TUM School of Life Sciences, Professur für Peptidbiochemie

Design, synthesis, and structure-function studies of peptides as inhibitors of the MIF/chemokine receptor axis

Christos Kontos

Vollständiger Abdruck der von der promotionsführenden Einrichtung

TUM School of Life Sciences

der Technischen Universität München zur Erlangung des akademischen Grades eines Doktors **der Naturwissenschaften (Dr.rer.nat.)** genehmigten Dissertation.

Vorsitzende: Prof. Dr. Lindsay Hall

Prüfende/-r der Dissertation:

1. Prof. Dr. Aphrodite Kapurniotu
2. Prof. Dr. Dieter Langosch
3. Prof. Dr. Alexander Bartelt

Die Dissertation wurde am 22.09.2021 bei der Technischen Universität München eingereicht und durch die TUM School of Life Sciences am 15.11.2021 angenommen.

Στον πατέρα μου, που με διάβαζε όταν ήμουν μικρός

What you leave behind is not what is engraved on stone monuments, but what is woven
into the lives of others
(Pericles)

Abstract

Atherosclerosis is an inflammatory disease with chemokines having fundamental importance on its progress. MIF is a pleiotropic cytokine with chemokine-like functions and promotes atherosclerosis via its receptors CXCR2 and CXCR4. Nevertheless, the interaction between MIF and the invariant chain CD74 has cardioprotective effects in the ischemic heart. The multifunctional CXCL12/CXCR4 axis is involved in athero- and cardioprotection, too. Therapeutic targeting of a specific chemokine/receptor axis emerges as an appealing approach but remains challenging due to the complex ligand/receptor network. Furthermore, receptor mimicry strategies for chemokine receptors remain challenging tasks due to the discontinuous GPCR epitope architecture.

The aim of the first part of my thesis was to develop engineered CXCR4 ectodomain-derived peptide mimics with MIF-specific binding properties ("msR4Ms"). The receptor mimics should attenuate the atheroprogessive MIF/CXCR4 pathway and spare the protective CXCL12/CXCR4 and MIF/CD74 pathways. Previous structure-activity relationship (SAR) studies on the MIF/CXCR4 interface indicated the ectodomain regions (ECDs) 97-110 from extracellular loop 1 (ECL1) and 182-196 from extracellular loop 2 (ECL2) but not ECL3 as the binding epitope of the receptor for MIF. Therefore, in this thesis ECL1(97-110) and ECL2(182-196) were chemically linked in three different ways to mimic the respective distance in the receptor with or without introducing the native disulfide bridge between their residues C109 and C186. The CXCR4 N-terminus which also had been implicated by the previous SAR studies was excluded to avoid interactions with CXCL12. Biophysical studies revealed ordered structures and a self-association propensity for most CXCR4 mimics related to the linkage of the ectodomain segments. All ordered msR4Ms bound to MIF with high affinity, while the mimics which did not contain the disulfide bridge had a high selectivity for MIF over CXCL12. Cell-based studies carried out in collaboration with cardiovascular experts resulted in the prioritization of the mimic msR4M-L1, which overall also exhibited the most favorable biophysical properties. The high binding affinity of the interaction of this lead mimic with MIF, the high binding selectivity to MIF over CXCL12 (>100-fold), as well as the lack of interference with MIF/CD74 complex formation were further validated by fluorescence polarization (FP) and microscale thermophoresis (MST) studies. Further studies carried out by our cardiovascular collaborators demonstrated an atheroprotective role and a therapeutic potency of msR4M-L1 *ex vivo* and *in vivo*. Studies using peptide arrays on msR4M-L1 and MIF revealed crucial residues and epitopes for their interaction in both the receptor mimic and cytokine sides, as an important basis for follow up minimization efforts and the design of next generation mimics (ngms).

The second part of the thesis focuses on SAR studies on the ectodomain regions of the receptor and the development of the ngms of CXCR4 with optimized sequence and high binding affinity to MIF. Shorter and mutated analogs of ECL1 and ECL2 were synthesized, and their secondary structures and binding affinity to MIF were determined. ECL1(102-110) and ECL2(187-195) were found to be the shortest ectodomain-derived peptides with significant binding to MIF. As previously for msR4Ms, ECL1(102-110) and ECL2(187-195) were connected based on their respective distance within the context of the receptor with seven different linker moieties resulting in seven ngms. The ngms were conformationally less ordered and more prone to self-associate than msR4M-L1, except for ngm-L5. All ngms bound strongly to MIF, but only the ones with natural amino acids in the linker bound CXCL12 as well, except for ngm-LD3. Interestingly, the MIF-specific ngms recognized the same MIF binding epitope as msR4M-L1, i.e. MIF(54-80).

In the third part of the thesis, the CXCR4 ngms were used together with the CXCR2 sequences involved in the MIF/CXCR2 binding interface aiming at developing chimeric receptor mimics (CRMs) of CXCR2 and CXCR4. Previous SAR studies on the

MIF/CXCR2 interaction identified the ECDs 108-120 from ECL1 and 184-198 from ECL2, here termed R2ECL1(108-120) and R2ECL2(184-198), respectively, as the binding epitopes of the receptor. SAR studies on these regions led to the R2ECL1(112-120) and R2ECL2(184-196) analogs as the shortest MIF-binding segments. For the development of CRMs, R2ECL2(184-196) was conjugated to four different CXCR4 ngms via linkers mimicking the C196-W112 distance in CXCR2. A disulfide bridge was formed between C196 and C109 of segments R2ECL2(184-196) and ECL1(102-110) respectively, and the oxidized CRMs were tested as well. R2ECL1(108-120) was not introduced into the CRMs, since ECL1(102-110), its CXCR4 homolog with remarkably high sequence identity, is already present in the ngm part of the CRM sequence. Next, chimeric mimics were biophysically characterized and, overall, a high exposure of hydrophobic residues on the surface was found. The oxidized CRMs were less ordered with a stronger self-association propensity than the reduced mimics. Of note, the oxidized mimics had a high binding affinity to MIF. Controversial findings were derived from the binding studies on the reduced mimics and MIF. Particularly, titrations with Fluos-CRM(reduced)/MIF and Alexa-488-MIF/CRM(reduced) showed strong and weak binding affinities, respectively. CRM-1/L5 and CRM-1//L5ox together with CRM-1/L4ox and CRM-1/LD3ox bound CXCL12 with high affinity. Noteworthy, CRM-1/LD3ox was the only mimic that exhibited high affinity binding to CXCL8 as well.

The fourth part of the thesis aimed at shedding light on the effect of MIF residues R87, L88, and R89 on MIF structure and its interaction with CXCR4. Our lab and our collaborators previously identified those three residues as a discontinuous extension of the MIF N-like loop that contributes to the MIF/CXCR4 interaction and recombinantly generated the triple alanine MIF mutant [R87A-L88A-R89A]-MIF for additional studies. This mutant showed a decreased affinity to the CXCR4 ectodomain segments and the mimics, while the contribution of the RLR motif for MIF binding to the CXCR4 N-terminus was further confirmed with peptide arrays.

The aim of the final part of the thesis was to study the peptide segment MIF(47-56), corresponding to the N-like loop of MIF, which contributes to the binding interface between MIF and CXCR2, and various different cyclic analogs thereof. Circular dichroism (CD) spectroscopy studies revealed significant effects of both the cyclization and the introduced spacers on peptide conformation. Cyclic analogs with shorter spacer segments were less disordered than the ones with longer spacers. Fluorescence spectroscopic titrations of Alexa-488-MIF with MIF(47-56) did not indicate any binding, suggesting that this 10-meric peptide segment of MIF blocks the MIF/CXCR2 interaction by binding to the receptor rather than MIF itself. Inhibitory studies in *in vitro* and *ex vivo* atherogenic systems conducted by our cardiovascular collaborators concluded that MIF(cyclo10), a cyclopeptide with a spacer length of 10 residues, is the lead peptide. This analog was then studied with respect to its proteolytic stability in human plasma *ex vivo* and a half life time of >8 h was found, consistent with a >16-fold improved stability compared to the linear precursor MIF(47-56).

Together, this thesis provides the peptide design, synthesis, and biophysical characterization of MIF-selective CXCR4 ectodomain-mimicking peptides with nanomolar affinities as a novel class of MIF-selective inhibitors for applications as drug leads in cardiovascular diseases, as well as their use as templates towards next generation mimics and chimeric mimics for dual targeting approaches. In addition, the thesis considerably adds to our SAR knowledge on the MIF/CXCR4 and MIF/CXCR2 binding interfaces and to the characterization of corresponding site-specific mutants and MIF-derived peptides as leads for anti-atherosclerotic molecules.

Zusammenfassung

Atherosklerose ist eine entzündliche Gefäßerkrankung, für deren Fortschreiten Chemokine eine grundlegende Bedeutung haben. MIF ist ein pleiotropes Zytokin mit chemokinähnlichen Funktionen und fördert die Atherosklerose über seine Rezeptoren CXCR2 und CXCR4. Die Interaktion zwischen MIF und der invarianten Kette CD74 hat jedoch kardioprotektive Auswirkungen auf das ischämische Herz. Die multifunktionale CXCL12/CXCR4-Achse ist ebenfalls an der Athero- und Kardioprotektion beteiligt. Die therapeutische Ausrichtung auf eine spezifische Chemokin-/Rezeptor-Achse stellt einen attraktiven Ansatz dar, bleibt aber aufgrund des komplexen Liganden-/Rezeptornetzwerks eine Herausforderung. Darüber hinaus sind Rezeptor-Mimikry-Strategien für Chemokin-Rezeptoren aufgrund der diskontinuierlichen GPCR-Epitop-Architektur molekular anspruchsvolle Ziele.

Das Ziel des ersten Teils dieser Arbeit war die Entwicklung von CXCR4-Ektodomänen-Peptid-Imitaten mit MIF-spezifischen Bindungseigenschaften ("msR4Ms"). Diese Rezeptor-*Mimics* sollten den atheroprogessiven MIF/CXCR4-Weg abschwächen und die schützenden CXCL12/CXCR4- und MIF/CD74-Wege verschonen. Frühere Studien zu den Struktur-Aktivitäts-Beziehungen (SAR) an der MIF/CXCR4-Schnittstelle wiesen auf die Ektodomänen-Regionen (ECDs) 97-110 der extrazellulären Schleife 1 (ECL1) und 182-196 der extrazellulären Schleife 2 (ECL2), nicht aber auf ECL3 als Bindungsepitop des Rezeptors für MIF hin. Daher wurden in dieser Arbeit ECL1(97-110) und ECL2(182-196) auf drei verschiedene Arten chemisch verknüpft, um den jeweiligen Abstand im Rezeptor mit oder ohne Einführung der nativen Disulfidbrücke zwischen ihren Resten C109 und C186 zu imitieren. Der N-Terminus von CXCR4, der in den früheren SAR-Studien ebenfalls eine Rolle gespielt hatte, wurde ausgeschlossen, um Wechselwirkungen mit CXCL12 zu vermeiden. Biophysikalische Untersuchungen wiesen auf das Vorhandensein geordneter Strukturen und eine gewisse Neigung zur Selbstassoziation für die meisten CXCR4-Imitate hin, was mit der Verknüpfung der Ektodomänensegmente zusammenhängt. Alle geordneten msR4Ms binden mit hoher Affinität an MIF, während die *Mimics*, die keine Disulfidbrücke enthalten, eine hohe Selektivität für MIF gegenüber CXCL12 aufweisen. Zellbasierte Studien, die in Zusammenarbeit mit Herz-Kreislauf-Forschern durchgeführt wurden, führten zu einer Priorisierung des Mimics msR4M-L1, das insgesamt auch die günstigsten biophysikalischen Eigenschaften aufwies. Die hohe Bindungsaffinität der Interaktion dieses Leit-*Mimics* mit MIF, die hohe Bindungsselektivität für MIF gegenüber CXCL12 (>100-fach) sowie die fehlende Interferenz mit der MIF/CD74-Komplexbildung wurden durch Fluoreszenzpolarisations- (FP) und mikroskalige Thermophorese-Studien (MST) validiert. Weitere Studien, die von unseren kardiovaskulären Kooperationspartnern durchgeführt wurden, zeigten eine atheroprotektive Rolle und eine therapeutische Wirksamkeit von msR4M-L1 *ex vivo* und *in vivo*. Studien unter Verwendung von Peptidarrays zu msR4M-L1 und MIF enthüllten entscheidende Reste und Epitope für ihre Interaktion sowohl auf der Seite des Rezeptormimikums als auch auf der Seite des Zytokins, was eine wichtige Grundlage für nachfolgende Minimierungsbemühungen und die Entwicklung von *Mimics* der nächsten Generation (NGMs) darstellt.

Der zweite Teil der Arbeit befasst sich mit SAR-Studien an den Ektodomänenregionen des Rezeptors und der Entwicklung der NGMs von CXCR4 mit optimierter Sequenz und hoher Bindungsaffinität zu MIF. Kürzere und mutierte Analoga von ECL1 und ECL2 wurden synthetisiert, und ihre Sekundärstrukturen und Bindungsaffinitäten zu MIF wurden bestimmt. ECL1(102-110) und ECL2(187-195) erwiesen sich als die kürzesten von der Ektodomäne abgeleiteten Peptide mit einer signifikanten Bindung an MIF. Wie zuvor bei den msR4Ms wurden ECL1(102-110) und

ECL2(187-195) auf der Grundlage ihres jeweiligen Abstands innerhalb des Rezeptorkontextes mit sieben verschiedenen Linker-Einheiten verbunden, was zu sieben NGMs führte. Die NGMs waren konformationell weniger geordnet und neigten eher zur Selbstassoziation als msR4M-L1, mit Ausnahme von NGM-L5. Alle NGMs banden stark an MIF, aber nur die mit natürlichen Aminosäuren im Linker banden auch CXCL12, mit Ausnahme von NGM-LD3. Interessanterweise erkannten die MIF-spezifischen NGMs das gleiche MIF-Bindungsepitop wie msR4M-L1, d. h. MIF(54-80).

Im dritten Teil der Arbeit wurden die CXCR4-NGMs zusammen mit den CXCR2-Sequenzen verwendet, die an der MIF/CXCR2-Bindungsschnittstelle beteiligt sind, mit dem Ziel, sogenannte chimäre Rezeptor-*Mimics* (CRMs) von CXCR2 und CXCR4 zu entwickeln. Frühere SAR-Studien zur MIF/CXCR2-Interaktion identifizierten die ECDs 108-120 von ECL1 und 184-198 von ECL2, hier als R2ECL1(108-120) bzw. R2ECL2(184-198) bezeichnet, als die Bindungsepitope des Rezeptors. SAR-Studien dieser Regionen führten zu den Analoga R2ECL1(112-120) und R2ECL2(184-196) als den kürzesten MIF-Bindungssegmenten. Für die Entwicklung von CRMs wurde R2ECL2(184-196) über Linker, die den C196-W112-Abstand in CXCR2 nachahmen, an vier verschiedene CXCR4-NGMs konjugiert. Zwischen C196 und C109 der Segmente R2ECL2(184-196) bzw. ECL1(102-110) wurde eine Disulfidbrücke gebildet und auch die oxidierten CRMs wurden getestet. R2ECL1(108-120) wurde nicht in die CRMs eingeführt, da ECL1(102-110), sein CXCR4-Homolog mit bemerkenswert hoher Sequenzidentität, bereits im NGM-Teil der CRM-Sequenz vorhanden ist. Anschließend wurden die chimären *Mimics* biophysikalisch charakterisiert, wobei insgesamt eine hohe Exposition von hydrophoben Resten auf der Oberfläche festgestellt wurde. Die oxidierten CRMs waren weniger geordnet und hatten eine stärkere Neigung zur Selbstassoziation als die reduzierten *Mimics*. Bemerkenswert ist, dass die oxidierten *Mimics* eine hohe Bindungsaffinität zu MIF aufwiesen. Die Bindungsstudien an den reduzierten *Mimics* und MIF erbrachten kontroverse Ergebnisse. Insbesondere Titrationen mit Fluos-CRM(reduziert)/MIF und Alexa-488-MIF/CRM(reduziert) zeigten starke bzw. schwache Bindungsaffinitäten. CRM-1/L5 und CRM-1//L5ox wiesen zusammen mit CRM-1/L4ox und CRM-1/LD3ox eine hochaffine Bindung an CXCL12 auf. Bemerkenswerterweise war CRM-1/LD3ox das einzige *Mimic*, das auch eine hohe Bindungsaffinität zu CXCL8 aufwies.

Der vierte Teil der Arbeit zielte darauf ab, die Auswirkungen der MIF-Reste R87, L88 und R89 auf die MIF-Struktur und seine Interaktion mit CXCR4 zu untersuchen. Unser Labor und unsere Kooperationspartner hatten diese drei Reste als eine diskontinuierliche Verlängerung der N-ähnlichen Schleife von MIF identifiziert, die zur Interaktion zwischen MIF und CXCR4 beiträgt, und rekombinant die Dreifach-Alanin-MIF-Mutante [R87A-L88A-R89A]-MIF für zusätzliche Studien erzeugt. Diese Mutante zeigte eine verringerte Affinität zu den CXCR4-Ektodomänensegmenten und den *Mimics*, während der Beitrag des RLR-Motivs zur MIF-Bindung an den CXCR4-N-Terminus mit Peptidarrays weiter bestätigt wurde.

Das Ziel des letzten Teils der Arbeit war die Untersuchung des Peptidsegments MIF(47-56), das der N-loop-artigen Schleife von MIF entspricht, die zur Bindungsstelle zwischen MIF und CXCR2 beiträgt, sowie verschiedener zyklischer Analoga davon. Zirkulardichroismus (CD)-Spektroskopiestudien zeigten signifikante Auswirkungen sowohl der Zyklisierung als auch der eingeführten Spacer auf die Peptidkonformation. Zyklische Analoge mit kürzeren Spacersegmenten waren weniger ungeordnet als solche mit längeren Spacern. Fluoreszenzspektroskopische Titrationen von Alexa-488-MIF mit MIF(47-56) ergaben keine Bindung, was darauf hindeutet, dass dieses 10-merische Peptidsegment von MIF die MIF/CXCR2-Interaktion durch Bindung an den Rezeptor und

nicht an MIF selbst blockiert. Inhibitionsstudien in *in vitro*- und *ex vivo*-Atherogenese-Assays, die von unseren kardiovaskulären Kooperationspartnern durchgeführt wurden, ergaben, dass MIF(cyclo10), ein Cyclopeptid mit einer Spacerlänge von 10 Resten, das vielversprechenste Peptid ist. Dieses priorisierte Analogon wurde dann im Hinblick auf seine proteolytische Stabilität in menschlichem Plasma *ex vivo* untersucht, und es wurde eine Halbwertszeit von >8 Stunden festgestellt, was einer >16-fach verbesserten Stabilität im Vergleich zum linearen Vorläufer MIF(47-56) entspricht.

Insgesamt liefert diese Arbeit das Peptiddesign, die Synthese und die biophysikalische Charakterisierung von MIF-selektiven CXCR4-Ektodomänen-nachahmenden Peptiden mit nanomolaren Affinitäten als eine neue Klasse von MIF-selektiven Inhibitoren für Anwendungen als Leitstrukturen für Medikamente bei kardiovaskulären Erkrankungen sowie ihre Verwendung als molekulare Template für *Mimics* der nächsten Generation und chimäre *Mimics* für duale *Targeting*-Ansätze. Darüber hinaus trägt die Arbeit wesentlich zu unserem SAR-Wissen über die MIF/CXCR4- und MIF/CXCR2-Bindungsstellen und zur Charakterisierung entsprechender ortsspezifischer Mutanten und von MIF abgeleiteter Peptide als Leitstrukturen für Moleküle gegen Atherosklerose bei.

Abbreviations

1-Nal	3-(1-naphthyl)-L-alanine
2,5-DHAP	2,5-Dihydroxyacetophenone
4-HCCA	Cyano-4-hydroxycinnamic acid
4-Pal	3-(4-Pyridyl)-L-alanine
6 Ahx	6-Aminohexanoic acid
8 Aoc	8-Aminooctanoic acid
12 Ado	12-Aminododecanoic acid
A	Absorbance
Å	Angstrom
Abs	Antibodies
AA	Aminoacid
Abu	Amino-butyric acid
ACN	Acetonitrile
Ac$_2$O	Acetic anhydride
Alexa	[6-amino-9-[2-carboxy-4-[5-(2,5-dioxopyrrol-1-yl)pentylcarbamoyl]phenyl]-4,5-disulfoxanthen-3-ylidene]azanium
ANS	8-Anilino-1-naphthalenesulfonic acid
App. K$_d$	Apparent dissociation constant
Asi	Aspartimide
a.u.	Arbitary unit
BBB	Blood Brain Barrier
BCA	Bicinchoninic acid
BiP	Biphenylalanine
BSA	Bovine serum albumin
C	Concentration
CD	Circular dichroism
Cha	Cyclohexylalanine
CD74	Cluster of Differentiation 74
COPD	Chronic Obstructive Pulmonary Disease
CVA	Cerebrovascular accident
CHD	Coronary heart disease
CRMs	Chimeric receptor mimics
CXCL	C-X-C motif ligand
CXCR	C-X-C Motif Chemokine Receptor
CVDs	Cardiovascular diseases
Da	Dalton
DIC	Diisopropylcarbodiimide
DIEA	Diisopropylethylamine
DMF	Dimethylformamid
DMSO	Dimethylsulfoxide
ε	Extinction coefficient
ECD	Ectodomain region
ECL	Extracellular loop
EDT	1,2-Ethanedithiol
ECs	Endothelial cells
EtOH	Ethanol
Eq	Equivalent
ESI-MS	Electrospray ionization mass spectrometry
FA	Formic acid
Fluos	5(6)-Carboxyfluorescein
Fmoc	9-Fluorenylmethoxycarbonyl
FP	Fluorescence polarization
GdnCl	Guanidinium-HCl
GPCR	G protein-coupled receptor
h	Hour
HCl	Hydrochloric acid

HFIP	1,1,1,3,3,3-Hexafluoro-2-propanol
HATU	2-(7-Aza-1H-benzotriazole-1-yl)-1,1,3,3-tetramethyluroniumhexafluorophosphate
HBTU	(2-(1H-benzotriazol-1-yl)-1,1,3,3-tetramethyluronium hexafluorophosphate
HDL	High-density lipoprotein C
HOBt	1-Hydroxybenzotriazole
IL-	Interleucine-
K^+	Potassium cation
LDL	Low-density lipoprotein C
M	Molar
MALDI-TOF-MS	Matrix-assisted laser desorption ionization mass spectrometry
MACE	Major adverse cardiovascular events (MACE)
MI	Myocardial infarction
MIF	Macrophage migration inhibitory factor
MIF-2	Macrophage migration inhibitory factor-2
MRE	Molar residue ellipticity
msR4M	MIF-specific CXCR4 mimic
MST	Microscale thermophoresis
MW	Molecular weight
Na^+	Sodium cation
ngm	Next generation mimics
NMR	Nuclear magnetic resonance
O2Oc	8-Amino-3,6-dioxaoctanoic acid
P	Polarization
RA	Rheumatoid arthritis
RP-HPLC	Reverse phase high performance liquid chromatography
R1ECL	CXCR1 extracellular loop
R2ECL	CXCR2 extracellular loop
RT	Room temperature
SAR	Structure-activity-relationship
sCD74	Soluble CD74
SD	Standard deviation
SPPS	Solid phase peptide synthesis
SDS	Sodium dodecyl sulfate
SMDs	Small molecule drugs
$t_{1/2}$	Half-life time
TAMRA	5-Carboxytetramethylrhodamin
tBu	Tert-butyl
TCA	Trichloroacetic acid
TFA	Trifluoroacetic acid
TIS	Triisopropylsilan
t_R	Retention time
Tris-HCl	2-Amino-2-(hydroxymethyl)-1,3-propanediol hydrochloride
Tris	(Tris(hydroxymethyl)aminomethane)
Trt	Trityl
ISO-1	(S,R)-3-(4-Hydroxyphenyl)-4,5-dihydro-5-isoxazole acetic acid, methyl ester
ISMs	Interaction surface mimics
UV	Ultraviolet
WT	Wild-type

Index

1. Introduction

1.1 Atherosclerosis and cardiovascular diseases (CVDs)

Arteriosclerosis is a pathological condition that occurs because of the hardening of the arterial walls [1]. In such a case, the blood might not be circulated correctly to all organs and tissues, and canonical functions of the organism would be hindered. Arteriosclerosis is divided into three subcategories, arteriolosclerosis, Monckeberg's arteriosclerosis, and atherosclerosis [2]. Arteriolosclerosis occurs when the wall of very small arteries is thickened, while Monckeberg's arteriosclerosis is involved with dysregulated calcification of the tunica media layer and deposition of calcium hydroxyapatite crystals [3] [4]. Atherosclerosis was first introduced as a medical term in 1904 by Felix Marchand and today refers to the most common kind of arteriosclerosis, in which lipids, connective tissues, and other substances are accumulated in and on the arterial walls [1, 5]. This buildup leads stepwise to the formation, destabilization, and rupture of plaques and thrombus development, leading to vascular diseases [6].

Cardiovascular diseases (CVDs) are classified as heart and blood vessel disorders. According to World Health Organization (WHO), among the CVDs are incorporated diseases of the blood vessels that supply the heart muscle (coronary heart disease, CHD), the brain (cerebrovascular disease, CVA), and the arms together with the legs (peripheral arterial disease). Rheumatic heart disease (damaged heart muscle and valves due to rheumatic fever), congenital heart disease (malformations of heart structure at birth), deep vein thrombosis, and pulmonary embolism (blood clots in the leg that could translocate to the veins of the heart and the lungs) are included in the CVDs, too. Two of the most known acute events of CVDs are myocardial infarction (MI) and stroke, belonging to CHD and CVA, respectively, and are mainly induced by preventing blood flowing to either the heart or the brain due to a blocked vein [7].

CVDs are the primary cause of mortality nowadays, even though a downward trend is observed for their mortal rates in the developed countries [8]. Estimations refer to 17.9 million deaths (31% of all global losses) worldwide for 2016 and 45% of all deaths in Europe the last decade [9]. Furthermore, the worldwide CVD-associated mortal cases are predicted to exceed 24 million by 2030 due to the expected increase in life expectancy and a more western lifestyle in developing countries [10] [11]. Researchers and organizations are aware and concerned about these numbers, and many initiatives have been taken to confront them. The most well-known is the "25 by 25", established by WHO and aiming to a 25% decreased risk of premature deaths by preventing and curing the CVD risk factors until 2025 [12].

Among them, tobacco smoking is considered as the leading risk factor for CVDs [13]. Suboptimal diet and particularly high uptake of low density lipoprotein C (LDL), glucose and sodium together low consumptions of whole grain and fruit intake is associated as well [14]. Furthermore, obesity, lack of physical activity, and modern life derived situations such as work, or socializing problems were shown to trigger CVDs in many cases [15] [16]. Increased age of the person and associated family history are included in the factors, too. Diseases such as diabetes, chronic kidney disease, hypertension and hyperlipidemia were shown to play an important role in the cause of CVDs, as well [14]. Particularly, hyperlipidemia and lipid oxidation trigger the initiation of atherosclerosis and share the same risk factors [17] [18].

1.1.1   Mechanisms of atherosclerosis

A hypothesis supports that atherosclerosis is a disease occurring due to our modern lifestyle, and a realignment of our daily life is required [19]. However, later it was proved that atherosclerosis and CVDs had been a cause of death since ancient times in diverse populations [20]. Other studies shed light on the mechanism of atherosclerosis and its vascular response after endothelial injury [21] [22] [23]. Inflammation and many different cells and mediators of the immune system were indispensable parts of atherosclerotic progress and the plaque rupture that leads to the CVDs [24] [25] [24b]. Conclusively, atherosclerosis is classified as a multistep lipid-driven chronic inflammatory disease and the main cause of CVDs [21a] [26] [27].

Atherosclerosis is initiated by endothelial damage caused by hypertension, smoking, hyperglycemia, or hypercholesterolemia [28] [29]. Through the dysfunctioned endothelial, low-density lipoprotein (LDL) and other lipids pass through to the subendothelial layer (intima), and get oxidized (oxLDL) by locally released reactive oxygen species (ROS) [21a] [27]. In this stage is mediated inflammatory signaling that leads to the penetration of the monocytes through their interactions with the endothelium adhesion molecules (VCAM-1, ICAM-1, E-selectin, P-selectin) into the intima [30] [31]. The migrated monocytes evolved in macrophages that internalize the oxLDL and transform to lipid-laden foam cells that mediate further the inflammation response. Accumulation of foam cells results in the formation of fatty streaks that get enlarged as time passes. The inflammatory triggered migration of vascular smooth cells (VSMCs) from the middle layer of the artery wall (tunica media) to the intima leads to the transition from an intimal fatty streak to an atheromatic plaque [32].

In advanced atherosclerosis is triggered the apoptosis of macrophages and, together with the concentration of cellular debris, lipids and death, result in the formation of the thrombogenic necrotic core inside the plaque [33] [34]. Moreover, except for monocytes, neutrophils, T lymphocytes and B lymphocytes play a vital role in the atheroprogessive stages, too [35] [25]. At the latest stage, a thrombus is formed, either due to the increased plaque growth or because of its rupture, and mediates an ischemic event (Figure 1) [26]. Even though the rupture of atherosclerotic plaques in their carotid and coronary arteries seems to be associated with the most major adverse cardiovascular events (MACE), the mechanisms behind it are unclear [36].
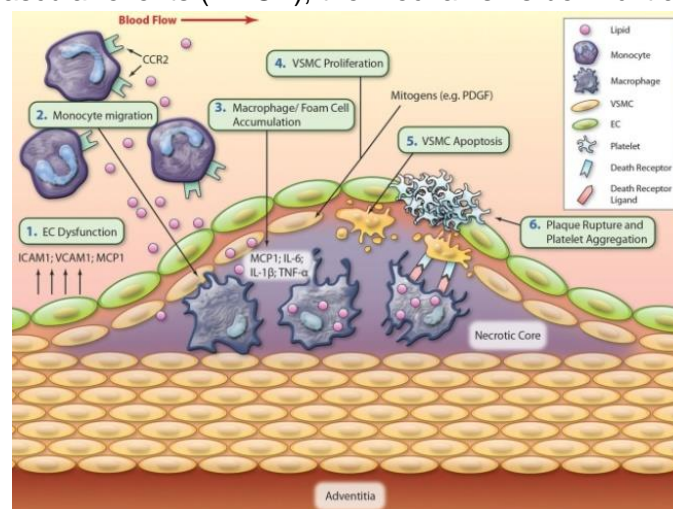
Figure 1. Stages of atherosclerotic progress. Initially, the dysfunction of ECs mediates the migration of monocytes to the intima and their differentiation to macrophages. Next, macrophages internalize the oxLDL, and foam cells are created before VSMC proliferation and apoptosis. Lastly, a plaque is formed on the intima surface and continues growing until its rupture (taken from Wang et al., ref. [37]).

1.1.2 Current drug-strategies against atherosclerosis

The possibility of a lethal MACE event has been remarkably decreased in the last decades. The obtained scientific knowledge about the CVD risk factors and preventive strategies against them seems to be a crucial parameter [8]. Additionally, active biomolecules against atherosclerosis were developed, with the majority of them aiming to reduce LDL concentration mainly, and secondary decrease the triglycerides, or increase the high density lipoprotein-C (HDL) levels [38]. Inhibitors of 3-hydroxy-3-methylglutaryl coenzyme A (HMG-CoA) reductase, also known as statins, is the most applied medication against atherosclerosis [39]. Statins induce the upregulation of the hepatocyte LDL receptors, which triggers the hepatic uptake of LDL from the circulation and thus its reduction [40]. The statin effect was beneficial in primary and secondary prevention, with significant mortality reduction, while they were shown to induce a slight increase in HDL-C levels, too [41] [42].

A similar essential mechanism of action was revealed for ezetimibe, a cholesterol absorption inhibitor, that remarkably reduced serum LDL levels by inducing the expression of LDL receptors [43] [44]. Another preventative therapy against CVD targets hypertension. Angiotensin-converting enzyme (ACE) inhibitors or calcium antagonists significantly decreased the possibility of a MACE event in high-risk patients [45] [46] [47]. Fibrates are agonists of peroxisome proliferator-activated receptor-α (PPAR-α), and they induce a reduction in the triglycerides and increase the HDL. Their administration, either as a single medication treatment, was beneficial for patients with hypertriglyceridemia [48]. Overall, the combination of two different types of molecules was shown to induce therapeutic results in patients.

For example, the combination of statins with ezetimibe or nianic acid reduced the LDL levels and the progress of carotid atherosclerosis, respectively [49]. Evolocumab and alirocumab are antibodies against PCSK9, and their administration together with statins decreased the LDL concentration and the CVD risk [50] [51]. Another approach combines aspirin, known for its antiplatelet activity, and P2Y12 antagonists such as ticagrelor resulting in fewer MACE events [52] [53]. However, the development of novel drugs to prevent a MACE event seems that has come to a standstill, and new strategies are needed [54].

A few market available drugs that inhibit IL-6 and IL-1β signaling pathways were clinically studied against CVDs [55]. Methotrexate is released against psoriasis and RA and blocked the IL-6 production in RA patients, but did not decrease CVD risk [56] [57] [58]. Colchicine is an alkaloid that was isolated from the *Colchicum autumnale* plant and has been used as a remedy from ancient times [59]. Currently is officially released for the treatment of Mediterranean fever (FMF) and acute gout flare. Studies on colchicine-treated CAD patients revealed reduced levels of IL-1β, IL-6, and MACE risk [60] [61] [62] [63] [64]. Canakinumab is a human IgGκ monoclonal antibody that targets IL-1β and is approved by FDA against RA and three rare but serious auto-inflammatory diseases, including FMF [65] [66]. Its anti-inflammatory effect proved to be protective in the clinical phase III trial, for patients after MI with increased CVD risk [67]. A possible alternative treatment is Anakinra (Kineret), a recombinant form of IL-1Ra that inhibits the IL-1/IL-1Ra and is released against rheumatoid arthritis, Cryopyrin-Associated Periodic Syndromes (CAPS), and Deficiency of Interleukin-1 Receptor Antagonist (DIRA) with benefical effect against CVDs [68] [69] [70].

1.2 **Macrophage Migration Inhibitory Factor (MIF)**

Macrophage migration inhibitory factor (MIF) was described for the first time in 1966 by John David as a soluble mediator of the function for which it is named [71]. MIF was cloned and expressed 23 years after its discovery and is consisted of 114 amino acids after the cleavage of the N-terminus methionine due to post-translational modification [72] [73]. The protein was classified as a cytokine and exhibited a broad functional repertoire, including regulation of the innate immunity, enzymatic and chemokine activities [74] [75] [76] [77]. The sequence of human MIF is 90% identical to its murine homolog, and they share similar secondary structures and activities [78].

MIF is a pleiotropic cytokine with enzymatic and chemokine activities and an upstream regulator of inflammatory signaling. The dysregulation of MIF has been associated with various immunological and inflammatory diseases [74]. Several studies shed light on its role as a disease-exacerbating factor. Circulating MIF values are at 5 ng/mL range in healthy adults, while those values were much higher in the first days of life. Furthermore, MIF increased levels correlated with the vascular and lung development, supporting an important role for these cytokines during the neonatal period [79]. A similar trend was obtained for another protein, known as D-dopachrome tautomerase (D-DT) or MIF-2 [80]. MIF-2 was initially determined as an enzyme that tautomerizes D-dopachrome with concomitant decarboxylation to give 5,6-dihydroxyindole and shares a 34% sequence identity with very similar topology to MIF [81] [80] [82].

The crystal structure of MIF was revealed by the group of Prof. Lolis 30 years after its discovery and revealed a well-ordered structure being in the trimeric form [83]. Even though MIF contains three cysteines, no disulfide bonding occurs. Each MIF monomer consists of two antiparallel α-helices and seven β-strands, four of which are β-sheet (Figure 2) [83] [84] [85]. The hydrophobic side chains of both α-helices face the β-sheet and form the hydrophobic core of the MIF, while the aromatic residues Y37, F50, Y96, W109, and F114 lead to a hydrophobic patch on the surface of the protein. On the other side, the interaction between α2-helix residues N73, R74, S77, K78, C81, and the C-terminus residues N111, S112, T113 form a hydrophilic surface [83].

Additionally, the C-terminus residues were shown to have an additional structural role as essential stabilizers of the MIF tertiary and quaternary structure [84]. A solvent channel in a barrel shape is formed through the center of the protein with broad charged ends and a narrow hydrophilic center [83]. Several residues of MIF could get connected through the solvent channel even though they are not closely located, as Y100 with P2, through aromatic interactions and a hydrogen bond network that involves H63 and M3 [86]. MIF is in the equilibrium between monomers and dimers under normal conditions and switches to a trimeric or even higher oligomeric state at concentrations higher than 10 µg/mL [84] [87]. Recombinant MIF was shown to have a remarkable stability against chemical and thermal denaturation studies, whereas it precipitates above 25 µM [76].
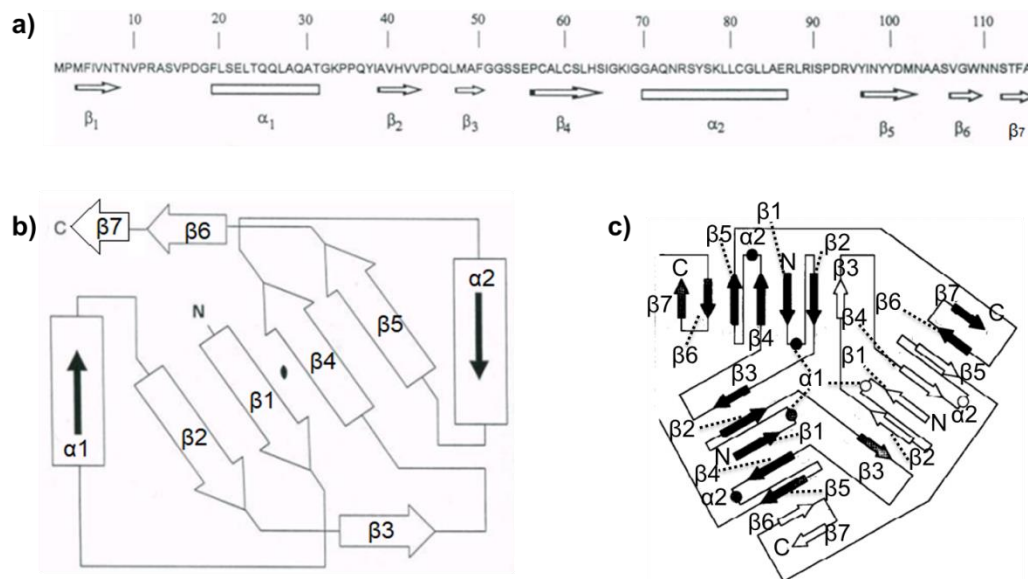
Figure 2. Formation of MIF based on its crystal structures. a Primary sequence of MIF with the secondary structure being noted below the residues (adapted from Sun et al, ref. [83] after taking into consideration the formation of β7 on the C-terminus, as suggested by Mischke et al., ref. [84] and Sugimoto et al., ref. [85]). **b** Tertiary structure of MIF as a monomer (adapted from Sun et al., ref. [83] as suggested by Mischke et al., ref. [84] and Sugimoto et al., ref. [85]). **c** Quaternary structure of MIF in the trimeric state (adapted from Sugimoto et al., ref. [85]).

1.2.1 MIF and its receptors

MIF is a multifunctional cytokine with various enzymatic activities. Firstly, MIF was found in 1996 to tautomerize D-dopachrome, although the tested substrate does not occur naturally, and the canonical substrate is still missing [75]. Mainly P2 and then the C-terminus and C81 of MIF were vital for its activity [88]. The two other MIF cysteines, C57 and C60, were crucial too, but for another enzymatic activity. Particularly, those residues are located on the beginning and ending of the oxidoreductase CXXC motif, i.e. CALC for MIF, and their mutations, especially of C60, significantly reduced the catalysis of the reduction of insulin and 2-hydroxyethyldisulfide [76]. Recently, MIF was found to act as PARP-1–dependent AIF-associated nuclease with the protein being recruited to the nucleus by Apoptosis-inducing factor (AIF), where it cleaves genomic DNA, with a crucial role played by E22 (Table 1) [89].

Besides, MIF acts as a chaperone under conditions of system restoration and heat stress removal and is carried out through invariant MHC class II, also known as CD74 [90] [91] [92]. SAR studies determined a functional role of the residues Y37, K67, and N110 and the surface of the catalytic pocket for the binding to CD74 [93]. The surface-exposed Y100 and its connection through H63, M3, P2 for the creation of a MIF solvent channel together with the MIF(80-87) belong to the hot spot region, too (Table 1) [86] [94]. Noteworthy, MIF requires an additional factor to mediate its cytoplasmic signaling through CD74, being either the single-pass transmembrane glycoprotein CD44, or the chemokine receptor CXCR4 (Figure 3) [91].

A breakthrough in MIF history was its identification as a ligand of the chemokine receptors CXCR2 and CXCR4 [77]. However, MIF does not have a typical CXC or any other chemokine motif; consequently, it could not be classified as a chemokine, even though it signals through chemokine receptors [83]. Due to this paradox MIF is characterized often as a cytokine with chemokine-like functions, or as

an atypical chemokine [77] [87]. MIF contains a *pseudo-(E)LR* motif constituted by the discontinued D44-X-R11 (i.e. DXR) motif with the D44 and R11 located in neighboring MIF monomer loops with the same topology to the chemokines' motif [95]. That motif, together with the N-like loop MIF(47-56) are essential for MIF signaling through CXCR2, and the findings were further confirmed by protein-protein docking and molecular dynamics simulations [96] [95] [97]. The theoretical approaches suggested an important role in the binding recognition of the P92, V95, I97 and K78, S61, H63 residues for hydrophobic and polar interactions, respectively, and of M102, A104, A105, V107, W109 for the subsequent signaling via the van der Waal forces [96]. Less information were released about the binding interface of the MIF to CXCR4, that highlighted a role of P2 and of the region between the 43th and 98th and particularly of MIF(67-81) [98]. The atypical chemokine could also interact with ACKR3, or also known as CXCR7, and with heterodimers of the receptors (Figure 3) [99] [100].
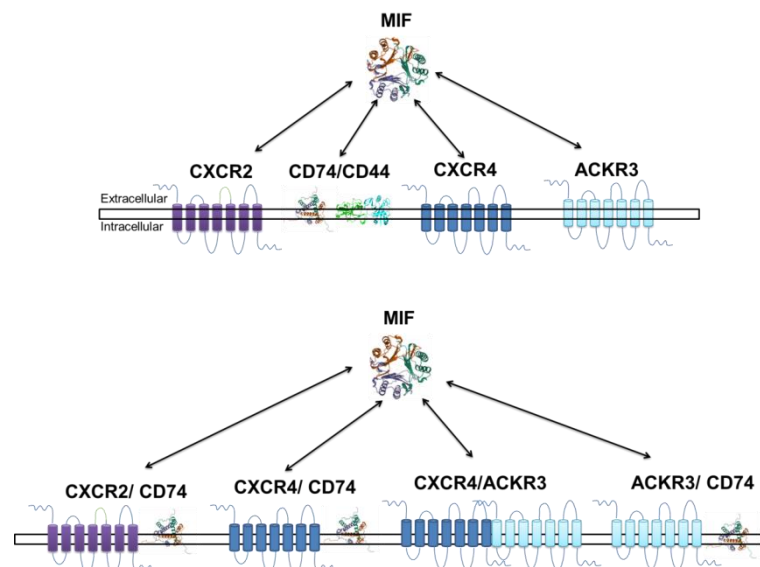
Figure 3. Interactions of MIF with its receptors. MIF was found to interact with the chemokine receptors CXCR2, CXCR4, the atypical ACKR3, the complex of transmembrane proteins CD74/CD44, and their heterodimers (PDB codes MIF:1MIF [83], CXCL12:3HP3 [101], CD74:1IIE [102], CD44:1uuh [103]).

Table 1. Essential residues of MIF for its interaction with receptors or for mediating enzyme activities.

Receptors/ Enzymatic activities	MIF residue	Reference
Receptors		
CXCR2	• D44 and R11, MIF(47-56) • P92, V95 I97, K78, S61, H63 M102, A104, A105, V107, W109	[95] [96] [97]
CXCR4	MIF(43-98), MIF(67-81)	[98]
CD74	• Y37, K67, and N110 • MIF(80-87) • Y100, H63, M3, P2	[86] [94] [93]
Enzymatic activities		
Tautomerase	P2, C81, C-terminus	[75]
Chaperone	• Y37, K67, and N110 • MIF(80-87) • Y100, H63, M3, P2	[86] [94] [93]
Oxidoreductase	C57, C60	[76]
Nuclease	E22	[89]

1.2.2 MIF and its role in atherosclerosis and other diseases

MIF orchestrates the inflammatory response with multiple signalling and functions. Particularly, MIF facilitates the pathogen sensing, recruits various immune cells and may mediates the migration and proliferation of specific cell types, contrary to its eponymous name [74]. MIF acts as a counter-regulator of the glucocorticoids hormones and their inflammatory protecting effects [104]. Furthermore, MIF is a regulator of cell cycle, growth and apoptosis with both beneficial and bad effects. MIF may block the apoptosis and promoter an extendend survival of monocytes and macrophages, which may result in a more efficient eradication of pathogens. However, the prolonged life of monocytes and macrophages could lead to side effects due to continued inflammatory response [74].

MIF has been found to be a proatherogenic factor that mediated T recruitment and B cell migration through its interactions with chemokine receptors [77] [87] [105]. Its inflammatory signaling induced the expression of adhesion molecules and stimulated the oxLDL uptake, too [106] [107]. MIF blockade reduced the atherosclerotic lesion size and led to regression of already established atherosclerotic lesions [77] [107]. MIF plays a role also in the rupture of the plaque. Particularly, mediates the secretion of plaque destabilization proteases and its deficiency resulted in increased SMC and collagen content in the neointimal area and less prone to rupture plaques [108].

MIF is associated with various types of cancers such as glioblastomas, melanoma, lung, breast, head and neck cancer. Data show that MIF is overexpressed in these malignancies in humans, and contributes to the dysregulation of the cell cycle, angiogenesis, and metastasis. Of note, the overexpression of MIF in tumors enhanced their aggression and the possibility to be lethal [109]. MIF has been found to be associated with diseases of the central nervous, the immune and the endocrine system, the gastrointestinal tract, the lung, the skin and the eye [110]. However MIF could mediate in many cases a double-edged role, for example in kidney diseases or exert a protective phenotype such as in ALS [111] [112].

1.2.3 MIF-based therapeutic approaches

Cytokines, chemokines, and their receptors are involved in signaling in many inflammatory diseases, and their blockade appeal as a promising therapeutic strategy. MIF is a cytokine with chemokine-like functions and its dysregulation has been associated with various immunological and inflammatory diseases. Thus, MIF targeting has attracted a rising scientific interest over the last years, with some of the developed drug candidates being in clinical phase trials.

Ibudilast (MN-166) is a pyrazolopyridine that inhibits phosphodiesterases 3,4,10, and 11 and is administrated for the treatment of ischemic stroke and bronchial asthma in Japan [113]. Later, it was further clarified as an allosteric inhibitor of the catalytic and chemotactic activity of MIF [114]. Particularly, it was identified as a blocker of the MIF/CD74 axis while its effect on PBMC expression and migration might hint its interference in CXCR2 and CXCR4 pathways, too [113] [115] [116]. Recently, Ibudilast was shown to decelerate MS in clinical phase II and will be further evaluated in the next stage [117]. ISO-1 is an isoxazoline, and the first developed small molecule that inhibits MIF biologic functions, while it has a beneficial activity against autoimmune and infectious diseases, as well as in cancer progression [118] [119]. The promising results from ISO-1 triggered more isoxazolines to be tested, such as ISO-

66 in melanoma and colon cancer models and CPSI-1306 against UVB-Induced Squamous Cell Carcinoma [120] [121]. Other small molecules that were preclinical tested and presented therapeutic input were in the categories of chromenes (T-614, anti-inflammatory against MS), chromenones (Orita-13 tautomerase inhibito), iminoquinones (N-acetyl-p-benzoquinone imine), benzoxazolones (MIF098, pulmonary hypertension,murine SLE), pyrimidazoles (K664–1 diabetes progression) and isocoumarins (SCD19, lung cancer) [122] [123] [124] [125].

Imalumab (BAX69), an anti-inflammatory recombinant, monoclonal antibody that binds specifically to oxMIF, is the only anti-MIF Ab in a clinical phase trial [126]. The anti-inflammatory Ab has been administrated in a clinical phase I study for the treatment of advanced solid tumors with an acceptable safety profile and promising results [127]. Other anti-MIF Abs such as NIH/IIID.9, Bax class (Bax B01, BaxG03, BaxM159) and nanobodies NbE10-NbAlb8-NbE10 remain in pre-clinical stage studies against atherosclerosis, endotoxic shock and inflammatory conditions [77] [126] [128] [129]. Noteworthy, Milatuzumab, a CD74 targeting Ab was shown to be clinically beneficial in patients with relapsed and refractory B-cell non-Hodgkin lymphoma (together with veltuzumab, a humanized anti-CD20 antibody) or refractory chronic lymphocytic leukaemia [130] [131]. Peptides that target the MIF/CD74 interaction still remain in preclinical studies. For example, the immunoglobin-derived peptide C36L1 was shown to have antitumor activity against melanoma, while peptides derived by Drα1β1 domain of MHC class II inhibited autoimmune encephalomyelitis and reduce permanent ischemic brain injury [132] [133]. In addition, the MIF derived peptides MIF(80-87), MIF(47-56) inhibited the MIF/CD74 and MIF/CXCR2, respectively, by binding to the receptors, while MIF(50-65) had an agonist activity to the CD74-mediated ERK [94] [97] [134].

1.3   GPCRs and chemokine receptors

G protein-coupled receptors (GPCRs), also known as seven transmembrane (7TM) receptors, is the largest integral membrane protein family, consisting of more than 800 members [135]. Their name originates from the structure and the seven times penetration to the cell membrane to couple to G proteins and activate the internal signaling. GPCRs are typical allosteric proteins, in which the agonist binds to the ectodomain and subsequently induces the binding to the intracellular protein complex and the signaling (e.g., a heterotrimeric G protein) [136]. The intracellular loops and parts of the seven transmembrane helices are quite highly conserved between GPCRs, and undergo significant conformational changes upon receptor activation. Contrariwise, the extracellular loops and sections of the transmembrane helices are highly diverse, and their structure is not affected so much by the binding [137]. GPCRs may also form dimers and higher homo- and hetero-oligomers [138].

GPCRs are divided in six different classes (A to F) based on the sequence and signaling similarities. Class A or rhodopsin-like family have a unique 8th helix and apalmitoylated cysteine at the C terminus of the receptor. Class B (secretin receptor family) and class C contain the metabotropic glutamate family, and the GABA, calcium-sensing, and taste receptors have an elongated N-terminus compared to class A receptors, consisting of 120 and 600 residues, respectively. The last three classes include fungal mating pheromone receptors (class D), cAMP receptors (class E), and frizzled/smoothened receptors (class F) [135].

The substrates of GPCRs are characterized by an extensive diversity, varying from amino acids and ions, peptide and peptide-based hormones, proteins (such as chemokines and proteases), to biogenic amines (like serotonin, dopamine), lipids and lipid-derived molecules, and environmental stimuli. GPCRs are in equilibrium which is shifted more to the active or inactive state in the presence of an agonist or an inverse agonist, respectively [139]. The antagonist is usually neutral and does not affect the equilibrium between the different states, while in the absence of any molecule the unordered one, which is in the lower enery state, is preferred [136].

GPCRs mediate plenty of physiological functions, including immune response and blood pressure regulation, but they could also get involved in pathogenesis. Particularly, they have an essential role in several diseases, including cancer, diabetes, obesity, and CNS, while they are targeted by almost one out of three approved therapeutics [140]. Almost all endogenous ligands function as agonists, whereas many drugs are designed to be antagonists or inverse agonists [139].

1.3.1   Chemokine receptors

Class A of the GPCRs is the most studied one and includes 80% of the GPCRs [136]. As mentioned above, there is a wide variety in the ligand of GPCRs and could be proteins, peptides, amines, alicarboxylic acid, steroids, nucleotides, melatonine, lipidsopsins or still unidentified for class A GPCRs. Herein, the interest will be focused on the class A GPCRs with chemokines as substrates, named chemokine receptors (Figure 4). Chemokine receptors are pleiotropic regulators of cell activities like immune response and are involved in the pathogenesis of many diseases, therefore, many research works focused on their pharmacological targeting [141] [142]. The first FDA-approved chemokine receptor drugs were maraviroc and AMD3100, two small molecules that are antagonists of the chemokine receptors CCR5 and CXCR4 and target HIV infection and specific cancer types, respectively

[143] [144]. More compounds are in clinical trials currently, with mogamulizumab, a monoclonal-antibody acting as a CCR4 antagonist, being the third market released drug targeting chemokine receptors for the treatment of mycosis fungoides or Sézary syndrome in 2019 [145] [140].
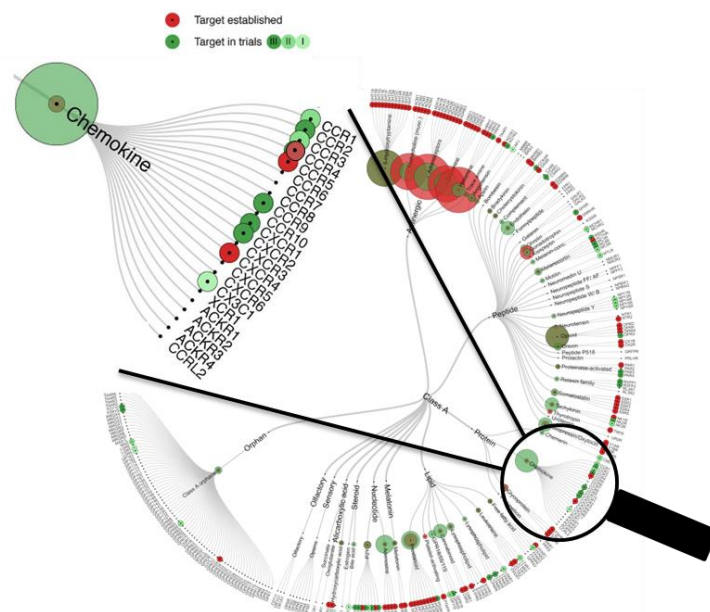
Figure 4. Classification of chemokine receptors among class A GPCRs and the clinical stage of their targeting. Chemokine receptors are the only category of GPCRs class receptors that has protein as ligands and consist of 23 receptors. Targeting with drug candidates is in clinical phase I for one of them (CXC3C1), clinical phase II for two (CCR1, CCR3), clinical phase III for four (CCR2, CCR9, CXCR1, CXCR2), while pharmaceutical molecules that focus on CCR4, CCR5 and CXCR4 are available on the market and the research for the other receptors remain in preclinical stage (no color: preclinical, very light green: clinical phase I, medium green: clinical phase II, deep green: clinical phase III, red: post clinical, adapted from Hauser et al., ref. [140]).

Chemokines, the substrates of the receptors of interest, are a group of 48 small proteins that consist of 70 to 80 amino acids with characteristic cysteine motifs. Based on these motifs, the ligands (L) of the chemokine receptors are classified according to the spacing (and presence) of the first two of these Cys residues, to CCLs (no residue in the between), CXCLs (one residue), CX3CL (three residues) and XCLs (the second Cys, and its disulfide bond partner are missing) (Figure 5a). CCLs and CXCLs are the major subfamilies of chemokines consisting of 28 and 17 proteins, while CX3CL and XCLs only by one and two, respectively. Chemokine receptors contain two conserved disulfide bonds that bridge N-terminus to ECL3 and ECL1 to ECL2 (Figure 5b). Chemokines may interact with multiple receptors, essentially of the same class, but could also bind to atypical chemokine receptors (ACKRs) that are conformationally similar but differ in signaling to the ordinary receptors (Figure 6) [146].

a)

C chemokine

CC chemokine

CXC chemokine

CX₃C chemokine

b)

Chemokine receptors

Figure 5. Overview of the structure of chemokines and chemokine receptors. a Chemokines have been divided into four main subfamilies, depending on the nature of the N-terminus cysteine motif. Particularly, in C chemokines there is a lack of a cysteine on the N-terminus and another one in the middle of the sequence, in CC chemokines the two cysteines of the N-terminus are directly juxtaposed, while in CXC and CX₃C chemokines there is one and three residues located in the between of them, respectively.**b** Chemokine receptors consist of seven transmembrane helices, with the N-terminus and the three extracellular loops (ECLs) outside of the membrane and the intracellular loops (ICLs) and the C-terminus inside. The disulphide bonds between N-terminus to ECL3 and ECL1 to ECL2 are indicated.

Figure 6. Overview of the chemokine and chemokine receptor interactome. Chemokines bind mainly to chemokine receptors of their own class and secondly of other class or atypical chemokine receptors (blue circle agonist, red square antagonist, yellow square unspecified activity (taken from Stone et al., ref [146]).

The binding of chemokines with their receptors was suggested to consist of two steps (two-site model) [142]. The chemokine recognition site 1 (CRS1) involves the N-loop and the closely located β3 region of the chemokine with the N-terminus and maybe the ECLs of the receptors. Next, in the chemokine recognition site 2 (CRS2), the N-terminus region of the chemokine interacts with the extracellular loops and the closely TM domains of the receptor [147]. CRS1 has been suggested to participate in the binding and the selectivity between the chemokine and the receptor and CRS2 in the receptor binding and activation by the chemokine [96]. However, the specific residues and the domains involved in CRS1 and CRS2 vary and are interaction-specific [142]. During the last years, it has been hypothesized that the two-site model could not include all the aspects of the binding mechanism. For example, the first released crystal structure of a chemokine receptor, CXCR4, uncovered chemokine recognition site 1.5 (CRS1.5), which involves interactions in an intermediate stage between CRS1 and CRS2 [148].

1.3.2   The chemokine receptor CXCR2

CXCR2, also known as IL-8RB, was firstly identified in neutrophils as the receptor of IL-8 and was encoded in 1991, adopting a typical chemokine receptor structure (Table 2) [149]. Sequence alignment analyses revealed another receptor, CXCR1, with which they share high homology in the entire sequence and the binding site [150]. Both receptors share CXCL1, CXCL6, and IL-8 (or CXCL8) as common ligands, while CXCR2 additionally recognizes CXCL2, CXCL3, CXCL5, CXCL7 as substrates, and the atypical chemokine MIF [77] [146]. Seven of the fifteen CXC ligands (CXCL1, -2, -3, -5, -6, -7, and -8) contain an ELR motif, all binding to chemokine receptor CXCR2 [151]. A possible explanation for the broad interactome repertoire of CXCR2 is the hydrophobic consistency of the N-terminus binding epitope of the receptor contrary to the charged one of CXCR1. Among all chemokines that contain the ELR motif, only CXCL6 and IL-8 exposed charged residues that could interact with CXCR1 N-terminus, while the hydrophobic residues are known for contributing to less specific interactions [152]. Among CXCR2 chemokine ligands, IL-8 has been found to be the most potent one [153]. The sequence of CXCR2 is quite conservative over the mice and generally for vertebrates [151]. The receptor is expressed mainly in myeloid cells and particularly in neutrophils (BM and blood) and basophils (blood), and its signaling promotes the release of neutrophils from the bone marrow [154] [155]. All ELR motif-containing chemokines exist in mice, including all the ligands of CXCR2, except for IL-8 [151].

Table 2. Sequence of CXCR2 and the location of residues on each topological domain of the receptor.

Topological domain	Sequence [a]
N-terminus	M^{1}EDFNMESDSFEDFWKGEDLSNYSYSSTLPPFLLDAAPCEPESLEINKYF^{50}
Transmembrane helix 1	V^{51}VIIYALVFLLSLLGNSLVMLVILY^{74}
Intracellular loop 1	S^{75}RVGRSVTD^{84}
Transmembrane helix 2	V^{85}YLLNLALADLLFALTLPIWA^{105}
Extracellular loop 1	A^{106}SKVNGWIFGTFLCK^{120}
Transmembrane helix 3	V^{121}VSLLKEVNFYSGILLLACISV^{142}
Intracellular loop 2	D^{143}RYLAIVHATRTLTQKRYLVK^{163}
Transmembrane helix 4	F^{164}ICLSIWGLSLLLALPVLLF^{183}

Topological domain	Sequence [a]
Extracellular loop 2	R[184]RTVYSSNVSPACYEDMGNNTANWR[208]
Transmembrane helix 5	M[209]LLRILPQSFGFIVPLLIMLFC[229]
Intracellular loop 3	Y[230]GFTLRTLFKAHMGQKHRAMR[251]
Transmembrane helix 6	V[252]IFAVVLIFLLCWLPYNLVLL[272]
Extracellular loop 3	A[273]DTLMRTQVIQETCERRNHIDR[294]
Transmembrane helix 7	A[295]LDATEILGILHSCLNPLIYA[315]
C-terminus	F[316]IGQKFRHGLLKILAIHGLISKDSLPKDSRPSFVGSSSGHTSTTL[360]

[a] The sequence is divided in different topological domains based on on Bradley et al, ref. [156].

CXCR2 has been found to form homodimers and heterodimers with the GPCRs δ-opioid, α1A-adrenoceptor, and AMPA Glu 1 [138]. The chemokine receptor was crystallized recently together either with its ligand IL-8 or with a small molecule. The IL-8/CXCR2 interaction follows the two-site model principles with an essential role of the N-terminus of the receptor in CRS1, CRS1.5, and of extracellular loops and TMs in CRS2. Particularly, the first 25 residues appear to align properly through the disulfide bridge C39-C286 and initiate the interaction with IL-8 (CRS1), and then through the N-terminus receptor PC motif (CRS1.5) it was induced the transition to CRS2. In the last stage of the binding, R208 (ECL2), R212 (TM5), and R278 (ECL3) are involved in ionic interactions with the ELR motif of the IL-8 while, Y197, T204 (ECL2), and T285 (ECL3) form hydrogen bonds with the chemokine. The large side chains of K108 and R184 were found to prohibit the deeper penetration of the chemokine to the TMs of the receptor [152]. Of note, the IL-8 dimer shares a similar tertiary structure with the MIF monomer [157]. Even though MIF does not have the typical cysteine motif, it contains a pseudo (E)LR motif that contributes to the binding to the chemokine receptor, as the respective motif of IL-8 [95]. However, the arrangement and topology of the secondary structure of MIF are entirely different from that of IL-8 [83]. Moreover, the binding epitope of the receptor is differentiated from ligand to ligand. First, the receptor ectodomains N-terminus(19-33), ECL1(108-120), ECL2(184-198), and secondly ECL2(198-212) and ECL3(286-300) appeared as contributors to the binding with MIF [97]. Overall in line, theoretical approaches indicated the necessity of the N-terminus hydrophobic residues located between the 28th and 39th residue, ECL2(187-192) and the residues Q40, Q83, and E284 for binding to the atypical chemokine [96]. Still there are no published data for the binding interface of CXCR2 with CXCL1, -2, -3, -5, -6, -7 (Figure 7, Table 3).
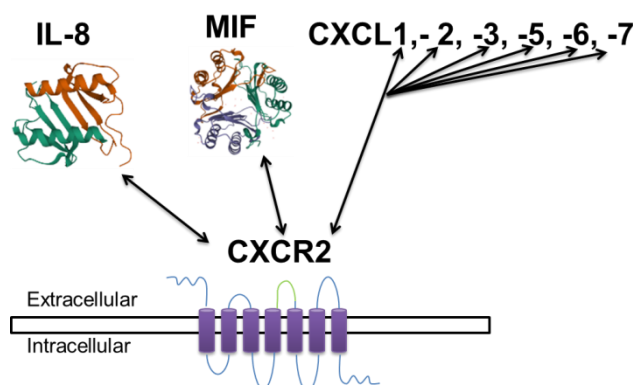
Figure 7. Interactions of CXCR2 with its ligands. CXCR2 was found to interact with the atypical chemokine MIF and the chemokines IL-8, CXCL1, -2, 3, -5, -6, 7 (PDB codes, MIF:1MIF, [83] IL-8:1IL8 [158]).

Table 3. Essential residues of CXCR2 for the interactions with its ligands.

Receptor	CXCR2 residue	References
IL-8	N-terminus(1-25), Y197, T204, R208, R212, R278, T285, disulfide bond C39- C286	[152]
MIF	N-terminus(19-33), ECL1(108-120) ECL2(184-198), 28th and 39th residue, ECL2(187-192) and the residues Q40, Q83, and E284	[96] [97]

1.3.2.1 CXCR2 and its role in atherosclerosis and other diseases

Neutrophils express CXCR2, which, if dysregulated, could be the mediator of several diseases [159]. For example, the chemokine receptor is protective against liver injury in lower concentrations but has a damaging role in higher ones [159-160]. Application of SCH-N, a CXCR2 antagonist small molecule, blocked the lung inflammation that leads to Chronic Obstructive Pulmonary Disease (COPD) [161]. Studies on CXCR2 deficient mice showed that the receptor contributes to the persistence of asthma through the allergenic fungi to *A. fumigatus* [162]. The blockade of CXCR2 mediated signaling might be beneficial against CNS diseases, too. The administration of the CXCR2 antagonists SB225002 and SB332235 in mice had a protective effect against inflammatory bowel disease, autoimmune encephalomyelitis and Alzheimer's disease [163] [164] [165]. Inhibition of IL-8/CXCR2 might be beneficial against various cancer types, too [166].

The pleiotropic inflammatory signaling through CXCR2 affects the CVDs, as well. Blockade of CXCR2 with a receptor-specific Ab resulted in decreased infarction size in mice, while its deficiency or inhibition by its antagonist SB265610 eliminated hypertension [167] [168]. More specifically, the MIF/CXCR2 axis has been shown to mediate monocyte arrest and chemotaxis, resulting in acceleration of atherosclerosis [77] [87]. Furthermore, the administration of G31P, a recombinant derivative form of IL-8 that blocks the binding of the chemokine to the receptor, reduced the infarction size [169]. The binding of CXCL1 to CXCR2 was shown to induce monocyte recruitment and be crucial in the initiation of atherosclerosis [170]. Additionally, CXCL5 and CXCR2 were defined as risk factors due to their increased levels during CAD [171].

On the other hand, CXCR2 could act as a cardioprotective factor, too. Particularly, the increased expression of CXCR2 on endothelial progenitor cells resulted in their accumulation in plaque and its resolution [172]. Moreover, CXCL5 decreased the cholesterol content of macrophages and prohibited their transformation to foam cells, most likely through CXCR2 [173]. In a mouse model after Ischemia/Reperfusion, the secreted by cardiomyocytes MIF mediates heart function and decreased infarction size through CXCR2 [174].

1.3.2.2 Targeting CXCR2 for drug development

Many CXCR2 antagonist small moleclues entered in clinical trials. Among them, the most promising seems to be Reparixin, a dual receptor inhibitor. Two phase I pilot studies showed safe and tolerable profile of the molecule in patients with HER-2-Negative Metastatic Breast Cancer and clinical phase II is on the way [175] [176]. Reparixin appeared to attenuate potentially myocardial Ischemia/Reperfusion after on-pump coronary artery bypass graft surgery due to its reduction the recruitment and diapedesis of neutrophils [177]. SCH527123 (naviraxin) was proved to be safe too, and reduced sputum neutrophils in patients with severe asthma [178]. MK-7123 (SCH527123) entered in clinical phase II against COPD but side effects appeared

which stopped the transition to the next phase [179]. Monoclonal antibodies that do not target CXCR2 but its main ligand, IL-8, are also in clinical trials. HuMax-IL8 (BMS-986253) exhibited good results in patients with metastatic or unresectable solid tumors in clinical phase I, while Abcream, an IL-8 monoclonal antibody, is used available on the market against psoriasis in China [180] [181].

1.3.3 The chemokine receptor CXCR4

CXCR4 was firstly discovered and cloned as a receptor for HIV-1 and initially named fusin, as it induces the fusion of the virus to cells [182]. The receptor adapts to the typical 7TM structure and is consisted of 352 amino acids (Table 4). CXCR4 is an essential mediator of the first steps in immune and central nervous system development and is the most highly conserved chemokine receptor in vertebrates [183]. The receptor is a vital factor at the earliest stages of B-cell lymphopoiesis, in the migration of multipotential hematopoietic cells to bone marrow (BM), and the formation of the cardiac septum and cerebellar neuronal layer [184]. Noteworthy, CXCR4 recruits neutrophils in the bone marrow, acting as an antagonist to the other MIF receptor, CXCR2, which is responsible for releasing them outside of the bone marrow [155]. Except for its very high expression in neutrophils (BM and blood) and monocytes (blood), CXCR4 could be found in high concentrations also in Germinal center B Cells, monocytes (BM), and macrophages (lung) [154]. According to PubMed abstracts, CXCR4 is the GPCR with the highest number of published papers and is the first one resolved in a crystal structure [140] [185].

Table 4. Sequence of CXCR4 and the location of residues on each topological domain of the receptor.

Topological domain	Sequence[a]
N-terminus	M[1]EGISIYTSDNYTEEMGSGDYDSMKEPCFREENANFNKI[39]
Transmembrane helix 1	F[40]LPTIYSIIFLTGIVGNGLVILVM[63]
Intracellular loop 1	G[64]YQKKLRSMTD[74]
Transmembrane helix 2	K[75]YRLHLSVADLLFVITLPFWAV[96]
Extracellular loop 1	D[97]AVANWYFGNFLCK[110]
Transmembrane helix 3	A[111]VHVIYTVNLYSSVLILAFISL[132]
Intracellular loop 2	D[133]RYLAIVHATNSQRPRKLLAE[153]
Transmembrane helix 4	K[154]VVYVGVWIPALLLTIPDFIF[174]
Extracellular loop 2	A[175]NVSEADDRYICDRFYPNDLWVV[197]
Transmembrane helix 5	V[198]FQFQHIMVGLILPGIVILSCYC[220]
Intracellular loop 3	I[221]IISKLSHSKGHQKRKALKT[2420]
Transmembrane helix 6	T[241]VILILAFFACWLPYYIGISID[262]
Extracellular loop 3	S[263]FILLEIIKQGCEFENTVH[281]
Transmembrane helix 7	K[282]WISITEALAFFHCCLNPILYAFL[305]
C-terminus	G[306]AKFKTSAQHALTSVSRGSSLKILSKGKRGGHSSVSTESESSSFHSS[352]

[a] The sequence is divided in different topological domains based on Rosenkilde et al., ref. [186].

CXCR4 has structural differences from other receptors, with its extracellular ends of TM1, TM4, and TM6 shifted, and its TM5 and TM7 longer than other GPCRs. However, it contains the conservative disulfide bridges N-terminus-ECL3 and ECL1-ECL2 that are crucial in forming the binding pocket for the substrate, as other GPCRs [185]. CXCR4 has been found to form homodimers and heterodimerize with the MIF receptors ACKR3 and CD74, as well as with the other GPCRS but non-chemokine

receptors BILF1, µ-, δ- and κ- opioid, α1A/B-adrenoreceptor, CB-2 receptor and the non-GPCRs CD4 and TCR [138]. The first released publication about CXCR4 crystal structure presented the receptor in dimeric form, with the domains ECL2(191-198), TM5 (F201, M205, L210), and ECL3(L266, L267) being crucial for homodimerization [185]. In this work, the receptor was complex with the small molecule IT1t or the peptide CVX15. Nevertheless, in the second released crystal structure, the receptor was crystallized together with vMIP-II, a CC chemokine encoded by Kaposi's sarcoma–associated herpesvirus in a monomeric form [148].

The CXCR4/vMIP-II interaction follows the two-site model principles. The N-terminus regions 23-27 and 27-31 of the receptors were involved in CRS1 and CRS1.5, while the D97 (ECL1), D262, and E288 (ECL3) with the chemokine in CRS2 [148]. Contrariwise, the binding of IT1t and CVX15 to the receptor did not follow the two-site model principles. For CVX15, a cyclic 16-mer derived by the horseshoe crab peptide polyphemusin, its first four amino acids and particularly R2 bound to the transmembrane residues H113, T117 (TM3), D171 (TM4), and ectodomain D187, Y190 (ECL2), respectively. Likewise, the ECL3 acidic residues of the receptor, D262, and E288, formed salt bridge and water-mediated interaction with R14 and the d-proline of the peptide. IT1t, an isothiourea derivative, recognizes a similar binding epitope, with the residues D97, C186, E288 of the CXCR4 being mainly involved [185].

CXCL12 is the most potent ligand of CXCR4, but their complex has not been crystallized, yet. However, authors that resolved the previous crystal structures correlated the topology of the receptor and tried to correlate it with the binding with the chemokine. Initially, it has been speculated that the basic residues of CVX15 and CXCL12 behave similarly and bind to the acidic residues D97, D187, and E288 of the receptor [185]. The crystal model with vMIP-II suggest an additional contribution of Y116, the sulfated Y21 (sY21), and the N-terminus (22-26) of the receptor for binding to CXCL12 [148].

Recently, computational and functional studies between CXCL12 and CXCR4 suggested an enriched two-site model in their interaction, including CRS0.5 and CRS1.5, two intermediate stages before CRS1 and CRS2. In CRS0.5, the first seven residues of the CXCR4 N-terminus form an anti-parallel β-sheet with the β1-strand of the chemokine. Then, the N-terminus region 21-26 of the receptor binds to the N-loop and 40s loop of the chemokine (CRS1). In CRS1.5, P27 and C28 (CXCR4) were packed against the C9-C50 bridge and the β3-strand of CXCL12 together with the formation of the E277(ECL3)-R12(N-loop) salt bridge. In CRS2, the model suggests the ionic interaction of CXCL12 to the engagement layer and the subsequent binding to the receptor's signal initiation layer, consisting of D97, D187, D262, and Y94, Y116, and E288, respectively. The E277-R12 interaction is not conservative among other CXC chemokines and receptors, indicating specificity of the CXCL12/CXCR4, while the ECL2 residues W195, Q200, and the negative charge of E179, D181, D182, are also crucial [187]. The importance of the ectodomain residues D10, D97, D187, F189, N192, L267, and H280 has been highlighted, too [188].

High-mobility group box 1 protein (HMGB1) is an alarmin that forms a heterocomplex with CXCL12 and, through it, could mediate signaling via CXCR4. The first indications suggest that the heterocomplex binds differently to the CXCR4 than CXCL12, but more data are needed to identify the hot spot regions of the interaction [189]. MIF was identified as a partial allosteric agonist of CXCR4, and its

binding evolves the N-terminus(1-27), ECL1(97-110), and ECL2(182-196) regions [98]. Ubiquitin is a protein that induces post-translational modifications in all eukaryotic cells and acts as an agonist of CXCR4, as CXCL12, but they differ in signaling and binding. Ubiquitin did not follow a two-site binding model, as it interacted with ECL2 and ECL3 of the receptor but not with the N-terminus [190]. The Rosetta docking model predicted interaction between the C-terminus of the protein with the ECL3 of the receptor and a high importance of the residues F29, F189, and K271 [191]. Human β2 and β3-defensin (hBD-2, -3) and the albumin-derived 16-mer EPI-X4 are other endogenous ligands of CXCR4, but they could not mediate any intracellular signalling [192] [141]. Furthermore, CXCR4 could bind to the exogenous HIV protein gp120, and promote the infection from the virus (Figure 8). SAR studies revealed that the mutation of specific N-terminus (E14, E15, D20, Y21, D22), ECL1 (D97), ECL2 (R183, D187, R188, F189, Y190, D193), and ECL3 (D262, E268, E277, K282, E288) residues decreased the affinity in the gp120-CXCR4 binding (Table 5) [193] [194]. HBD-2, hBD-3, CXCL12 but not MIF or ubiquitin are able to bind to CXCR4 and block its interaction with gp120 and HIV-1 cell entry [98].
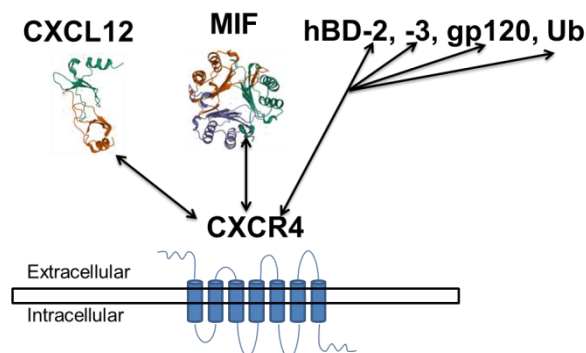
Figure 8 Interactions of CXCR4 with its receptors. CXCR4 was found to interact with the atypical chemokine MIF, the chemokine CXCL12, the human β defensins hBD2, hBD3, ubiquitin, and the virus proteins gp120 (PDB codes, MIF:1MIF [83], CXCL12:3HP3 [101]).

Table 5. Important residues of CXCR4 for the interactions with its ligands.

Receptor	CXCR4 residue	Reference
CXCL12	N-terminus (1-7, 21-26), D10, P27, C28, Y94, D97, Y116, D187, F189, N192, D262, L267, E277, H280, E288,	[150] [187] [188]
MIF	1-27, 97-110, 182-196	[98]
gp120	E14, E15, D20, Y21, D22, D97, R183, D187, R188, F189, Y190, D193), D262, E268, E277, K282, E288	[193] [194]
vMIP-II	N-terminus (23-31), D97, D262, E288	[148]
CVX15	H113, T117, D171, D187, Y190, D262, E288	[185]
IT1t	D97, C186, E288	[185]

1.3.3.1 CXCR4 and its role in atherosclerosis and other diseases

CXCR4 is a multifunctional receptor with various roles in diseases through its signaling after interacting with MIF and CXCL12. Particularly for atherosclerosis, CXCR4 has been found to play a double-edged role. The binding of the MIF to the receptor has been shown to trigger T recruitment and B cell migration promoting early-stage atherosclerosis [77] [87] [105]. However, CXCR4 appears to mediate atheroprotective signaling as well since it induced the localization of B1 cells and the

increase of IgM in plasma [195]. Its interaction with CXCL12 has a cardiobeneficial input, mainly.

The blockade of the CXCL12/CXCR4 interaction in bone marrow increased circulating neutrophils and their recruitment in plaques, enhancing their enlargement and destabilization [196]. Additionally, the vascular signaling through this axis decreased the endothelial permeability and promoted the least inflammatory phenotype of SMC [197]. Moreover, the binding between CXCL12 and CXCR4 mobilized progenitor cells and leukocytes, protecting against myocardial ischemia [198]. Another cardioprotective aspect of this interaction promotes ischaemic preconditioning that decreases the infarct size after ischemia and reperfusion but also triggers the cardioprotective neoangiogenesis after MI [199] [200]. On the other hand, the same axis may lead to the recruitment of pro-inflammatory cells to the ischemic heart [201]. Furthermore, the mobilization of SMC through CXCL12/CXCR4 was associated with increased neointima formation in injury-induced restenosis [202]. To sum up, the CXCL12/CXCR4 axis mediates atheroprotection before an ischemic event and adopts a double-edged role that depends on several factors [198].

The CXCL12/CXCR4 signaling is involved in the promotion of several types of cancer, autoimmune, and kidney diseases [203] [204] [205]. Additionally, the interaction of the receptor with MIF triggers the inflammatory signaling in many diseases, including CNS diseases and cancer metastasis [109] [110]. Therefore, many therapeutical strategies targeted CXCR4, with the most known molecule being AMD3100, an FDA approved antagonist of CXCR4, to treat patients with non-Hodgkin's lymphoma and multiple myeloma [144]. AMD3100 may be beneficial in various malignant or hereditary immunological disorders such as WHIM syndrome and physiopathological processes like hepatopulmonary syndrome, too [206].

SAR studies on AMD3100 led to new, more potent cyclam analogs such AMD3465 with improved pharmacokinetic profile [207] [196]. Non-cyclam analogs such as bisamine derivative and bis-tertiary amines were applied as CXCR4 antagonists, too [208]. Mavorixafor, previously known as X4P-001, AMD11070, or AMD070, is a tetrahydroquinoline derivative and acts as an oral, selective, allosteric inhibitor of the chemokine receptor CXCR4. Currently, it is administrated against hypogammaglobulinemia, infections, and myelokathexis (WHIM) syndrome in clinical phase III and in clinical phase II to treat renal cell carcinoma (together with axitinib, a tyrosine kinase inhibitor) or Warts [209] [210]. Isothiourea, quinazoline, purine, and guanide or dipicolylamine-zinc(II)-based CXCR4 antagonists were generated as well with promising preclinical efficiency [211] [212] [213] [214].

1.3.3.2 Targeting CXCR4 for drug development

The first steps on peptide antagonists of CXCR4 were carried based on polyphemusin II, an antimicrobial peptide isolated from horseshoe crab [215]. In 1992, there was synthesized the first polyphemusin II analogs and identified as inhibitors of HIV-1 infection *in vitro* [216]. Some years after, it was clarified that its antivirus activity derives from its antagonism to CXCR4 [217]. The follow-up SAR studies concluded to BL-8040 (F-benzoyl-TN14003, or T-140) with the strongest inhibitory effect against HIV-1 entry [218]. Nowadays, BL-8040 is tested together with other inhibitors against cancer in later clinical phases. Particularly, BL-8040 was administrated together with cytarabine for the treatment of relapsed/refractory acute myelogenous leukemia, and is currently in clinical phase III [219]. In a clinical phase IIa trial BL-8040,

pembrolizumab (programmed cell death 1 inhibitor) and chemotherapy exhibited beneficial effects against pancreatic cancer [220]. In another peptide design, Polyphemusin II-derived important residues were introduced on a macrocyclic β-hairpin mimetic template, generating the POL class of CXCR4 inhibitors [221]. SAR studies led to the more pharmacokinetically stable and safe POL6326 (balixafortide) that entered in clinical trials [222] [223]. LY2510924, a CXCR4 antagonist that was developed after a medium-throughput screen, is enrolled in clinical phase II in patients with advanced refractory solid tumors, together with Durvalumab (programmed death 1, PD-1, inhibitor) [224] [225].

Regarding anti-CXCR4 antibodies, Ulocuplumab presented beneficial effects to the patients with relapsed multiple myeloma in clinical phase Ib/II (together with lenalidomide and dexamethasone) [226]. PF-06747143, an IgG1 antibody that acts as CXCR4 antagonist, showed preclinical therapeutic inhibition of primary acute myeloid and chronic lymphocytic leukemia and entered clinical phase I [227] [228] [229]. Another Ab with receptor antagonist activity that showed promising preclinical results is LY2624587, for the treatment of hematologic malignancies [230].

1.4 Peptide mimicry approaches
1.4.1 Introduction on peptides, peptidomimetics and their modifications

The first step in peptide synthesis was done in 1903 by Emil Fischer, who achieved to couple two amino acids through acyl chlorides [231]. Insulin was the first applied peptide therapeutic, isolated from animal pancreases for the treatment of type 1 diabetes. However, the 51-amino acid peptide/protein could not be synthesized with the protocols of that period, and this limited the development of other peptide drugs until the 1960s. Then, Robert Bruce Merrifield introduced the solid phase peptide synthesis (SPPS) in 1963, an affordable and significantly faster protocol than the existing ones, and was awarded for his discovery with the Nobel prize 21 years later [232]. Currently, approximately 80 peptide drugs are available on the global market, with more than half being released in the last twenty years. Four out of five of them act as an agonists, and one out of two are applied against oncology, metabolic indication, or endocrinology [233].

Peptides have several advantages over other drug molecules, such as standardized and low-cost production, high efficiency and potency for their substrates, with remarkably selectivity and tolerability. Contrariwise, peptide bonds are prone to be cleaved, resulting in a poor pharmacokinetic profile. Additionally, peptides struggle to fuse in membranes and may tend to aggregate or face chemical modifications, such as oxidation [234]. Those obstacles are usually overcome with chemical modifications and the transition from peptides to peptidomimetics [235]. Lately, the division of peptidomimetics has been proposed in four classes based on the grade of chemical modifications on the peptide backbone and sequence. Class A mimetics are peptides with few changes in the residues and the backbone, while class B mimetics have more drastic alternations in their sequence (foldamers, peptoids, β-peptides). Class C mimetics have the backbone replaced with a non-peptidic scaffold and a topological exposure of the key residues as the peptide when class D mimetics are small molecules with the same activities as some particular peptides but without any relationship to peptide side chains [236].

To enhance the drug-like properties of the peptide mimetics, some substitutions aim at a peptide bond modification. The replacement of the carbonyl oxygen or of the whole ketone group (C=O) of the bond led to the creation of thioamide (S=C-NH), sulfonamide (O2S-NH), phosphonamide (P2S-NH), or an 3-aminooxetane bond [235]. Likewise, methylation on the Nα of the peptide bond or acetylation on the N-terminus of the peptide hinders its proteolytic degradation or aggregation [237] [238]. Other approaches are substituting the natural L-amino acids of the sequences with non-natural ones that contain on their side chain other reactive groups or with natural D-amino acids (Figure 9a). Another effectively proved strategy aims at the cyclization of the linear peptides [238]. The macrocycles are between the two terminuses of the peptides, one of them with the side chain of an amino acid or is formed through two side chains of amino acids (Figure 9b) [235]. Noteworthy, bicyclic peptides that are cyclized through two bonds have also been formed with great properties and perspectives as the therapeutics of tomorrow [239].
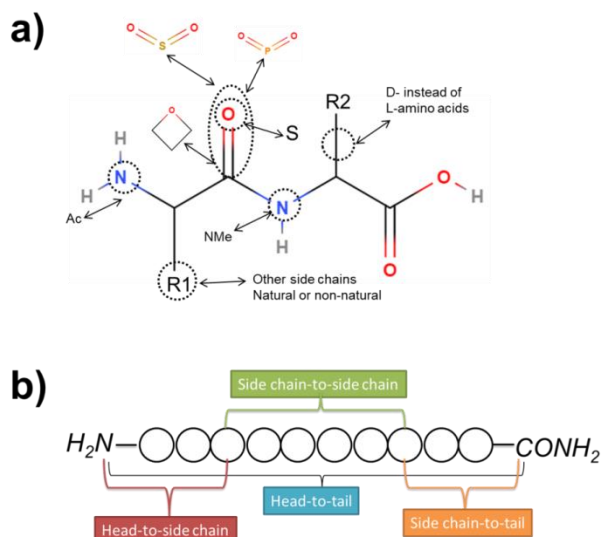
Figure 9. Substitutions on peptide sequence for enhancing drug-like properties.a Modification on the amino, carbonyl, or side-chain group of amino acids **b** Different cyclization strategies between the terminuses and the side chains of the peptide.

1.4.2   Peptide mimicry strategies on binding epitopes of proteins

Peptides could serve as various tools in research, including mimicking the binding sites of a protein. Class A or B peptidomimetics, with few alternations on the peptide sequence, have been studied more than the less peptide-like mimics class C and D. One challenge that should often be overcome is the imitation of the well-ordered structure of the binding epitopes. Chemical modifications might induce the formation of ordered structures and therefore are applied [240].

Helices are stabilized through intramolecular hydrogen bonds between neighboring residues. To enhance the helix-formation in the mimics, macrocyclization was applied between i and i+3 and i+4 if it was wished to mimic one helical turn or with i+7 for two helical turns. One approach involves the cross-linking of cysteines with or without an intermediate organic molecule or a lactam bridge between an acidic and a basic residue. The hydrocarbon peptide stapling technique is an alternative technique in which the particular side chain groups are cross-linked with a carbohydrate alkene chain. The N-terminus capping or the application of well-ordered unnatural oligomeric forms (foldamers) also induce the helical formation. Regarding β-sheet/turn mimetics, small conformational rigid molecules and the pro-Pro dipeptide promote the β-strand or β-turn formation. Macrocyclization, disulfide bridges, and aromatic interactions could stabilize β-hairpin (Figure 10) [236].
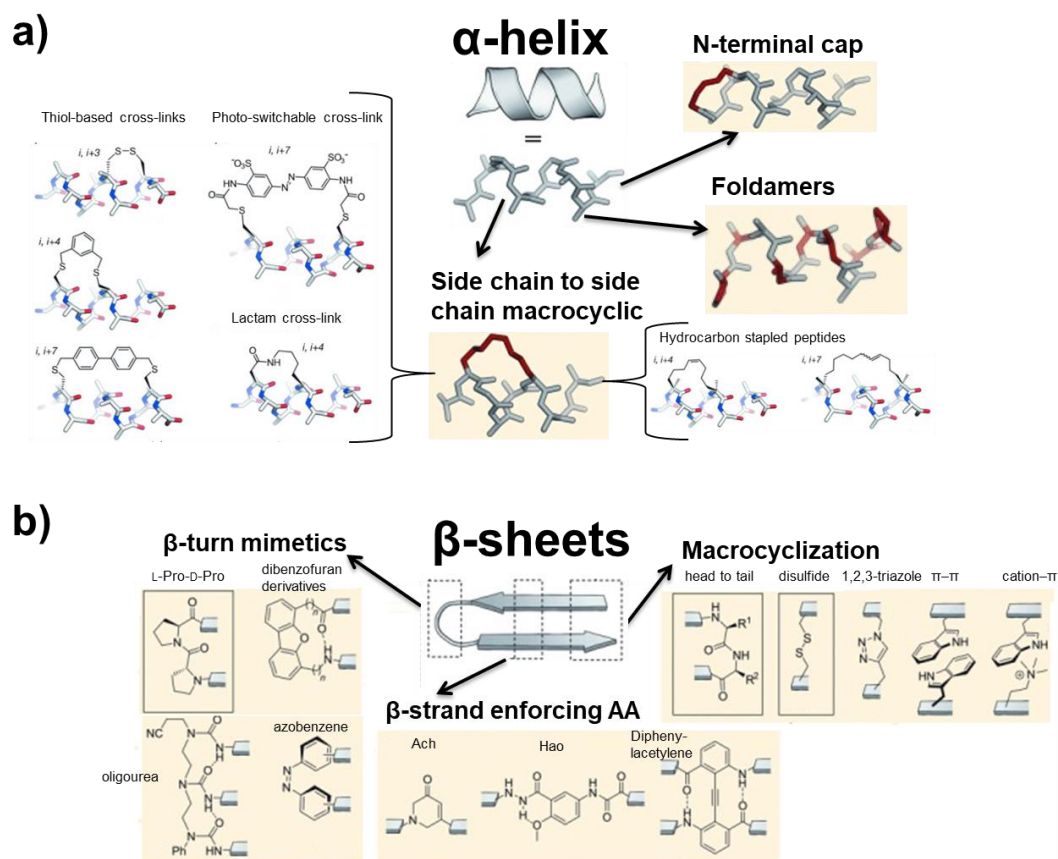
Figure 10. Chemical modifications on peptide-based mimetics to induce ordered conformation. **a** Macrocyclization through side chains, introduction of foldamers or N-terminus acetyl group for the enhancement of α-helix formation. **b** Substitutions of amino acids with organic molecules or other amino acids for the induction of β-sheet formation (adapted from Marta Pelay-Gimeno et al., ref. [236]).

Peptidomimetics may have to be connected if the binding epitope that they present consists of discontinuous regions. For example, the IAPP cross-amyloid interaction surface with Aβ was imitated by connecting the two hot spots regions with three amino acids resulting in nanomolar inhibitors [237]. In another template, the binding ectodomain interface of the class B GPCR corticotropin-releasing factor receptor type 1 (CRF1) was applied on a tripeptide, and the generated mimic was able to bind to urocortin 1, a ligand of CRF1 [241]. The integrin-binding RGD motif was inserted on the scaffold of the cyclic cystine ladder motif of θ-defensins and restricted in a β-sheet/turn conformation. The lead analog inhibited the αvβ3 integrin in the low nanomolar range [242]. Another scaffold that has been discovered recently is the knob-socket model. In this case, it was introduced a four-residue motif, in which a single residue (knob) from the one part of the secondary structure packs into a cavity formed by three residues (socket) in the opposite one [243]. Following these principles, it was developed a peptide that mimics the epitope of an antibody (Cetuximab) in its interaction with an antigen (EGFR), with high specificity and potency [244].

Another study developed an organic molecule that allows the conjugation of three complementarity determining region (CDR)-loops of each variable domain of antibodies, with the generated mimic binding to TNFα in the micromolar range [245]. A complex of natural, non-natural amino acids and an organic molecule led to the creation of a scaffold that could expose two different cyclic peptides on the surface, but without determining its biophysical or binding properties [246]. A much bigger

scaffold, i.e. an antibody was used for conjugation of all extracellular loops of CXCR4. The mimic was recognized by anti-CXCR4 antibodies, while it could bind to CXCL12 and the HIV protein gp120 that belong to the receptor's substrates [247]. The B1 domain of Streptococcal protein G was applied as a scaffold in a mimicking strategy of the CCR3 ectodomain (Figure 11). The most potent CCR3 mimic had a dissociation equilibrium constant ligand to the receptor's ligand eotaxin in the low micromolar range [248].
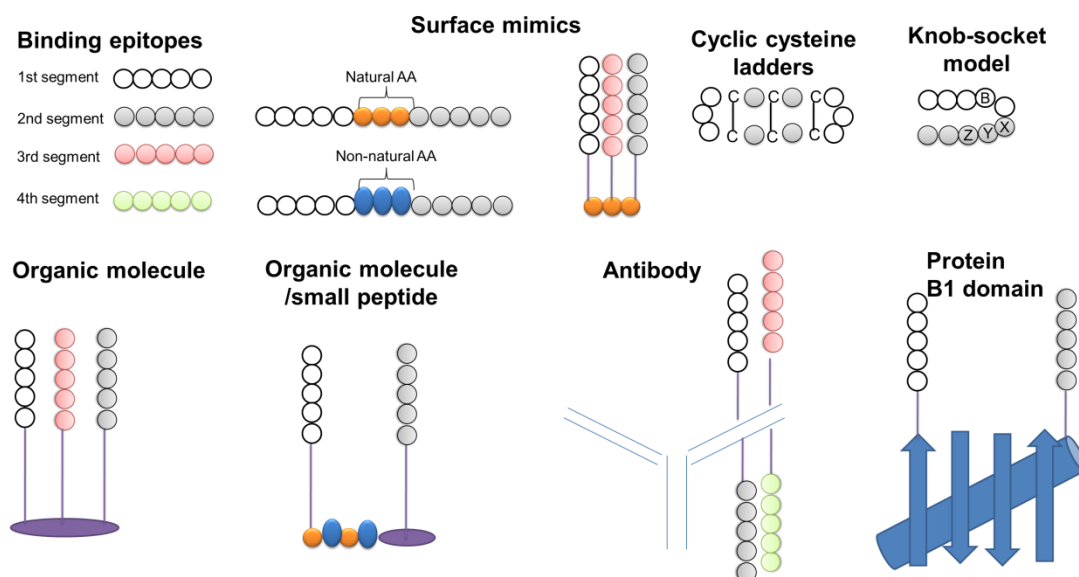
Figure 11. Scaffolds for mimicking binding epitopes of proteins. Discontinued hot spot segments could be linked via amino acids that may be flexible or constrained in an ordered structure (surface mimics, cyclic cysteine ladders, Knob-socket model). Additionally, the bindings epitopes might be conjugated on an organic molecule, an organic molecule/peptide complex, the V_H and V_L regions of an Ab, or the surface of the Protein B1 domain.

1.4.3 Chemokine and chemokine receptor mimics as therapeutics

The crystalization of chemokine receptors was achieved only in the last decade, with the CXCR4 being the first one that its structure was resolved [185]. This novel finding triggered the generation CXCR4 mimics and particularly of its ectodomain for therapeutical studies. Particularly, the first two or all three extracellular loops were connected with a tandem of non-natural amino acids having carboxyhydrate chains as the side chain group in the presence or absence of an additional ECL1-ECL2 disulfide linkage. The mimic that contained the three extracellular loops and the disulfide bridge was the only one that blocked the HIV infection, with the IC50 being at the micromolar range [249]. A similar analog that included the extended ECL2 was shown to bind to gp120 and CXCL12 with higher affinity than the first one. The latest analog could additionally inhibit the CXCL12-mediated signaling and was recognized by anti-CXCR4 antibodies [250]. In another strategy, the V_H and V_L regions and especially the CDRs of the HIV neutralizing antibody b12 hosted the three extracellular loops and the N-terminus of the receptor. Even though all the N-terminus and almost all the ECL2 residues of the receptor are presented on the b12, only four residues of each ECL1 and ECL3 are introduced to the antibody. However, this did not affect the potency of the ectodomain mimic, with strong binding to CXCL12 and blocking of its signaling through the receptor.

Additionally, the CXCR4 mimic could bind to gp120 and generate the production of anti-CXCR4 antibodies [247].

Another approach for mimicking chemokine receptors involved the conjugation of their ectodomain sections on the B1 domain of Streptococcal protein G that acted as a soluble scaffold. In the first trial, the attachment of the N-terminus and ECL3 of CCR3 led to a mimic that could bind to eotaxin-1, -2 and -3, all substrates of the receptor, at a low micromolar range [251] [248]. Following the same principles, it was generated the ectodomain mimic of CCR2, with a similar affinity to the receptor's ligand CCL2. Noteworthy, the conjugation of the N-terminus of CCR2 and the ECL3 of CCR3 or the vice-versa resulted in chimeric receptor mimics that could not recognize any of the substrates of the receptors [248]. Likewise, a chimeric receptor mimic of CXCR1 and CXCR2 was generated, with two receptors that shared high sequence homology and tested against the common ligand of the receptors, IL-8 [150]. The determined K_d for the interaction between the chimeric mimic and the chemokine was at 0.7 µM, similar to one of CXCR1 mimic and eight times improved compared to the CXCR2 mimic [252].

2. Aims of the thesis

Capitalizing on previous findings about the MIF/CXCR4 binding interface, the first part of the current thesis had the following aims:

1. Design and development of novel MIF-specific CXCR4 mimics ("msR4Ms") that will spare the MIF/CD74 and CXCL12/CXCR4 cardioprotective pathway.
2. Biophysical characterization (secondary structure, self-association) of msR4Ms and surfacal hydrophobicity studies on lead mimics to determine their structure and function relationships.
3. Binding studies via fluorescence spectroscopy between msR4Ms and CXCR4 ligands (MIF, CXCL12) and prioritization of a potent MIF-specific binder.
4. FP and MST studies for the interaction between the lead mimic and CXCR4 ligands (MIF, CXCL12) and for its effect on the MIF/CD74 complex formation.
5. SAR studies on the msR4Ms/MIF interaction and mapping of crucial residues.The lead mimic should then be studied *in vitro, ex vivo and in vivo* by collaborators from the group of Prof. Bernhagen.

In the second part of this thesis, the two segments of msR4Ms, ECL1 and ECL2 were shortened based on SAR studies. Based on these findings the next aims were:

1. Design and development of next generation mimics ("ngms") of CXCR4 with MIF-specific binding potency and more favorable drug-like properties.
2. Biophysical characterization (secondary structure, self-association, surface hydrophobicity) of ngms to determine drug-like properties.
3. Binding studies with CXCR4 ligands (MIF, CXCL12) and MIF binding epitope of msR4M-L1 to conclude in lead ngms for further studies. The lead mimic should then be studied *in vitro, ex vivo and in vivo* by collaborators from the group of Prof. Bernhagen.

In the third part of my thesis, SAR studies on the CXCR2 ectodomain binding segments with MIF uncovered the hot spot region of the receptor. Together with the results of the studies on the ngms, the aims were:

1. Design and development of novel chimeric receptor mimics (CRMs) of the MIF receptors, CXCR2 and CXCR4 with enhanced MIF-binding properties.
2. Biophysical characterization (secondary structure, self-association, surfacal hydrophobicity) of CRMs to determine their structure and function relationships.
3. Binding studies with the ligand of CXCR4 (CXCL12), CXCR2 (IL-8) and their common ligand (MIF) for the evaluation of their MIF-specificity of CRMs. The lead mimic should then be studied *in vitro, ex vivo and in vivo* by collaborators from the group of Prof. Bernhagen.

The last part of my thesis focused on the MIF and its binding interface with CXCR4 (R87, L88 and R89) and CXCR2 [MIF(47-56)], but from different research angles. Particularly, the aims were:

1. Biophysical characterization (secondary structure, surfacal hydrophobicity) of the triple alanine mutation effect on the RLR motif of MIF.
2. Binding studies between the triple alanine mutated MIF or an RLR-containig MIF 15-mer and CXCR4 ectodomain segments or mimics to determine the role of these residues in the interaction with the receptor.
3. Determination of the secondary structure of MIF(47-56) and its cyclic analogs.
4. Priorization of a lead MIF cyclic analog based on SAR studies and test *in vitro* its proteolytic stability in human plasma and compare with MIF(47-56).
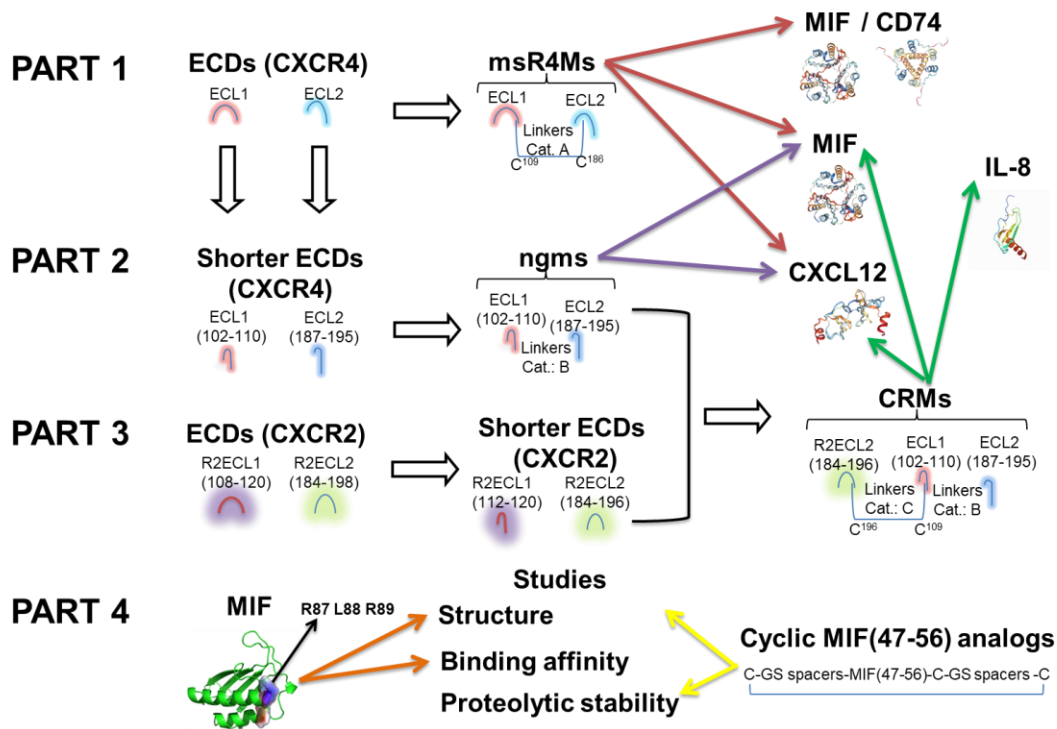
Scheme 1. Aims of my thesis. Part 1 Ectodomains ECL1 and ECL2 (ECDs) of CXCR4, known MIF substrates, were linked (Linkers Cat.A: 6 Ahx-12 Ado, O2Oc-12 Ado, G_7) using rational peptide design approaches to generate MIF specific CXCR4 mimics (msR4Ms). Their biophysical properties, their affinities with MIF and CXCL12 and the lead mimic effect on MIF/CD74 complex were determined. **Part 2** Size and sequence optimization studies of ECDs led to ECL1(102-110) and ECL2(187-195) as improved MIF binders. The 9-mers were connected after rational design and ngms were generated. Ngms were biophysically characterized and their binding affinities to MIF and CXCL12 were identified (Linkers Cat.B: 6 Ahx-12 Ado, 8 Aoc, O1Pen-O1Pen, D_3, G_3, K_3, R_3). **Part 3** Previous studies identified the ECDs of CXCR2 that interact with MIF. Current SAR studies identified segments R2ECL1(112-120) and R2ECL2(184-196) as the hot spot regions. Following rational design strategy, the second domain was conjugated to previously potent ngms and generated the respective CRMs. CRMs were biophysical characterized their app. K_{ds} with the substrates of their receptors were calculated (Linkers Cat.C: G-12 Ado). **Part 4** On the left side a triple alanine mutated in the CXCR4 binding motif MIF was biophysically tested and its affinity with receptor's domains and mimic was determined. On the right side MIF(47-56) and its cyclic analogs were biophysically characterized and their proteolytical stabilities were studied.

3. Materials & Methods
3.1 Materials
3.1.1 Chemicals

Table 6. Chemicals.

Chemicals	Company (City, country)
Protected natural and non-natural amino acids (AA)	Iris Biotech (Marktredwitz, GER)
Acetaldheyde	Roth (Karlsruhe, GER)
Acetic anhydride (Ac$_2$O)	Sigma-Aldrich (St. Louis, USA)
Acetone	Isotec Inc. (Miamisburg, USA)
Acetonitrile (ACN)	VWR (Ismaning, GER)
8-Anilino-1-naphthalenesulfonic acid (ANS)	Sigma-Aldrich (St. Louis, USA)
2-(7-Aza-1H-benzotriazole-1yl)-1,1,3,3-tetramethyluronium (HATU)	Bachem (Bubendorf, CHE)
(2-(1H-Benzotriazol-1-yl)-1,1,3,3-tetramethyluronium hexafluorophosphate (HBTU)	Iris Biotech (Marktredwitz, GER)
Carbon dioxide (CO$_2$), UN1013	Westfallen (Münster, GER)
5-Carboxytetramethylrhodamin (TAMRA)	Novabiochem/Merck KGaA, (Darmstadt, GER)
5(6)-Carboxyfluorescein (Fluos)	Sigma-Aldrich (St. Louis, USA)
Chloranil	Fluka (Seelze, GER)
Cyano-4-hydroxycinnamic acid (4-HCCA)	Sigma-Aldrich (St. Louis, USA)
Diethyl ether (Et$_2$O)	Roth (Karlsruhe, GER)
2,5-Dihydroxyacetophenone (2,5-DHAP)	Bruker Daltonics (Bremen, GER)
N,N-Diisopropylcarbodiimide (DIC)	Fluka (Seelze, GER)
N,N-Diisopropylethylamine (DIEA)	Sigma-Aldrich (St. Louis, USA)
N,N-Dimethylformamide (DMF)	CLN (Niederhummer, GER)
Dimethylsulfoxide (DMSO)	Roth (Karlsruhe, GER)
1,2-Ethanedithiol (EDT)	Sigma-Aldrich (St. Louis, USA)
Ethanol (EtOH)	CLN (Niederhummer, GER)
9-Fluorenylmethoxycarbonyl-Rink amide MBHA resin (Fmoc-Rink amide)	Novabiochem/Merck KGaA, (Darmstadt, GER)
Formic acid (FA)	Roth (Karlsruhe, GER)
GdnHCl	Roth (Karlsruhe, GER)
Hellmanex	Hellma Analytics (Müllheim, GER)
Hydrochloric acid (HCl)	Roth (Karlsruhe, GER)
1,1,1,3,3,3-Hexafluor-2-propanol (HFIP)	Sigma-Aldrich (St. Louis, USA)
1-Hydroxybenzotriazol (HOBt)	Sigma-Aldrich (St. Louis, USA)
Isopropanol (iPrOH)	Roth (Karlsruhe, GER)
Methanol (MeOH)	VWR (Ismaning, GER)
Nitrogen (N$_2$) 5.0, UN1066	Westfallen (Münster, GER)
Ninhydrin	Fluka (Steinheim, GER)
Phenol	Sigma-Aldrich (St. Louis, USA)
Piperidine	Iris Biotech (Marktredwitz, GER)
Pyridine	Roth (Karlsruhe, GER)
Potassium chloride (KCl)	Merck (Darmstadt, GER)
Potassium dihydrogen phosphate (KH$_2$PO$_4$)	Fluka (Steinheim, GER)
Sodium chloride (NaCl)	Merck (Darmstadt, GER)
Sodium dihydrogen phosphate (NaH$_2$PO4)	Merck (Darmstadt, GER)
Sodium hydrogen phosphate dihydrate (Na$_2$HPO$_4$ x 2 H$_2$O)	Merck (Darmstadt, GER)
Sodium hydroxide (NaOH)	Sigma-Aldrich (St. Louis, USA)
Thioanisol	Fluka (Steinheim, GER)
Trifluroacetic acid (TFA)	Iris Biotech (Marktredwitz, GER)
Trifluoracetic acid (TFA) for HPLC (>99.0%)	Sigma-Aldrich (St. Louis, USA)
Tris (tris(hydroxymethyl)aminomethane)	Roth (Karlsruhe, GER)
Tween 20	Roth (Karlsruhe, GER)

3.1.2 Buffers/Solutions

Table 7. Buffers and solutions.

Buffers	Preparation
1×b	10 mM NaPPi in aqueous solution, pH 7.4
2×b	20 mM NaPPi in aqueous solution, pH 7.2
1×PBS	Provided by the lab of Prof. Kapurniotu
10 mM Tris, pH 8.0	Provided by the lab of Prof. Bernhagen
80% B	80% HPLC buffer B: 20% HPLC buffer A
Acetaldehyde/Chloranil test solution I	2% v/v acetaldehyde in DMF
Acetaldehyde/Chloranil test solution II	2% w/v chloranil in DMF
HPLC buffer A	0.058% v/v TFA in water
HPLC buffer B	0.05% v/v TFA in 9:1 ACN: water
Kaiser test solution I	5% w/v Ninhydrin in EtOH
Kaiser test solution II	40 g Phenol in 10 mL EtOH
Kaiser test solution III	2 mL of aqueous 0.001M KCN in 100 mL pyridine
Reagent K	TFA: water: phenol: thioanisole: EDT 82.5%: 5%: 5%: 5%: 2.5%
MALDI-Solution A	97% v/v acetone, 0.1% TFA in aqueous solution
MALDI-Solution A (matrix)	Aqueous solution of 97% v/v acetone, 0.1% TFA, saturated by 4-HCCA
MALDI-Solution B	16.67% v/v FA, 33.34% v/v iPrOH in aqueous solution
MALDI-Solution B (matrix)	Aqueous solution of 16.67% v/v FA, 33.34% v/v iPrOH, saturated by 4-HCCA
MALDI-Solution C (matrix)	Aqueous solution of 49.95% v/v ACN, 0.1%TFA v/v, 10% w/v 2,5-DHAP in aqueous

3.1.3 Peptides

The CXCR4 mimic msR4M-L1(2xAla) was purified and the CXCR2 or CXCR4 ectodomain derived peptides R2ECL1(108-120), CXCR4 (1-27), as well as the mimics msR4M-L1(5xAla) and msR4M-L1(7xAla) were both synthesized and purified by Kathleen Hille. The peptides [Arom]-ECL2 and [R188Cit]-ECL2(184-196) were both synthesized by Núria Gimeno Magán. The ectodomain derived peptides ECL1(100-110), ECL2(176-200), the MIF cyclic analogs and all MIF derived peptides except for MIF(55-80), MIF(57-80), MIF(58-80), MIF(81-94), MIF(82-95) were purchased by Peptide Specialities GmbH (PSL, Heidelberg, GER).

3.1.4 Proteins

Table 8. Proteins.

Proteins	Manufacturer/supplier (City or University, country)
Alexa-488-MIF	Provided by the group of Prof. Bernhagen (LMU, GER)
Alexa-647-MIF	Provided by the group of Prof. Bernhagen (LMU, GER)
Alexa-488-[R87A-L87A-R89A]-MIF	Provided by the group of Prof. Bernhagen (LMU, GER)
C57S-MIF	Provided by the group of Prof. Bernhagen (LMU, GER)
CXCL12	Provided by the group of Dr. von Hundelshausen (LMU, GER) or purchased from Peprotech (Hamburg, GER)
IL-8	Purchased from Peprotech (Hamburg, GER)
MIF	Provided by the group of Prof. Bernhagen (LMU, GER)
MIF(10xAla)	Provided by the group of Prof. Bernhagen (LMU, GER)
MIF-2	Provided by the group of Prof. Bernhagen (LMU, GER))
Peptide calibrant for MALDI	Sigma-Aldrich (St. Louis, USA)
[R87A-L87A-R89A]-MIF	Provided by the group of Prof. Bernhagen (LMU, GER)
sCD74	Purchased from R&D Systems (Minnesota, USA)

3.1.5 Organic molecules

Table 9. Organic molecules.

Organic molecules	Supplier (University, country)
ISO-1	Provided by the group of Prof. Bernhagen (LMU, GER)

3.1.6 Materials

Table 10. Materials.

Materials	Company (City, country)
Capillaries, Monolith NT.115	NanoTemper Technologies (Munich, GER)
Cellstar® Tubes, 15 mL	Greiner Bio-One (Frickenhausen, GER)
Cellstar® Tubes, 50 mL	Greiner Bio-One (Frickenhausen, GER)
Cellulose disks	Intavis (Cologne, GER)
Crimp Caps N20	Rloland Vetter Laborbedarf OHG (Ammerbuch, GER)
Cuvette, quartz	Hellma Analytics (Müllheim, GER)
Disposable hypodermic needles, 100 Sterican Gr.18	BRAND (Wertheim, GER)
Filter, Millex-FG, 0.2 µm	Merck (Darmstadt, GER)
Glass reaction vessel	CS-Bio Inc (California, USA)
Glass vials 20 mL with plastic lids	Roth (Karlsruhe, GER)
Microcentrifuge tubes 2.0 mL with lid	BRAND (Wertheim, GER)
MTP 384 target plate polished steel BC	Bruker Daltonics (Bremen, GER)
Pasteur pipette	BRAND (Wertheim, GER)
Pasteur pipettes, glass, 145 mm	BRAND (Wertheim, GER)
PCR tubes, 0.2 mL	BRAND (Wertheim, GER)
Pipette tips, 2-200 µL, yellow	BRAND (Wertheim, GER)
Pipette tips, 100-1000 µL, blue	BRAND (Wertheim, GER)
Pipette tips, 0.5-10 µL	Axygen (Union City, USA)
Plastic reaction tubes 10 mL	CS-Bio Inc (California, USA)
Reaction vessel, 1.5 mL	Sarstedt (Nümbrecht, GER)
Syringe, BD Discardit II, sterile, 2 mL	Becton Dickinson (Franklin Lakes, USA)
Syringe, BD Discardit II, sterile, 10 mL	Becton Dickinson (Franklin Lakes, USA)
Syringe, BD Discardit II, sterile, 20 mL	Becton Dickinson (Franklin Lakes, USA)

3.1.7 Devices

Table 11. Devices.

Devices	Company (City, country)
Analytical balance T-215D (d=0.01mg)	Denver Instrument Sartorius (Göttingen, GER)
Analytical balance AW-220.S2 (d=0.1mg)	4 more labor (Grasbrunn, GER)
Centrifuge Labofuge Ae	Heraeus Sepatech (Osterode, GER)
Dionex Ultimate 3000 Pump	Thermoscientific (Langenselbold , GER)
Dionex Ultimate 3000 Variable Wavelength Detector (VWD)	Thermoscientific (Langenselbold , GER)
Dry freezer Alpha 1-2 LD plus	CHRIST (Osterode, GER)
Eppendorf centrifuge 5417C	Netheler-Hinz GmbH (Hamburg, GER)
FDP-223 polarizer	JASCO (Pfungstadt, GER)
FDP-243 polarizer	JASCO (Pfungstadt, GER)
FreeZone 2.5 Plus	LABCONCO (Kansas City, USA)
Heating block neoBlock 1	NeoLab (Heidelberg, GER)
Heraeus Function Line T6	Thermoscientific (Langenselbold , GER)
Herafreeze HFU 586 Basic	Heraeus (Hanau, GER)
HPLC degassing unit DG-2080-53	JASCO (Pfungstadt, GER)
HPLC low pressure gradient unit LG-2080-02S	JASCO (Pfungstadt, GER)
HPLC pump PU-2080 Plus	JASCO (Pfungstadt, GER)

Devices	Company (City, country)
HPLC pump PU-2089	JASCO (Pfungstadt, GER)
HPLC UV/Vis detector UV-2075	JASCO (Pfungstadt, GER)
HPLC UV/Vis detector UV-2077 Plus	JASCO (Pfungstadt, GER)
Magnetic stirrer RSM-10 / RSM-ECO	PHOENIX Instrument (Garbsen, GER)
Magnetic stirrer Topolino	Carl Roth (Karlsruhe, GER)
MALDI-TOF Mass Spectrometer	Bruker Daltonics (Bremen, GER)
Monolith NT.115 (green/red filters)	NanoTemper Technologies (Munich, GER)
Multilabel plate reader 2030 VictorTM X3	PerkinElmer Inc (Waltham, USA)
Multipep RSi	Intavis (Cologne, GER)
Nucleosil 100 C18, 33 mm length, ID 8 mm, 7 µm particle size	Grace (Columbia, USA)
Peptide synthesizer CS-Bio 336x	CS-Bio Inc (California, USA)
pH-Meter	Mettler Toledo (Greifensee, CHE)
Ps-150j Spectropolarimeter Power Supply J-715-150s	JASCO (Pfungstadt, GER)
PTC-351S Peltier	JASCO (Pfungstadt, GER)
PTC-423L Peltier Controller	JASCO (Pfungstadt, GER)
HPLC column Reprosil Gold 200 C18, 250 mm length, ID 8 mm, 10 µm particle size	Dr. Maisch-GmbH (Herrenberg, GER).
HPLC precolumn Reprosil Gold 200 C18, 30 mm length, ID 8 mm, 10 µm particle size	Dr. Maisch-GmbH (Herrenberg, GER).
HPLC column Reprospher 100 C18-DE, 250 mm length, ID 8 mm, 7 µm particle size	Dr. Maisch-GmbH (Herrenberg, GER).
HPLC precolumn Reprospher 100 C18-DE, 30 mm length, ID 8 mm, 7 µm particle size	Dr. Maisch-GmbH (Herrenberg, GER).
Scotsman AF100 Flaker	Ice Machines UK Ltd (Ash Vale, GBR)
Shaker CAT S20	CAT (Staufen, GER)
Spectrofluorometer FP-6500	JASCO (Pfungstadt, GER)
Spectropolarimeter J-715	JASCO (Pfungstadt, GER)
Ultrapure water unit TKA MikroPure	TKA (Niederelbert, GER)
Ultrasonic bath SONOREX	Bandelin (Berlin, GER)
UV-Vis spectrophotometer V630	JASCO (Pfungstadt, GER)
Vortex Mixer Vortex Genie 2	Scientific Industries (New York, USA)

3.1.8 Biological fluids

Table 12. Biological fluids.

Materials	Company (City, country)
Human plasma from healthy donors	Provided by the group of Prof. Bernhagen (LMU, GER)

3.2 Methods

3.2.1 Fmoc-Solid phase peptide synthesis (SPPS) methodology

Peptides were synthesized following the principles of the Fmoc-SPPS strategy [253]. The N-terminus of each amino acid was protected with the Fmoc group. Depending on the amino acid, additional protection of the side chain might be required for avoiding side reactions during the elongation of the peptide on the resin. All CXCR2 and CXCR4-derived peptides and mimics were developed on Fmoc-Rink amide MBHA resin. Initially, the resin was swelled and shortly Fmoc-deprotected for 2 and 5 min with 25% piperidine in DMF. After swelling the resin with DMF to remove piperidine traces, the first amino acid was loaded on the resin. The coupling of the Fmoc-protected amino acid (3-fold molar excess) was carried out together with HBTU (3-fold molar excess) and DIEA (4.5-fold molar excess) for 2 h. The only exception was when Fmoc-Cys(Trt)-OH was the first loaded amino acid on the resin. To avoid racemization, it was preferred the HOBT/DIC protocol [254]. In particular, Fmoc-Cys(Trt)-OH (3-fold molar excess), HOBt (3-fold molar excess), and DIC (4.5-fold molar excess) were dissolved in DMF and stirred at 4°C for 10 min and an additional 10 min at room temperature (RT). The amino acid was activated and coupled to the Fmoc-deprotected resin for 1.5 h.

Next, DMF-swelling and drying of the resin were required before determining the substitution level with UV-spectroscopy (see chapter 3.2.1.1 for more details). A part of the free-amine-resin might not be coupled with the Fmoc-protected amino acid. In order to minimize the risks of obtaining hard-removable side products and lower yields during the peptide synthesis, the resin was acetylated after the coupling with Ac$_2$O and DIEA, both in 10-fold molar excess. The peptide was elongated further with repeating circles of Fmoc-deprotection, Fmoc-amino acid coupling, acetylation, and swelling with DMF in the between of each step (Scheme 2). After each Fmoc-deprotection and Fmoc-protected amino acid coupling step, the effectiveness of the reaction was examined by the Kaiser test. The only exception was the case of coupling Fmoc-proline. In this case, the Fmoc-deprotection and the subsequent amino acid coupling were tested with the chloranil test. The subtraction of the N-terminus Fmoc was carried out with two washes of either via 25% piperidine/DMF for 5 and 20 min or 0.1M HOBt in 20% piperidine/DMF for 3 and 9 min. The solution that was applied was dependent on the sequence and the presence of aspartic acid (see chapter 3.2.1.7).

Conjugation of amino acids on the resin may follow different conditions, depending on their difficulty to couple. For all amino acids, natural or non-natural, the couplings were carried out with HATU or HBTU as the activator and DIEA as the base. Amino acids and activators were weighted in a glass vial, vortexed until everything was dissolved, and transported into the syringe with the Fmoc-deprotected resin after the subsequent addition of DIEA. Overall, couplings may vary on the total times applied until their successful conjugation, on the selected activator, and the required time for each reaction. More details are provided in the respective synthesis chapters in the results. Fmoc-Cys(Trt)-OH was coupled under different conditions to guarantee both its successful coupling and the lack of racemization. In particular, the coupling was carried out with the N-terminus protected amino acid (3-fold molar excess), HATU (3-fold molar excess), and in comparison with the other amino acids, less amount of DIEA (3.375-fold molar excess) for 35 min, twice [255].

Acetytalion was brought about as described above but for 15 min instead of 40 min, and Fmoc-deprotection methodology is described in detail in 3.2.1.2. Automated SPPS followed overall the same experimental route, without the possibility of applying Kaiser or Chloranil test (see chapter 3.2.1.5 for additional details).

AA: Amino acid
Ac₂O: Acetic anhydride
Ac: Acetyl
DIEA: Diisopropylethylamine
DMF: Dimethylformamid
Fmoc: Fluorenylmethyloxycarbonyl
HBTU: (2-(1*H*-benzotriazol-1-yl)-1,1,3,3-tetramethyluronium hexafluorophosphate
R: side chain of AA
R1: side chain of another AA
● : resin
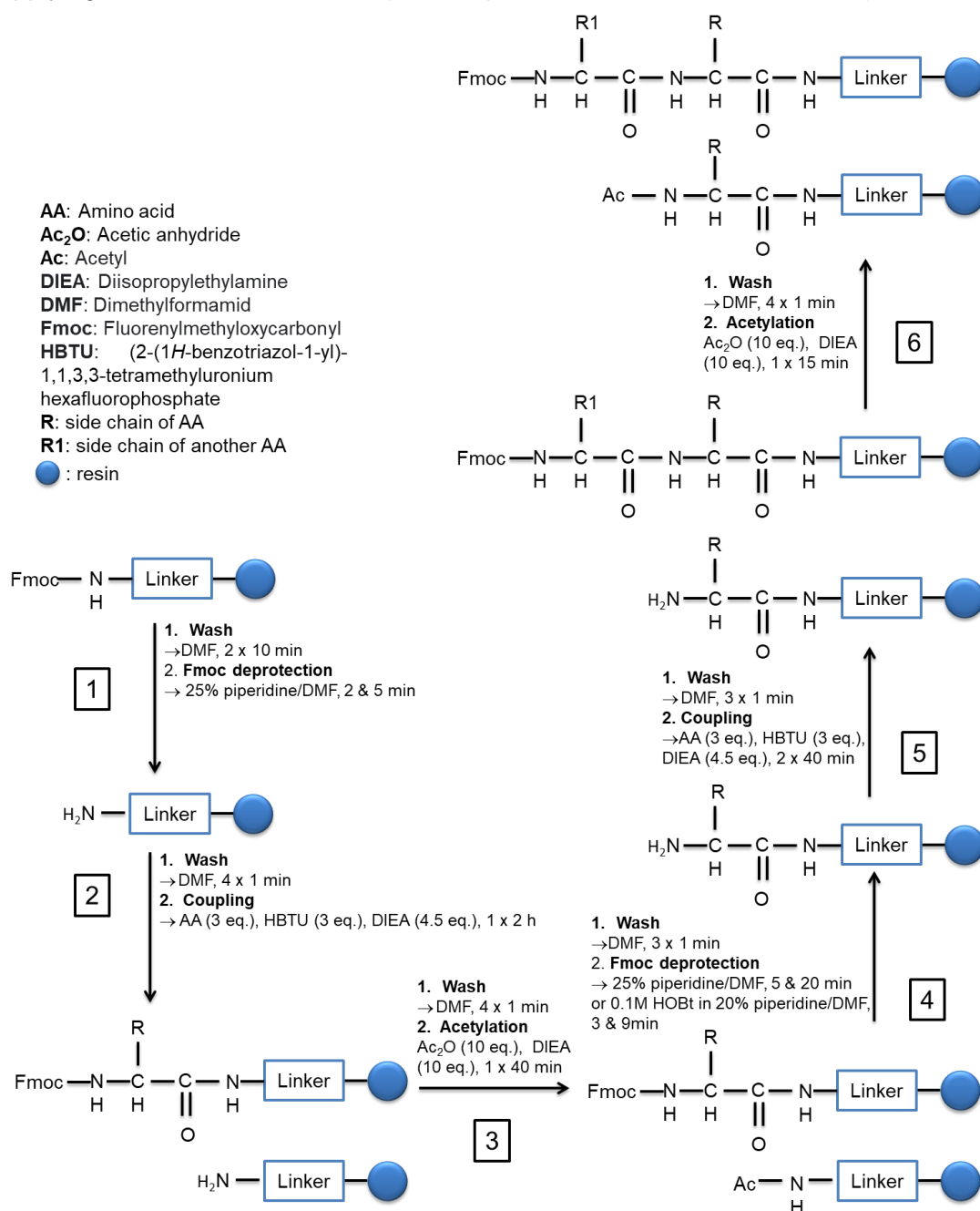
Scheme 2. Applied Fmoc-SPPS protocol. At step 1, Fmoc-protecting group is removed from the resin. At step 2, the first amino acid is loaded, and at step 3, the rest of the uncoupled resin is acetylated. At step 4, the Fmoc is cleaved from the Fmoc-amino acid-resin. At step 5, the following amino acid is coupled (coupling conditions are indicative and may vary), and at step 6, acetylation is carried out. Each synthesis continued further with repetitive circles of steps 4, 5, and 6.

3.2.1.1 Determination of substitution level after the coupling of the first amino acid

Essential parameters of peptide synthesis, such as the amounts of amino acid and the rest of coupling reagents, are pending on the substitution of the resin after the conjugation of the first amino acid. An amount of 3 mg and below of Fmoc-

amino acid-resin was weighted in a volumetric flask, mixed with 10 mL of 25% v/v piperidine in DMF, and incubated for 10 min in RT. During the incubation, the Fmoc group was cleaved from the resin and formed the dibenzofulvene-piperidine adduct, which exhibits its UV absorbance maximum at 290 nm with ε=5800 mol^{-1}·L·cm^{-1} [256] [257]. A part of the solution was then transported to a 1-cm quartz cuvette, and its absorbance was recorded at its maximum. Before this measurement and under the same conditions, the background of 25% v/v piperidine in DMF was monitored and subtracted. The final value was applied to Lambert–Beer's law equation to calculate the substitution level (S.L.) as indicated in Equation 1. This process was carried out three times in total and the final S.L. of the Fmoc-amino acid-resin was calculated as the mean of these three values.

Equation 1. Determination of substitution level of resin.

$$S.L. = \frac{A \times V}{\varepsilon \times m}$$

S.L.: Substitution level (mmol/g)
A: Absorption
V: Volume of solution (=10 mL)
ε: molar attenuation coefficient of dibenzofulvene-piperidine at 290 nm (=5800 L mol^{-1} cm^{-1})
m: (g)

3.2.1.2 Fmoc-deprotection of N-terminus after coupling Asp

Aspartimide formation on the side chain of an aspartic acid remains up to nowadays a major pitfall in peptide synthesis (Figure 12) [258]. The yield of this undesired cyclization of the side chain of aspartic acid to a cyclic imide is increased as the peptide gets elongated due to the repeating Fmoc-deprotection circles [259] [260]. Other studies have provided proof that this side reaction is sequence-dependent [261]. Taking into consideration the sequence of msR4Ms, the first developed peptides, their aspartic residues did not appear to be prone to aspartimide formation. Therefore, it was followed the conventional Fmoc deprotection with 25% piperidine in DMF and two circles of 5 and 20 min each. However, the synthesized peptides contained the side product, and their purification did not lead to satisfying results. One approach to avoid aspartimide formation suggests adding small amounts of organic molecules to the standard Fmoc cleavage solution [262]. On the other hand, researchers focused their attention on β-carboxyl protection of the Asp. They support the replacement of the tBu protecting group with other more bulky ones to suppress the side reaction [260].

MsR4Ms were synthesized again with the additives on the Fmoc-cleavage solution. It was preferred since it has been studied in a broader range of time with success and is more cost-efficient than the bulky protection of β-carboxyl groups approach. All peptides were Fmoc-deprotected with the conventional method until the first coupling of aspartic residue on the resin. From this residue and until the end of the synthesis, Fmoc-deprotection was carried out with a solution of 0.1 M HOBt in 20% piperidine in DMF for 3 and 9 min ('Short HOBt protocol') [263] [261]. Aspartimide was not formed with the 'Short HOBt protocol' and the method was applied as described above to all peptides that contained aspartic acids.
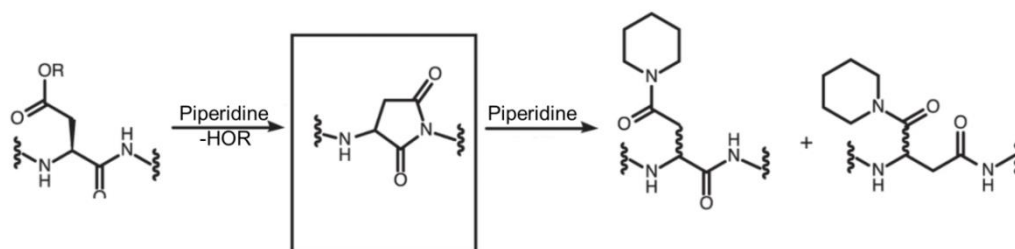
Figure 12. Aspartimide formation in aspartic acid-containing sequences. The side reaction occurs during Fmoc-SPPS and may lead to racemized α- and β-piperidides (adapted from Micsonai et al., ref. [258]).

3.2.1.3 Kaiser test

Elongation of peptides is achieved with several repetitions of Fmoc-deprotection and Fmoc-amino acid coupling. An easy, fast and affordable check of monitoring these reactions is required. Kaiser test was developed in the early 1970s and remained the most applicable method for controlling the efficiency of the Fmoc-deprotection and Fmoc-amino acid coupling [264]. The test is performed to detect either the presence of free primary amine after Fmoc-deprotection (dark blue colored beads) or its absence after a coupling step (yellow/colorless beads). Few beads of peptide-resin are transported into a glass test tube and three drops of each of the Kaiser test solution were added (Table 13). The test tube was slightly shaken and placed on the Heating block neoBlock 1, in which it was heated for 5 min at 110°C. Under these conditions, a free primary amine, if present, interacts with ninhydrin and results in the formation of a complex with the characteristic Ruhemann's blue color or due to the lack of any primary amine, no interaction takes place, and the color of the beads remains colorless/yellow [265].

Table 13. Kaiser test solutions and their constince.

Kaiser test solutions	Content
Solution I	5% w/v Ninhydrin in EtOH
Solution II	40 g Phenol in 10 mL EtOH
Solution III	2 mL of aqueous 0.001M KCN in 100 mL pyridine

3.2.1.4 Acetaldehyde/Chloranil test

Kaiser test is a quick and efficient method for detecting the process of coupling and Fmoc-deprotection during peptide synthesis, but as mentioned above, it is limited only for the detection of primary amines. However, the N-terminus of Pro has a secondary amine instead and the Kaiser test will not provide us insights whether the Fmoc of the Fmoc-Pro-peptide-resin is cleaved and the subsequent amino acid is coupled. Under these circumstances, acetaldehyde/chloranil test was applied. The required solutions were not older than one month and they were stored in fridge after their use (Table 14). Three drops of each of solution were added into a glass test tube together with few beads of peptide-resin and let at RT for 5 min after short mixing. Dark-blue green colored beads indicated the presence of an unprotected amino-group, while colorless to yellowish beads indicated its absence.

Table 14. Acetaldehyde/Chloranil test solutions and their constince.

Acetaldehyde/Chloranil test solutions	Content
Solution I	2% v/v acetaldehyde in DMF
Solution II	2% w/v chloranil in DMF

46

3.2.1.5 Automated solid-phase peptide synthesis (SPPS)

Automated solid-phase peptide synthesis (SPPS) is a suitable technology to produce fast and efficient the desired peptides. Several automated synthesizers, apply heat or microwave to reduce the coupling and subsequently the peptide synthesis time. However, peptide researchers have shown that higher temperatures favor side reactions, including the aspartimide formation [266]. In the current work, various peptides were synthesized fully or partially via the automated peptide synthesizer CS 336X (CS-Bio Inc, CA, USA). Fmoc-amino acid(s)-resin was transported in a glass reaction vessel in which Fmoc-deprotection, coupling, acetylation, and DMF-washes in the between took place. Fmoc-deprotection was performed essentially as described above, either with 20% v/v piperidine in DMF (5 and 20 min) or with the same solution containing 0.1 M HOBt (3 and 9 min), depending on the absence or the presence of aspartic acid in sequence, respectively. Fmoc-amino acid and activator (HATU or HBTU) were weighted in a plastic reaction tube and dissolved in a DIEA/DMF solution prior to its transportation to the glass reaction vessel, and coupling took place. Each amino acid was coupled either with HBTU twice for 40 min or one time with HATU for 1 h and twice with HBTU. Likewise, Ac_2O was added in another plastic reaction tube, and the capping was carried out as the coupling. All equivalents of the coupling and acetylation reagents were kept constant, as described. Couplings of Fmoc-Cys(Trt)-OH, Fmoc-non natural amino acids and N-terminus labeling were not applied in the synthesizer in order to avoid either racemization or insufficient yields. After the end of the automated synthesis, Fmoc-peptide-resin was transported back in the syringe either for further elongation of the sequence or for cleavage.

3.2.1.6 N-terminus labeling of peptides

Peptides may be applied in several assays and systems which require their labeling for monitoring the results. The chosen approach for synthesizing the labeled peptides was to conjugate the selected label on the side-chain group protected peptide-resin via Fmoc-SPPS chemistry. Either 20 or 40 mg of Fmoc-peptide-resin were swelled with DMF, Fmoc-deprotected, and subsequently washed with DMF before the coupling. 5(6) carboxyfluorescein (Fluos) was coupled in 3-fold molar excess together with HATU (3-fold molar excess) and DIEA (4.5-fold molar excess) for 2 h, two times. 5-TAMRA (5-Carboxytetramethylrhodamin) was coupled with the same reagents and molar excess as Fluos but only once, overnight. All couplings and storage of the labeled peptide resin were done in light-protected conditions to protect the photosensitive fluorophores. In the case of biotin, it was necessary first to attach aminohexanoic acid as a spacer between the molecule and the resin. Coupling of 6-(Fmoc-amino)hexanoic acid (Fmoc-6 Ahx-OH) was achieved with a 3-fold molar excess of the spacer under the presence of HBTU (3-fold molar excess) and DIEA (4.5-fold molar excess) for 1 h, three times. After Fmoc-deprotection and DMF-wash of Fmoc-6 Ahx-peptide-resin, biotin was N-terminusly conjugated under the same conditions that were applied for Fmoc-6 Ahx-OH.

3.2.1.7 Deprotection of side chains and cleavage of peptide from the resin

A successful peptide synthesis ends when the last amino acid is coupled on the resin. However, the peptide is still not ready for purification. Detachment of peptides from the solid support of resin and eliminating the side chain protected group is a necessary procedure before injection to the RP-HPLC. This process occurs with aqueous TFA solution in Fmoc-SPPS unless the peptide contains nucleophilic functional groups, such as Trp, Met, Tyr, and Cys. These residues might get chemically modified due to the generation of highly reactive cationic species during the cleavage process. To quench these cations and prevent undesired side reactions, scavengers (nucleophilic reagents) are added to the TFA [267]. Among several mixtures, the most used one is Reagent K (TFA: water: phenol: thioanisole: EDT 82.5%: 5%: 5%: 5%: 2.5%) and all peptides described here were cleaved using it [267]. 40 mg peptide-resin were incubated with 1 mL of Reagent K for 3 h under shaking at RT. Peptide-containing cleavage solution was collected in a plastic centrifugation tube with the two thirds of the volume being filled with two times distilled cold water. Next, cold Et_2O was added to the plastic centrifugation tube (Cellstar® Tubes, 15 mL) to fill it and the mixture was gently shaken and centrifuged for 3 min at 3000 rpm. The organic phase was discarded, Et_2O was re-added, and the process was repeated. After three ether extractions, the cleavage solution was diluted with water to reduce the TFA percentage below 10%. The solution was frozen, lyophilized, and the crude peptide was obtained in powder the next day.

3.2.1.8 Formation of intra-peptide disulfide bridges

The crystal structure of CXCR4 provided several conformational insights for the receptor, such as the presence of a disulfide bond connecting Cys109 (ECL1) and Cys186 (ECL2). Both residues are present in msR4M-L1 and msR4M-L2 sequences and were connected via an intra-peptide disulfide bridge, forming their oxidized analogs msR4M-L1ox and msR4M-L2ox, respectively. Disulfide bridges were created for both peptides in a crude peptide solution of 1 mg/mL in aqueous 3 M guanidinium chloride (GdnCl) 0.1 M ammonium carbonate (NH_4HCO_3) solution, containing 40% DMSO. Likewise, msR4M-LS was generated with 0.3 mg/mL ECL1 and 0.5 mg/mL ECL2 in the same buffer, but it contained 20% DMSO instead. The mixtures were stirred in RT for at least 3 h.

3.2.2 Purification and characterization of peptides

3.2.2.1 Reversed-phase HPLC (RP-HPLC)

Reversed-phase HPLC (RP-HPLC) is a common and efficient purification method of peptides. Herein, the stationary phase consisted of a column made up of 18 carbon atoms on each chain (C18) chemically bound to a silica support tandem with a shorter length column (pre-column) having the same internal diameter and particle size. A tandem system of Reprosil Gold 200 C18 columns (250 and 30 mm length, 8 mm internal diameter, 10 µm particle size) and another of Reprospher 100 C18-DE (250 and 30 mm length, 8 mm internal diameter, 7 µm particle size) were applied for peptide separation and purification. The mobile phase was composed of the polar HPLC buffer A (0.058% v/v TFA in water) and the less polar HPLC buffer B (0.05% v/v TFA in 9:1 ACN: water) [253]. Each analytic program had the flow rate set

at 2 mL/min, while the consistency of the mobile phase changed during the time as described in the Table 15.

Table 15. Applied HPLC-gradient programs.

HPLC-programs Number/Name	Time (min)	Buffer A (%)	Buffer B (%)
1. "Fast Aβ"	0	90	10
	1	90	10
	31	10	90
2. "Fast Aβ 20-80-60m"	0	80	20
	1	80	20
	60	20	80
3. "Slow Aβ"	0	70	30
	7	70	30
	37	30	70
4. "40-80% B for Nle3"	0	60	40
	7	60	40
	8	50	50
	38	20	80
	38.5	0	100
	40	0	100
5. "Fast-fast Aβ"	0	90	10
	1	90	10
	7	10	90

For each program, the mobile phase composition was kept constant to its t=0 min conditions at least for 10 min before injection. Crude peptide or purified peptide that needed repurification was dissolved in a TFA mixture: buffer A: buffer B (15%: 17%: 68%) and injected for analysis. Peptide peaks were collected based on their absorbance at 280 nm if Tyr or Trp are present in the sequence, 254 nm if Phe but not Tyr, Trp, and 214 nm if none of the above residues in present in the peptide sequence. Fluos- and TAMRA-labeled peptides were purified after following their absorbance at 432 nm. All collected samples were frozen and lyophilized before the determination of their molecular weights.

3.2.2.2 Matrix-Assisted Laser Desorption/Ionization time-of-flight mass spectroscopy (MALDI-TOF-MS)

MALDI-TOF-MS (Bavarian Center for Biomolecular Mass Spectrometry, BayBioMS) was mainly applied for the detection of the molecular weight of the synthesized peptides. Few spots of peptide powder were dissolved in either solution A or B and mixed in 1-to-1 proportionality with the respective solution A (matrix) or B (matrix) saturated by cyano-4-hydroxycinnamic acid (4-HCCA). A drop of the mixed solution was transported on the MTP 384 target plate, dried completely and washed with an aqueous solution of 10 mM $NH_4H_2PO_4$ 0.1% TFA for suppressing matrix cluster ions. For some peptides, their powder was dissolved immediately in solution C (matrix) and spotted on the target plate (Table 16). Peptide calibrant was used for the calibration and precise determination of the molecular weights of the samples.

The analysis was performed on positive ion mode for the detection of monoisotopic mass (M is monoisotopic mass) [268].

Table 16. Solutions that were applied in MALDI-TOF-MS analysis.

Name	Solution (Composition)
Solution A	97% v/v acetone, 0.1% TFA in aqueous solution
Solution A (matrix)	Aqueous solution of 97% v/v acetone, 0.1% TFA, saturated by 4-HCCA
Solution B	16.67% v/v FA, 33.34% v/v iPrOH in aqueous solution
Solution B (matrix)	Aqueous solution of 16.67% v/v FA, 33.34% v/v iPrOH, saturated by 4-HCCA
Solution C (matrix)	Aqueous solution of 49.95% v/v ACN, 0.1%TFA v/v, 10% w/v 2,5-DHAP in aqueous

3.2.3 Synthesis of peptide arrays using CelluSpots method

Peptide arrays were generated on cellulose membrane (Intavis Bioanalytical Instruments AG) using the Intavis MultiPep RSi automated multiple peptide synthesizer on the Celluspot method (Intavis, Cologne, GER). Cellulose membrane was mounted into 384-well-footprint synthesis frames (CelluSpots frames, Intavis Bioanalytical Instruments AG), and the individual amine-derivatized cellulose disks of 2.7 mm diameter were ready for peptide synthesis [269]. The procedure was based on the principles of Fmoc-SPPS with repeating circles of Fmoc-deprotection, Fmoc-amino acid coupling, and acetylation steps in RT. The discs were washed with DMF in between of each step, dried with EtOH, and all solutions were pulled through the disks via vacuum [270]. Fmoc-deprotection was performed using 2 and 4 µL 20% v/v piperidine in DMF for 5 and 10 min and the acetylation with 4 µL 5% v/v Ac$_2$O in DMF for 5 min. All coupling solutions were prepared in DMF, and the ones containing the N-terminus protected amino acid were substituted every 24 h by fresh ones. Coupling of each amino acid was performed twice with the addition of 0.6 µL of Fmoc-protected amino acid (0.5 M), 0.3 µL of HOBt (1.1 M), and 0.3 µL of DIC (1.1 M) on each disk for a minimum time 30 and 40 min.

Following the coupling of the last amino acid, the N-terminus was deprotected four times (5, 10, and two times 15 min subsequently) and acetylated three times (5 min each time) by 4 µL of the respective solution for each time. The disks were washed with DMF, dried with EtOH and air, and stored at -20°C. Peptides were side-chain deprotected, dissociated from cellulose membrane, and spotted onto coated glass slides by the group of Prof. Bernhagen. Additionally, the microarrays were blocked for unspecific binding, probed with 3 µM biotinylated recombinant human MIF, and developed with horse-radish peroxidase (HRP)-conjugated streptavidin. Chemiluminescence intensity was quantified with a LICOR Odyssey Fc Dual-Mode Imaging System (LICOR), and after being corrected for spot-specific background signal and checked for false positives, the values were provided back to us for interpretation.

3.2.4 Preparation and concentration determination of stock solutions

Many different stock solutions were prepared of either peptides or proteins. Concentrations, solutions, and methodologies may vary, depending on the requirement of the assay. In order to clarify how the stock was prepared in each case, the preparations procedures were classified in the following categories:

- Preparation of labeled peptide stock solutions

After HPLC and MALDI analysis, an amount of pure Fluos-peptide was dissolved in cold HFIP and filtered (0.2 µm). UV-Vis spectrum of the filtered solution was recorded between 200 and 600 nm, and the absorbance at 432 nm (ε_{432} = 22770 $M^{-1} \cdot cm^{-1}$) was applied in the Lambert-Beer law for the concentration determination of the Fluos-peptide [271]. Based on the emission of the labeled peptide, substocks in the 1-5.33 µM range were prepared. Stock solutions of TAMRA-msR4M-L1 were prepared by dissolving an aliquot of the known amount in aqueous 20 mM NaPPi (2×b), pH 7.2. The aliquot amount was estimated the previous day when the labeled-peptide was dissolved in HFIP and analyzed by UV-Vis spectroscopy. Its absorbance at 547 nm (ε_{547} = 71391 $M^{-1} \cdot cm^{-1}$) was introduced in Lambert-Beer law and the TAMRA-msR4M-L1 concentration was determined. In both cases, the labeled peptide was evaporated and reconstituted in a cold solution of 80% buffer B: 20% buffer A (80% B), aliquoted, frozen immediately, lyophilized, and stored as a powder form at -20°C until the day of the assay.

- Preparation of unlabeled peptide stock solutions

All peptides were HPLC purified in TFA salt form, and their purity was determined with MALDI-TOF-MS. An amount higher than 1 mg of each peptide was weighed in an analytical balance and dissolved by a cold of solution of 80% B. Peptide was aliquoted, frozen immediately, lyophilized, and stored as a powder form at -20°C. Shortly before each experiment, the required peptide aliquot was dissolved in HFIP, vortexed gently, and stored on ice until the measurement. Peptides were not constituted in HFIP but in other solutions in the following cases:

o Studies of MIF(47-56) and MIF-cyclic analogs with Circular Dichroism (CD) spectroscopy: Peptides were dissolved in aqueous 10 mM NaPPi (1×b), pH 7.4

o Studies of the effect of msR4M-L1 in the Alexa-647-MIF/sCD74 complex: msR4M-L1 stock solution was prepared in aqueous 10 mM Tris, pH 8.0.

All substock solutions were made with serial dilutions in the same buffer that the stock was.

- Preparation of unlabeled and labeled MIF, MIF mutants and MIF-2 stock solutions

All proteins were expressed, purified, folded in a known concentration, labeled if necessary, and provided for assays by the group of Prof. Bernhagen (LMU, GER). Proteins were stored in 4°C and constituted in aqueous 20 mM NaPPi (2×b), pH 7.2, except for Alexa-647-MIF, which was prepared in aqueous 10 mM Tris, pH 8.0. All substock solutions were made with serial dilutions in the same buffer that the stock was.

- Preparation of CXCL12 stock solutions

In fluorescence spectroscopic titrations of Fluos-msR4Ms and CXCL12, the chemokine was constituted in aqueous 2×b, pH 7.2, and provided by the group of Dr. von Hundelshausen (LMU, GER). In the rest cases, the protein was purchased from

Peprotech (Hamburg, GER), dissolved in two times distilled H_2O and stored at -80°C until the titration took place. The protein stock solution was prepared for the Fluorescence spectroscopic titrations of Fluos-ngms, Fluos-CRMs, and CXCL12 and for fluorescence polarization spectroscopy studies in two times distilled H_2O. Regarding microscale thermophoresis, CXCL12 stock solution was prepared in aqueous 2×b, pH 7.2, after prior dissolution in two times distilled H_2O. All substock solutions were prepared with serial dilutions of the stock under the same dissolving conditions.

- Preparation of sCD74 stock solutions

sCD74 was purchased from R&D Systems (Minnesota, USA), dissolved in aqueous 1×PBS, pH 7.2, and stored at - 20°C until its titrations were carried out. For the fluorescence polarization spectroscopic titrations, the stock and the substock solutions were prepared in the same buffer. In the case of microscale thermophoretic studies, the stock and the substock solutions consisted of aqueous 10 mM Tris, 0.5×PBS, pH 8.

- Determination of peptide concentration via bicinchoninic acid (BCA) protein assay

BCA protein assay was performed for the quantification of peptide powders that were weighted below 1 mg. With this method, peptides can reduce Cu^{+2} to Cu^{+1} in an alkaline solution (the biuret reaction) and concludes in a purple color formation by bicinchoninic acid that exhibits a strong linear absorbance at 562 nm [272]. The kit was used to determine the exact amount of MIF(51-67) with reference MIF(56-69), R2ECL2(188-198) with reference R2ECL2(186-198) and CRM-1/L4 with reference CRM-1/L4ox in order to apply them in biophysical assays.

- Exchange of trifluoroacetate counter-ion of msR4M-L1 before their *in vivo* administration

All peptides were obtained after HPLC purification in TFA-salt form. Prior to its *in vivo* administration to Apoe-/- mice, the lead mimic msR4M-L1 was dissolved in cold 5 mM aqueous HCl in a 200 µg/mL concentration after intensive shaking, frozen and lyophilized. The same process was repeated three additional times [273]. Finally, msR4M-L1 was dissolved in a concentration of 50 µg/mL in two times distilled water frozen and lyophilized before handling the group of Prof. Bernhagen.

3.2.5 Circular Dichroism Spectroscopy (CD)

Circular dichroism spectroscopy (CD) is a widely used method of determining the secondary structure of peptides and proteins. CD may not provide insights into the secondary structure of particular residues like NMR or X-ray crystallography. However, it is significantly more time-and cost-efficient and a method with minimized amount demands. The optical activity of peptides is due to the asymmetric α-carbon atoms in all amino acids except for Gly and the asymmetry of the polypeptide chain in proteins [274]. The alignment of the chromophore amides in arrays causes the shift of their optical transitions or split into multiple transitions due to "exciton" interactions, resulting in characteristic CD spectra for structure [275]. CD-spectra of α-helical peptides or proteins have the minima on their negative bands at 222 nm and 208 nm. Peptides/proteins with β-sheet or unordered conformation have minimum between 215 and 220 nm and maximum of 195 nm (Figure 13a) [276]. Other studies shed more light on the spectra, and their interpretation might give more details about the nature of the α-helix or β-sheet (Figure 13b, c) [277].
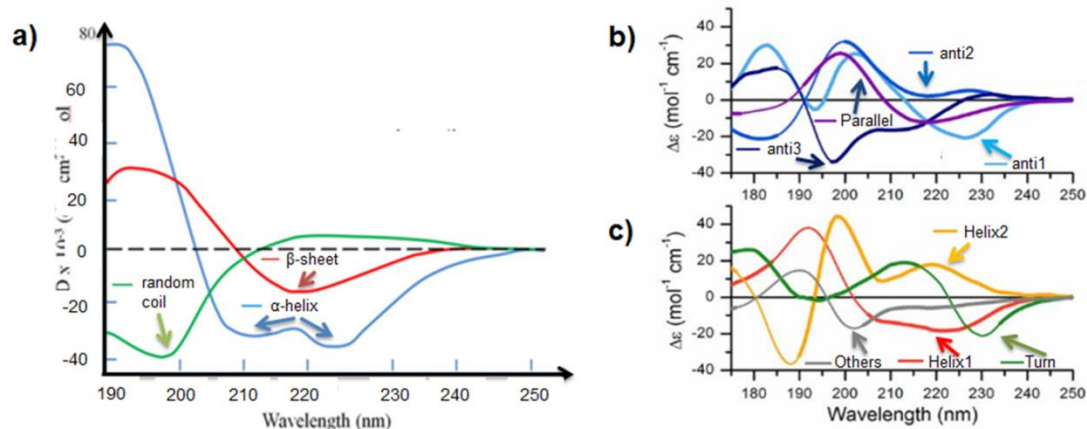
Figure 13. Templates of CD far-UV spectra and their corresponding secondary structures. a A 190-250 nm template of CD far-UV spectra with the characteristic signal shape of α-helix in blue, β-sheet in red and random coil in green (adapted from Wei et al., ref. [276]). **b** CD far-UV spectra templates in the 175-250 nm range with the characteristic signal shape of parallel β-sheet in purple (parallel), left-hand twisted antiparallel in light blue (anti1), relaxed antiparallel in blue (anti2) and right-hand twisted antiparallel in dark blue (anti3) (adapted from Micsonai et al., ref. [277]). **c** As in b with the characteristic signal shape of regular α-helix in red (helix1), distorted α-helix in yellow (helix2), turn in green (turn) and 3_{10} helix in grey (Others) (adapted from Micsonai et al., ref. [277]).

3.2.5.1 Concentration dependence studies

Circular dichroism spectra were recorded on a JASCO J-715 spectro-polarimeter (JASCO, Pfungstadt, GER) using already applied protocols [278]. Far-UV CD spectra were obtained between 195 and 250 nm in a continuous scanning mode with a scanning speed of 100 nm/min. The response time was set at 1 s, the intervals at 0.1 nm, and the bandwidth at 1 nm. All scans were carried out at RT, and the presented spectra are average of three spectra. CXCR2 and CXCR4-derived peptides and mimics were freshly dissolved in cold HFIP at 1 mM and measured in final conditions of aqueous 1×b, pH 7.4, 1% HFIP. Peptide stock solutions were diluted into the buffer-containing quartz cuvette in a concentration range varying from 1 to 50 µM, mixed, and then measured. Under the same conditions, they were collected the spectra of MIF(38-80), MIF(50-80), MIF(54-80) between 1 and 5 µM and the 1:1 mixture of ECL1 and ECL2, with the concentration of each ectodomain peptide being equal to 5 µM. MIF(47-56) and its cyclic derived analogs were dissolved at a final concentration of 5, 10, 20, 50 or 100 µM in aqueous 1×b, pH 7.4, vortexed, and transferred to quartz cuvettes for being measured. Stock solutions of proteins were prepared folded in aqueous 2×b, pH 7.2 and kept for a short time in 4°C before the signal analysis at aqueous 1×b, pH 7.4.

All spectra were measured at RT in quartz cuvettes of 0.2, 0.5, 1 or 2 cm and represent an average of three recorded spectra. The background spectrum of the assay buffer alone was subtracted from the CD spectrum of each sample's measurement and then the raw data were converted to mean residue ellipticities (MRE). Dynode voltage values were below 1000 V and did not interfere with CD measurements. MRE was calculated based on Equation 2.

Equation 2. Determination of MRE.

$$\text{MRE}\left[\frac{\deg \cdot \text{cm}^2}{\text{dmol}}\right] = \frac{100 \cdot \theta}{c \cdot d \cdot n}$$

MRE: mean residue ellipticity (deg·cm^2·dmol^{-1})
θ: ellipticity
c: concentration (M)
l: optical path length (cm)
n: number of amino acids

The deconvolution of the obtained spectra and the estimation of the secondary structure of the proteins was performed after importing the data to the Dichroweb online software (http://dichroweb.cryst.bbk.ac.uk/html/home.shtml) analyzing them with the program Contin LL via the reference spectra Set 7 [279] [280] [281].

3.2.5.2 Interaction studies

CD spectroscopy was applied for studies on the secondary structure of peptides and MIF mixtures in various concentrations. The experimental setup was maintained essentially the same as described in chapter 3.2.5.1, and the spectra were analysed based on their ellipticities. Spectra of peptide and MIF were firstly individually measured in the required concentrations and then another sample with their mixture on the same concentrations and conditions (aqueous 1×b, pH 7.4, 1% HFIP) was analyzed. The measured ellipticity from the peptide/MIF sample was compared with the expected signal herein named "Sum", which was obtained by the mathematical addition of their individual spectra.

3.2.6   Fluorescence spectroscopy

3.2.6.1 Titrations between labeled-analyte and titrant

Fluorescence emission was monitored with a JASCO FP-6500 fluorescence spectrophotometer (JASCO, Pfungstadt, GER), based on previously described experimental protocols [282] [238]. Fluos-peptide or Alexa-488-MIF were applied as analytes and unlabeled peptides or proteins as titrants. All peptide stock and substock solutions were freshly prepared in cold HFIP. Unlabeled and labeled MIF (wild-type and mutants), CXCL12 (when titrated with Fluos-msR4Ms) and MIF-2 and were folded in aqueous 2×b, pH 7.2. Stock solutions of CXCL12 and IL-8 that were applied in the titrations with Fluos-ngms and Fluos-CRMs, were prepared in two times distilled water. Labeled-analyte and unlabeled titrant were mixed in assay buffer and measured in final conditions of aqueous 1×b, pH 7.4, containing 1% HFIP. Under the final measuring conditions, the labeled peptide or protein is in the low nanomolar range (5-26.7 nM), while the concentration of the titrant varies from 0.05 to 40000 nM. In the case of the titration with the DMSO-dissolved ISO-1, Alexa-488-MIF had a concentration of 50 nM, and ISO-1 varied from 0.1 to 500 µM in aqueous 1xb, pH 7.4, containing 0.5% DMSO.

All mixtures were measured in a quartz cuvette at RT. The excitation wavelength was set at 492 nm, and the fluorescence emission spectra were obtained between 500 and 600 nm within 2-3 min following the solution preparation. Apparent K_{ds} (app. K_{ds}) were calculated based on the emission at 519 nm for Alexa-488-MIF and 522 nm for Fluos-peptide by applying 1/1 binding models and were means (±SD)

from three binding curves. Sigmoidal curve fittings and estimation of affinities of interactions (app. K_d) were performed with Origin software using the Equation 3.

Equation 3. **Determination of app. K_d by Origin software** [282].

$$F = F_0 + \frac{F_{max} - F_0}{1 + 10^{[(\log K_d - L) \cdot s]}}$$

F: fluorescence intensity
F_0: fluorescence intensity of the Fluos-labeled peptide
F_{max}: maximal fluorescence intensity
$\log K_d$: logarithm of the dissociation constant
L: concentration of the ligand
s: slope of the curve

In case that the calculated K_d is below 20-fold of the concentration of the labeled-analyte, a second mathematic formula was additionally applied using the GraFit software to calculate the dissociation constant (Equation 4).

Equation 4. Determination of app. K_d by GraFit software [282].

$$F = F_{min} + (F_{max} - F_{min}) \cdot \frac{\sqrt{\frac{[E_0] + [L_0] + [K_d]}{2} - \frac{([E_0] + [L_0] + [K_d])^2}{4} - [E_0] \cdot [L_0]}}{[L_0]}$$

F: fluorescence emission
F_{min}: minimum fluorescence emission
F_{max}: maximum fluorescence emission
L_0: concentration of the labeled peptide
E_0: concentration of the unlabeled peptide
K_d: dissociation constant (app. K_d)

3.2.6.2 ANS binding studies

8-anilino-1-naphthalenesulfonic acid (ANS) is a fluorescent dye that binds to exposed hydrophobic surfaces of proteins and may provide insights into their solvent-exposed residues and their unfolding propensity [283] [270]. The binding interaction between ANS and the hydrophobic species of peptides or proteins leads to an increased fluorescence emission and a blue shift for its maxima. Thus, the comparison of the fluorescence over increased ligand concentration may shed light on the solvent-exposed hydrophobic content and the changes on the surface, if any. JASCO FP-6500 fluorescence spectrophotometer (JASCO, Pfungstadt, GER) was applied for monitoring the changes of the fluorescence emission of the dye. Parameters were set up as 355 nm for the excitation wavelength, 5 nm the bandwidth, 1 s the response time, 1 nm of data pitch, while the scanning speed was 100 nm/min and the spectra were recorded between 355 and 650 nm. Peptides and ANS were always mixed in a constant proportionality 1 to 2 and measured immediately after with the final measuring conditions being aqueous 1×b, pH 7.4, 1% HFIP. Under the same conditions, a spectra with the same ANS amount but without the peptide was recorded. Its signal was subtracted from the peptide/ANS spectra before analyzing the data to remove the background emission.

3.2.6.3 Fluorescence Polarization Spectroscopy (FP)

Fluorescence polarization spectroscopy (FP) is an alternative technique for the measurement of ligand binding. Its principle is that fluorescent molecules when excited by polarized light, emit light with a degree of polarization that has inverse proportionality to molecular rotation speed. Consequently, the observed polarization will be differentiated between the cases of labeled-molecule A and labeled-molecule A/unlabeled-molecule B due to the different rotation of the label. Thus, FP might be used as a technique for the measurement of ligand binding [284]. FDP-223 and FDP-243 polarizers were attached to the JASCO FP-6500 fluorescence spectrophotometer for monitoring the titrations. The bandwidth was set for both excitation and emission at 5 nm, time response at 0.5 s, sensitivity at medium and the excitation wavelength at 492 nm. The fluorescence polarization was recorded at 522 nm for Fluos-peptides and at 519 nm for Alexa-488-MIF.

Peptides and protein solutions were prepared as described in the chapter 3.2.4, mixed in the quartz cuvette with the assay buffer, and measured. Fluos-msR4M-L1 was titrated against MIF and CXCL12 at aqueous 1×b, pH 7.4, 0.5% HFIP, while the final measuring conditions between Alexa-488-MIF and msR4M-L1 were aqueous 1×b, pH 7.4, 2% HFIP. The final concentration of the labeled molecule was kept constant (5 nM for Fluos-msR4M-L1 and 10 nM for Alexa-488-MIF), and measurements were done within 2-3 min following preparation of the solution. Regarding Alexa-488-MIF and sCD74 mixtures, they were prepared at aqueous 1×b, 2% HFIP, 0.01×PBS and incubated at RT for approximately 4 h before measurement. For the competition experiments with msR4M-L1, Alexa-488-MIF was mixed and pre-incubated shortly with a 20-fold excess of msR4M-L1. Then, sCD74 was added and the mixtures were under the same conditions and incubation time as previously. Measurements were obtained inside a quartz cuvette at RT after adjustment of the angles of the polarizers. Bandwidth was set for both excitation and emission at 5 nm, time response at 0.5 s, sensitivity at medium, and the excitation wavelength at 492 nm. The fluorescence emission was recorded at 519 nm for Alexa-488-MIF and at 522 nm for Fluos-msR4M-L1. Polarization (P) was calculated using the Equation 5.

Equation 5. Calculation of polarization (P) values [284].

$$P = \frac{I_{\parallel} - G \times I_{\perp}}{I_{\parallel} + G \times I_{\perp}}$$

I$_{\perp}$: intensity of emitted light polarized perpendicular to the excitation light (polarizer on the excitation side: 90°, polarizer on the emission side: 0°)
I$_{\parallel}$: intensity of emitted light polarized parallel to the excitation light
(polarizer on the excitation side: 90°, polarizer on the emission side: 90°)

G is a correction factor which depends on each instrument and the specific optical components used to measure fluorescence polarization. Its value should be determined following the instrumental documentation and should be re-calculated every time after installing the polarizers on the spectrophotometer. Here it is calculated from the Equation 6, based on the polarization of a sample containing the labeled-analyte alone [284].

Equation 6. Calculation of correction factor G.

$$G = \frac{i_\perp}{i_\parallel}$$

i$_\perp$: intensity of emitted light polarized perpendicular to the excitation light
(polarizer on the excitation side: 0°, polarizer on the emission side: 90°)
i$_\parallel$: intensity of emitted light polarized parallel to the excitation light
(polarizer on the excitation side: 0°, polarizer on the emission side: 0°)

3.2.7   Microscale Thermophoresis (MST) binding assays

MST titrations were monitored by Monolith NT.115 with green/red filters (NanoTemper Technologies, Munich, GER) at Biophysics Core Facility at the School of Biology of LMU Munich with the contribution of Markus Brandhofer (group of Prof. Bernhagen). MST power was set at 80% and LED power at 80 and 95% for the titrations with Alexa-647-MIF and TAMRA-msR4M-L1, respectively. MST traces were tracked for 40 s, with the laser being switched off for the first 5 s, turned on for the next 30 s, and switched again off for the last 5 s. Stock and substock solutions of analytes and titrants were prepared as described in chapter 3.2.4, mixed in 1:1 proportionality, incubated for a specific time in RT and/or 37°C, before the transportation on the capillaries and the measurements.

Mixtures of TAMRA-msR4M-L1 and MIF or CXCL12 were incubated at RT for 8-12 min with the concentration of the labeled analyte being constant at 100 nM, while proteins varied from subnanomolar to low μM. Samples were measured under final conditions of aqueous 2×b, pH 7.2, 0.1% Tween 20 at 37°C and analyzed using the signal from an MST-on time of 1.5 s (Figure 14a). Alexa-647-MIF/sCD74 mixtures (1:1) were incubated at RT for 3 h, and after their load in the capillaries, it followed an additional incubation for 15 min at 37°C. In the final measuring conditions, 20 nM of Alexa-647-MIF was titrated against 0.1976 to 809.25 nM sCD74 in aqueous 10 mM Tris, 0.25×PBS, 0.01% BSA, pH 8, at 37°C.

To study the role of msR4M-L1 on the MIF/sCD74 binding, Alexa-647-MIF and msR4M-L1 were pre-mixed in aqueous 10 mM Tris, pH 8.0, leading to concentrations of 40 and 400 nM respectively, and incubated at RT for 10 min. Afterward, sCD74 was added to the pre-mixed solution in 1:1 proportionality, and titrations were performed as above. The reported measurement values were obtained from the signal from the MST-on time of 30 s (Figure 14b). For each sample, the fluorescence intensity was normalized using the Equation 7 [285]:
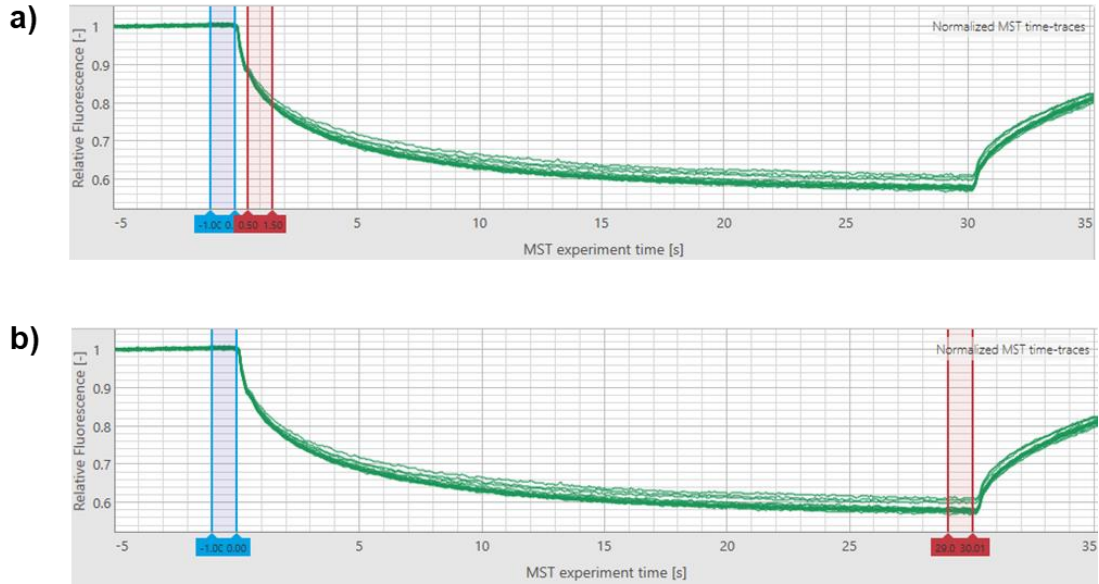
Equation 7. Calculation of F$_{norm}$ [285].

$$F_{norm} = \frac{F_{hot}}{F_{cold}} \times 1000$$

F$_{norm}$: normalized fluorescence, [‰]
F$_{hot}$: fluorescence on MST-on time of 1.5 or 30 s, a.u.
F$_{cold}$: initial fluorescence, before laser was switched on, a.u.

Figure 14. Representative signal of a titration analyzed by MST. Before the application of IR laser (-5 to 0 s), the sample is homogeneous and the fluorescence is stable (F_{cold} indicated in blue in both Figures a and b). Immediately after the laser activation, there is a temperature-induced change in the fluorescence emission. IR-laser remained switched on for a total of 30 s and then it was switched off. **a, b** Mean fluorescence emission between 0.5-1.5 s (a) or 29-30 s (b) after IR-laser was switched on was considered as F_{hot} (indicated in red in both Figures a and b).

However, in some cases, the curves may start at different F_{norm} levels and/or show different amplitudes, making comparing them difficult. To overcome this problem, ΔF_{norm} was introduced. To determine it, the F_{norm} of the lowest concentration of its titration (unbound state) is subtracted from all data points of the same curve and ΔF_{norm} is calculated as shown in Equation 8.

Equation 8. Calculation of ΔF_{norm} [286].

$$\Delta F_{norm} = F_{norm} - F_{norm(unbound\,state)}$$

ΔF_{norm}: baseline subtracted normalized fluorescence
F_{norm}: normalized fluorescence of the sample
$F_{norm\,(unbound\,state)}$: normalized fluorescence of the unbound state, as determined by MO.Affinity Analysis software version 2.3, NanoTemper Technologies

Thus, by definition, ΔF_{norm} is 0 in the unbound state and might adopt positive or negative values, if binding occurs, depending on the direction of the response amplitude. In case that the amplitudes may differ, the response curve with the smaller amplitude might mistakenly be interpreted as a non-binder. For that reason, the fraction bound normalization might be applied as an alternative, if there is binding. All F_{norm} values of a curve are divided by the curve amplitude, resulting in the fraction bound (FB) for each data point. FB can take values between 0 to 1 and is calculated using the Equation 9 [285]:

Equation 9. Calculation of FB [285].

$$FB = \frac{F_{norm} - F_{norm(unbound\,state)}}{F_{norm(bound\,state)} - F_{norm(unbound\,state)}}$$

FB: fraction bound

Data from all curves were interpreted with FB normalization, except for the TAMRA-msR4M-L1 to CXCL12 titration in which ΔF_{norm} was applied. All app. K_{ds} were calculated as described above and were means ($\pm$SD) from three binding curves.

3.2.8 Proteolytic stability studies of peptides in human plasma *in vitro*

A previously developed proteolytic stability assay for quantifying the peptide present in plasma after a specific time was applied to study the proteolytic stability of MIF (47-56) and MIF(cyclo10) [287]. 44 µL of human plasma derived by voluntary healthy donors were added to 20 µg aliquoted peptide powder, and the incubations were carried out at 37°C for the required time. After the incubation time, the samples were pipetted and with 44 µL of aqueous 10% v/v trichloroacetic acid (TCA) and vortexed shortly. The samples were kept on ice for 10 min prior to their centrifugations in 20200 g for 4 min with an Eppendorf centrifuge 5417C (Netheler-Hinz GmbH (Hamburg, GER). Supernatants were separated from precipitates and mixed in 1 to 2 proportionality with a solution consisting of 80% B. As next, the mixed supernatants were analyzed by RP-HPLC at 214 nm using a Nucleosil 100 C18 column (Grace) (length 33 mm length, ID 8 mm, 7 µm particle size) and a flow rate at 2.0 mL/min. HPLC program 5 was applied and the collected peaks were further characterized by MALDI-TOF-MS (Bruker Daltonics, Bremen, GER).

4 Results

4.1 MIF-specific CXCR4 mimics (msR4Ms)

The MIF/CXCR4 pathway is shown to trigger pro-atherogenic signaling and therefore the MIF/CXCR4 interaction appears to be a potential therapeutic target for the treatment of atherosclerosis [77]. Nevertheless, MIF and CXCR4 also exhibit cardioprotective activities via their interactions with CD74 and CXCL12, respectively [288] [289] [268] [197]. A MIF/CXCR4-specific targeting strategy that would spare the MIF/CD74 and CXCL12/CXCR4 interactions appeals thus a promising anti-atherosclerotic strategy [290]. Among other functions, rationally designed peptides could mimic the binding interface between proteins and receptors and block their interaction [240]. Previous studies on MIF/CXCR4 interaction interface revealed the necessity of the sequences 97-110 derived by extracellular loop 1 (ECL1) and of 182-196 derived by extracellular loop 2 (ECL2) of the receptor for the complex formation [98]. Herein, those two ectodomains derived peptides (ECDs) were chemically linked aiming at generating MIF-specific CXCR4 mimics (msR4Ms) that will not interfere in the MIF or CXCR4 mediated cardioprotective pathways (Scheme 3).
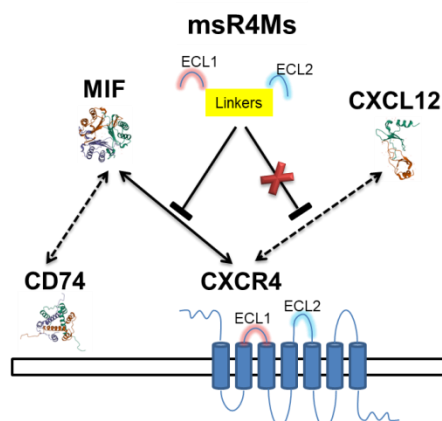
Scheme 3. Development of msR4Ms and the desired blockade of the atheroprogressive pathways. The CXCR4 mimics were developed after bonding of fragment 97-110 derived by extracellular loop 1 (ECL1) with the 182-196 fragment, derived by extracellular loop 2 (ECL2). The linked analogs aimed to act as MIF-specific CXCR4 mimics (msR4Ms) that will inhibit the atheroprogressive pathway (solid line) MIF/CXCR4 and spare the cardioprotective (dashed line) MIF/CD74 and CXCL12/CXCR4. The chemokines and the transmembrane protein are demonstrated based on their published structures (MIF:1MIF, CXCL12:3HP3, CD74:1IIE) [83] [101] [102] (adapted from Kontos et al., ref. [291]).

All peptides were synthesized using standard Fmoc-SPPS protocols and purified by HPLC and their purity was confirmed by MALDI-TOF-MS or ESI-MS. Initially, the secondary structure and the self-association propensity of the msR4Ms and ECDs were determined, as well as the exposure of hydrophobic residues of selected mimics Fluorescence spectroscopic titrations between the msR4Ms and MIF or CXCL12 uncovered two mimics (msR4M-L1, -L2) with ordered secondary structures that bound MIF but not CXCL12 with high affinity. Further studies were carried out to monitor the interactions between the prioritized peptide, msR4M-L1, and the two CXCR4 ligands with FP and MST. The last two techniques were applied to determine the effect of msR4M-L1 on MIF/CD74 binding. Furthermore, SAR studies mapped the binding interface and crucial residues of the MIF/msR4M-L1 interaction on both sides. Finally, the lead mimic was provided to the group of Prof. Bernhagen for additional *in vitro*, *ex vivo*, and *in vivo* studies (Scheme 4).
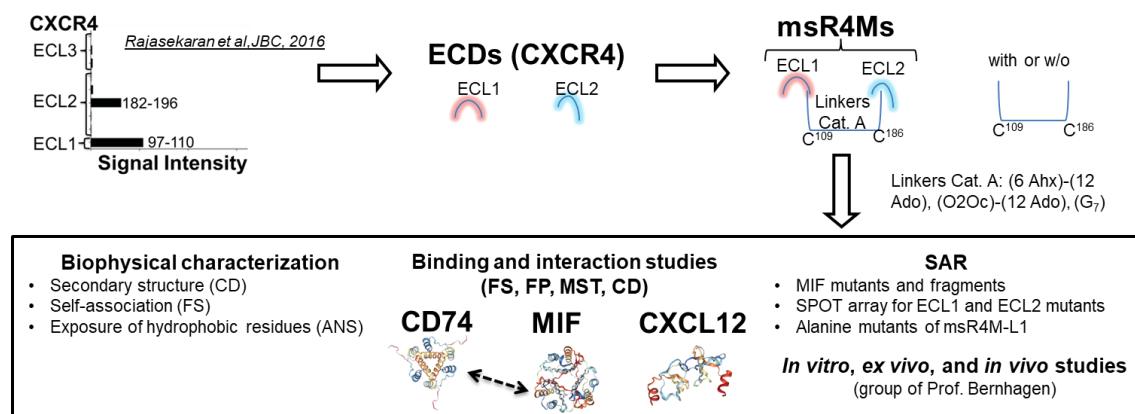
Scheme 4. Overview of the development and studies of msR4Ms. The development of MIF-specific receptor mimics (msR4Ms) and the applied linkers are shown, while the msR4Ms were tested both in reduced and oxidized form. Studies of msR4Ms aimed to determine their biophysical properties and their binding affinities with the CXCR4 ligands. Additional experiments were carried out for the lead mimic msR4M-L1 to define its effect on the MIF/CD74 formation, and its binding interface with MIF. The prioritized mimic was provided to collaborators from the group of Prof. Bernhagen for further studies. The chemokines and the transmembrane protein are demonstrated based on their published structures (MIF:1MIF, CXCL12:3HP3, CD74:1IIE) [83] [101] [102].

4.1.1 Design of msR4Ms

The MIF-selective peptide ectodomain mimics of CXCR4, msR4Ms, were designed to consist of the chemically linked ectodomain peptides (ECDs), ECL1 and ECL2, located at the 97-110 and 182-196 region of CXCR4, respectively (Scheme 5a). Initially, the crystal structure model of CXCR4 was imported at Jmol for measuring the distance between the D182 and K110 (Scheme 5b). Based on this, either 6 Ahx-12 Ado (12 Ado: 12-amino-dodecanoic acid) or O2Oc-12 Ado (O2Oc: 8-amino-3,6-dioxaoctanoic acid) were introduced as linkers between ECL1 and ECL2 for the generation of msR4M-L1 or msR4M-L2, respectively (Scheme 5c, d). As proposed from the X-ray crystallography, ECL1 and ECL2 are connected to each other via a disulfide bridge between C109 and C186. This bridge was applied additionally to msR4M-L1 and msR4M-L2 leading to the msR4M-L1ox and msR4M-L2ox analogs. Two more peptides were designed to provide more insights into the role of linkage. MsR4M-LS consisted of ECL1 and ECL2 linked only via the disulfide bridge. In contrast, no disulfide bond was present at msR4M-LG7, but seven glycines between the C-terminus of ECL1 and N-terminus of ECL2 as linkers (Scheme 5e).
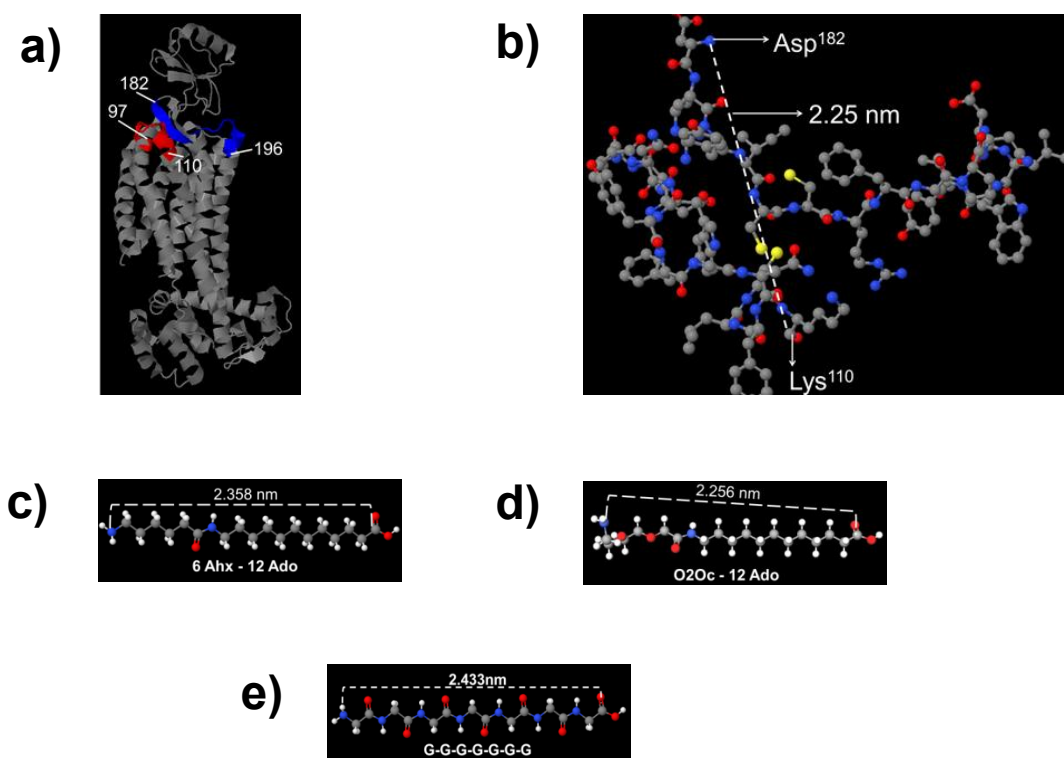
Scheme 5. Design of linkers for msR4Ms. **a** Ribbon structure of human CXCR4 showing highlighted the regions of ECL1 (in red) and ECL2 (in blue), with their N- and C-terminus residues being indicated. **b** Zoomed view of **a** as spheres (blue: nitrogen, red: oxygen, yellow: sulfur, grey: carbon, white: hydrogen) focusing on ECL1 and ECL2 with the measured length (2.25 nm) between the carbon of the C-terminus of Lys[110] and the nitrogen of the N-terminus of Asp[182] being shown. **c, d, e** Estimated lengths of the 6 Ahx-12 Ado (c), O2Oc-12 Ado (d) and $(G)_7$ (e) linkers that were visualized by Molview and introduced between ECL1 and ECL2 for the development of msR4M-L1, -L2 and -LG7, respectively. The crystal structure for a and b was visualized by Jmol (http://www.jmol.org) and obtained from protein data bank (PDB code: 4RWS) as published by Qin and colleagues [148] (adapted from Kontos et al., ref. [291]).

4.1.2 Synthesis, purification mass determination of msR4Ms

Fmoc-SPPS was applied for the synthesis of msR4Ms, as described in chapter 3.2.1. In brief, V196 was loaded on the free N-terminus of Rink resin after its Fmoc-deprotection, and the substitution level was determined. Sequences were elongated with either double or triple couplings of amino acids, with differentiations on the activator, eq. of DIEA, and the coupling time as depicted in Scheme 6.
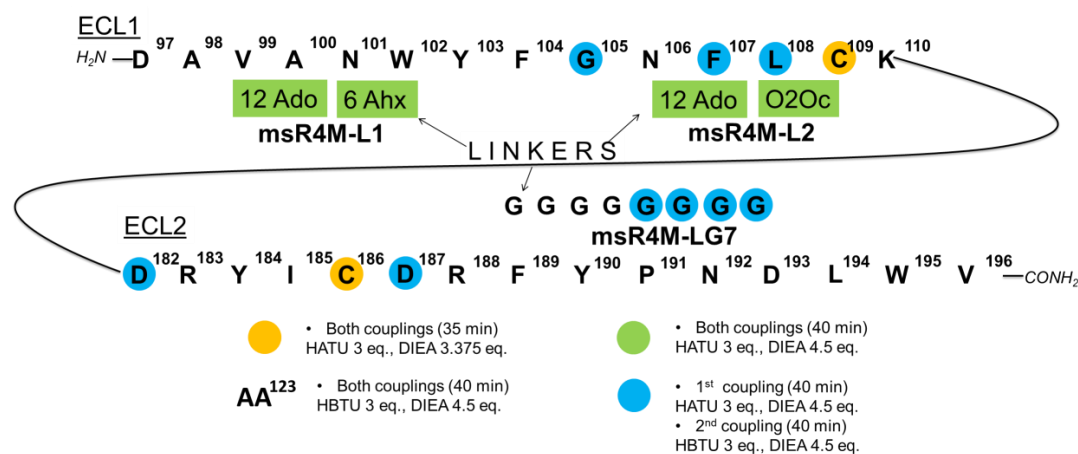
Scheme 6. Conditions of couplings for the syntheses of msR4Ms and ECDs. All amino acids (AA) were coupled with three equivalents (eq.), based on the substitution level that was determined after the load of the first amino acid on Rink-resin. Equivalents of activator and base, together with the coupling time, may vary, as indicated.

Initially, the N-terminus deprotection of every amino acid on each peptide was done with the 25% v/v piperidine/DMF protocol. At the end of the syntheses of msR4Ms and secondary of ECL2, it was noted not only the desired but also a side product with a MW reduced by 18 Da. Many researchers reported similar cases due to the aspartimide (Asi) formation as peptide sequence gets elongated and more exposed to piperidine for the cleavage of Fmoc. A common strategy to prevent this is to alternate to milder Fmoc-deprotection strategies, like the 'Short HOBt protocol' (chapter 3.2.1.2). In a new synthesis of msR4M-L1, 'Short HOBt protocol' was applied after the coupling of the D193 and until the end of the synthesis. The final product was examined by HPLC-ESI-MS in parallel to the initial synthesis. Noteworthy, the side product with -18 Da was absent in the newer synthesis, confirming that its presence in the initial generated msR4M-L1 was due to Asi formation (Figure 15). ECL2 and msR4Ms were resynthesized following the 'Short HOBt protocol' after the coupling of D193 and ECL1 with the 25% v/v piperidine/DMF protocol. All peptides were cleaved from the solid support and side-chain deprotected with Reagent K and lyophilized prior to their purification or oxidation.
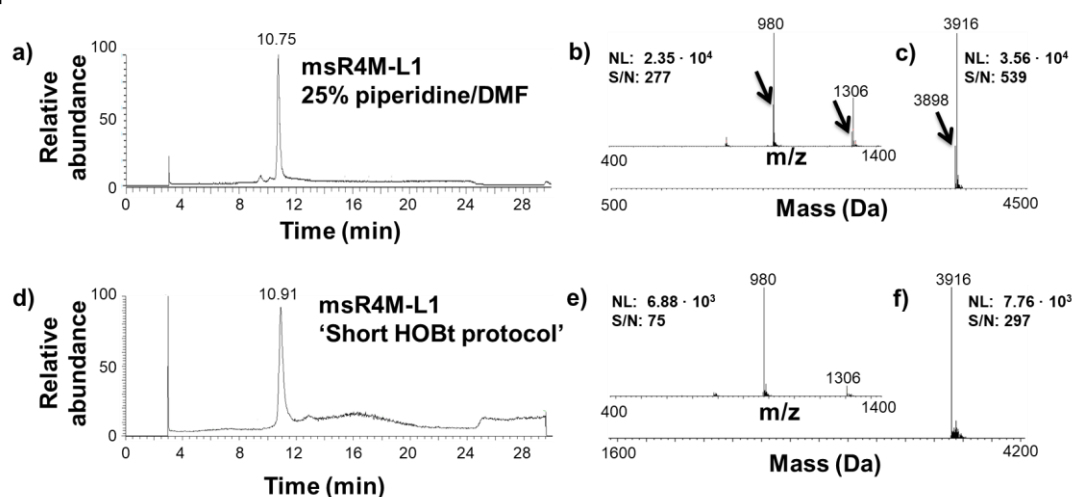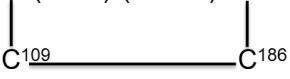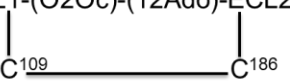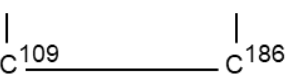
Figure 15. Estimation of RP-HPLC purified msR4M-L1 purity after syntheses following either 25% piperidine/DMF or 'Short HOBt protocol' for Fmoc-deprotection. a, d Chromatogram of purified msR4M-L1 after being synthesized following either the 25% piperidine/DMF (a) or 'Short HOBt protocol' (d) for Fmoc-deprotection, with respective retention times at 10.75 min and 10.91 min. **b, c, e f** ESI-MS spectra obtained by the main peaks of msR4M-L1 after being synthesized following either the 25% piperidine/DMF (b) or 'Short HOBt protocol' (e) for Fmoc-deprotection. Peaks derived by the ESI-MS spectra in (b) and (e) were deconvoluted to the respective MW 3916, having together either the Asi side product (c) or not (f). The peaks that indicate the Asi side product are pointed with an arrow.

The formation of disulfide bonds in msR4M-L1ox and msR4M-L2ox was carried out after dissolving lyophilized crude peptide at 1 mg/mL in aqueous 3 M guanidinium chloride (GdnCl), 0.1 M ammonium carbonate (NH_4HCO_3) solution containing 40% DMSO. Another disulfide bridged peptide, msR4M-LS, was synthesized by dissolving crude ECL1 and ECL2 in 3 M GdnCl 0.1 M NH_4HCO_3 solution, containing 20% DMSO, in a concentration of 0.3 and 0.5 mg/mL, respectively. Oxidations were performed under stirring in RT for a minimum of 3 h. Peptides were purified with RP-HPLC and their purity was estimated by MALDI-TOF-MS (Table 17, Figures 16-17). In two cases, spectra of msR4M-L2ox and –LS showed surprisingly many peaks. This result might occur either because of sample impurities or due to non-sufficient crystallization of the peptides and the appearance of artifacts. To solve this out, both

peptides were provided for HPLC-ESI-MS analysis and the data indicated a high purity for both of them (Figure 18).

Table 17. Sequences, abbreviation and characterization of synthesized msR4Ms and ECDs by RP-HPLC and MALDI-TOF-MS.

Peptide sequence[a]	Peptide abbreviation	HPLC Pr.No.	t_R (min) [b]	Yield (%) [c]	[M+H]+ expected [d]	[M+H]+ found[d]
ECL1-(6Ahx)-(12 Ado) ECL2	msR4M-L1	1	22.16	19.4	3912.92	3913.66
ECL1-(O2Oc)-(12 Ado)-ECL2	msR4M-L2	1	20.41	24.2	3944.93	3945.48
ECL1-(6Ahx)-(12Ado)-ECL2 C^{109}———C^{186}	msR4M-L1ox	1[e]	22.50	19.9	3910.90	3911.36
ECL1-(O2Oc)-(12Ado)-ECL2 C^{109}———C^{186}	msR4M-L2ox	1	20.75	18.2	3942.91	3943.46
ECL1 ECL2 C^{109}———C^{186}	msR4M-LS	3[g]	21.95		3618.68	3618.78
ECL1-(G)$_7$-ECL2	msR4M-LG7	1	20.00	7.4	4001.85	4003.19
D^{97}AVANWYFGNFLCK^{110}	ECL1	1	19.10	20.0	1646.79	1669.24[f]
D^{182}RYICDRFYPNDLWV^{196}	ECL2	1	19.95	21.0	1973.94	1974.37

ECL1 and ECL2 were dissolved and analyzed by MALDI-TOF-MS in a mixture of MALDI solutions A and A (matrix), while msR4Ms in a mixture of MALDI solutions B and B (matrix); **[a]** peptides were synthesized with free amino-N-terminus and amidated C-terminus; **[b]** HPLC retention time of the pure product; **[c]** % yield with regard to crude peptide after cleavage; **[d]** monoisotopic molar mass with an additional hydrogen [M+H]+; **[e]** the stationary phase was a tandem of Reprospher 100 C18-DE columns (250 and 30 mm length, 8 mm internal diameter, 7 µm particle size), in the rest cases Reprosil Gold 200 C18 columns were applied (250 and 30 mm length, 8 mm internal diameter, 10 µm particle size); **[f]** monoisotopic molar mass with an additional sodium [M+Na]+ (adapted from Kontos et al., ref. [291]).
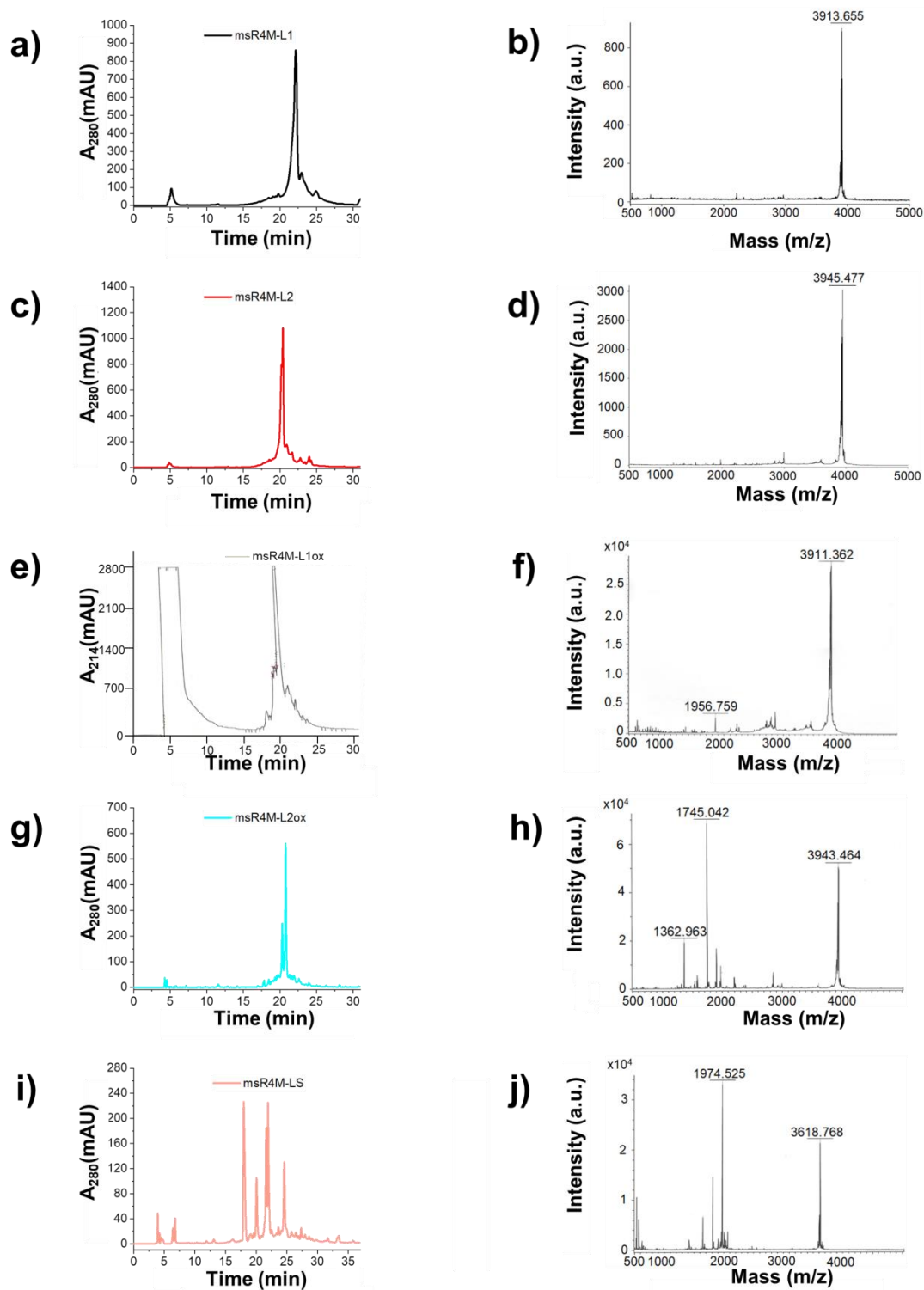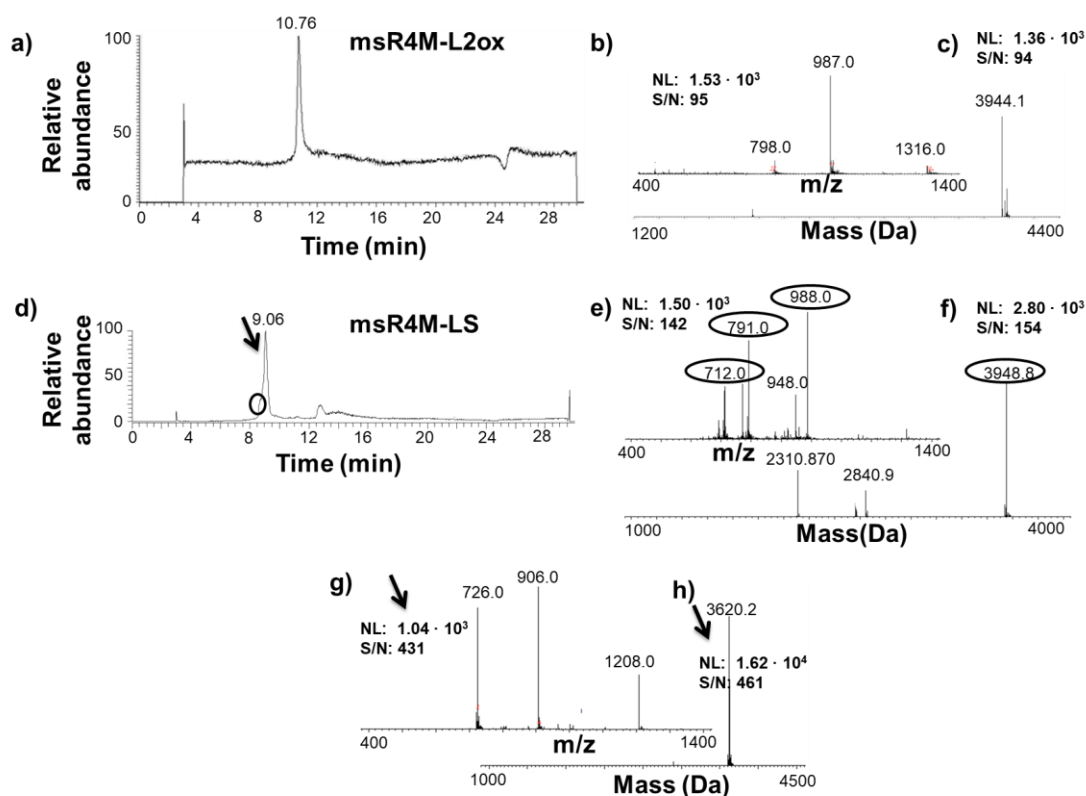
Figure 16. HPLC purification of msR4Ms and verification of their purity by MALDI. a, c, e, g, i Representative C18 HPLC chromatograms (absorbance at 214 or 280 nm) of crude msR4M-L1, msR4M-L2, msR4M-L1ox, msR4M-L2ox and msR4M-LS with respective retention times: a) 22.16 min, c) 20.41 min, e) 22.50 min, g) 20.75 min and i) 21.95 min following SPPS and cleavage. **b, d, f, h, j** MALDI-TOF-MS spectra of HPLC-purified msR4M-L1 (b), msR4M-L2 (d), msR4M-L1ox (f), msR4M-L2ox (h) and msR4M-LS (j) with respective experimental determined masses [M+H]⁺: b) 3913.655 Da, d) 3945.477 Da, f) 3911.362 Da, h) 3943.464 Da and j) 3618.768 Da (adapted from Kontos et al., ref. [291]).
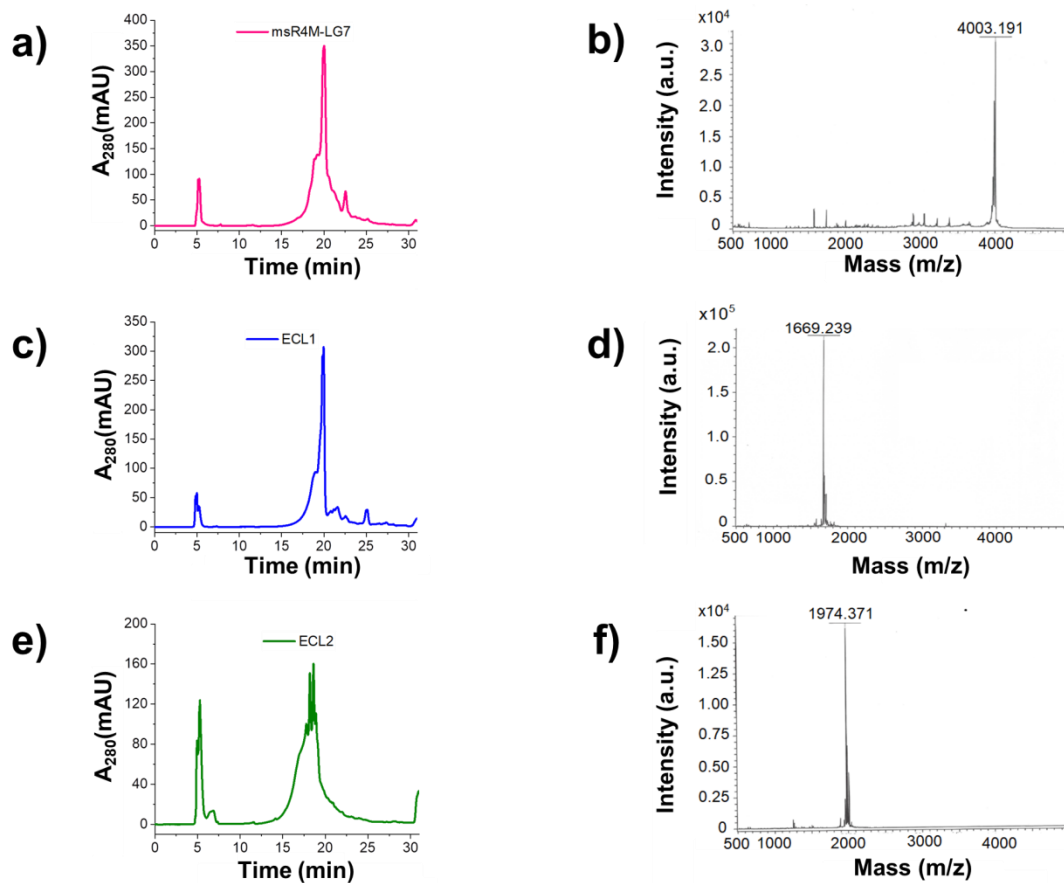
Figure 17. HPLC purification of msR4M-LG7 and ECDs and verification of their purity by MALDI. a, c, e Representative C18 HPLC chromatograms (absorbance at 280 nm) of crude msR4M-LG7, ECL1 and ECL2 with respective retention times: a) 20.00 min, c) 19.10 min and e) 19.95 min, following SPPS and cleavage. **b, d, f** MALDI-TOF-MS spectra of HPLC-purified msR4M-LG7 (b), ECL1 (d) and ECL2 (f) with respective experimental determined masses [M+H]$^+$ or [M+Na]$^+$: b) 4003.191 Da, d) 1669.239 Da and f) 1974.371 Da.

Figure 18. Estimation of purity for msR4M-L2ox and msR4M-LS after RP-HPLC purification. a, d Chromatograms of purified msR4M-L2ox (a) and msR4M-LS (d) with respective retention times at 10.76 min and 9.06 min. The main peak of msR4M-LS is pointed with an arrow and the shoulder before the main peak is indicated in a circle. **b, e, g** ESI-MS spectra obtained by the main peak of msR4M-L2ox (b), the shoulder (e) and the main peak (g) of msR4M-LS. **c, f, h** Peaks derived by the ESI-MS spectra in (b), (e) and (g) were deconvoluted to the respective MWs 3944.1 Da (c), 3948.8 (f) and 3620.2 (h).

4.1.3 Biophysical characterization

4.1.3.1 Conformational and concentration dependence studies via CD spectroscopy

CD spectroscopy was applied for the determination of the secondary structure of msR4Ms and ECDs. A stock solution of each peptide was freshly prepared in HFIP, and spectra were collected under final conditions of aqueous 1×b, pH 7.4, containing 1% HFIP. Peptides were measured in various concentrations for recording whether there is any effect of the increasing concentration in their conformation and oligomerization state. Spectra of msR4M-L1 exposed a β-sheet-characteristic signal with minima at 223 nm and positive signal below 208 nm, while peptide aggregated at 20 µM (Figure 19a). MsR4M-L2 exhibited its minima at 212.5 nm and positive signal below 203 nm, which fits the signal of a β-sheet structure formation prior to its remarkable signal reduction at 7.5 µM due to oligomerization (Figure 19b). Both msR4M-L1 and msR4M-L2 precipitated at 50 µM.

The oxidized analogs of msR4M-L1, -L2 exhibited similar spectra to the reduced ones. In particular, msR4M-L1ox and msR4M-L2ox had their minima at 225 nm and 211.5 nm, while they reached positive MRE values below 208 nm and 201 nm, respectively (Figure 19c, d). Except for msR4M-L2ox that remained soluble, the msR4M-L1ox and msR4M-LG7 precipitated at 50 µM, when msR4M-LS was insoluble already from the 5 µM. From all the mimics, msR4M-LG7 was the only one in a non-ordered state. The glycine-linked CXCR4 mimic showed spectra with an extended

negative signal and minima in similar wavelengths to ECL1. Notably, ECL1 exhibited a broad negative signal below 225 nm and minima at 200 nm, showing some ordered state traces in an overall unfolded peptide (Figure 19e, f). The minima of ECL2 was recorded below 200 nm, and its spectral shape indicated a random coil conformation until its precipitation at 20 µM, like ECL1 (Figure 19g). Summarized results and comparison of the spectra of the peptides are described in 'Discussion' (see 5.1).
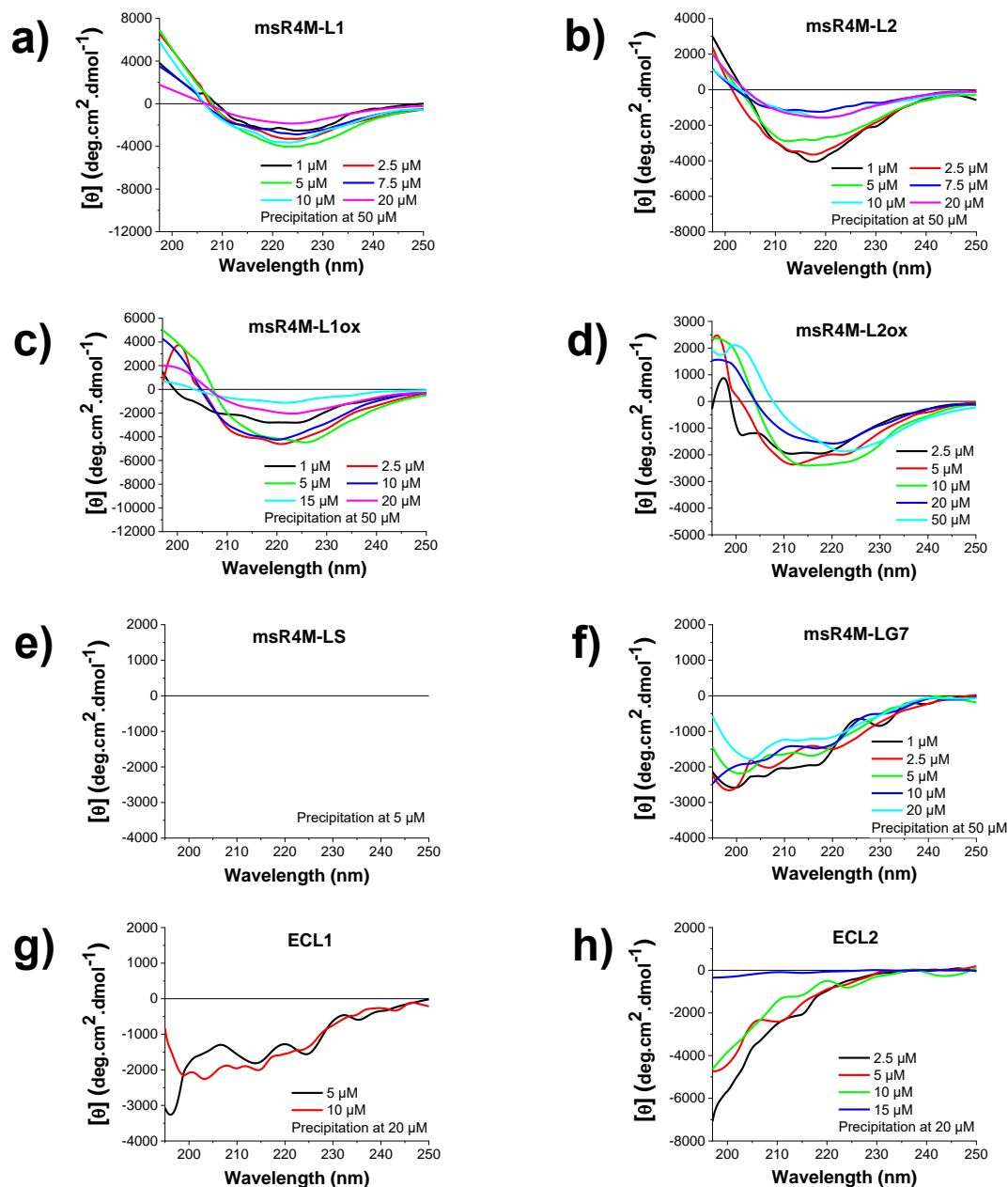
Figure 19. Spectra of msR4Ms and ECDs in various concentrations for the determination of the conformation, as determined by far-UV CD spectroscopy. a, b, c, d, e, f, g, h CD spectra of msR4M-L1 (a), msR4M-L2 (b), msR4M-L1ox (c), msR4M-L2ox (d), msR4M-LS (e), msR4M-LG7 (f), ECL1 (g) and ECL2 (h) at increasing concentrations at final measuring conditions of aqueous 1×b, pH 7.4, containing 1% HFIP. Mean residue ellipticity (MRE) plotted over the wavelength between 197.5 and 250 nm for a, b, 197 and 250 nm for c, g and 195-250 nm for d, e, f (adapted from Kontos et al., ref. [291]).

Individual spectra of ECL1 and ECL2 showed their minima in the lower wavelengths, suggesting a random coil conformation of each peptide. When both

peptides were mixed at 1:1, the minimum remained at 200 nm, indicating that linking is important for the β-sheet formation as found in msR4M-L1 and msR4M-L2 (Figure 20).
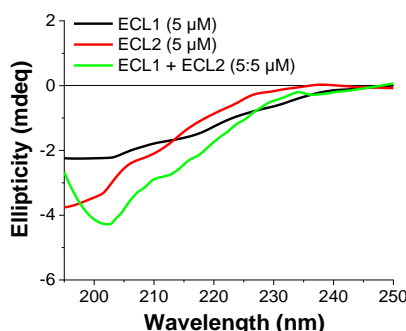
Figure 20. Spectra of ECL1 and ECL2 and their mixture as determined by far-UV CD spectroscopy.CD spectra of ECL1 and ECL2 alone, each at 5 μM and their mixture at final measuring conditions of aqueous 1×b, pH 7.4, containing 1% HFIP. Ellipticity (θ) plotted over the wavelength between 195-250 nm (adapted from Kontos et al., ref. [291]).

4.1.3.2 Self-association studies via fluorescence spectroscopy

Fluorescence spectroscopic titrations of N-terminusly fluorescence-labeled with unlabeled peptides were performed for the determination of their self-assembly propensity. Assays were carried out in final conditions of aqueous 1×b, pH 7.4, containing 1% HFIP, and labeled peptide concentration equal to 5 nM. MsR4Ms seem more prone to self-assemble with K_{ds} varying from 46.6 to 280 nM. In particular, studies on msR4M-L1 indicated an increase in the fluorescence emission with a sigmoidal binding curve being shaped and an app. K_d of 142.0 ± 48.9 nM calculated (Figure 21a, b). Increased concentrations of msR4M-L2 resulted in the enhanced fluorescence intensity of its respective labeled analog in the 10-fold molar excess range and led to an app. K_d of 69.5 ± 61.9 nM (Figure 21c, d). Similar to its non-oxidized analog, msR4M-L1ox self-associated with a high affinity and an app. K_d of 117.5 ± 9.4 nM was obtained (Figure 21e, f). The formation of a disulfide bond between C109 and C186 in msR4M-L2ox appears to slightly decrease the self-association propensity, since the determined app. K_d at 280.0 ± 29.7 nM was more than four times weaker in comparison to the reduced analog (Figure 21g, h). The glycine-linked msR4M-analog is the one with the strongest self-assembly with an app. K_d equal to 46.6 ± 6.0 nM (Figure 21i, j). Data for msR4M-LS were not recorded due to its unfavorable soluble properties in HFIP. On the other hand, extracellular domain peptides ECL1 and ECL2 did not show a strong tendency for self-association with the app. K_{ds} being estimated above 10000 nM for both of them (Table 18, Figure 22).
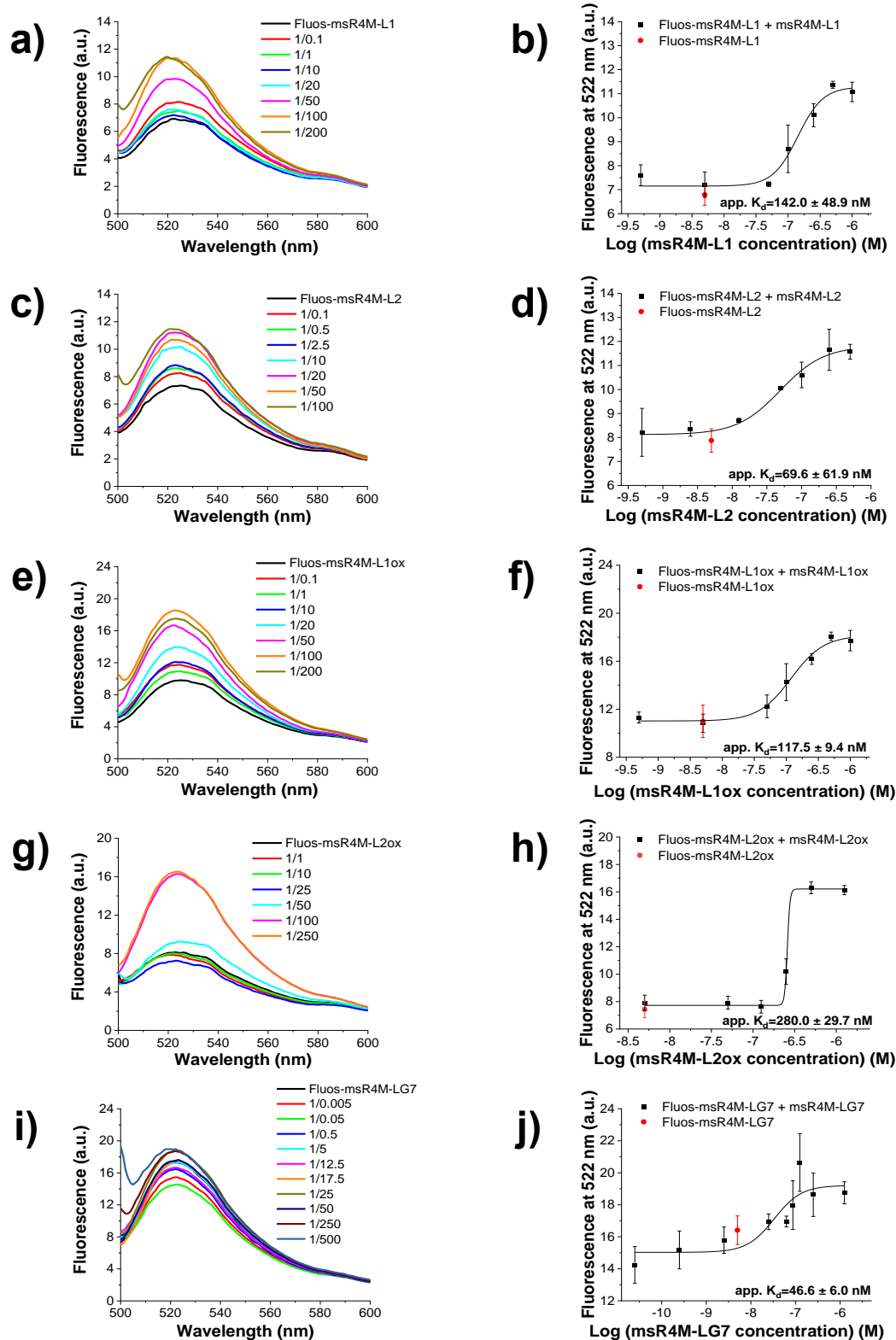
Figure 21. Fluorescence spectroscopic titrations for the determination of apparent affinities (app. K_{ds}) for the self-association of msR4Ms. a, c, e, g, i Fluorescence spectra between 500 and 600 nm of each Fluos-msR4M (5 nM) alone and its mixtures with various amounts of its respective unlabeled partner msR4M-L1 (a), msR4M-L2 (c), msR4M-L1ox (e), msR4M-L2ox (g) and msR4M-LG7 (i); the molar ratios of Fluos-msR4M/msR4M are indicated. **b, d, f, h, j** Binding curves derived from the fluorescence emission at 522 nm of Fluos-msR4M (5 nM) at different concentrations of its respective unlabeled partner msR4M-L1 (b), msR4M-L2 (d), msR4M-L1ox (f), msR4M-L2ox (h) and msR4M-LG7 (j). Data shown are means (±SD) from three independent titration experiments which were performed in aqueous 1×b, pH 7.4, containing 1% HFIP (adapted from Kontos et al., ref. [291]).
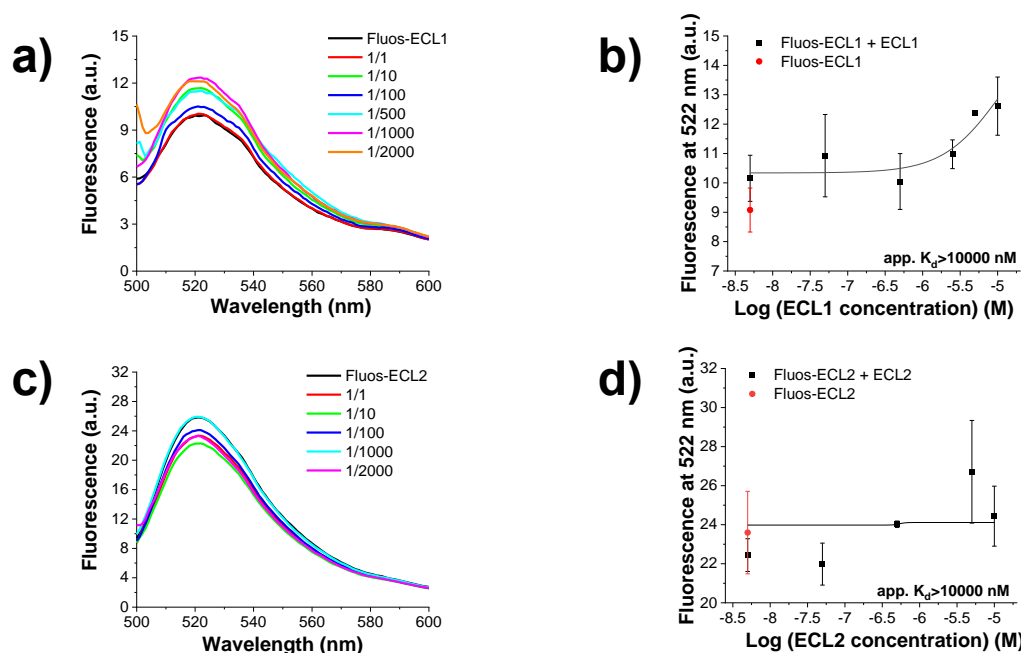
Figure 22. Fluorescence spectroscopic titrations for the determination of apparent affinities (app. K_{ds}) for the self-association of ECDs. a, c Fluorescence spectra between 500 and 600 nm of each Fluos-ECD (5 nM) alone and its mixtures with various amounts of its respective unlabeled partner ECL1 (a) and ECL2 (c); the molar ratios of Fluos-ECD/ECD are indicated. **b, d** Binding curves derived from the fluorescence emission at 522 nm of Fluos-ECD (5 nM) at different concentrations of its respective unlabeled partner ECL1 (b) and ECL2 (d). Data shown are means (±SD) from three independent titration experiments which were performed in aqueous 1×b, pH 7.4, containing 1% HFIP.

Table 18. Apparent affinities (app. K_{ds}) of self-association of msR4Ms and ECDs, as determined by fluorescence spectroscopic titrations (adapted from Kontos et al., ref. [291]).

msR4Ms and ECDs	Fluos-peptide/peptide app. K_d (±SD) (nM)[a]
msR4M-L1	142.0 (±48.9)
msR4M-L2	69.5 (±61.9)
msR4M-L1ox	117.5 (±9.4)
msR4M-L2ox	280.0 (±29.7)
msR4M-LS	n.d. [b]
msR4M-LG7	46.6 (±6.0)
ECL1	> 10000
ECL2	> 10000

[a]: App. K_{ds} are means (±SD) from three independent titration experiments which were performed in aqueous 1×b, pH 7.4, containing 1% HFIP. [b]: n.d., non-determined.

4.1.3.3 ANS binding studies

Fluorescence spectroscopy is a tool with a broad range of applications in biophysical studies, including the investigation of hydrophobic species on the surface of a compound of interest. With the appropriate experimental setup, the addition of 8-anilino-1-naphthalenesulfonic acid (ANS), and the monitoring of its increased fluorescence emission at its maximum at 469 nm, we can obtain insights whether hydrophobic residues are present or not on the surface of the peptide or the protein. Peptides were dissolved in HFIP and measured in quartz cuvette under final measuring conditions of aqueous 1×b, pH 7.4, 1% HFIP and a constant 2-fold excess of ANS compared to the concentration of the peptide. Fluorescence emission did not differentiate to baseline for msR4M-L1 between 0.5 and 2 µM, but it became significant

after 3 µM and reached even 54.24 a.u. at 15 µM before its precipitation at 20 µM (Figure 23a, b). ANS failed to bind to msR4M-L2 until 2 µM, which changed with the increase of the concentrations until at 15µM of peptide the emission reached a plateau at ~ 26 a.u (Figure 23c, d). Summarized results and comparison of the spectra of the peptides are described in 'Discussion' (see 5.1).
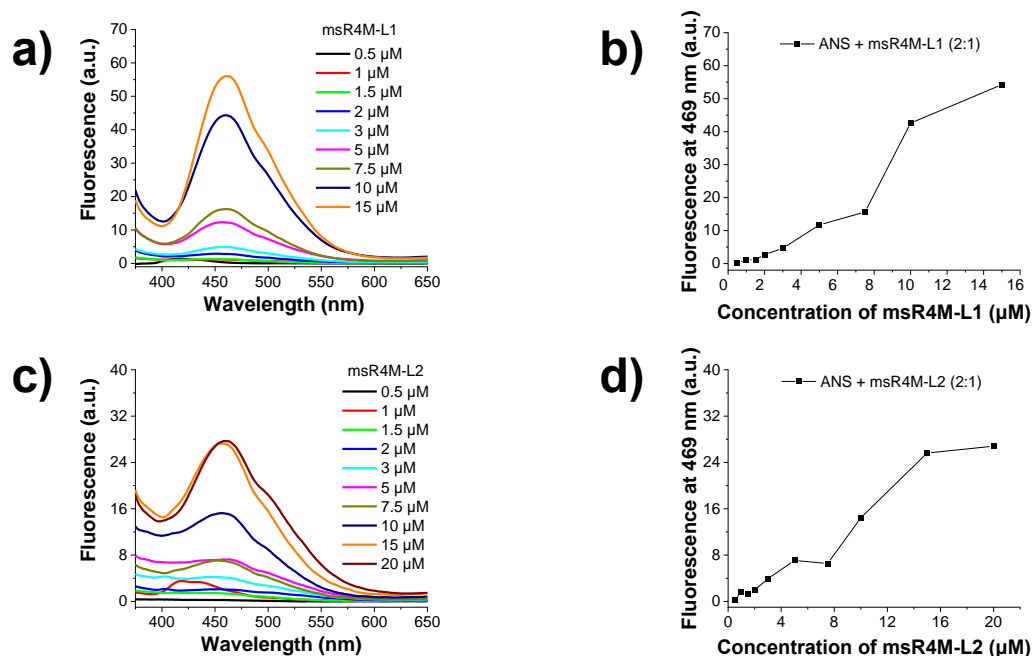

Figure 23. Effect of the binding of ANS to msR4M-L1, -L2, as recorded by fluorescence spectroscopy. a, c Spectra between 375 and 650 nm of mixtures between ANS and msR4Ms in constant 2:1 proportionality; the concenctrations of msR4M-L1 (a) and msR4M-L2 (c) are indicated. **b, d** Fluorescence emission at 469 nm over increased concentrations of msR4M-L1 (b) and msR4M-L2 (d) that were mixed with ANS in a constant 1:2 proportionality. Spectra of ANS alone were subtracted from the spectra of of peptide/ANS mixtures and measurements were performed in aqueous 1×b, pH 7.4, containing 1% HFIP.

4.1.4   Interactions of msR4Ms with MIF studies

4.1.4.1 Determination of binding affinities to MIF via fluorescence spectroscopy

Fluorescence spectroscopic titrations were applied for the determination of the binding affinities of the peptides to MIF. Measurements were carried out at aqueous 1×b, pH 7.4, containing 1% HFIP final conditions and the app. K_d was calculated based on the fluorescence emission of the Fluos-peptide or Alexa-488-MIF. The concentration of the labeled-peptides in the measuring conditions was kept constant at 5 nM, and their fluorescence emission at 522 nm was plotted against increasing concentration of MIF. The fluorescence emission values of Fluos-msR4Ms were plotted versus MIF concentrations. Overall, the results suggested a high affinity between the mimics and the atypical chemokine, as Fluos-msR4M-L1 and Fluos-msR4M-L2 had app. K_{ds} of 40.7 ± 4.0 nM and 18.6 ± 2.9 nM to MIF, respectively (Figure 24a-d). Their oxidized analogs showed a strong binding as well, with Fluos-msR4M-L1ox binding to MIF with an app. K_d of 28.9 ± 2.5 nM and msR4M-L2ox of 105.3 ± 44.9 nM (Table 19, Figure 24e-h).
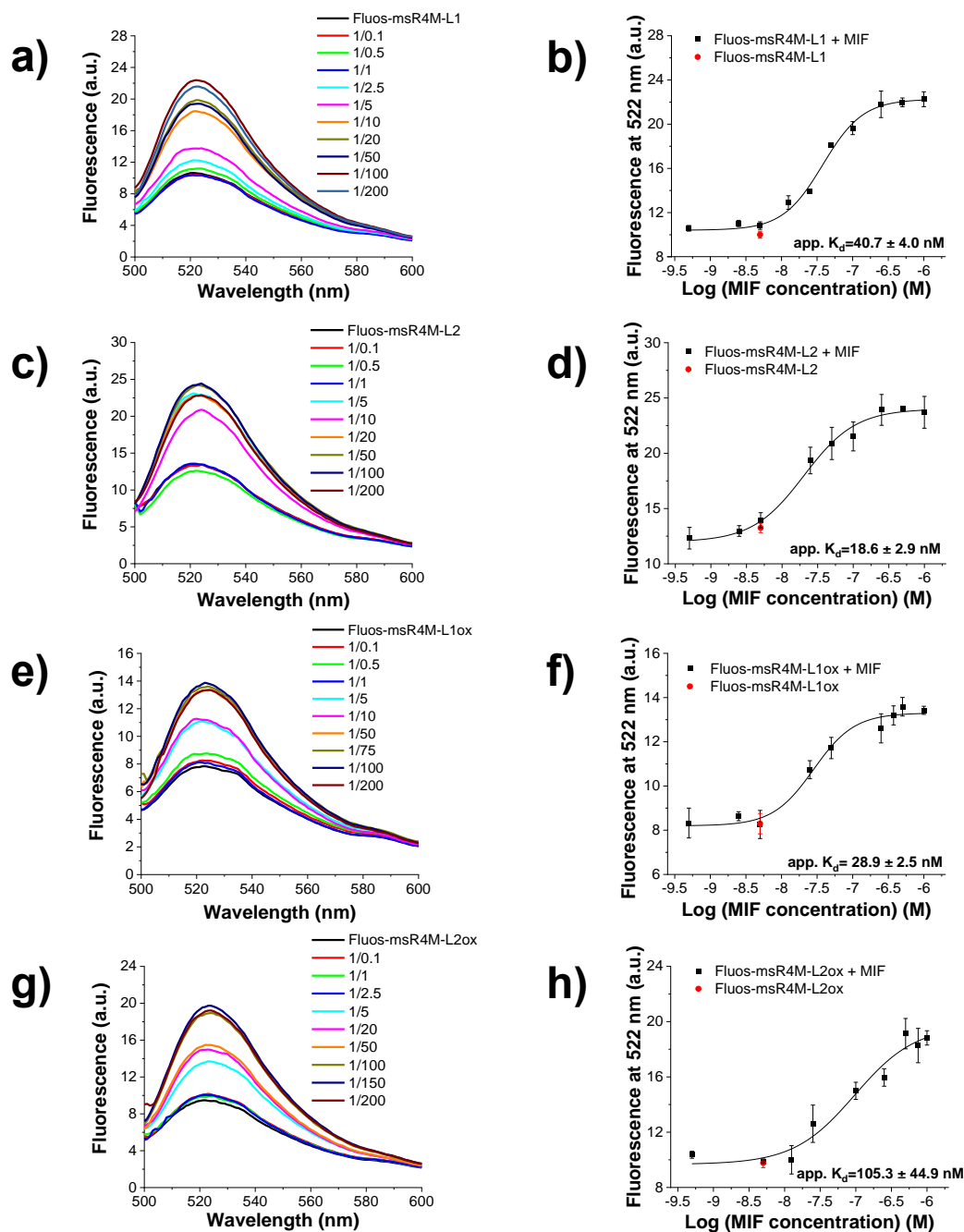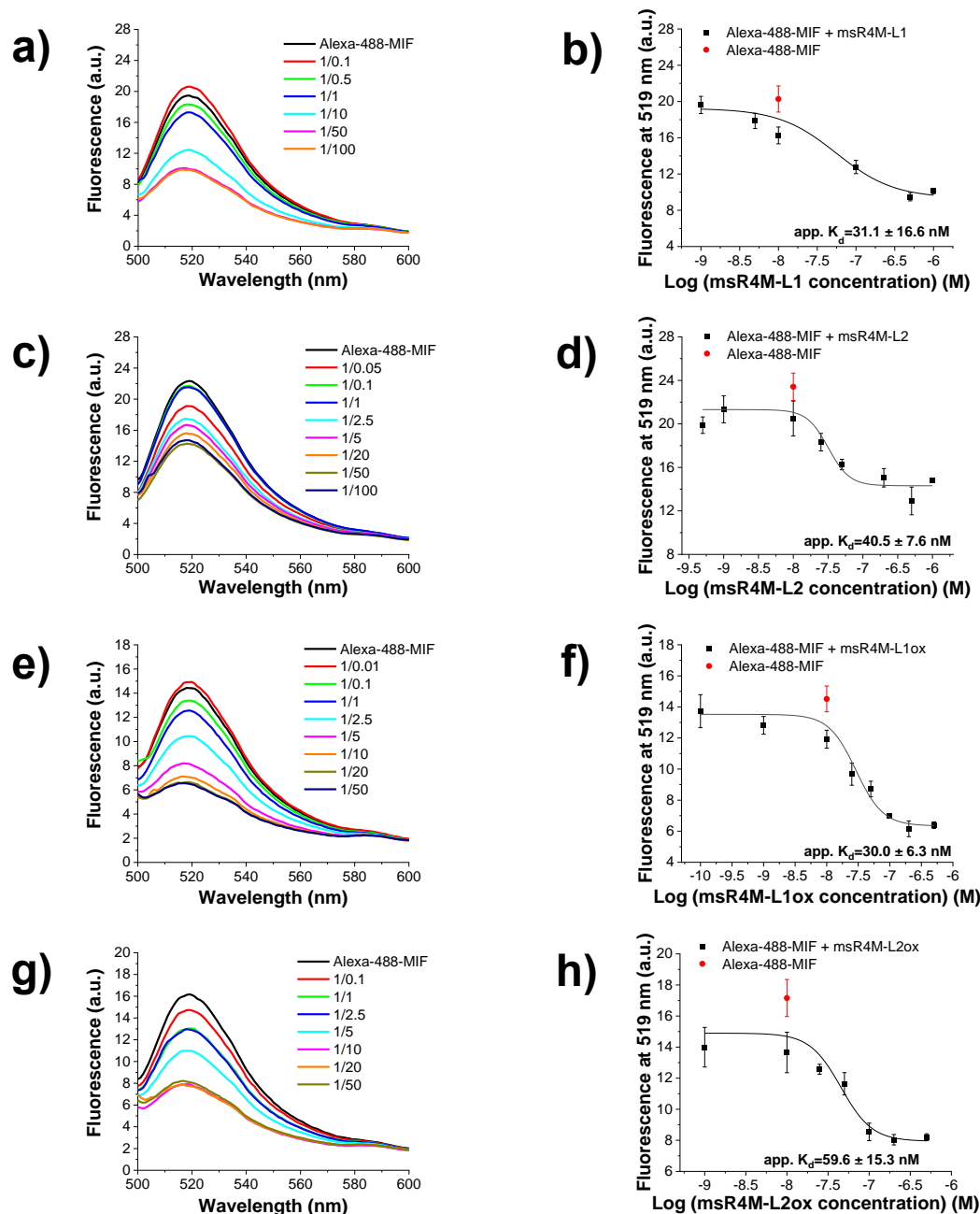
Figure 24. Fluorescence spectroscopic titrations of Fluos-msR4Ms with MIF for the determination of apparent affinities (app. K_{ds}). a, c, e, g Fluorescence spectra between 500 and 600 nm of 5 nM of Fluos-msR4M-L1 (a), Fluos-msR4M-L2 (c), Fluos-msR4M-L1ox (e) and Fluos-msR4M-L2ox (g) alone and their mixtures with various amounts of MIF; the molar ratios of Fluos-msR4Ms/MIF are indicated. **b, d, f, h** Binding curves derived from the fluorescence emission at 522 nm of 5 nM of Fluos-msR4M-L1 (b), Fluos-msR4M-L2 (d), Fluos-msR4M-L1ox (f) and Fluos-msR4M-L2ox (h) at different concentrations of MIF. Data shown are means (±SD) from three independent titration experiments which were performed in aqueous 1×b, pH 7.4, containing 1% HFIP (adapted from Kontos et al., ref. [291]).

The experimental setup and the low concentration of the labeled-peptide made the system reliable for determining the affinity between Fluos-msR4M-LS and MIF. Surprisingly, the disulfide-bonded peptide, which lacks any additional linkers, showed the strongest affinity among msR4Ms to MIF and resulted in an app. K_d of 6.9 ± 2.0 nM (Figure 25a-b). Contrariwise, the fluorescence emission of Fluos-msR4M-LG7 did not differentiate in the presence of MIF, indicating a very weak affinity and an app. K_d

above 2500 nM (Figure 25c-d). The fluorescence emission of Fluos-ECL2 failed to reach its upper plateau until 5000 nM of MIF, suggesting an app. K_d above this concentration point (Figure 25e-f).
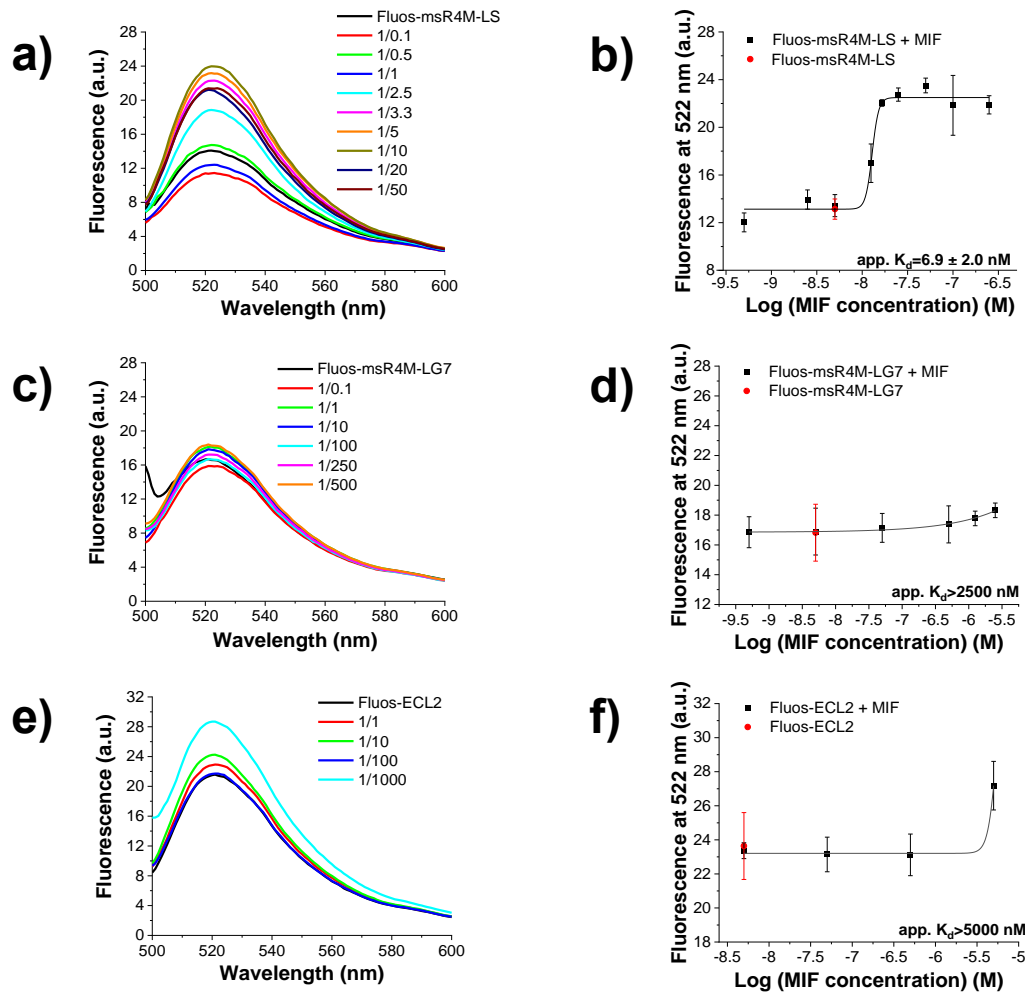
Figure 25. Fluorescence spectroscopic titrations of Fluos-msR4M-LS, -LG7, Fluos-ECL2 with MIF for the determination of apparent affinities (app. K_{ds}). a, c, e Fluorescence spectra between 500 and 600 nm of 5 nM of Fluos-msR4M-LS (a), Fluos-msR4M-LG7 (c) and Fluos-ECL2 (e) alone and their mixtures with various amounts of MIF; the molar ratios of Fluos-peptide/MIF are indicated. **b, d, f** Binding curves derived from the fluorescence emission at 522 nm of 5 nM of Fluos-msR4M-LS (b), Fluos-msR4M-LG7 (d) and Fluos-ECL2 (f) at different concentrations of MIF. Data shown are means (±SD) from three independent titration experiments which were performed in aqueous 1×b, pH 7.4, containing 1% HFIP (adapted from Kontos et al., ref. [291]).

Likewise, the fluorescence emission of Alexa-488-MIF (10 nM) at 519 nm was plotted versus increased concentration of the peptide for the estimation of the binding affinity. Overall, the results were in agreement with the Fluos-peptide-basedfindings. Alexa-488-MIF was already saturated by a 5-molar excess of msR4M-L1 and the estimated app. K_d was 31.1 ± 16.6 nM (Figure 26a-b). Likewise, msR4M-L2 bound firmly to MIF with app. K_{ds} 40.5 ± 7.6 nM (Figure 26c-d). The introduction of a disulfide bond did not significantly differentiate the app. K_{ds}, which were 30.0 ± 6.3 nM for msR4M-L1ox and 59.6 ± 15.3 nM, for msR4M-L2ox (Figure 26e-h). MsR4M-LS was not tested due to its unfavorable soluble properties. Titrations of Alexa-488-MIF against CXCR4 ectodomain peptides ECL1 and ECL2 showed a medium to relative low affinity to MIF with the calculated app. K_{ds} being 345.2 ± 79.4 nM and 2458 ± 1054 nM, respectively (Table 19, Figure 27). Of note, Alexa-488-MIF exhibited a higher affinity to

msR4Ms and ECDs than to ISO-1, an organic molecule that is known as an MIF inhibitor [119]. Final measuring conditions were slightly differentiated to 50 nM of the Alexa-488-analyte at 1xb, pH 7.4, 1% HFIP, 0.5% DMSO and the determined app. K_d was 14.42 ± 4.42 μM (see Appendix Figure A1). Interestingly, under the previously applied conditions for labeled-protein/peptides titrations, Alexa-488 had a high propensity to self-associate with an app. K_d equal to 24.8 ± 1.3 nM (see Appendix Figure A2). Summarized results and comparison of the binding affinities of the peptides are described in 'Discussion' (see 5.1).

Figure 26. Fluorescence spectroscopic titrations of Alexa-488-MIF with msR4Ms for the determination of apparent affinities (app. K_{ds}). a, c, e, g Fluorescence spectra between 500 and 600 nm of Alexa-488-MIF (10 nM) alone and its mixtures with various amounts of msR4M-L1 (a), msR4M-L2 (c), msR4M-L1ox (e) and msR4M-L2ox (g); the molar ratios of Alexa-488-MIF/peptides are indicated. **b, d, f, h** Binding curves derived from the fluorescence emission at 519 nm of Alexa-488-MIF (10 nM) at different concentrations of msR4M-L1 (b), msR4M-L2 (d), msR4M-L1ox (f) and msR4M-L2ox (h). Data shown are means (±SD) from three independent titration experiments which were performed in aqueous 1×b, pH 7.4, containing 1% HFIP (adapted from Kontos et al., ref. [291]).
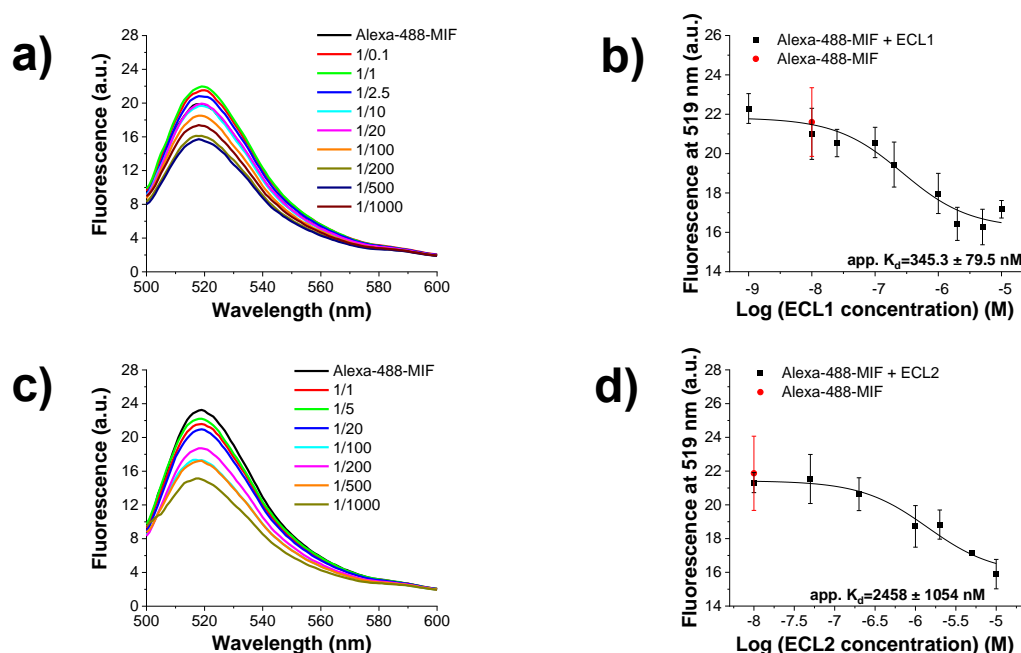
Figure 27. Fluorescence spectroscopic titrations of Alexa-488-MIF with ECDs for the determination of apparent affinities (app. K$_{ds}$). a, c Fluorescence spectra between 500 and 600 nm of Alexa-488-MIF (10 nM) alone and its mixtures with various amounts of ECL1 (a) and ECL2 (c); the molar ratios of Alexa-488-MIF/peptides are indicated. **b, d** Binding curves derived from the fluorescence emission at 519 nm of Alexa-488-MIF (10 nM) at different concentrations of ECL1 (b) and ECL2 (d). Data shown are means (±SD) from three independent titration experiments which were performed in aqueous 1×b, pH 7.4, containing 1% HFIP (adapted from Kontos et al., ref. [291]).

Table 19. Apparent affinities (app. K$_{ds}$) between msR4Ms and ECDs with MIF, as determined by fluorescence spectroscopic titrations (adapted from Kontos et al., ref. [291]).

msR4Ms and ECDs	Fluos-peptide/MIF app. K$_d$ (nM)[a]	Alexa-488-MIF/peptide app. K$_d$ (nM)[a]
msR4M-L1	40.7 (±4.0)	31.1 (±16.6)
msR4M-L1ox	28.9 (±2.5)	30.0 (±6.3)
msR4M-L2	18.6 (±2.9)	40.5 (±7.6)
msR4M-L2ox	105.3 (±44.9)	59.6 (±15.3)
msR4M-LS	6.9 (±2.0)	n.d.[b]
msR4M-LG7	> 2500	n.d.[b]
ECL1	n.d.[b]	345.2 (±79.4)
ECL2	> 5000	2458 (±1054)

[a]: App. K$_{ds}$ are means (±SD) from three independent titration experiments which were performed in aqueous 1×b, pH 7.4, containing 1% HFIP. [b]: n.d., non-determined.

4.1.4.2 Determination of binding affinities of msR4M-L1 to MIF via fluorescence polarization (FP)

Fluorescence polarization (FP) spectroscopy was applied additionally to determine the binding affinity between msR4M-L1 and MIF. As a binding assay based on the polarization, a general property of fluorescent molecules, FP has the advantage that the fluorescence emission is less dye dependent and susceptible to environmental interferences than in other fluorescence intensity-based assays [284]. The final concentration of the labeled analytes Fluos-msR4M-L1 and Alexa-488-MIF was kept constant at 5 and 10 nM, respectively, as for the fluorescence spectroscopy. The measuring conditions were aqueous 1×b, pH 7.4, while the HFIP percentage varied, being 0.5% in the titrations of the Fluos-msR4M-L1 and 2% of Alexa-488-MIF. P values

were recorded in the wavelength with the maximum emission, depending on the label and the calculated app. K_{ds} were congruent to the fluorescence spectroscopy findings. FP titrations of Fluos-msR4M-L1 to MIF led to an app. K_d of 24.4 ± 5.3 nM, while the reverse titration with Alexa-488-MIF and msR4M-L1 to 10.6 ± 1.2 nM (Figure 28).
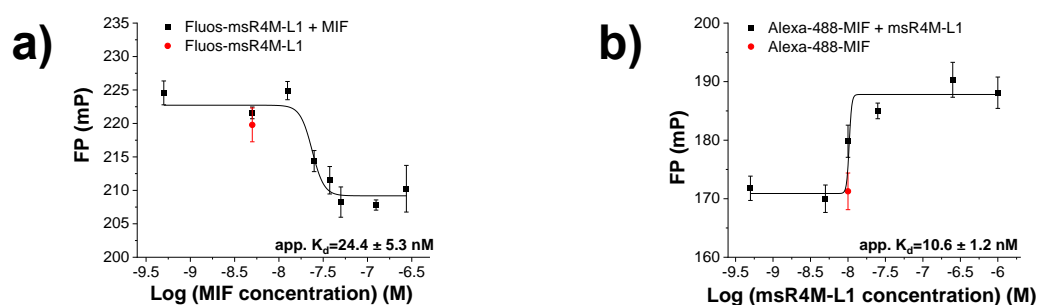
Figure 28. Determination of apparent affinities (app. K_{ds}) of the Fluos-msR4M-L1/MIF with Alexa-488-MIF/msR4M-L1 titrations by fluorescence polarization. a, b FP signal (mP) of either 5 nM Fluos-msR4M-L1 at 522 nm (a) or 10 nM of Alexa-488-MIF at 519 nm (b) plotted at different concentrations of MIF or msR4M-L1, respectively. Data shown are means (±SD) from three independent titration experiments which were performed in aqueous 1×b, pH 7.4, containing 0.5% HFIP for Fluos-msR4M-L1/MIF and 2% HFIP for Alexa-488-MIF/msR4M-L1 (adapted from Kontos et al., ref. [291]).

4.1.4.3 Determination of binding affinities to MIF via Microscale Thermophoresis (MST)

Microscale Thermophoresis (MST) is another approach to measure the dissociation constants of the interactions [285]. MST utilizes a tiny amount of labeled analyte and unlabeled titrant mixtures and is loaded on the capillaries. Their fluorescence is recorded without, with, and again without IR-laser heating. The extracted normalized fluorescence value (F_{norm}) is a quotient between F_{hot} (fluorescence at a specific time point after IR-laser is switched on) and F_{cold} (before IR-laser is switched on) and is plotted against the increasing concentration of the titrant for the calculation of the app. K_d. N-terminusly labeled TAMRA-msR4M-L1 was chosen as the labeled analyte, mixed with MIF, and incubated in RT for 8-12 min. Measurements were obtained at aqueous 2×b, pH 7.2, 0.05% Tween 20 at 37°C, and its F_{hot} was recorded based on the MST signal at 1.5 s, and the data were further analysed and presented as fraction bound. The different experimental setup, the alternate label of msR4M-L1, and the lack of HFIP did not significantly affect the affinity between msR4M-L1 and MIF, since the calculated app. K_d at 77.2 ± 37.1 nM is similar to the previous calculated from fluorescence spectroscopy and FP (Figure 29).
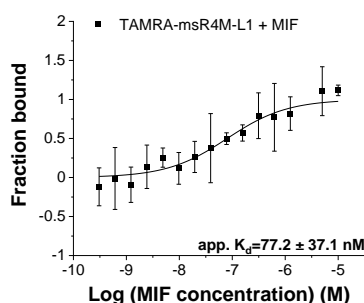
Figure 29. Determination of apparent affinity (app. K_d) of the titration of TAMRA-msR4M-L1 with MIF by MST. Fraction bound of 100 nM TAMRA-msR4M-L1 at different concentrations of MIF. As F_{cold} it was considered the mean fluorescence derived by the MST signal between -1 and 0 s, and as F_{hot} the mean fluorescence derived by the MST signal between 0.5 and 1.5 s prior to their normalization. Data shown are means (±SD) from three independent titration experiments which were performed in aqueous 2×b, pH 7.2, 0.1% Tween 20 (adapted from Kontos et al., ref. [291]).

4.1.4.4 Interactions with MIF by CD spectroscopy

CD spectroscopy may provide insights into the structure not only of the individual compounds of interest and but also of their mixtures [237]. Previously, MIF and msR4Ms were shown to have ordered secondary structures and bind strongly. However, it remains unknown whether their interactions affect their ordered structures or not. Herein, mixtures of msR4M-L1, -L1ox, or -L2 with MIF were measured in different proportionality, under the already described experimental setup and final measuring conditions aqueous 1×b, pH 7.4, 1% HFIP. Mixtures of msR4M-L1 and MIF at 1:1 (5:5 µM) did not differentiate from the sum of their single spectra, suggesting that there is no conformational change (Figure 30a). Similar results were obtained in a 10-fold excess (5:0.5 µM) of msR4M-L1 over MIF (Figure 30b). Spectra of msR4M-L1ox/MIF and msR4M-L2ox/MIF mixtures at 10:1 had identical signal and structure with the respective sums, too (Figure 30c, d). The results indicate that the interactions of selected msR4Ms with MIF do not affect their structures. Summarized results and comparison of the spectra of the peptides are described in 'Discussion' (see 5.1).
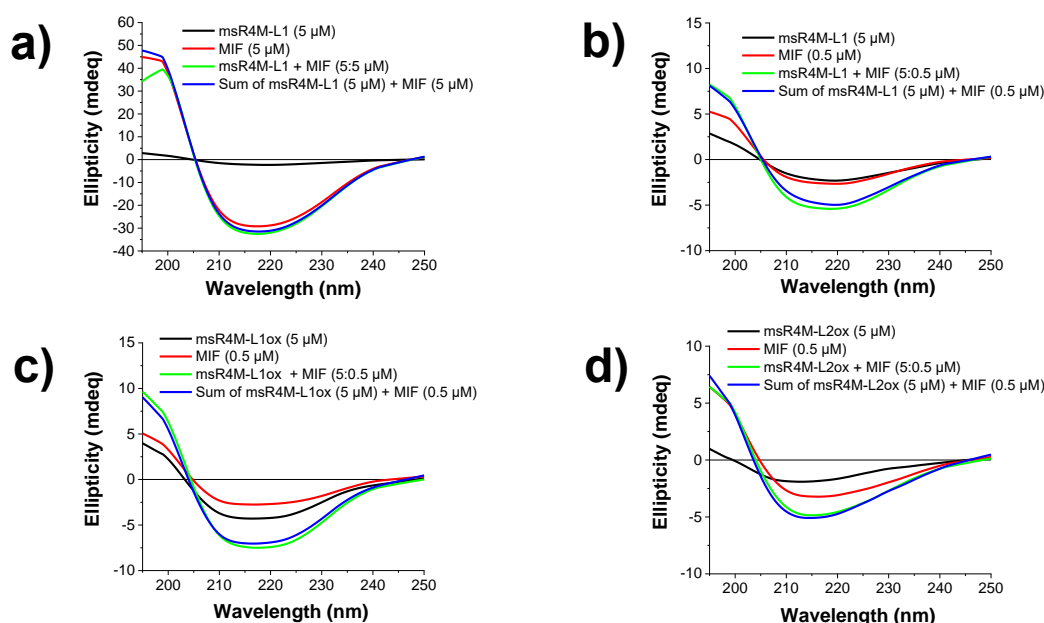
Figure 30. Studies on secondary structure of msR4Ms-MIF mixtures through CD spectroscopy. a, b, c, d CD spectra of msR4Ms and MIF alone, msR4Ms-MIF mixture and sum of the ellipticity of the derived peptide and protein individual spectra. The analyzed peptides were msR4M-L1 (a, b), msR4M-L1ox (c) and msR4M-L2ox (d). Concentrations and ratios are indicated. Measurements were performed in aqueous 1×b, pH 7.4, containing 1% HFIP. Ellipticity (θ) plotted over the wavelength between 195 and 250 nm.

4.1.5 Interaction studies between msR4Ms and CXCL12

4.1.5.1 Determination of binding affinities to CXCL12 via fluorescence spectroscopy

Herein, it was questioned the specificity of msR4Ms over CXCL12, the other ligand of CXCR4. Fluorescence spectroscopic titrations were pursued between Fluos-msR4Ms and CXCL12 under the same final conditions as for MIF. Neither Fluos-msR4M-L1 nor Fluos-msR4M-L2 had an increased fluorescence intensity in the presence of CXCL12, resulting in app. K_{ds} higher than 6340 nM for both peptides (Figure 31a-d). Contrariwise, their oxidized analogs showed a strong affinity to CXCL12. More specifically, Fluos-msR4M-L1ox binds to CXCL12 with an app. K_d of 84.6 ± 42.1 nM, while the estimated app. K_d between Fluos-msR4M-L2ox and CXCL12

was equal to 54.8 ± 10.3 nM (Figure 31e-h). Fluos-msR4M-LS, another disulfide bridged but not additionally linked analog, binds even stronger to CXCL12, with an app. K_d of 17.4 ± 4.7 nM (Figure 31i-j). Collectively, the disulfide bond may be a pivotal factor for the binding of msR4Ms to CXCL12 (Table 20). Summarized results and comparison of the binding affinities of the peptides are described in 'Discussion' (see 5.1).
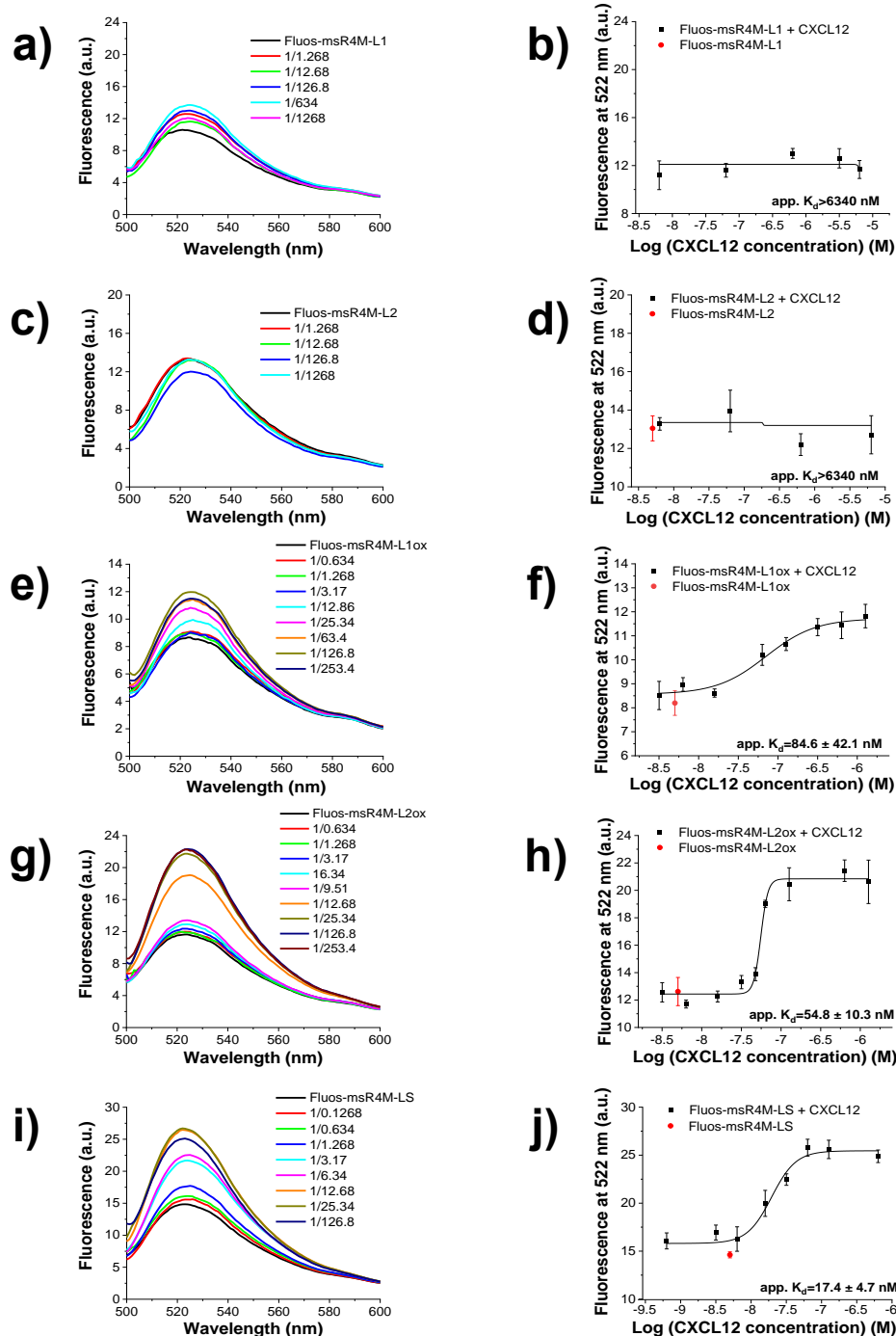
Figure 31. Fluorescence spectroscopic titrations of Fluos-msR4Ms with CXCL12 for the determination of apparent affinities (app. K_{ds}). a, c, e, g, i Fluorescence spectra between 500 and 600 nm of 5 nM of Fluos-msR4M-L1 (a), Fluos-msR4M-L2 (c), Fluos-msR4M-L1ox (e), Fluos-msR4M-L2ox (g) and Fluos-msR4M-LS (i) alone and their mixtures with various amounts of CXCL12; the molar ratios of Fluos-msR4Ms/CXCL12 are indicated. **b, d, f, h, j** Binding curves derived from the fluorescence emission at 522 nm of 5 nM of Fluos-msR4M-L1 (b), Fluos-msR4M-L2 (d), Fluos-msR4M-L1ox (f), Fluos-msR4M-L2ox (h) and Fluos-msR4M-LS (j) at different concentrations of CXCL12. Data shown are means (±SD) from three independent titration experiments which were performed in aqueous 1×b, pH 7.4, containing 1% HFIP. (adapted from Kontos et al., ref. [291]).

79

Table 20. Apparent affinities (app. K_{ds}) between msR4Ms and CXCL12, as determined by fluorescence spectroscopic titrations (adapted from Kontos et al., ref. [291]).

msR4Ms	Fluos-msR4Ms/CXCL12 app. K_d (nM)[a]
msR4M-L1	> 6340
msR4M-L2	> 6340
msR4M-L1ox	84.6 (±42.1)
msR4M-L2ox	54.8 (±10.3)
msR4M-LS	17.4 (±4.7)
msR4M-LG7	n.d.[b]

[a]: App. K_{ds} are means (±SD) from three independent titration experiments which were performed in aqueous 1×b, pH 7.4, containing 1% HFIP. [b]: n.d., non-determined.

4.1.5.2 Determination of binding affinities to CXCL12 via FP

In the chapters 4.1.4.1 and 4.1.5.1, fluorescence spectroscopy was applied for testing the selectivity of msR4Ms between MIF and CXCL12. Previous findings indicated an MIF-specificity of msR4M-L1 over CXCL12. To investigate further these findings, FP was pursued recording the titration between Fluos-msR4M-L1 and CXCL12. Measurements were obtained in aqueous 1×b, pH 7.4, containing 0.5% HFIP, which were the same conditions applied for the FP assay between Fluos-msR4M-L1 and MIF in chapter 4.1.4.2. The P values of the labeled-peptide did not alternate after the addition of CXCL12 and the estimated app. K_d is > 2500 nM and indicates a higher than 100-fold weaker affinity of Fluos-msR4M-L1 to CXCL12 than MIF (Figure 32).
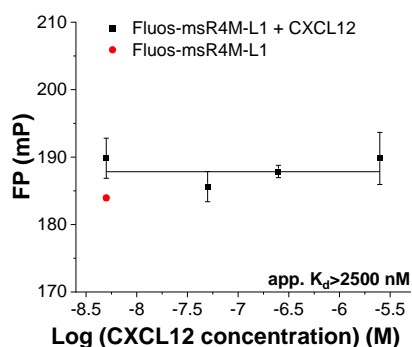
Figure 32. Determination of apparent affinity (app. K_d) of the Fluos-msR4M-L1/CXCL12 titration by fluorescence polarization. FP signal (mP) of 5 nM Fluos-msR4M-L1 at 522 nm plotted at different concentrations of CXCL12. Data shown are means (±SD) from three independent titration experiments which were performed in aqueous 1×b, pH 7.4, containing 0.5% HFIP (adapted from Kontos et al., ref. [291]).

4.1.5.3 Determination of binding affinities to CXCL12 via MST

Microscale thermophoretic titrations provided data in chapter 4.1.4.3 that concluded in an interaction between TAMRA-msR4M-L1 and MIF with an app. K_d equal to 77.2 ± 37.1 nM. Measurements were performed under final conditions of aqueous 2×b, pH 7.2, containing 0.1% Tween 20 at 37°C. Under the same conditions it was tested the TAMRA-msR4M-L1 binding specificity. Labeled-msR4M-L1 was titrated against CXCL12 and exhibited an app. K_d higher than 3125 nM (Figure 33). The result comes into agreement with findings from the fluorescence spectroscopy and FP assays, in which the affinity was above 6340 and 2500 nM, respectively.
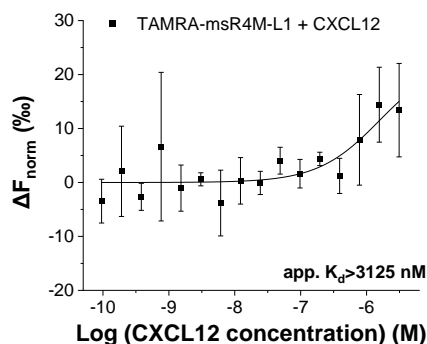
Figure 33. Determination of apparent affinity (app. K_d) of the titration of TAMRA-msR4M-L1 with CXCL12 by MST. Change of normalized fluorescence (ΔF_{norm}) of 100 nM TAMRA-msR4M-L1 at different concentrations of CXCL12. As F_{cold} it was considered the mean fluorescence derived by the MST signal between -1 and 0 s, and as F_{hot} the mean fluorescence derived by the MST signal between 0.5 and 1.5 s prior to their normalization. Data shown are means (±SD) from five independent titration experiments which were performed in aqueous 2×b, pH 7.2, 0.1% Tween 20 (adapted from Kontos et al., ref. [291]).

4.1.6 Competition studies of msR4M-L1 and sCD74 for binding to MIF

4.1.6.1 Determination of binding affinities of Alexa-488-MIF to sCD74 in the presence and absence of msR4M-L1 with FP

An anti-atherosclerotic MIF-specific CXCR4 mimic, except for its specific binding to MIF compared to CXCL12, should also spare the MIF-atheroprotective pathways. MIF-CD74 interaction triggers cardioprotective signaling and should be maintained [289]. MsR4M-L1 showed its MIF-specificity against CXCL12, and as next, it was questioned whether its interaction with MIF hinders the MIF/CD74 complex formation or not. Initially, Alexa-488-MIF was titrated at a constant final concentration of 10 nM against HA-tagged soluble ectodomain of CD74 (HA-tagged sCD74$_{73-232}$) without the presence of msR4M-L1. Mixtures of Alexa-488-MIF/sCD74 were prepared in aqueous 1×b, pH 7.4, containing 2% HFIP and 0.01×PBS and incubated for 4 h in RT before their measurements took place.

Likewise, in the competition experiments, Alexa-488-MIF was pre-mixed with 20-fold excess of msR4M-L1 and incubated shortly prior to the addition of sCD74 and the titration of the mixtures, as above. Previous studies between Alexa-488-MIF and msR4M-L1 in chapter 4.1.4 showed saturation between the labeled-protein and msR4M-L1 in this proportionality. Alexa-488-MIF and sCD74 retained their affinity in the presence of msR4M-L1, with the app. K_d calculated equal to 114.4 ± 47.0 nM and 89.4 ± 55.3 nM without and with msR4M-L1, respectively (Figure 34a, b). These non-differentiated app. K_{ds} indicate non-competitive binding mechanisms between msR4M-L1 and sCD74 for the binding to MIF.
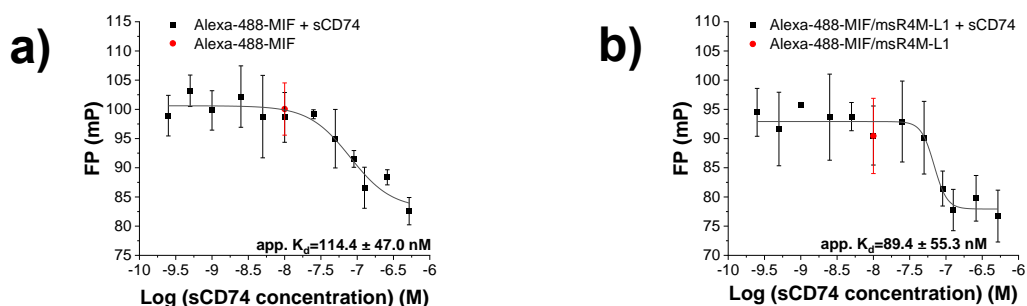
Figure 34. Determination of apparent affinities (app. K$_{ds}$) of the titration of Alexa-488-MIF, with or without msR4M-L1, with sCD74 by fluorescence polarization. a, b FP signal (mP) at 519 nm of 10 nM Alexa-488-MIF (a) and 10 nM Alexa-488-MIF/200 nM msR4M-L1 (b) plotted at different concentrations of sCD74. Data shown are means (±SD) from three independent titration experiments which were performed in aqueous 1×b, pH 7.4, containing 2% HFIP and 0.01×PBS (adapted from Kontos et al., ref. [291]).

4.1.6.2 Determination of binding affinities of Alexa-647-MIF to sCD74 in the presence and absence of msR4M-L1 with MST

Further studies on the possible effect of msR4M-L1 in the formation of the MIF/CD74 complex were performed in addition to the above FP assays. Herein, MST was utilized to determine the binding affinity between Alexa-647-MIF and sCD74 either in the presence or the absence of msR4M-L1. Alexa-647-MIF was mixed with sCD74 in aqueous 10 mM Tris, 0.25×PBS, 0.005% BSA, and incubated for 3h in RT and 15 min in 37°C. All mixtures contained 20 nM of the labeled protein and variable concentrations of sCD74, and their fluorescence emission was measured after the end of their incubation period at 37°C. For the competitive binding experiments, Alexa-647-MIF was pre-mixed with 10-fold excess of msR4M-L1 and shortly incubated before the subsequent addition of sCD74. Mixtures were handled and analyzed as described. The app. K$_d$ between Alexa-647-MIF and sCD74 was calculated at 33.9 ± 5.0 nM (Figure 35a). Importantly, their affinity did not change in the presence of msR4M-L1, since the respective dissociation constant was 34.5 ± 14.4 nM (Figure 35b). Results suggested lack of competition between msR4M-L1 and CD74 for the binding to MIF and agree with the FP-findings of chapter 4.1.6.1. Summarized results and comparison of the binding affinities of the titrations are described in 'Discussion' (see 5.1).
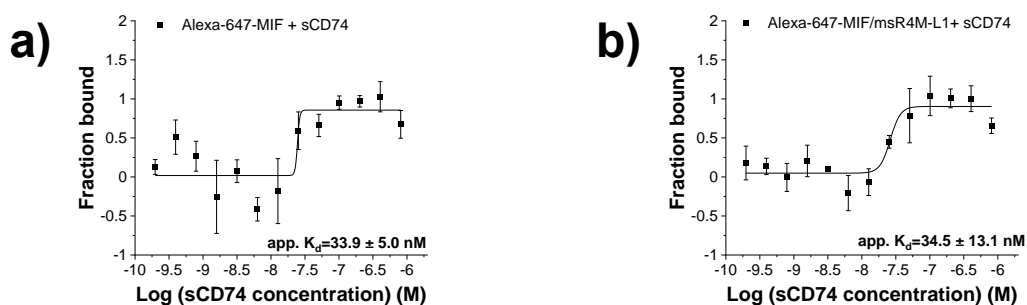
Figure 35. Determination of apparent affinities (app. K$_{ds}$) of the titration of Alexa-647-MIF, with or without msR4M-L1, with sCD74 by MST. a, b Fraction bound of sCD74 against 20 nM Alexa-647-MIF (a) or 20 nM Alexa-647-MIF/ 200nM msR4M-L1 (b) is plotted at different concentrations of the titrant. As F$_{cold}$ it was considered the mean fluorescence derived by the MST signal between -1 and 0 s, and as F$_{hot}$ the mean fluorescence derived by the MST signal between 29 and 30 s prior to their normalization. Data shown are means (±SD) from three independent titration experiments which were performed in aqueous 10mM Tris, 0.25×PBS, 0.005% BSA in 37°C (adapted from Kontos et al., ref. [291]).

4.1.7 Mapping crucial residues of MIF for the interaction to msR4M-L1 and other msR4Ms

4.1.7.1 Determination of binding affinities of msR4Ms to MIF fragments

As presented previously, Fluos-msR4M-L1 had a strong affinity to MIF according to derived studies by fluorescence spectroscopy, FP and MST. MIF consists of 114 residues, and the initial studies focused on determining the MIF epitope in which Fluos-msR4M-L1 can bind with a comparable K_d to the determined one against the whole protein. The titrations were performed as already described, with 5 or 10 nM of the labeled analyte being measured against increased titrant concentrations at 1×b, pH 7.4, 1% HFIP.

Studies of binding of Fluos-msR4M-L1 to the MIF partial sequences in the region 2-32 revealed that the mimic could not bind any of them strongly, since the app. K_{ds} for MIF(2-16), MIF(6-23), MIF(13-27) and MIF(18-32) were above 20000 nM (Figure 36). In the same range were estimated the dissociation constants for MIF(23-38) and MIF(28-43), but a different result was obtained for MIF(38-80). Fluos-msR4M-L1 and MIF(38-80) share an app. K_d of 57.1 ± 7.8 nM, which became higher than 2000 nm when the next fragment MIF(69-90) was tested (Figure 37). Fluos-msR4M-L1 and fragments MIF(76-90) and MIF(81-94) did not bind until 20000 nM suggesting app. K_{ds} in a higher concentration. On the contrary, the labeled peptide bound to MIF(81-95) and MIF(81-102) with the calculated dissociation constants being equal to 481.1 ± 43.5 and 480.2 ± 83.1 nM, respectively (Figure 38). Further studies on the MIF region between 82nd and 115th amino acid indicated a very weak affinity, as the app. K_{ds} between Fluos-msR4M-L1 and MIF(82-95), MIF(86-100), MIF(91-105) and MIF(101-115) were estimated above either 10000 nM or 20000 nM (Figure 39). As MIF(38-80) appeared to be the binding interface of MIF for msR4M-L1, additional studies were carried out for narrowing even more to the hot spot region.

Fluorescence spectroscopic titrations of Fluos-msR4M-L1 with fragments MIF(38-60) and MIF(38-64) did not indicate any binding below 20000 nM, suggesting app. K_{ds} above this latest measured point (Figure 40a-d). The affinity between the mimic and MIF fragments improved significantly after elongation of the C-terminus with the app. K_d for MIF(38-68) and MIF(38-72) being equal to 696.3 ± 26.3 nM and 160.7 ± 89.6 nM, respectively(Figure 40e-h). The addition of another four amino acids on the C-terminus brought an even more improved app. K_d between Fluos-msR4M-L1 and MIF(38-76) at 42.2 ± 27.9 nM (Figure 41a, b). Labeled mimic and MIF(50-60) did not bind until 5000 nM, contrarywise to the C-terminus elongated MIF(50-80) that regained a strong affinity with an app. K_d of 55.2 ± 9.9 nM (Figure 41c-f). The fluorescence emission of the analyte remained undifferentiated for the 17-mer MIF(51-67) until its highest measured point at 20000 nM (Figure 41g, h). As MIF(50-80) retained the strong affinity that was previously determined for MIF(38-80), the next tested fragments focused on the further shortening of the 31-mer. Fluos-msR4M-L1 and MIF(54-80) bound strongly with a calculated app. K_d at 70.6 ± 14.2 nM, which became seven times worse after eliminating S54 for the fragment MIF(55-80) (Figure 42a-d). The labeled-mimic was able to bind to MIF(56-69) and MIF(57-80) as well but not as strong as with MIF(54-80), with the dissociation constants being determined 1819 ± 491 nM and 283.1 ± 57.7 nM, respectively (Figure 42e-h). Likewise, the labeled-analyte managed to bind to MIF(58-80) with an app. K_d at 540.4 ± 206.3 nM, but not to MIF(60-74) until 20000 nM (Figure 43a-d). Fluos-msR4M-L1 and MIF(60-80) had a micromolar affinity and,

more precisely, an app. K_d at 1758 ± 272 nM, which turned to be above 10000 nM for the 19-mer MIF(62-80), after the subtraction of MIF residues C60 and S61 (Table 21, Figure 43e-h). Summarized results and comparison of the binding affinities of msR4Ms to the different MIF fragments are described in 'Discussion' (see 5.1).
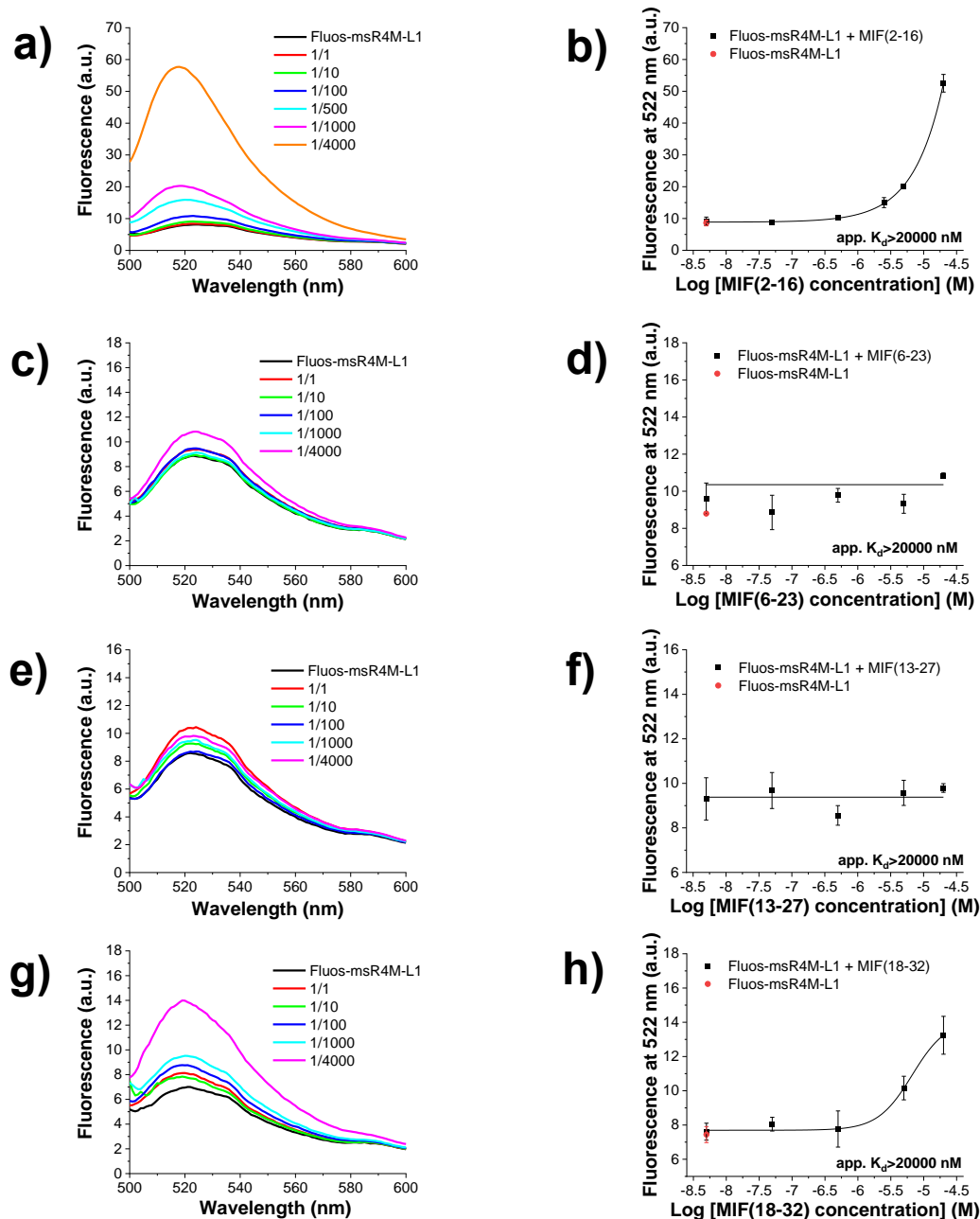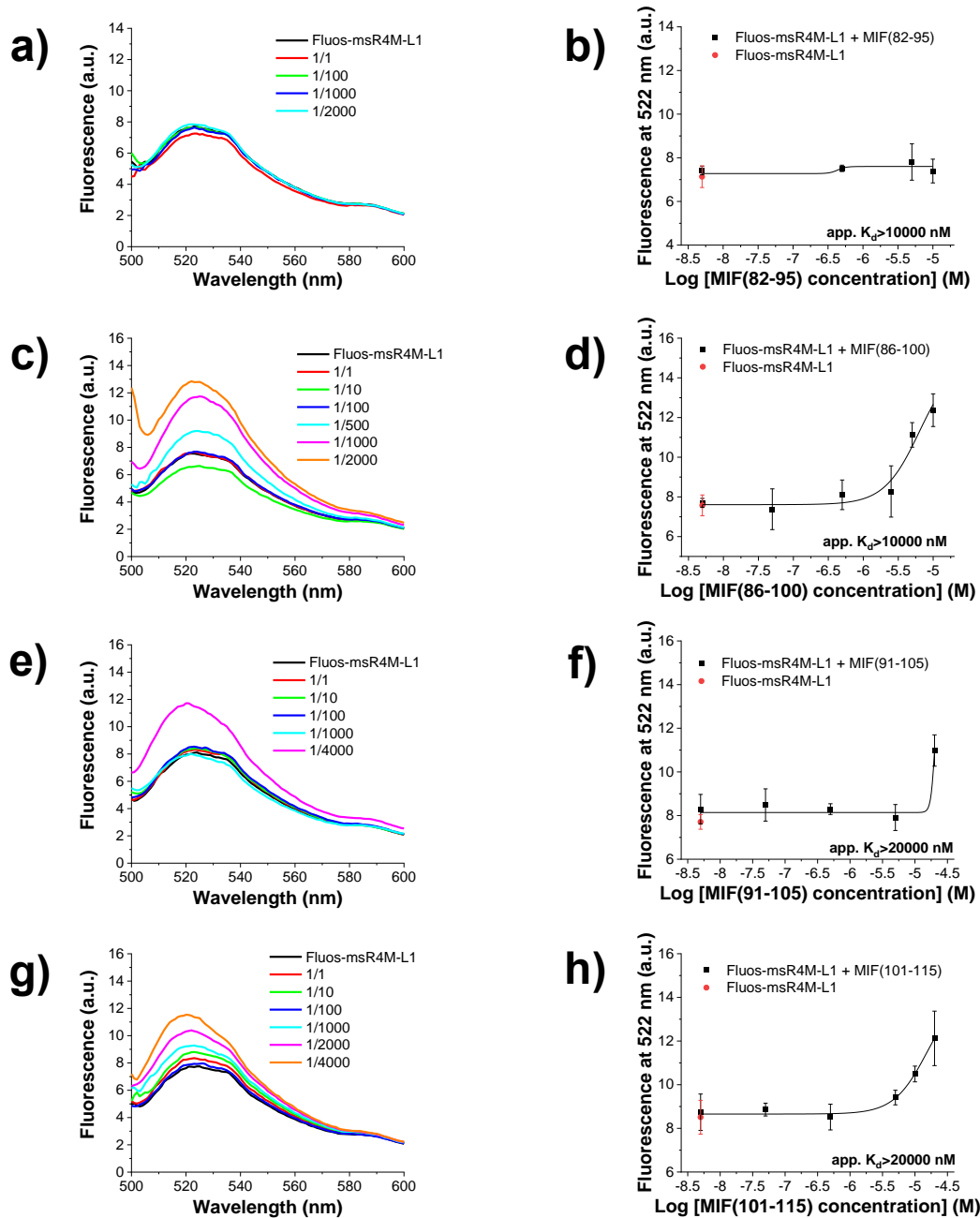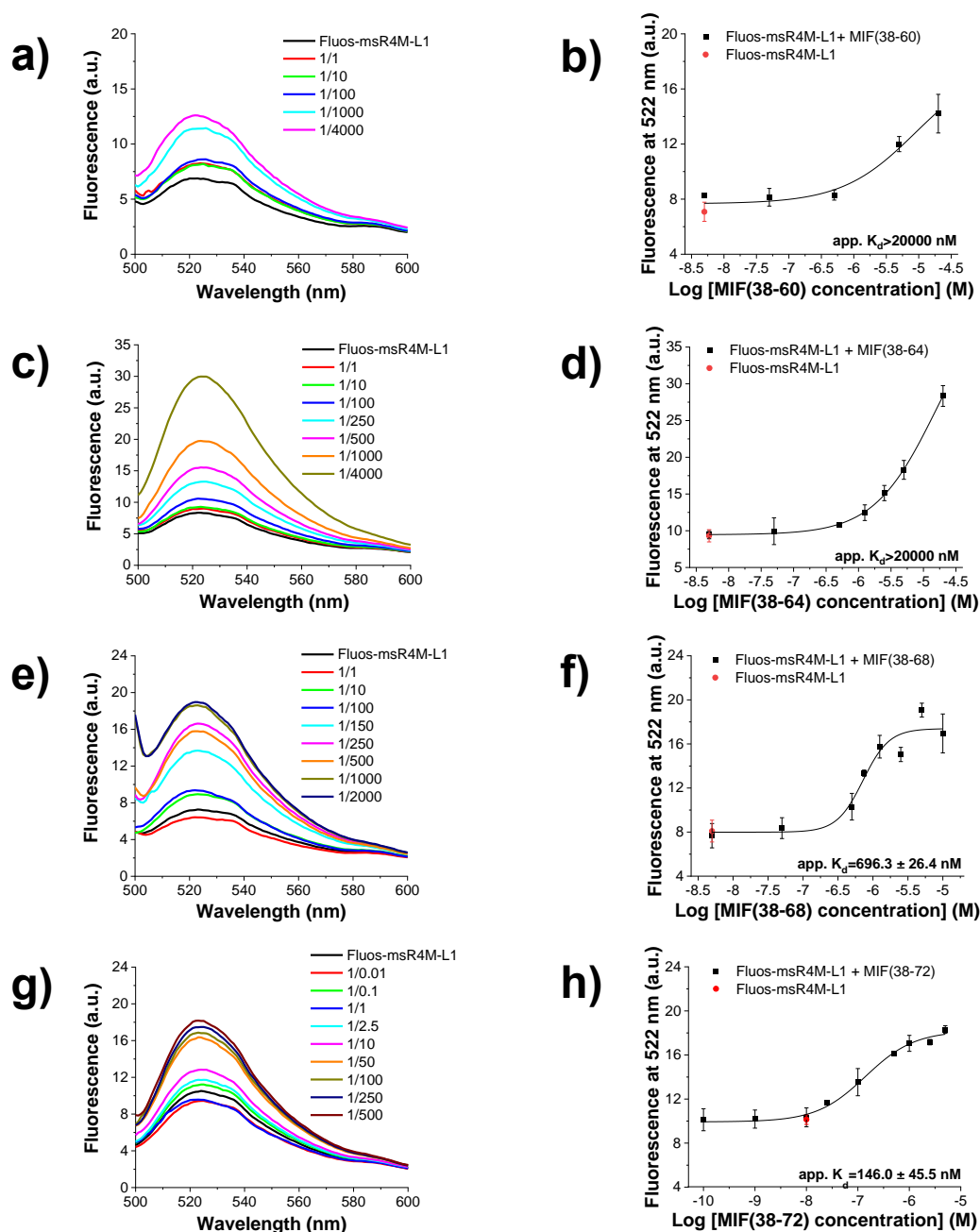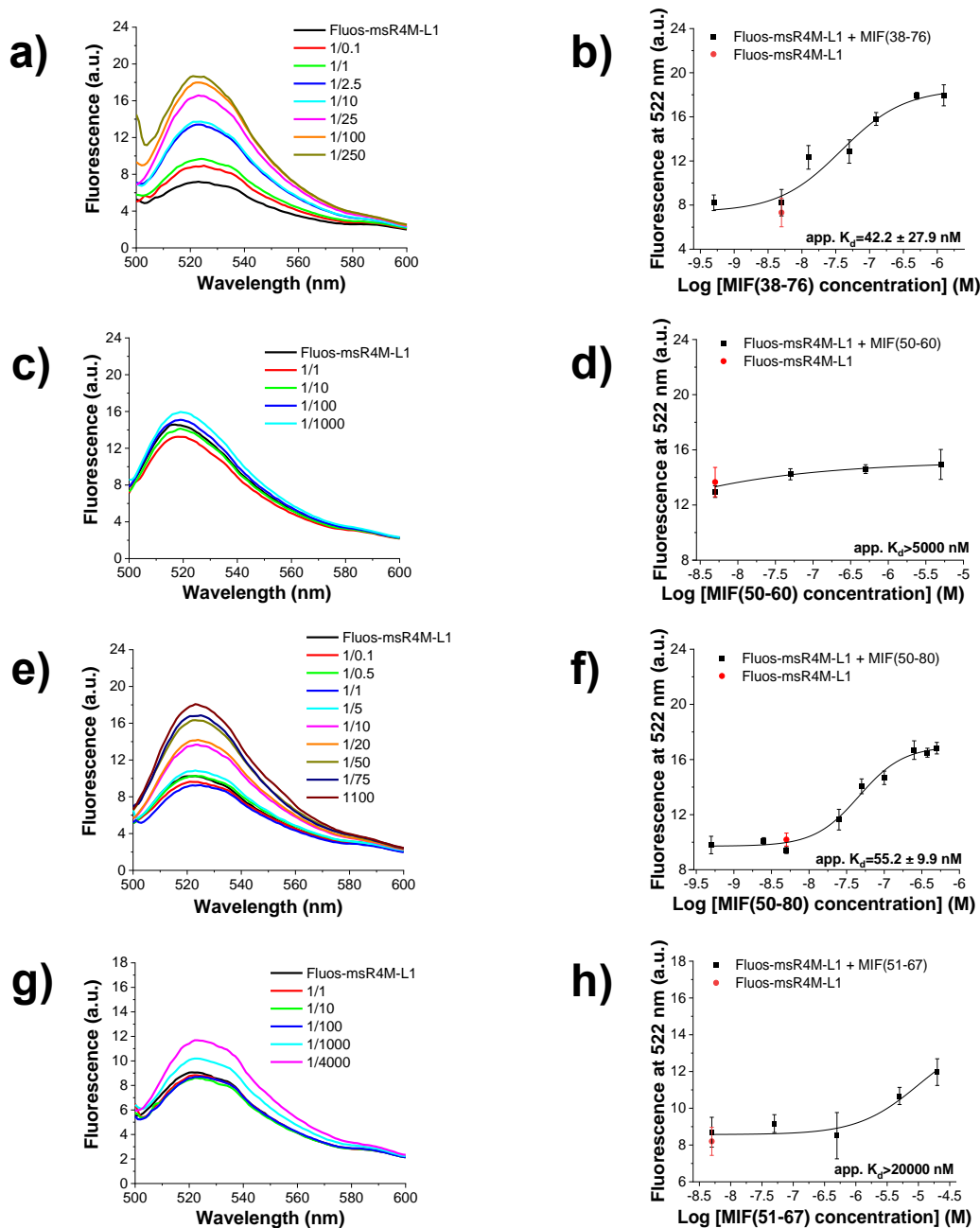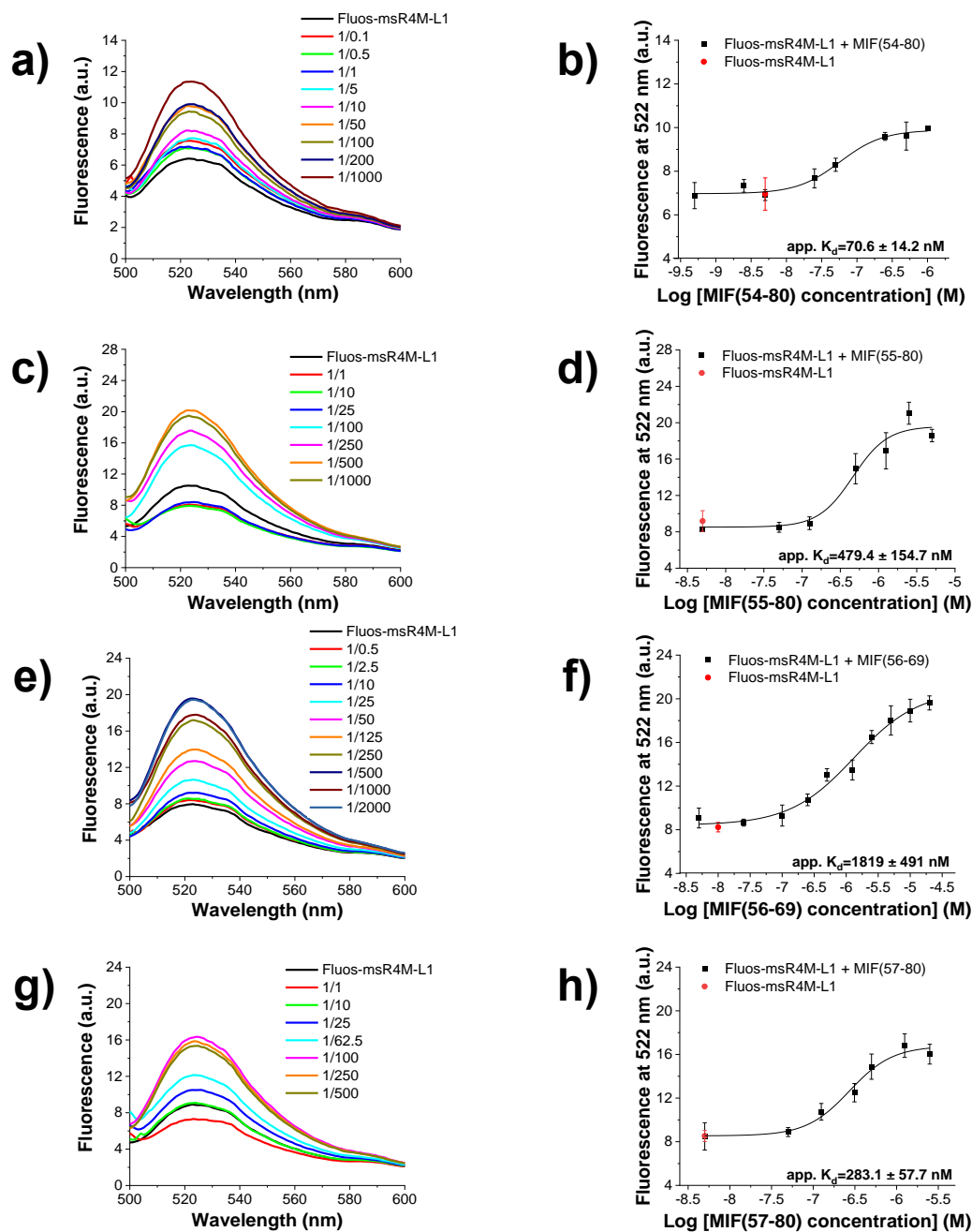

Figure 36. Fluorescence spectroscopic titrations of Fluos-msR4M-L1 with MIF(2-16), MIF(6-23), MIF(13-27) and MIF(18-32) for the determination of apparent affinities (app. K_{ds}). a, c, e, g Fluorescence spectra between 500 and 600 nm of Fluos-msR4M-L1 (5 nM) alone and its mixtures with various amounts of MIF(2-16) (a), MIF(6-23) (c), MIF(13-27) (e) and MIF(18-32) (g); the molar ratios of Fluos-msR4M/MIF fragments are indicated. **b, d, f, h** Binding curves derived from the fluorescence emission at 522 nm of Fluos-msR4M-L1 (5 nM) at different concentrations of MIF(2-16) (b), MIF(6-23) (d), MIF(13-27) (f) and MIF(18-32) (h). Data shown are means (±SD) from three independent titration experiments which were performed in aqueous 1×b, pH 7.4, containing 1% HFIP (adapted from Kontos et al., ref. [291]).
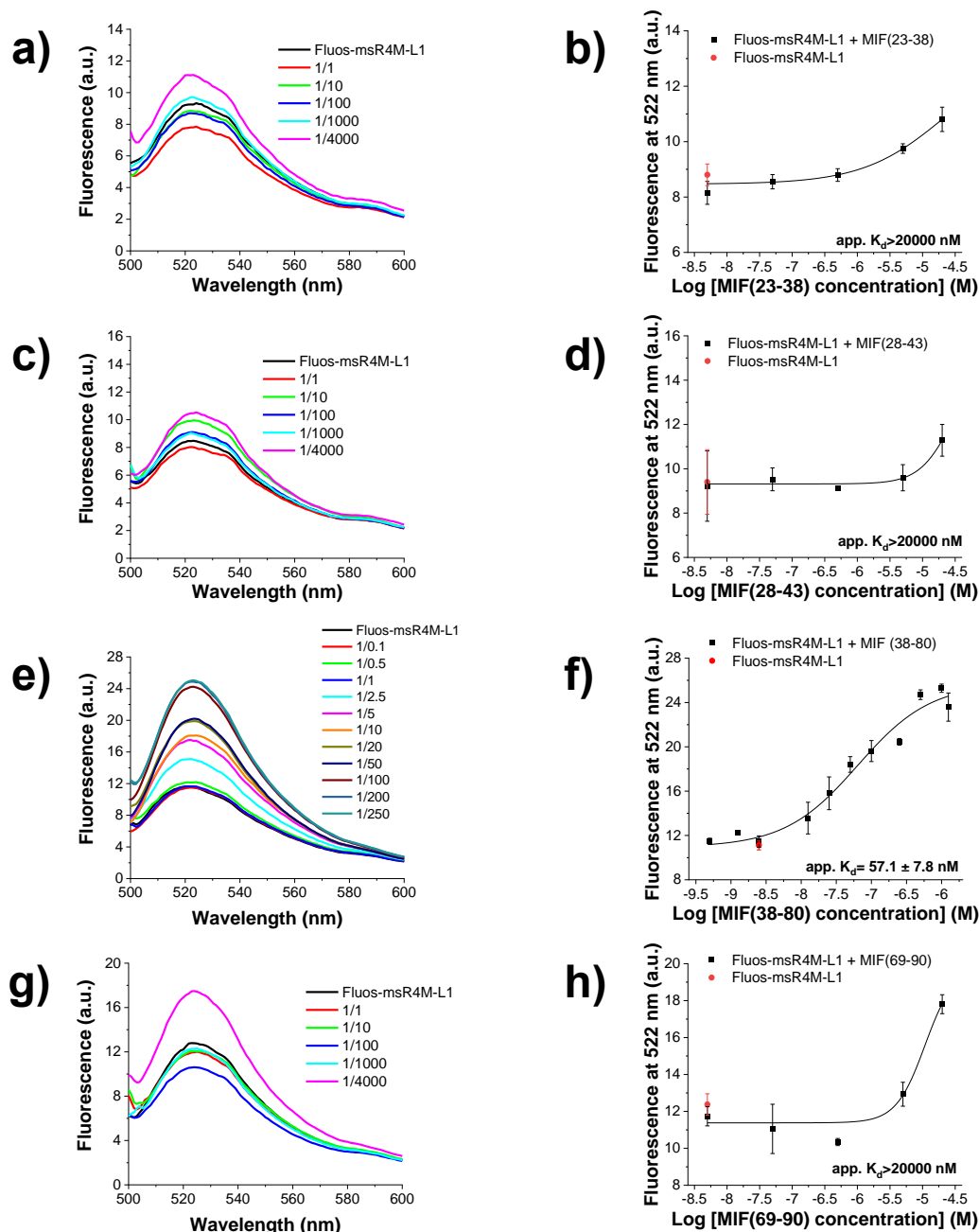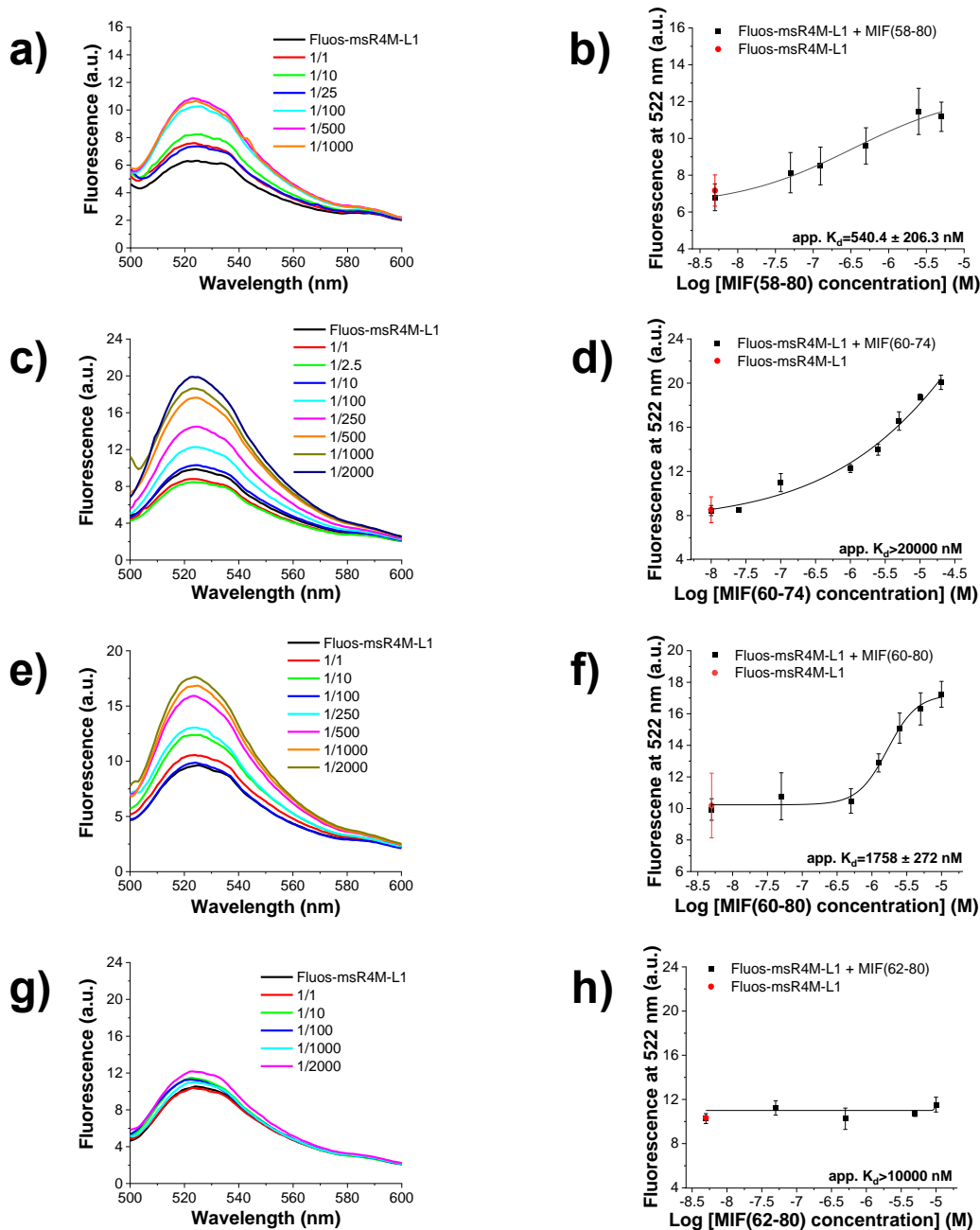
Figure 37. Fluorescence spectroscopic titrations of Fluos-msR4M-L1 with MIF(23-38), MIF(28-43), MIF(38-80) and MIF(69-90) for the determination of apparent affinities (app. K_{ds}). a, c, e, g Fluorescence spectra between 500 and 600 nm of Fluos-msR4M-L1 (5 nM) alone and its mixtures with various amounts of MIF(23-38) (a), MIF(28-43) (c), MIF(38-80) (e) and MIF(69-90) (g); the molar ratios of Fluos-msR4M/MIF fragments are indicated. **b, d, f, h** Binding curves derived from the fluorescence emission at 522 nm of Fluos-msR4M-L1 (5 nM) at different concentrations of MIF(23-38) (b), MIF(28-43) (d), MIF(38-80) (f) and MIF(69-90) (h). Data shown are means (±SD) from three independent titration experiments which were performed in aqueous 1×b, pH 7.4, containing 1% HFIP (adapted from Kontos et al., ref. [291]).
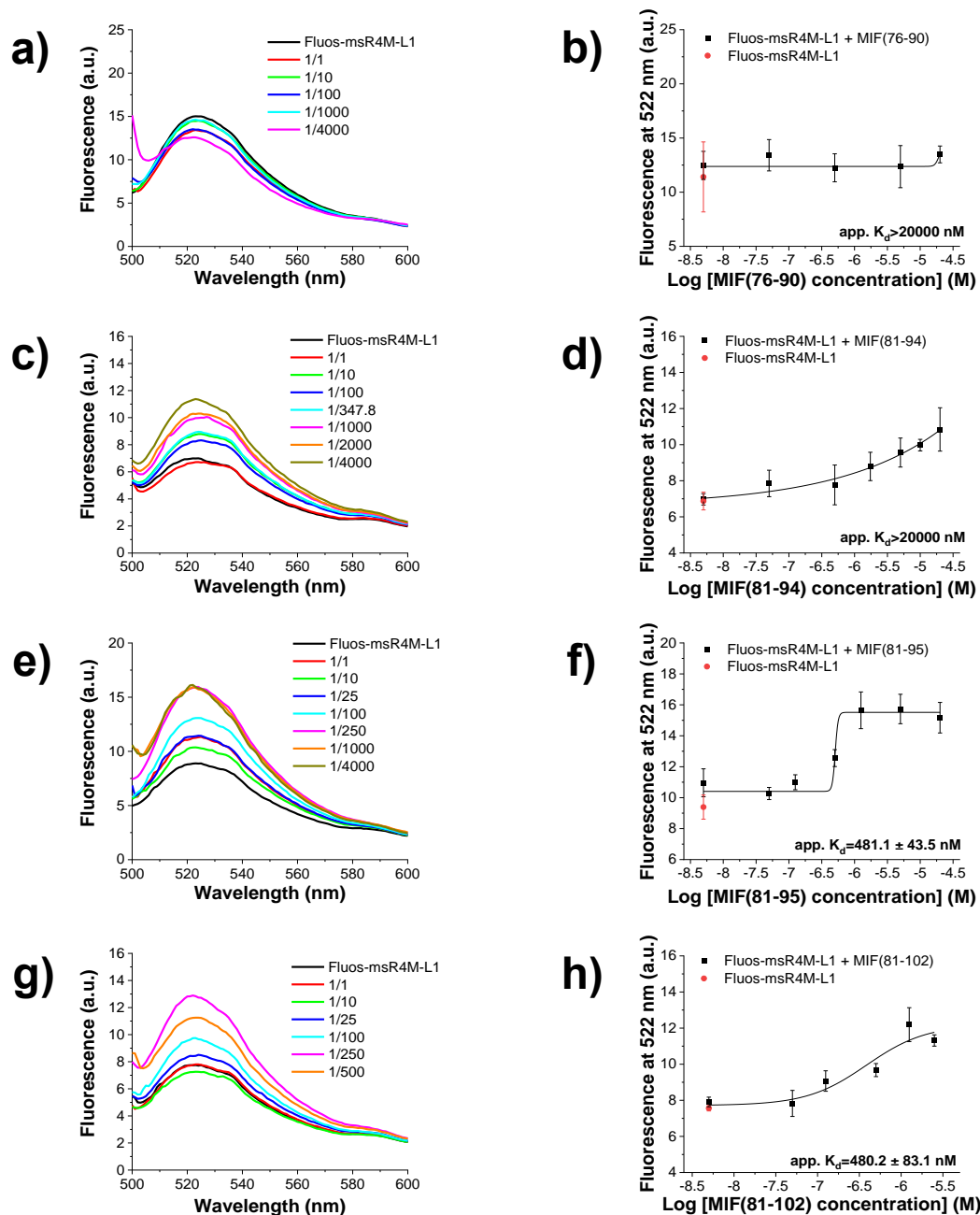
Figure 38. Fluorescence spectroscopic titrations of Fluos-msR4M-L1 with MIF(76-90), MIF(81-94), MIF(81-95) and MIF(81-102) for the determination of apparent affinities (app. K$_{ds}$). a, c, e, g Fluorescence spectra between 500 and 600 nm of Fluos-msR4M-L1 (5 nM) alone and its mixtures with various amounts of MIF(76-90) (a), MIF(81-94) (c), MIF(81-95) (e) and MIF(81-102) (g); the molar ratios of Fluos-msR4M/MIF fragments are indicated. **b, d, f, h** Binding curves derived from the fluorescence emission at 522 nm of Fluos-msR4M-L1 (5 nM) at different concentrations of MIF(76-90) (b), MIF(81-94) (d), MIF(81-95) (f) and MIF(81-102) (h). Data shown are means (±SD) from three independent titration experiments which were performed in aqueous 1×b, pH 7.4, containing 1% HFIP.

Figure 39. Fluorescence spectroscopic titrations of Fluos-msR4M-L1 with MIF(82-95), MIF(86-100), MIF(91-105) and MIF(101-115) for the determination of apparent affinities (app. K$_{ds}$). a, c, e, g Fluorescence spectra between 500 and 600 nm of Fluos-msR4M-L1 (5 nM) alone and its mixtures with various amounts of MIF(82-95) (a), MIF(86-100) (c), MIF(91-105) (e) and MIF(101-115) (g); the molar ratios of Fluos-msR4M/MIF fragments are indicated. **b, d, f, h** Binding curves derived from the fluorescence emission at 522 nm of Fluos-msR4M-L1 (5 nM) at different concentrations of MIF(82-95) (b), MIF(86-100) (d), MIF(91-105) (f) and MIF(101-115) (h). Data shown are means (±SD) from three independent titration experiments which were performed in aqueous 1×b, pH 7.4, containing 1% HFIP.

Figure 40. Fluorescence spectroscopic titrations of Fluos-msR4M-L1 with MIF(38-60), MIF(38-64), MIF(38-68) and MIF(38-72) for the determination of apparent affinities (app. K_{ds}). a, c, e, g Fluorescence spectra between 500 and 600 nm of Fluos-msR4M-L1 (5 nM for a,c,e and 10 nM for g) alone and its mixtures with various amounts of MIF(38-60) (a), MIF(38-64) (c), MIF(38-68) (e) and MIF(38-72) (g); the molar ratios of Fluos-msR4M-L1/MIF fragments are indicated. **b, d, f, h** Binding curves derived from the fluorescence emission at 522 nm of Fluos-msR4M-L1 (5 nM for b, d, f and 10 nM for h) at different concentrations of MIF(38-60) (b), MIF(38-64) (d), MIF(38-68) (f) and MIF(38-72) (h). Data shown are means (±SD) from three independent titration experiments which were performed in aqueous 1×b, pH 7.4, containing 1% HFIP (adapted from Kontos et al., ref. [291]).

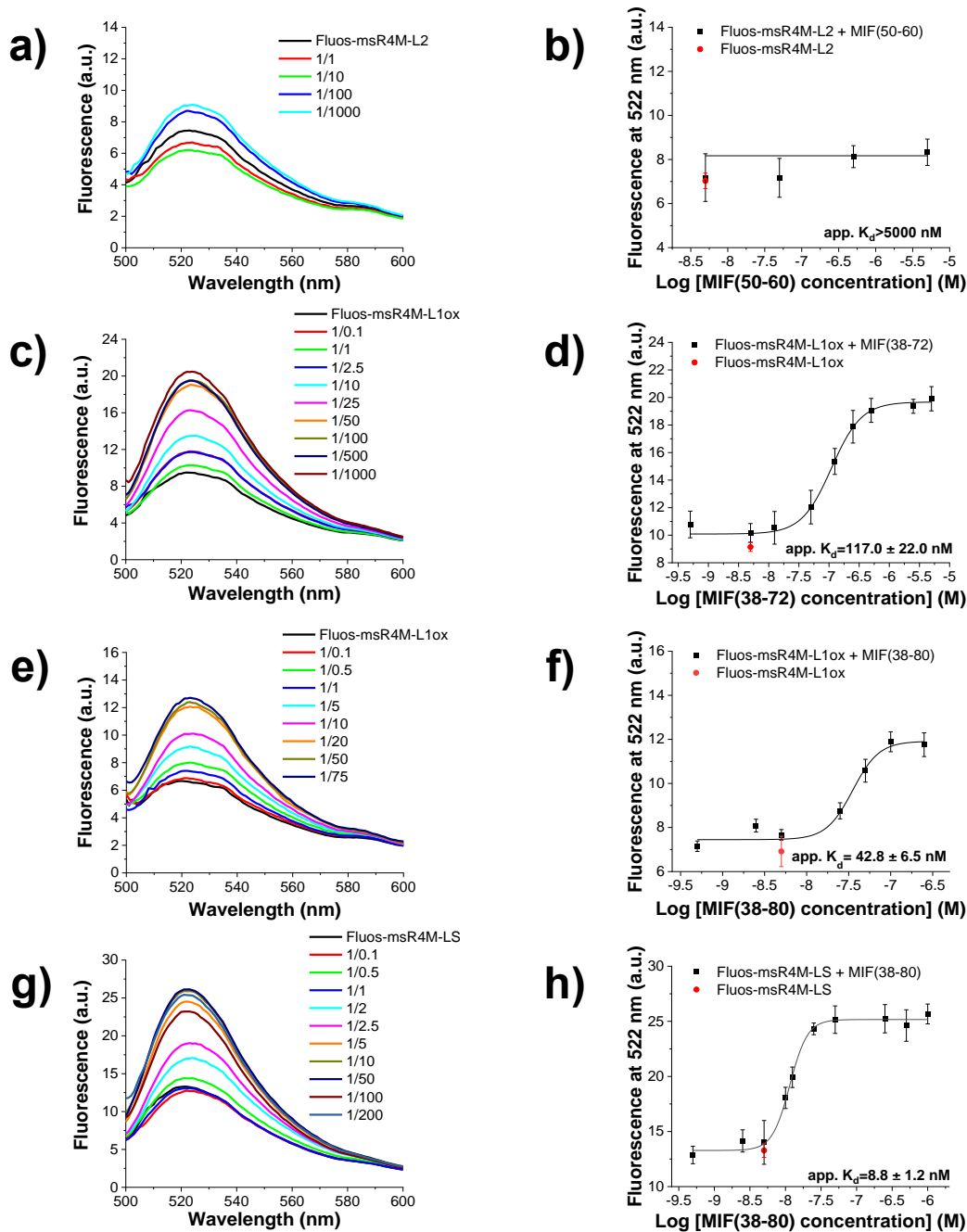**Figure 41. Fluorescence spectroscopic titrations of Fluos-msR4M-L1 with MIF(38-76), MIF(50-60), MIF(50-80) and MIF(51-67) for the determination of apparent affinities (app. K$_{ds}$). a, c, e, g** Fluorescence spectra between 500 and 600 nm of Fluos-msR4M-L1 (5 nM for a,c,e and 10 nM for g) alone and its mixtures with various amounts of MIF(38-76) (a), MIF(50-60) (c), MIF(50-80) (e) and MIF(51-67) (g); the molar ratios of Fluos-msR4M-L1/MIF fragments are indicated. **b, d, f, h** Binding curves derived from the fluorescence emission at 522 nm of Fluos-msR4M-L1 (5 nM for b, d, f and 10 nM for h) at different concentrations of MIF(38-76) (b), MIF(50-60) (d), MIF(50-80) (f) and MIF(51-67) (h). Data shown are means (±SD) from three independent titration experiments which were performed in aqueous 1×b, pH 7.4, containing 1% HFIP.

Figure 42. Fluorescence spectroscopic titrations of Fluos-msR4M-L1 with MIF(54-80), MIF(55-80), MIF(56-69) and MIF(57-80) for the determination of apparent affinities (app. K_{ds}). a, c, e, g Fluorescence spectra between 500 and 600 nm of Fluos-msR4M-L1 (5 nM for a,c,g and 10 nM for e) alone and its mixtures with various amounts of MIF(54-80) (a), MIF(55-80) (c), MIF(56-69) (e) and MIF(57-80) (g); the molar ratios of Fluos-msR4M-L1/MIF fragments are indicated. **b, d, f, h** Binding curves derived from the fluorescence emission at 522 nm of Fluos-msR4M-L1 (5 nM for b, d, h and 10 nM for f) at different concentrations of MIF(54-80) (b), MIF(55-80) (d), MIF(56-69) (f) and MIF(57-80) (h). Data shown are means (±SD) from three independent titration experiments which were performed in aqueous 1×b, pH 7.4, containing 1% HFIP (adapted from Kontos et al., ref. [291]).

90

Figure 43. Fluorescence spectroscopic titrations of Fluos-msR4M-L1 with MIF(58-80), MIF(60-74), MIF(60-80) and MIF(62-80) for the determination of apparent affinities (app. K_{ds}). a, c, e, g Fluorescence spectra between 500 and 600 nm of Fluos-msR4M-L1 (5 nM for a,e,h and 10 nM for c) alone and its mixtures with various amounts of MIF(58-80) (a), MIF(60-74) (c), MIF(60-80) (e) and MIF(62-80) (g); the molar ratios of Fluos-msR4M-L1/MIF fragments are indicated. **b, d, f, h** Binding curves derived from the fluorescence emission at 522 nm of Fluos-msR4M-L1 (5 nM for b, f, h and 10 nM for d) at different concentrations of MIF(58-80) (b), MIF(60-74) (d), MIF(60-80) (f) and MIF(62-80) (h). Data shown are means (±SD) from three independent titration experiments which were performed in aqueous 1×b, pH 7.4, containing 1% HFIP (adapted from Kontos et al., ref. [291]).

Table 21. Apparent affinities (app. K_{ds}) of interaction between Fluos-msR4M-L1 and MIF fragments, as determined by fluorescence spectroscopic titrations (adapted from Kontos et al., ref. [291]).

Overall screen of MIF(2-115)		Screen of binding region MIF(38-80)	
MIF(fragment)	Fluos-msR4M-L1/ MIF(fragment) app. K_d (nM)[a]	MIF(fragment)	Fluos-msR4M-L1/ MIF(fragment) app. K_d (nM)[a]
MIF(2-16)	> 20000	MIF(38-80)	57.1 (±7.8)
MIF(6-23)	> 20000	MIF(38-60)	> 20000
MIF(13-27)	> 20000	MIF(38-64)	> 20000
MIF(18-32)	> 20000	MIF(38-68)	696.3 (±26.3)
MIF(23-38)	> 20000	MIF(38-72)	160.7 (±89.6)[b]
MIF(28-43)	> 20000	MIF(38-76)	42.2 (±27.9)
MIF(38-80)	57.1 (±7.8)	MIF(50-60)	> 5000
MIF(69-90)	> 20000	MIF(50-80)	55.2 (±9.9)
MIF(76-90)	> 20000	MIF(51-67)	> 20000[b]
MIF(81-94)	> 20000	MIF(54-80)	70.6 (±14.2)
MIF(81-95)	481.1 (±43.5)	MIF(55-80)	479.4 (±154.7)
MIF(81-102)	480.2 (±83.1)	MIF(56-69)	1819 (±491)
MIF(82-95)	> 10000	MIF(57-80)	283.1 (±57.7)
MIF(86-100)	> 20000	MIF(58-80)	540.4 (±206.3)
MIF(91-105)	> 10000	MIF(60-74)	> 20000[b]
MIF(101-115)	> 20000	MIF(60-80)	1758 (±272)
		MIF(62-80)	> 10000

[a] App. K_{ds}, are means (±SD) from three independent titration experiments which were performed in aqueous 1×b, pH 7.4, containing 1% HFIP. Titrations were applied with 5 nM of Fluos-msR4M-L1, except for [b], in which Fluos-msR4M-L1 was used at 10 nM.

Additional studies on selected MIF fragments between the 38th and the 80th residue were carried out against the other msR4Ms. The set goal was to figure out whether they follow a similar pattern to msR4M-L1 on binding to MIF or not. Fluos-msR4M-L2 failed to bind to MIF(50-60) until 5000 nM, while labeled-msR4M-L1ox had a strong affinity with fragments MIF(38-72) and MIF(38-80) with app. K_{ds} 117.0 ± 22.0 nM and 42.8 ± 6.5 nM, respectively (Figure 44a-f). MIF(38-80) was titrated against Fluos-msR4M-LS as well, with a strong affinity estimated and an app. K_d of 8.8 ± 1.2 nM (Figure 44g, h). Titrations between the labeled-msR4M-L2 and fragments MIF(50-80) and MIF(54-80) showed app. K_{ds} of 30.9 ± 20.4 nM and 52.9 ± 25.6 nM, respectively (Figure 45a-d). The calculated dissociation constants between Fluos-msR4M-L1ox and fragments MIF(54-80) and MIF(56-69) varied from 146.8 ± 46.7 nM for the 27-mer to 2146 ± 930 for the 14-mer (Figure 45e-h). Labeled-msR4M-LS and MIF(50-80) bound with an app. K_d of 20.9 ± 1.8 nM (Figure 45i, j). In a similar manner to msR4M-L1 analog, the estimated app. K_{ds} between labeled-msR4M-L2 and MIF(62-80) were above 5000 nM when the Fluos-msR4M-L1ox and MIF(60-74) shared an app. K_d of 785.1 ±1 51.7 nM (Figure 46a-d). All oxidized msR4Ms were titrated against MIF(62-80) with the determined app. K_{ds} being above 5000 nM for Fluos-msR4M-L1ox, 1251.0 ± 30.0 nM for Fluos-msR4M-L2ox and equal to 33.9 ± 2.1 nM for Fluos-msR4M-LS (Table 22, Figure 46e-j).

Figure 44. Fluorescence spectroscopic titrations of Fluos-msR4Ms with MIF(50-60), MIF(38-72) and MIF(38-80) for the determination of apparent affinities (app. K_{ds}). a, c, e, g Fluorescence spectra between 500 and 600 nm of 5 nM of Fluos-msR4M-L2 (a), Fluos-msR4M-L1ox (c, e) and Fluos-msR4M-LS (g) alone and their mixtures with various amounts of MIF(50-60) (a), MIF(38-72) (c) and MIF(38-80) (e, g); the molar ratios of Fluos-msR4Ms/MIF fragments are indicated. **b, d, f, h** Binding curves derived from the fluorescence emission at 522 nm of Fluos-msR4M-L2 (b), Fluos-msR4M-L1ox (d, f) and Fluos-msR4M-LS (h) at different concentrations of MIF(50-60) (b), MIF(38-72) (d) and MIF(38-80) (f, h). Data shown are means (±SD) from three independent titration experiments which were performed in aqueous 1×b, pH 7.4, containing 1% HFIP.
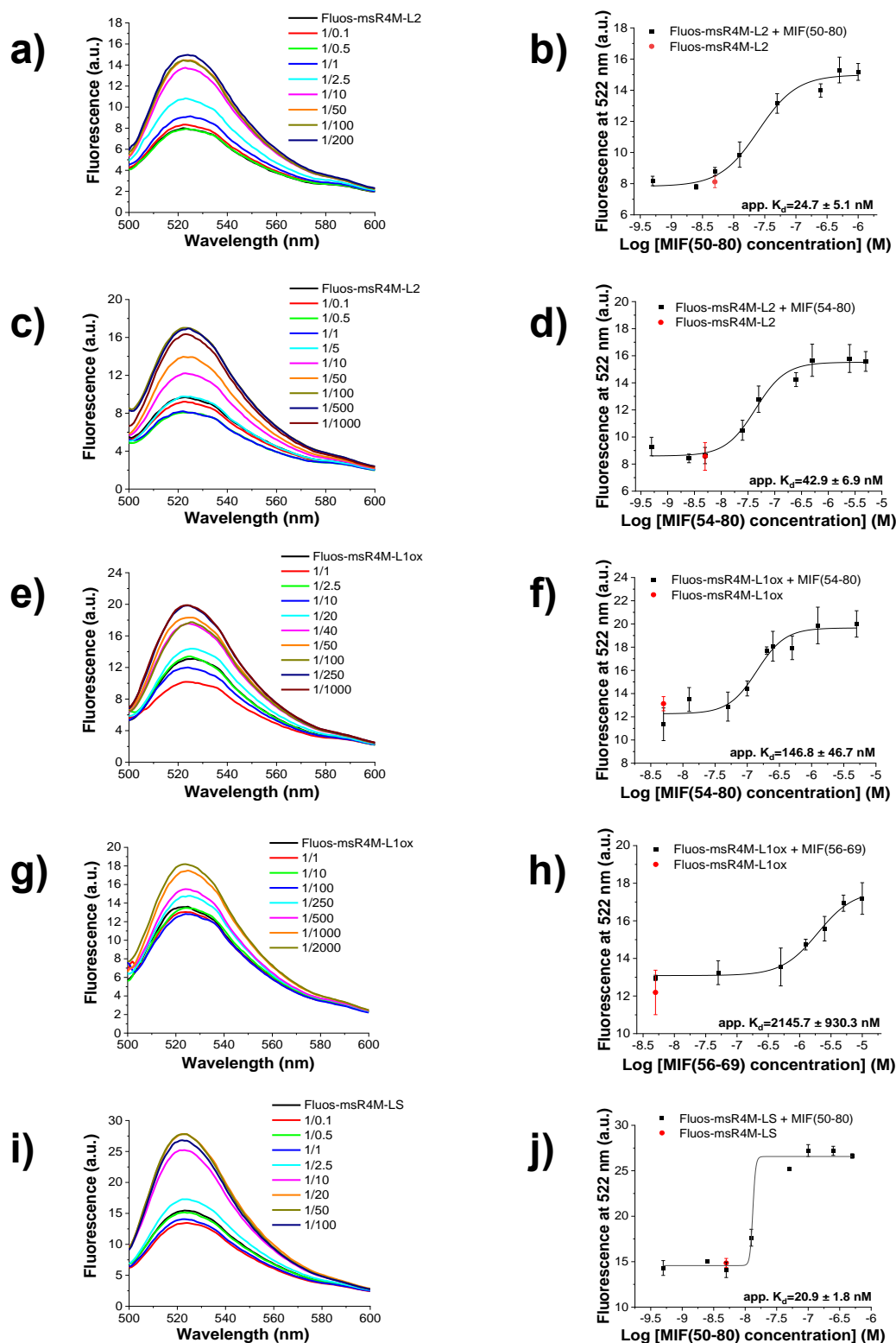
Figure 45. Fluorescence spectroscopic titrations of Fluos-msR4Ms with MIF(50-80), MIF(54-80) and MIF(56-69) for the determination of apparent affinities (app. K$_{ds}$). a, c, e, g, i Fluorescence spectra between 500 and 600 nm of 5 nM of Fluos-msR4M-L2 (a, c), Fluos-msR4M-L1ox (e, g) and Fluos-msR4M-LS (i) alone and their mixtures with various amounts of MIF(50-80) (a, i), MIF(54-80) (c, e) and MIF(56-69) (g); the molar ratios of Fluos-msR4Ms/MIF fragments are indicated. **b, d, f, h, j** Binding curves derived from the fluorescence emission at 522 nm of Fluos-msR4M-L2 (b, d), Fluos-msR4M-L1ox (f, h) and Fluos-msR4M-LS (j) at different concentrations of MIF(50-80) (b, j), MIF(54-80) (d, f) and MIF(56-69) (j). Data shown are means (±SD) from three independent titration experiments which were performed in aqueous 1×b, pH 7.4, containing 1% HFIP.
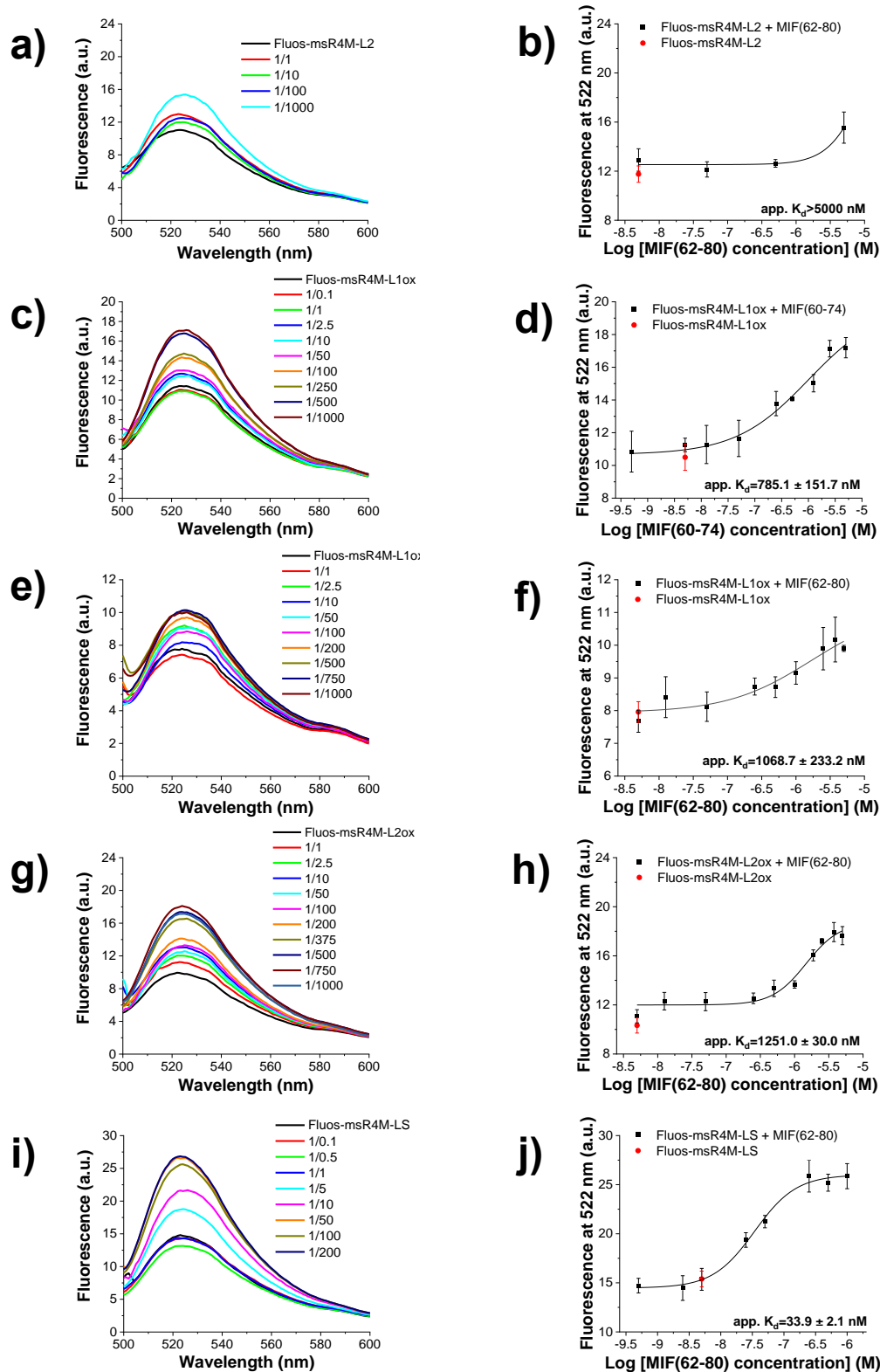
Figure 46. Fluorescence spectroscopic titrations of Fluos-msR4Ms with MIF(62-80) and MIF(60-74) for the determination of apparent affinities (app. K_{ds}). a, c, e, g, i Fluorescence spectra between 500 and 600 nm of 5 nM of Fluos-msR4M-L2 (a), Fluos-msR4M-L1ox (c, e), Fluos-msR4M-L2ox (g) and Fluos-msR4M-LS (i) alone and their mixtures with various amounts of MIF(62-80) (g); the molar ratios of Fluos-msR4Ms/MIF fragments are indicated. **b, d, f, h, j** Binding curves derived from the fluorescence emission at 522 nm of Fluos-msR4M-L2 (b), Fluos-msR4M-L1ox (d, f), Fluos-msR4M-L2ox (h) and Fluos-msR4M-LS (j) at different concentrations of MIF(62-80). Data shown are means (±SD) from three independent titration experiments which were performed in aqueous 1×b, pH 7.4, containing 1% HFIP.

95

Table 22. Apparent affinities (app. K_{ds}) of interaction between Fluos-msR4M-L2, -L1ox, -L2ox, -LS and MIF fragments, as determined by fluorescence spectroscopic titrations.

MIF (fragment)	Fluos-msR4M-L2/MIF(fragment) app. K_d (nM)[a]	Fluos-msR4M-L1ox/MIF(fragment) app. K_d (nM)[a]	Fluos-msR4M-L2ox/MIF(fragment) app. K_d (nM)[a]	Fluos-msR4M-LS/MIF(fragment) app. K_d (nM)[a]
MIF(38-72)	n.d.[b]	117.0 (±22.0)	n.d.[b]	n.d.[b]
MIF(38-80)	n.d.[b]	42.8 (±6.5)	n.d.[b]	8.8 (±1.2)
MIF(50-80)	30.9 (±20.4)	n.d.[b]	n.d.[b]	20.9 (±1.8)
MIF(54-80)	52.9 (±25.6)	146.8 (±46.7)	n.d.[b]	n.d.[b]
MIF(56-69)	n.d.[b]	2146 (±930)	n.d.[b]	n.d.[b]
MIF(60-74)	n.d.[b]	785.1 (±151.7)	n.d.[b]	n.d.[b]
MIF(62-80)	>5000	>5000	1251.0 (±30.0)	33.9 (±2.1)

[a]: App. K_{ds} are means (±SD) from three independent titration experiments which were performed in aqueous 1×b, pH 7.4, containing 1% HFIP. [b]: n.d., non-determined.

4.1.7.2 Conformational studies of MIF fragments via CD spectroscopy

As previously shown, fragment MIF(38-80) and the shorter MIF(50-80) and MIF(54-80) appeared contain the hot spot regions for the MIF interaction with msR4M-L1. MIF is a well-structured protein, but it is unknown whether MIF fragments as peptides retain an ordered conformation or not. CD spectroscopy was applied to clarify this. The final measuring conditions were the same that were used in the fluorescence spectroscopic titrations that suggested those regions as crucial for the interaction with the lead mimic, i. e aqueous 1×b, pH 7.4, 1 % HFIP.

All MIF fragments were soluble and their 1 to 5 µM obtained spectra showed the random coil indicative signal with the characteristic minima below 200 nm. Furthermore, the peptides exhibited a broad weak negative band between 215 nm and 230 nm at -2000 deg·cm^2·dmol^{-1}, suggesting the presence of few ordered species in the overall unordered sequences. MIF(38-80) and MIF(50-80) reached at their minima values varying in the -8000 to -12000 deg·cm^2·dmol^{-1} and -15000 to -19000 deg·cm^2·dmol^{-1} range, respectively (Figure 47a, b). Together, the data propose the lack of aggregation for those two fragments. Likewise, the 27-mer MIF(54-80) maintained its minima below 200 nm (Figure 47c). A slight subsequent reduction of its MRE signal was noticed as the concentration increased, maybe due to its self-association.
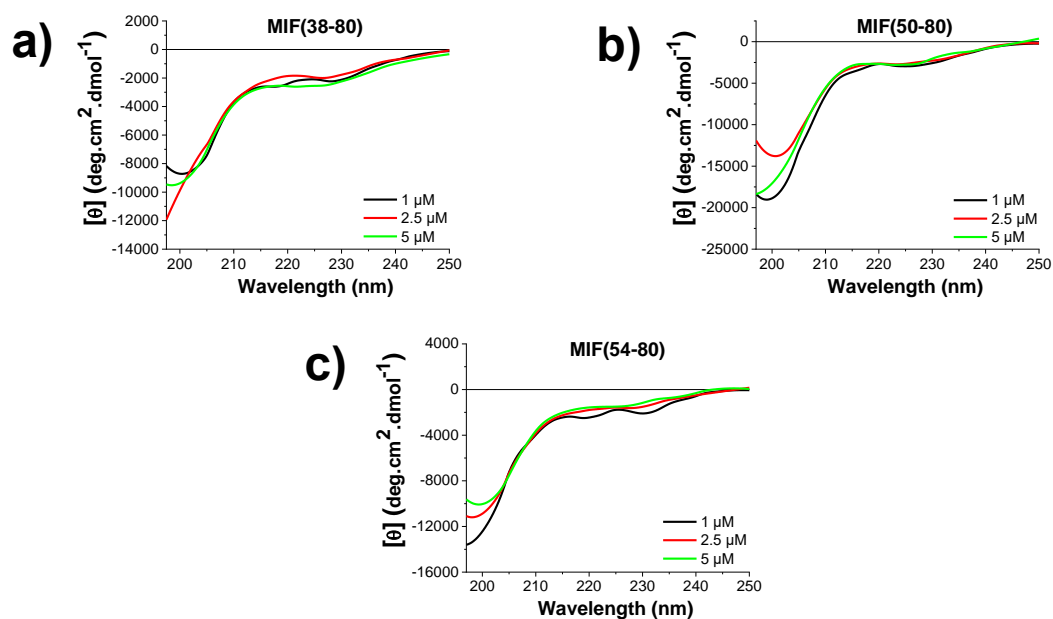
Figure 47. Spectra of MIF fragments in various concentrations for the determination of the conformation, as determined by far-UV CD spectroscopy. a, b, c CD spectra of MIF(38-80) (a), MIF(50-80) (b) and MIF(54-80) (c) at increasing concentrations at final measuring conditions of aqueous 1×b, pH 7.4, containing 1% HFIP. Mean residue ellipticity (MRE) plotted over the wavelength between 197.5 and 250 nm for a, 197 and 250 nm for b, c.

4.1.7.3 Determination of binding affinities of msR4M-L1 to mutants of MIF

The importance of residues and fragments of MIF for its interactions with other receptors and its subsequent activities is of particular interest for the design of an optimized MIF-specific inhibitor. MIF/CXCR4 interaction is known to involve P2 and residues 43-98 from the extended N-like loop of MIF [98]. After its fluorescence spectroscopic titrations with WT-MIF, the prioritized CXCR4-ectodomain mimic msR4M-L1 was further titrated against mutants of the cytokine for the determination of the residues of the binding interface. In the titration against the C57S-MIF mutant, there was no plateau reached and the app. K_d was higher than 2500 nM or at least 62.5-fold higher than the respective dissociation constant with WT-MIF (Figure 48a, b). In a similar manner, the importance of the MIF N-like loop in the interaction with the CXCR4-ectodomain of CXCR4 was confirmed. In particular, Fluos-msR4M-L1 lost its affinity to the 47-56 alanine mutated MIF or, in other words, MIF(10xAla), with the app. K_d estimated to be higher than 500 nM (Figure 48, d).
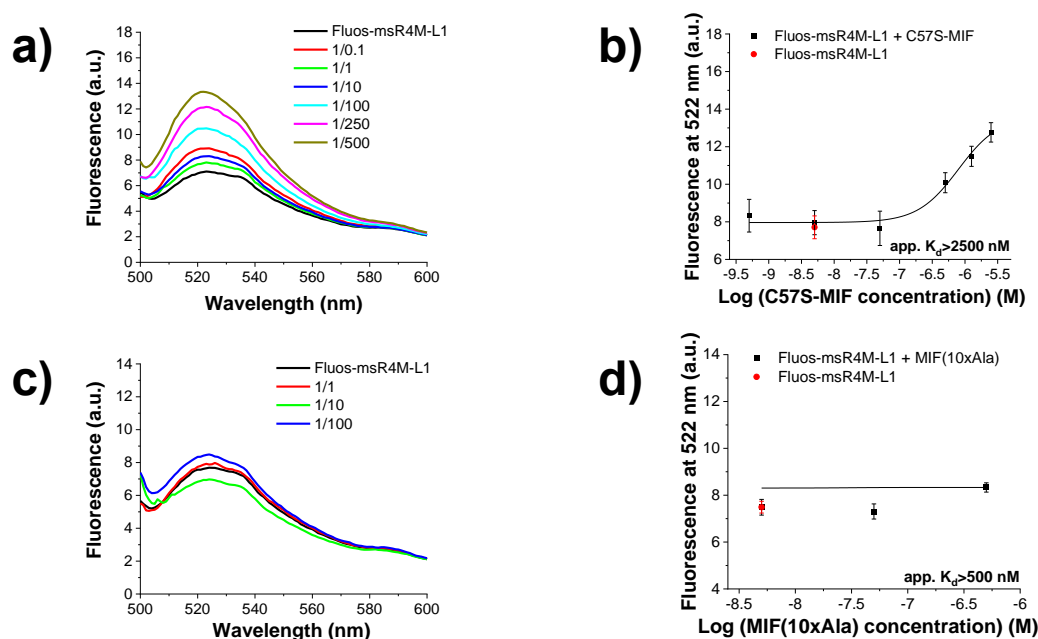
Figure 48. Fluorescence spectroscopic titrations of Fluos-msR4M-L1 with MIF mutants C57S-MIF and MIF(10xAla) for the determination of apparent affinities (app. K$_{ds}$). a, c Fluorescence spectra between 500 and 600 nm of Fluos-msR4M-L1 (5 nM) alone and their mixtures with various amounts of C57S-MIF (a) and MIF(10xAla) (c); the molar ratios of Fluos-msR4M-L1/MIF mutants are indicated. **b, d** Binding curves derived from the fluorescence emission at 522 nm of Fluos-msR4M-L1 (b) at different concentrations of C57S-MIF (b) and MIF(10xAla) (d). Data shown are means (±SD) from three independent titration experiments which were performed in aqueous 1×b, pH 7.4, containing 1% HFIP (adapted from Kontos et al., ref. [291]).

4.1.8 Mapping crucial residues of msR4M-L1 for the binding to MIF
4.1.8.1 SPOT array analysis of ECL1 & ECL2 fragments

The characterization of the binding interface between CXCR4 and its structural properties attracted the interest of researchers, with the recent crystallization of the CXCR4 structure providing more insights [148]. In 2007 it was published that CXCR4 has another ligand, MIF, and nine years later motives contributing to their binding interface were identified [77] [98]. Mainly, ectodomain of CXCR4 seems to be actively involved and especially the residues 43-98 from the extended N-like loop of MIF and the CXCR4 side residues 1-27 of N-terminus, 97-110 of extracellular loop 1 (ECL1), and 182-196 of extracellular loop 2 (ECL2)[98]. As described in chapter 4.1.1., the followed CXCR4-ectodomain mimic approach was based on the covalent linkage between these extracellular loop 1 and -2 fragments for the generation of msR4Ms.

SPOT array analysis was initially used for tracing the essential residues of the interaction of the mimic with MIF. MsR4Ms consist of ECL1 and ECL2, linked together and having a sequence of 29, 31 or 36 residues. The mimics could not be synthesized with the current method due to a possible low yield because of their long sequence that may result in intermediate acetylated side products and false positives/negatives. Hence, on the cellulose membrane there were generated the 14-mer ECL1 or the 15-mer ECL2. Both ECDs are present in all msR4Ms, including the lead compound msR4M-L1. WT and mutated peptides were synthesized, cleaved, and incubated with 3 µM biotinylated recombinant human MIF with the chemiluminescence intensity being quantified via a horse-radish peroxidase (HRP)-conjugated streptavidin.

Single-alanine mutants of ECL1 showed that all residues except for D97A and C109A are important. The introduction of two subsequent alanine mutations in ECL1

sequence suggested an important role of the pair residues 101-102 and 103-104 and of the region 105-108 for the affinity with MIF, while D97-A98 and V99-A100 appear to be involved, too. Studies on triple-alanine mutated ECL1 peptides narrowed down further the number of essential residues and underlined the necessity of the region 102-108. What is of great interest is the presence of four aromatic residues inside this ECL1 fragment, which appear to be actively involved in the interaction with MIF. All four singe-alanine mutations in these aromatic positions showed three times reduced chemiluminescence intensity in comparison to native ECL1. Similar reduced intensity was observed for the W102A-Y103A-F104A and W102A-F104A-F107A ECL1 mutants, too (Figure 49a). The studies were continued in the ECL2 sequence following the same strategy that was applied for ECL1. Immobilized 15-mers of ECL2 were alanine mutated residue-by-residue suggesting a crucial role of residues 187-189, 192, and 194-196 for the interaction with MIF (Figure 49b).

Figure 49. Alanine scanning of ECL1, ECL2 and estimation of their binding to MIF, by peptide arrays. a, b Peptide array analysis using Cellulspot method of ECL1 and ECL2 mutated analogs for determination of msR4M-L1 critical residues for MIF binding. 14-meric single, double or triple alanine or glycine mutants of ECL1 (a) and 15-meric single alanine mutants of ECL2 (b) sequences were synthesized and immobilized on glass slides. The intensity of each spot was quantified after incubation with biotinylated MIF and the substituted residues are bolded and underlined. Substitutions that led to significant reduced in binding are included in the red boxes in red. At the bottom panel it is summarized the findings of the arrays in the sequences of ECL1 and ECL2: amino acids that are circled indicate are characterized as important residues and those that are circled in red were substituted for the generation of msR4M-L1 mutants (adapted from Kontos et al., ref. [291]).

4.1.8.2 Design and synthesis of alanine mutated and other msR4M-L1 analogs

MsR4M-L1 is a CXCR4-ectodomain mimic with a high affinity to MIF, consisting of the 14-mer ECL1 and 15-mer ECL2 being linked via the non-natural amino acids 6 Ahx and 12 Ado. Uncovering pivotal mediators of the msR4M-L1/MIF binding mechanism may provide us insights not only for the specificity of the interaction but also for developing next generation mimics with increased potency and drug-favorable properties. The previously described SPOT array analysis presented data for W102, Y103, F104, F107 from ECL1 and F189, Y190, W195 from ECL2 as key aromatic residues for the interaction with MIF. Next, the methodology was switched from the synthesis of the ECL1 and ECL2 mutants on the cellulose membrane to the Fmoc-

SPPS and the peptide generation on the solid support of the resin before its purification and biophysical testing. Three alanine mutated msR4M-L1 analogs were synthesized for this purpose together with Kathleen Hille (lab of Prof. Kapurniotu). In msR4M-L1(2xAla) sequence, F104 and F107 are substituted, while for msR4M-L1(5xAla) W102, Y103, F189, Y190 and W195 were replaced by alanines. The third analog, msR4M-L1(7xAla) has all seven previously mentioned aromatic amino acids exchanged with alanines, with Y184 left as the only aromatic residue of the sequence. To improve the solubility properties of msR4M-L1, a three-lysine tag was conjugated on the N-terminus of the peptide, resulting in msR4M-K3L1 analog. Each of the three lysines were coupled for 40 min, twice, with 3 eq. of AA, 3 eq. of HBTU and 4.5 eq. of DIEA, and the peptide was obtained pure after applying HPLC and MALDI-TOF-MS (Table 23, Figure 50).

Table 23. Sequences, abbreviation and characterization of synthesized alanine msR4M-L1 mutants and the msR4M-K3L1 analog, by RP-HPLC and MALDI-TOF-MS.

Peptide sequence[a]	Peptide abbrev-iation	HPLC Pr.No.	t_R (min)[b]	Yield (%) [c]	[M+H]+ expected [d]	[M+H]+ found [d]
DAVANWY**A**GN**A**LCK-(6Ahx)-(12 Ado)- DRYICDRFYPNDLWV	msR4M-L1(2xAla)	I) 1 II)2	I)19.80 II)27.75	4.1	3761.53	3761.26
DAVAN**AA**FGNFLCK-(6Ahx)-(12 Ado)- DRYICDR**AA**PNDL**A**V	msR4M-L1(5xAla)	I) 1 II)2	I)19.20 II)25.6	17.6	3420.48	3423.47
DAVAN**AAA**GN**A**LCK-(6Ahx)-(12 Ado)- DRYICDR**AA**PNDL**A**V	msR4M-L1(7xAla)	I) 2 II)1	I)21.10 II)17.5	10.8	3268.42	3271.11
KKKDAVANWYFGNFLCK-(6Ahx)-(12 Ado)- DRYICDRFYPNDLWV	msR4M-K3L1	1	20.80	5.9	4297.21	4298.01

msR4M-K3L1 was dissolved and analyzed by MALDI-TOF-MS in a mixture of MALDI solutions B and B (matrix), with bold are indicated the substituted and the additional conjugated amino acids; **[a]** Peptides were synthesized with free amino-N-terminus and amidated C-terminus; **[b]** HPLC retention time of the pure product, the stationary phase was a tandem of Reprosil Gold 200 C18 columns (250 and 30 mm length, 8 mm internal diameter,10 μm particle size); **[c]** % yield with regard to crude peptide after cleavage; **[d]** monoisotopic molar mass with an additional hydrogen [M+H]+.
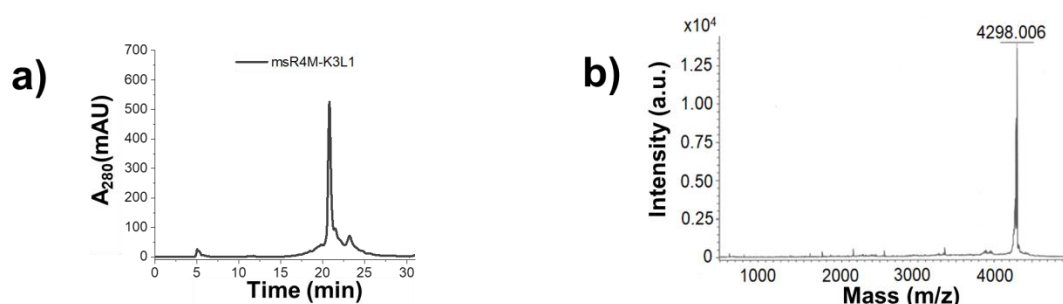
Figure 50. HPLC purification of msR4M-K3L1 and verification of its purity by MALDI. a Representative C18 HPLC chromatogram (absorbance at 280 nm) of crude msR4M-K3L1 with retention time 20.80 min following SPPS and cleavage. **b** MALDI-TOF-MS spectra of HPLC-purified msR4M-K3L1 with experimental determined mass [M+H]+: 4298.006 Da.

4.1.8.3 Conformational studies via CD spectroscopy

The secondary structure of msR4Ms was estimated in chapter 4.1.3.1 by circular dichroism spectroscopic studies. Contrary to individual ECL1 and ECL2 fragments, all linked via non-natural amino acids, ectodomain mimics appear to have ordered structures. MsR4M-L1 exhibited a minimum at 223 nm and a positive signal below 208 nm, consisted with significant contents of β-sheet structure. Spectra at 10 and 20 μM had a gradual decrease in the signal intensity indicating oligomerization of

the peptide, while precipitation occured at 50 µM. MsR4M-L1(2xAla) showed similar solubility properties and a concentration-dependent signal but with a different shape. The introduction of two alanines in positions 104 and 107 instead of phenylalanines was sufficient to disrupt the ordered structure. The double mutant exposed at 1 and 5 µM minima at 202 nm and a second but less intense one at 217 nm, while at 10 µM, the respective minima were shifted at 206 nm and 221 nm. At 20 µM the minima were observed at 201 and 216 nm but herein with similar signal intensity. The minimum at 216-217 nm indicate β-sheet and the existence of a second minimum with a 1.5-fold more intense signal at 201 nm proposed that the peptide is mainly unordered (Figure 51a).

MsR4M-L1(5xAla) was determined to have random coil too. The peptide was analyzed from 1 to 50 µM without getting precipitated and exposed a minimum at 200 nm in all concentrations. The negative signal at 216-217 nm might be due to β-sheet traces in the peptide, but the peptide is considered to be mainly unordered (Figure 51b). MsR4M-L1(7xAla), which combines all the alanine substitutions of the previous two analogs in one sequence, is random coil and did not precipitate until the concentration of 50 µM (Figure 51c). The K3-conjugated analog msR4M-K3L1 appears to be more ordered than the alanine mutants of CXCR4-mimic. Its minima is exposed approximately at 223 nm in all spectra and the peptide precipitated at 50 µM, as msR4M-L1. In comparison to the native mimic, msR4M-K3L1 did not exhibit a strong positive signal below 208 nm. Overall, msR4M-K3L1 has β-sheet formation but the introduction of the K3-tag did not improve the solubility properties (Figure 51d).
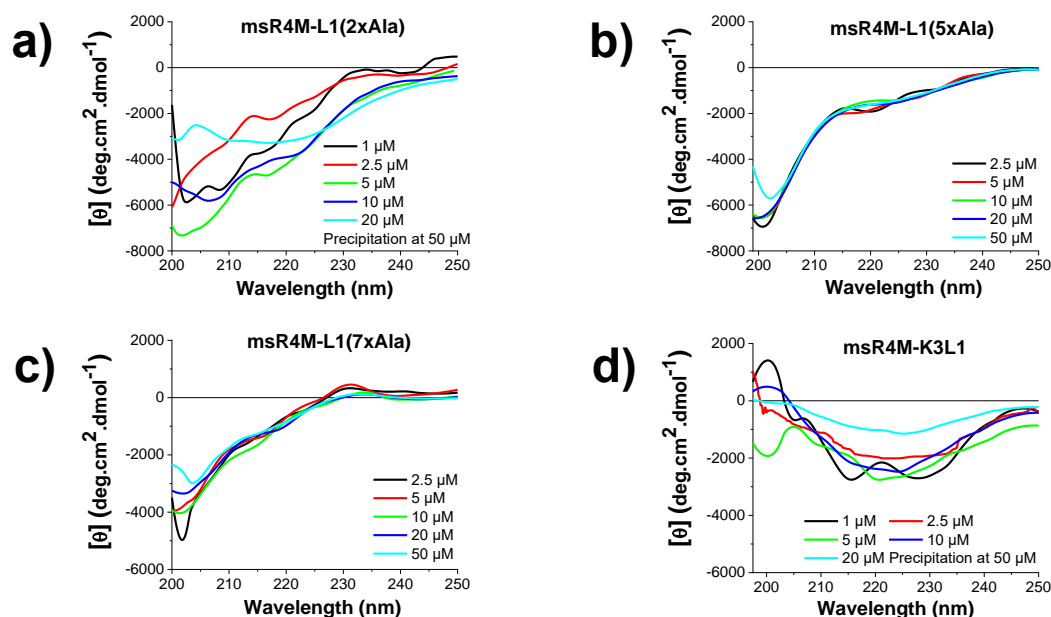
Figure 51. Spectra of alanine msR4M-L1 mutants and of msR4M-K3L1 analog in various concentrations, as determined by far-UV CD spectroscopy. a, b, c, d, CD spectra of msR4M-L1(2xAla) (a), msR4M-L1(5xAla) (b), msR4M-L1(7xAla) (c) and msR4M-K3L1 (d) at increasing concentrations at final measuring conditions of aqueous 1×b, pH 7.4, containing 1% HFIP. Mean residue ellipticity (MRE) plotted over the wavelength between 200 and 250 nm for a, b, c and 197.5 and 250 nm for d (adapted from Kontos et al., ref. [291]).

4.1.8.4 Determination of binding affinities to MIF via fluorescence spectroscopy

MsR4M-L1 is a CXCR4 mimic with a high affinity to MIF. Fluorescence spectroscopic titrations of 5 nM of Fluos-msR4M-L1 with various MIF concentrations

showed an app. K_d equal to 40.7 ± 4.0 nM in aqueous 1×b, pH 7.4, 1% HFIP. Under the same conditions, alanine mutants of labeled msR4M-L1 were titrated against MIF, and their affinity was monitored. Substitutions of F104 and F107 in the msR4M-L1(2xAla) analog resulted in the loss of the affinity with MIF and an app. K_d above 1500 nM, as no upper plateau was reached until this latest measuring point (Figure 52a-b). Replacement of the five aromatic residues W102, Y103, F188, Y189, W195 by alanines led to a 4-fold decreased affinity compared to the native mimic and an app. K_d of 161.3 ± 11.2 nM between Fluos-msR4M-L1(5xAla) and MIF (Figure 52c-d). Fluorescence emission of labeled-msR4M-L1(7xAla) did not change over the increased addition of MIF amount and the app. K_d was estimated to be in the micromolar range, if not higher (Figure 52e-f). Summarized results and comparison of the binding affinities of the peptides are described in 'Discussion' (see 5.1).
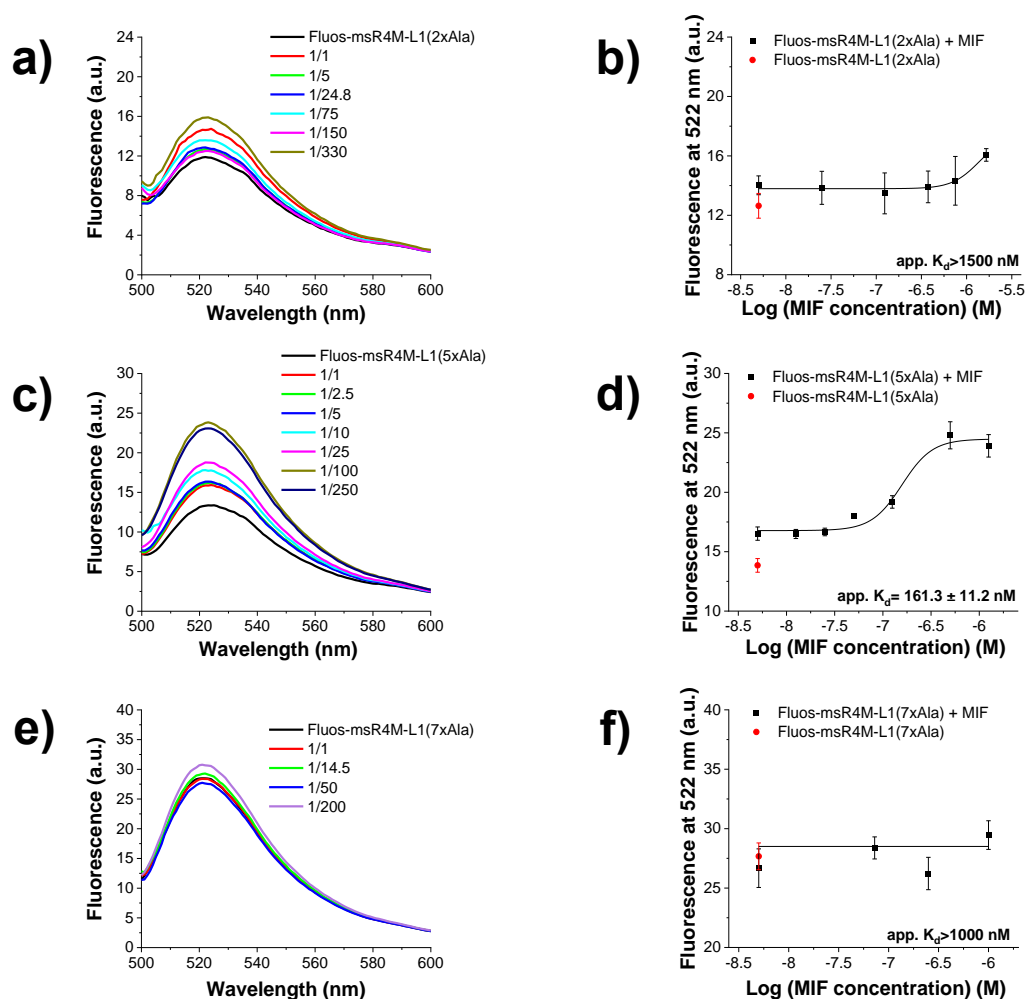
Figure 52. Fluorescence spectroscopic titrations of alanine Fluos-msR4M-L1 mutants with MIF for the determination of apparent affinities (app. K_{ds}). a, c, e Fluorescence spectra between 500 and 600 nm of 5 nM of Fluos-msR4M-L1(2xAla) (a), Fluos-msR4M-L1(5xAla) (c) and Fluos-msR4M-L1(7xAla) (e) alone and their mixtures with various amounts of MIF; the molar ratios of Fluos-peptide/MIF are indicated. **b, d, f** Binding curves derived from the fluorescence emission at 522 nm of Fluos-msR4M-L1(2xAla) (b), Fluos-msR4M-L1(5xAla) (d) and Fluos-msR4M-L1(7xAla) (f) at different concentrations of MIF. Data shown are means (±SD) from three independent titration experiments which were performed in aqueous 1×b, pH 7.4, containing 1% HFIP (adapted from Kontos et al., ref. [291]).

In agreement to these findings, Alexa-488-MIF and msR4M-L1(7xAla) appear to have an app. K_d above 10000 nM (Figure 53a-b). In this experimental setup with 10 nM of Alexa-488-MIF as analyte and peptide as the titrant under always the same

measuring conditions aqueous 1×b, pH 7.4, 1% HFIP, the app. K_d to msR4M-L1 was determined 31.1 ± 16.6 nM. The addition of three lysines on the N-terminus did not alternate the affinity of the mimic since the app. K_d between the labeled protein and the msR4M-K3L1 analog was 27.4 ± 11.3 nM (Figure 53c-d). In conclusion, F104 and F107, and secondary the rest five aromatic residues, are vital for the interaction with MIF, while the attachment of a K3-tag on the N-terminus did not affect the binding to the cytokine (Table 24).
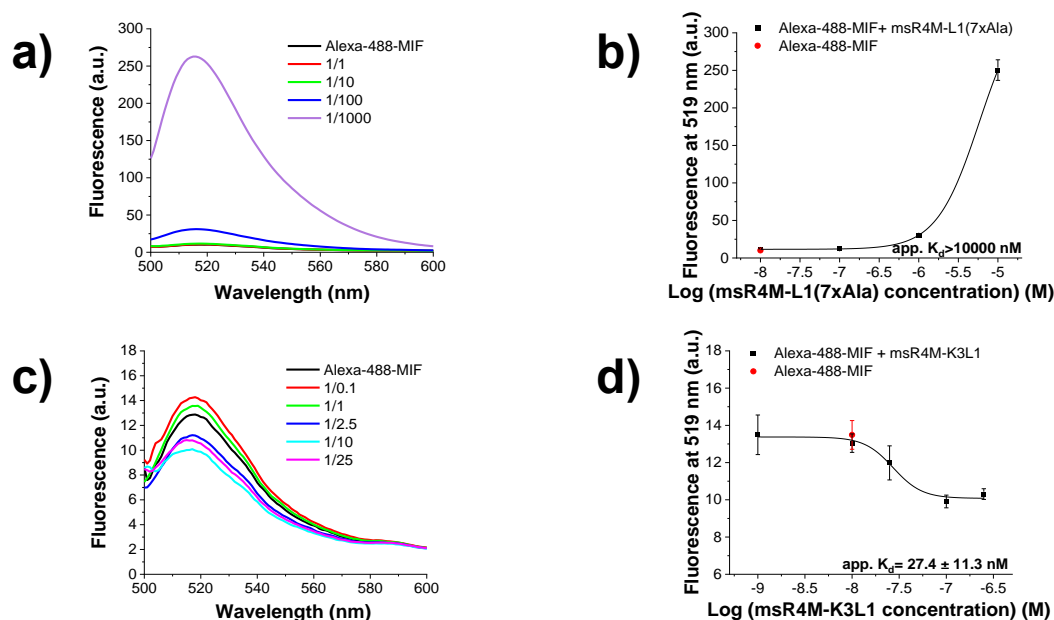
Figure 53. Fluorescence spectroscopic titrations of Alexa-488-MIF with msR4M-L1(7xAla) and msR4M-K3L1 for the determination of apparent affinities (app. K_{ds}). a, c Fluorescence spectra between 500 and 600 nm of Alexa-488-MIF (10 nM) alone and its mixtures with various amounts of msR4M-L1(7xAla) (a) and msR4M-K3L1 (c); the molar ratios of Alexa-488-MIF/peptides are indicated. **b, d** Binding curves derived from the fluorescence emission at 519 nm of Alexa-488-MIF (10 nM) at different concentrations of msR4M-L1(7xAla) (ECL1) (b) and msR4M-K3L1 (ECL1). Data shown are means (±SD) from three independent titration experiments which were performed in aqueous 1×b, pH 7.4, containing 1% HFIP.

Table 24. Apparent affinities (app. K_{ds}) of interaction between alanine msR4M-L1 mutants or msR4M-K3L1 and MIF, as determined by fluorescence spectroscopic titrations (adapted from Kontos et al., ref. [291]).

Peptide	Fluos-peptide/MIF app. K_d (nM)[a]	Alexa-488-MIF/peptide app. K_d (nM)[a]
msR4M-L1(2xAla)	> 2000	n.d.[b]
msR4M-L1(5xAla)	161.3 (±11.2)	n.d.[b]
msR4M-L1(7xAla)	>1000	>10000
msR4M-K3L1	n.d.[b]	27.4 (±11.3)

[a]: App. K_{ds} are means (±SD) from three independent titration experiments which were performed in aqueous 1×b, pH 7.4, containing 1% HFIP. [b]: n.d., non-determined.

4.1.9 Determination of binding affinity of msR4M-L1 to MIF-2 via fluorescence spectroscopy

MIF shares a 34% of sequence identity with and MIF-2, and their crystal structures revealed many similarities between the two proteins [292] [80]. Among several common functions, it was questioned whether they share substrates as well, and particularly CXCR4. So far, no data were available to confirm or dismiss it. Due to the nature of a chemokine receptor, it is hard to isolate it in sufficient amount for titration

and unaffordable to purchase it from the market. MsR4M-L1 as ectodomain mimic of CXCR4 was applied as a substitute of the receptor and investigated whether it interacts with MIF-2 or not by fluorescence spectroscopy, following already described protocols. Titrations between Fluos-msR4M-L1 and MIF-2 showed binding, and the sigmoidal curve derived by the fluorescence emission of the labelled analyte over the increased titrant concentration suggested an app. K_d of 161.3 ± 11.2 nM (Figure 54).
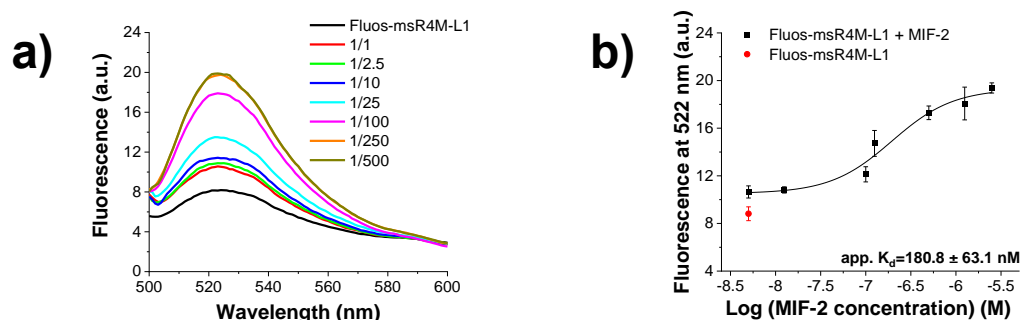
Figure 54. Fluorescence spectroscopic titrations of Fluos-msR4M-L1 with MIF-2 for the determination of apparent affinity (app. K_d). a Fluorescence spectra between 500 and 600 nm of 5 nM of Fluos-msR4M-L1 alone and its mixtures with various amounts of MIF-2; the molar ratios of Fluos-msR4M-L1/MIF-2 are indicated. **b** Binding curve derived from the fluorescence emission at 522 nm of Fluos-msR4M-L1 at different concentrations of MIF-2. Data shown are means (±SD) from three independent titration experiments which were performed in aqueous 1×b, pH 7.4, containing 1% HFIP.

4.1.10 Conclusions of msR4Ms

The peptides were synthesized following established SPPS methodologies with a particular protocol for the N-terminus Fmoc cleavage to avoid the aspartimide (Asi) formation. ECDs and msR4Ms shared different biophysical properties. Notably, the ectodomain-derived peptides mainly lacked ordered structure contrary to the linked with non-natural amino acids mimics that formed β-sheet. No oligomerization of ECDs was recorded until 10 µM, but the peptides precipitated at 20 µM. Contrariwise, msR4Ms self-associated in the nanomolar range and precipitated at 50 µM, except for msR4M-L2ox that remained soluble in this concentration (Table 25). The effect of the linkage became even more apparent with the interaction studies with MIF and the enhanced binding that the linked with non-natural amino acid mimics showed over MIF, compared to ECDs. Noteworthy, msR4M-LG7, the only mimic with natural amino acids as linkers, neither formed any ordered structure nor bound to MIF. Additional binding studies with CXCL12 demonstrated that the introduction of a disulfide bridge in msR4Ms played an important role in binding CXCL12 (Table 26). MsR4M-L1 and msR4M-L2 were the only mimics that bound specifically MIF, with the first one being more ordered, less prone to self-associate, and more potent and specific *in vitro* than the second, and thus, prioritized for further testing (Table 25, 26).

Two additional binding assays, FP and MST, were used to monitor the interaction of the prioritized mimic with the two CXCR4 ligands. The findings of both techniques agreed with the fluorescence spectroscopic data about an app. K_d in the low nanomolar range of msR4M-L1 for MIF and in the micromolar range for CXCL12. The MIF-specificity of msR4M-L1 was more extensively studied with those two assays, and particularly if the mimic affected the cardioprotective MIF/CD74 complex formation. Of note, the lead mimic did not interfere in the interaction between the MIF and CD74, showing its selectivity in blocking only the atheroprogressive MIF/CXCR4 and spare the cardioprotective MIF/CD74 interaction. Next, the mapping of the MIF/msR4M-L1 binding epitope uncovered the segments MIF(54-80), ECL1(102-108), and ECL2(188-

196) as hot spot regions with a vital role of MIF N-like loop between the 47th and 57th amino acid and the aromatic residues of mimic F104 and F107 (Table 25). The lead mimic was studied by the group of Prof. Bernhagen and inhibited the MIF-mediated proatherogenic inflammatory signaling *in vitro* and *ex vivo*. Lastly, msR4M-L1 was administrated in Apoe$^{-/-}$ mice and brought about a significant reduction in the atherosclerotic progress, showing a therapeutic potency *in vivo* [291].

Table 25. Defined biophysical properties of msR4Ms, analogs and mutants of msR4M-L1 and ECDs after CD and fluorescence spectroscopy studies with ANS.

Peptide	Secondary structure	Precip. (µM)	Hydrophobic residues on the surface
msR4Ms and ECDs			
msR4M-L1	β-sheet	50	Medium exposure
msR4M-L2	β-sheet	50	Medium exposure
msR4M-L1ox	β-sheet	50	n.d. [b]
msR4M-L2ox	β-sheet	>50	n.d. [b]
msR4M-LS	n.d. [b]	5	n.d. [b]
msR4M-LG7	r.c. [a]	50	n.d. [b]
ECL1	r.c. [a]	20	n.d. [b]
ECL2	r.c. [a]	20	n.d. [b]
Alanine mutants and analogs of msR4M-L1			
msR4M-L1(2xAla)	r.c. [a]	50	n.d. [b]
msR4M-L1(5xAla)	r.c. [a]	>50	n.d. [b]
msR4M-L1(7xAla)	r.c. [a]	>50	n.d. [b]
msR4M-K3L1	β-sheet + r.c. [a]	50	n.d. [b]

Peptides were biophysically characterized in aqueous 1×b, pH 7.4, containing 1% HFIP. [a]: r.c., random coil, [b]: n.d., non-determined.

Table 26. Determined app. K_{ds} of self-assembly of msR4Ms and of their binding affinities with MIF, and CXCL12, as derived by fluorescence spectroscopic titrations (adapted from Kontos et al., ref. [291]).

Peptide	app. K_d (±SD) (nM) [a] (self-assembly)	app. K_d (±SD) (nM) [a] (Fluos-peptide/MIF)	app. K_d (±SD) (nM) [a] (Alexa-488-MIF/peptide)	app. K_d (±SD) (nM) [a] (Fluos-peptide/CXCL12)
msR4Ms and ECDs				
msR4M-L1	142.0(±48.9)	40.7 (±4.0)	31.1 (±16.6)	> 6340
msR4M-L2	69.5 (±61.9)	28.9 (±2.5)	30.0 (±6.3)	> 6340
msR4M-L1ox	117.5 (±9.4)	18.6 (±2.9)	40.5 (±7.6)	84.6 (±42.1)
msR4M-L2ox	280.0 (±29.7)	105.3 (±44.9)	59.6 (±15.3)	54.8 (±10.3)
msR4M-LS	n.d. [b]	6.9 (±2.0)	n.d. [b]	17.4 (±4.7)
msR4M-LG7	46.6 (±6.0)	> 2500	n.d. [b]	n.d. [b]
ECL1	> 10000	n.d. [b]	345.2 (±79.4)	n.d. [b]
ECL2	> 10000	> 5000	2458 (±1054)	n.d. [b]
Alanine mutant and analogs of msR4M-L1				
msR4M-1(2xAla)	n.d. [b]	> 2000	n.d. [b]	n.d. [b]
msR4M-1(5xAla)	n.d. [b]	161.3 (±11.2)	n.d. [b]	n.d. [b]
msR4M-1(7xAla)	n.d. [b]	> 1000	> 10000	n.d. [b]
msR4M-K3L1	n.d. [b]	n.d. [b]	27.4 (±11.3)	n.d. [b]

[a]: App. K_{ds} are means (±SD) from three independent titration experiments which were performed in aqueous 1×b, pH 7.4, containing 1% HFIP. [b]: n.d., non-determined.

4.2 Structure-activity relationship (SAR) studies on ECL1 and ECL2

MsR4Ms consisted of the ectodomain sections of CXCR4, ECL1, and ECL2. In chapter 4.1.8.1, SPOT array analysis studies indicated the existence of active regions of ECL1 and ECL2 that may be shorter and have higher affinities for MIF than the native 14-mer and 15-mer, respectively. Therefore, shorter fragments of ECL1 and ECL2 were synthesized to shed more light on this hypothesis. For analogs of ECL1, the sequence of the one terminus was kept constant, while a step-by-step removal of residues from C-terminus amino acid occurred. Regarding ECL2, the SPOT array analysis suggested a non-important role of V196, so mainly the N-terminus shortening of ECL2 occurred to 195-ending fragment and not at position 196. Besides, fragments ending in L194 or V196 were synthesized to test the importance of C-terminus residues.

The secondary structure and the binding affinity of the shorter ECDs were determined and resulted in the segments with the highest affinity for MIF. Capitalizing on these findings, additional studies aimed further to optimize the biophysical or binding properties of the peptides. To achieve this, mutants and analogs of the most potent shorter analogs of ECL1 and ECL2 were developed and analyzed via CD and fluorescence spectroscopy with MIF as their native analogs. All these SAR studies resulted in sequence and sized optimized analogs of ECL1 and ECL2 that could be applied in future MIF-targeting studies (Scheme 7).
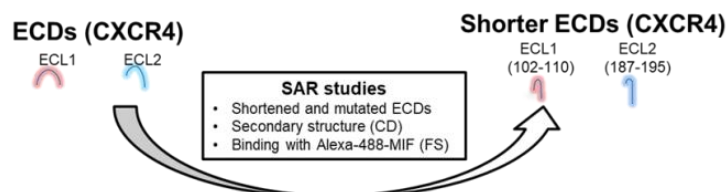
Scheme 7. Overview of the development and studies of shorter ECDs. Studies of shorter ECDs aimed on the determination of their biophysical properties and their binding affinities with MIF.

4.2.1 Synthesis, purification and mass determination of shorter analogs of ECL1 and ECL2

Fmoc-SPPS was applied for the synthesis of the shorter ECL1 and ECL2 analogs, as previously. Briefly, the first amino acid was loaded on the Fmoc-deprotected Rink-resin and the substitution level was estimated with UV-Vis spectroscopy. Synthesis continued with double couplings of amino acids that may differ in the activator, the DIEA equivalents and the reaction duration as shown in Schemes 8 and 9. Fmoc-group was cleaved from the N-terminus using the normal protocol except for the residues after the D193 for analogs of ECL2. For those, it was preferred the 'Short HOBt protocol' for reducing the possibility of Asi side reaction. Simultaneous cleavage of the side-chain protection and of the peptide from the resin was mediated by Reagent K. Lyophilized powder of crudes was dissolved in TFA/80% B and purified via RP-HPLC. The collected peaks were dissolved in MALDI solution A and their MWs were determined by MALDI-TOF-MS. All found masses agreed with the theoretical masses and the yield varied between 3.0 and 33.1% for shorter fragments of ECL1 and 8.1 and 17.6% for ECL2 analogs (Table 27, Figures 55-58).
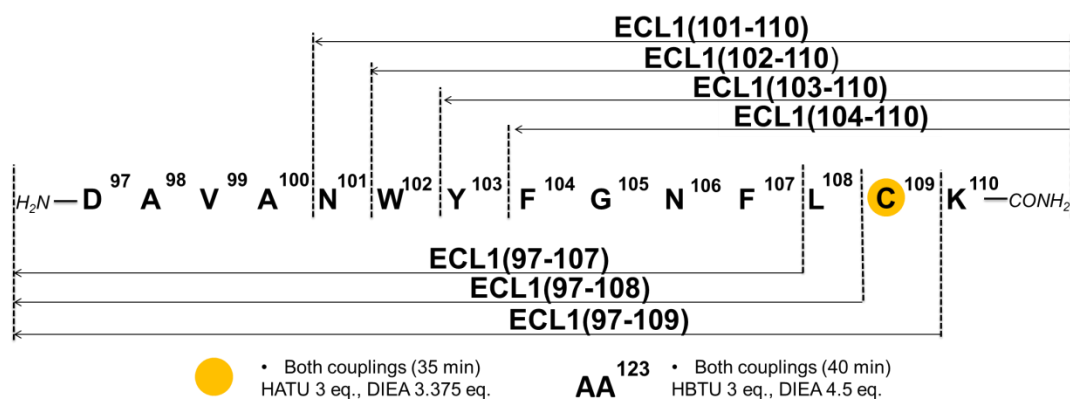
Scheme 8. Conditions of couplings for the syntheses of shorter analogs of ECL1. All amino acids (AA) were coupled on resin with 3 equivalents (eq.), based on the substitution level that was determined after the load of the first amino acid on Rink-resin. Equivalents of activator and base, together with the coupling time may vary, as indicated.
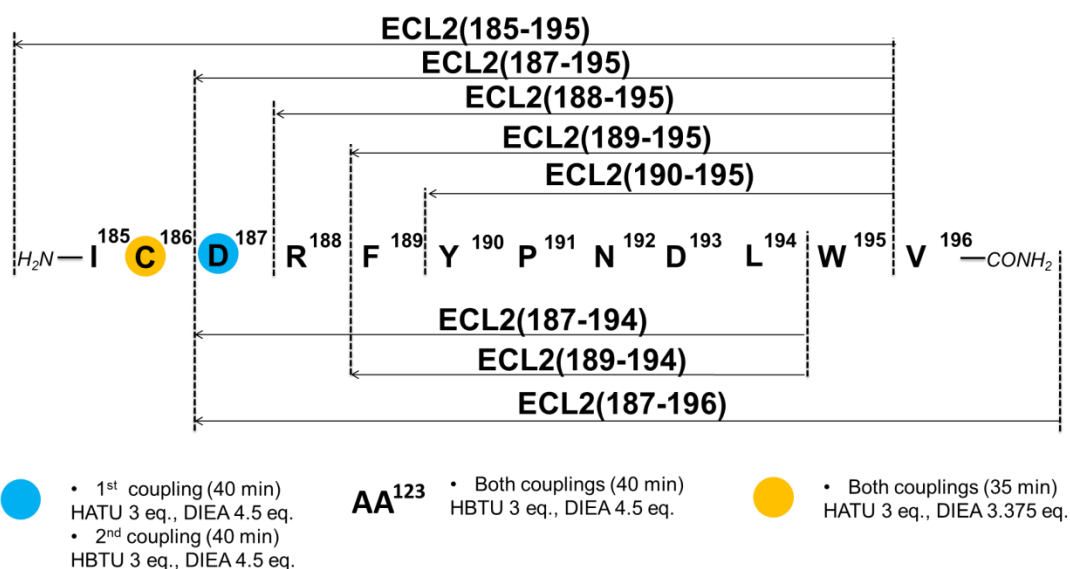
Scheme 9. Conditions of couplings for the syntheses of shorter analogs of ECL2. All amino acids were coupled on resin with 3 equivalents (eq.), based on the substitution level that was determined after the load of the first amino acid on Rink-resin. Equivalents of activator and base, together with the coupling time may vary, as indicated.

Table 27. Sequences, abbreviation and characterization of synthesized shorter ECL1 and ECL2 peptides by RP-HPLC and MALDI-TOF-MS.

Peptide sequence[a]	Peptide abbreviation	HPLC Pr.No.	t_R (min)[b]	Yield (%)[c]	[M+H]$^+$ expected [d]	[M+H]$^+$ found[d]
DAVANWYFGNF	ECL1(97-107)	1	19.20	12.0	1302.60	1324.83[e]
DAVANWYFGNFL	ECL1(97-108)	3	21.50	3.0	1415.68	1437.76[e]
DAVANWYFGNFLC	ECL1(97-109)	1	20.55	33.1	1518.69	1540.93[e]
ANWYFGNFLCK[f]	ECL1(100-110)	[g]				
NWYFGNFLCK	ECL1(101-110)	1	19.30	13.8	1289.61	1312.85[e]
WYFGNFLCK	ECL1(102-110)	1	19.65	10.5	1176.57	1198.72[e]
YFGNFLCK	ECL1(103-110)	1	18.60	8.8	990.47	990.67
FGNFLCK	ECL1(104-110)	1	16.74	9.9	826.42	849.61[e]
ICDRFYPNDLW	ECL2(185-195)	1	18.50	17.6	1440.68	1440.99
DRFYPNDL	ECL2(187-194)	1	14.95	9.1	1038.51	1038.70

Peptide sequence[a]	Peptide abbreviation	HPLC Pr.No.	t_R (min)[b]	Yield (%)[c]	[M+H]+ expected [d]	[M+H]+ found[d]
DRFYPNDLW	ECL2(187-195)	1	18.00	8.8	1224.59	1224.82
DRFYPNDLWV	ECL2(187-196)	1	17.95	16.1	1323.65	1324.03
RFYPNDLW	ECL2(188-195)	1	17.65	18.1	1109.56	1109.58
FYPNDL	ECL2(189-194)	1	15.00	8.1	767.38	789.57[e]
FYPNDLW	ECL2(189-195)	1	18.80	9.5	953.46	975.61[e]
YPNDLW	ECL2(190-195)	1	17.45	8.4	806.39	828.31[e]

Peptides were dissolved and analyzed by MALDI-TOF-MS in a mixture of MALDI solutions A and A (matrix); [a] Peptides were synthesized with free amino-N-terminus and amidated C-terminus; [b] HPLC retention time of the pure product, the stationary phase was a tandem of Reprosil Gold 200 C18 columns (250 and 30 mm length, 8 mm internal diameter, 10 µm particle size); [c] % yield with regard to crude peptide after cleavage; [d] monoisotopic molar mass with an additional hydrogen [M+H]+; [e] monoisotopic molar mass with an additional sodium [M+Na]+ and [f] peptide was purchased with acetylated amino-N-terminus and carboxylated C-terminus, [g] purchased by PSL (Heidelberg, GER).
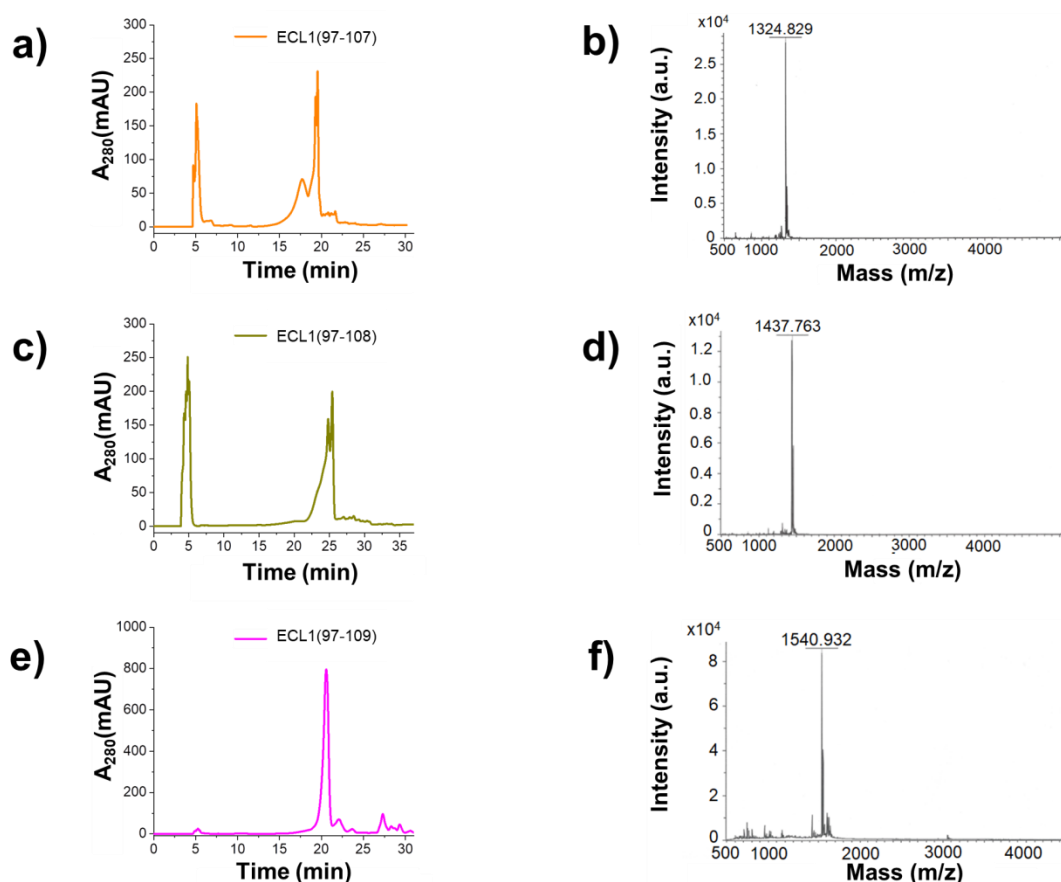

Figure 55. HPLC purification of C-terminus shortened analogs of ECL1 and verification of their purity by MALDI. a, c, e Representative C18 HPLC chromatogram (absorbance at 280 nm) of crude ECL1(97-107), ECL1(97-108) and ECL1(97-109) with respective retention times: a) 19.20 min, c) 21.50 min and e) 20.55 min, following SPPS and cleavage. **b, d, f** MALDI-TOF-MS spectra of HPLC-purified ECL1(97-107), ECL1(97-108) and ECL1(97-109) with respective experimental determined masses [M+H]+: b) 1324.829 Da, d) 1437.763 Da and f) 1540.932 Da.
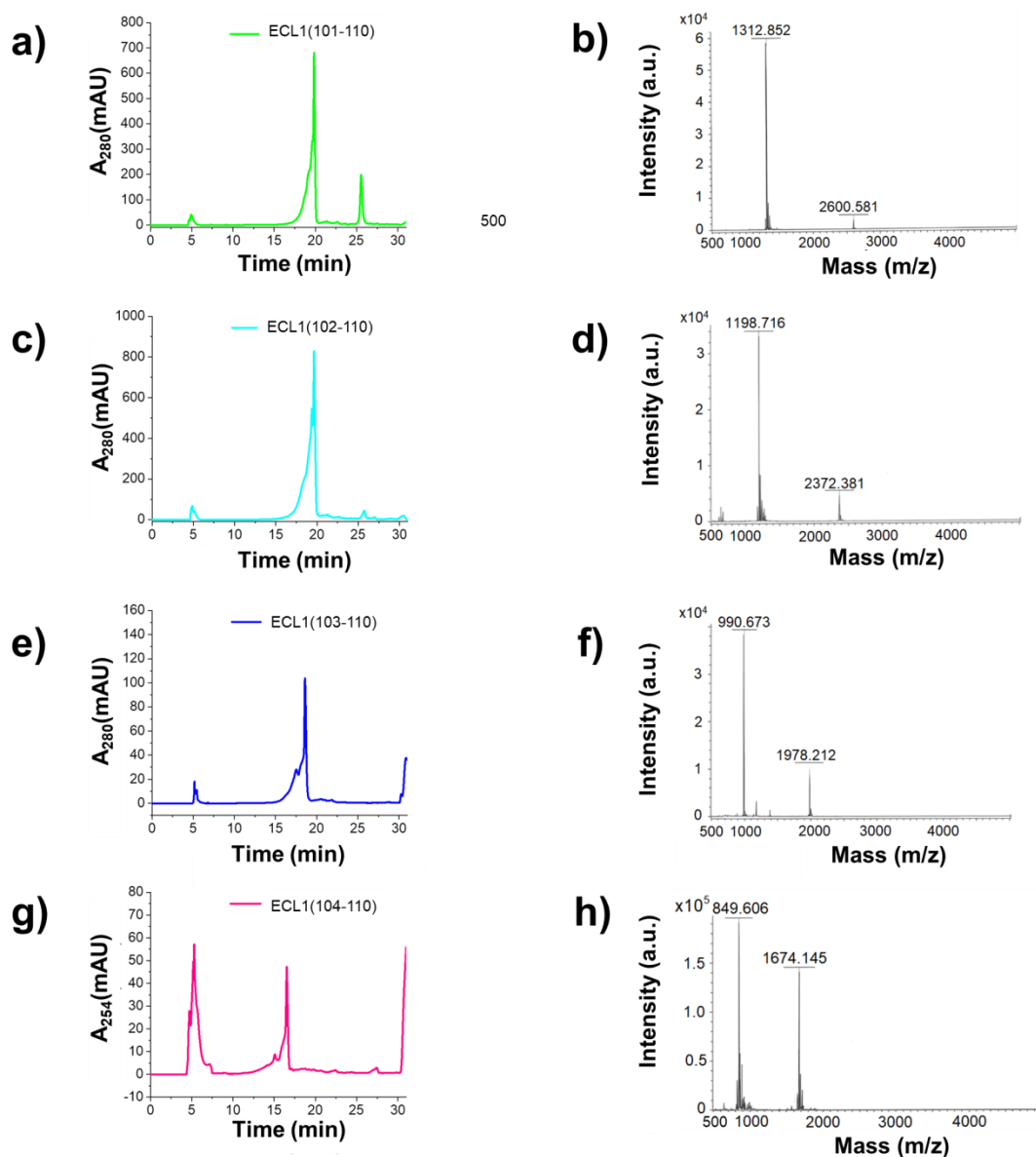
Figure 56. HPLC purification of N-terminus shortened analogs of ECL1 and verification of their purity by MALDI. a, c, e, g Representative C18 HPLC chromatogram (absorbance at 280 or 254 nm) of crude ECL1(101-110), ECL1(102-110), ECL1(103-110) and ECL1(104-110) with respective retention times: a) 19.30 min, c) 19.65 min, e) 18.60 min and g) 16.74 min, following SPPS and cleavage. The peaks that are eluted at the end of the chromatogram (tR=31 min) are due to the formation of non-covalent aggregates. **b, d, f, h** MALDI-TOF-MS spectra of HPLC-purified ECL1(101-110), ECL1(102-110), ECL1(103-110) and ECL1(104-110) with respective experimental determined masses [M+H]+: b) 1312.852 Da, d) 1198.716 Da, f) 990.673 and h) 849.606 Da.
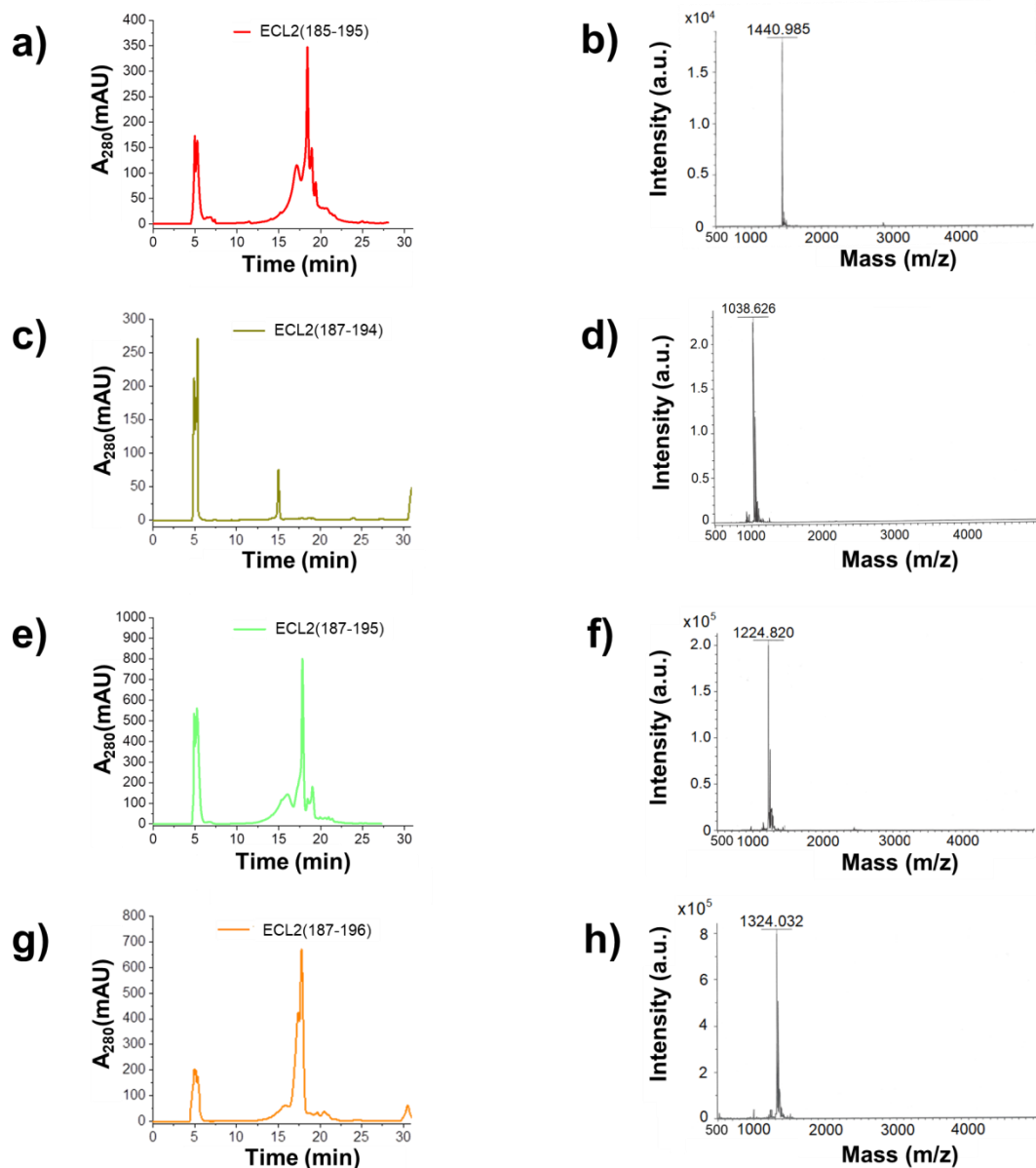
Figure 57. HPLC purification of shortened analogs of ECL2 and verification of their purity by MALDI. **a, c, e, g** Representative C18 HPLC chromatogram (absorbance at 280 nm) of crude ECL2(185-195), ECL2(187-194), ECL2(187-195) and ECL2(187-196) with respective retention times: a) 18.50 min, c) 14.95 min, e) 18.00 min and g) 17.95 min, following SPPS and cleavage. **b, d, f, h** MALDI-TOF-MS spectra of HPLC-purified ECL2(185-195), ECL2(187-194), ECL2(187-195) and ECL2(187-196) with respective experimental determined masses [M+H]⁺: b) 1440.985 Da, d) 1038.626 Da, f) 1224.820 Da, h) 1324.032 Da.
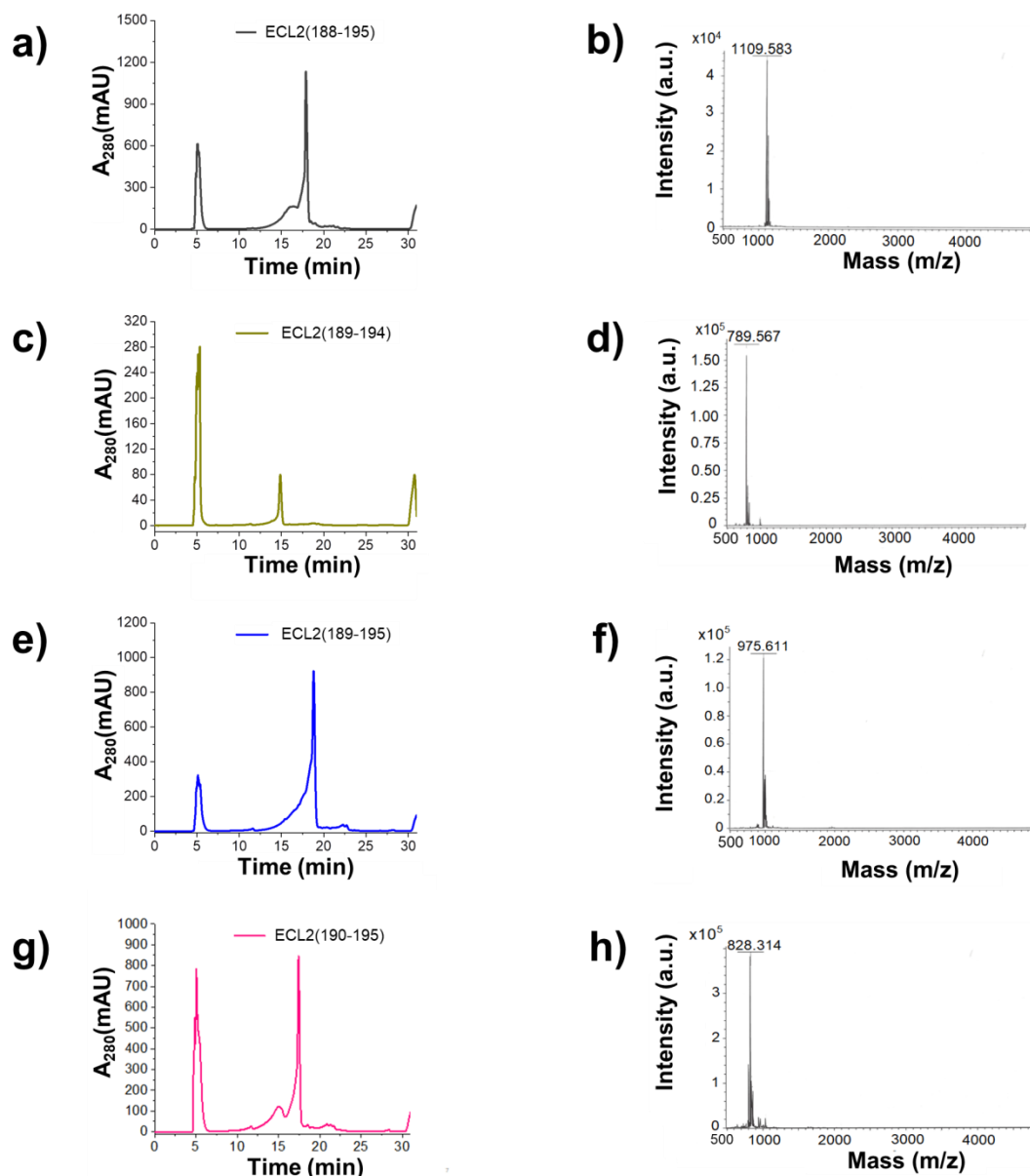
Figure 58. HPLC purification of shortened analogs of ECL2 and verification of their purity by MALDI.
a, c, e, g Representative C18 HPLC chromatogram (absorbance at 280 nm) of crude ECL2(188-195), ECL2(189-194), ECL2(189-195) and ECL2(190-195) with respective retention times: a) 17.65 min, c) 15.00 min, e) 18.80 min and g) 17.40 min, following SPPS and cleavage. **b, d, f, h** MALDI-TOF-MS spectra of HPLC-purified ECL2(188-195), ECL2(189-194), ECL2(189-195) and ECL2(190-195) with respective experimental determined masses [M+H]$^+$: b) 1109.583Da, d) 789.567 Da, f) 975.611 Da and h) 828.314 Da.

4.2.2 Conformational and concentration dependence studies via CD spectroscopy

The secondary structure of ECL1 and ECL2 shorter analogs were conformationally studied by far-UV CD spectroscopy. Peptides were measured under the same experimental conditions that were used for the native ECL1, ECL2, and msR4Ms. The differences in the scans over the increasing concentration contributed to understanding more of the aggregation and the solubility of the peptides of interest. Previously recorded spectra of the 14-mer ECL1 (see 4.1.3) showed a negative signal below 225 nm and a minima at 200 nm and indicating mostly random coil.

ECL1(97-107) had very similar spectra and solubility properties to ECL1, with a random coil indicative signal and precipitation at 20 µM (Figure 59a). There was no concentration dependence of the CD signal of the 11-mer, contrary to the elongated ECL1(97-108). Spectrum at 5 µM of the 12-mer had its minimum at 216 nm, two slightly less intense minima at 209 and 222 nm and reached positive MRE values below 200 nm, while the spectra at 10 µM and 20 µM shared a similar signal to ECL1 and ECL1(97-107). Together the data suggested that ECL1(97-108) is mainly ordered at 5 µM forming β-sheet and secondly α-helix, while peptide unfolded and switched to a less ordered state at 10 µM and 20 µM (Figure 59b). The peptide precipitated at 50 µM, as well as ECL1(97-109). However, the recorded spectra of ECL1(97-109) showed broad minima between 205 and 220 nm and MRE values approaching the baseline at 195 nm, suggesting that ECL1(97-109) is mainly ordered but still contains unordered species (Figure 59c).

Additional CD spectroscopy studies were carried out for the N-terminus shorter analogs ECL1(100-110), ECL1(101-110), and ECL1(102-110) and presented an overall similar signal shape with the native peptide (Figure 59d-f). Further elimination of W102 and Y103 led to a slight differentiation in the spectra, with the respective peptides having the initiation of their negative signal below 215 nm and their minima below 200 nm, indicating the lack of any sign of ordered structure (Figure 59g, h). Interestingly, from all these unordered peptides, only ECL1(102-110) exposed the π-π-indicative positive wide band in the wavelength range between 225 and 235 nm (Figure 59f). All N-terminus shortened analogs had better soluble properties compared to the 14-mer, with ECL1(101-110) and ECL1(102-110) precipitating at 50 µM and the rest peptides remaining soluble until that concentration. ECL1(103-110) and ECL1(104-110) spectra presented a decreased signal at 50 µM compared to the lower concentrations, proposing the aggregation of the peptides in that point. No other concentration-dependent signal was observed for the other peptides. Summarized results and comparison of the spectra of the peptides are described in 'Discussion' (see 5.2).
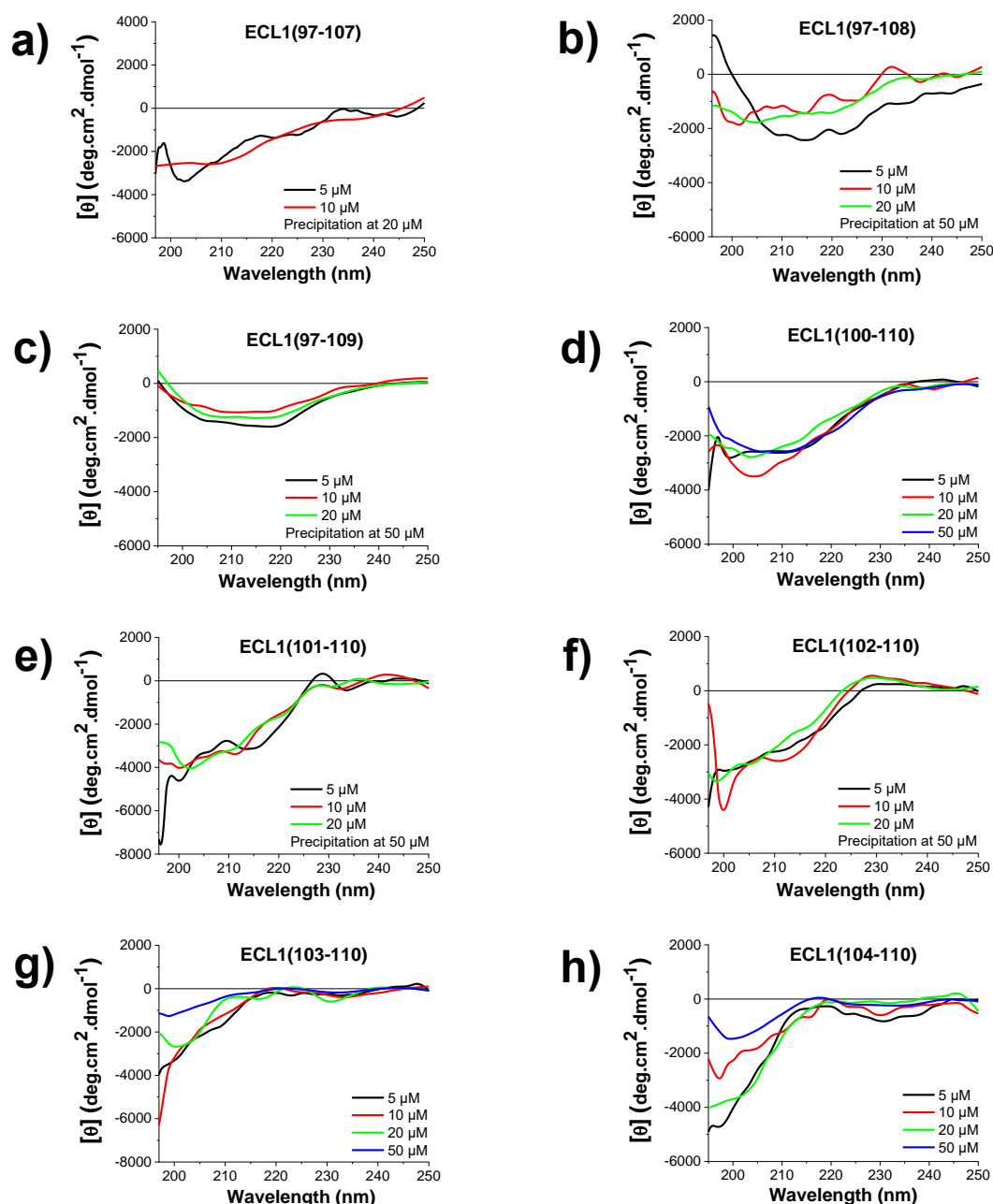
Figure 59. Spectra of shorter analogs of ECL1 in various concentrations for the determination of the conformation, as determined by far-UV CD spectroscopy. a, b, c, d, e, f, g, h CD spectra of ECL1(97-107) (a), ECL1(97-108) (b), ECL1(97-109) (c), ECL1(100-110) (d), ECL1(101-110) (e), ECL1(102-110) (f), ECL1(103-110) (g) and ECL1(104-110) (h) at increasing concentrations at final measuring conditions of aqueous 1×b, pH 7.4, containing 1% HFIP. Mean residue ellipticity (MRE) plotted over the wavelength between 197 and 250 nm for a, f, g, 196 and 250 nm for b, e 195 and 250 nm for c, d, h.

Regarding ECL2, the other ectodomain peptide of interest, its spectra had the random-coil characteristic minimum below 200 nm. The same negative peak appeared in the spectra of all shorter analogs of ECL2 in an overall similar MRE values range at -6000 deg·cm^2·dmol^{-1}, except for ECL2(190-195), which exposed stronger minima in the 200 nm area (5-10 μM). What differentiates the spectra of some peptides is the positive signal between 220 and 240 nm, which does not occur for the native ECL2. ECL2(185-195) does not have any positive band in this particular wavelength section, and the signal is comparable with the baseline (Figure 60a). Contrariwise, ECL2(187-194),

ECL2(187-195) and ECL2(187-196) exposed weak broad positive bands, but for ECL2(188-195), ECL2(189-194), ECL2(189-195) and ECL2(190-195) the recorded values at maxima are higher (Figure 60b-h). Of note, shorter ECL2 analogs showed enhanced solubility without any precipitation until 50 μM except for ECL2(188-195), which precipitated at 20 μM, as the 15-mer. Spectra of ECL2(190-195) appeared to have the same shape but with stronger signal intensity at 5 and 10 μM, suggesting its oligomerization in higher concentrations (Figure 60h). None of the shorter shorter derived peptide exhibited a concentration dependent CD signal, contrary to ECL2 that aggregated at 15 μM. This finding suggests a pivotal role of the terminus residues of ECL2 in its self-associaton.
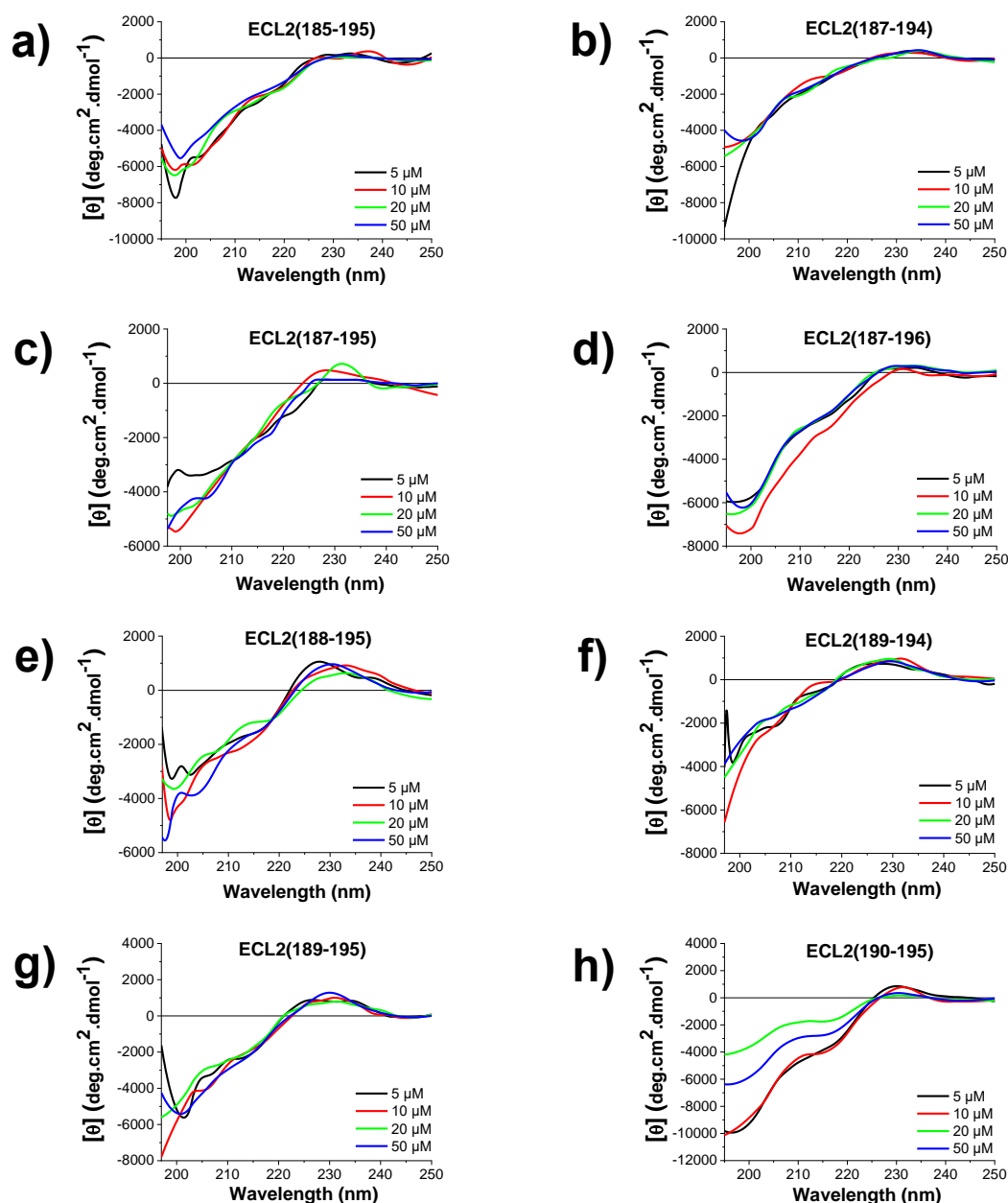
Figure 60. Spectra of shorter analogs of ECL2 in various concentrations for the determination of the conformation, as determined by far-UV CD spectroscopy. a, b, c, d, e, f, g, h CD spectra of ECL2(185-195) (a), ECL2(187-194) (b), ECL2(187-195) (c), ECL2(187-196) (d), ECL2(188-195) (e), ECL2(189-194) (f), ECL2(189-195) (g) and ECL2(190-195) (h) at increasing concentrations at final measuring conditions of aqueous 1×b, pH 7.4, containing 1% HFIP. Mean residue ellipticity (MRE) plotted over the wavelength between 195 and 250 nm for a, b, d, h 197.5 and 250 nm for c, 197 and 250 nm for e, f, g.

4.2.3 Determination of binding affinities to MIF via fluorescence spectroscopy

Fluorescence spectroscopic titrations in chapter 4.1.4.1 provided us insights about the binding between Alexa-488-MIF and ECDs. ECL1 and ECL2 are CXCR4 fragments with medium (345.2 ± 79.4 nM) and low (2458 ± 1054 nM) affinity to MIF, respectively. The followed size optimization strategy for these fragments aimed not only at the elimination of the non-necessary amino acids for the interaction but also in the increase of the affinity between the peptides and the atypical chemokine. However, the first tested analog ECL1(97-107) had an app. K_d above 10000 nM (Figure 61a, b). Likewise, ECL1(97-108) did not have a strong affinity to MIF since the app. K_d appeared to be above 20000 nM (Figure 61c, d). Things changed drastically with the addition of the next amino acid, C109, with the K110 missing fragment ECL1(97-109) showing an almost 6-fold improved affinity to MIF than ECL1, with the app. K_d being calculated at 60.1 ± 9.6 nM (Table 28, Figure 61e, f).

The elimination of N-terminus amino acids D97, A98, V99 appears to improve the binding potency of the peptide with Alexa-488-MIF until a point before it leads to the loss of the affinity. The decreased fluorescence emission of the labeled cytokine over increased ECL1(100-110) concentration suggested ab app. K_d equal to 214.5 ± 72.3 nM, quite similar to the one of the native peptide (Figure 61a, b). Additional removal of A100 and N101 residues affected even more positively the interaction and led to the first ECL1 fragments with double-digit nanomolar affinity. In particular, a step-by-step residual elimination was further followed for the generation of ECL1(101-110) and ECL1(102-110) analogs with the app. K_{ds} being equal to 45.2 ± 14.0 nM and 86.3 ± 9.2 nM, respectively (Figure 61c-f). However, the subsequent elimination of W102 and Y103 led to significantly worse binding affinities. ECL1(103-110) returned to the three-digit nanomolar app. K_d (533.8 ± 95.7 nM), while the value for ECL1(104-110) was estimated to be above 10000 nM (Table 28, Figure 61g-j). Conclusively, the shortest ECL1 fragment that's binds strongly to MIF is ECL1(102-110). Summarized results and comparison of the binding affinities of the peptides are described in 'Discussion' (see 5.2).
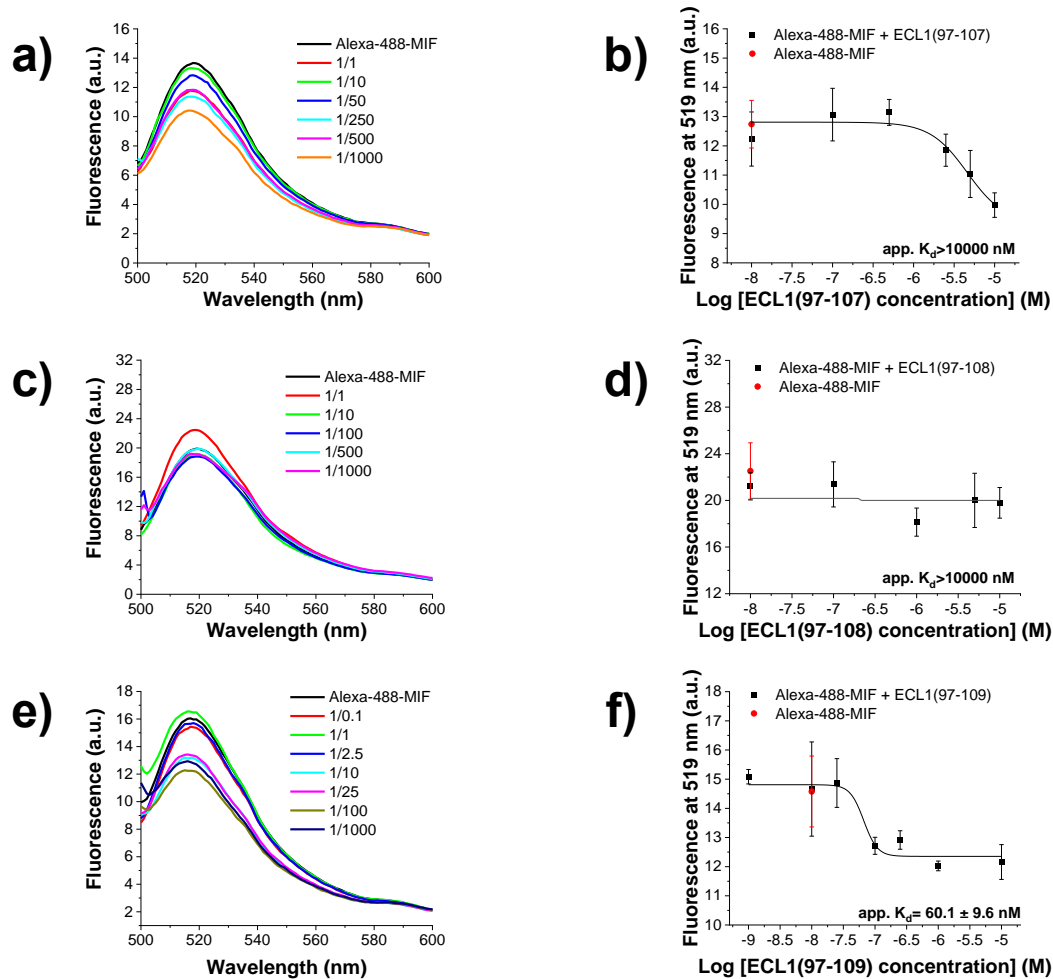
Figure 61. Fluorescence spectroscopic titrations of Alexa-488-MIF with C-terminus shortened analogs of ECL1 for the determination of apparent affinities (app. K_{ds}). a, c, e Fluorescence spectra between 500 and 600 nm of Alexa-488-MIF (10 nM) alone and its mixtures with various amounts of ECL1(97-107) (a), ECL1(97-108) (c) and ECL1(97-109) (e); the molar ratios of Alexa-488-MIF/peptides are indicated. **b, d, f** Binding curves derived from the fluorescence emission at 519 nm of Alexa-488-MIF (10 nM) against increasing concentration of ECL1(97-107) (b), ECL1(97-108) (d) and ECL1(97-109) (f). Data shown are means (±SD) from three independent titration experiments which were performed in aqueous 1×b, pH 7.4, containing 1% HFIP.
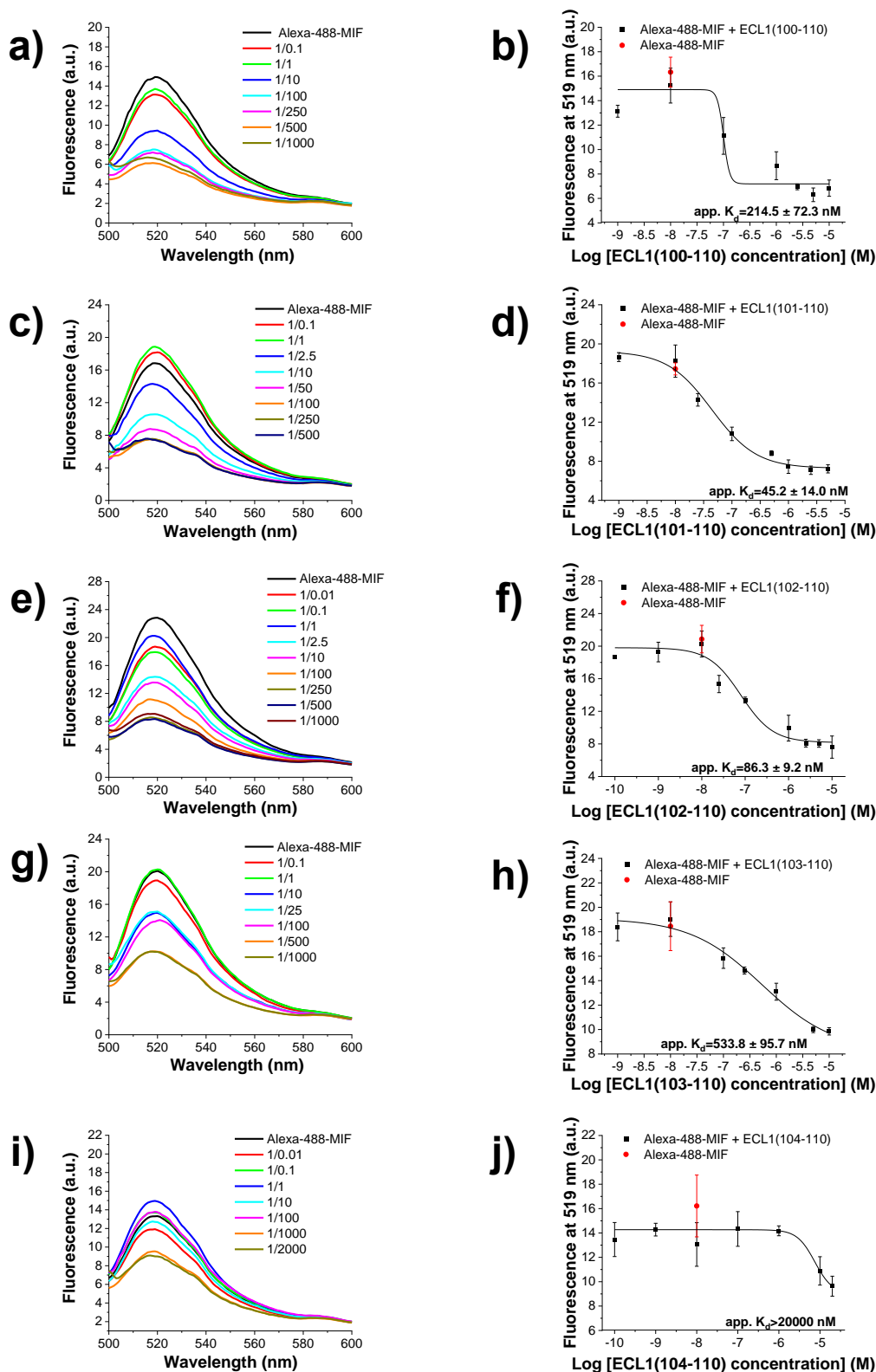
Figure 62. Fluorescence spectroscopic titrations of Alexa-488-MIF with N-terminus shortened analogs of ECL1 for the determination of apparent affinities (app. K_{ds}). a, c, e, g, i Fluorescence spectra between 500 and 600 nm of Alexa-488-MIF (10 nM) alone and its mixtures with various amounts of ECL1(100-110) (a), ECL1(101-110) (c), ECL1(102-110) (e), ECL1(103-110) (g) and ECL1(104-110) (i) ; the molar ratios of Alexa-488-MIF/peptides are indicated. **b, d, f, h, j** Binding curves derived from the fluorescence emission at 519 nm of Alexa-488-MIF (10 nM) at different concentrations of ECL1(100-110) (b), ECL1(101-110) (d), ECL1(102-110) (f), ECL1(103-110) (h) and ECL1(104-110) (j). Data shown are means (±SD) from three independent titration experiments which were performed in aqueous 1×b, pH 7.4, containing 1% HFIP.

117

Table 28. Apparent affinities (app. K_{ds}) of interaction between Alexa-488-MIF and shorter analogs of ECL1, as determined by fluorescence spectroscopic titrations.

Shorter analogs of ECL1	Alexa-488-MIF/peptide app. K_d (±SD) (nM)
ECL1	345.2 (±79.4)
ECL1(97-107)	>20000
ECL1(97-108)	>10000
ECL1(97-109)	60.1 (±9.6)
ECL1(100-110)	214.5 (±72.3)
ECL1(101-110)	45.2 (±14.0)
ECL1(102-110)	86.3 (±9.2)
ECL1(103-110)	533.8 (±95.7)
ECL1(104-110)	>20000

App. K_{ds}, are means (±SD) from three independent titration experiments which were performed in aqueous 1×b, pH 7.4, containing 1% HFIP.

Regarding size optimization studies of ECL2, the first tested peptide was ECL2(185-195). The 11-mer reached a medium affinity for the labeled-analyte with the calculated app. K_d at 323.7 ± 30.1 nM being more than 7-fold improved in comparison with the one obtained from ECL2 (Figure 63a, b). Alexa-488-MIF failed to get saturated by ECL2(187-194), as its fluorescence emission did not reach any down plateau and the app. K_d was above 10000 nM (Figure 63c, d). The addition of the crucial amino acid W195 led to ECL2(187-195), the analog with the strongest affinity to MIF. Particularly, the labeled cytokine and the the 9-mer shared an app. K_d equal to 285.6 ± 35.2 nM (Table 29, Figure 63e, f). However, the subsequent addition of V196 led to an abrogation of the interaction between Alexa-488-MIF and ECL2(187-196) until 10000 nM, at least (Table 29, Figure 63g, h).

ECL2(187-195), the ECL2 analog with the highest binding affinity to Alexa-488-MIF, was further shortened to figure out whether there is a shorter core region. The elimination of D187 weakened the affinity between the peptide and the protein, with the calculated app. K_d between ECL2(188-195) and MIF being equal to 3774.3 ± 1773.0 nM (Figure 64a, b). The fluorescence emission of the labeled analyte against ECL2(189-194) did not reach any plateau until the highest concentration at 20000 nM thus the app. K_d is above this point (Figure 64c, d). Similarly, the fluorescence signal in the titrations of Alexa-488-MIF to ECL2(189-195) and ECL2(190-195) did not differientiate upon increased titrant concentrations, indicating app. K_{ds} above 20000 nM and 10000 nM, respectively (Table 29, Figure 65e-h).
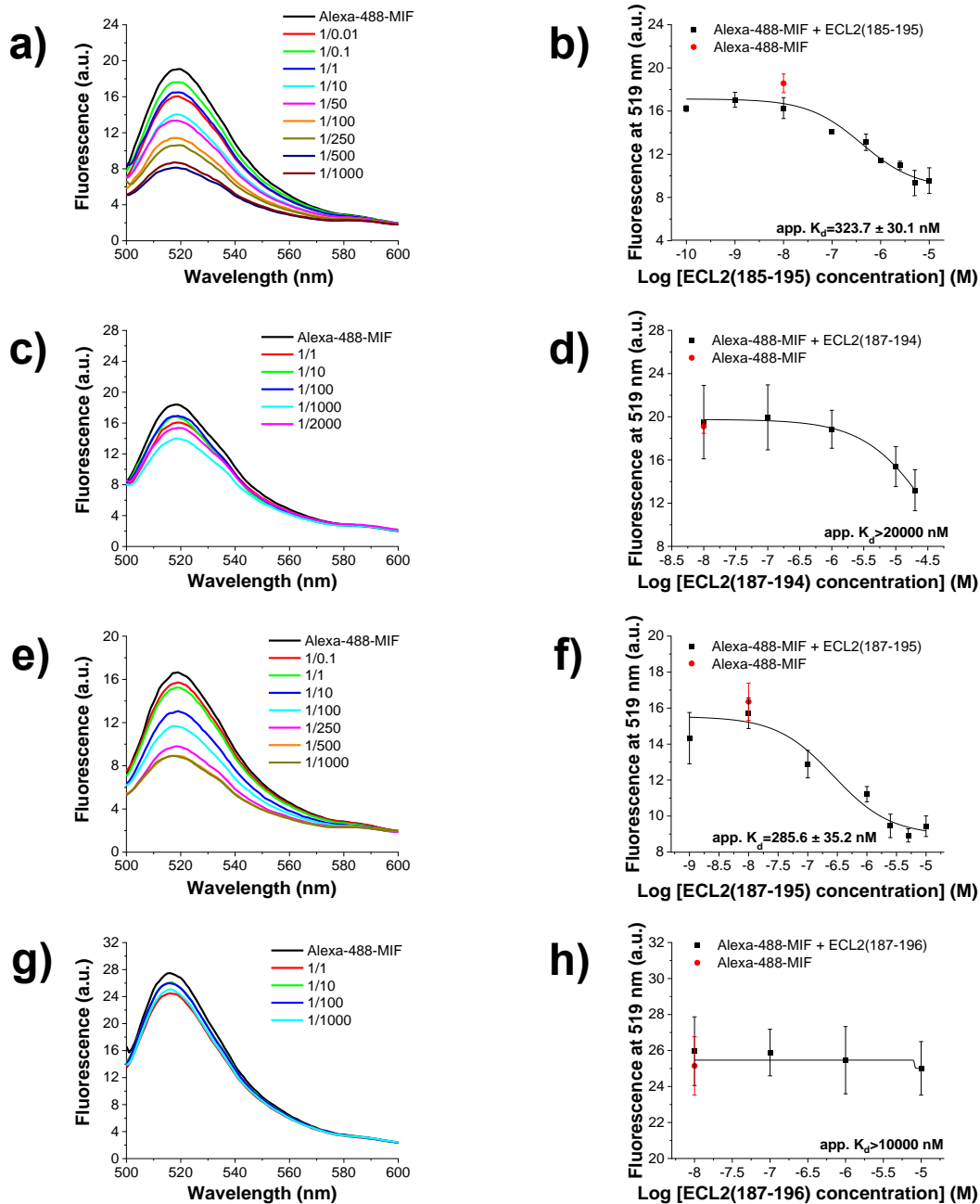
Figure 63. Fluorescence spectroscopic titrations of Alexa-488-MIF with shorter analogs of ECL2 for the determination of apparent affinities (app. K_{ds}). a, c, e, g Fluorescence spectra between 500 and 600 nm of Alexa-488-MIF (10 nM) alone and its mixtures with various amounts of ECL2(185-195) (a), ECL2(187-194) (c), ECL2(187-195) (e) and ECL2(187-196) (g); the molar ratios of Alexa-488-MIF/peptides are indicated. **b, d, f, h** Binding curves derived from the fluorescence emission at 519 nm of Alexa-488-MIF (10 nM) at different concentrations of ECL2(185-195) (b), ECL2(187-194) (d), ECL2(187-195) (f) and ECL2(187-196) (h). Data shown are means (±SD) from three independent titration experiments which were performed in aqueous 1×b, pH 7.4, containing 1% HFIP.
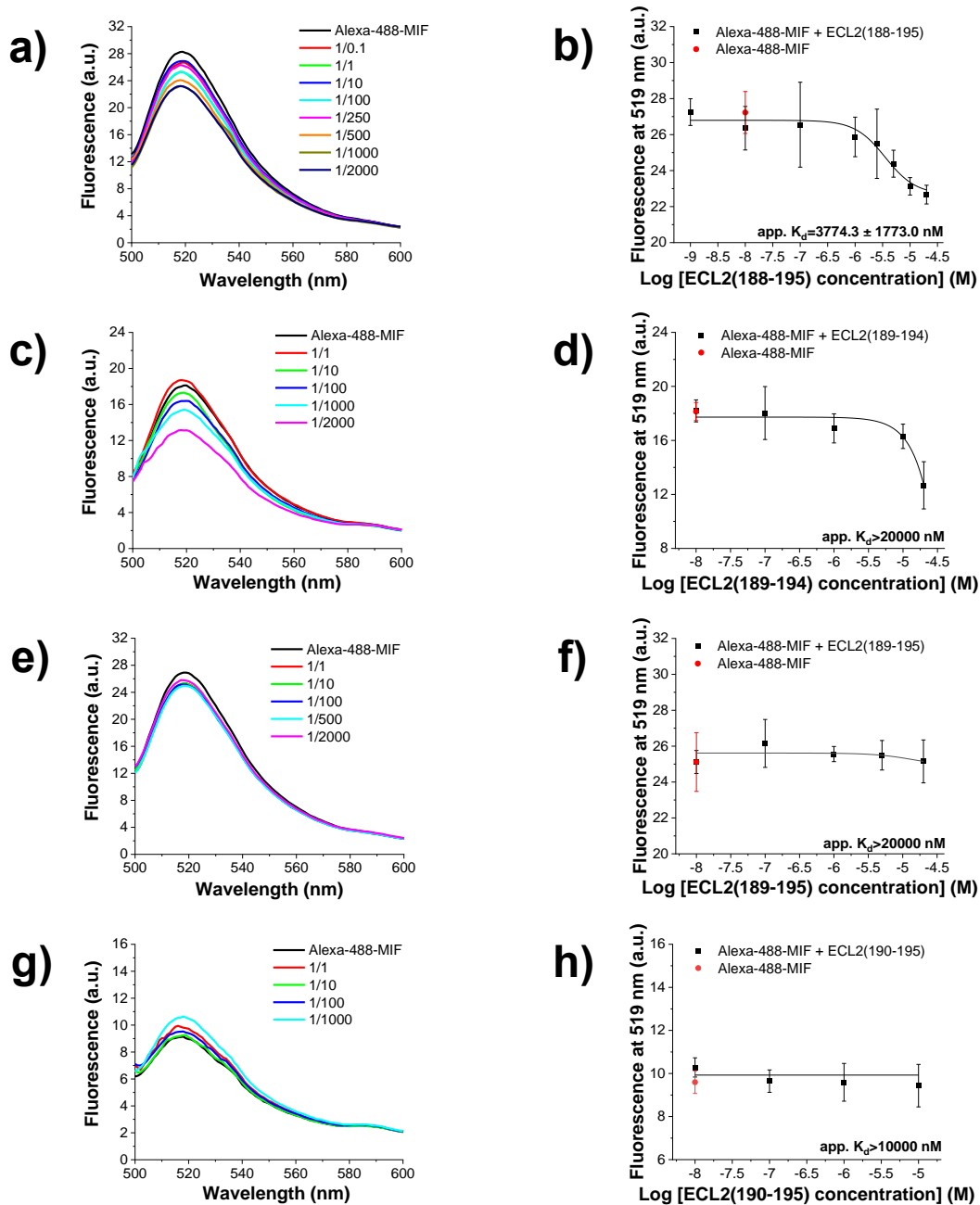
Figure 64. Fluorescence spectroscopic titrations of Alexa-488-MIF with shorter analogs of ECL2(187-195) for the determination of apparent affinities (app. K_{ds}). a, c, e, g Fluorescence spectra between 500 and 600 nm of Alexa-488-MIF (10 nM) alone and its mixtures with various amounts of ECL2(188-195) (a), ECL2(189-194) (c), ECL2(189-195) (e) and ECL2(190-195) (g); the molar ratios of Alexa-488-MIF/peptides are indicated. **b, d, f, h** Binding curves derived from the fluorescence emission at 519 nm of Alexa-488-MIF (10 nM) at different concentrations of ECL2(188-195) (b), ECL2(189-194) (d), ECL2(189-195) (f) and ECL2(190-195) (h). Data shown are means (±SD) from three independent titration experiments which were performed in aqueous 1×b, pH 7.4, containing 1% HFIP.

Table 29. Apparent affinities (app. K_{ds}) of interaction between Alexa-488-MIF and the shorter analogs of ECL2, as determined by fluorescence spectroscopic titrations.

Shorter analogs of ECL2	Alexa-488-MIF/peptide app. K_d (±SD) (nM)
ECL2	2458 (±1054)
ECL2(185-195)	323.7 (±30.1)
ECL2(187-194)	>20000
ECL2(187-195)	285.6 (±35.2)
ECL2(187-196)	>10000
ECL2(188-195)	3774.3 (±1773.0)
ECL2(189-194)	>20000
ECL2(189-195)	>20000
ECL2(190-195)	>10000

App. K_{ds}, are means (±SD) from three independent titration experiments which were performed in aqueous 1×b, pH 7.4, containing 1% HFIP.

4.2.4 Synthesis, purification and mass determination of ECL1(102-110), ECL1, ECL2(187-195) and ECL2 analogs

SAR studies in ECL1 and ECL2 and fluorescence spectroscopic titrations to determine their binding affinities to Alexa-488-MIF revealed ECL1(102-110) and ECL2(187-195) as the shortest potent binders of the atypical chemokine. Of note, both 9-mers exhibited a remarkably stronger affinity to MIF in comparison to the native sequences. As next, it was examined a sequence optimization of the peptides to obtain new derivatives with even higher affinity to MIF and improved solubility properties. All residues of both peptides were replaced one-by-one by alanines to test the specific effect of each residue. Additionally, one or two lysines were conjugated on the N-terminus of ECL1(102-110) for the generation of K-ECL1(102-110) and the KK-ECL1(102-110) analogs. For the generation of [2xPal]-ECL1(102-110) both F104 and F107 were substituted by 4-Pal. To examine further the effect of particular aromatic amino acids, mutations were introduced additionally on the native ECL1 and ECL2 sequences for the synthesis of [W102Cha]-ECL1and [Arom]-ECL2.

All peptides were synthesized and purified according to the previously described Fmoc-SPPS and RP-HPLC protocols. In brief, the synthesis was performed on the Fmoc-deprotected Rink-resin, and after the load of the first amino acid, UV-Vis spectroscopy was applied for the determination of the substitution level. Synthesis continued with double couplings of amino acids with some changes on the nature of the activator, DIEA equivalents, and the coupling duration as shown in Schemes 8 and 9. The normal protocol was applied for the cleavage of the Fmoc-group from the N-terminus, with the exception of ECL2 analogs. In particular, after D193 residue was coupled, the Fmoc-deprotection was carried out with the 'Short HOBt protocol' to hinder the Asi formation. Cleavage of both side-chain protected groups and peptide from the resin was achieved with Reagent K. Crude was lyophilized, and the obtained powder was dissolved in TFA/80% B, purified via RP-HPLC, and the collected peaks were dissolved in MALDI solution A prior to their MALDI-TOF-MS analysis (Figure 65-69). Yields were in the 5.6-49.2% range for the ECL1(102-110) and [W102Cha]-ECL1analogs, while they varied between 6.5 and 23.2% for analogs of ECL2(187-195), and [Arom]-ECL2 (Table 30, 31).
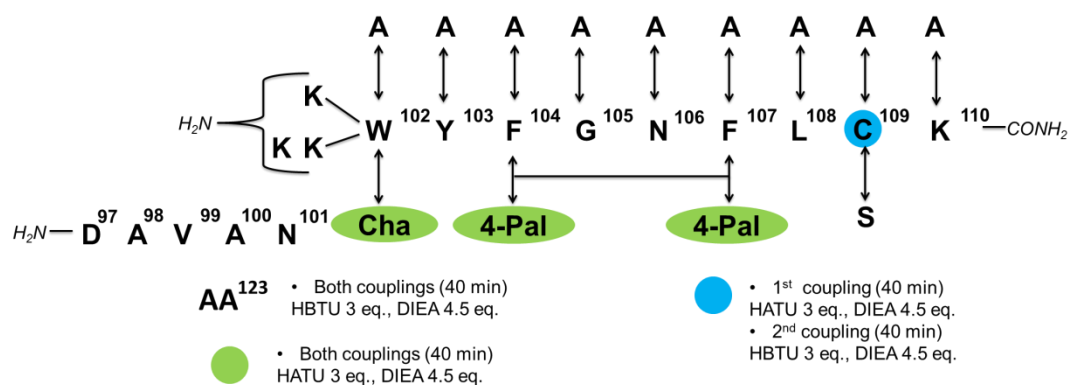
Scheme 8. Conditions of couplings for the synthesis of substituted analogs of ECL1(102-110) and ECL1. All amino acids were coupled with 3 equivalents (eq.), based on the substitution level that was determined after the load of the first amino acid on Rink-resin. Equivalents of activator and base, together with the coupling time may vary, as indicated.

Table 30. Sequences, abbreviation and characterization of synthesized substituted analogs of ECL1(102-110) and [W102Cha]-ECL1 by RP-HPLC and MALDI-TOF-MS.

Peptide sequence[a]	Peptide abbreviation	HPLC Pr.No.	t_R (min) [b]	Yield (%)[c]	[M+H]+ expected [d]	[M+H]+ found[d]
AYFGNFLCK	[W102A]-ECL1(102-110)	1	17.77	6.6	1061.53	1083.68[e]
W**A**FGNFLCK	[Y103A]-ECL1(102-110)	1	19.15	20.1	1084.55	1106.50[e]
WY**A**GNFLCK	[F104A]-ECL1(102-110)	1	17.60	7.9	1100.54	1122.76[e]
WYF**A**NFLCK	[G105A]-ECL1(102-110)	1	20.50	19.8	1190.59	1212.56[e]
WYFG**A**FLCK	[N106A]-ECL1(102-110)	1	20.30	17.2	1133.57	1155.47[e]
WYFGN**A**LCK	[F107A]-ECL1(102-110)	1	17.75	13.5	1100.54	1138.51[f]
WYFGNF**A**CK	[L108A]-ECL1(102-110)	1	18.00	6.4	1134.53	1156.57[e]
WYFGNFL**A**K	[C109A]-ECL1(102-110)	1	18.95	49.2	1144.60	1166.74[e]
WYFGNFLC**A**	[K110A]-ECL1(102-110)	1	21.60	15.7	1119.51	1141.60[e]
KWYFGNFLCK	K-ECL1(102-110)	1	17.85	31.0	1304.67	1326.59[e]
KKWYFGNFLCK	KK-ECL1(102-110)	1	17.45	11.1	1432.76	1495.14[g]
WYFGNFL**S**K	[C109S]-ECL1(102-110)	1	19.05	20.5	1160.6	1182.55[e]
WY**X₁**GN**X₁**LCK	[2xPal]-ECL1(102-110)	1	11.35	10.2	1178.55	1200.81[e]
DAVAN**X₂**YFGNFLCK	[W102Cha]-ECL1	1	20.40	5.6	1614.79	1635.91[e]

Peptides were dissolved and analyzed by MALDI-TOF-MS in a mixture of MALDI solutions A and A (matrix), with bold are indicated the substituted and the additional conjugated amino acids; **X₁**: 4-Pal, 3-(4-pyridyl)-L-alanine; **X₂**: Cha, cyclohexylalanine; **[a]** Peptides were synthesized with free amino-N-terminus and amidated C-terminus; **[b]** HPLC retention time of the pure product, the stationary phase was a tandem of Reprosil Gold 200 C18 columns (250 and 30 mm length, 8 mm internal diameter,10 μm particle size); **[c]** % yield with regard to crude peptide after cleavage; **[d]** monoisotopic molar mass with an additional hydrogen [M+H]+; **[e]** monoisotopic molar mass with an additional sodium [M+Na]+; **[f]** monoisotopic molar mass with an additional potassium [M+K]+ and **[g]** monoisotopic molar mass with an additional sodium and an additional potassium [M+Na]+.

122
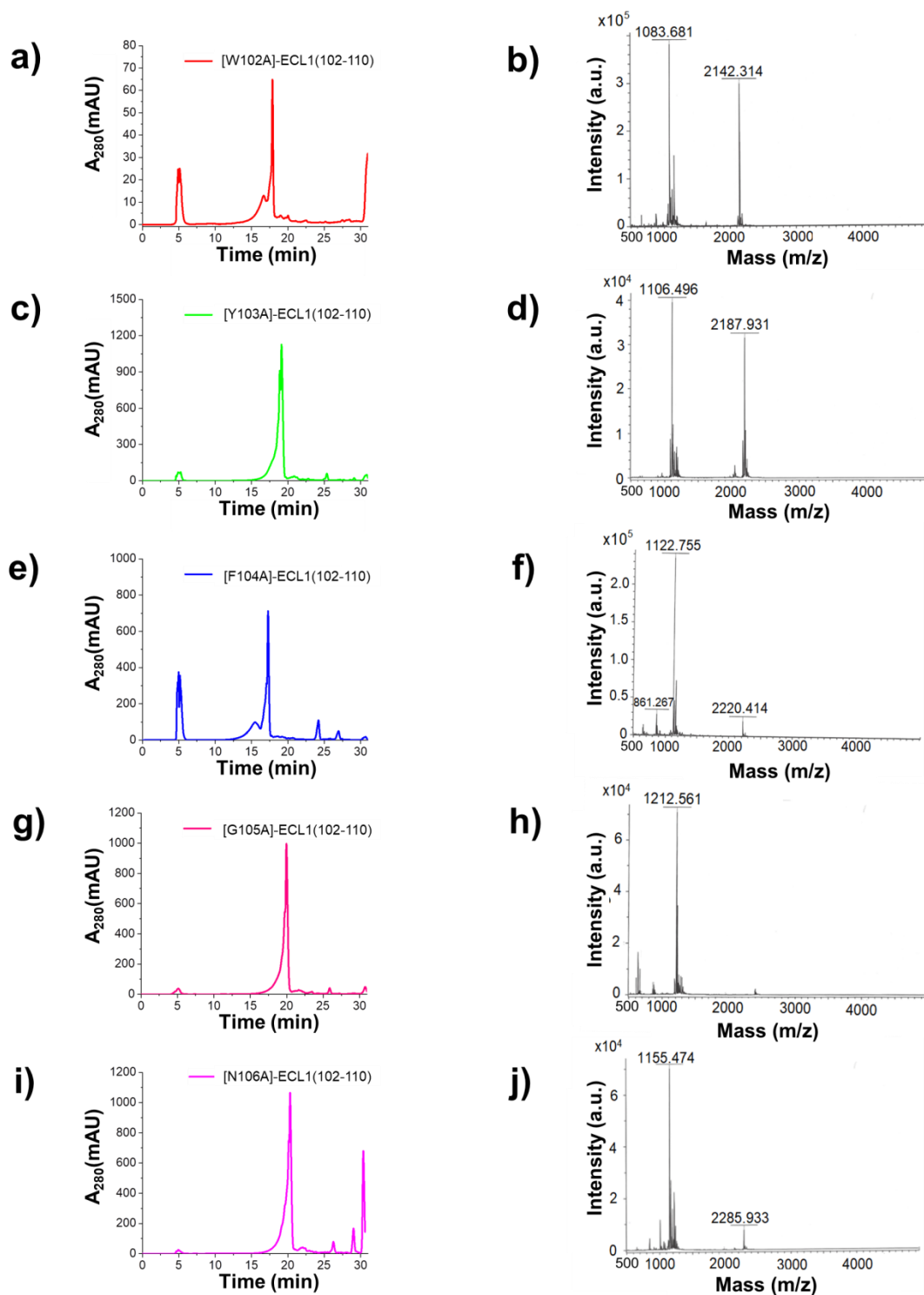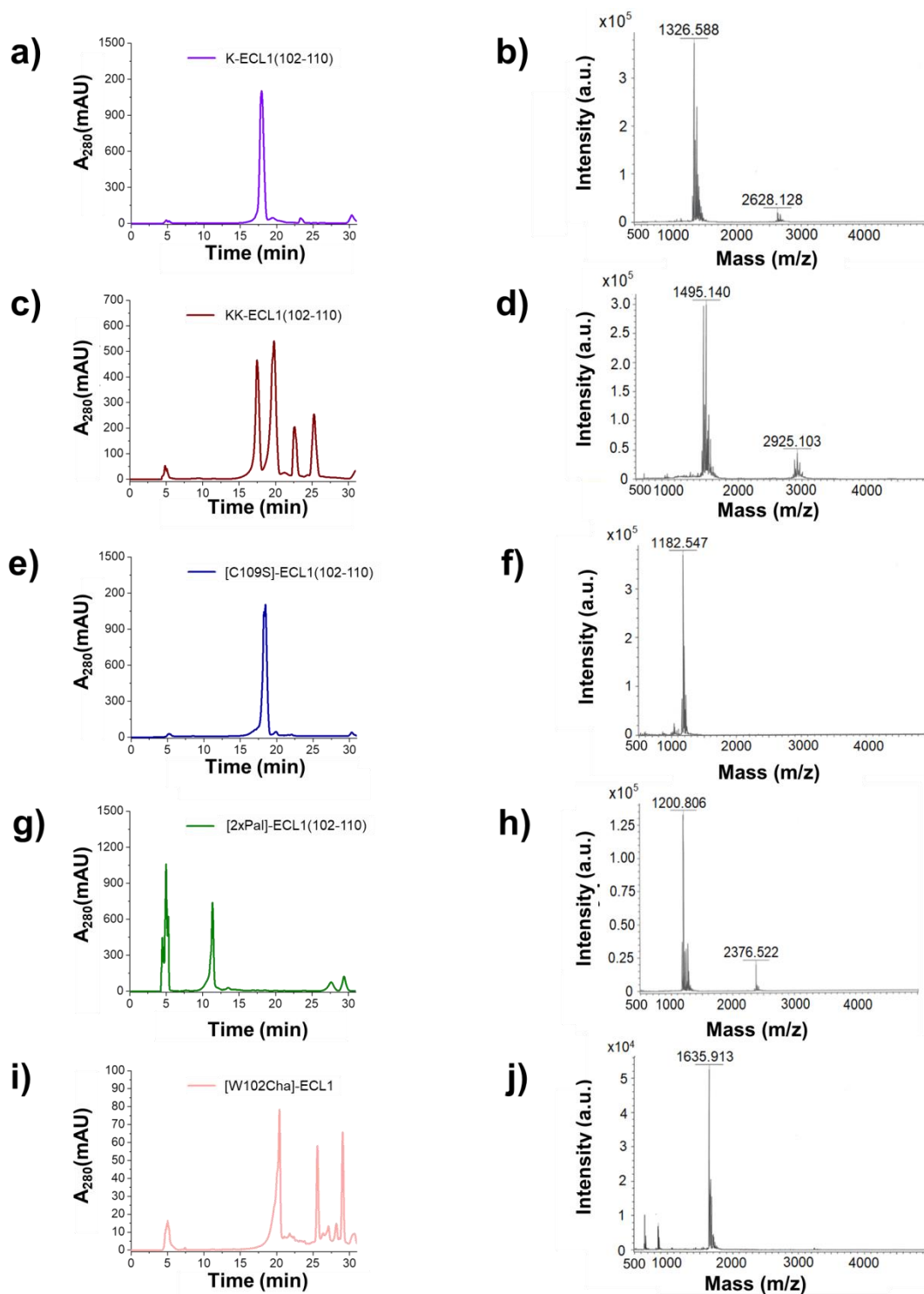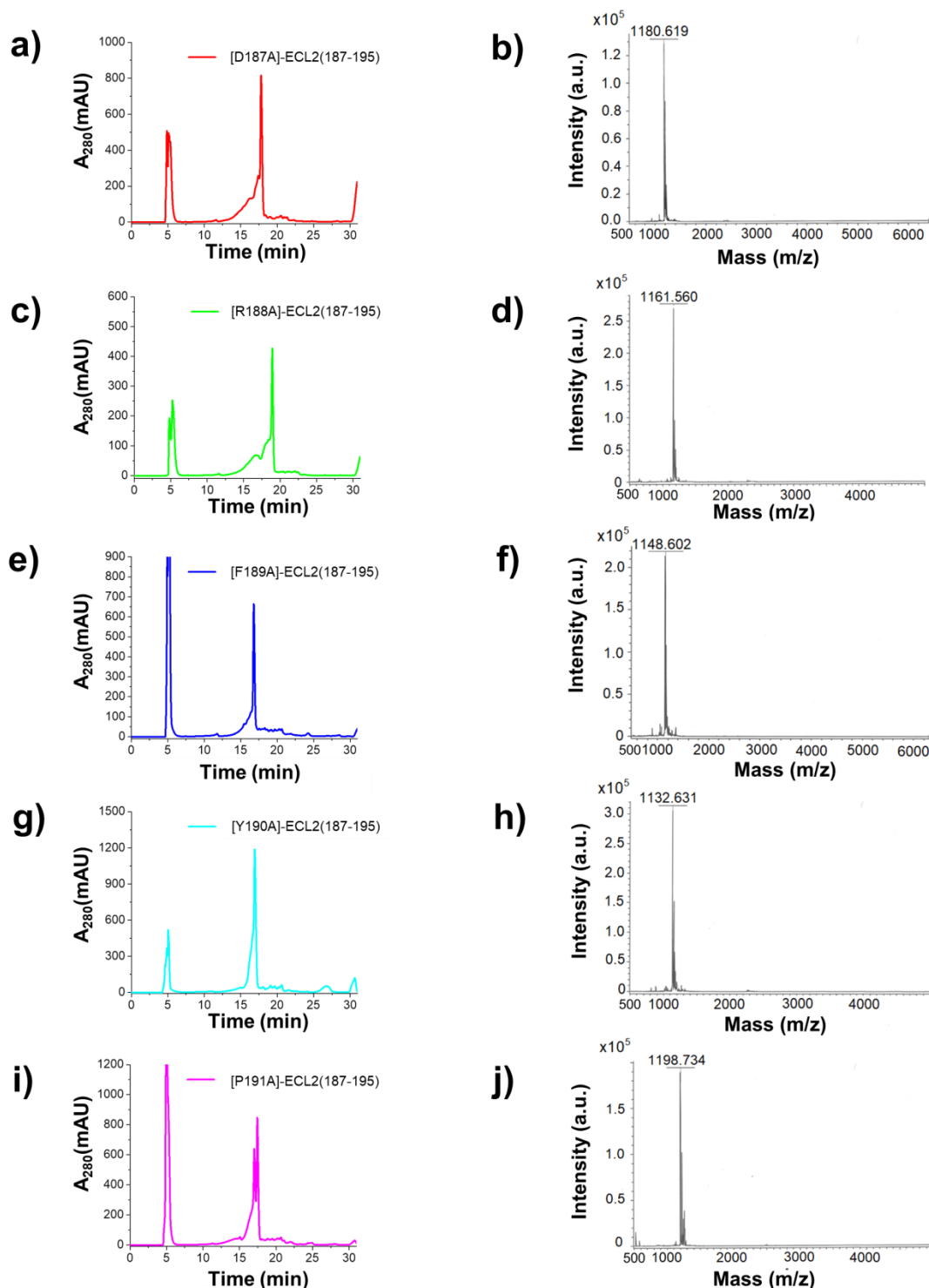
Figure 65. HPLC purification of alanine substituted analogs of ECL1(102-110) at positions 102, 103, 104, 105 and 106 and verification of their purity by MALDI. a, c, e, g, i Representative C18 HPLC chromatogram (absorbance at 280 nm) of crude [W102A]-ECL1(102-110), [Y103A]-ECL1(102-110), [F104A]-ECL1(102-110), [G105A]-ECL1(102-110) and [N106A]-ECL1(102-110) with respective retention times: a) 17.77 min, c) 19.15 min, e) 17.60 min, g) 20.50 min and i) 20.30 min, following SPPS and cleavage. The peaks that are eluted at the end of the chromatogram (t_R=31 min) are due to the formation of non-covalent aggregates. **b, d, f, h, j** MALDI-TOF-MS spectra of HPLC-purified [W102A]-ECL1(102-110), [Y103A]-ECL1(102-110), [F104A]-ECL1(102-110), [G105A]-ECL1(102-110) and [N106A]-ECL1(102-110) with respective experimental determined masses [M+H]$^+$: b) 1083.681 Da, d) 1106.496 Da, f) 1122.755 Da, h) 1212.561 Da and j) 1155.474 Da.
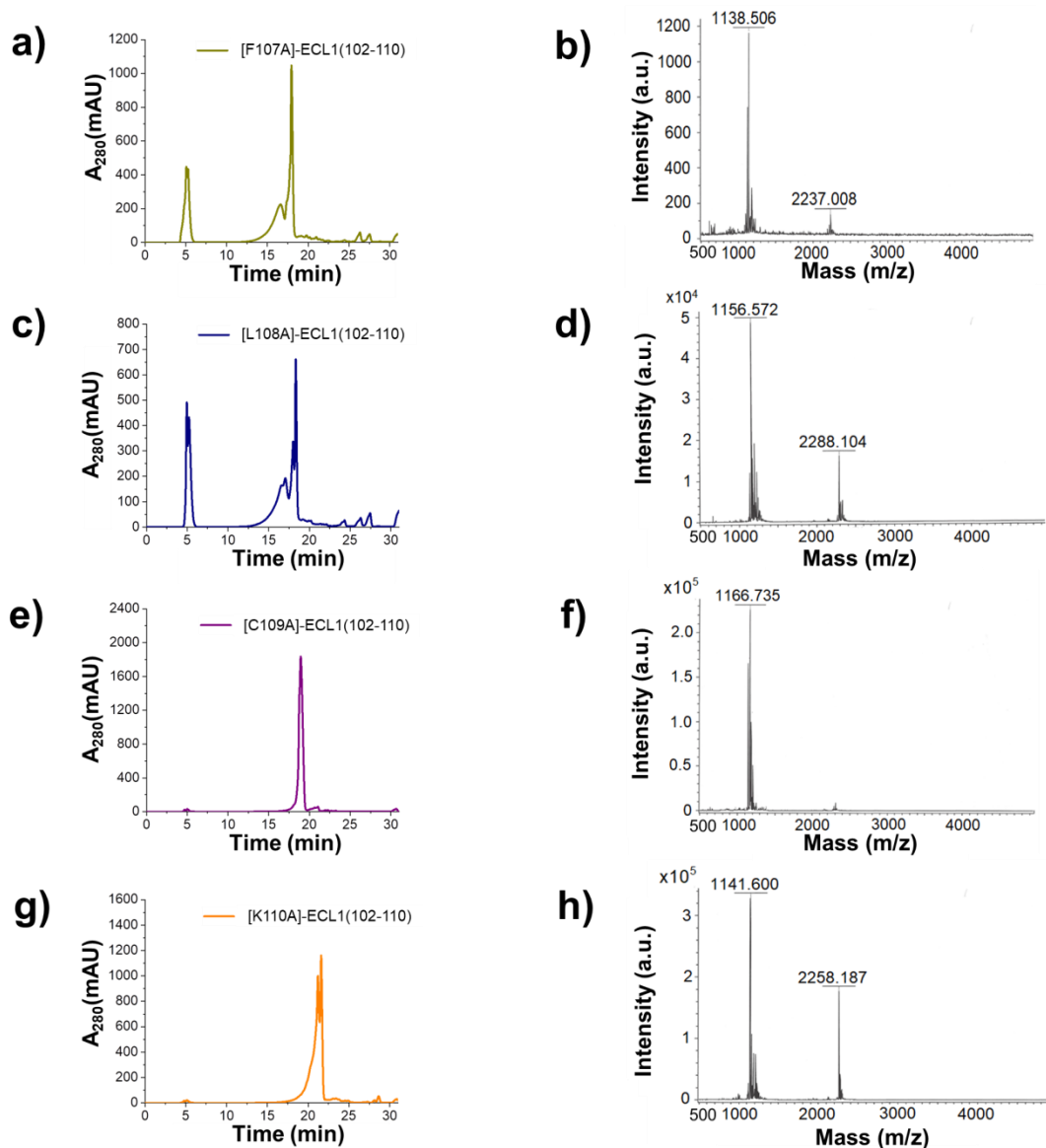
Figure 66. HPLC purification of alanine substituted analogs of ECL1(102-110) at positions 107, 108, 109 and 110 and verification of their purity by MALDI. a, c, e, g Representative C18 HPLC chromatogram (absorbance at 280 nm) of crude [F107A]-ECL1(102-110), [L108A]-ECL1(102-110), [C109A]-ECL1(102-110) and [K110A]-ECL1(102-110) with respective retention times: a) 17.75 min, c) 18.00 min, e) 18.95 min and g) 21.60 min, following SPPS and cleavage. **b, d, f, h** MALDI-TOF-MS spectra of HPLC-purified [F107A]-ECL1(102-110), [L108A]-ECL1(102-110), [C109A]-ECL1(102-110) and [K110A]-ECL1(102-110) with respective experimental determined masses [M+H]$^+$: b) 1138.506 Da, d) 1156.572 Da, f) 1166.735 Da and h) 1141.600 Da.

Figure 67. HPLC purification of analogs of ECL1(102-110) and ECL1 and verification of their purity by MALDI. a, c, e, g, i Representative C18 HPLC chromatogram (absorbance at 280 nm) of crude K-ECL1(102-110), KK-ECL1(102-110), [C109S]-ECL1(102-110), [2xPal]-ECL1(102-110) and [W102Cha]-ECL1with respective retention times: a) 17.85 min, c) 17.45 min, e) 19.05 min, g) 11.35 min and i) 20.40 min, following SPPS and cleavage. The peaks that are eluted at the end of the chromatogram (tR=31 min) are due to the formation of non-covalent aggregates. **b, d, f, h, j** MALDI-TOF-MS spectra of HPLC-purified K-ECL1(102-110), KK-ECL1(102-110), [C109S]-ECL1(102-110), [2xPal]-ECL1(102-110) and [W102Cha]-ECL1with respective experimental determined masses [M+H][+]: b) 1326.588 Da, d) 1495.140 Da, f) 1182.547 Da, h) 1200.806 Da and j) 1635.913 Da.
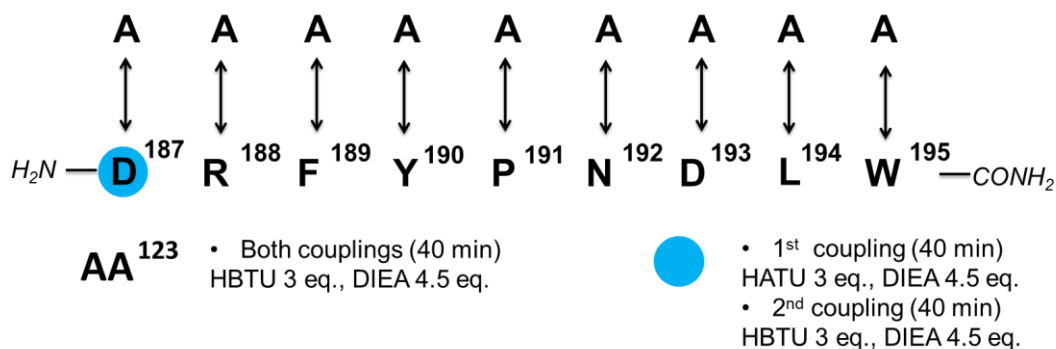
Scheme 9. Conditions of couplings for the synthesis of alanine substituted analogs of ECL2(187-195). All amino acids were coupled with 3 equivalents (eq.), based on the substitution level that was determined after the load of the first amino acid on Rink-resin. Equivalents of activator and base, together with the coupling time may vary, as indicated.

Table 31. Sequences, abbreviation and characterization of synthesized substituted analogs of ECL2(187-195) and [Arom]-ECL2 by RP-HPLC and MALDI-TOF-MS.

Peptide sequence[a]	Peptide abbreviation	HPLC Pr.No.	t_R (min) [b]	Yield (%)[c]	[M+H]$^+$ expected [d]	[M+H]$^+$ found[d]
ARFYPNDLW	[D187A]-ECL2(187-195)	1	15.88	11.7	1180.60	1180.62
D**A**FYPNDLW	[R188A]-ECL2(187-195)	1	18.92	6.5	1139.52	1161.56[e]
DR**A**YPNDLW	[F189A]-ECL2(187-195)	1	15.90	10.3	1148.56	1148.60
DRF**A**PNDLW	[Y190A]-ECL2(187-195)	1	17.50	19.4	1132.56	1132.63
DRFY**A**NDLW	[P191A]-ECL2(187-195)	1	17.44	16.5	1198.57	1198.73
DRFYP**A**DLW	[N192A]-ECL2(187-195)	1	18.55	23.2	1181.58	1181.78
DRFYPN**A**LW	[D193A]-ECL2(187-195)	1	17.91	18.0	1180.60	1180.68
DRFYPND**A**W	[L194A]-ECL2(187-195)	1	15.73	7.3	1182.54	1182.47
DRFYPNDL**A**	[W195A]-ECL2(187-195)	1	14.74	8.7	1109.54	1109.64
DR**X$_1$**ICDRF**X$_1$**PNDL**X$_2$**V	[Arom]-ECL2	4	33.90	16.9	2104.97	2105.43

Peptides were dissolved and analyzed by MALDI-TOF-MS in a mixture of MALDI solutions A and A (matrix), with bold are indicated the substituted amino acids; **X$_1$**:BiP, biphenylalanine; **X$_2$:** 1-Nal, 3-(1-naphthyl)-L-alanine; **[a]** Peptides were synthesized with free amino-N-terminus and amidated C-terminus; **[b]** HPLC retention time of the pure product; **[c]** % yield with regard to crude peptide after cleavage; **[d]** monoisotopic molar mass with an additional hydrogen [M+H]$^+$ and **[e]** monoisotopic molar mass with an additional sodium [M+Na]$^+$.

Figure 68. HPLC purification of alanine substituted analogs of ECL2(187-195) at positions 187, 188, 189, 190 and 191 and verification of their purity by MALDI. a, c, e, g, i Representative C18 HPLC chromatogram (absorbance at 280 nm) of crude [D187A]-ECL2(187-195), [R188A]-ECL2(187-195), [F189A]-ECL2(187-195), [Y190A]-ECL2(187-195) and [P191A]-ECL2(187-195) with respective retention times: a) 15.88 min, c) 18.92 min, e) 15.90 min, g) 17.50 min and i) 17.44 min, following SPPS and cleavage. **b, d, f, h, j** MALDI-TOF-MS spectra of HPLC-purified [D187A]-ECL2(187-195), [R188A]-ECL2(187-195), [F189A]-ECL2(187-195), [Y190A]-ECL2(187-195) and [P191A]-ECL2(187-195) with respective experimental determined masses [M+H]$^{+}$: b) 1180.619 Da, d) 1161.560 Da, f) 1148.602 Da, h) 1132.631 Da and j) 1198.734 Da.
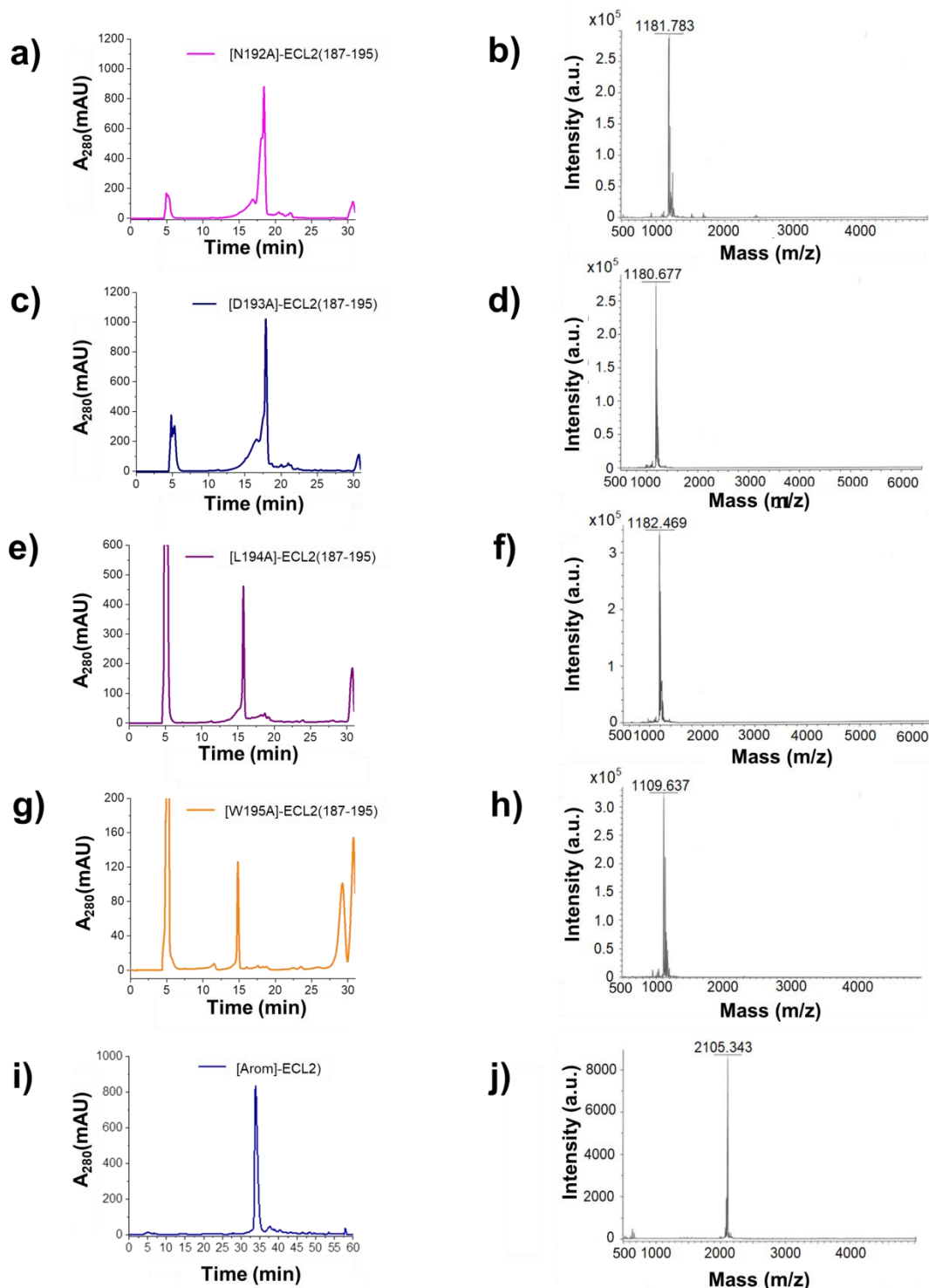
Figure 69. HPLC purification of alanine substituted analogs of ECL2(187-195) at positions 192, 193, 194, 195 and [Arom]-ECL2 and verification of their purity by MALDI. a, c, e, g, i Representative C18 HPLC chromatogram (absorbance at 280 nm) of crude [N192A]-ECL2(187-195), [D193A]-ECL2(187-195), [L194A]-ECL2(187-195), [W195A]-ECL2(187-195) and [Arom]-ECL2 with respective retention times: a) 18.55 min, c) 17.91 min, e) 15.73 min, g) 14.74 min and i) 33.90 min, following SPPS and cleavage. The peaks that are eluted at the end of the chromatogram (tR=31 min) are due to the formation of non-covalent aggregates. **b, d, f, h, j** MALDI-TOF-MS spectra of HPLC-purified [N192A]-ECL2(187-195), [D193A]-ECL2(187-195), [L194A]-ECL2(187-195), [W195A]-ECL2(187-195) and [Arom]-ECL2 with respective experimental determined masses $[M+H]^+$: b) 1181.783 Da, d) 1180.677 Da, f) 1182.469 Da, h) 1109.637 Da and j) 2105.343 Da.

4.2.5 Conformational and concentration dependence studies via CD spectroscopy

The conformation of all ECD analogs was determined by far-UV CD spectroscopy. Spectra were monitored between 1 and 50 µM following the already described experimental procedure and conditions. ECL1(102-110) derived spectra contained a broad positive peak between 225 and 235 nm, with the maxima at 230 nm. All single alanine mutants of ECL1(102-110) maintained this characteristic positive peak, with the exception of [W102A]-ECL1(102-110) and [Y103A]-ECL1(102-110) that had values very close to the baseline. Except for the maxima, [F104A]-ECL1(102-110) and [G105A]-ECL1(102-110) exposed their random coil indicative minima at 200 nm with MRE values equal to -3000 and -2000 deg·cm^2·dmol^{-1}, respectively. [N106A]-ECL1(102-110) was the only peptide with an ordered structure, with its minima between 214 and 218 nm and its positive values below 207 nm, indicating a β-sheet structure. The minima of [F107A]-ECL1(102-110) returned to 200 nm with MRE values between -3000 and -5000 deg·cm^2·dmol^{-1}, suggesting the presence of a random coil. A broad minima below 218 nm with its peak between 202 and 208 nm and an upward trend below 200 nm was noticed for [L108A]-ECL1(102-110), suggesting mainly of unordered species.

Both [C109A]-ECL1(102-110) and [K110A]-ECL1(102-110) exhibited their minima below 200 nm between -2500 and -4000 deg·cm^2·dmol^{-}1, and the positive π-π indicative bands at 230 nm. The rest of the alanine mutants exhibited the random coil indicative signal with the minima below 20 µM. Regarding their solubility properties, [N106A]-ECL1(102-110), as well as ECL1(102-110), precipitated at 50 µM, while [K110A]-ECL1(102-110) at 20 µM. All other alanine mutants showed more favorable soluble properties without any precipitation occurring until 50 µM. Spectra of [N106A]-ECL1(102-110) and [L108A]-ECL1(102-110) exhibited a reduced signal at 20 and 50 µM, respectively, suggesting the oligomerization of the peptides at these concentrations. No significant differentiation was noticed for the rest of these single alanine mutants (Figure 70). Summarized results and comparison of the spectra of the peptides are described in 'Discussion' (see 5.2).
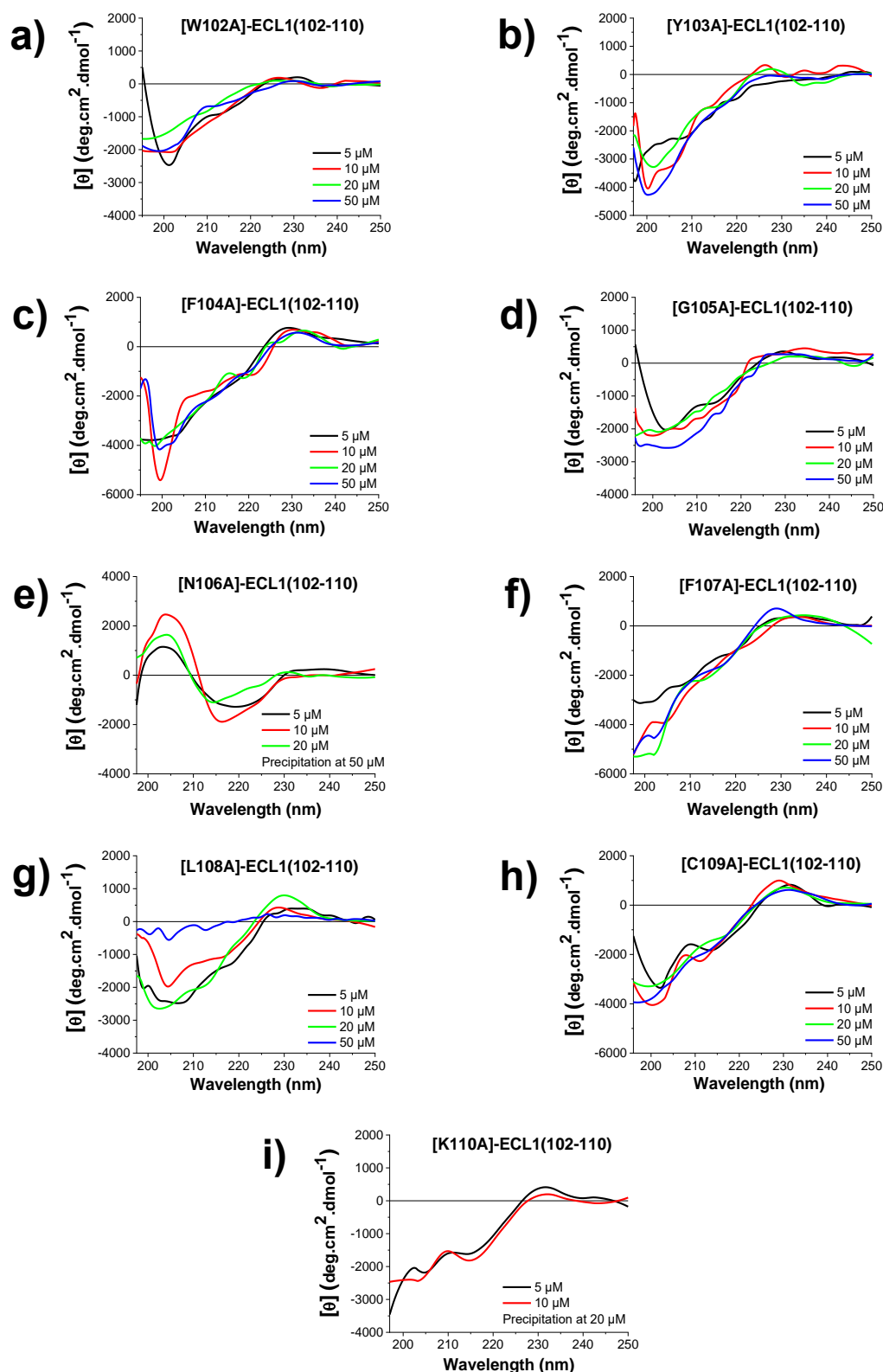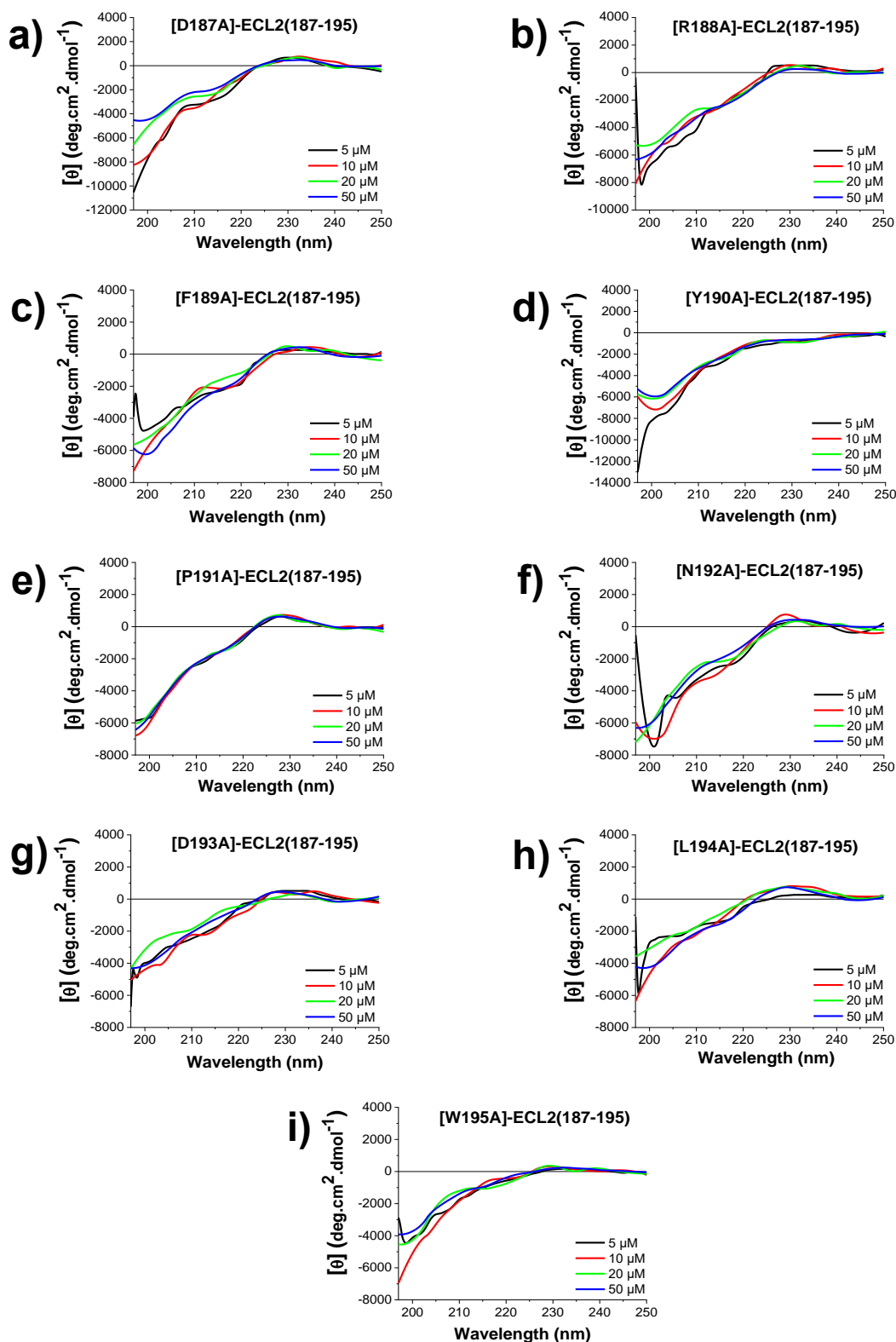
Figure 70. Spectra of single alanine mutants of ECL1(102-110) in various concentrations for the determination of the conformation, as determined by far-UV CD spectroscopy. a, b, c, d, e, f, g, h, i CD spectra of [W102A]-ECL1(102-110) (a), [Y103A]-ECL1(102-110) (b), [F104A]-ECL1(102-110) (c), [G105A]-ECL1(102-110) (d), [N106A]-ECL1(102-110) (e), [F107A]-ECL1(102-110) (f), [L108A]-ECL1(102-110) (g), [C109A]-ECL1(102-110) (h) and [K110A]-ECL1(102-110) (i) at increasing concentrations at final measuring conditions of aqueous 1×b, pH 7.4, containing 1% HFIP. Mean residue ellipticity (MRE) plotted over the wavelength between 195 and 250 nm for a, c, 197 and 250 nm for b, i, 196 and 250 nm for d, h and 197.5 and 250 nm for e, f, g.

130

Regarding the rest ECL1(102-110) analogs, all retained the 200 nm minima between -4000 and -6000 deg·cm^2·dmol^{-1} and the unordered structure of the non-mutated peptide. Peptides differentiated more in the 225 to 235 nm region, in which K-ECL1(102-110) had a stable weak positive signal (Figure 71a). Contrariwise, KK-ECL1(102-110) spectra did not show any remarkable signal in this wavelength region, while [C109S]-ECL1(102-110) and [2xPal]-ECL1(102-110) exhibited broad intense maxima at 230 nm (Figure 71b-d). Concerning the range of their intensities at their minima at 200 nm, K-ECL1(102-110) varied between -3000 and -5000 deg·cm^2·dmol^{-1} and KK-ECL1(102-110) between -4000 and -6000 deg·cm^2·dmol^{-1}.

Both [C109S]-ECL1(102-110) and [2xPal]-ECL1(102-110) exposed their minima at deg·cm^2·dmol^{-1}. The highest measured concentration was 50 µM for those peptides, except for KK-ECL1(102-110), which precipitated at this concentration, and its spectra were recorded until 20 µM. Peptides exposed constant spectra in all tested concentrations. Interestingly, another mutant, not of the shortened ECL1 but of the native sequence, the 14-mer [W102Cha]-ECL1appears to have an ordered structure, as the β-sheet indicative minima at 216 nm suggested (Figure 71e). Peptide precipitated at 50 µM, while its spectra at 10 and 20 µM had a 20% increased intensity at its minima, maybe due to oligomerization.
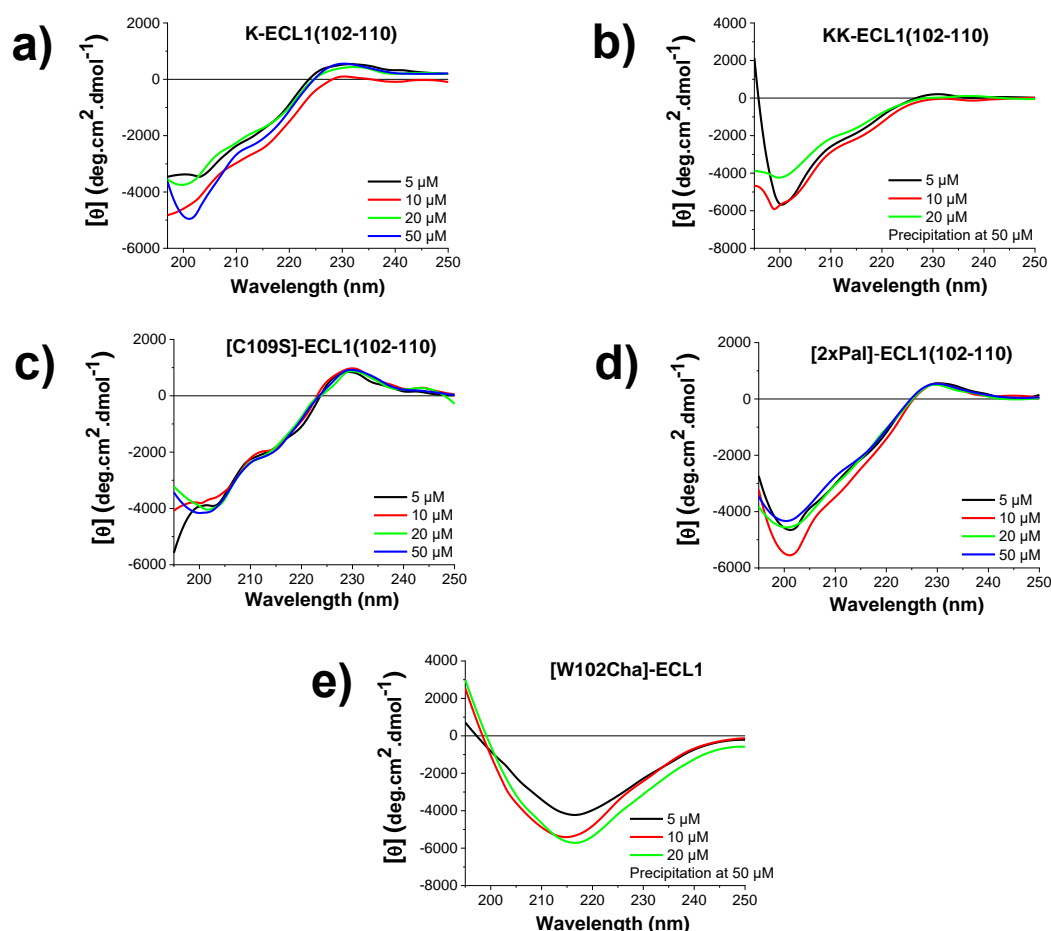
Figure 71. Spectra of analogs of ECL1(102-110) and ECL1 in various concentrations for the determination of the conformation, as determined by far-UV CD spectroscopy. a, b, c, d, e CD spectra of K-ECL1(102-110) (a), KK-ECL1(102-110) (b), [C109S]-ECL1(102-110) (c), [2xPal]-ECL1(102-110) (d) and [W102Cha]-ECL1(e) at increasing concentrations at final measuring conditions of aqueous 1×b, pH 7.4, containing 1% HFIP. Mean residue ellipticity (MRE) plotted over the wavelength between 195 and 250 nm.

ECL2(187-195) was previously shown to expose a random coil characteristic signal with strong minima below 200 nm. All single alanine mutants of the size optimized analog had spectra with similar shape and MRE values to the native one. A weak positive peak between 225 and 235 nm was noticed in ECL2(187-195), which may suggest the existence of π-π interactions. In some spectra of ECL2(187-195) mutants, this positive band obtained even higher MRE values for the mutants [D187A]-ECL2(187-195), [P191A]-ECL2(187-195), [L194A]-ECL2(187-195) (Figure 72a, e, h). The maxima had similar intensities in the spectra of [R188A]-ECL2(187-195), [F189A]-ECL2(187-195), [N192A]-ECL2(187-195) and [D193A]-ECL2(187-195) to the one derived from the native 9-mer. However, the maxima were not present for [Y190A]-ECL2(187-195) and [W195A]-ECL2(187-195) (Figure 72), proposing the lack of the previously noticed aromatic interactions. Similar to ECL2(187-195), all single alanine mutants showed favorable soluble properties and did not precipitate until 50 µM. Substitutions of D187 and Y190 by alanines led to a partial reduction of the signal intensity at the 20 and 50 µM obtained spectra, indicating an aggregation propensity in this range. Native peptide and the rest of the alanine mutants showed no concentration-dependent signal in their 5 to 50 µM measured spectra.

[R188Cit]-ECL2(184-196), a mutant of ECL2, exhibited random-coil indicative spectra with minima at 200 nm. The reduced intensity of the 20 and 50 µM derived spectra may pinpoint for self-association in this concentration range (Figure 73a). Peptide remained soluble until 50 µM, contrary to [Arom]-ECL2 that precipitated in this concentration. The 15-mer [Arom]-ECL2 showed spectra with minima at 225 nm at 5 and 10 µM, which appears to be associated with the β-sheet/β-turn formation. The intensity of the minima was reduced to half at 20 µM, possibly due to oligomerization (Figure 73b).

Figure 72. Spectra of single alanine mutants of ECL2(187-195) in various concentrations for the determination of the conformation, as determined by far-UV CD spectroscopy. a, b, c, d, e, f, g, h, i CD spectra of [D187A]-ECL2(187-195) (a), [R188A]-ECL2(187-195) (b), [F189A]-ECL2(187-195) (c), [Y190A]-ECL2(187-195) (d), [P191A]-ECL2(187-195) (e), [N192A]-ECL2(187-195) (f), [D193A]-ECL2(187-195) (g), [L194A]-ECL2(187-195) (h) and [W195A]-ECL2(187-195) (i) at increasing concentrations at final measuring conditions of aqueous 1×b, pH 7.4, containing 1% HFIP. Mean residue ellipticity (MRE) plotted over the wavelength between 197 and 250 nm for a, b, c, d, f, g, h 195 and 250 nm for e and 196 and 250 nm for i.

133
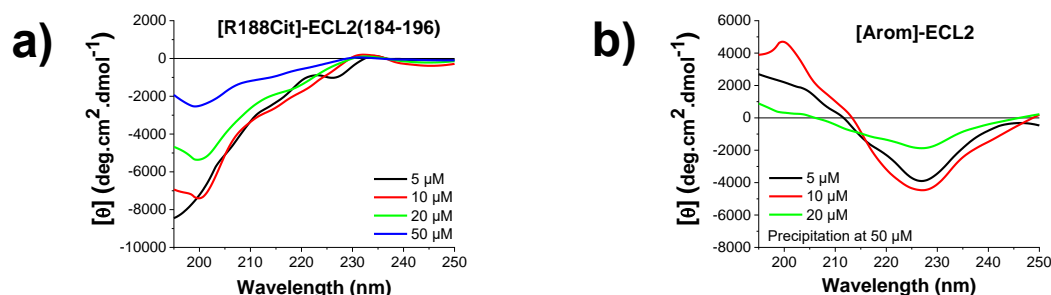
Figure 73. Spectra of [R188Cit]-ECL2(184-196) and [Arom]-ECL2 in various concentrations for the determination of the conformation, as determined by far-UV CD spectroscopy. a, b CD spectra of [R188Cit]-ECL2(184-196) (a) and [Arom]-ECL2 (b) at increasing concentrations at final measuring conditions of aqueous 1×b, pH 7.4, containing 1% HFIP. Mean residue ellipticity (MRE) plotted over the wavelength between 195 and 250 nm.

4.2.6 Determination of binding affinities to MIF with fluorescence spectroscopy

ECL1(102-110) and ECL2(187-195) had a high (86.3 ± 9.2 nM) and medium (285.6 ± 35.2 nM) affinity to MIF, remarkably improved compared to the long native peptides. The next posed question was whether these 9-mers could reach even lower dissociation constant values by a step-by-step alanine mutation of each of their residues. The previous size optimization studies underlined the importance of W102 and Y103 in the ECL1(102-110) sequence, with their elimination leading to a significant drop in the affinity with MIF. Likewise, [W102A]-ECL1(102-110) and [Y103A]-ECL1(102-110) mutants indicated the increased app. K_{ds} of 1280.3 ± 239.7 nM and 524.9 ± 70.2 nM (Figure 74a-d). Taking over phenylalanine with an alanine at position 104 slightly reduced the affinity with MIF concluding to an app. K_d of 179.4 ± 64.1 nM (Figure 74e-f).

Of note, alanine mutations at positions 105 and 106 led to a failure of reaching the plateau of the bound state with the app. K_{ds} of both [G105A]-ECL1(102-110) and [N106A]-ECL1(102-110) being estimated as higher than 10000 nM (Figure 74g-j). Alanine mutations of Phe and Leu at positions 107 and 108 led to the increased dissociation constants 286.5 ± 51.7 nM and 316.4 ± 49.7 nM, respectively (Figure 75a-d). Replacement of C109 with Ala led to a 10-fold decreased affinity between peptide and atypical chemokine, and particularly the calculated app. K_d was equal to 842.3 ± 129.0 nM (Figure 75e-f). The presence on the C-terminus of the only charged residue of the sequence seems to be important for the interaction with MIF since the [K110A]-ECL1(102-110) had an app. K_d above 10000 nM for binding to MIF (Figure 75g, h). Summarized results and comparison of the binding affinities of the peptides are described in 'Discussion' (see 5.2).
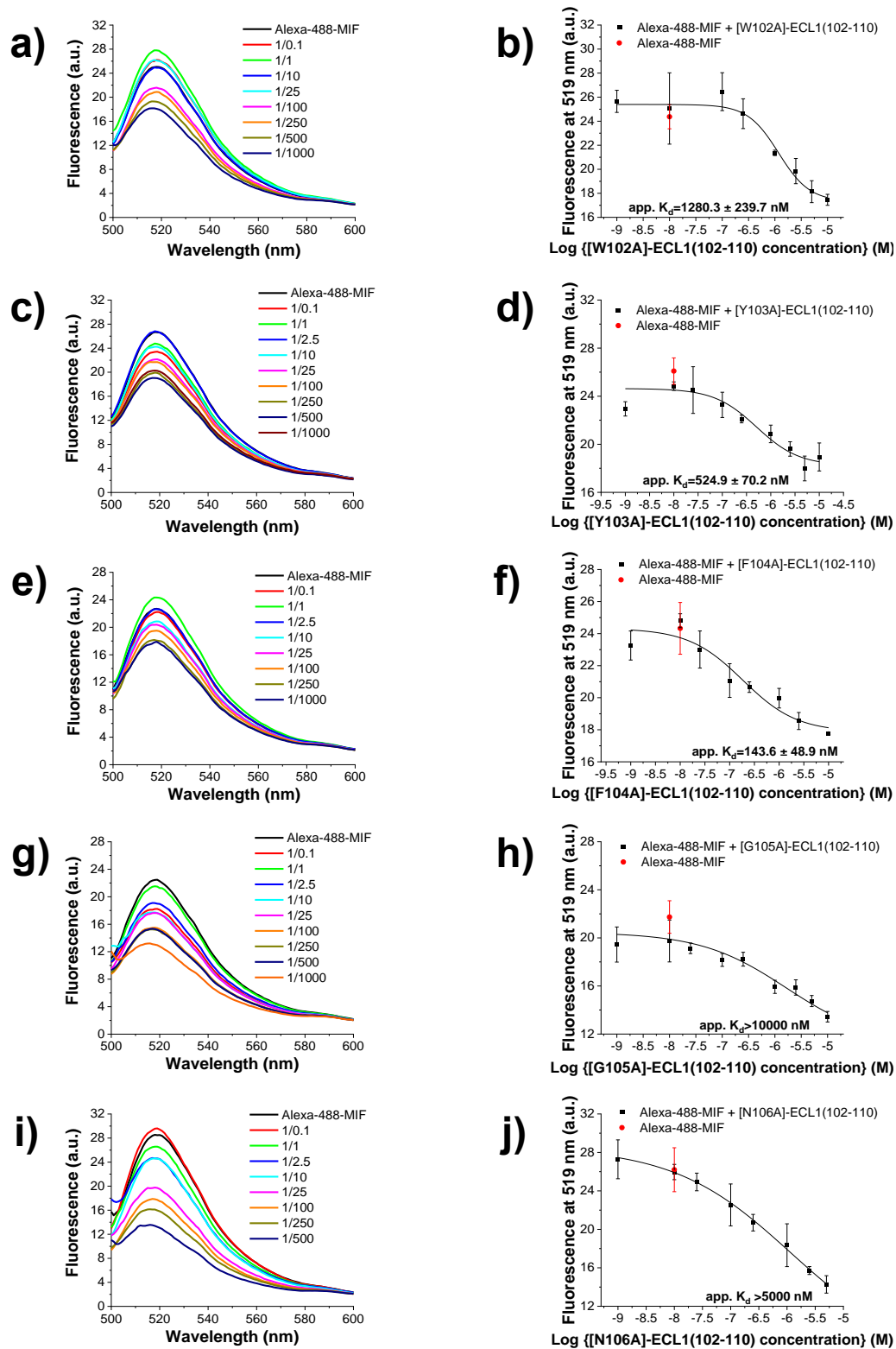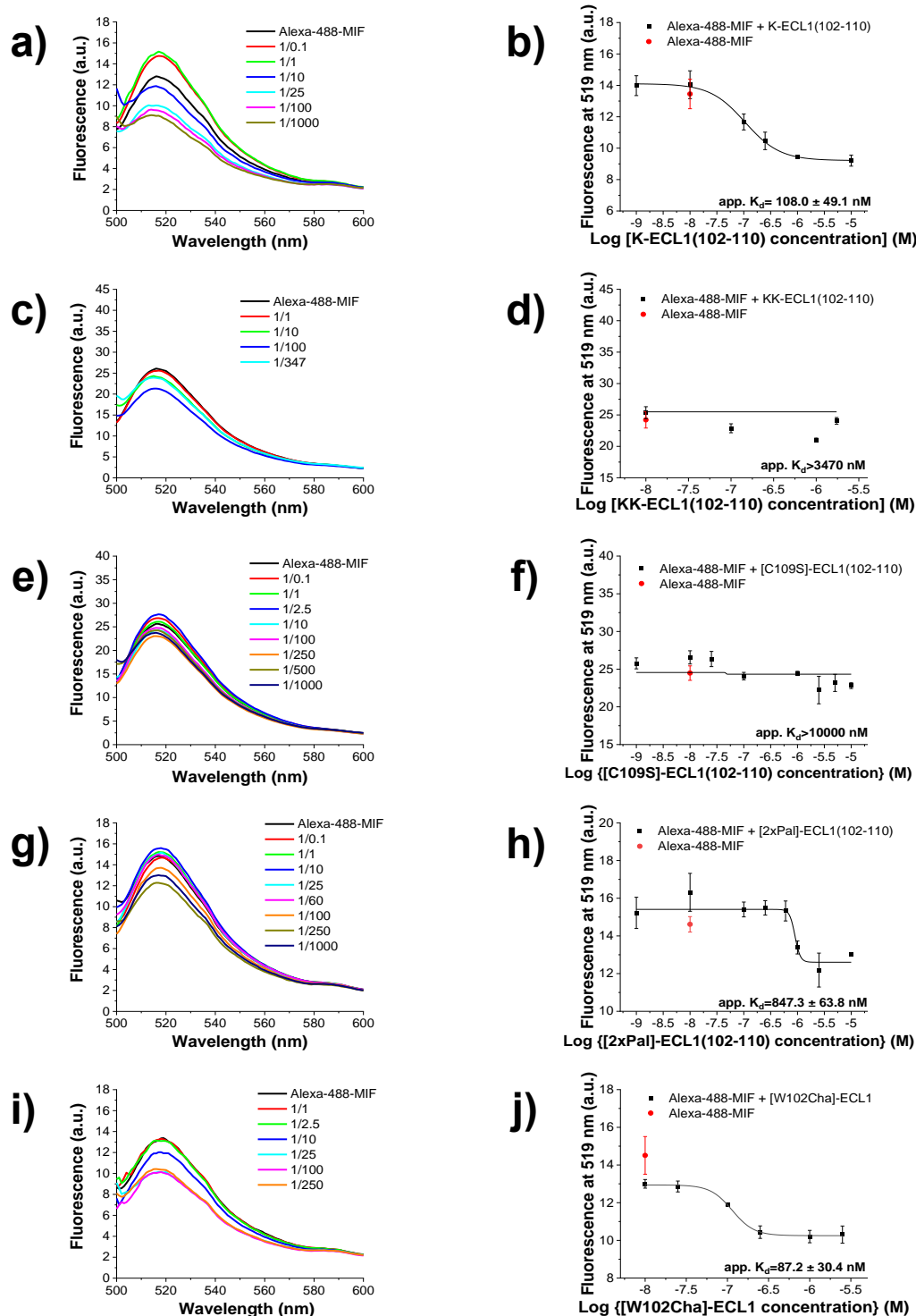
Figure 74. Fluorescence spectroscopic titrations of Alexa-488-MIF with alanine substituted analogs of ECL1(102-110) at positions 102, 103, 104, 105 and 106 for the determination of apparent affinities (app. K$_{ds}$). a, c, e, g, i Fluorescence spectra between 500 and 600 nm of Alexa-488-MIF (10 nM) alone and its mixtures with various amounts of [W102A]-ECL1(102-110) (a), [Y103A]-ECL1(102-110) (c), [F104A]-ECL1(102-110) (e), [G105A]-ECL1(102-110) (g) and [N106A]-ECL1(102-110) (i) ; the molar ratios of Alexa-488-MIF/peptides are indicated. **b, d, f, h, j** Binding curves derived from the fluorescence emission at 519 nm of Alexa-488-MIF (10 nM) at different concentrations of [W102A]-ECL1(102-110) (b), [Y103A]-ECL1(102-110) (d), [F104A]-ECL1(102-110) (f), [G105A]-ECL1(102-110) (h) and [N106A]-ECL1(102-110) (j). Data shown are means (±SD) from three independent titration experiments which were performed in aqueous 1×b, pH 7.4, containing 1% HFIP.

135
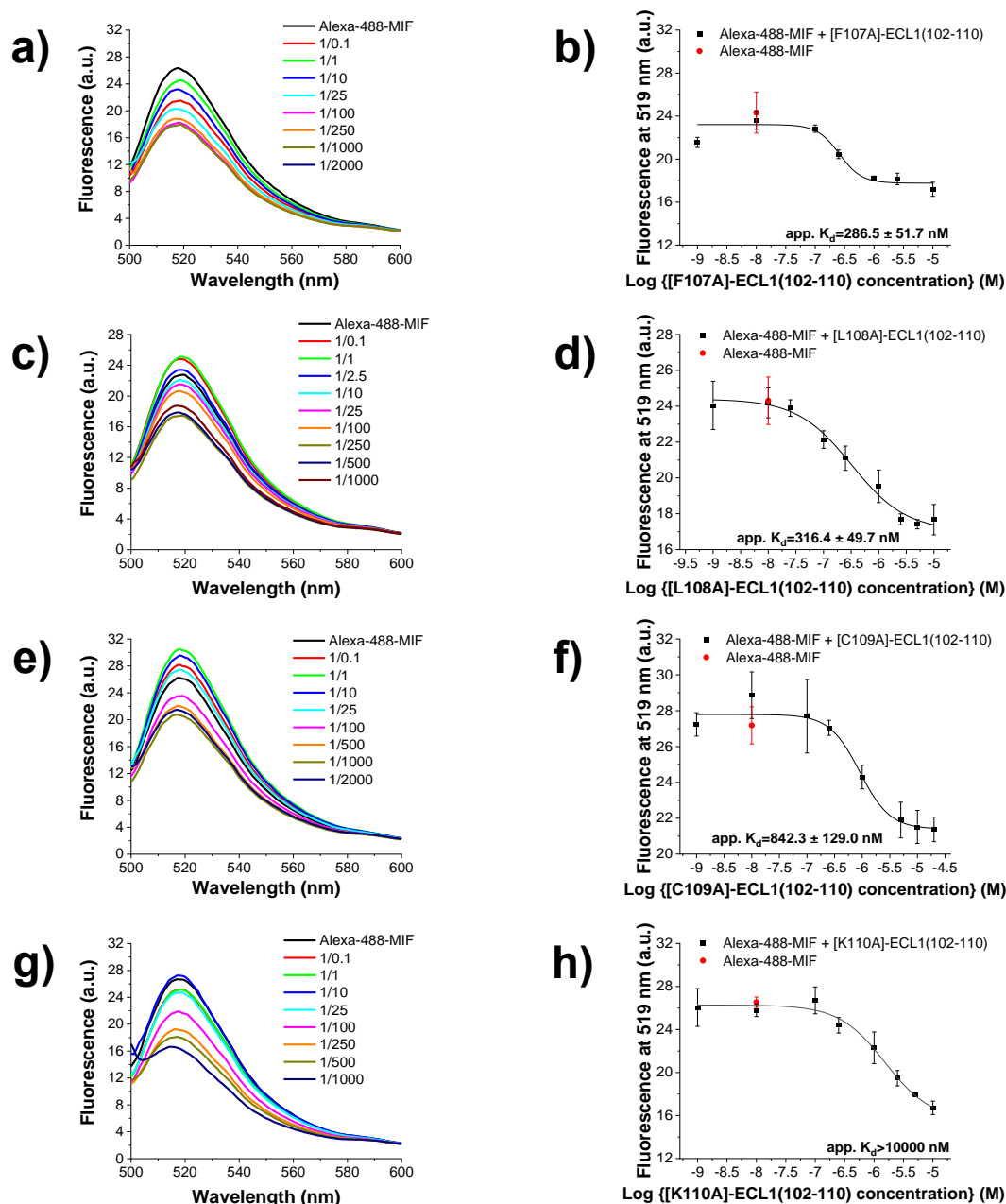
Figure 75. Fluorescence spectroscopic titrations of Alexa-488-MIF with alanine substituted analogs of ECL1(102-110) at positions 107, 108, 109 and 110 for the determination of apparent affinities (app. K_{ds}). a, c, e, g Fluorescence spectra between 500 and 600 nm of Alexa-488-MIF (10 nM) alone and its mixtures with various amounts of [F107A]-ECL1(102-110) (a), [L108A]-ECL1(102-110) (c), [C109A]-ECL1(102-110) (e) and K110A (ECL1) (g); the molar ratios of Alexa-488-MIF/peptides are indicated. **b, d, f, h** Binding curves derived from the fluorescence emission at 519 nm of Alexa-488-MIF (10 nM) at different concentrations of [F107A]-ECL1(102-110) (b), [L108A]-ECL1(102-110) (d), [C109A]-ECL1(102-110) (f) and [K110A]-ECL1(102-110) (h). Data shown are means (±SD) from three independent titration experiments which were performed in aqueous 1×b, pH 7.4, containing 1% HFIP.

The conjugation of a single K on the N-terminus of ECL1(102-110) did not affect the affinity of the K-ECL1(102-110) generated analog to MIF (app. K_d=108.0 ± 49.1 nM, Figure 76a, b). On the contrary, the addition of a second extra N-terminus K disrupted the binding, since the dissociation constant of KK-ECL1(102-110) to Alexa-488-MIF was above 10000 nM (Figure 76c, d). The fluorescence emission of the labeled MIF did not differentiate upon increasing concentration of C109S(102-110), suggesting an app. K_d above 10000 nM (Figure 76e, f). The substitution of F104 and

F107 by two 4-Pal residues concluded to a 10-fold increase in the app. K_d (847.3 ± 63.8 nM) (Figure 76g, h). Alexa-488-MIF and the 14-mer [W102Cha]-ECL1 shared a high affinity with the app. K_d being equal to 87.2 ± 30.4 nM (Table 32, Figure 76i, j).

Figure 76. Fluorescence spectroscopic titrations of Alexa-488-MIF with analogs of ECL1(102-110) and ECL1 for the determination of apparent affinities (app. K_{ds}). a, c, e, g, i Fluorescence spectra between 500 and 600 nm of Alexa-488-MIF (10 nM) alone and its mixtures with various amounts of K-ECL1(102-110) (a), KK-ECL1(102-110) (c), [C109S]-ECL1(102-110) (e), [2xPal]-ECL1(102-110) (g), and and [W102Cha]-ECL1(i); the molar ratios of Alexa-488-MIF/peptides are indicated. **b, d, f, h, j** Binding curves derived from the fluorescence emission at 519 nm of Alexa-488-MIF (10 nM) at different concentrations of K-ECL1(102-110) (b), KK-ECL1(102-110) (d), [C109S]-ECL1(102-110) (f), [2xPal]-ECL1(102-110) (h) and [W102Cha]-ECL1(j). Data shown are means (±SD) from three independent titration experiments which were performed in aqueous 1×b, pH 7.4, containing 1% HFIP.

Table 32. Apparent affinities (app. K_{ds}) of interactions between Alexa-488-MIF and mutants or analogs of ECL1(102-110) or [W102Cha]-ECL1, as determined by fluorescence spectroscopic titrations.

Mutants and analogs of ECL1(102-110) and ECL1	Alexa-488-MIF/peptide app. K_d (±SD) (nM)
ECL1(102-110)	86.3 (±9.2)
[W102A]-ECL1(102-110)	1280.3 (±239.7)
[Y103A]-ECL1(102-110)	524.9 (±70.2)
[F104A]-ECL1(102-110)	179.4 (±64.1)
[G105A]-ECL1(102-110)	>10000
[N106A]-ECL1(102-110)	>10000
[F107A]-ECL1(102-110)	286.5 (±51.7)
[L108A]-ECL1(102-110)	316.4 (±49.7)
[C109A]-ECL1(102-110)	842.3 (±129.0)
[K110A]-ECL1(102-110)	>10000
K-ECL1(102-110)	108.0 (±49.1)
KK-ECL1(102-110)	>10000
[C109S]-ECL1(102-110)	>10000
[2xPal]-ECL1(102-110)	847.3 (±63.8)
[W102Cha]-ECL1	87.2 (±30.4)

App. K_{ds}, are means (±SD) from three independent titration experiments which were performed in aqueous 1×b, pH 7.4, containing 1% HFIP.

Single alanine mutations did not bring any improvement in the interaction between ECL2 and MIF, as well. The affinity was significantly decreased to the micromolar range in all the cases with [P191A]-ECL2(187-195) and [L194A]-ECL2(187-195) having the app. K_{ds} above 10000 and 20000 nM, respectively. In a similar manner, all the rest single alanine mutants demonstrated dissociation constants higher than 40000 nM (Figure 77, 78). The only exception was the [Y190A]-ECL2(187-195), in which the affinity was determined at the three-digit nanomolar range and, more specifically, at 893.8 ± 82.6 nM (Table 33, Figure 77 g, h). Two other analogs of ECL2, [R188Cit]-ECL2(184-196) and [Arom]-ECL2 were titrated against Alexa-488-MIF as well, and their dissociation constants were estimated to be above 20000 and 2500 nM, respectively (Table 33, Figure 79).
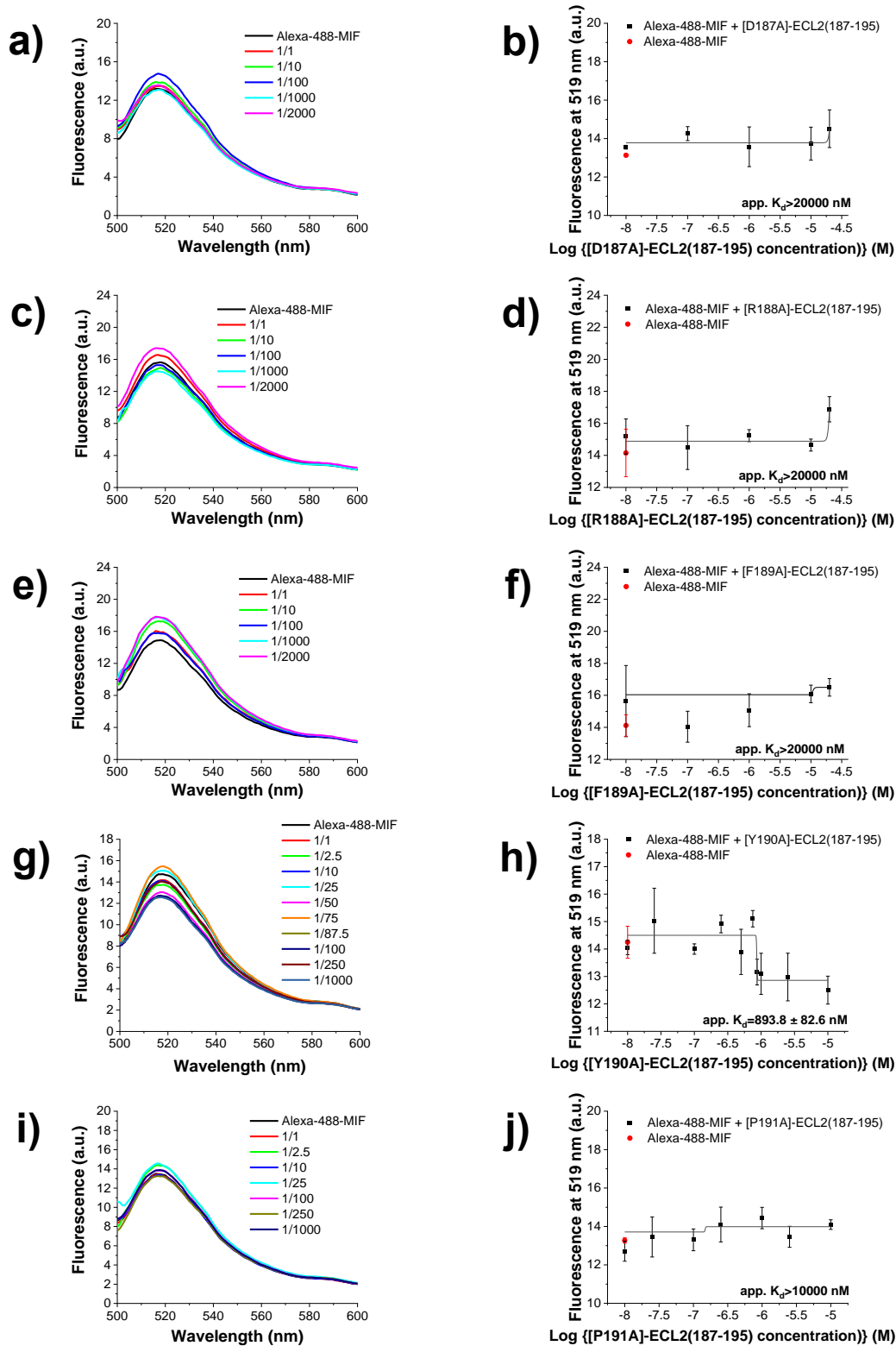
Figure 77. Fluorescence spectroscopic titrations of Alexa-488-MIF with alanine substituted analogs of ECL2(187-195) at positions 187, 188, 189, 190 and 191 for the determination of apparent affinities (app. K_{ds}). a, c, e, g, i Fluorescence spectra between 500 and 600 nm of Alexa-488-MIF (10 nM) alone and its mixtures with various amounts of [D187A]-ECL2(187-195) (a), [R188A]-ECL2(187-195) (c), [F189A]-ECL2(187-195) (e), [Y190A]-ECL2(187-195) (g) and [P191A]-ECL2(187-195) (i); the molar ratios of Alexa-488-MIF/peptides are indicated. **b, d, f, h, j** Binding curves derived from the fluorescence emission at 519 nm of Alexa-488-MIF (10 nM) at different concentrations of [D187A]-ECL2(187-195) (b), [R188A]-ECL2(187-195) (d), [F189A]-ECL2(187-195) (f), [Y190A]-ECL2(187-195) (h) and [P191A]-ECL2(187-195) (j). Data shown are means (±SD) from three independent titration experiments which were performed in aqueous 1×b, pH 7.4, containing 1% HFIP.
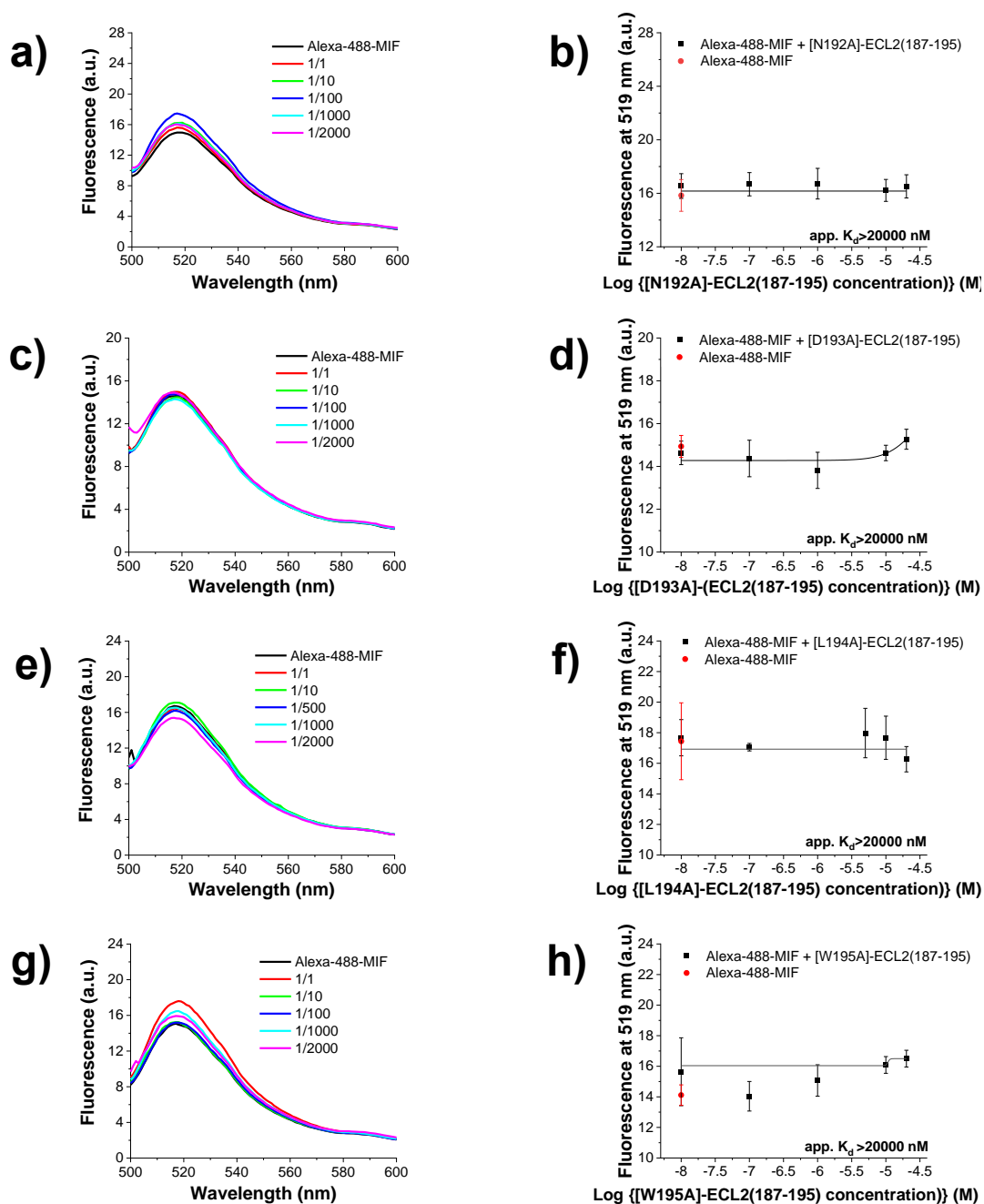
Figure 78. Fluorescence spectroscopic titrations of Alexa-488-MIF with alanine substituted analogs of ECL2(187-195) at positions 192, 193, 194 and 195 for the determination of apparent affinities (app. K_{ds}). a, c, e, g Fluorescence spectra between 500 and 600 nm of Alexa-488-MIF (10 nM) alone and its mixtures with various amounts of [N192A]-ECL2(187-195) (a), [D193A]-ECL2(187-195) (c), [L194A]-ECL2(187-195) (e) and [W195A]-ECL2(187-195) (g); the molar ratios of Alexa-488-MIF/peptides are indicated. **b, d, f, h** Binding curves derived from the fluorescence emission at 519 nm of Alexa-488-MIF (10 nM) at different concentrations of [N192A]-ECL2(187-195) (b), [D193A]-ECL2(187-195) (d), [L194A]-ECL2(187-195) (f) and [W195A]-ECL2(187-195) (h). Data shown are means (±SD) from three independent titration experiments which were performed in aqueous 1×b, pH 7.4, containing 1% HFIP.
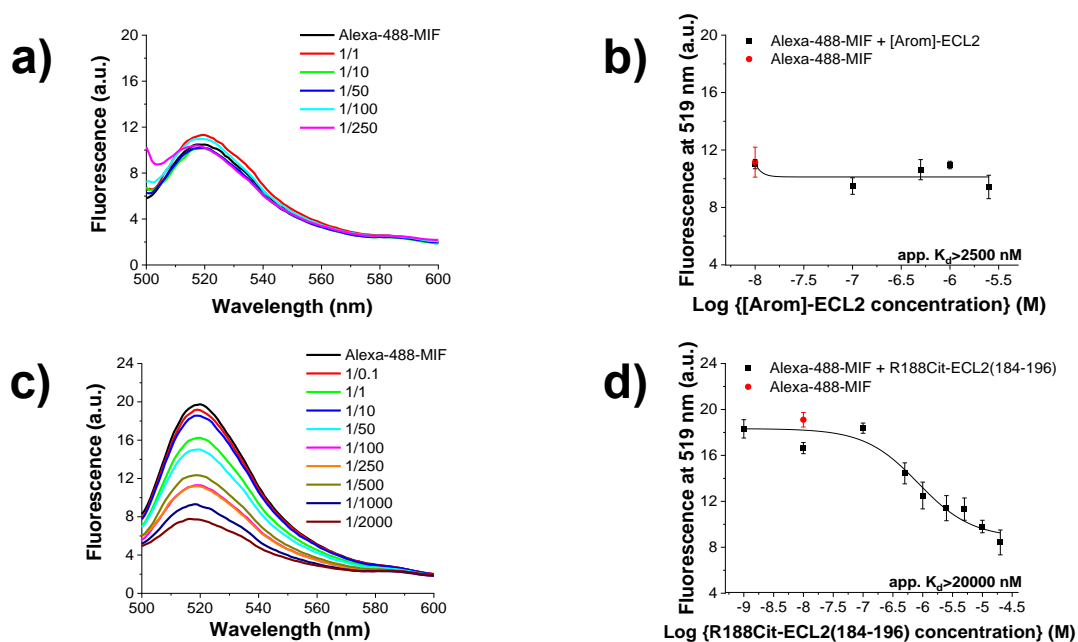
Figure 79. Fluorescence spectroscopic titrations of Alexa-488-MIF with [R188Cit]-ECL2(184-196) and [Arom]-ECL2 for the determination of apparent affinities (app. K_{ds}). a, c Fluorescence spectra between 500 and 600 nm of Alexa-488-MIF (10 nM) alone and its mixtures with various amounts of [R188Cit]-ECL2(184-196) (a) and [Arom]-ECL2 (c) the molar ratios of Alexa-488-MIF/peptides are indicated. **b, d** Binding curves derived from the fluorescence emission at 519 nm of Alexa-488-MIF (10 nM) at different concentrations of [R188Cit]-ECL2(184-196) (b) and [Arom]-ECL2 (d). Data shown are means (±SD) from three independent titration experiments performed in aqueous 1×b, pH 7.4, containing 1% HFIP.

Table 33. Apparent affinities (app. K_{ds}) of interaction between Alexa-488-MIF and alanine mutants of ECL2(187-195) or analogs of ECL2, as determined by fluorescence spectroscopic titrations.

Alanine mutants of ECL2(187-195) and analogs of ECL2	Alexa-488-MIF/peptide app. K_d (±SD) (nM)
ECL2(187-195)	285.6 (±35.2)
[D187A]-ECL2(187-195)	>20000
[R188A]-ECL2(187-195)	>20000
[F189A]-ECL2(187-195)	>20000
[Y190A]-ECL2(187-195)	893.8 (±82.6)
[P191A]-ECL2(187-195)	>10000
[N192A]-ECL2(187-195)	>20000
[D193A]-ECL2(187-195)	>20000
[L194A]-ECL2(187-195)	>20000
[W195A]-ECL2(187-195)	>20000
[R188Cit]-ECL2(184-196)	>20000
[Arom]-ECL2	>2500

App. K_{ds}, are means (±SD) from three independent titration experiments which were performed in aqueous 1×b, pH 7.4, containing 1% HFIP.

4.2.7 Conclusions of SAR studies on ECL1 and ECL2

SAR studies on ECL1 and ECL2 sequence, the two CXCR4-derived segments that, when conjugated together via linkers generated msR4Ms, aimed to develop shorter ECD with increased affinity for MIF. ECL1 analogs retained the random coil with traces of ordered structure of the native peptide, except for ECL1(97-109) that seemed to be more in a β-sheet than an unordered state. Regarding ECL2 analogs, the flexibility and the lack of

order were induced even more in the shorter peptides. Notably, the size minimization led to the shorter ECL1 and ECL2 analogs that were more soluble than the native peptides under the CD measuring conditions (Table 34). Except for increased solubility, some shortened ECD analogs had enhanced binding to MIF, compared to long ones, according to the data derived by fluorescence spectroscopic titrations. The shortest and most binders for MIF were the 9-mers ECL1(102-110) and ECL2(187-195), with 4-fold and 8.6-fold improved dissociations constants compared to ECL1 and ECL2, respectively (Table 35).

Table 34. Defined biophysical properties of shorter analogs of ECL1 and ECL2, after CD spectroscopy studies.

Shorter analogs of ECL1	Secondary structure	Precip. (µM)	Shorter analogs of ECL2	Secondary structure	Precip. (µM)
ECL1	r.c. [a]	20	ECL2	r.c. [a]	20
ECL1(97-107)	r.c. [a]	20	ECL2(185-195)	r.c. [a]	>50
ECL1(97-108)	r.c. [a]	50	ECL2(187-194)	r.c. [a]	>50
ECL1(97-109)	β-sheet + r.c.[a]	50	ECL2(187-195)	r.c. [a]	>50
ECL1(100-110)	r.c. [a]	>50	ECL2(187-196)	r.c. [a]	>50
ECL1(101-110)	r.c. [a]	50	ECL2(188-195)	r.c. [a]	20
ECL1(102-110)	r.c. [a]	50	ECL2(189-194)	r.c. [a]	50
ECL1(103-110)	r.c. [a]	>50	ECL2(189-195)	r.c. [a]	>50
ECL1(104-110)	r.c. [a]	>50	ECL2(190-195)	r.c. [a]	>50

Peptides were biophysically characterized in aqueous 1×b, pH 7.4, containing 1% HFIP. [a]: r.c., random coil,

Table 35. Determined app. K_{ds} of shorter analogs of ECL1 and ECL2 with Alexa-488-MIF, as derived by fluorescence spectroscopic titrations.

Shorter analogs of ECL1	app. K_d (±SD) (nM) [a] (Alexa-488-MIF/peptide)	Shorter analogs of ECL2	app. K_d (±SD) (nM) [a] (Alexa-488-MIF/peptide)
ECL1(97-107)	>20000	ECL2(185-195)	323.7 (±30.1)
ECL1(97-108)	>10000	ECL2(187-194)	>20000
ECL1(97-109)	60.1 (±9.6)	ECL2(187-195)	285.6 (±35.2)
ECL1(100-110)	214.5 (±72.3)	ECL2(187-196)	>10000
ECL1(101-110)	45.2 (±14.0)	ECL2(188-195)	3774.3 (±1773.0)
ECL1(102-110)	86.3 (±9.2)	ECL2(189-194)	>20000
ECL1(103-110)	533.8 (±95.7)	ECL2(189-195)	>20000
ECL1(104-110)	>20000	ECL2(190-195)	>10000

[a]: App. K_{ds} are means (±SD) from three independent titration experiments which were performed in aqueous 1×b, pH 7.4, containing 1% HFIP.

Next, more SAR studies were carried out in these analogs to check whether it is possible to maintain or induce an even stronger binding to MIF and have improved solubility. CD spectra of the analogs [N106A]-ECL1(102-110) and [W102Cha]-ECL1 suggested a mainly β-sheet structure with some random coil traces, while the rest mutants and analogs of ECL1(102-110) remained unordered. Likewise, all ECL2(187-195) mutants and [R188Cit]-ECL2(184-196) did not obtain any ordered structure, except for [Arom]-ECL2 (Table 36). The substitutions of F104, F107, or L108 with alanine of ECL1(102-110) or the conjugation of lysine on the N-terminus resulted in mutants with a slightly weaker affinity for MIF. All the rest alanine mutants and analogs of the 9-mer had remarkably decreased binding potency compared to the native peptide, except for [W102Cha]-ECL1. Similar to ECL1(102-110), the single alanine mutated ECL2(187-195) and the other ECL2 analogs had micromolar affinities for MIF, except for [Y190A]-ECL2(187-195) (Table 36). To sum up, any change on ECL1(102-110) or ECL2(187-195) disrupted its binding with MIF, and the native peptides were prioritized for further studies.

Table 36. Biophysical properties of alanine mutants and other analogs of ECL1(102-110), ECL1, ECL2(187-195) and ECL2 with Alexa-488-MIF.

Shorter analogs of ECL1 [b]	Secondary structure	Precip. (µM)	Shorter analogs of ECL1 [b]	Secondary structure	Precip. (µM)
ECL1(102-110)	r.c. [a]	50	ECL2(187-195)	r.c.	>50
Alanine mutants of ECL1(102-110)			**Alanine mutants of ECL2(187-195)**		
[W102A]-ECL1(102-110)	r.c. [a]	>50	[D187A]-ECL2(187-195)	r.c. [a]	>50
[Y103A]-ECL1(102-110)	r.c. [a]	>50	[R188A]-ECL2(187-195)	r.c. [a]	>50
[F104A]-ECL1(102-110)	r.c. [a]	>50	[F189A]-ECL2(187-195)	r.c. [a]	>50
[G105A]-ECL1(102-110)	r.c. [a]	>50	[Y190A]-ECL2(187-195)	r.c. [a]	>50
[N106A]-ECL1(102-110)	β-sheet + r.c.	50	[P191A]-ECL2(187-195)	r.c. [a]	>50
[F107A]-ECL1(102-110)	r.c. [a]	>50	[N192A]-ECL2(187-195)	r.c. [a]	>50
[L108A]-ECL1(102-110)	r.c. [a]	>50	[D193A]-ECL2(187-195)	r.c. [a]	>50
[C109A]-ECL1(102-110)	r.c. [a]	>50	[L194A]-ECL2(187-195)	r.c. [a]	>50
[K110A]-ECL1(102-110)	r.c. [a]	20	[W195A]-ECL2(187-195)	r.c. [a]	>50
Analogs and mutants of ECL1(102-110), ECL1			**Analogs of ECL2**		
K-ECL1(102-110)	r.c. [a]	>50	[R188Cit]-ECL2(184-196)	r.c. [a]	>50
KK-ECL1(102-110)	r.c. [a]	50	[Arom]-ECL2	β-sheet	50
[C109S]-ECL1(102-110)	r.c. [a]	>50			
[2xPal]-ECL1(102-110)	r.c. [a]	>50			
[W102Cha]-ECL1	β-sheet + r.c. [a]	50			

Peptides were biophysically characterized in aqueous 1×b, pH 7.4, containing 1% HFIP. [a]: r.c., random coil,

Table 37. Determined app. K_{ds} of shorter analogs of alanine mutants and other analogs of ECL1(102-110), ECL1, ECL2(187-195) and ECL2 with Alexa-488-MIF, as derived by fluorescence spectroscopic titrations.

Shorter analogs of ECL1 [b]	app. K_d (±SD) (nM) (Alexa-488-MIF/peptide [a])	Shorter analogs of ECL2	app. K_d (±SD) (nM) (Alexa-488-MIF/peptide [a])
ECL1(102-110)	86.3 (±9.2)	ECL2(187-195)	285.6 (±35.2)
Alanine mutants of ECL1(102-110)		**Alanine mutants of ECL2(187-195)**	
[W102A]-ECL1(102-110)	1280.3 (±239.7)	[D187A]-ECL2(187-195)	>20000
[Y103A]-ECL1(102-110)	524.9 (±70.2)	[R188A]-ECL2(187-195)	>20000
[F104A]-ECL1(102-110)	179.4 (±64.1)	[F189A]-ECL2(187-195)	>20000
[G105A]-ECL1(102-110)	>10000	[Y190A]-ECL2(187-195)	893.8 (±82.6)
[N106A]-ECL1(102-110)	>10000	[P191A]-ECL2(187-195)	>10000
[F107A]-ECL1(102-110)	286.5 (±51.7)	[N192A]-ECL2(187-195)	>20000
[L108A]-ECL1(102-110)	316.4 (±49.7)	[D193A]-ECL2(187-195)	>20000
[C109A]-ECL1(102-110)	842.3 (±129.0)	[L194A]-ECL2(187-195)	>20000
[K110A]-ECL1(102-110)	>10000	[W195A]-ECL2(187-195)	>20000
Analogs and mutants of ECL1(102-110), ECL1		**Analogs of ECL2**	
K-ECL1(102-110)	108.0 (±49.1)	[R188Cit]-ECL2(184-196)	>20000
KK-ECL1(102-110)	>10000	[Arom]-ECL2	> 2500
[C109S]-ECL1(102-110)	>10000		
[2xPal]-ECL1(102-110)	847.3 (±63.8)		
[W102Cha]-ECL1	87.2 (±30.4)		

[a]: App. K_{ds} are means (±SD) from three independent titration experiments which were performed in aqueous 1×b, pH 7.4, containing 1% HFIP.

## 4.3   Next generation of MIF-specific receptor mimics (ngms)

Previously, msR4Ms were shown to imitate the CXCR4 ectodomain, with the reduced ones exhibiting MIF-specific binding properties without interfering with CXCL12, the other ligand of the receptor. The soluble CXCR4 mimics consisted of the 14-mer ECL1 and the 15-mer ECL2, covalently connected to each other with linkers, with or without a disulfide bridge. SAR studies of the ECDs resulted in the ECL1(102-110) and ECL2(187-195) as the shortest potent binders of MIF. Herein, the next generation mimics (ngms) of CXCR4 were developed, consisting of the shorter ECDs ECL1(102-110) and ECL2(187-195) covalently linked to each other (Scheme 10). The aims for the newer mimics were to have enhanced binding potency to MIF, without any affinity to CXCL12 and being more soluble than msR4Ms.
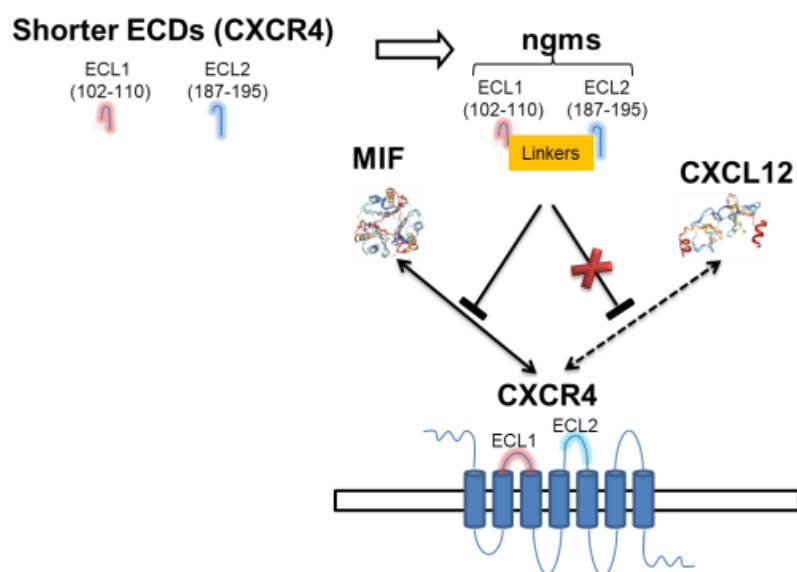
Scheme 10. Development of ngms and the desired blockade of the atheroprogressive pathways.
The next generation mimics (ngms) of CXCR4 mimics were developed after linkage of fragment 102-110 derived by extracellular loop 1 (ECL1) and of 187-195 derived by extracellular loop 2 (ECL2). The newer mimics linked analogs aimed to inhibit the atheroprogressive pathways (solid line) MIF/CXCR4 and spare the atheroprotective (dashed line) CXCL12/CXCR4. The chemokines and the transmembrane protein are demonstrated based on their published structures (MIF:1MIF, CXCL12:3HP3) [83] [101].

Similar to msR4Ms, ngms were synthesized with various linkers between their ECDs, being either natural or non-natural amino acids. The synthesized peptides were synthesized and purified as the rest peptides previously in order to be biophysically characterized. Particularly, there were estimated the secondary structures, the self-association propensities, and the hydrophobicity content on the surface of ngms. Next, the binding strength of the mimics and MIF and CXCL12 was determined via fluorescence spectroscopic titrations. Further studies examined whether ngms recognize the same binding epitope to MIF, i.e. MIF(54-80) as msR4M-L1 (Scheme 11).
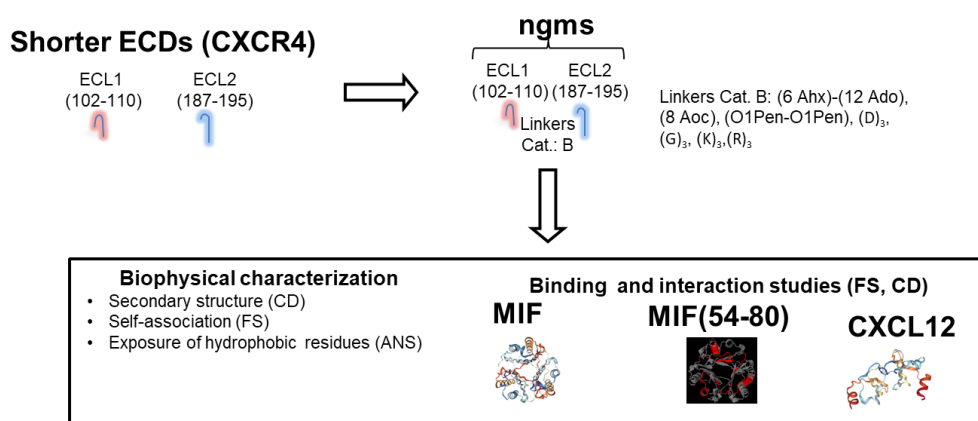
Scheme 11. Overview of the development and studies of ngms. The development of next generation mimics (ngms) and the applied linkers are shown. Studies of ngms aimed on the determination of their biophysical properties and their binding affinities with CXCR4 ligands and the MIF hot spot region for the interaction with msR4M-L1. The structures of the demonstrated chemokines are based on their published structures (MIF:1MIF, CXCL12:3HP3, IL-8:1IL8) [83] [101] [158].
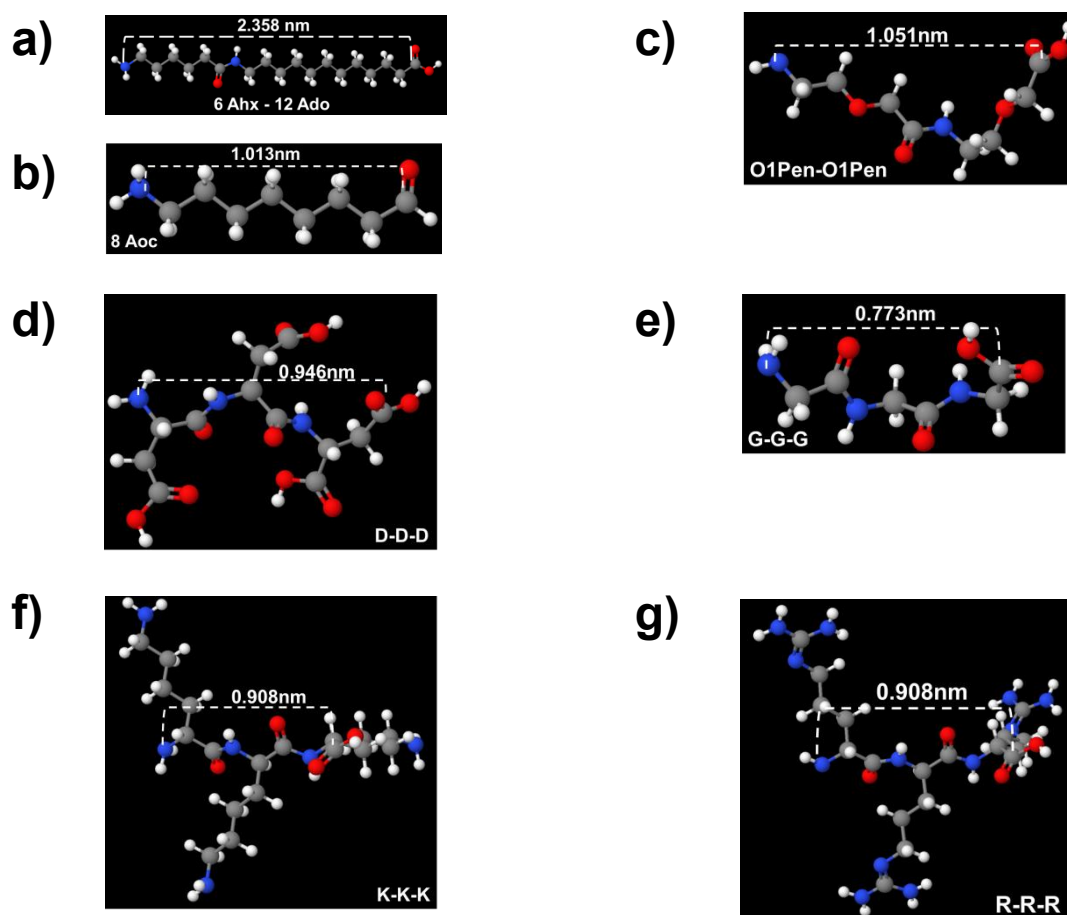
4.3.1 Design of ngms

ECL1(102-110) and ECL2(187-195) are located closer to CXCR4 compared to ECL1 and ECL2, with the distance between K110 and D187 being 0.95 nm, according to the crystal structure of the receptor (Scheme 12a, b). As for the design of msR4Ms, a rational design strategy was applied, and it was desired to introduce linkers between the two shorter ectodomain fragments that will imitate their determined distance from the X-ray model (Scheme 12c).
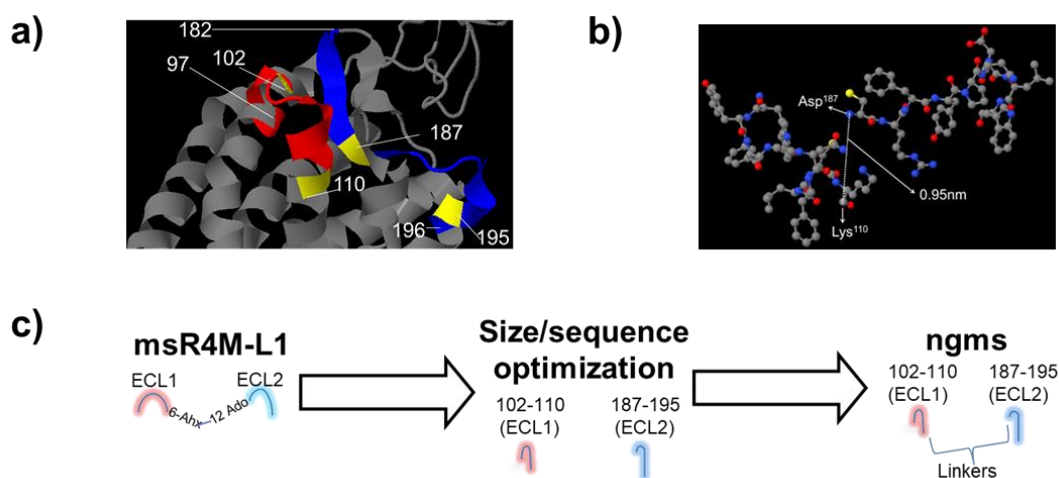
Scheme 12. Design and development of ngms. a Ribbon structure of human CXCR4 with highlighted the regions of ECL1 (in red) and ECL2 (in blue) with their N- and C-terminus residues being indicated**.** Residues W102, K110, D187 and W195 are highlighted in yellow. **b** Zoomed view of **a** as spheres (blue: nitrogen, red: oxygen, yellow: sulphur, grey: carbon, white: hydrogen) focusing on ECL1(102-110) and ECL2(187-195) with the measured length (0.95 nm) between Lys[110] of the ECL1(102-110) C-terminus and Asp[187] of the ECL2(187-195) N-terminus being shown. **c** Strategy for the transition of msR4Ms to ngms. MsR4Ms consisted of ECL1 and ECL2 and their sequences were shortened to ECL1(102-110) and ECL2(187-195) with the elimination of non-essential amino acids for the interaction with MIF, as suggested in chapter 4.2. For the generation of ngms, linkers should be introduced between the C-terminus of K110 and D187. Crystal structure for **a** and **b** was obtained from protein data bank (PDB code: 4RWS) as published by Qin and colleagues and visualized by Jmol (http://www.jmol.org) [148].

The dipeptide of the two non-natural amino acids 6 Ahx and 12 Ado was calculated in chapter 4.1.1. and estimated to cover a distance of 2.358 nm. Even though the determined length is longer than the distance of ECL1(102-110) and

ECL2(187-195), it was chosen to be introduced between those two peptides for the generation of the next generation mimic (ngm)-L3 analog, in order to provide insights for the effect of the length of the linkers. (Scheme 13a). Taken into consideration the 0.95 nm length between K110 and D187 and trying to imitate it, 8 Aoc and the tandem O1Pen-O1pen were introduced between ECL1(102-110) and ECL2(187-195) resulting in the development of ngm-L4 and ngm-L5, respectively (Scheme 13b, c). Except for non-natural amino acids, it was tried additionally as an alternative approach the linking of C-and N- terminuses of size optimized ECL1 and ECL2 via natural amino acids. Studies on Molview indicated that three amino acids in a row might mimic the distance between K110 and D187. To obtain new mimics with enhanced solubility, the three subsequent amino acids were applied initially as negatively charged and, in particular, aspartic acids (ngm-LD3, Scheme 13d). Ngm-LG3 was developed next, with three glycines between ECL1(102-110) and ECL2(187-195) (Scheme 13e). Likewise, two other ngms were designed but with basic amino acids applied as linkers. The introduction of three subsequent lysines led to the generation of ngm-LK3 and three in row arginines to ngm-LR3 (Scheme 13f, g).

Scheme 13. Design of linkers for the generation of ngms. a, b, c, d, e, f, g Estimated lengths of the tandem 6 Ahx-12 Ado that was applied for the development of ngm-L3 (a), 8 Aoc for ngm-L4 (b), O1Pen-O1Pen for ngm-L5 (c), D-D-D for ngm-LD3 (d), G-G-G for ngm-LG3 (e), K-K-K for ngm-LK3 (f) and R-R-R for ngm-LR3 (g). All linkers were introduced between the C-terminus of ECL1(102-110) and the N-terminus of ECL2(187-195) for the development of the respective ngms. Linkers were designed on Molview and visualized as spheres (blue: nitrogen, red: oxygen, grey: carbon, white: hydrogen) by applying Jmol (http://www.jmol.org) [148].

## 4.3.2 Synthesis, purification and mass determination of ngms

Synthesis of ngms was carried out using Fmoc-SPPS, as it was already described. Shortly, Fmoc-Rink resin was N-terminusly deprotected for the conjugation of W195. Then, UV-Vis spectroscopy was applied for the determination of the substitution level of the resin. Based on this, the synthesis continued further with the following amino acids being coupled twice, while the activator, the equivalents of the base, and the time may vary as described in Scheme 14. The N-terminus cleavage of the Fmoc group followed the normal protocol for W195 and L194 and the 'Short HOBt protocol' for the rest amino acids to prevent Asi formation [263] [261]. After the end of the synthesis, Reagent K was applied for the cleavage of the peptide from the resin and its side-chain deprotection prior its lyophilization. Each crude ngm was dissolved in TFA/80% B and purified by RP-HPLC.The MWs of the collected peaks were determined after dissolving it in MALDI solution B and MALDI-TOF-MS analysis (Figure 80, 81). Experimental determined MWs were in accordance with the expected values, and the yield of all ngms was in the 34.7-37.7% range, except for ngm-LD3, which showed a yield of 26.8% (Table 38).

Table 38. Sequences, abbreviation and characterization of synthesized ngms by RP-HPLC and MALDI-TOF-MS.

Peptide sequence[a]	Peptide abbreviation	HPLC Pr.No.	t_R (min) [b]	Yield (%)[c]	[M+H]$^+$ expected [d]	[M+H]$^+$ found[d]
[ECL1(102-110)] -6 Ahx-12 Ado- [ECL2(187-195)]	ngm-L3	1	22.60	36.7	2693.36	2693.54
[ECL1(102-110)] – 8 Aoc - [ECL2(187-195)]	ngm-L4	1	21.35	37.4	2524.24	2524.38
[ECL1(102-110)]- O1pen-O1pen - [ECL2(187-195)]	ngm-L5	1	19.75	37.7	2585.23	2586.08
[ECL1(102-110)] - D-D-D - [ECL2(187-195)]	ngm-LD3	1	18.40	26.8	2728.22	2728.16
[ECL1(102-110)] - G-G-G - [ECL2(187-195)]	ngm-LG3	1	20.25	37.4	2554.20	2555.23
[ECL1(102-110)] - K-K-K - [ECL2(187-195)]	ngm-LK3	1	18.70	35.1	2767.42	2767.26
[ECL1(102-110)] - R-R-R - [ECL2(187-195)]	ngm-LR3	1	19.16	34.7	2851.44	2851.82

Peptides were dissolved and analyzed by MALDI-TOF-MS in a mixture of MALDI solutions B and B (matrix); **[a]** Peptides were synthesized with free amino-N-terminus and amidated C-terminus; **[b]** HPLC retention time of the pure product, the stationary phase was a tandem of Reprosil Gold 200 C18 columns (250 and 30 mm length, 8 mm internal diameter,10 μm particle size); **[c]** % yield with regard to crude peptide after cleavage and **[d]** monoisotopic molar mass with an additional hydrogen [M+H]$^+$.
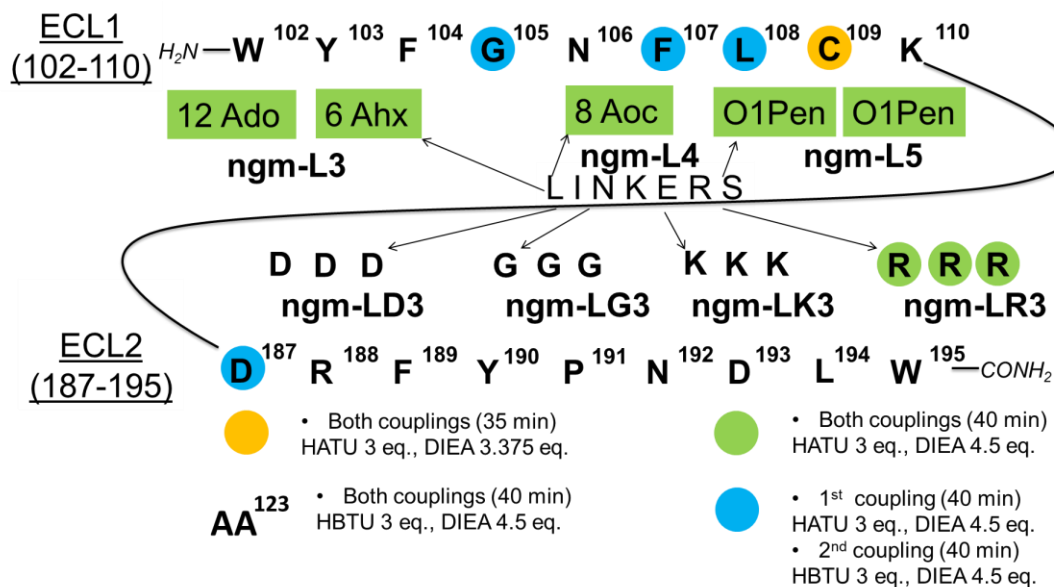
Scheme 14. Conditions of couplings for the syntheses of ngms. All amino acids were coupled with 3 equivalents (eq.), based on the substitution level that was determined after the load of the first amino acid on Rink-resin. Equivalents of activator and base, together with the coupling time may vary, as indicated.
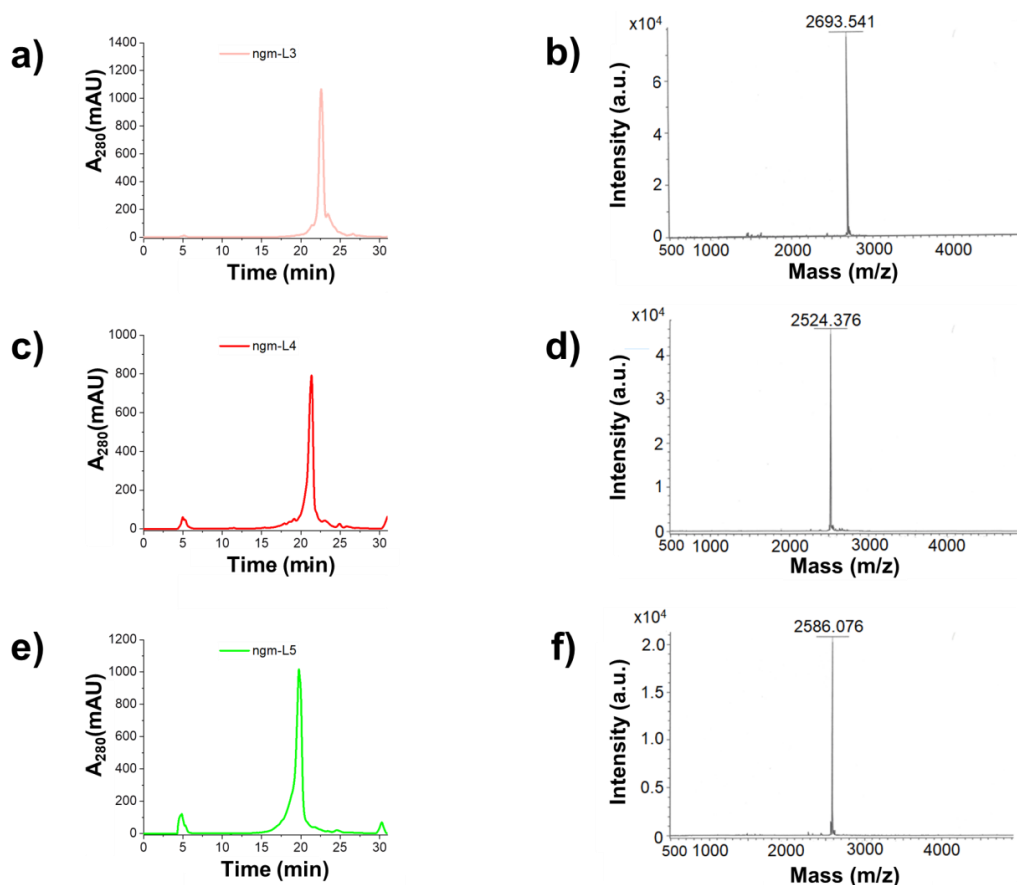
Figure 80. HPLC purification of ngms with non natural amino acids introduced as linkers and verification of their purity by MALDI. a, c, e Representative C18 HPLC chromatogram (absorbance at 280 nm) of crude ngm-L3, ngm-L4 and ngm-L5 with respective retention times: a) 22.60 min, c) 21.35 min and e) 19.75 min, following SPPS and cleavage. **b, d, f** MALDI-TOF-MS spectra of HPLC-purified ngm-L3, ngm-L4 and ngm-L5 with respective experimental determined masses [M+H]+: b) 2693.541 Da, d) 2524.376 Da and f) 2586.076 Da.

148
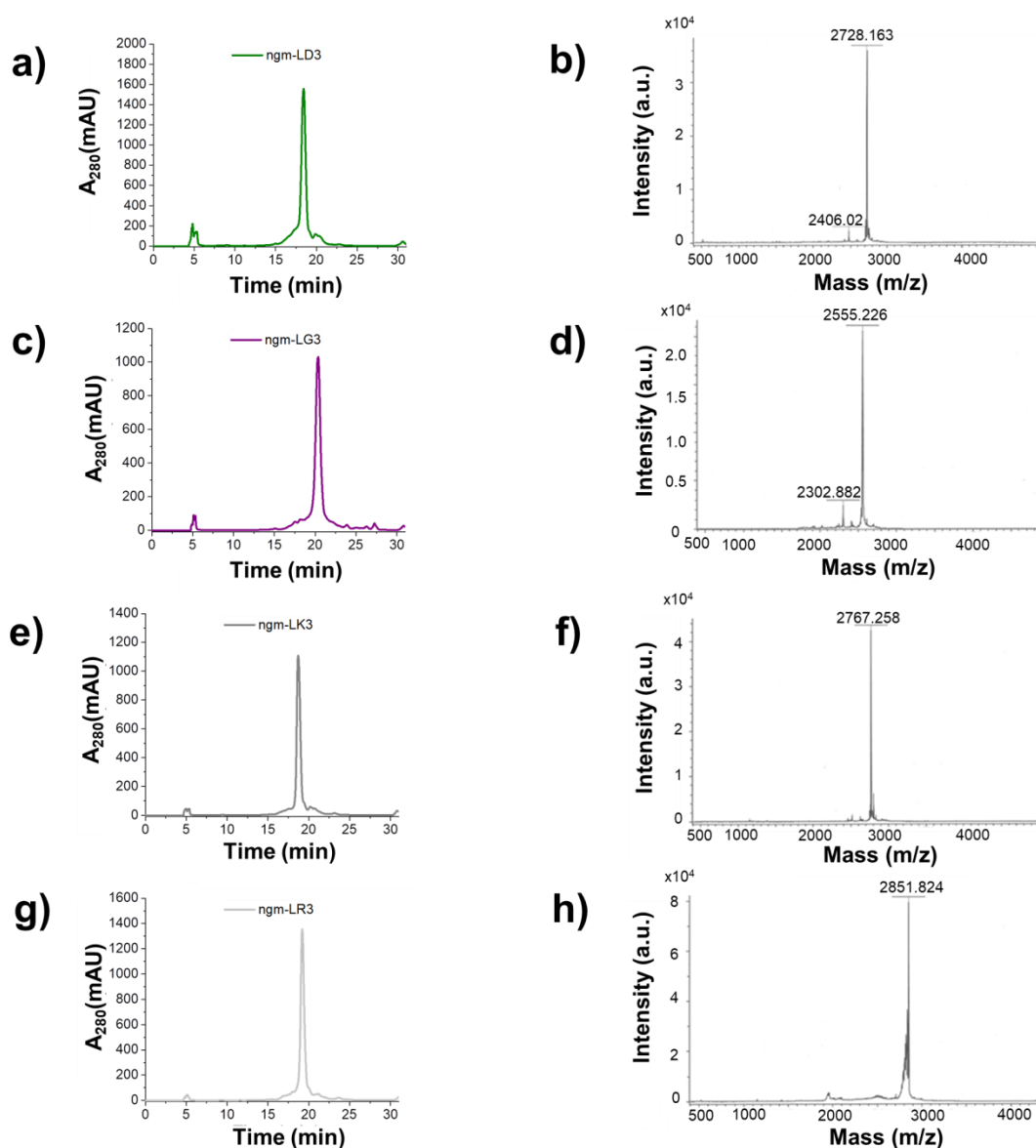
Figure 81. HPLC purification of ngms with natural amino acids introduced as linkers and verification of their purity by MALDI. a, c, e, g Representative C18 HPLC chromatogram (absorbance at 280 nm) of crude purified ngm-LD3, ngm-LG3, ngm-LK3 and ngm-LR3 with respective retention times: a) 18.40 min, c) 20.25 min, e) 18.70 min and g) 19.16 min, following SPPS and cleavage. **b, d, f, h** MALDI-TOF-MS spectra of HPLC-purified ngm-LD3, ngm-G3, ngm-LK3 and ngm-LR3 with respective experimental determined masses [M+H]$^+$: b) 2728.163 Da, d) 2555.226 Da, f) 2767.258 Da and h) 2851.824 Da.

4.3.3 Biophysical characterization

4.3.3.1 Conformational and concentration dependence studies via CD spectroscopy

The secondary structure of all ngms was determined by far-UV CD spectroscopy. Spectra were recorded from 1 to 50 μM under the same experimental conditions that were applied previously for the msR4M studies. Interestingly, the extracted signal provided additional information for the oligomerization and the solubility of the peptides in the tested concentrations. Ngm-L3 shared the same linker with msR4M-L1 but here connected the size optimized ECL1 and ECL2 fragments instead of the native 14-mer and 15-mer, respectively. The newly developed mimic was soluble at its stock at 1 mM HFIP but precipitated at the final measuring conditions with aqueous 1×b, pH 7.4, 1% HFIP even from 2.5 μM concentration. Spectra of ngm-L4 at 2.5 and 5

149

µM exhibited the random coil indicative minima at 200 nm, with a wide maximum appearing between 225 and 235 nm but just in the 2.5 µM spectra. The subsequently measured concentration at 10 µM showed the same signal shape but with the half intensity, suggesting an oligomerization of the peptide, before its precipitation at 20 µM (Figure 82a). Likewise, the formation of the ngm-L5 appeared to be unordered but with slightly more favorable soluble properties. In particular, its π-π interaction indicative positive band between 225 and 235 nm was present in all measured concentration points together with its random coil- characteristic minima at 200 nm. Peptide showed a 25% reduced signal in the spectra at 20 µM, while it precipitated at 50 µM (Figure 82b).

Contrariwise to the non-natural amino acid linked ngms, the acidic and basic amino acid linked analogs remained soluble until 50 µM. Ngm-LD3 exposed minima at 200 nm with its MRE values being approximately equal to -8000 deg·cm^2·dmol^{-1} for the measured points between 2.5 and 10 µM and -4500 deg·cm^2·dmol^{-1} between 20 and 50 µM. By analyzing further the results, this reduction of the signal in the two highest concentration points and the decrease of the maxima from 500 to 150 for the respective concentrations were associated with the presence of oligomers in the two highest measured concentration points (Figure 82c). The maxima in the wavelengths between 225 and 235 nm is present in the ngm-LG3 spectra of 2.5, 10, and 20 µM (Figure 82d). Spectra of all tested concentrations exhibited their strongest minima at 200 nm. In parallel, second less intense but broad minima were noticed between 211 and 217 nm for 2.5 and 5 µM spectra. Minima were slightly shifted to 213 and 220 nm for measurements obtained at 10 and 20 µM of the peptide. The lack of charge in the linkers affected the solubility of the peptide, which did not remain soluble at 50 µM.

Substitutions of the three neutral glycines with the basic lysines led to the ngm-LK3 analog that was soluble at 50 µM and exposed stronger minima at 200 nm. More specifically, the obtained MRE values were approximately at -8000 deg·cm^2·dmol^{-1} for 2.5 and 5 µM, at -5500 deg·cm^2·dmol^{-1} for 10 and 20 µM, and at -3000 deg·cm^2·dmol^{-1} for 50 µM. Together with the concentration-dependent intensity of the maxima at 225-235 nm, these findings suggested the aggregation of the peptide in the higher concentrations (Figure 82e). Similarly, the arginine-linked peptide ngm-LR3 exhibited a concentration-dependent random coil indicative signal, which became weaker at 20 µM and reduced to half at 50 µM. As all previous ngms, the positive broadband between 225 and 235 nm is present in all spectra of ngm-LR3, too (Figure 82f). Summarized results and comparison of the spectra of the peptides are described in 'Discussion' (see 5.3).
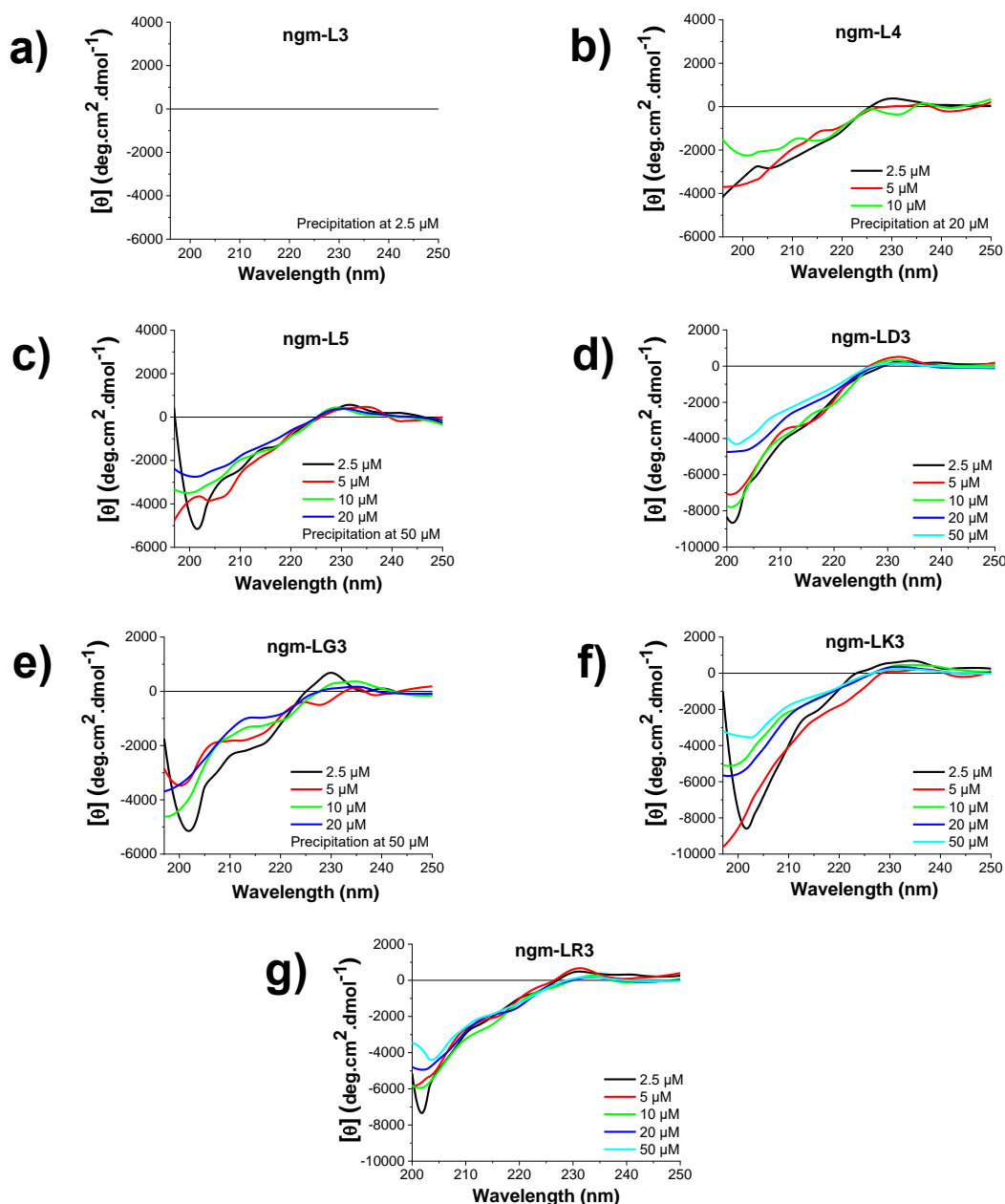
Figure 82. Spectra of ngms in various concentrations for the determination of the conformation, as determined by far-UV CD spectroscopy. a, b, c, d, e, f, g CD spectra of ngm-L3 (a), ngm-L4 (b), ngm-L5 (c), ngm-LD3 (d), ngm-LG3 (e), ngm-LK3 (f) and ngm-LR3 (g) at increasing concentrations at final measuring conditions of aqueous 1×b, pH 7.4, containing 1% HFIP. Mean residue ellipticity (MRE) plotted over the wavelength between 196 and 250 nm for a, 197 and 250 nm for b, d, e, 200 and 250 nm for c, f.

### 4.3.3.2 Self-association studies via fluorescence spectroscopy

CD spectroscopy data indicated a tendency of self-assembly for the ngms in many cases, likewise to msR4Ms. The self-association propensities of ngms were studied further with fluorescence spectroscopic studies between Fluos-labeled-ngm as the analyte and the respective non-labeled peptide playing the role of the titrant. The experimental setup was the same that was applied for the respective titrations of msR4Ms in chapter 4.1.3.2. Ngm-L4 showed a strong tendency to self-associate as its titrations indicated an app. K_d of 47.9 ± 15.7 nM, contrary to the other non-natural amino acid-linked peptide (Figure 83a, b). Fluorescence emission of labeled-ngm-L5 did not differentiate against increased unlabeled peptide concentration until its highest

151

measured concentration point at 500 nM, suggesting a dissociation constant above this point (Figure 83c, d).
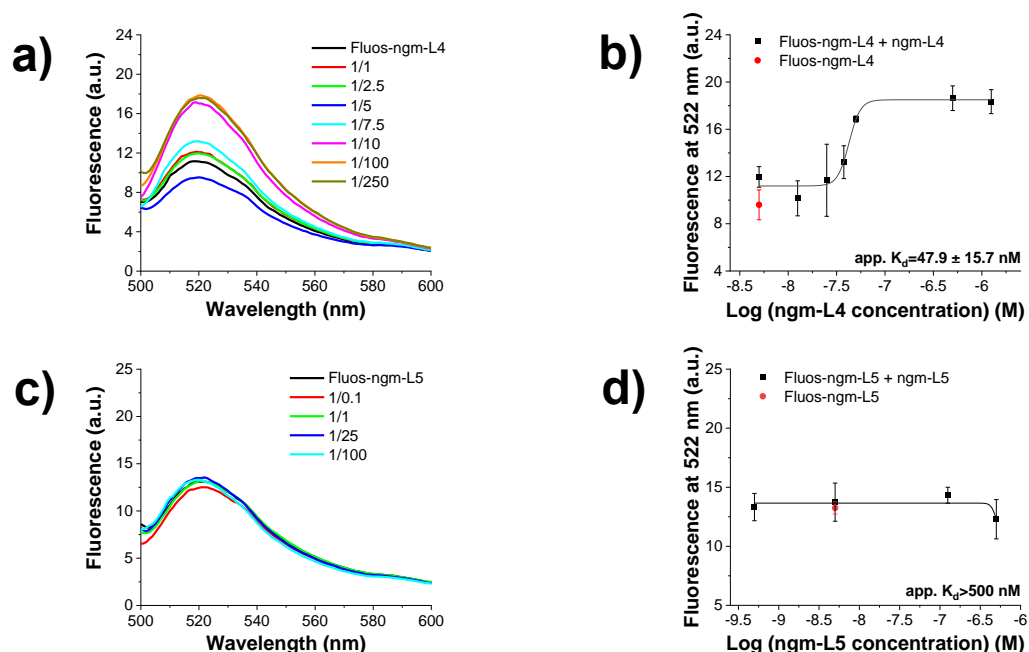
Figure 83. Fluorescence spectroscopic titrations for the determination of apparent affinities (app. K_{ds}) for the self-association of ngms linked with non-natural amino acids. a, c Fluorescence spectra between 500 and 600 nm of each Fluos-ngm (5 nM) alone and its mixtures with various amounts of its respective unlabeled partner ngm–L4 (a) and ngm-L5 (c); the molar ratios of Fluos-ngm/ngm are indicated. **b, d** Binding curves derived from the fluorescence emission at 522 nm of Fluos-ngm (5 nM) at different concentrations of its respective unlabeled partner ngm–L4 (b) and ngm-L5 (d). Data shown are means (±SD) from three independent titration experiments which were performed in aqueous 1×b, pH 7.4, containing 1% HFIP.

The ngms with the natural amino acids applied as linkers showed a self-association assembly behavior similar to ngm-L4. In particular, Fluos-ngm-LD3 and -LG3 exhibited a strong tendency to self-assemble with the app. K_{ds} estimated 64.4 ± 18.3 and 76.9 ± 15.5 nM, respectively (Figure 84a-d). In the case of ngm-LK3, when the labeled analyte was saturated, the fluorescence emission was doubled and indicated an app. K_d of 41.2 ± 9.9 nM (Figure 84e, f). Of note, the strongest self-assembling propensity was noticed for ngm-LR3 that had an app. K_d of 16.2 ± 4.3 nM (Table 39, Figure 84g, h). Summarized results and comparison of the binding affinities of the peptides are described in 'Discussion' (see 5.3).
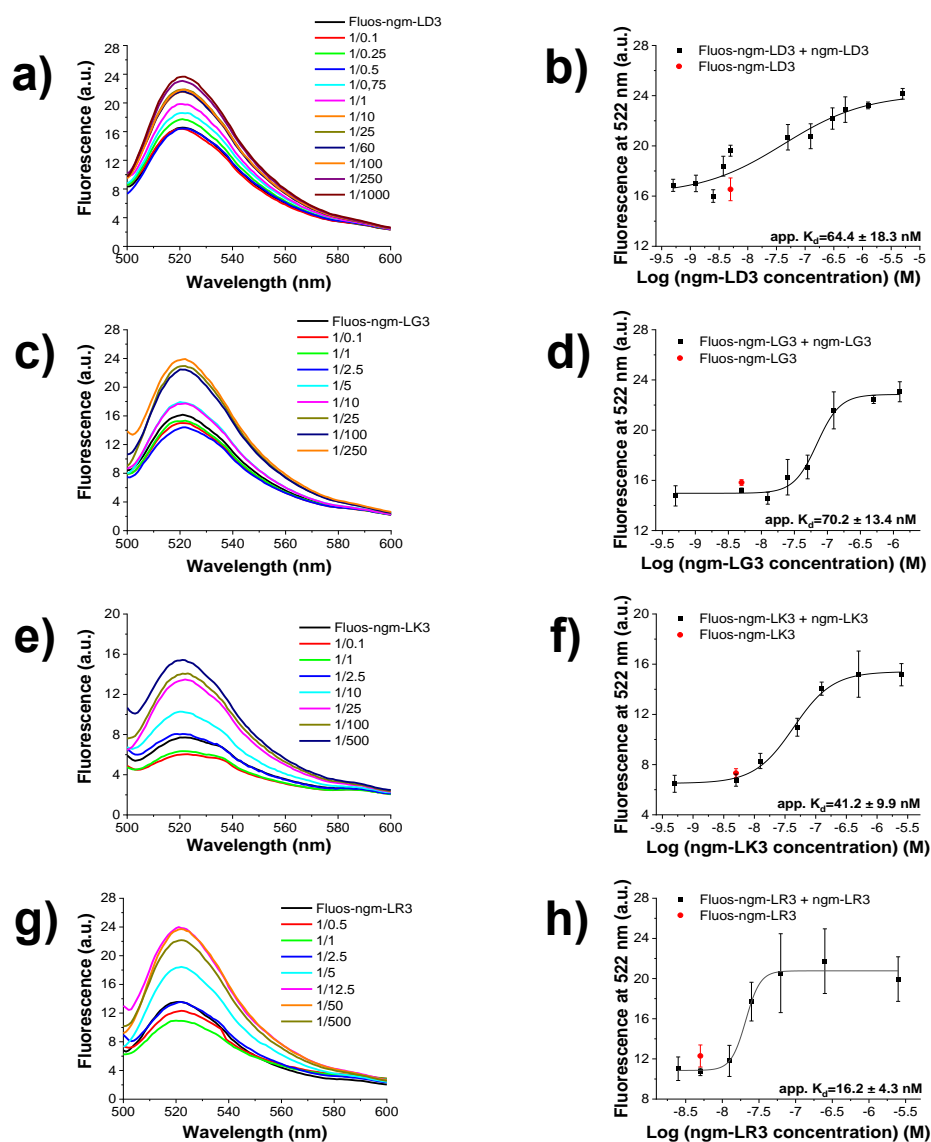
Figure 84. Fluorescence spectroscopic titrations for the determination of apparent affinities (app. K_{ds}) for the self-association of ngms linked with natural amino acids.a, c, e, g Fluorescence spectra between 500 and 600 nm of each Fluos-ngm (5 nM) alone and its mixtures with various amounts of its respective unlabeled partner ngm-LD3 (a), ngm-LG3 (c), ngm-LK3 (e) and ngm-LR3 (g) ; the molar ratios of Fluos-ngm/ngm are indicated. **b, d, f, h** Binding curves derived from the fluorescence emission at 522 nm of Fluos-ngm (5 nM) at different concentrations of its respective unlabeled partner ngm-LD3 (b), ngm-LG3 (d), ngm-LK3 (f) and ngm-LR3 (h). Data shown are means (±SD) from three independent titration experiments which were performed in aqueous 1×b, pH 7.4, containing 1% HFIP**.**

Table 39. Apparent affinities (app. K_{ds}) of self-association of ngms, as determined by fluorescence spectroscopic titrations.

ngms	Fluos-ngm/ngm app. K_d (±SD) (nM)[a]
ngm-L3	n.d.[b]
ngm-L4	47.9 (±15.7)
ngm-L5	>500
ngm-LD3	64.4 (±18.3)
ngm-LG3	70.2 (±13.4)
ngm-LK3	41.2 (±9.9)
ngm-LR3	16.2 (±4.3)

[a]: App. K_{ds} are means (±SD) from three independent titration experiments which were performed in aqueous 1×b, pH 7.4, containing 1% HFIP. [b]: n.d., non-determined.

4.3.3.3 ANS binding studies

After determining the self-assembly propensity, further fluorescence spectroscopic studies were applied for the biophysical characterization of the ngms. Unlabelled ngms and ANS were mixed in various concentrations, having constant 1:2 proportionality, and their surface hydrophobicity was monitored, as in 4.1.3.3. First, the linked via non-natural amino acid mimics, ngm-L4 is very prone to exhibit hydrophobic residues on its surface. Peptide and ANS began to interact already from 5 µM of the peptide with the label emission being 13.6 a.u., while the respective values at 10 and 20 µM of the peptide were 48.2 a.u. and 133.9 a.u (Figure 85a, b). Contrariwise, the ANS emission was significantly reduced when it was mixed with ngm-L5, reaching 5.7 and 18.8 a.u. at 10 and 20 µM, respectively (Figure 85c, d).
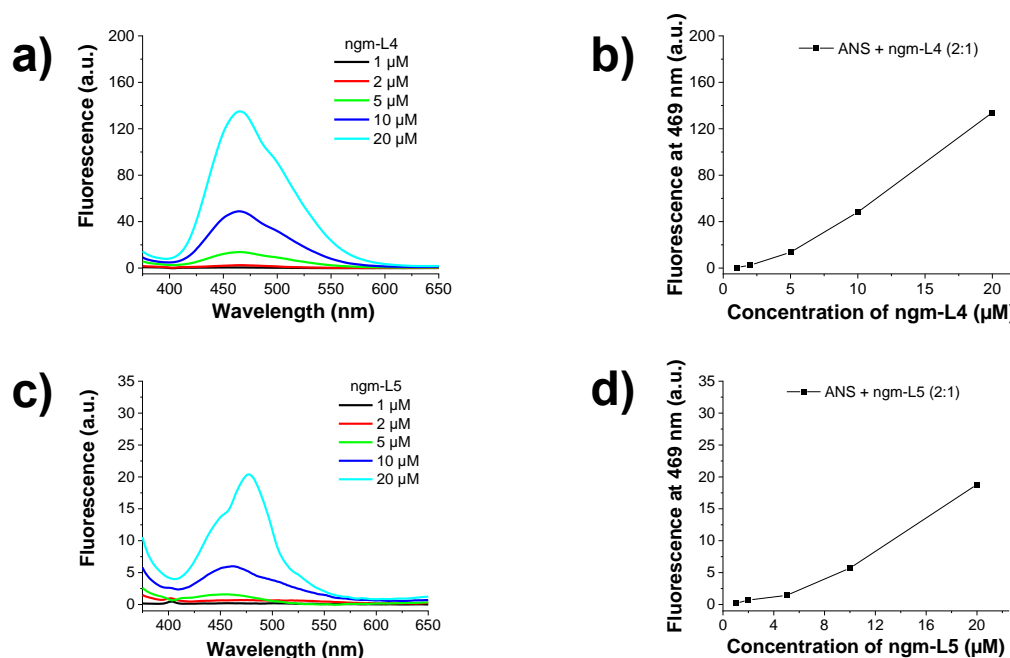
Figure 85. Effect of the binding of ANS to ngms that are linked with non-natural amino acids, as recorded by fluorescence spectroscopy. a, c Spectra between 375 and 650 nm of mixtures between ANS and ngms in constant 2:1 proportionality; the concencrations of ngm-L4 (a) and ngm-L5 (c) are indicated. **b, d** Fluorescence emission at 469 nm over increased concentrations of ngm-L4 (b) and ngm-L5 (d) that were mixed with ANS in a constant 1:2 proportionality. Spectra of ANS alone were subtracted from the spectra of peptide/ANS mixtures and measurements were performed in aqueous 1×b, pH 7.4, containing 1% HFIP.

ANS emission varied significantly when it was mixed with mimics that were linked with natural amino acids, always in 2-fold excess of the label. The dependency of emission on the linkage residues became apparent when the label did not emit above 4 a.u. when mixed with 35 µM ngm-LD3, while it exceeded 14 a.u. against 5 µM of ngm-LG3 (Figure 86a-d). The high exposure of hydrophobic residues of ngm-LG3 became even more intense at 10 and 20 µM with ANS emission at 63.1 and 247.5 a.u., respectively (Figure 86c, d). Compared to its interaction with ngm-LG3, the label exhibited reduced values for ngm-LK3, reaching 16.1 a.u. against 10 µM and 88.2 a.u. against 20 µM of the peptide (Figure 86e, f). The other linked via basic residues mimic, ngm-LR3, precipitated already from 10 µM. Its mixtures with ANS showed high emission already at 3.5 and 5 µM, with the respective values being 17.5 a.u. and 48.2 a.u (Figure 86g, h). Summarized results and comparison of the spectra of the peptides are described in 'Discussion' (see 5.3).
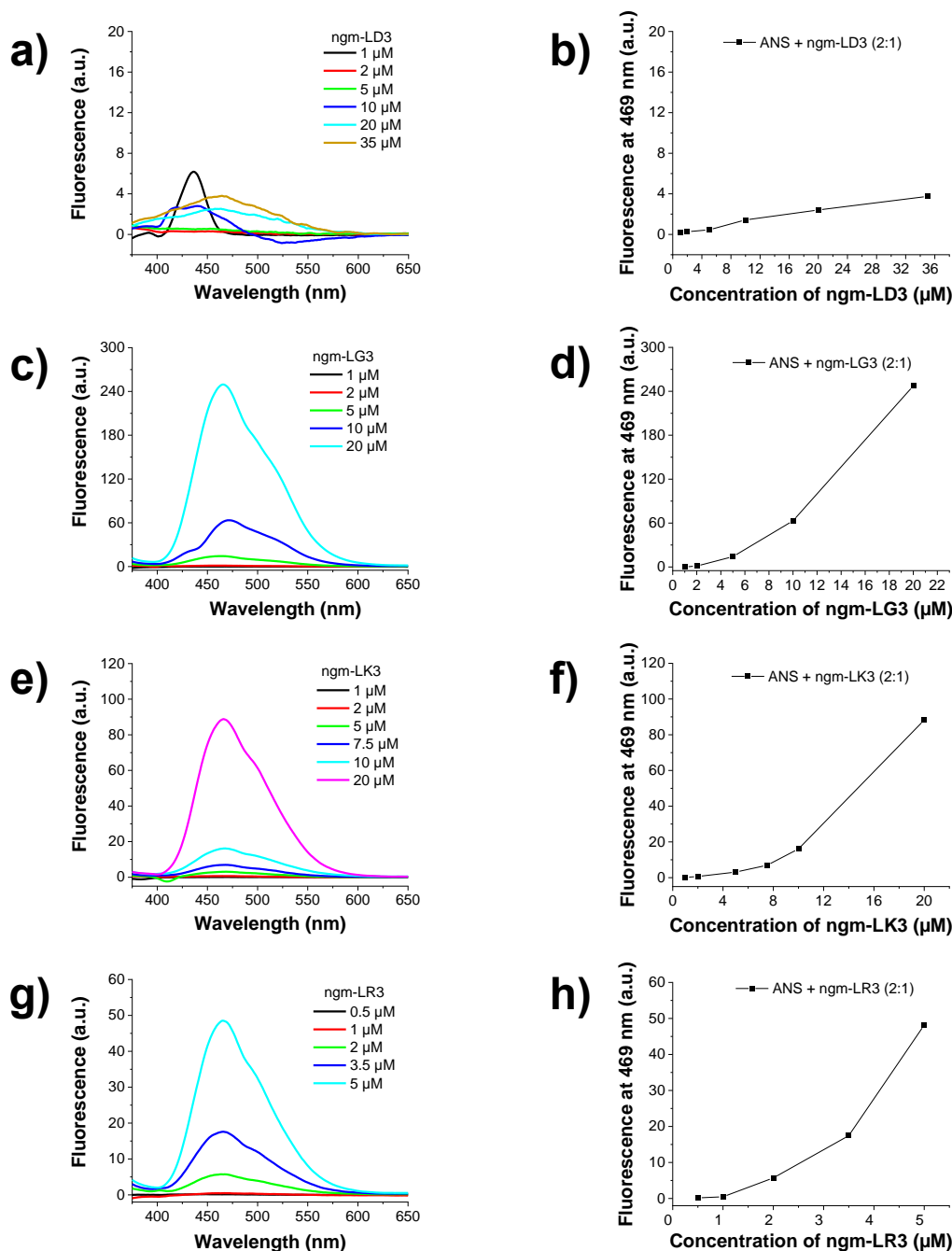
Figure 86. Effect of the binding between ANS and ngm that are linked with natural amino acids, as recorded by fluorescence spectroscopy. a, c, e, g Spectra between 375 and 650 nm of mixtures between ANS and ngms in constant 2:1 proportionality; the concenctrations of ngm-LD3 (a), ngm-LG3 (c), ngm-LK3 (e) and ngm-LR3 (g) are indicated. **b, d, f, h** Fluorescence emission at 469 nm over increased concentrations of ngm-LD3 (b), ngm-LG3 (d), ngm-LK3 (f) and ngm-LR3 (h) that were mixed with ANS in a constant 1:2 proportionality. Spectra of ANS alone were subtracted from the spectra of of peptide/ANS mixtures and measurements were performed in aqueous 1×b, pH 7.4, containing 1% HFIP.

4.3.4   Interactions between ngms and MIF

4.3.4.1 Determination of binding affinities to MIF via fluorescence spectroscopy

Ngms were designed based on the previous studies of ECL1 and ECL2, aiming to retain and improve the affinity of msR4M-L1 with MIF, despite the elimination of several residues. All peptides were N-terminusly Fluos-labeled and titrated against

155

increasing concentration of the atypical chemokine. The experimental conditions of Fluos-msR4Ms/MIF fluorescence spectroscopic titrations were kept unchanged for these assays, as well. Although in Fluos-ngm-L3 analog ECL1(102-110) and ECL2(187-195) are covalently linked with 6 Ahx and 12 Ado, and their estimated distance differentiates from the theoretical one, its calculated app. K_d at 44.4 ± 16.4 nM was in a very similar range to the determined one from Fluos-msR4M-L1/MIF titration (Figure 87a, b). Of note, the rationally linked peptides Fluos-ngm-L4 and Fluos-ngm-L5 demonstrated 3.4- and 2.8-fold improved affinities than msR4M-L1 with MIF and the calculated app. K_{ds} were 11.9 ± 4.8 nM and 14.3 ± 5.7 nM, respectively (Figure 87c-f).
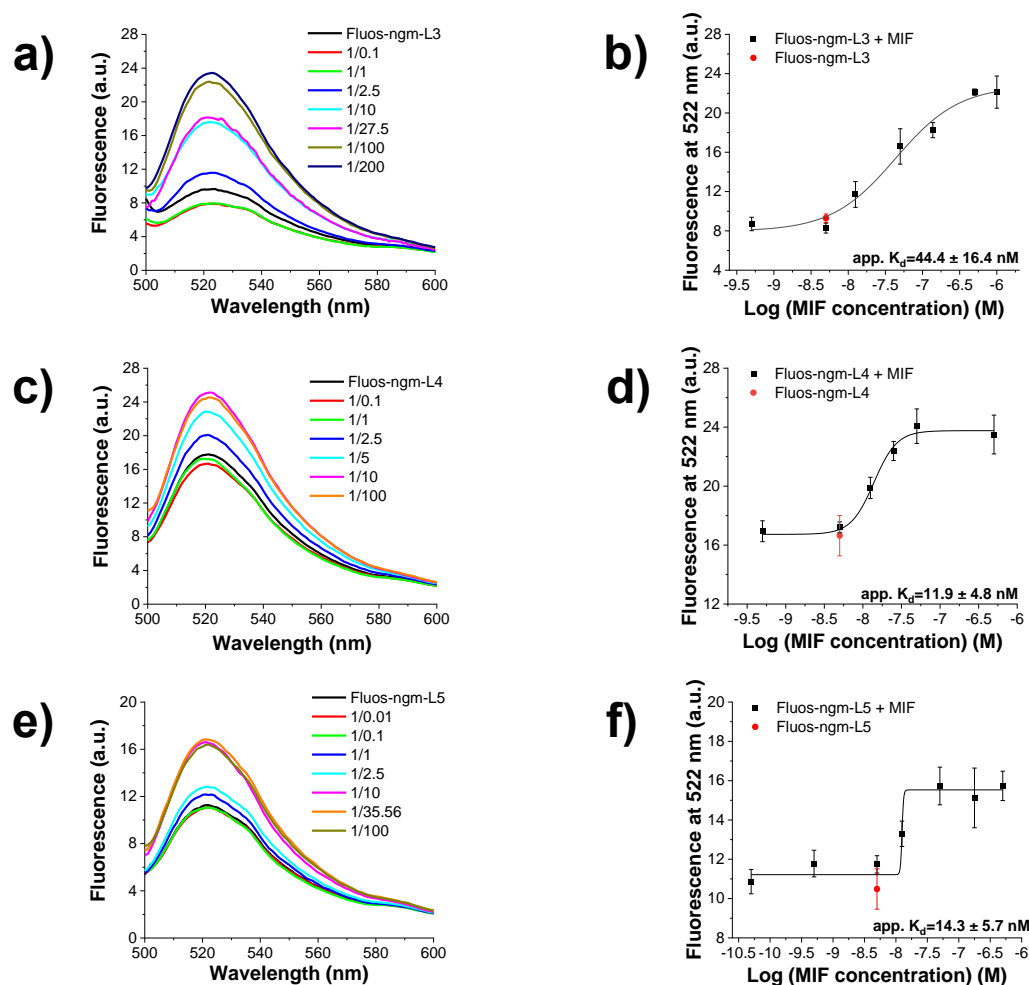
Figure 87. Fluorescence spectroscopic titrations of Fluos-ngms linked by non-natural amino acids with MIF for the determination of apparent affinities (app. K_{ds}). a, c, e Fluorescence spectra between 500 and 600 nm of 5 nM of Fluos-ngm-L3 (a), Fluos-ngm-L4 (c) and Fluos-ngm-L5 (e) alone and their mixtures with various amounts of MIF; the molar ratios of Fluos-ngms/MIF are indicated. **b, d, f** Binding curves derived from the fluorescence emission at 522 nm of Fluos-ngm-L3 (b), Fluos-ngm-L4 (d) and Fluos-ngm-L5 (f) at different concentrations of MIF. Data shown are means (±SD) from three independent titration experiments which were performed in aqueous 1×b, pH 7.4, containing 1% HFIP.

The high affinity between ngms and MIF was retained even when natural amino acids replaced the non-natural ones as linkers. Titrations between Fluos-ngm-LD3 and Fluos-ngm-LG3 with MIF indicated dissociation constants at 36.0 ± 22.2 nM and 35.0 ± 19.6 nM, respectively (Figure 88a-d). Likewise, the significant increase of the fluorescence emission of Fluos-ngm-LK3 and Fluos-ngm-LR3 against the increasing concentration of MIF presented the respective app. K_{ds} equal to 36.4 ± 7.5 nM and 16.8 ± 6.2 nM (Figure 88e-f). Conclusively, all Fluos-ngms demonstrated similar

affinity to msR4M-L1 for binding to MIF. Summarized results and comparison of the binding affinities of the peptides are described in 'Discussion' (see 5.3)
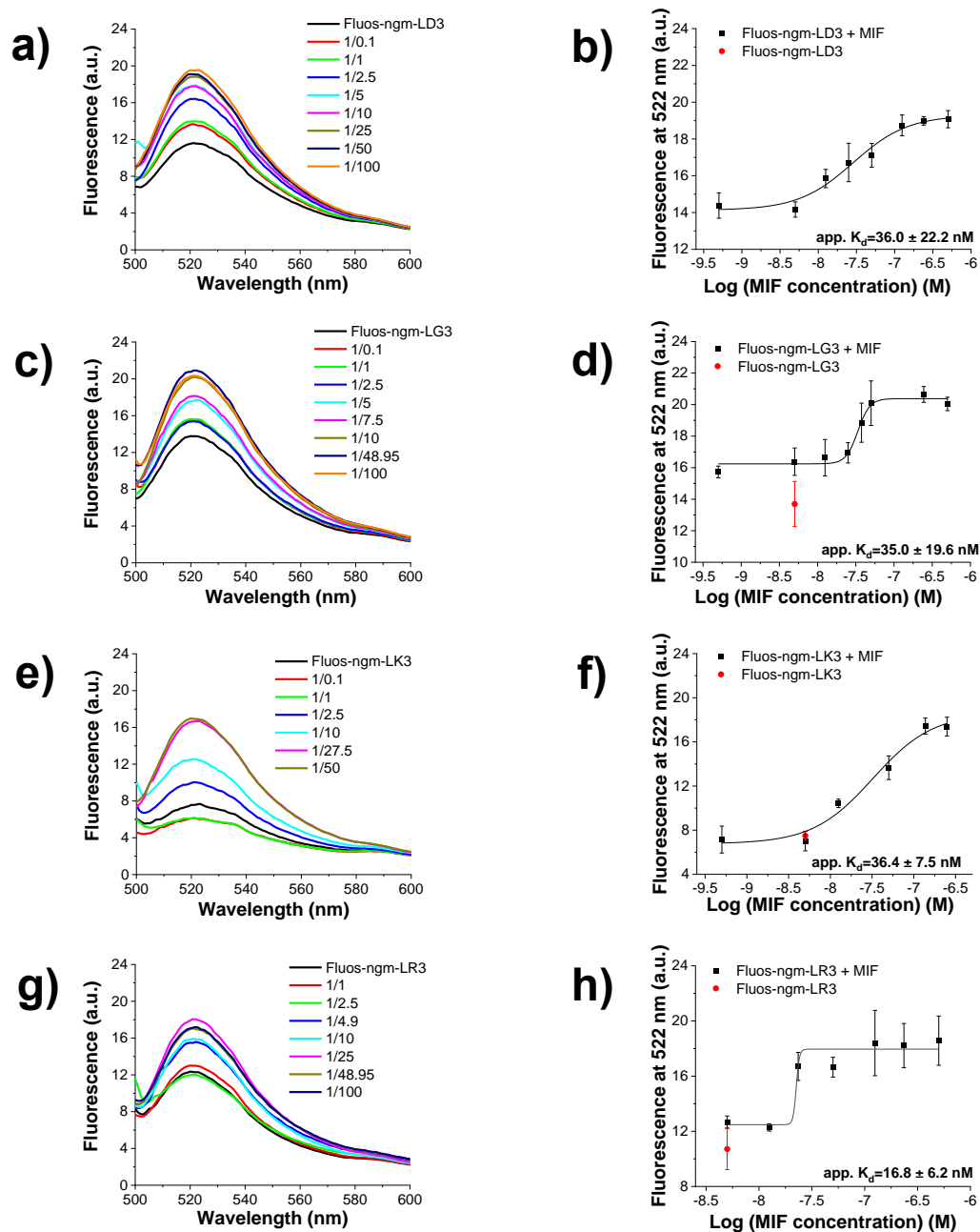
Figure 88. Fluorescence spectroscopic titrations of Fluos-ngms linked by natural amino acids with MIF for the determination of apparent affinities (app. K_{ds}). a, c, e, g Fluorescence spectra between 500 and 600 nm of 5 nM of Fluos-ngm-LD3 (a), Fluos-ngm-LG3 (c), Fluos-ngm-LK3 (e) and Fluos-ngm-LR3 (g) alone and their mixtures with various amounts of MIF; the molar ratios of Fluos-ngms/MIF are indicated. **b, d, f, h** Binding curves derived from the fluorescence emission at 522 nm of of Fluos-ngm-LD3 (b), Fluos-ngm-LG3 (d), Fluos-ngm-LK3 (f) and Fluos-ngm-LR3 (h) at different concentrations of MIF. Data shown are means (±SD) from three independent titration experiments which were performed in aqueous 1×b, pH 7.4, containing 1% HFIP.

The next question was whether improved affinity would be observed in the vice-versa titrations, i.e. of Alexa-488-MIF with non-labeled ngms. All linked by non-natural amino acids peptides had an app. K_d below 50 nM, with the lowest one being at 11.7 ± 7.3 nM between Alexa-488-MIF and ngm-L3 (Figure 89a, b). The decreased fluorescence emission of Alexa-488-MIF over the increased concentrations of the

peptides indicated dissociation constants of 43.2 ± 20.2 nM and 41.8 ± 16.4 nM for ngm-L4 and ngm-L5, respectively (Figure 89c-f). The obtained values are marginally increased to the 31.1 ± 16.6 nM that originates from the interaction between the labeled protein and msR4M-L1 (Table 40).
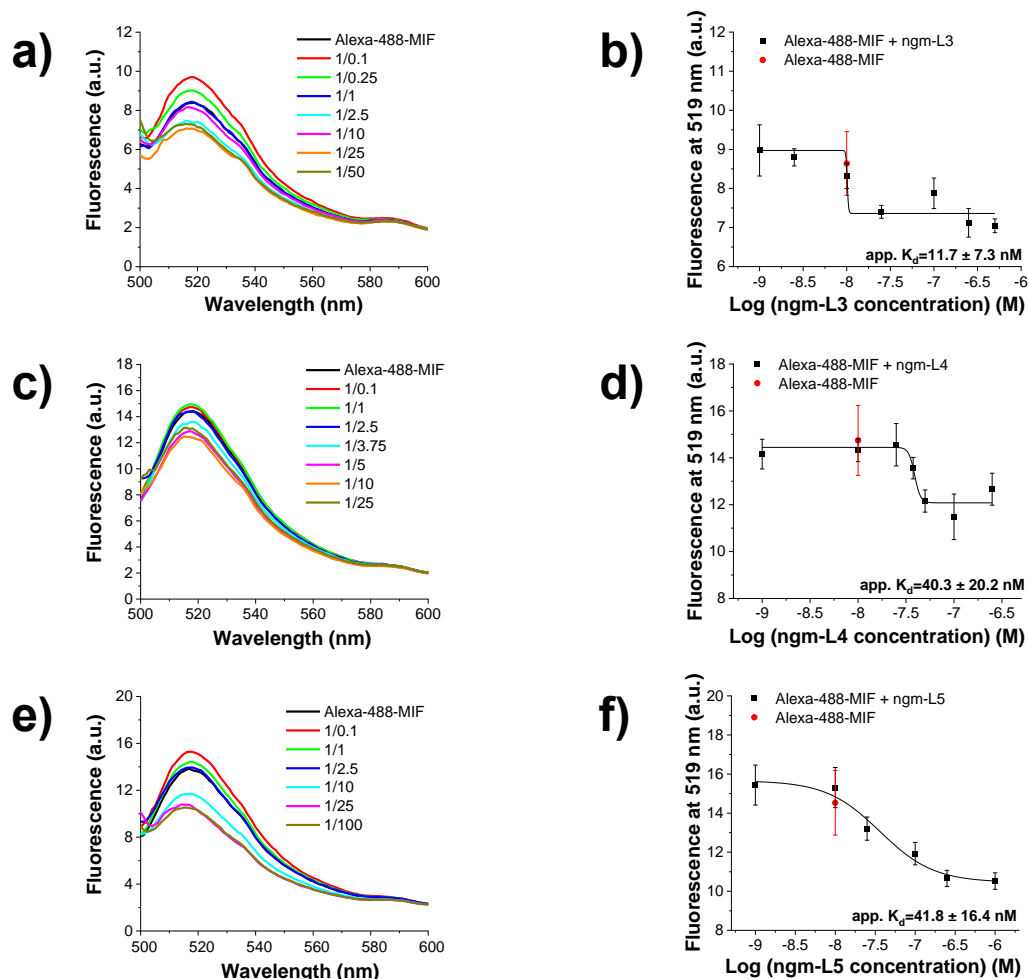
Figure 89. Fluorescence spectroscopic titrations of Alexa-488-MIF with linked by non-natural amino acids ngms for the determination of apparent affinities (app. K$_{ds}$). a, c, e Fluorescence spectra between 500 and 600 nm of Alexa-488-MIF (10 nM) alone and its mixtures with various amounts of ngm-L3 (a), ngm-L4 (c) and ngm-L5 (e); the molar ratios of Alexa-488-MIF/peptides are indicated. **b, d, f** Binding curves derived from the fluorescence emission at 519 nm of Alexa-488-MIF (10 nM) at different concentrations of ngm-L3 (b), ngm-L4 (d) and ngm-L5 (f). Data shown are means (±SD) from three independent titration experiments which were performed in aqueous 1×b, pH 7.4, containing 1% HFIP.

Regarding the ngms linked via natural amino acids, the app. K$_{ds}$ varied from two-digit nanomolar to micromolar. Ngm-LD3, with a three-aspartic acid covalent linkage between ECL1(102-110) and ECL2(187-195), comes as the next binder having a dissociation constant equal to 246.5 ± 21.7 nM (Figure 90a, b). When ngm-LG3 was applied as the titrant, surprisingly, the fluorescence emission of the analyte got increased instead of decreased. However, no upper plateau was achieved until 5000 nM, indicating an app. K$_d$ above this concentration. No measurements were recorded above this point due to the weak presence of light scattering and the possible presence of aggregates in higher concentrations (Figure 90c, d). Among ngms, ngm-LK3 is the more potent binder of MIF with an app. K$_d$ of 44.8 ± 10.3 nM followed by ngm-LR3, another peptide which is linked via basic residues, with an app. K$_d$ of 110.1 ± 28.1 nM (Table 40, Figure 90e-h).
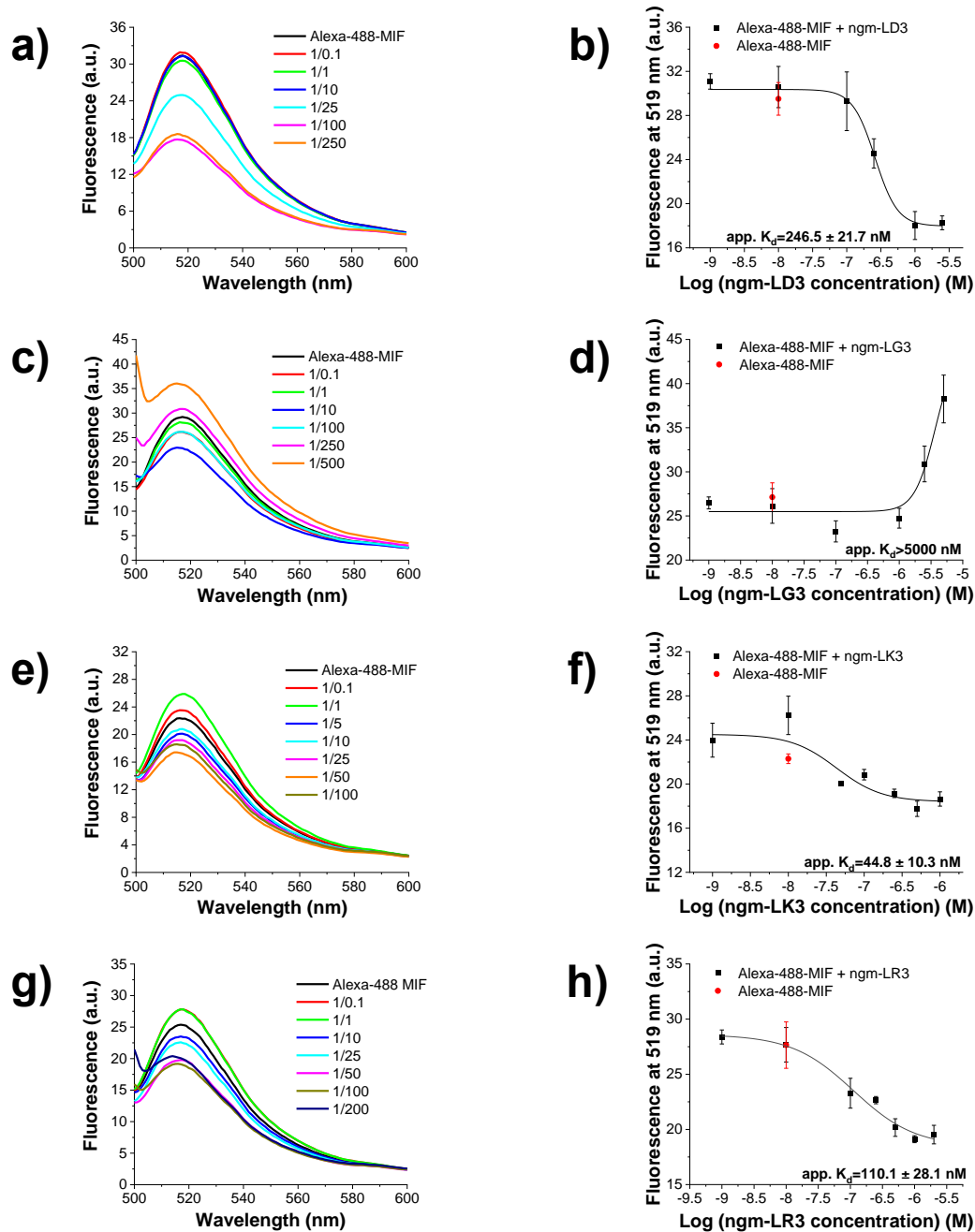
Figure 90. Fluorescence spectroscopic titrations of Alexa-488-MIF with linked by natural amino acids ngms for the determination of apparent affinities (app. K_{ds}). a, c, e, g Fluorescence spectra between 500 and 600 nm of Alexa-488-MIF (10 nM) alone and its mixtures with various amounts of ngm-LD3 (a), ngm-LG3 (c), ngm-LK3 (e) and ngm-LR3 (g); the molar ratios of Alexa-488-MIF/peptides are indicated. **b, d, f, h** Binding curves derived from the fluorescence emission at 519 nm of Alexa-488-MIF (10 nM) at different concentrations of ngm-LD3 (b), ngm-LG3 (d), ngm-LK3 (f) and ngm-LR3 (h). Data shown are means (±SD) from three independent titration experiments which were performed in aqueous 1×b, pH 7.4, containing 1% HFIP.

Table 40. Apparent affinities (app. K_{ds}) of interaction between ngms and MIF, as determined by fluorescence spectroscopic titrations.

ngms	Fluos-ngm/MIF app. K_d (±SD) (nM)	Alexa-488-MIF/ngm app. K_d (±SD) (nM)
ngm-L3	44.4 (±16.4)	11.7 (±7.3)
ngm-L4	11.9 (±4.8)	43.2 (±20.2)
ngm-L5	14.3 (±5.7)	41.8 (±16.4)
ngm-LD3	36.0 (±22.2)	246.5 (±21.7)
ngm-LG3	35.0 (±19.6)	>5000
ngm-LK3	36.4 (±7.5)	44.8 (±10.3)
ngm-LR3	16.8 (±6.2)	110.1 (±28.1)

App. K_{ds}, are means (±SD) from three independent titration experiments which were performed in aqueous 1×b, pH 7.4, containing 1% HFIP.

4.3.4.2 Interactions with MIF by CD spectroscopy

Titrations between labeled-ngms and MIF indicated strong bindings with app. K_{ds} varying from 11 to 47 nM. However, it remains unanswered whether this interaction causes any structural change in the peptides or the cytokine. To shed light on this topic, mixtures of ngms and MIF were analyzed through CD spectroscopy, and the obtained signal was compared to the expected for the identification of possible changes. MIF was shown to have a well-ordered structure, contrary to all ngms that adopted a random coil. From all the peptides, ngm-L4 and ngm-L5 had the weaker minima below 200 nm, suggesting the existence of more ordered traces compared to mimics linked via natural amino acids. The derived signals from ngm-L4/MIF and ngm-L5/MIF mixtures at 5:1 (5:1 µM) were very similar to the sums of the single spectra of the peptides and the protein, suggesting no conformation changes (Figure 91a, b).

Comparison between the expected and the experimentally determined ellipticity between ngm-LD3, ngm-LG3 and their mixtures with MIF (5:1 µM) showed no significant differences (Figure 91c, d). Likewise, the secondary structure remained unchanged after the mix of ngm-LK3 and MIF (Figure 91e). However, this was not the case for the other mimic that was linked with basic residues, the ngm-LR3. Sum and mixture of ngm-LR3 and MIF exposed similar signal shapes with broad minima between 207 and 224 nm that reached strong positive values below 203 nm, but with different ellipticity intensities. In particular, the experimental spectra exposed approximately 15% reduced signal at the region of the minima and 30% increased ellipticity below 195 nm. Of note, the spectrum of the ngm-LR3/MIF mixture seems very similar to the one of MIF alone with slightly more intense negative ellipticity values between 205 and 215 nm (Figure 91f).
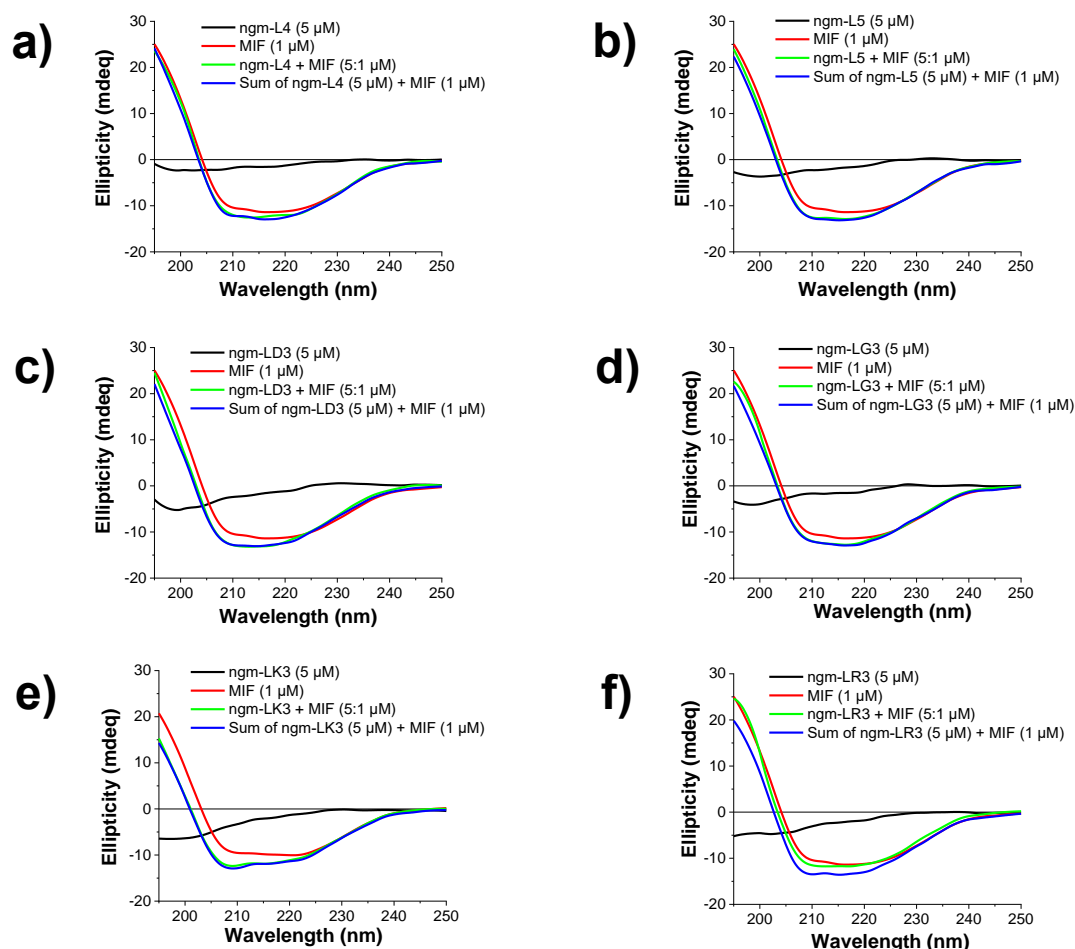
Figure 91. Studies on secondary structure of ngms-MIF mixtures (5:1) through CD spectroscopy. a, b, c, d, e, f CD spectra of ngms and MIF alone, ngms-MIF mixture and sum of the ellipticity of the derived peptide and protein individual spectra. The analyzed peptides were ngm-L4 (a), ngm-L5 (b), ngm-LD3 (c), ngm-LG3 (d), ngm-LK3 (e) and ngm-LR3 (f). Concentrations and ratios are indicated. Measurements were performed in aqueous 1×b, pH 7.4, containing 1% HFIP. Ellipticity (θ) plotted over the wavelength between 195 and 250 nm.

4.3.5 Determination of binding affinities to MIF(54-80) via fluorescence spectroscopy

Previously, in chapter 4.1.7.1, fluorescence spectroscopic titrations were carried out between Fluos-msR4Ms and various MIF-derived peptides to determine the region of the atypical chemokine that is prone to bind to the mimics. Among all MIF sequenced peptides, from 10-mers to 43-mers, MIF(54-80) appeared to be the shortest MIF fragment in which the Fluos-labeled analog of the lead peptide msR4M-L1 retained its strong affinity in similar range as against the whole MIF sequence. Next generation mimics are generated after size and sequence optimization studies in the two parts of ECL1 and ECL2 and have a 40% reduced molecular weight in comparison to msR4Ms. As shown in chapter 4.3.4.1, newly developed peptides remain strong binders of MIF like msR4Ms. However, it still remains unknown whether ngms bind strongly to the MIF region between the 54th and 80th residue as the first tested peptides.

Fluos-ngms were titrated with MIF(54-80) and the fluorescence emission of their mixtures was monitored via fluorescence spectroscopy. Measurements were pursued under the same conditions as in the previous chapters. The increased fluorescence emission of the labeled ngm-L5 upon the titration with MIF indicated an

app. K_d equal to 70.1 ± 40.8 nM (Figure 92a, b). Likewise, the fluorescence emission of unsaturated labeled-ngm-LD3 was increased over elevated titrant concentration by approximately 35% until the saturation was fulfilled and the app. K_d was 173.1 ± 68.8 nM (Figure 92c, d). The affinity between the labeled analyte and the unlabeled titrant was weakened when the three amino acids that linked ECL1(102-110) and ECL2(187-195) were basic. In particular, the estimated app. K_{ds} of labeled ngm-LK3 and ngm-LR3 with MIF(54-80) were 490.9 ± 123.4 nM and 1249.6 ± 138.2 nM, respectively (Table 41, Figure 92e-h).
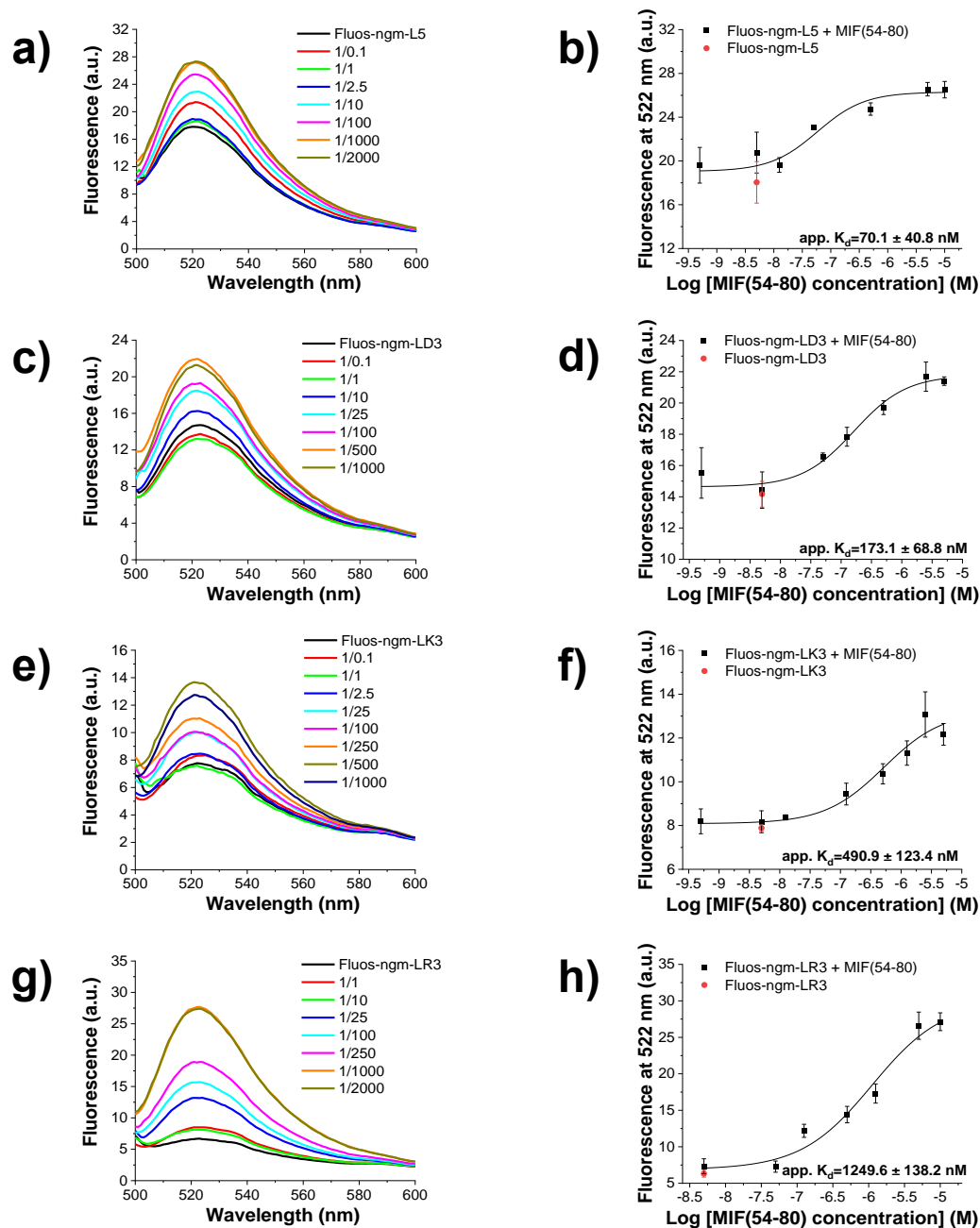
Figure 92. Fluorescence spectroscopic titrations of selected Fluos-ngms with MIF(54-80) for the determination of apparent affinities (app. K_{ds}). a, c, e, g Fluorescence spectra between 500 and 600 nm of 5 nM of Fluos-ngm-L5 (a), Fluos-ngm-LD3 (c), Fluos-ngm-LK3 (e) and Fluos-ngm-LR3 (g) alone and their mixtures with various amounts of MIF(54-80); the molar ratios of Fluos-ngms/MIF(54-80) are indicated. **b, d, f, h** Binding curves derived from the fluorescence emission at 522 nm of Fluos-ngm-L5 (b), Fluos-ngm-LD3 (d), Fluos-ngm-LK3 (f) and Fluos-ngm-LR3 (h) at different concentrations of MIF(54-80). Dat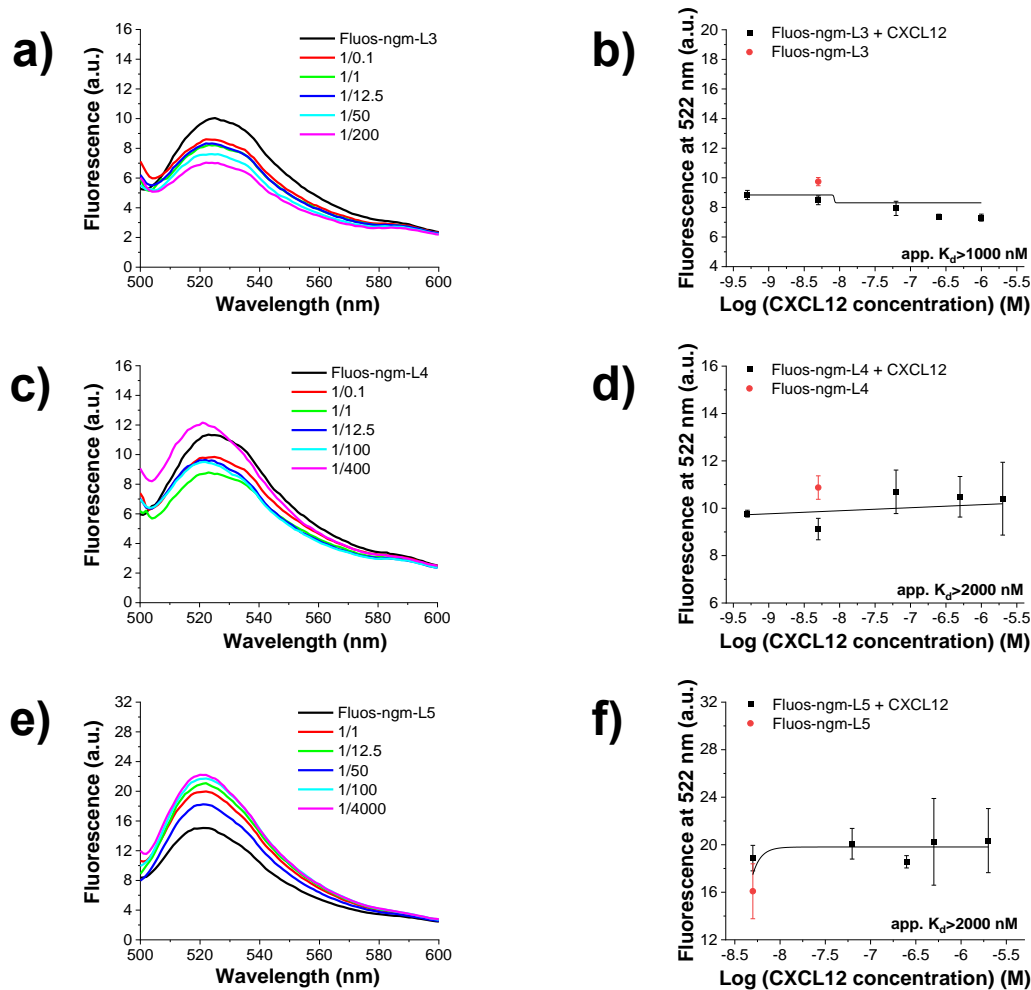a shown are means (±SD) from three independent titration experiments which were performed in aqueous 1×b, pH 7.4, containing 1% HFIP.

Table 41. Apparent affinities (app. K_{ds}) of interaction between Fluos-ngms and MIF(54-80), as determined by fluorescence spectroscopic titrations.

ngms	Fluos-ngm/MIF(54-80) app. K_d (±SD) (nM)
ngm-L3	n.d. [b]
ngm-L4	n.d. [b]
ngm-L5	70.1 (±40.8)
ngm-LD3	173.1 (±68.8)
ngm-LG3	n.d. [b]
ngm-LK3	490.9 (±123.4)
ngm-LR3	1249.6 (±138.2)

App. K_{ds}, are means (±SD) from three independent titration experiments which were performed in aqueous 1×b, pH 7.4, containing 1% HFIP. [b]: n.d., non-determined

4.3.6 Determination of binding affinities to CXCL12 via fluorescence spectroscopy

Firstly generated mimics of CXCR4, msR4Ms, were not only tested as binders of MIF but against CXCL12, the other ligand of the receptor CXCR4. In those studies, the oxidized analogs were able to interact with CXCL12 but the reduced not. Nevertheless, ngms, as shorter versions of msR4Ms, maintain the C109 of ECL1 but not the C186 of ECL2. Thereafter, it is impossible to generate an intra-peptide disulfide bond in the newer CXCR4 mimics. As next, labeled ngms were tested whether they can bind to CXCL12 or they maintain the MIF specificity, as the non-oxidized msR4Ms to MIF.
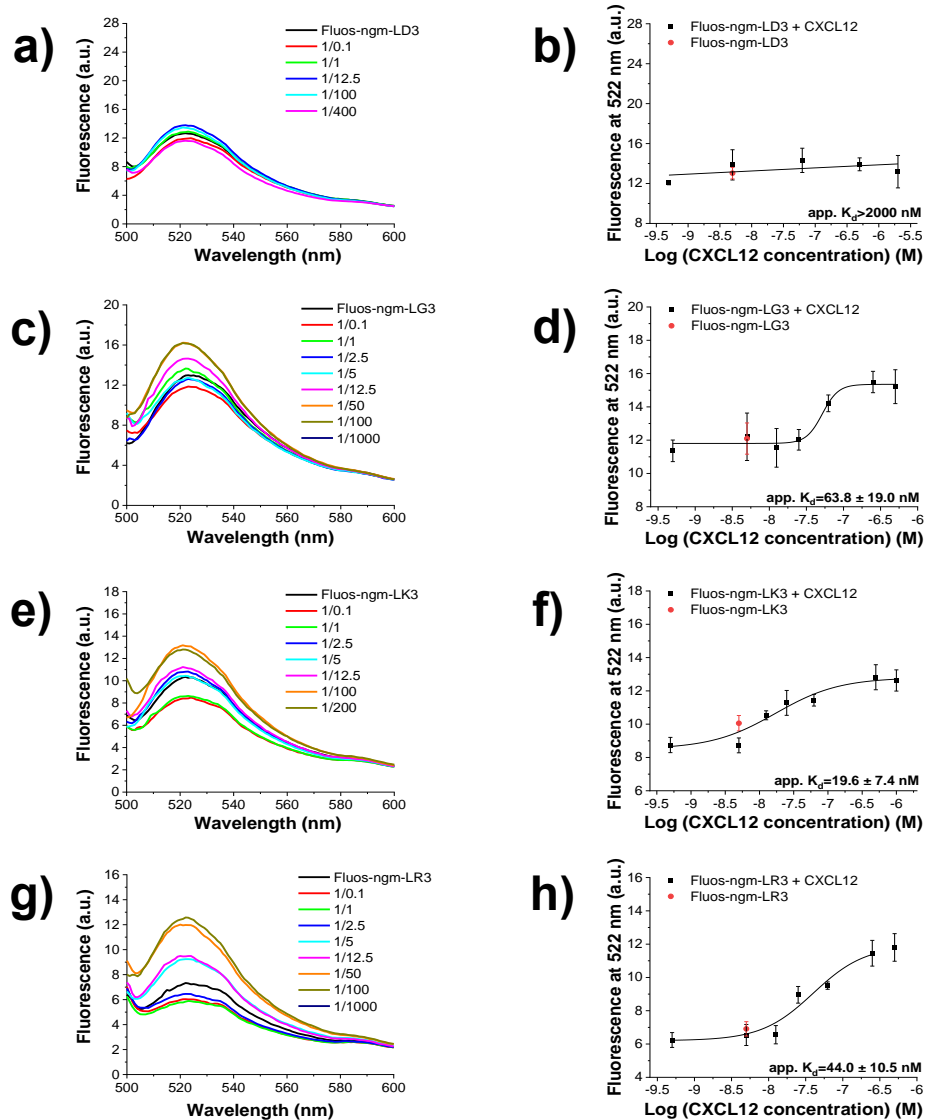
Fluorescence spectroscopic titrations of Fluos-ngms with CXCL12 were carried out at the same conditions that were described for Fluos-msR4Ms/CXCL12 and Fluos-ngms/MIF interactions, i.e. 1xb, pH 7.4, 1% HFIP. Fluorescence emission of labeled-ngms that were linked with natural amino acids against an increased amount of the chemokine remained unchanged. These findings suggested dissociation constants between those Fluos-ngms and MIF above this highest measured concentration point. Particularly, Fluos-ngm-L3 and CXCL12 had an app. K_d above 1000 nM, while the respective values for Fluos-ngm-L4 and -L5 were estimated to higher than 2000 nM (Table 42, Figure 93).

Figure 93. Fluorescence spectroscopic titrations of Fluos-ngms linked by non-natural amino acids with CXCL12 for the determination of apparent affinities (app. K_{ds}). a, c, e Fluorescence spectra between 500 and 600 nm of 5 nM of Fluos-ngm-L3 (a), Fluos-ngm-L4 (c) and Fluos-ngm-L5 (e) alone and their mixtures with various amounts of CXCL12; the molar ratios of Fluos-ngms/CXCL12 are indicated. **b, d, f** Binding curves derived from the fluorescence emission at 522 nm of Fluos-ngm-L3 (b), Fluos-ngm-L4 (d) and Fluos-ngm-L5 (f) at different concentrations of CXCL12. Data shown are means (±SD) from three independent titration experiments which were performed in aqueous 1×b, pH 7.4, containing 1% HFIP.

Ngms linked via natural amino acids exhibited diverse binding properties with CXCL12. Interestingly, the newer mimics exposed either strong nanomolar or weak micromolar affinity. Fluos-ngm-LD3 belongs to the second category, with its fluorescence emission remaining unchanged until 2000 nM of CXCL12 (Figure 94 a, b). Contrariwise, labeled-ngm-LG3 showed strong binding to the chemokine with an app. K_d of 63.8 ± 19.0 nM (Figure 94 c, d). Similar potency was observed for the lysine and arginine linked ngms, with Fluos-ngm-LK3 and -LR3 and CXCL12 sharing dissociation constants of 19.6 ± 7.4 nM and 44.0 ± 10.5 nM, respectively (Table 42, Figure 94 e-h). Summarized results and comparison of the binding affinities of the peptides are described in 'Discussion' (see 5.3).

Figure 94. Fluorescence spectroscopic titrations of Fluos-ngms linked by natural amino acids with CXCL12 for the determination of apparent affinities (app. K$_{ds}$). a, c, e, g Fluorescence spectra between 500 and 600 nm of 5 nM of Fluos-ngm-LD3 (a), Fluos-ngm-LG3 (c), Fluos-ngm-LK3 (e) and Fluos-ngm-LR3 (g) alone and their mixtures with various amounts of CXCL12; the molar ratios of Fluos-ngms/CXCL12 are indicated. **b, d, f, h** Binding curves derived from the fluorescence emission at 522 nm of Fluos-ngm-LD3 (b), Fluos-ngm-LG3 (d), Fluos-ngm-LK3 (f) and Fluos-ngm-LR3 (h) at different concentrations of CXCL12. Data shown are means (±SD) from three independent titration experiments which were performed in aqueous 1×b, pH 7.4, containing 1% HFIP.

Table 42. Apparent affinities (app. K$_{ds}$) of interaction between Fluos-ngms and CXCL12, as determined by fluorescence spectroscopic titrations.

ngms	Fluos-ngms/CXCL12 app. K$_d$ (±SD) (nM)
ngm-L3	>1000
ngm-L4	>2000
ngm-L5	>2000
ngm-LD3	>2000
ngm-LG3	63.8 (±19.0)
ngm-LK3	19.6 (±7.4)
ngm-LR3	44.0 (±10.5)

App. K$_{ds}$, are means (±SD) from three independent titration experiments which were performed in aqueous 1×b, pH 7.4, containing 1% HFIP.

4.3.7 Conclusions of ngms

Ngms were successfully synthesized and purified following well-established protocols with high yields. The newer CXCR4 mimics exhibited different biophysical properties than the first generated peptides. Particularly, all ngms were found to lack any ordered structure. The linked via charged natural amino acids mimics had the highest flexibility and remained soluble until 50 μM, at least, in CD measuring conditions. The hydrophobicity content on the surface of the ngms varied from very limited (ngm-L5,-LD3) to moderate/relatively high (ngm-L4, -LG3, -LK3) or even high (ngm-LR3) (Table 43).

Table 43. Defined biophysical properties of ngms after CD and fluorescence spectroscopy studies with ANS.

Peptide	Secondary structure	Precip. (μM)	Hydrophobic residues on the surface
ngm-L3	r.c. [a]	2.5	n.d. [b]
ngm-L4	r.c. [a]	20	Quite high exposure
ngm-L5	r.c. [a]	50	Very low exposure
ngm-LD3	r.c. [a]	>50	No exposure
ngm-LG3	r.c. [a]	50	Quite high exposure
ngm-LK3	r.c. [a]	>50	Medium exposure
ngm-LR3	r.c. [a]	>50	High exposure

Peptides were biophysically characterized in aqueous 1×b, pH 7.4, containing 1% HFIP. [a]: r.c., random coil, [b]: n.d., non-determined.

Next, all ngms exhibited a strong self-association propensity, except for ngm-L5 that did not self-assemble until 500 nM. The N-terminus labeled ngms had a strong binding to MIF, and all but the ones bonded with basic amino acids recognized the same binding interface on the chemokine as the msR4M-L1 previously. In the reverse experimental setup with the labeled-MIF as the analyte, ngm-LG3 and ngm-LD3 fully and partially lost their bindings to the chemokine, while the rest ngms maintained the strong affinity (Table 44). The ngms that were linked with non-acidic natural amino acids were strong binders of CXCL12, with dissociation constants comparable to the respective ones with MIF. Contrariwise, ngm-LD3 and the non-natural amino acid-linked mimics were MIF-specific binders and did not interfere with the chemokine. The two most soluble newer MIF-specific mimics, ngm-LD3 and then ngm-L5, could be prioritized for further testing.

Table 44. Determined app. K_{ds} of self-assembly of ngms and of their binding interactions with MIF, MIF(54-80) and CXCL12, as derived by fluorescence spectroscopic titrations.

Peptide	app. K_d (±SD) (nM) [a] (self-assembly)	app. K_d (±SD) (nM) [a] (Fluos-ngm/MIF)	app. K_d (±SD) (nM) [a] (Alexa-488-MIF/ngm)	app. K_d (±SD) (nM) [a] (Fluos-ngm/ MIF(54-80)	app. K_d (±SD) (nM) [a] (Fluos-ngm/CXCL12)
ngm-L3	n.d.[b]	44.4 (±16.4)	11.7 (±7.3)	n.d.[b]	>1000
ngm-L4	47.9 (±15.7)	11.9 (±4.8)	43.2 (±20.2)	n.d.[b]	>2000
ngm-L5	>500	14.3 (±5.7)	41.8 (±16.4)	70.1 (±40.8)	>2000
ngm-LD3	64.4 (±18.3)	36.0 (±22.2)	246.5 (±21.7)	173.1 (±68.8)	>2000
ngm-LG3	70.2 (±13.4)	35.0 (±19.6)	>5000	106.4 (±31.9)	63.8 (±19.0)
ngm-LK3	41.2 (±9.9)	36.4 (±7.5)	44.8 (±10.3)	490.9 (±123.4)	19.6 (±7.4)
ngm-LR3	16.2 (±4.3)	16.8 (±6.2)	110.1 (±28.1)	1249.6 (±138.2)	44.0 (±10.5)

[a]: App. K_{ds} are means (±SD) from three independent titration experiments which were performed in aqueous 1×b, pH 7.4, containing 1% HFIP. [b]: n.d., non-determined.

4.4   SAR studies on ECL1 and ECL2 analogs of CXCR2

Previously published spot-array data indicated the CXCR2 fragments between the 108th and 120th residue and 184th and 198th residue of the extracellular loop 1 and 2 respectively, termed as R2ECL1(108-120) and R2ECL2(184-198), as binders of MIF, among others [97]. Based on these, it was desired to examine further these peptides and their shorter analogs and determine their secondary structures via CD and binding affinities with MIF via fluorescence spectroscopy. These SAR studies aimed at mapping the core region of the CXCR2 ectodomain for binding to MIF (Scheme 15).
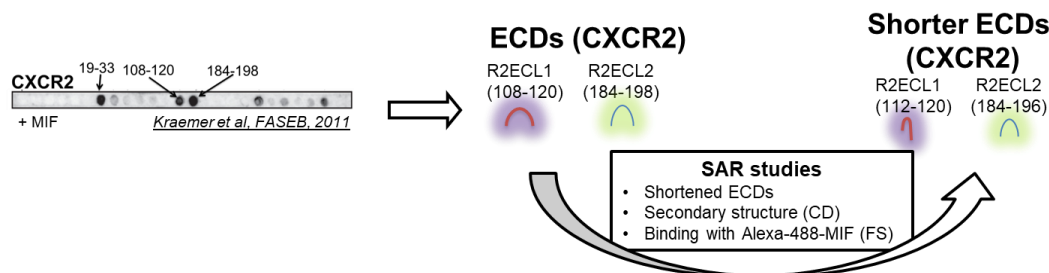
Scheme 15. Overview of the development and studies of ECDs analogs of CXCR2. Studies of shorter ECDs aimed on the determination of their biophysical properties and their binding affinities with MIF.

4.4.1   Synthesis of R2ECL1(108-120) and R2ECL2(184-198) analogs

R2ECL1(108-120) and R2ECL2(184-198) were systematically N-or C-terminusly shortened and synthesized on a Rink resin, following the Fmoc-SPPS described protocols. The protocol of couplings differentiated slightly in some cases regarding the coupling times, the activator, the equivalents of DIEA, and the time, as described in Scheme 16. All N-terminus Fmoc groups were cleaved with the normal protocol, and cleaved with Reagent K as previously described. Lyophilized crude peptides were dissolved in TFA/80% B, analyzed by RP-HPLC and their peaks were dissolved in MALDI solution A before their MALDI-TOF-MS analyses (Figure 95-97). Theoretical and experimental determined MWs were in agreement after taking into consideration the addition of Na$^+$ or K$^+$ in a few cases, while the yield was in the 13.7-23.6% and 4.4-5.6% range for R2ECL1 and R2ECL2 analogs, respectively (Table 45).

Table 45. Sequences, abbreviation and characterization of synthesized R2ECL1 and R2ECL2 analogs by RP-HPLC and MALDI-TOF-MS.

| Peptide sequence[a]	Peptide abbreviation	HPLC Pr.No.	t_R (min)[b]	Yield (%)[c]	[M+H]$^+$ expected[d]	[M+H]$^+$ found[d]
KVNGWIFGTFLCK	R2ECL1(108-120)	1	18.61	13.7	1511.83	1534.27[e]
KVNGWIFGTFLC	R2ECL1(108-119)	1	21.25	16.8	1383.73	1405.95[e]
NGWIFGTFLCK	R2ECL1(110-120)	1	20.70	19.4	1284.66	1306.80[e]
GWIFGTFLCK	R2ECL1(111-120)	1	18.90	15.6	1170.62	1193.00[e]
WIFGTFLCK	R2ECL1(112-120)	1	20.57	19.1	1113.60	1135.69[e]
IFGTFLCK	R2ECL1(113-120)	1	16.85	23.6	927.52	949.81[e]
FGTFLCK	R2ECL1(114-120)	1	16.45	19.2	814.43	854.62[f]
RRTVYSSNVSPACYE	R2ECL2(184-198)	1	12.34	4.9	1730.21	1730.94
RRTVYSSNVSPAC	R2ECL2(184-196)	1	11.85	5.6	1438.73	1439.00
TVYSSNVSPACYE	R2ECL2(186-198)	1	13.51	5.0	1418.63	1441.11[e]
YSSNVSPACYE	R2ECL2(188-198)	1	13.30	4.4	1218.52	1240.65[e]

Peptides were dissolved and analyzed by MALDI-TOF-MS in a mixture of MALDI solutions A and A (matrix); **[a]** Peptides were synthesized with free amino-N-terminus and amidated C-terminus; **[b]** HPLC retention time of the pure product, the stationary phase was a tandem of Reprosil Gold 200 C18 columns (250 and 30 mm length, 8 mm internal diameter,10 μm particle size); **[c]** % yield with regard to crude peptide ; **[d]** monoisotopic molar mass with an extra hydrogen [M+H]$^+$; **[e]** monoisotopic molar mass with an extra sodium [M+Na]$^+$; **[f]** monoisotopic molar mass with an extra potassium [M+K]$^+$.
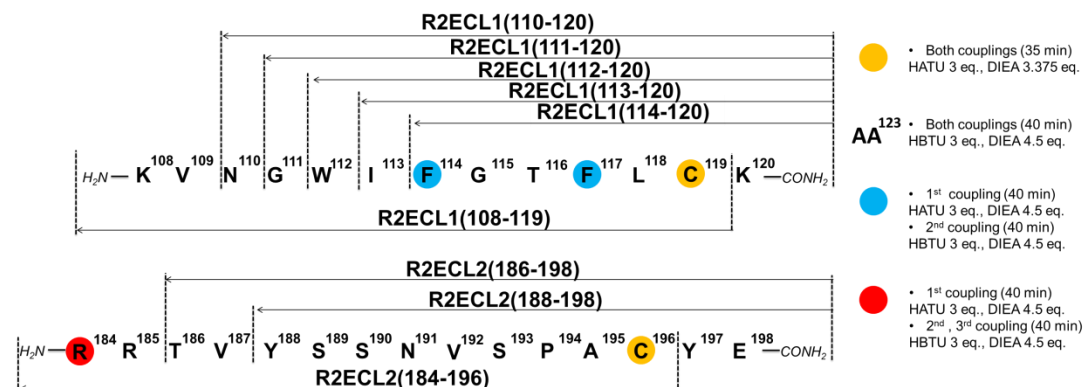
Scheme 16. Conditions of couplings for the syntheses of R2ECL1 and R2ECL2 analogs. All amino acids were coupled with 3 equivalents (eq.), based on the substitution level that was determined after the load of the first amino acid on Rink-resin. Equivalents of activator and base, together with the coupling time may vary, as indicated.
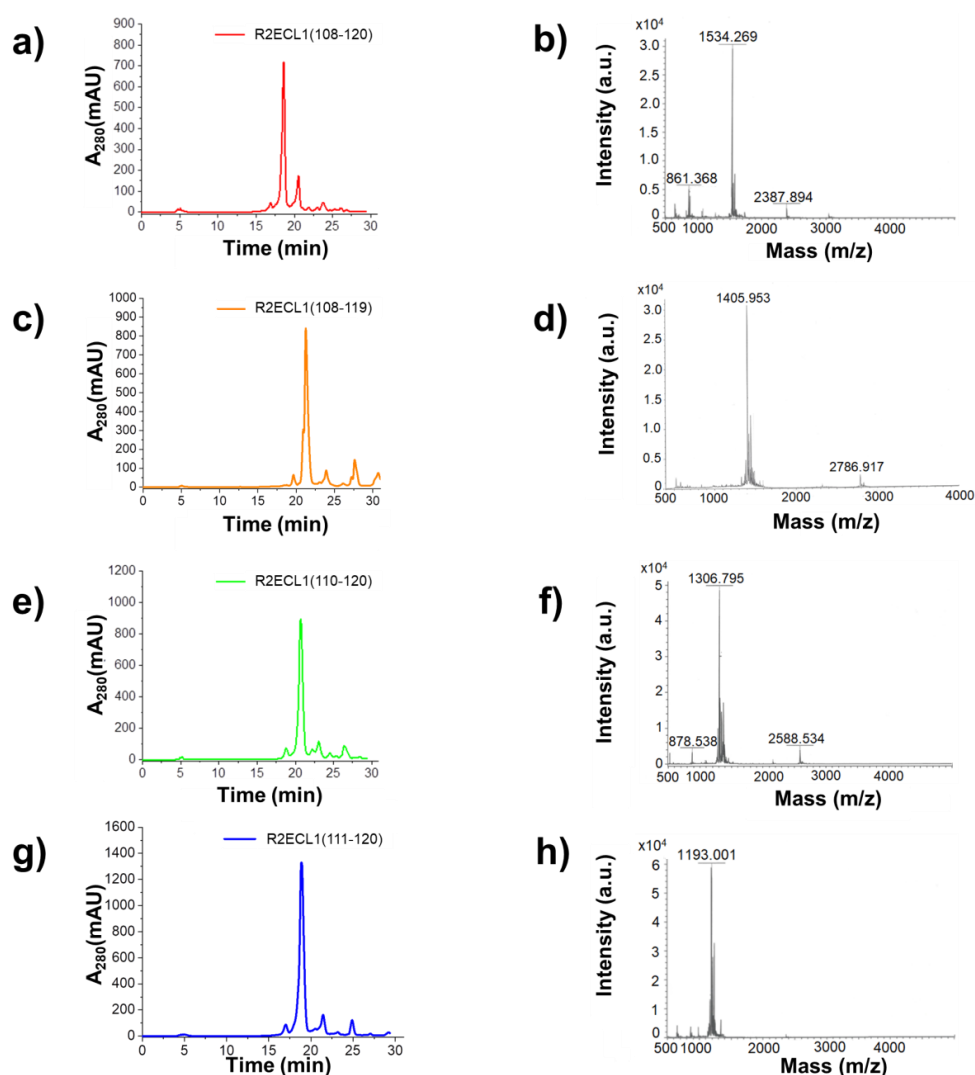
Figure 95. HPLC purification of R2ECL1(108-120), R2ECL1(108-119), R2ECL1(110-120), and R2ECL1(111-120) and verification of their purity by MALDI. a, c, e, g Representative C18 HPLC chromatogram (absorbance at 280 nm) of crude R2ECL1(108-120), R2ECL1(108-119), R2ECL1(110-120) and R2ECL1(111-120) with respective retention times: a) 18.61 min, c) 21.25 min, e) 20.70 min and g) 18.90 min, following SPPS and cleavage. **b, d, f, h** MALDI-TOF-MS spectra of HPLC-purified R2ECL1(108-120), R2ECL1(108-119), R2ECL1(110-120) and R2ECL1(111-120) with respective experimental determined masses [M+H]$^+$: b) 1534.269 Da, d) 1405.953 Da, f) 1306.795 Da and h) 1193.001 Da.
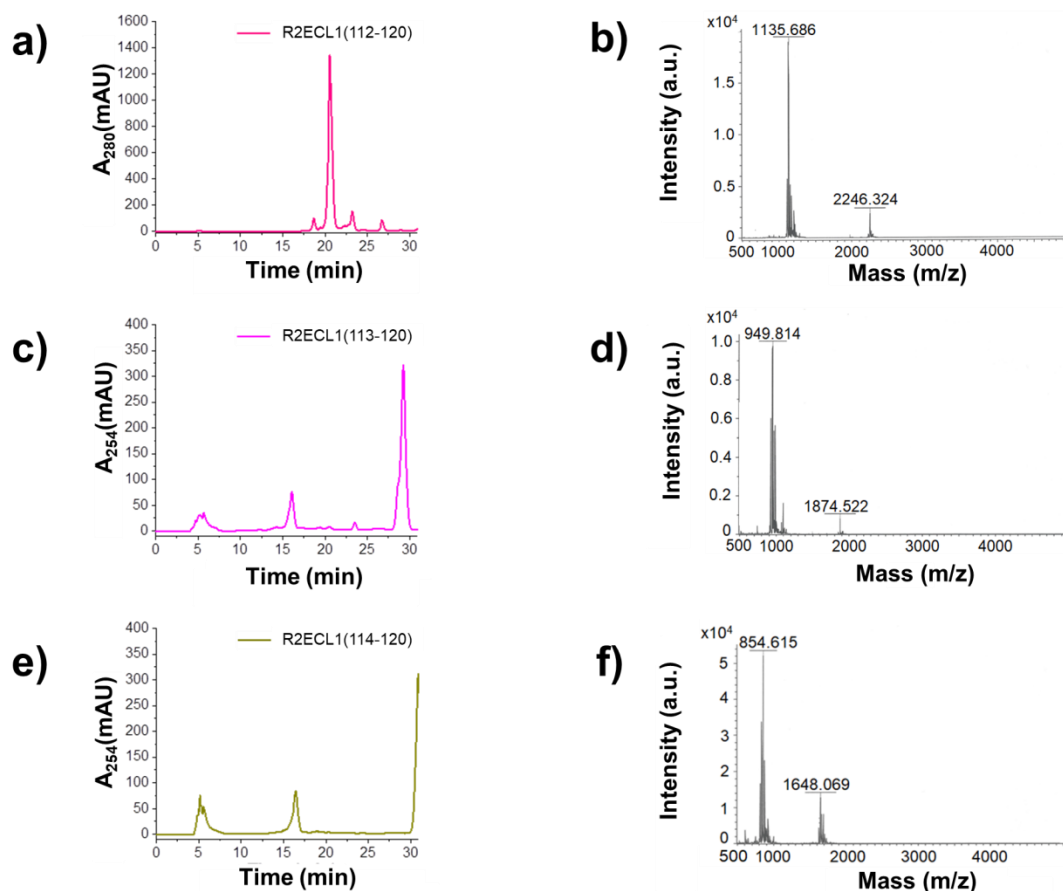
Figure 96. HPLC purification of R2ECL1(112-120), R2ECL1(113-120) and R2ECL1(114-120) and verification of their purity by MALDI. a, c, e Representative C18 HPLC chromatogram (absorbance at 280 nm for a, c and at 254 nm for e) of crude R2ECL1(112-120), R2ECL1(113-120) and R2ECL1(114-120) with respective retention times: a) 20.57 min, c) 16.85 min and e) 16.45 min, following SPPS and cleavage. The peaks that are eluted at the end of the chromatogram (tR=31 min) are due to the formation of non-covalent aggregates. **b, d, f** MALDI-TOF-MS spectra of HPLC-purified R2ECL1(112-120), R2ECL1(113-120) and R2ECL1(114-120) with respective experimental determined masses [M+H]$^+$: b) 1135.686 Da, d) 949.814 Da and f) 854.615 Da.
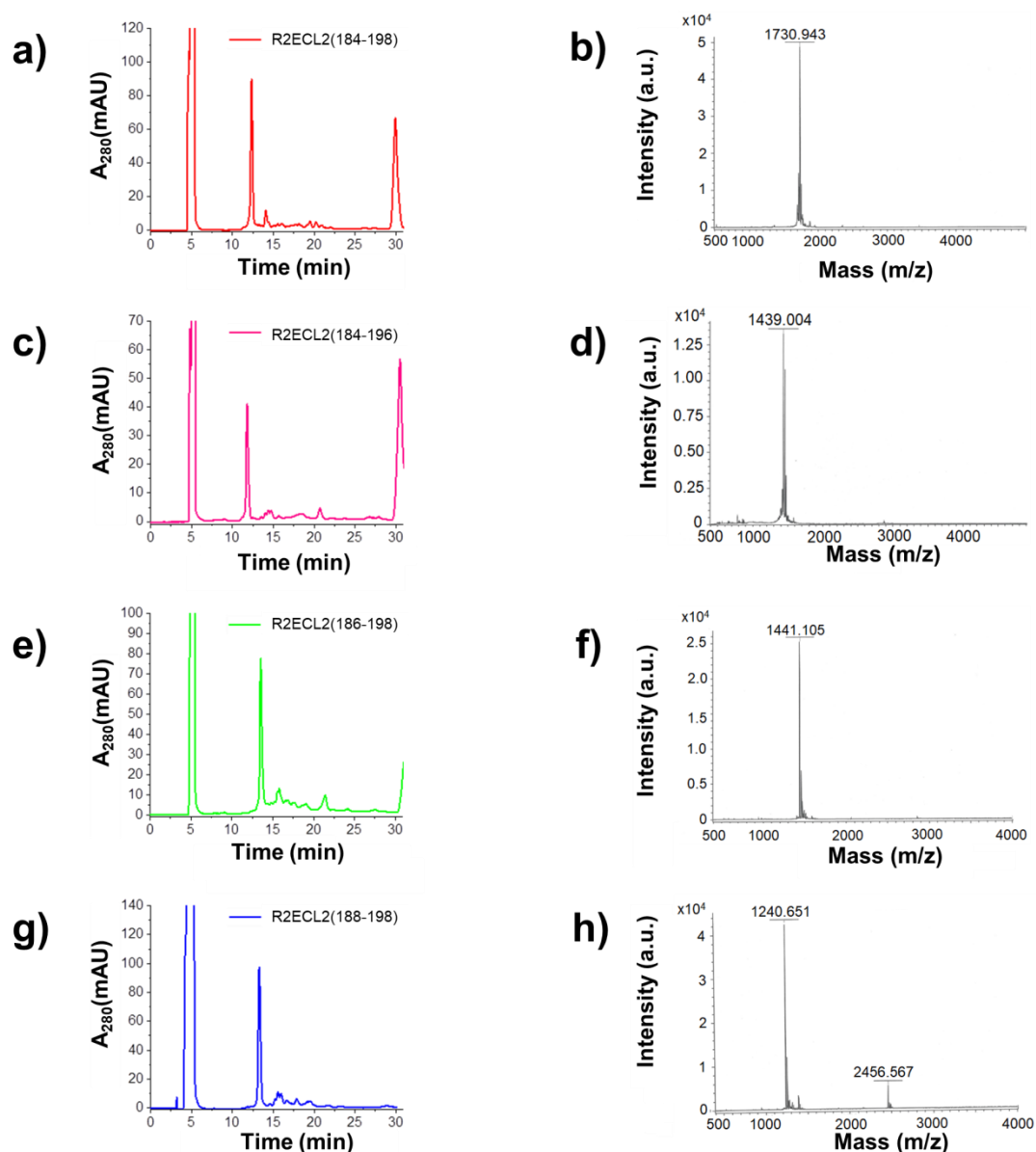
Figure 97. HPLC purification of R2ECL2(184-198) and its shorter analogs and verification of their purity by MALDI. a, c, e, g Representative C18 HPLC chromatogram (absorbance at 280 nm) of crude R2ECL2(184-198), R2ECL2(184-196), R2ECL2(186-198) and R2ECL2(188-198) with respective retention times: a) 12.34 min, c) 11.85 min, e) 13.51 min and g) 13.30 min, following SPPS and cleavage. The peaks that are eluted at the end of the chromatogram (tR=31 min) are due to the formation of non-covalent aggregates. **b, d, f, h** MALDI-TOF-MS spectra of HPLC-purified R2ECL2(184-198), R2ECL2(184-196), R2ECL2(186-198) and R2ECL2(188-198) with respective experimental determined masses $[M+H]^+$: b) 1730.943 Da, d) 1439.004 Da, f) 1441.105 Da and h) 1240.651 Da.

## 4.4.2 Conformational and concentration dependence studies via CD spectroscopy

R2ECL1 and R2ECL2 peptides were structurally studied by CD spectroscopy. Peptide solutions were measured between 5 and 50 µM as described before, and their spectra between 197 and 250 nm provided insights for their secondary structure, aggregation, and solubility properties. The sequence between the 108th and 120th residues derived by extracellular loop 1 of CXCR2, or in other words R2ECL1(108-120), exposed a concentration-dependent signal including both characteristic minima of a random coil and β-turn structure. The peptide contains a mainly unordered structure at

5 and 20 µM, while for the spectra at 10 and 50 µM the minima at 225-230 nm and at 200 nm were equal. As next, the N-terminus residues of the R2ECL1(108-120) analog remained untouched, and the K120 was extracted (Figure 98a). R2ECL1(108-119) maintained its solubility until 50 µM, even after the absence of K120, and exhibited β-sheet-indicative spectra for 5 and 10 µM. The shape of the spectrum remained similar for 50 µM but with a weaker signal. At 20 µM the 12-mer slightly differentiated, exhibiting a minimum at 216 nm (Figure 98b).

Spectra slightly differentiated after eliminating the residues K108 and V109 and the generation of the more β-sheet containing analog R2ECL1(110-120). As the native peptide, the 11-mer did not precipitate until 50 µM. Peptide showed spectra for at 5 and 10 µM that contained two minima, one at 218 nm and the other at 200 nm. Interestingly, the R2ECL1(110-120) switched to a mainly ordered structure at 20 and 50 µM. The first minimum was slightly shifted at 222 nm, and the values below 200 nm were increased from -2000 to 0 deg·cm^2·dmol^{-1} (Figure 98c). Subsequent elimination of N110 led to the R2ECL1(111-120) analog that had the characteristic β-sheet spectra from 5 µM. The signal shape of the spectra remained similar but its intensity became weaker for the 20 µM, while at 50 µM the minimum is shifted from 219 nm to 226 nm (Figure 98d).

R2ECL1(112-120) followed a similar pattern. Its minima at 220 nm for 5 and 10 µM was slightly shifted to the right of the x-axis for 50 µM, with the peptide having a spectrum with a lower intensity at 20 µM (Figure 98e). The first elimination of an aromatic residue had a strong effect on the secondary structure of the W112 missing R2ECL1(113-120). Its weak minima at 232 nm and its positive signal at 225 nm led to the assumption of β-turn traces in the structure. A second and stronger minimum was exposed at 200 nm, indicating an overall non-ordered structure for peptides in the 5 to 50 µM range (Figure 98f). Surprisingly, the subtraction of F113 in the sequence led to the insoluble R2ECL1(114-120). The 7-mer precipitated at 5 µM, when all the rest R2ECL1 analogs maintained their solubility until 50 µM. Summarized results and comparison of the spectra of the peptides are described in 'Discussion' (see 5.4).
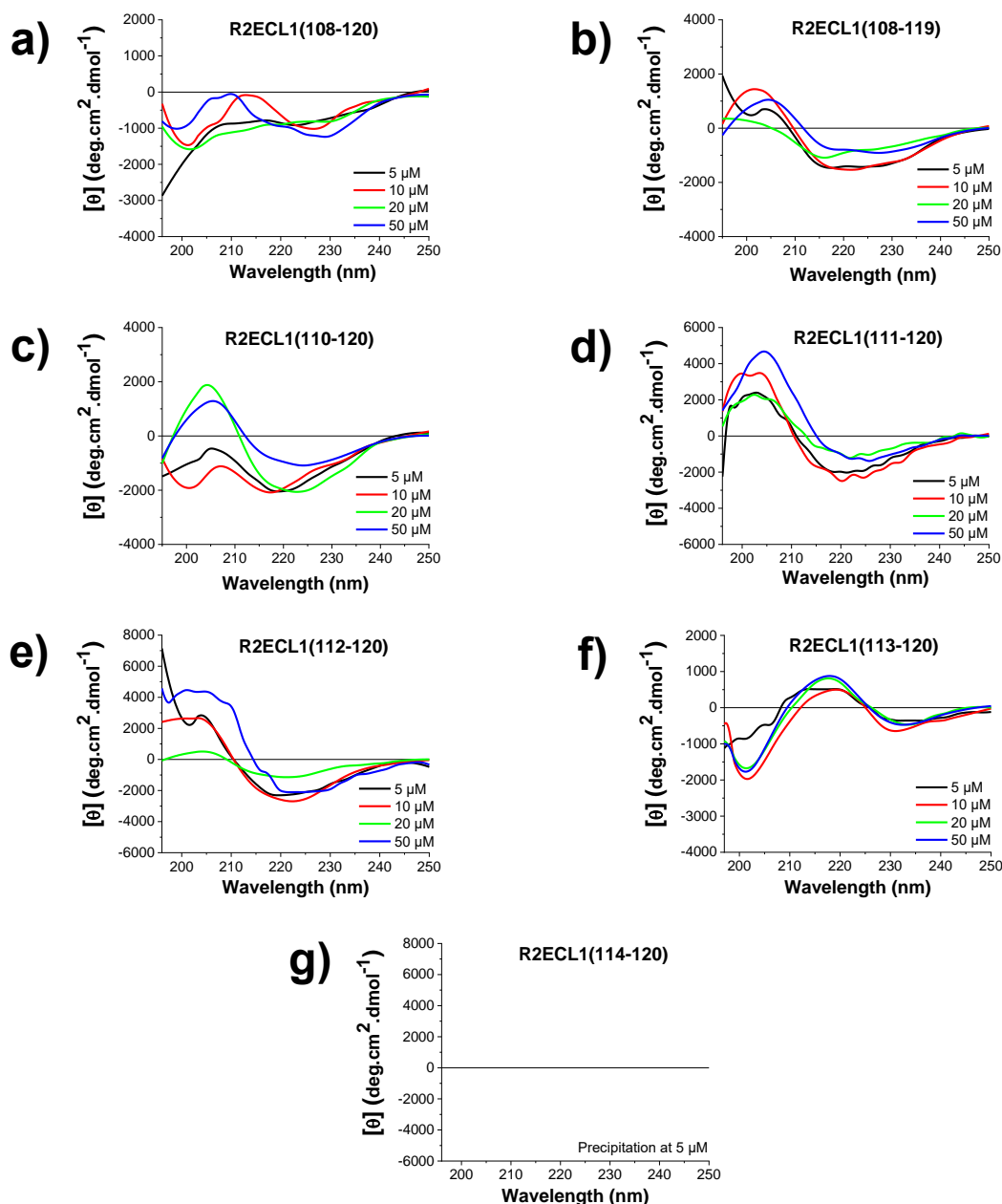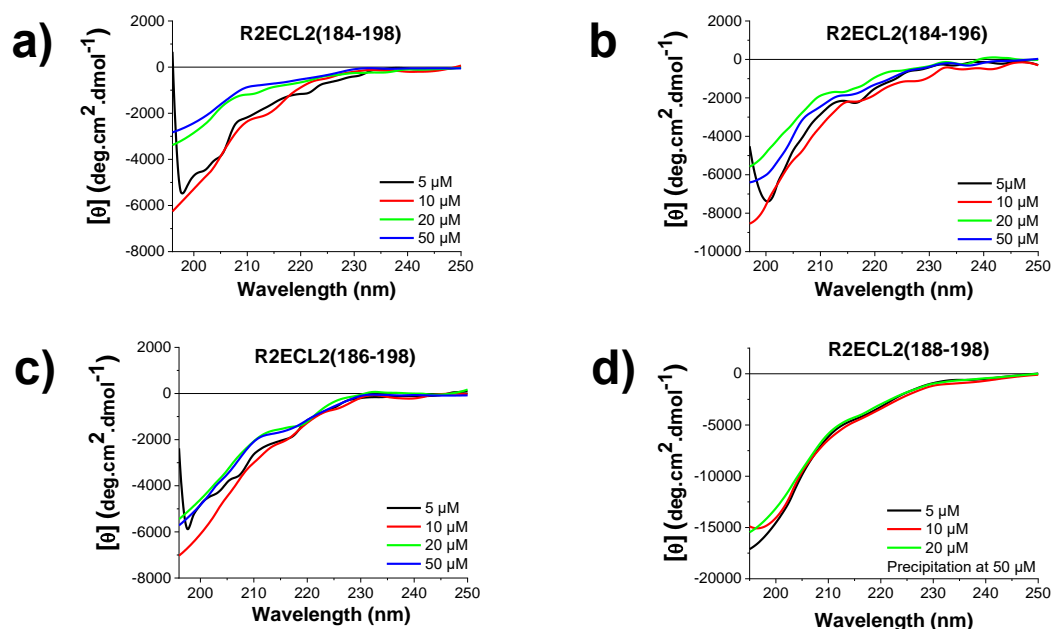
Figure 98. Spectra of R2ECL1(108-120) and its shorter analogs in various concentrations for the determination of the conformation, as determined by far-UV CD spectroscopy. a, b, c, d, e, f, g CD spectra of R2ECL1(108-120) (a), R2ECL1(108-119) (b), R2ECL1(110-120) (c), R2ECL1(111-120) (d), R2ECL1(112-120) (e), R2ECL1(113-120) (f) and R2ECL1(114-120) (g) at increasing concentrations at final measuring conditions of aqueous 1×b, pH 7.4, containing 1% HFIP. Mean residue ellipticity (MRE) plotted over the wavelength between 196 and 250 nm for a, d, e and 195 and 250 nm for b, c, f.

Further secondary structure studies were carried out for the peptide that contained the sequence between the 184th and 198th residue of CXCR2, derived by the second extracellular loop and abbreviated as R2ECL2(184-198). The 15-mer exhibited random coil characteristic spectra with strong minima below 200 nm. Peptide remained soluble until 50 µM, but its notable decrease in the signal intensity at 20 and 50 µM may be indicative of oligomerization in this concentration range (Figure 99a). The elimination of the C-terminus Y197 and E198 did not affect the secondary structure or the solubility of the peptide. R2ECL2(184-196) exposed strong negative minima with MRE values equal to -8000 deg·cm^2·dmol^{-1} for 5 and 10 µM below 200 nm. At the same wavelength

region and for the spectra between 20 and 50 µM, the signal intensity was reduced by approximately 25% (Figure 99b). The N-terminus shortened analog R2ECL2(186-198) did not differentiate from the previous analogs without having any ordered structure. Interestingly, the peptide reached -6000 deg·cm^2·dmol^{-1} at its minima below 200 nm and did not aggregate until 50 µM (Figure 99c). A further shortening led to the R2ECL2(188-198) analog, with 3-fold increased MRE values at its random-coil indicative minima in the 5-20 µM range before its precipitation at 50 µM (Figure 99d).

Figure 99. Spectra of R2ECL2(184-198) and its shorter analogs in various concentrations for the determination of the conformation, as determined by far-UV CD spectroscopy. a, b, c, d CD spectra of R2ECL2(184-198) (a), R2ECL2(184-196) (b), R2ECL2(186-198) (c) and R2ECL2(188-198) (d) at increasing concentrations at final measuring conditions of aqueous 1×b, pH 7.4, containing 1% HFIP. Mean residue ellipticity (MRE) plotted over the wavelength between 196 and 250 nm for a, c, 197 and 250 nm for b and 195 and 250 nm.

4.4.3 Determination of binding affinities to MIF via fluorescence spectroscopy

CXCR2 and MIF share a binding interface that involves extracellular loop 1 and 2 segments, among others [97]. However, the precise dissociation constants of the interaction between the loops and the atypical chemokine remained unidentified. Moreover, data about the hot spot region of the ectodomain are still missing. To investigate their binding affinities, MIF was conjugated with Alexa-488 and titrated with various extracellular loop peptide fragments. Titrations were followed using fluorescence spectroscopy under the already applied conditions for the CXCR4 mimic studies. As previously, the decreased fluorescence emission of Alexa-488-MIF over the subsequent addition of an increased amount of peptide led to the separation between the unbound and bound state. Fluorescence spectroscopic titrations of R2ECL1(108-120) showed an app. K_d of 255.7 ± 85.0 nM (Figure 100a, b). The elimination of K120 led to R2ECL1(108-119) with a reduced affinity and an app. K_d above 2500 nM (Figure 100c, d). Switching to N-terminus shortening to determine the core region of R2ECL1, R2ECL1(110-120) and R2ECL1(111-120) showed app. K_{ds} above 10000 nM and equal to 586.4 ± 74.7 nM, respectively (Table 46, Figure 100e-h).
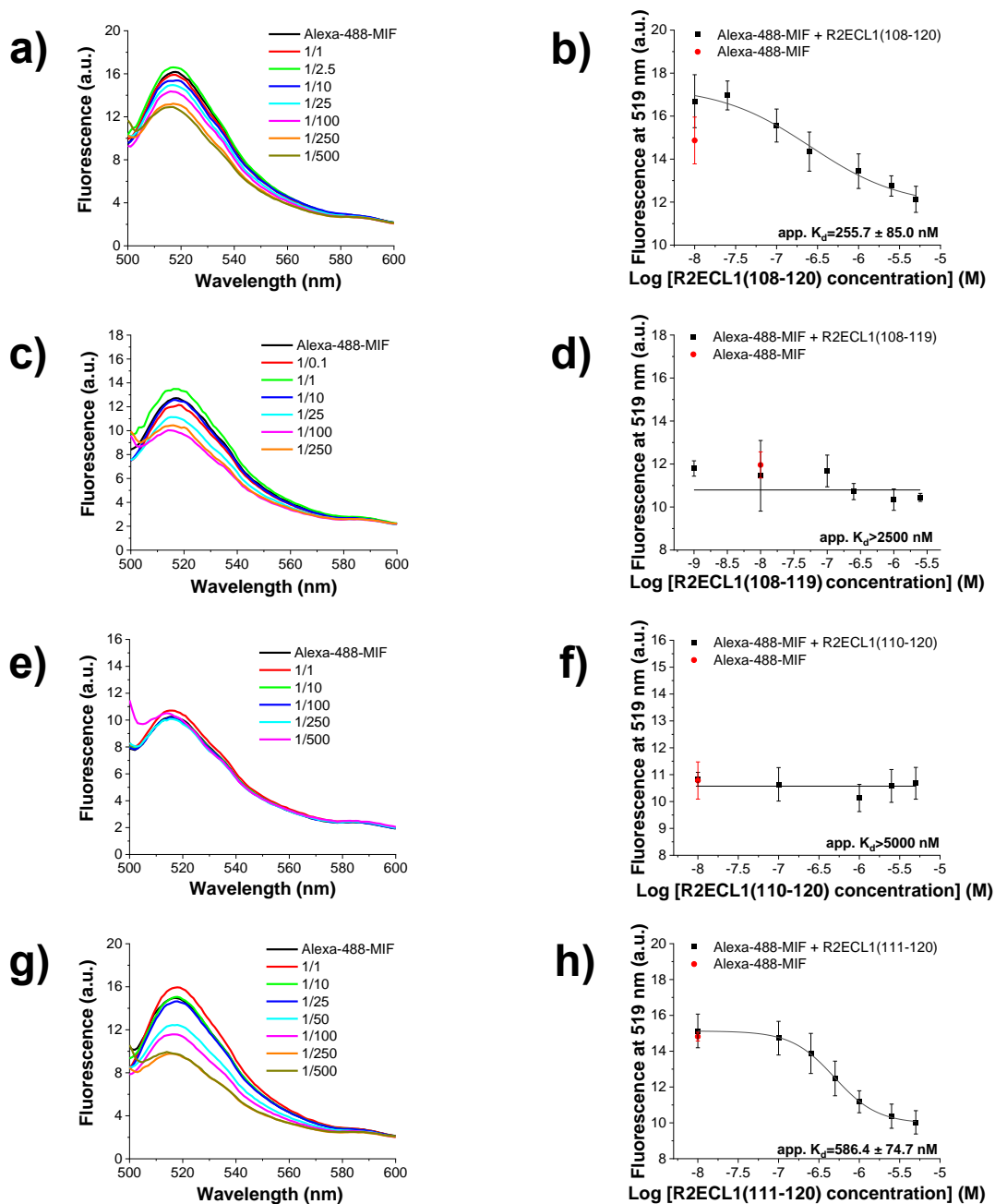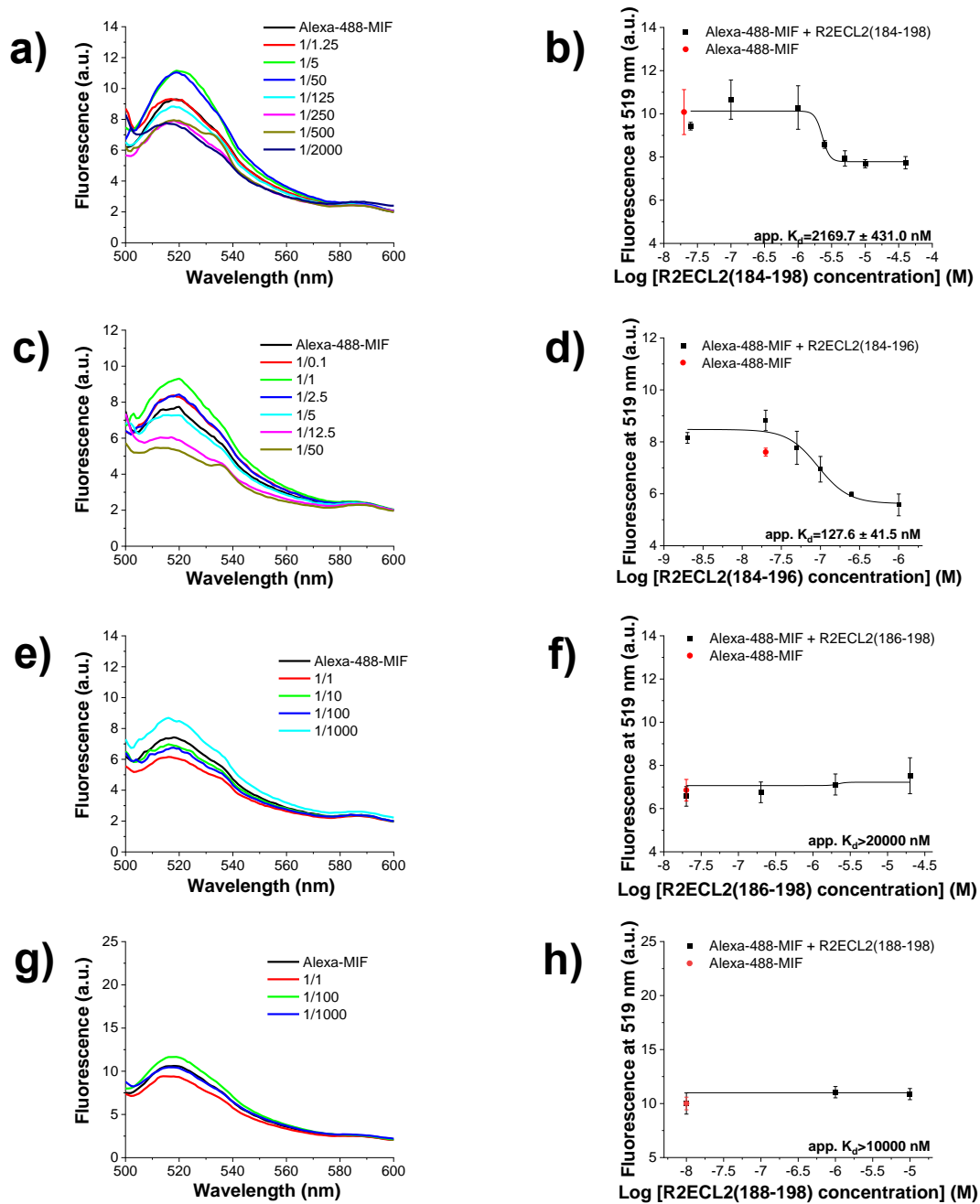
Figure 100. Fluorescence spectroscopic titrations of Alexa-488-MIF with R2ECL1(108-120), R2ECL1(108-119), R2ECL1(110-120) and R2ECL1(111-120) for the determination of apparent affinities (app. K_{ds}). a, c, e, g Fluorescence spectra between 500 and 600 nm of Alexa-488-MIF (10 nM) alone and its mixtures with various amounts of R2ECL1(108-120) (a), R2ECL1(108-119) (c), R2ECL1(110-120) (e) and R2ECL1(111-120) (g); the molar ratios of Alexa-488-MIF/peptides are indicated. **b, d, f, h** Binding curves derived from the fluorescence emission at 519 nm of Alexa-488-MIF (10 nM) at different concentrations of R2ECL1(108-120) (b), R2ECL1(108-119) (d), R2ECL1(110-120) (f) and R2ECL1(111-120) (h). Data shown are means (±SD) from three independent titration experiments which were performed in aqueous 1×b, pH 7.4, containing 1% HFIP.

Likewise, the generated R2ECL1(112-120) after the subtraction of G111 had a very similar affinity with app. K_d equal to 564.7 ± 167.7 nM (Figure 101a, b). Contrariwise, Alexa-488-MIF failed to bind to shorter analogs R2ECL1(113-120) and R2ECL1(114-120) until 10000 and 1000 nM of the titrant, respectively. These findings suggested weak binding between the latest tested R2ECL1 analogs and Alexa-488-MIF and dissociation constants above those concentrations (Table 46, Figure 101c-f).

174
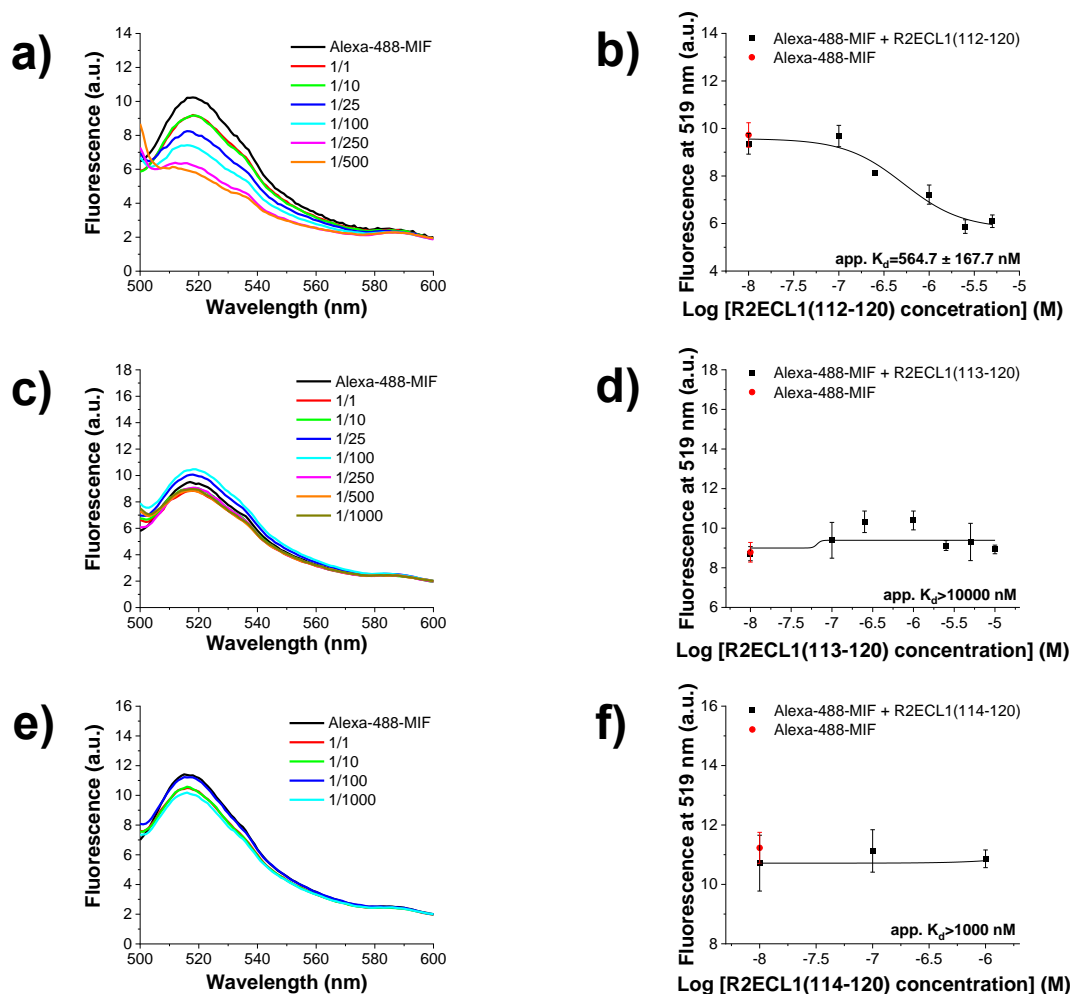
Figure 101. Fluorescence spectroscopic titrations of Alexa-488-MIF with R2ECL1(112-120), R2ECL1(113-120) and R2ECL1(114-120) for the determination of apparent affinities (app. K_{ds}). a, c, e Fluorescence spectra between 500 and 600 nm of Alexa-488-MIF (10 nM) alone and its mixtures with various amounts of R2ECL1(112-120) (a), R2ECL1(113-120) (c) and R2ECL1(114-120) (e); the molar ratios of Alexa-488-MIF/peptides are indicated. **b, d, f** Binding curves derived from the fluorescence emission at 519 nm of Alexa-488-MIF (10 nM) at different concentrations of R2ECL1(112-120) (b), R2ECL1(113-120) (d) and R2ECL1(114-120) (f). Data shown are means (±SD) from three independent titration experiments which were performed in aqueous 1×b, pH 7.4, containing 1% HFIP.

The app. K_d of Alexa-488-MIF to R2ECL2(184-198) was found in the micromolar range, and particularly equal to 2169.7 ± 431.0 nM (Figure 102a, b). The elimination of the two C-terminus residues Y197 and E198, led to a 17-fold improved affinity for R2ECL2(184-196) with an app. K_d at 127.6 ± 41.4 nM (Figure 102c, d). On the other hand, keeping untouched the C-terminus of the native peptide and eliminating the first two residues on the N-terminus had the opposite results. R2ECL2(186-198) and Alexa-488-MIF did not have a significant binding and the app. K_d was estimated to be above 20000 nM (Figure 102e, f). Similar findings were determined for the shorter analog R2ECL2(188-198) and no change in the fluorescence emission of the labeled analyte was detected until 10000 nM of the peptide titrant (Table 46, Figure 102g, h). Summarized results and comparison of the binding affinities of the peptides are described in 'Discussion' (see 5.4).

Figure 102. Fluorescence spectroscopic titrations of Alexa-488-MIF with R2ECL2(184-198), R2ECL2(184-196), R2ECL2(186-198) and R2ECL2(188-198) for the determination of apparent affinities (app. K_{ds}). a, c, e, g Fluorescence spectra between 500 and 600 nm of Alexa-488-MIF (20 nM for a, c, e, 10 nM for g) alone and its mixtures with various amounts of R2ECL2(184-198) (a), R2ECL2(184-196) (c), R2ECL2(186-198) (e) and R2ECL2(188-198) (g); the molar ratios of Alexa-488-MIF/peptides are indicated. **b, d, f, h** Binding curves derived from the fluorescence emission at 519 nm of Alexa-488-MIF (20 nM for b, d, f, 10 nM for h) at different concentrations of R2ECL2(184-198) (b), R2ECL2(184-196) (d), R2ECL2(186-198) (f) and R2ECL2(188-198) (h). Data shown are means (±SD) from three independent titration experiments which were performed in aqueous 1×b, pH 7.4, containing 1% HFIP.

Table 46. Apparent affinities (app. K_{ds}) of interaction between Alexa-488-MIF and R2ECL1 or R2ECL2 analogs, as determined by fluorescence spectroscopic titrations.

R2ECL1 or R2ECL2 analogs	Alexa-488-MIF/R2ECL1 or R2ECL2 analog app. K_d (±SD) (nM)[a]
R2ECL1(108-120)	255.7 (±85.0)
R2ECL1(108-119)	>10000
R2ECL1(110-120)	>10000
R2ECL1(111-120)	586.4 (±74.7)
R2ECL1(112-120)	564.7 (±167.7)
R2ECL1(113-120)	>10000
R2ECL1(114-120)	>1000
R2ECL2(184-198)	2169.7 (±431.0)[b]
R2ECL2(184-196)	86.8 (±22.8)[b]
R2ECL2(186-198)	>10000[b]
R2ECL2(188-198)	>10000

[a] App. K_{ds}, are means (±SD) from three independent titration experiments which were performed in aqueous 1×b, pH 7.4, containing 1% HFIP. Titrations were applied with 10 nM of Alexa-488-MIF, except for [b], in which Alexa-488-MIF was used at 20 nM.

4.4.4 Conclusions of SAR studies on ECL1 and ECL2 analogs of CXCR2

CXCR2 ectodomain-derived analogs were developed, and their biophysical and binding properties were determined to narrow down the interaction interface of the receptor with MIF. Despite of their limited size, some extracellular loop 1 analogs had ordered structure. Particularly, the CD spectra of R2ECL1(111-120), R2ECL1(112-120), R2ECL1(108-119), and partially R2ECL1(110-120) were indicative of β-sheet, while the rest were mainly random coil. The ordered structure of specific fragments might be associated with their aromatic and hydrophobic composition and the elimination of charged or polar residues in the sequence. R2ECL2(184-198) and its analogs were unordered and remained soluble until at least 50 μM, as well as the R2ECL1(108-120) analogs, except for R2ECL1(114-120). Binding studies uncovered R2ECL1(112-120) and R2ECL2(184-196) as the hot spot regions with the same and remarkably higher affinity to MIF than R2ECL1(108-120) and R2ECL2(184-198), respectively and could be prioritized for future studies (Table 47).

Table 47. Defined biophysical properties of R2ECL1(108-120) or R2ECL2(184-198) analogs by CD spectroscopy and their apparent affinities (app. K_{ds}) of interaction with Alexa-488-MIF, as determined by fluorescence spectroscopic titrations.

Peptide	Secondary structure	Precip. (μM)	Alexa-488-MIF/peptide app. K_d (±SD) (nM)[a]
R2ECL1(108-120)	r.c. [c] + β-sheet	> 50	255.7 (±85.0)
R2ECL1(108-119)	β-sheet	> 50	>10000
R2ECL1(110-120)	r.c. [c] + β-sheet	> 50	>10000
R2ECL1(111-120)	β-sheet	> 50	586.4 (±74.7)
R2ECL1(112-120)	β-sheet	> 50	564.7 (±167.7)
R2ECL1(113-120)	r.c. [c]	> 50	>10000
R2ECL1(114-120)	n.d. [d]	5	>1000
R2ECL2(184-198)	r.c. [c]	> 50	2169.7 (±431.0)[b]
R2ECL2(184-196)	r.c. [c]	> 50	86.8 (±22.8)[b]
R2ECL2(186-198)	r.c. [c]	> 50	>10000[b]
R2ECL2(188-198)	r.c. [c]	> 50	>10000

[a] App. K_{ds}, are means (±SD) from three independent titration experiments which were performed in aqueous 1×b, pH 7.4, containing 1% HFIP. Titrations were applied with 10 nM of Alexa-488-MIF, except for [b], in which Alexa-488-MIF was used at 20 nM. [c] :r.c., random coil [d]: n.d., non-determined

4.5   CXCR2 and CXCR4 chimeric receptor mimics (CRMs)

MIF is classified as a cytokine with proatherogenic chemokine-like functions through the chemokine receptors CXCR2 and CXCR4 [77]. CXCR4 mimics were developed, and the hot spot regions of the CXCR2 ectodomains were uncovered in previous chapters. Herein, it was aimed to conjugate the binding interface of CXCR2 on ngms, the newer and shorter CXCR4 mimics, and the generation of chimeric receptor mimics (CRMs) of both MIF receptors. Particularly, CRMs were synthesized with the introduction of the R2ECL2(184-196) segment via a (12 Ado)-G tandem to two ngms bonded with non-natural amino acids (ngm-L4, -L5) and two with natural charged ones (ngm-LD3, -LK3). The dual mimic should distinguish between the different pathways and have enhanced binding to MIF without interfering with the atheroprotective CXCL12/CXCR4 axis (Scheme 17).
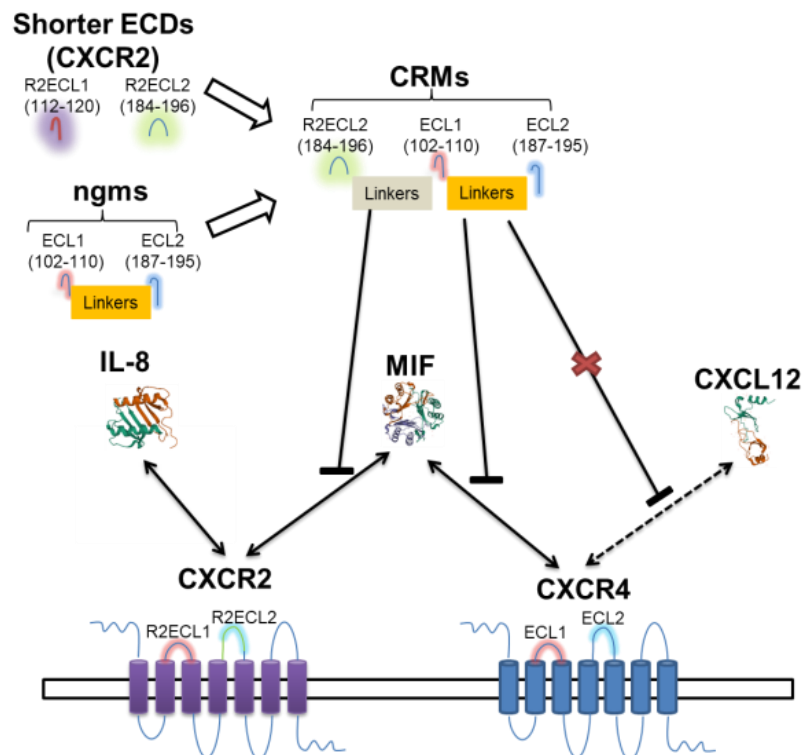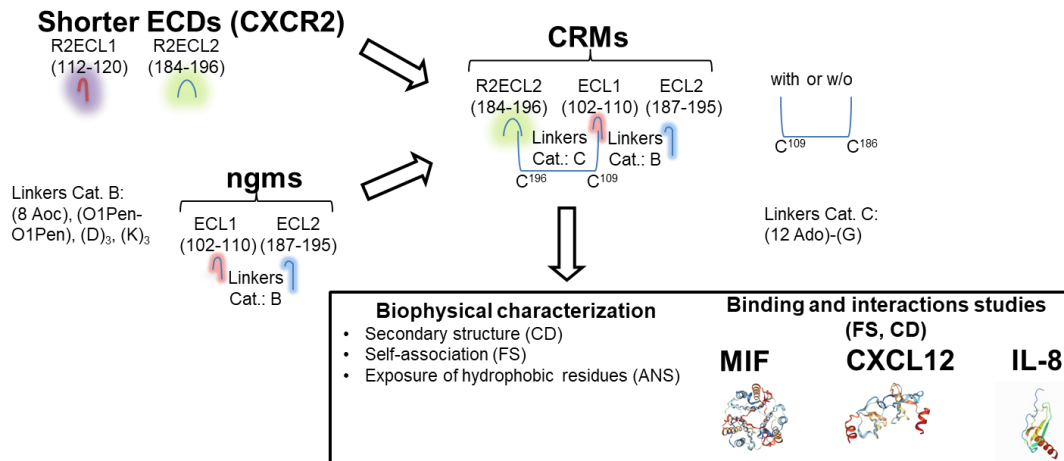

Scheme 17. Development of CRMs and the desired blockade of the atheroprogressive pathways.
The chimeric receptor mimics (CRMs) of CXCR2 and CXCR4 were developed after linkage of fragment 184-196 derived by extracellular loop 2 of CXCR2, abbreviated as R2ECL2(184-196) with selected ngms. The newer mimics aimed to inhibit the atheroprogressive pathways (solid line) MIF/CXCR4 and MIF/CXCR2 and spare the cardiobeneficial CXCL12/CXCR4. The IL-8/CXCR2 pathway might be desired to be blocked in future studies, since it has disease-exacerbating signalling but is mediating essential functions, too. The chemokines are demonstrated based on their published structures (MIF:1MIF, CXCL12:3HP3, IL-8:1IL8) [83] [101] [158].

CRMs were synthesized and obtained pure after HPLC and MALDI-TOF-MS analysis and were tested both in reduced, and disulfide bridged form (C196-C109). The first studies on CRMs involved its biophysical characterization, as previously for msR4Ms and ngms. Mainly, CD spectroscopy was applied to estimate secondary structure and fluorescence spectroscopy to determine the hydrophobicity content of the surface and the self-assembly of the mimics. The latest technique was used to calculate the dissociation constants between CRMs and MIF, CXCL12, and IL-8 and to evaluate its specificity (Scheme 18).

Scheme 18. Overview of the development and studies of CRMs. The development of chimeric receptor mimics (CRMs) and the applied of linkers are shown, while the CRMs were tested both in reduced and oxidized form. Studies of CRMs aimed on the determination of their biophysical properties and their binding affinities with the CXCR2 and CXCR4 ligands. The chemokines are demonstrated based on their published structures (MIF:1MIF, CXCL12:3HP3, IL-8:1IL8) [83] [101] [158].

4.5.1 Design of CRMs

CXC chemokine receptors share relatively high sequence similarity and homology, especially in the transmembrane helices 1, 2, 3, 4, 6, the intracellular loops 1 and 2, and the extracellular loop 1. The two MIF receptors CXCR2 and CXCR4, have overall high homology with a 38.6% similarity and 31.9% identity in their entire sequences (Figure 103a). Both receptors interact with MIF via their N-terminus, ECL1 and ECL2, while ECL3 is involved only in the MIF/CXCR2 interaction [97] [98]. Interestingly, a high similarity was observed for the ECL1 domain but not for ECL2 and N-terminus of the MIF receptors. Size optimized studies revealed ECL1 segments 112-120 of CXCR2 and 102-110 of CXCR4, and ECL2 segments 184-196 of CXCR2 and 187-195 of CXCR4 as the core regions for the interaction with MIF. On the one hand, the minimized ECL1 segments of the receptors showed a remarkably high homology, with a 77.7% identity in the residues. On the other hand, the size optimized analogs of ECL2 did not share any significant sequence similarity (Figure 103b).
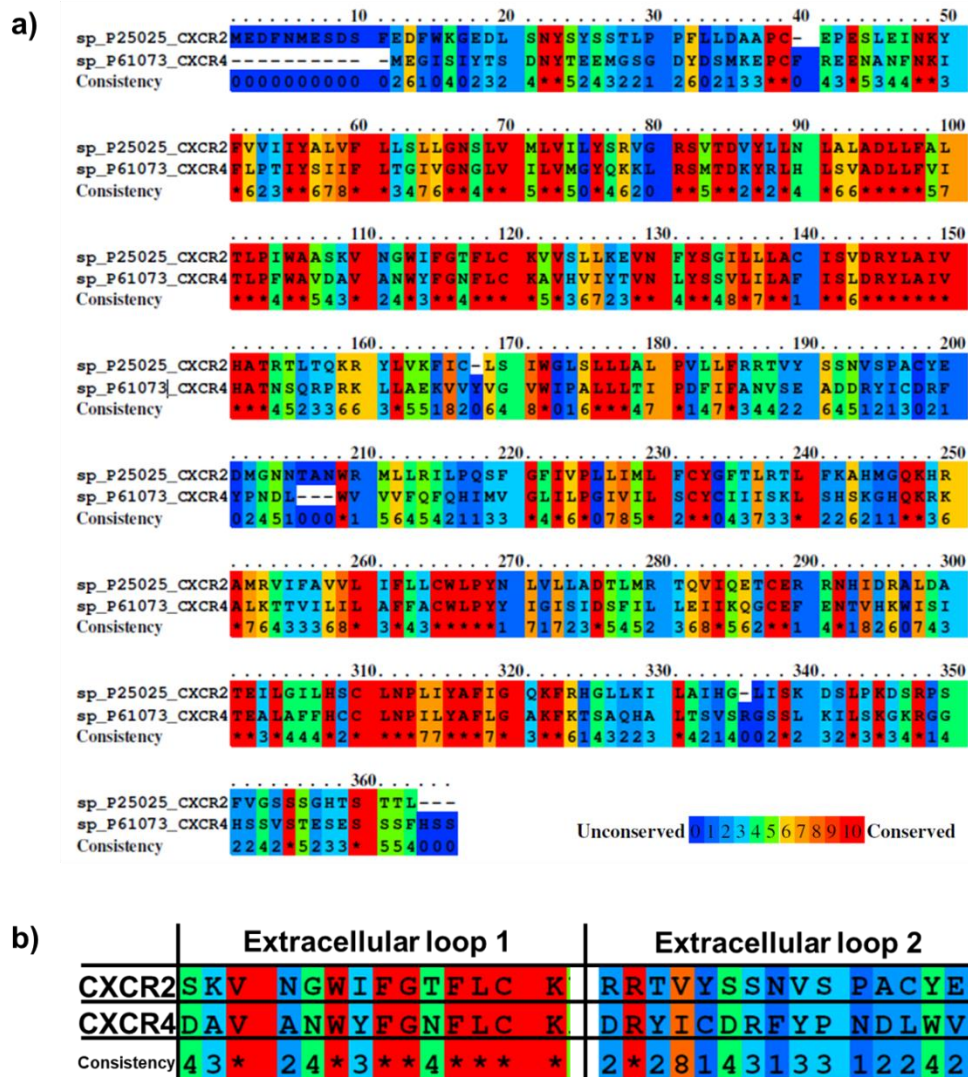
Figure 103. Sequence alignment between CXCR2 and CXCR4 by PRofile ALIgNEment (PRALINE). a Scanning of the full CXCR2 and CXCR4 sequence and evaluation of the consistency between their residues. **b** Similar to a but for the binding epitopes of CXCR2 and CXCR4 with MIF and in particular for CXCR2 the peptides R2ECL1(108-120), including S107 for the perfomance of sequence alignment, R2ECL2(184-198) and for CXCR4 the ECL1 and ECL2. The applied programm was the PRALINE (https://www.ibi.vu.nl/programs/pralinewww/) with the conservation levels being shown according to the transition colour code (blue: unconserved, red: conserved) with the following settings: Exchange weights matrix: BLOSUM62, Associated gap penalties: 12 Open 1 Extension Progressive alignment strategy: PSI-BLAST pre-profile processing (Homology-extended alignment) PSI-BLAST Iterations:3, E-value cut-off of: 0.01 DB:NR [293].

Based on the high identity of the extracellular loop 1 of CXCR2, -R4, and the previously generated CXCR4 mimics, i.e. the ngms, we aimed to develop chimeric receptor mimics (CRMs) that will imitate the ectodomain binding regions of both receptors. To develop the chimeric mimics, it was desired to follow the same strategy as applied to design msR4Ms and ngms in chapters 4.1.1. and 4.3.1. and study the regions of interest in a CXCR2 model. However, at that moment, there was neither X-ray nor NMR structure available of the receptor. An alternative was to apply CXCR1 for the studies, which shares with CXCR2 75% sequence identity all over their sequence. In particular, R2ECL1(108-120) and the respective R1ECL1(99-111) segment of CXCR1 have an identical sequence. Between R2ECL2(184-198)/R1ECL2(175-189) and R2ECL2(184-196)/R1ECL2(175-187) the sequence identity was 46.7% and 38.5%, respectively (Figure 104).

180
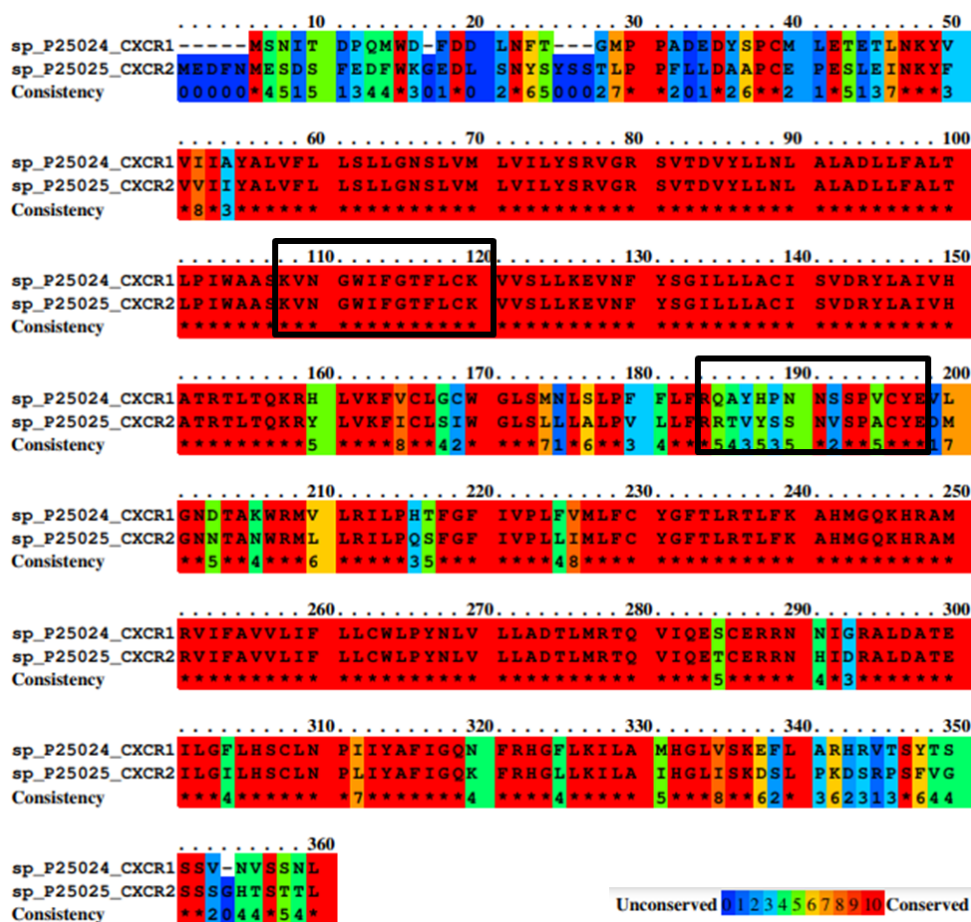
Figure 104. Sequence alignment between CXCR1 and CXCR2 by PRofile ALIgNEment (PRALINE). Scanning of the full CXCR1 and CXCR2 sequence and evaluation of the consistency between their residues. In first box is shown the R2ECL1(108-120) and the 99-111 (R1ECL1) region, while in the second box they are included the sequences of R2ECL2(184-198) and 175-189 (R1ECL2) The applied programm was the PRALINE (https://www.ibi.vu.nl/programs/pralinewww/) with the conservation levels being shown according to the transition colour code (blue: unconserved, red: conserved) with the following settings: Exchange weights matrix: BLOSUM62, Associated gap penalties: 12 Open 1 Extension Progressive alignment strategy: PSI-BLAST pre-profile processing (Homology-extended alignment) PSI-BLAST Iterations:3, E-value cut-off of: 0.01 DB:NR [293].

To overcome the limitation with the lack of CXCR2 structure, a solid-state NMR-derived model of its adjacent receptor CXCR1 was applied instead for developing CRMs. Segments R1ECL1(99-111) and R1ECL2(175-189) were the homologues of R2ECL1(108-120) and R2ECL2(184-198) (Scheme 19a-c). The W103-C187 distance was equal to 1.761 nm, and it was hypothesized that it is similar to the one between the respective residues W112 and C196 of CXCR2 (Scheme 19d). Next, a similar design strategy for msR4Ms and ngms was applied. In particular, it was designed that the sequence of ngms would be taken as the basis and elongated with the introduction of linkage chemistry on the N-terminus and the subsequent conjugation of the MIF binding region for CXCR2, R2ECL2(184-196). The other binding domain of the receptor, R2ECL1(112-120), was not introduced since its 77.7% identical to the ECL1(102-110) segment of CXCR4, which is present in the sequence of ngms and may mimic the extracellular loop 1 of both receptors. The linkage between the 13-mer and the ngms, ECL1(102-110)-Linkers-ECL2(187-195), was applied to simulate the distance in the CXCR2 between the C196 and the W112. Of note, W112 of CXCR2 is the homolog of W102 of CXCR4, the N-terminus residue of ECL1(102-110), and ngms (Scheme 19a).

Molview was applied to estimate the length of possible linkers, as previously. The 12 Ado-G tandem was estimated to be 1.582 nm, which is close to the 1.761 nm of C196-W112 and thus introduced as linkers between R2ECL2(184-196) and the N-terminus of ngm-L4, -L5, -LD3, and –LK3 for the generation of the respective CRM-1/L4, /L5, /LD3 and /LK3 (Scheme 19e, f). According to CXCR1, CXCR4, and other chemokine receptor models, there is a disulfide linkage between the cysteines of ECL1 and ECL2. In all sequences of CRMs, there is a C109 located in the ECL1(102-110) and a C196 in the R2ECL2(184-196), but none in the ECL2(187-195). An additional disulfide bond was formed between the two cysteines of CRMs and resulting to their respective oxidized analogs CRM-1/L4ox, /L5ox,/ LD3ox, and /LK3ox (Scheme 19f).
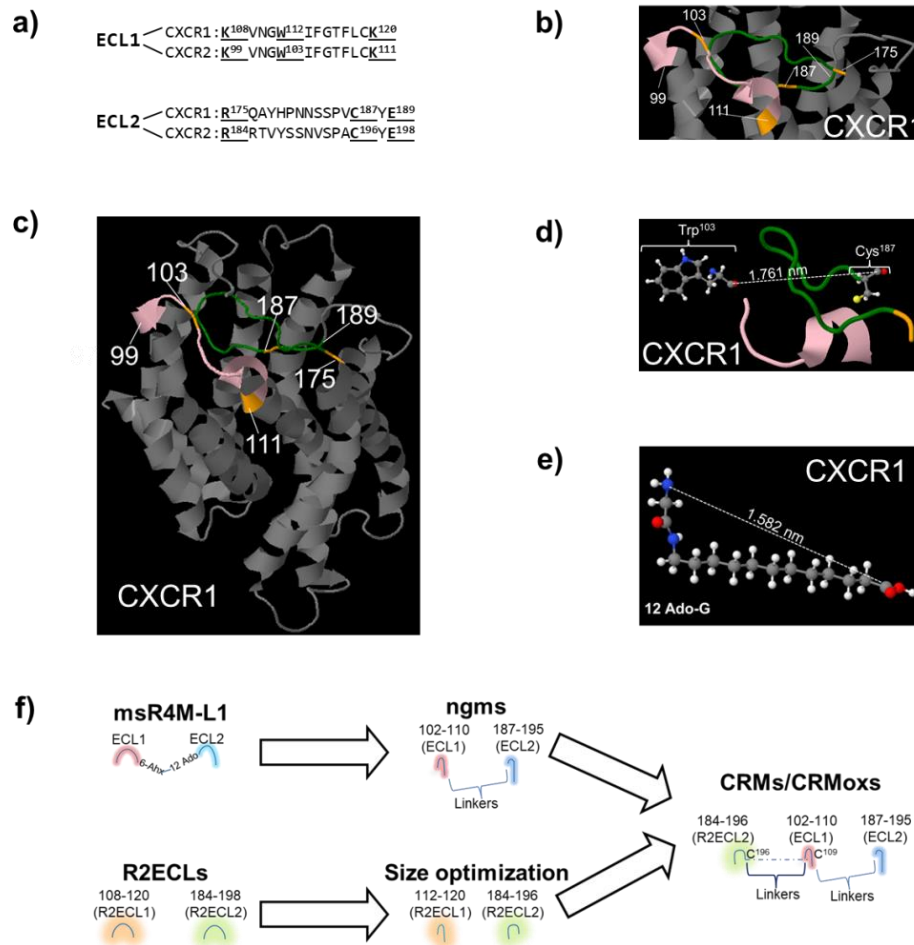
Scheme 19. Applied design strategy for the design of CRMs. a Sequences of CXCR2 ectodomain peptides R2ECL1(108-120) and R2ECL2(184-198) and their homologous peptides 99-111 (R1ECL1) and 175-189 (R1ECL2) of CXCR1. The homologous residues K108 (CXCR2)/K99 (CXCR1), W112 (CXCR2)/W103 (CXCR1) and K120 (CXCR2)/K111 (CXCR1) of ECL1 domain and R175 (CXCR2)/R184 (CXCR1), C187 (CXCR2)/C196 (CXCR1) and E189 (CXCR2)/E198 (CXCR1) of ECL2 domain are bolded and underlined. **b** Ribbon structure of human CXCR1 with highlighted the regions of 99-111 (R1ECL1) in pink and 175-189 (R1ECL2) in green. Residues of CXCR1 W103, K111, R175 and C187 are colored in yellow and the N- and C-terminus of 99-111 (R1ECL1) and 175-189 (R1ECL2) are indicated. **c** Zoomed out of **b**. **d** Zoomed view of **b** focusing on 103-111 (R1ECL1) and 175-187 (R1ECL2) and showing residues W103 and C187 as spheres (blue: nitrogen, red:oxygen, yellow: sulfur, grey: carbon, white: hydrogen). The measured length (1.761 nm) is between the C-terminus of C187 and the N-terminus of W103. **e** Estimated lengths of the tandem of 12 Ado and G linker that was introduced between R2ECL2(184-196) [294] and ngms for the development of CRM-1 mimics. **f** Applied design strategy for the evolution of CRMs. R2ECL2(184-196) was N-terminusly conjugated on ngms with the introduced linkers to mimic the distance of C196 and W112 of CXCR2, based on the findings on the respective segments on the homologous receptor CXCR1. NMR structure for b, c and d was obtained from protein data bank (PDB code: 2LNL) as published by Ho Park and colleagues and visualized by Jmol (http://www.jmol.org) [294]. Linkers for d and e were designed on Molview and visualized by applying Jmol as the engine.

4.5.2 Synthesis, purification and mass determination of CRMs

CRMs were synthesized following the already described principles of Fmoc-SPPS, as described previously, and W195 was loaded on Rink resin. After determining its substitution level, the synthesis was continued further step by step, either manually or by the automatic synthesizer. Depending on the position, the amino acid may be coupled twice or three times with conditions varying for the activator, the equivalents of the base, and the time as described in Scheme 20. For residues 194 and 195, the N-terminus protection was removed with the normal protocol. Though, after the coupling of D193 and until the end of the synthesis, the Fmoc group was removed using the 'Short HOBt protocol' to exclude any possible Asi formation. All CRMs were side-chain deprotected and cleaved from the resin with Reagent K and lyophilized before their purification via RP-HPLC. Prior to their injections, crudes of reduced CRMs were dissolved in TFA/80% B, while for the oxidized analogs, the reduced crudes were dissolved in 3M GdnCl, 40% DMSO and oxidized for 2 h in RT. Peptides were dissolved in MALDI solution C (matrix) and analyzed via MALDI-TOF-MS without any significant difference between the theoretical and the expected masses, while their yield varied from 6.5 to 21.4% (Tables 48, 49 and Figures 105, 106).
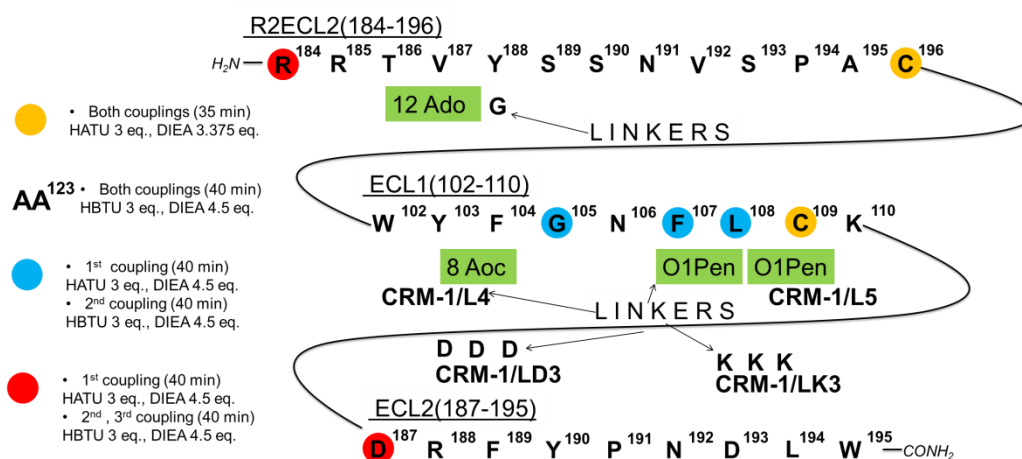
Scheme 20. Conditions of couplings for the syntheses of CRMs. All amino acids were coupled with 3 equivalents (eq.), based on the substitution level that was determined after the load of the first amino acid on Rink-resin. Equivalents of activator and base, together with the coupling time may vary, as indicated.

**Table 48.** Sequences and abbreviation of CRMs.

Sequence	Peptide abbreviation
R2ECL2(184-196)-12 Ado-G-ngm-L4	CRM-1/L4
184-196 (R2ECL2)-12 Ado- G-ngm-L4 C196 ——————— C109	CRM-1/L4ox
R2ECL2(184-196)-12 Ado-G-ngm-L5	CRM-1/L5
184-196 (R2ECL2)-12 Ado- G-ngm-L5 C196 ——————— C109	CRM-1/L5ox
R2ECL2(184-196)-12 Ado- G-ngm-LD3	CRM-1/LD3
184-196 (R2ECL2)-12 Ado- G-ngm-LD3 C196 ——————— C109	CRM-1/LD3ox
R2ECL2(184-196)-12 Ado-G-ngm-LK3	CRM-1/LK3
184-196 (R2ECL2)-12 Ado- G-ngm-LK3 C196 ——————— C109	CRM-1/LK3ox

Table 49. Characterization of synthesized CRMs by RP-HPLC and MALDI-TOF-MS.

Peptide abbreviation	HPLC Pr.No.	t_R (min)[b]	Yield[c]	[M+H]$^+$ expected[d]	[M+H]$^+$ found[d]
CRM-1/L4	2	30.42	6.5	4199.16	4199.80
CRM-1/L4ox	2	33.22	10.7	4197.16	4198.61
CRM-1/L5	1	20.18	18.7	4260.15	4260.67
CRM-1/L5ox	2	31.62	18.6	4258.15	4258.76
CRM-1/LD3	1	21.52	16.0	4403.14	4403.21
CRM-1/LD3ox	2	32.17	21.4	4401.14	4400.97
CRM-1/LK3	1	20.85	15.7	4442.34	4442.49
CRM-1/LK3ox	2	29.28	16.8	4440.34	4440.96

Peptides were dissolved and analyzed by MALDI-TOF-MS in MALDI solution C (matrix); [a] Peptides were synthesized with free amino-N-terminus and amidated C-terminus; [b] HPLC retention time of the pure product; the stationary phase was a tandem of Reprosil Gold 200 C18 columns (250 and 30 mm length, 8 mm internal diameter,10 µm particle size); [c] % yield with regard to crude peptide after cleavage; [d] monoisotopic molar mass with an additional hydrogen [M+H]$^+$.
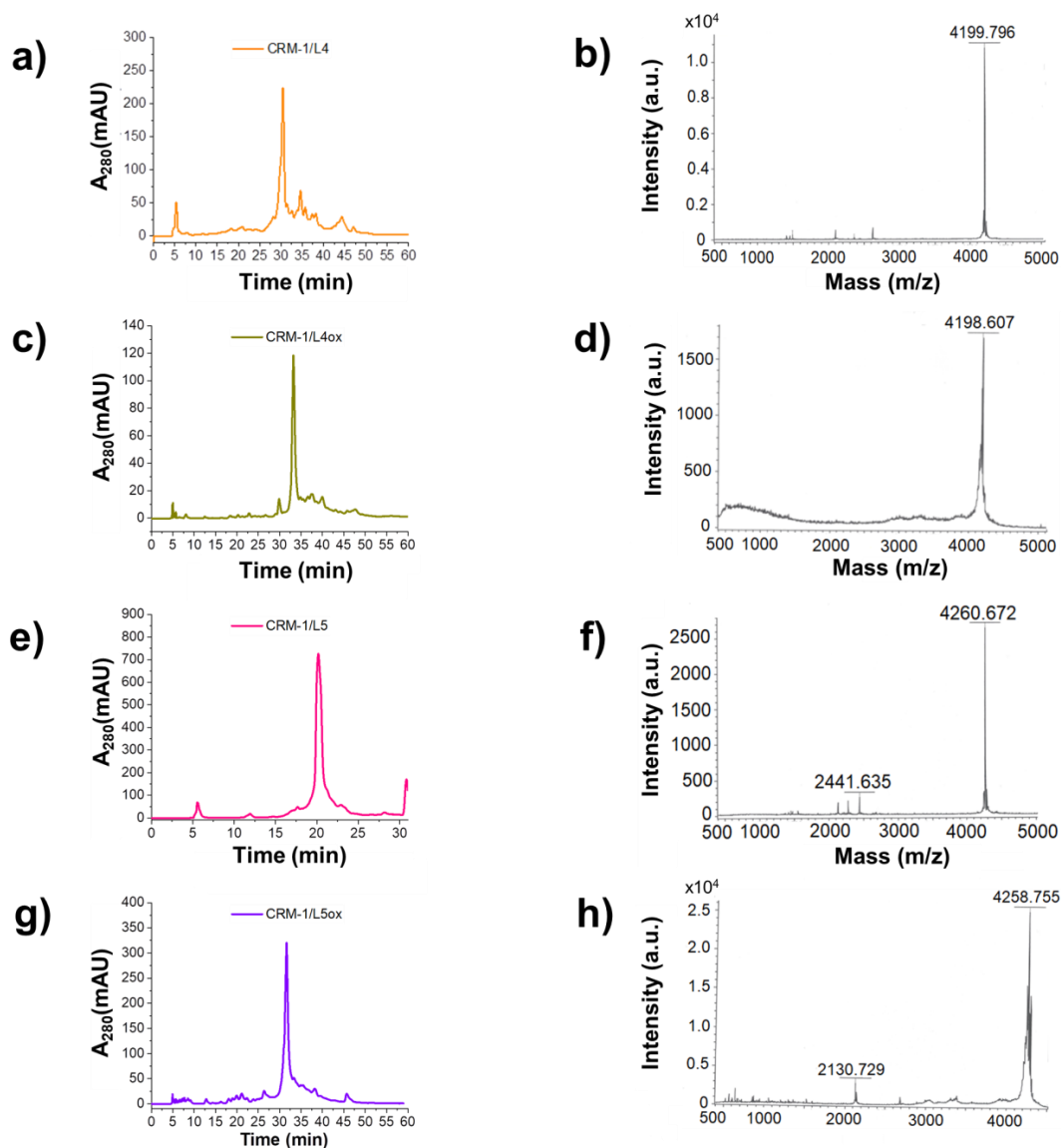
Figure 105. HPLC purification of CRM-1/L4, CRM-1/L5 and their oxidized analogs and verification of their purity by MALDI. a, c, e, g Representative C18 HPLC chromatogram (absorbance at 280 nm) of crude purified CRM-1/L4, CRM-1/L4ox, CRM-1/L5 and CRM-1/L5ox with respective retention times: a) 30.42 min, c) 33.22 min, e) 20.18 min and g) 31.62 min, following SPPS and cleavage. **b, d, f, h** MALDI-TOF-MS spectra of HPLC-purified CRM-1/L4 (b), CRM-1/L4ox (d), CRM-1/L5 (f) and CRM-1/L5ox (h) with respective experimental determined masses $[M+H]^+$: b) 4199.796 Da, d) 4198.607 Da, f) 4260.672 Da and h) 4258.755 Da.
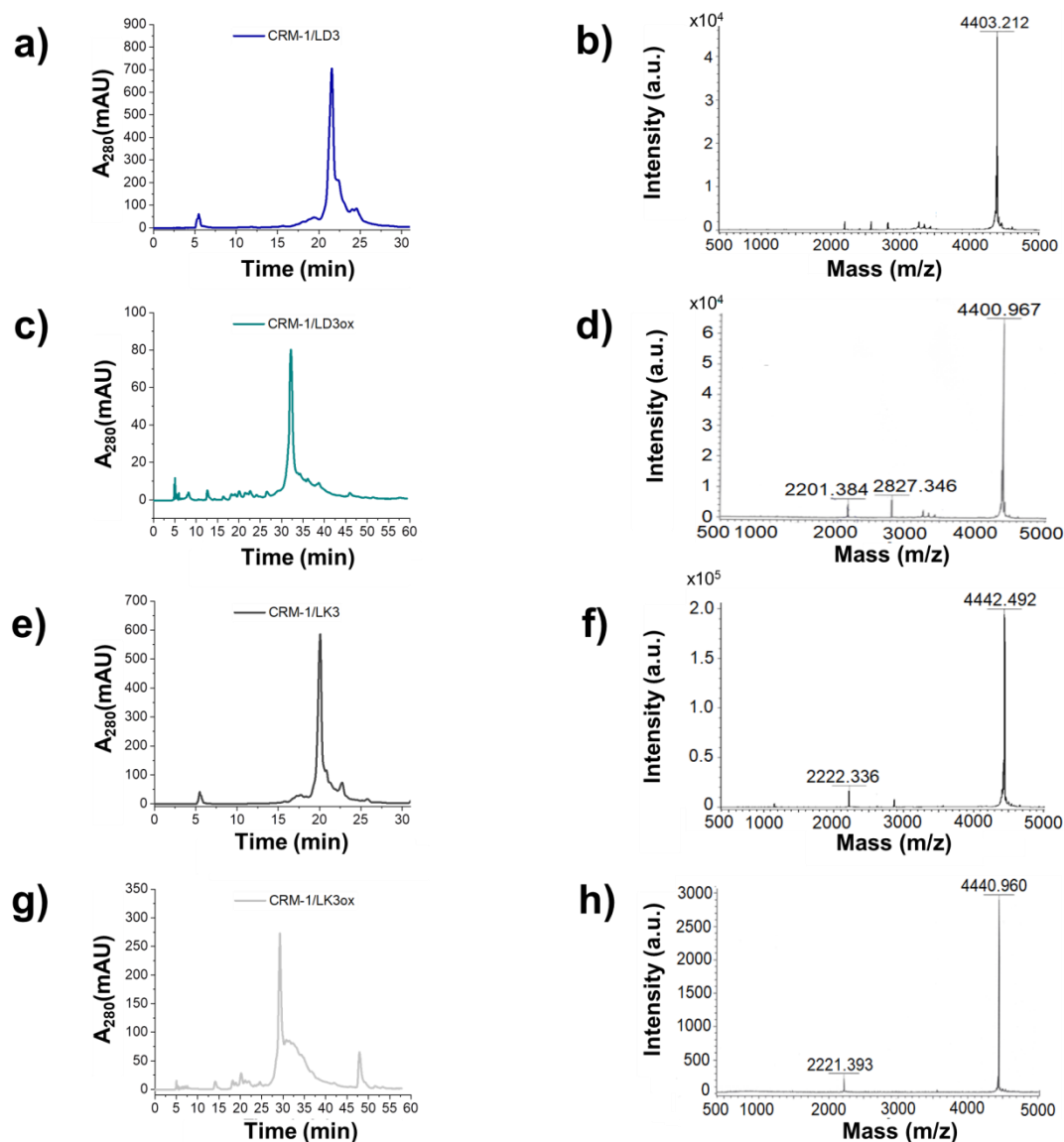
Figure 106. HPLC purification of CRM-1/LD3, CRM-1/LK3 and their oxidized analogs and verification of their purity by MALDI. a, c, e, g Representative C18 HPLC chromatogram (absorbance at 280 nm) of crude purified CRM-1/LD3, CRM-1/LD3ox, CRM-1/LK3 and CRM-1/LK3ox with respective retention times: a) 21.52 min, c) 32.17 min, e) 20.85 min and g) 29.28 min, following SPPS and cleavage. **b, d, f, h** MALDI-TOF-MS spectra of HPLC-purifiedCRM-1/LD3 (b), CRM-1/LD3ox (d), CRM-1/LK3 (f) and CRM-1/LK3ox (h) with respective experimental determined masses [M+H]$^{+}$: b) 4403.212 Da, d) 4440.967 Da, f) 4442.492 Da and h) 4440.960 Da.

4.5.3 Biophysical characterization

### 4.5.3.1 Conformational and concentration dependence studies via CD spectroscopy

After the successful synthesis and purification of the CRMs, the next set goal was to determine their secondary structures. As before, CD spectroscopy was applied for getting more information on the conformation. Spectra were recorded in the previously described experimental setup in a 1 to 20 or 50 µM concentration range, depending on the solubility of the peptide. Both CRM-1/L4 and CRM-1/L4ox exhibited similar signal-shaped spectra between the 1 to 5 and 10 to 20 µM concentrations but with weaker signal intensity in the higher concentrations, suggesting the oligomerization of the peptide above 5 µM. CRM-1/L4 showed broad minima at - 3000 deg·cm^{2}·dmol^{-1}

between 217 and 226 nm, while the minima of the oxidized analog were shifted to the 204-218 nm region (Figure 107a, b). Likewise, both conformations are present in CRM-1/L5, with the respective characteristic minima noted at 216 and 199 nm, contrary to CRM-1/L5ox, which differentiated to an unordered structure and exhibited its minima at 201 nm. Both peptides exposed reduced signal intensity at 20 μM, indicating their oligomerization at this concentration (Figure 107c, d).

Interestingly, CRM-1/LD3 appears to have the most ordered structure with its minima at 222 nm and. The peptide spectra recorded positive MRE values either below 206 nm at 5 and 10 μM or below 210 nm at 1, 2.5, and 20 μM. The minima of the peptide at 5 and 10 μM was slightly stronger than the rest measured spectra (Figure 107e). The effect of the concentration in the peptide conformation became even more apparent in its disulfide-bridged analog, CRM-1/LD3ox. At 1 μM, the oxidized analog had a minimum at 195 nm being in a random coil. On the contrary, the spectrum at 2.5 μM had two additional minima at 207 and 217 nm, revealing the presence of ordered structure, too. The oxidized analog had two minima in the spectra of 5 and 10 μM, at 208-211 and 217-221 nm region. At 195 nm the MRE values were approaching the baseline, indicating the presence of α-helix species. Peptide retained the α-helix signal at 20 μM, but with less signal intensity due to self-association (Figure 107f).

Of note, all mimics precipitated at 50 μM, except for CRM-1/LK3 and CRM-1/LK3ox. The lysine-linked peptides remained soluble in this concentration but aggregated as suggested by the weaker signal in comparison to the spectra from lower concentration (Figure 107g, h). Each spectrum of the non-oxidized analog exhibited a strong minimum at 200 nm or below, characteristic of a random coil. Simultaneously, at 1 and 2.5 μM the peptide presented other minima at 216 nm but with half intensity (Figure 107g). Similarly, CRM-1/LK3ox exposed one and strong minima at the 200 nm region, which became less intense at 20 and 50 μM, most likely due to self-association (Figure 107h). Summarized results and comparison of the spectra of the peptides are described in 'Discussion' (see 5.5).
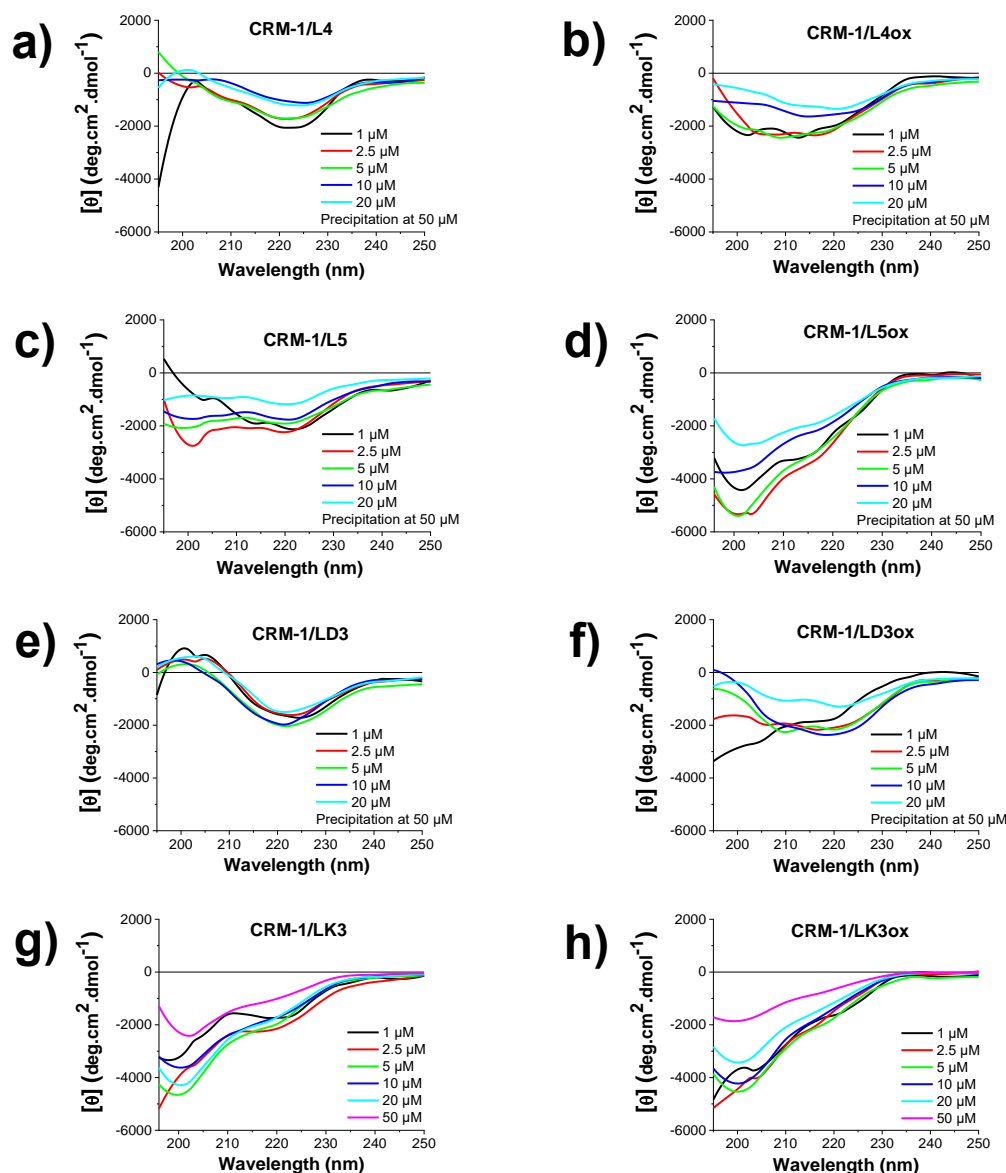
Figure 107. Spectra of CRMs in various concentrations for the determination of the conformation, as determined by far-UV CD spectroscopy. a, b, c, d, e, f, g, h CD spectra of CRM-1/L4 (a), CRM-1/L4ox (b), CRM-1/L5 (c), CRM-1/L5ox (d), CRM-1/LD3 (e), CRM-1/LD3ox (f), CRM-1/LK3 (g) and CRM-1/LK3ox (h) at increasing concentrations at final measuring conditions of aqueous 1×b, pH 7.4, containing 1% HFIP. Mean residue ellipticity (MRE) plotted over the wavelength between 195 and 250 nm for a, b, c, e, f, h and 196 and 250 nm for d, g.

4.5.3.2 Self-association studies via fluorescence spectroscopy

Following the same experimental setup to msR4Ms and ngms, Fluos-CRMs were titrated against their respective non-labeled analogs but with different analyte concentrations in the final measuring conditions. More specifically, due to the close-to-noise emission of Fluos-CRMs in the 5 nM, it was decided to increase the concentration. The labeled-analyte concentration was kept constant in all titration measurements but varied between the peptides due to the different emission intensities. For example, stock solutions of Fluos-CRM-1/L4ox and Fluos-CRM-1/L5ox were prepared at 2.5 µM, and measured at a concentration of 12.5 nM in the final measuring conditions showing a strong tendency to self-associate and app. K_d of 20.5 ± 6.8 nM and 38.9 ± 2.4 nM, respectively. Labeled CRM-1/LD3 and its oxidized analog did not share the same self-assembly tendency. In particular, Fluos-CRM-1/LD3 (12.5

188

nM) and Fluos-CRM-1/LD3ox (26.7 nM) had app. K_{ds} above 1250 nM and equal to 67.8 ± 13.7 nM, respectively (Figure 108a-d). Contrariwise to the other oxidized CRMs, the emission of Fluos-CRM-1/LK3ox (12.5 nM) did not reach the plateau until 5 µM of the unlabeled peptide, suggesting an app. K_d above this (Table 50, Figure 108e, f).
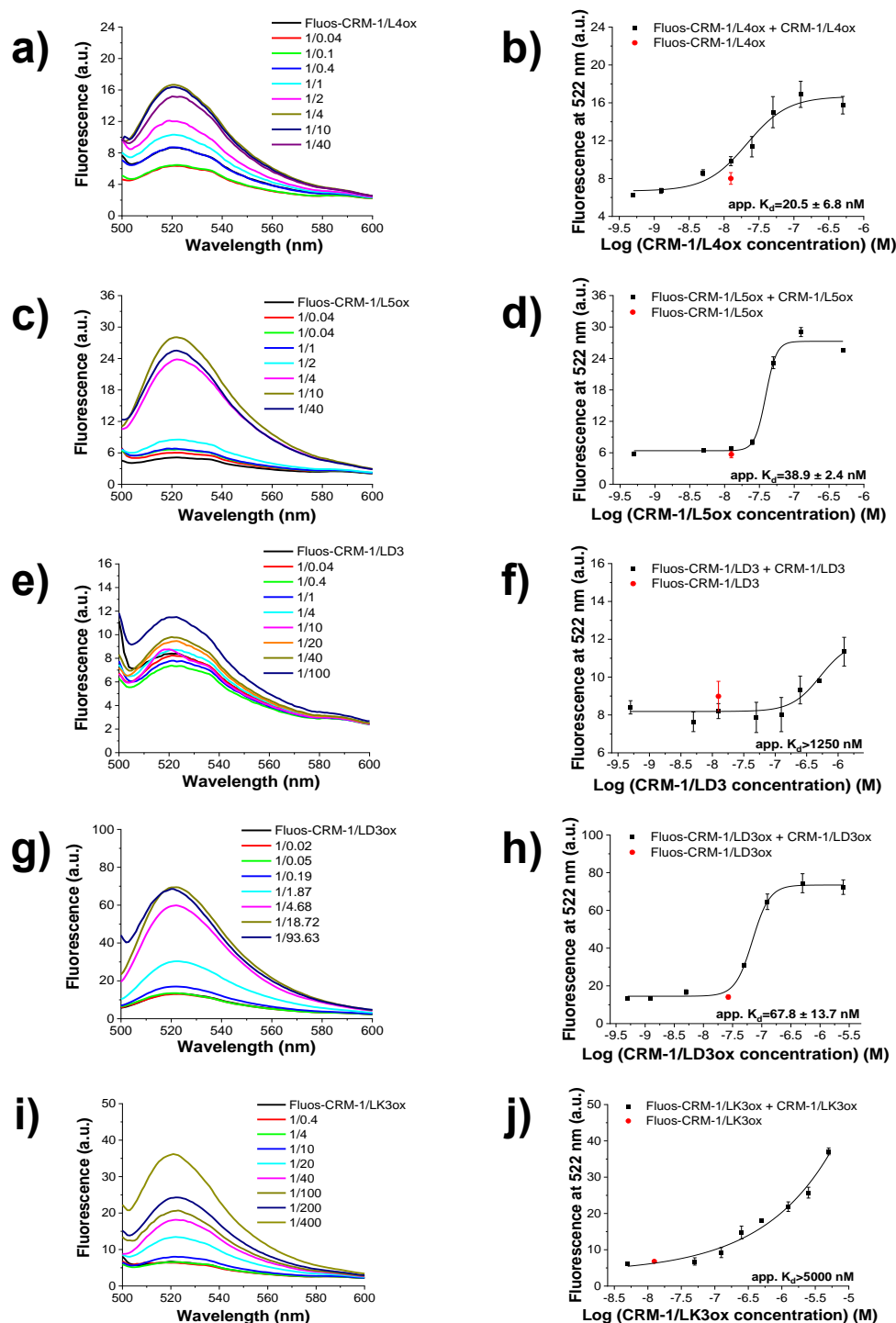
Figure 108. Fluorescence spectroscopic titrations for the determination of apparent affinities (app. K_{ds}) for the self-association of CRM-1/L4ox, /L5ox, /LD3 , /LD3ox and/LK3ox. a, c, e, g, i Fluorescence spectra between 500 and 600 nm of each Fluos-CRM (12.5 nM) alone and its mixtures with various amounts of its respective unlabeled partner CRM-1/L4ox (a), CRM-1/L5ox (c), CRM-1/LD3 (e); CRM-1/LD3ox (g) and CRM-1/LK3ox (i) the molar ratios of Fluos-CRM/CRM are indicated. **b, d, f, h, j** Binding curves derived from the fluorescence emission at 522 nm of Fluos-CRM (12.5 nM) at different concentrations of its respective unlabeled partner CRM-1/L4ox (b), CRM-1/L5ox (d), CRM-1/LD3 (f); CRM-1/LD3ox (h) and CRM-1/LK3ox (j). Data shown are means (±SD) from three independent titration experiments which were performed in aqueous 1×b, pH 7.4, containing 1% HFIP.

Table 50. Apparent affinities (app. K_{ds}) of self-association for CRMs, as determined by fluorescence spectroscopic titrations.

CRMs	Fluos-CRM/CRM app. K_d (±SD) (nM)[a]
Fluos-CRM-1/L4	n.d.[b]
Fluos-CRM-1/L4ox	20.5 (±6.8)
Fluos-CRM-1/L5	n.d.[b]
Fluos-CRM-1/L5ox	38.9 (±2.4)
Fluos-CRM-1/LD3	>1250
Fluos-CRM-1/LD3ox	67.8 (±13.7)
Fluos-CRM-1/LK3	n.d.[b]
Fluos-CRM-1/LK3ox	>5000

[a]: App. K_{ds} are means (±SD) from three independent titration experiments which were performed in aqueous 1×b, pH 7.4, containing 1% HFIP. [b]: n.d., non-determined.

4.5.3.3 ANS binding studies

CD spectroscopy gave us insights about CRMs and their significantly different secondary structures depending on their linkers and the presence of disulfide bonds. Next, it was investigated whether the chimeric mimics expose on their surface hydrophobic residues via their binding with ANS (constantly in 2-fold excess over the peptide). The fluorescence emission of ANS was tracked at its maxima at 469 nm through fluorescence spectroscopy, as previously described in chapters 4.1.3.3 and 4.3.3.3. The ANS emission was increased significantly over the increased CRM-1/L4 concentration, reaching 12.4 a.u. at 2 µM of the peptide, 48 a.u. at 3.5 µM, 75.6 a.u. at 5 µM and 244 a.u. at 10 µM (Figure 109a, b). Likewise, ANS exhibited 11.6 a.u. at 2 µM of CRM-1/L4ox, 71.9 a.u. at 3.5 µM, 77.5 a.u. at 5 µM and 287.4 a.u. at 10 µM. Both reduced and oxidized peptides precipitated at 20 µM (Figure 109c, d). CRM-1/L5 appeared to expose many hydrophobic amino acids on its surface, as well as the ANS emission with values equal to 12.8 a.u. of 2 µM of the peptide, 85 a.u. of 5 µM and 169.7 a.u. of 7 µM indicated (Figure 109e, f). Peptide precipitated at 10 µM, contrary to its oxidized analog that remained soluble until this concentration. However, CRM-1/L5ox seems to have a similar high exposure of hydrophobic residues with an even slightly increased ANS emission (Figure 109g, h). Summarized results and comparison of the spectra of the peptides are described in 'Discussion' (see 5.5).
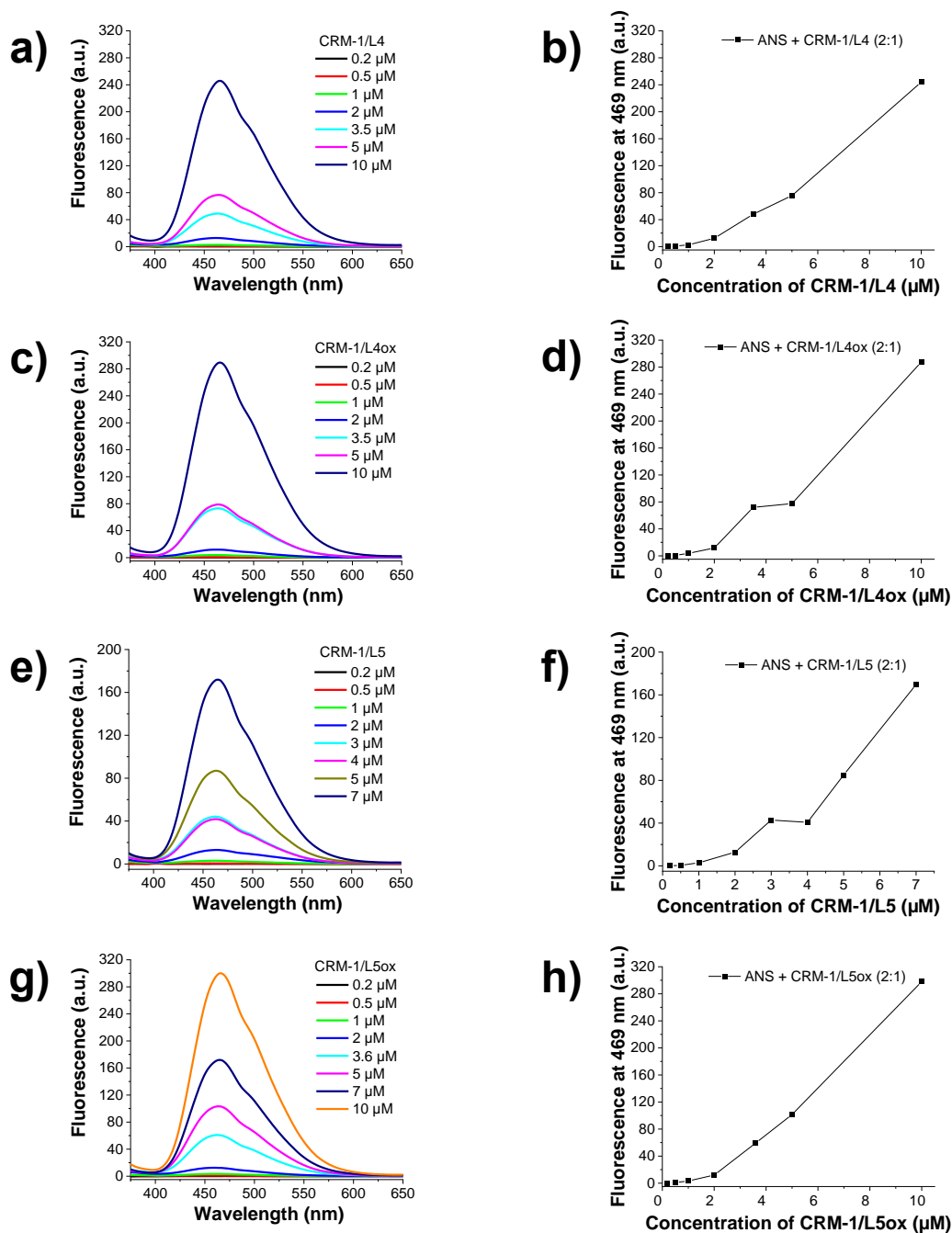
Figure 109. Effect of the binding of ANS to CRM-1/L4, /L4ox, /L5 and /L5ox, as recorded by fluorescence spectroscopy. a, c, e, g Spectra between 375 and 650 nm of mixtures between ANS and CRMs in constant 2:1 proportionality; the concenctrations of CRM-1/L4 (a), CRM-1/L4ox (c), CRM-1/L5 (e) and CRM-1/L5ox (g) are indicated. **b, d, f, h** Fluorescence emission at 469 nm over increased concentrations of CRM-1/L4 (b), CRM-1/L4ox (d), CRM-1/L5 (f) and CRM-1/L5ox (h) that were mixed with ANS in a constant 1:2 proportionality. Spectra of ANS alone were subtracted from the spectra of of peptide/ANS mixtures and measurements were performed in aqueous 1×b, pH 7.4, containing 1% HFIP.

ANS and CRM-1/LD3 (always in 2-fold excess in favor of the label) shared a high affinity, suggesting an intense exposure of hydrophobic residues on the surface of the peptide. In particular, the fluorescence emission of the label at its maxima exceeded 17.9 a.u. already from 5 µM of the peptide and reached 57.4 and 102.6 a.u. at 10 and 20 µM, respectively (Figure 110a, b). CRM-1/LD3ox followed a similar pattern to the reduced analog, with the ANS emission equal to 16.9 a.u. at 5 µM of the peptide, 38.4 a.u. at 10 µM, and 99.5 a.u. at 20 µM (Figure 110c, d). The label showed an even

stronger affinity for CRM-1/LK3ox, as it emitted 31.4 a.u. after adding 5 µM of CRM-1/LK3ox, 67.5 a.u. after 10 µM and 270.9 after 20 µM (Figure 110e, f).
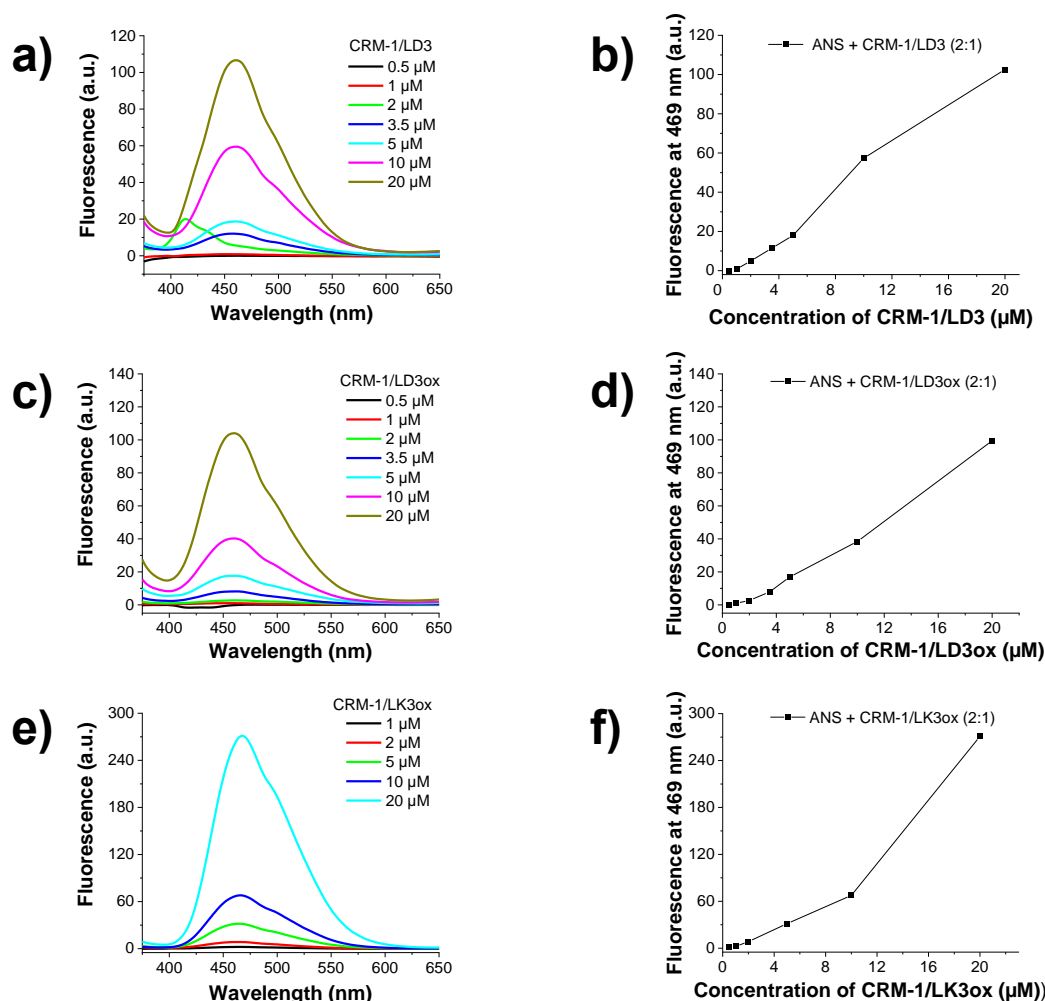

Figure 110. Effect of the binding of ANS to CRM-1/LD3, /LD3ox and LK3ox, as recorded by fluorescence spectroscopy. a, c, e Spectra between 375 and 650 nm of mixtures between ANS and CRMs in constant 2:1 proportionality; the concenctrations of CRM-1/LD3 (a), CRM-1/LD3ox (c) and CRM-1/LK3ox (e) are indicated. **b, d, f** Fluorescence emission at 469 nm over increased concentrations CRM-1/LD3 (b), CRM-1/LD3ox (d) and CRM-1/LK3ox (f) that were mixed with ANS in a constant 1:2 proportionality. Spectra of ANS alone were subtracted from the spectra of of peptide/ANS mixtures and measurements were performed in aqueous 1×b, pH 7.4, containing 1% HFIP.

4.5.4 Interactions between CRMs and MIF
4.5.4.1 Determination of binding affinities to MIF via fluorescence spectroscopy

Fluorescence spectroscopic titrations were carried out for the determination of the binding affinity between CRMs and MIF, as for the previous mimics. The same measuring conditions were maintained the same, i.e. aqueous 1×b, pH 7.4, 1% HFIP. Concerning the labeled analyte concentration, Alexa-488-MIF was kept constant at 10 nM in all titrations and measurements. However, Fluos-labeled peptides had to be added in a higher concentration than the 5 nM that were titrated previously, due to the significantly reduced fluorescence emission of the Fluos-CRMs, compared to msR4Ms and ngms. In principle, Fluos-CRMs were applied in the minimum concentration (12.5 to 83.4 nM) to reduce the aggregation possibility and maintain a sufficient emission for determining a binding.

Fluos-CRM-1/L4 (26.7 nM) was titrated against 2000 nM of MIF, and the lack of upper plateau indicated app. K_d above this concentration (Figure 111a, b). On the other hand, titrations of labeled CRM-1/L4ox (12.5 nM) against MIF showed a four to 5-fold increase in the fluorescence emission after saturation, suggesting app. K_d of 265.0 ± 57.2 nM (Figure 111c, d). Similarly, the dissociation constants of Fluos-CRM-1/L5 (26.7 nM) and Fluos-CRM-1/L5ox (12.5 nM) were estimated to be above 1000 nM and equal to 281.1 ± 26.3 nM, respectively (Figure 111e-h).
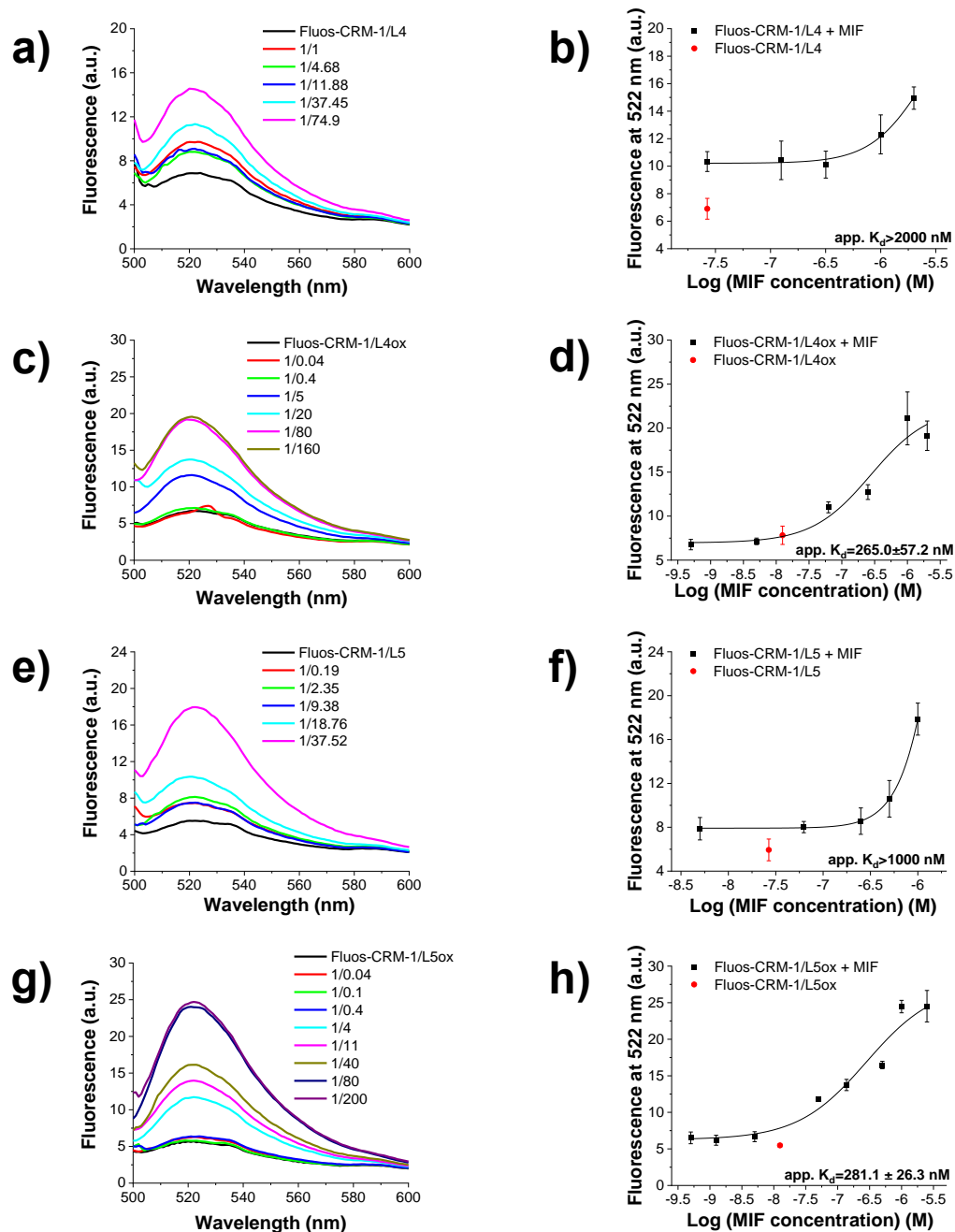
Figure 111. Fluorescence spectroscopic titrations of Fluos-CRM-1/L4, /L4ox, /L5, /L5ox with MIF for the determination of apparent affinities (app. K_{ds}). a, c, e, g Fluorescence spectra between 500 and 600 nm of 26.7 nM Fluos-CRM-1/L4 (a), 12.5 nM Fluos-CRM-1/L4ox (c), 26.7 nM Fluos-CRM-1/L5 (e) and 12.5 nM Fluos-CRM-1/L5ox (g) alone and its mixtures with various amounts of MIF; the molar ratios of Fluos-CRMs/MIF are indicated. **b, d, f, h** Binding curves derived from the fluorescence emission at 522 nm of 26.7 nM Fluos-CRM-1/L4 (b), 12.5 nM Fluos-CRM-1/L4ox (d), 26.7 nM Fluos-CRM-1/L5 (f) and 12.5 nM Fluos-CRM-1/L5ox (h) at different concentrations of MIF. Data shown are means (±SD) from three independent titration experiments which were performed in aqueous 1×b, pH 7.4, containing 1% HFIP.

Fluos-CRM-1/LD3 (26.7 nM) did not have a strong affinity with MIF as the app. K_d above 2000 nM suggested (Figure 112a, b). Contrariwise, the respective oxidized analog Fluos-CRM-1/LD3ox (26.7 nM) bound to the atypical chemokine at least tweny times stronger in comparison to the reduced one, with an app. K_d of 97.3 ± 1.4 nM (Figure 112c, d). Neither Fluos-CRM-1/LK3 (12.5 nM) nor Fluos-CRM-1/LK3ox (26.7 nM) got saturated by MIF, with the dissociation constants being estimated above 500 and 1000 nM, respectively (Figure 112e-h).
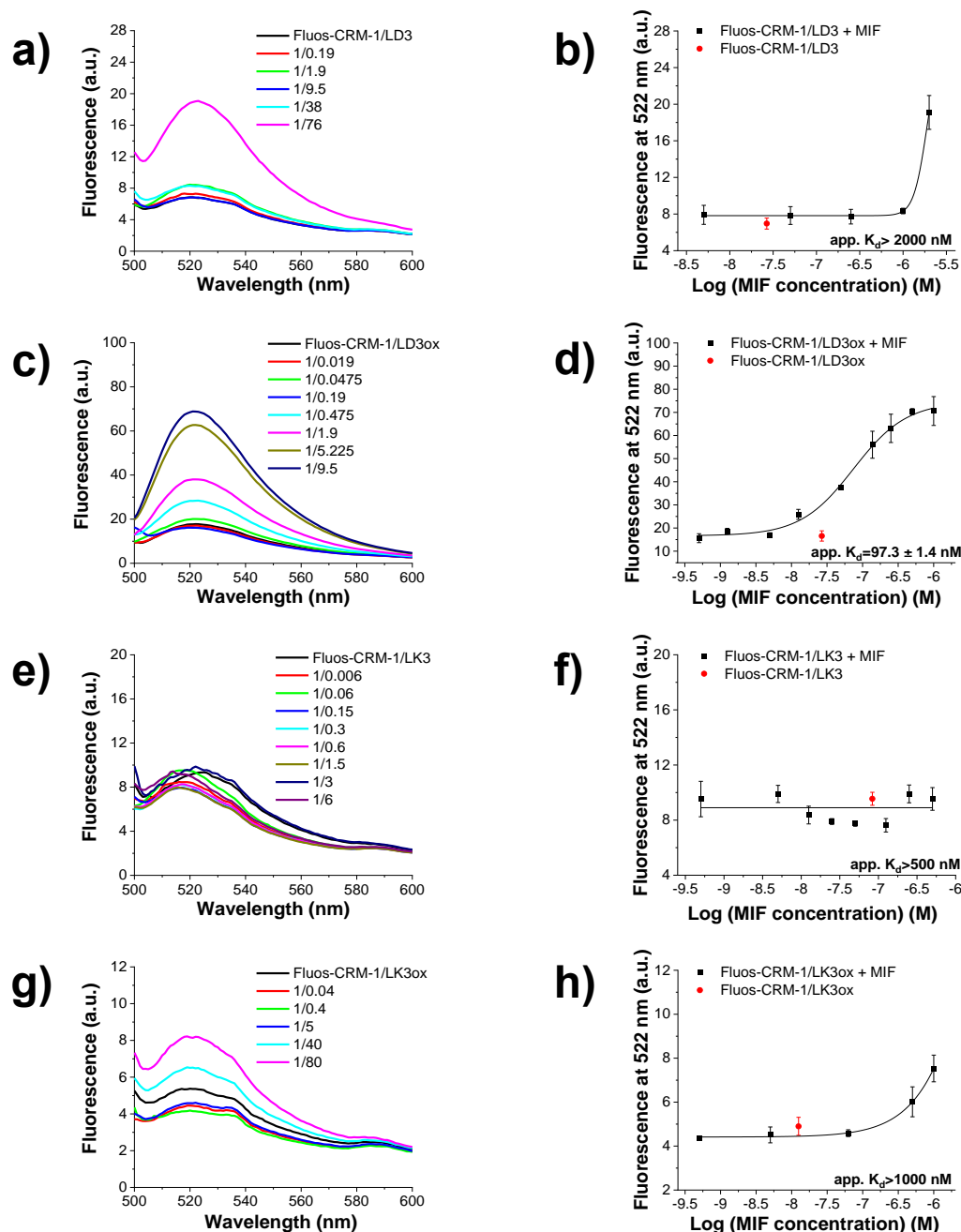
Figure 112. Fluorescence spectroscopic titrations of Fluos-CRM-1/LD3, /LD3ox, /LK3, /LK3ox with MIF for the determination of apparent affinities (app. K_{ds}). a, c, e, g Fluorescence spectra between 500 and 600 nm of 26.7 nM Fluos-CRM-1/LD3 (a), Fluos-CRM-1/LD3ox (c), 83.4 nM Fluos-CRM-1/LK3 (e) and 12.5 nM Fluos-CRM-1/LK3ox (g) alone and its mixtures with various amounts of MIF; the molar ratios of Fluos-CRMs/MIF are indicated. **b, d, f, h** Binding curves derived from the fluorescence emission at 522 nm of 26.7 nM Fluos-CRM-1/LD3 (b), Fluos-CRM-1/LD3ox (d), 83.4 nM Fluos-CRM-1/LK3 (f) and 12.5 nM Fluos-CRM-1/LK3ox (h) at different concentrations of MIF. Data shown are means (±SD) from three independent titration experiments which were performed in aqueous 1×b, pH 7.4, containing 1% HFIP.

Reversely to this experimental setup, Alexa-488-MIF was titrated against increasing concentration of non-labeled CRMs to identify the dissociation constants. Both CRM-1/L4 and CRM-1/L4ox showed a very strong affinity with the labeled-protein, with the respective calculated app. K_{ds} being 18.5 ± 3.0 nM and 21.2 ± 6.1 nM (Figure 113a-d). Similarly, CRM-1/L5 and CRM-1/L5ox bound firmly to Alexa-488-MIF with dissociation constants equal to 19.8 ± 5.9 nM and 22.8 ± 3.2 nM, respectively (Table 51, Figure 113e-h).
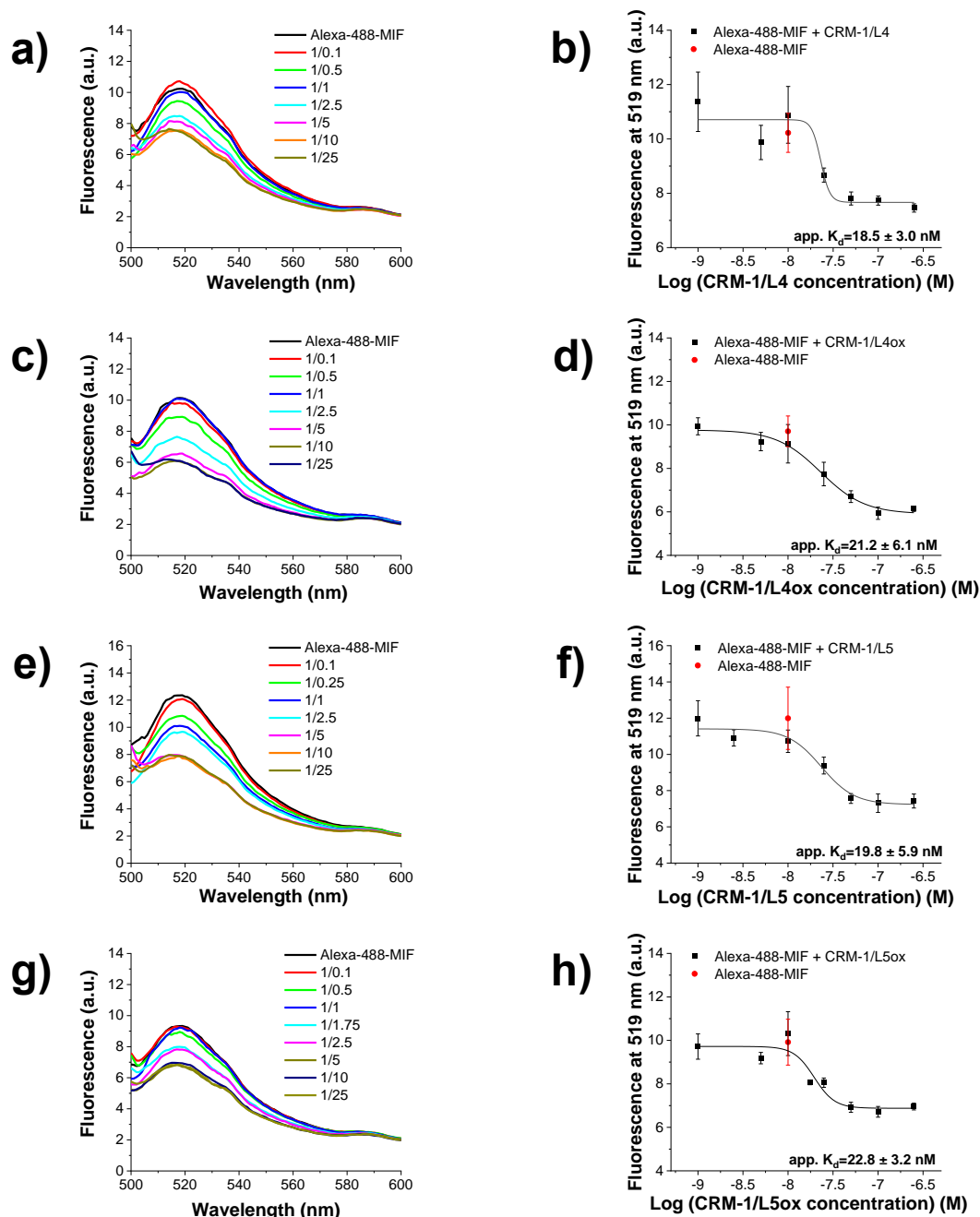
Figure 113. Fluorescence spectroscopic titrations of Alexa-488-MIF with CRM-1/L4, CRM-1/L4ox, CRM-1/L5 and CRM-1/L5ox for the determination of apparent affinities (app. K_{ds}). a, c, e, g Fluorescence spectra between 500 and 600 nm of Alexa-488-MIF (10 nM) alone and its mixtures with various amounts of CRM-1/L4 (a), CRM-1/L4ox (c), CRM-1/L5 (e) and CRM-1/L5ox (g); the molar ratios of Alexa-488-MIF/peptides are indicated. **b, d, f, h** Binding curves derived from the fluorescence emission at 519 nm of Alexa-488-MIF (10 nM) at different concentrations of CRM-1/L4 (b), CRM-1/L4ox (d), CRM-1/L5 (f) and CRM-1/L5ox (h). Data shown are means (±SD) from three independent titration experiments which were performed in aqueous 1×b, pH 7.4, containing 1% HFIP.

CRM-1/LD3 and CRM-1/LD3ox shared similar binding potency to Alexa-488-MIF and exhibited app. K_{ds} at 25.9 ± 14.5 nM and at 26.4 ± 7.7 nM, respectively (Figure 114a-d). Interestingly, the non-oxidized and the oxidized analog of the ngm-LK3-based CRM had different binding affinities to the labeled-ACK. In the first case, the fluorescence emission in the various Alexa-488-MIF and CRM-1/LK3 mixtures did not reach a plateau until 250 nM of titrant, indicating the incomplete saturation (Figure 114e, f). Contrariwise, there was a 40% reduction of Alexa-488-MIF fluorescence emission at its maxima in the titration with CRM-1/LK3ox, suggesting an app. K_d of 35.2 ± 4.1 nM (Table 51, Figure 114g, h). Summarized results and comparison of the binding affinities of the peptides are described in 'Discussion' (see 5.5).
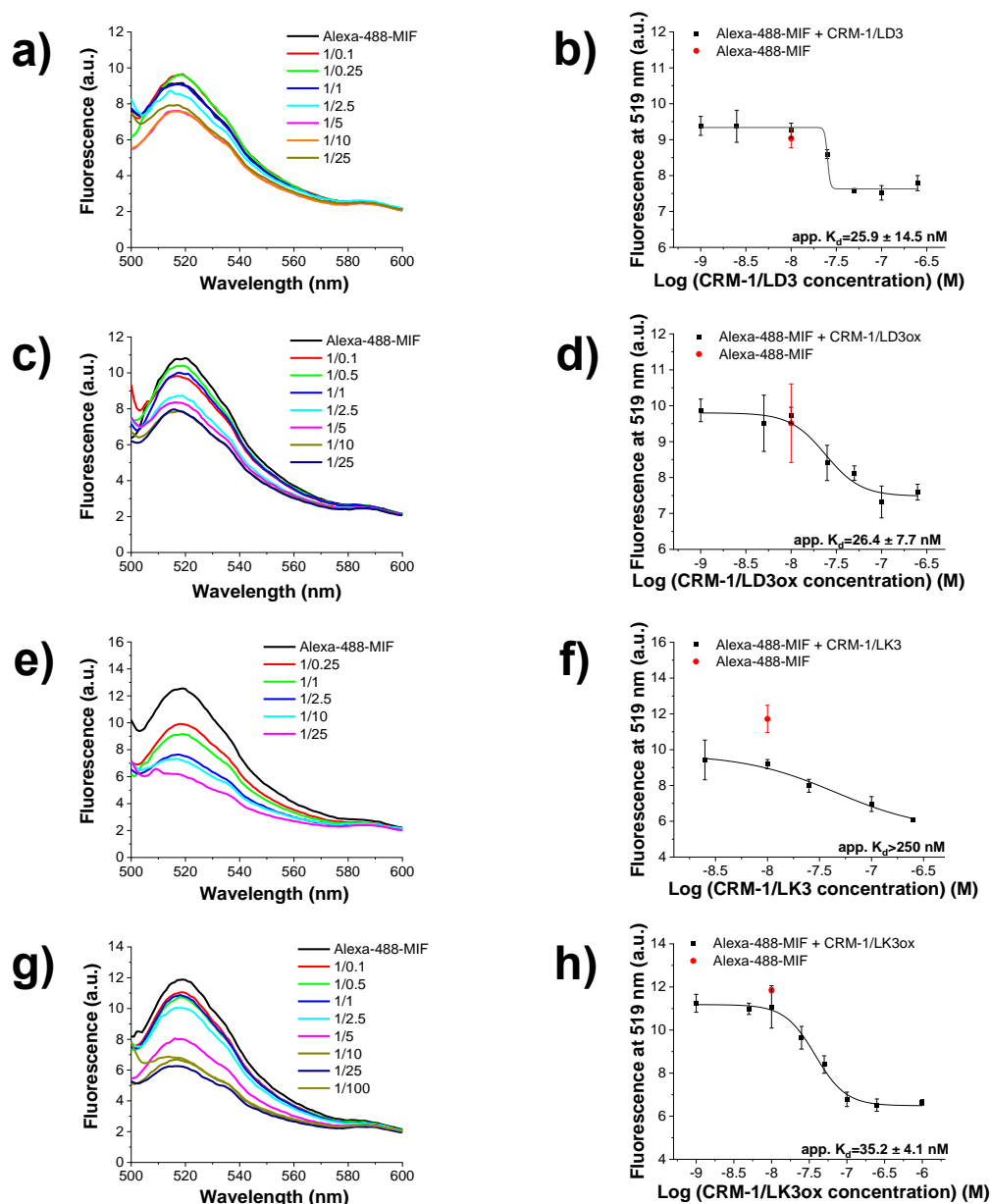
Figure 114. Fluorescence spectroscopic titrations of Alexa-488-MIF with CRM-1/LD3, CRM-1/LD3ox, CRM-1/LK3 and CRM-1/LK3ox for the determination of apparent affinities (app. K_{ds}). a, c, e, g Fluorescence spectra between 500 and 600 nm of Alexa-488-MIF (10 nM) alone and its mixtures with various amounts of CRM-1/LD3 (a), CRM-1/LD3ox (c), CRM-1/LK3 (e) and CRM-1/LK3ox (g); the molar ratios of Alexa-488-MIF /peptides are indicated. **b, d, f, h** Binding curves derived from the fluorescence emission at 519 nm of Alexa-488-MIF (10 nM) at different concentrations of CRM-1/LD3 (b), CRM-1/LD3ox (d), CRM-1/LK3 (f) and CRM-1/LK3ox (h). Data shown are means (±SD) from three independent titration experiments which were performed in aqueous 1×b, pH 7.4, containing 1% HFIP.

Table 51. Apparent affinities (app. K_{ds}) of interaction between CRMs and MIF, as determined by fluorescence spectroscopic titrations.

CRMs	Fluos-CRM/MIF app. K_d (±SD) (nM)	Alexa-488-MIF/CRM app. K_d (±SD) (nM)
CRM-1/L4	>2000	18.5 (±3.0)
CRM-1/L4ox	265.0 (±57.2)	21.2 (±6.1)
CRM-1/L5	>2000	19.8 (±5.9)
CRM-1/L5ox	281.1 (±26.3)	22.8 (±3.2)
CRM-1/LD3	>2000	25.9 (±14.5)
CRM-1/LD3ox	97.3 (±1.4)	26.4 (±7.7)
CRM-1/LK3	>500	>250
CRM-1/LK3ox	>2000	35.2 (±4.1)

App. K_{ds}, are means (±SD) from three independent titration experiments which were performed in aqueous 1×b, pH 7.4, containing 1% HFIP.

4.5.4.2 Interactions between CRMs and MIF by CD spectroscopy

Receptor-substrate interactions were shown in many cases to cause changes in the structure of the formed complexes. CRMs that were designed to mimic the MIF receptors CXCR2 and CXCR4 were identified as potent binders of the atypical chemokine. In order to investigate their interactions, CD spectroscopy was applied for additional studies on the secondary structures of their mixtures. Neither CRM-1/L4 nor CRM-1/L4ox mixtures with MIF differentiated than expected, which is the sum of their individual spectra. Consequently, when mimics and protein were mixed in a 5 to 1 proportionality there was no conformational change in their secondary structures (Figure 115a, b). Contrariwise, mixtures between either CRM-1/L5 or CRM-1/L5ox with MIF exposed a different signal than expected. The mixture of CRM-1/L5 and MIF exhibited a broad minimum between 213 and 226 nm, slightly shifted if compared to the expected between 209 and 221 nm. Moreover, the minimum derived by the experimentally obtained spectrum exposed 25% reduced ellipticity than the sum of the individual spectra. Below 202 nm, both spectra reached positive mdeq with very similar signal intensity values (Figure 115c).

Similarly, spectra of CRM-1/L5ox and MIF mixtures and the sum of their individual spectra sum exhibited their minima in the 210-221 nm and 207-218 nm region, respectively. The theoretically expected signal exposed a 15-20% increased ellipticity with stronger intensity at 208-211 nm, compared to the experimentally determined. The signal of the mixture reached positive ellipticity at 201.4 nm, while the sum at 199.7 nm and the ellipticities of both shared similar intensity below this point (Figure 115d). The mixture of CRM-1/LD3 and MIF exhibited a similar spectrum with a slightly sharper minimum at 219-221 nm and reduced intensity in the 209-219 nm region in comparison to the sum (Figure 115e). Experimentally determined ellipticities of the CRM-1/LD3ox and CRM-1/LK3ox mixture with MIF were in agreement with the expected ones (Figure 115f, g).
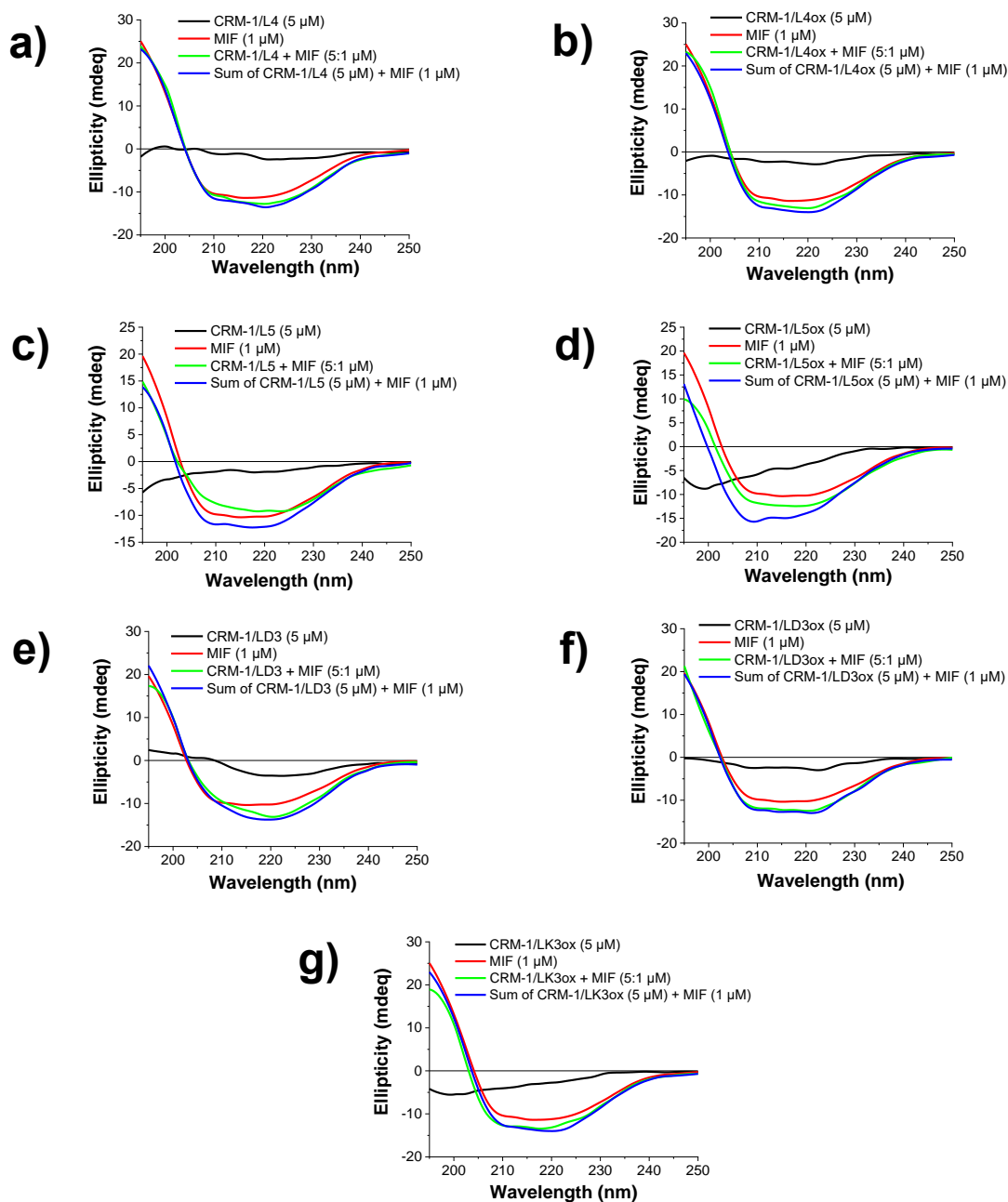
Figure 115. Studies on secondary structure of CRMs-MIF mixtures through CD spectroscopy.a, b, c, d, e, f, g CD spectra of CRMs and MIF alone, CRMs-MIF mixture and sum of the ellipticity of the derived peptide and protein individual spectra. The analyzed peptides were CRM-1/L4 (a), CRM-1/L4ox (b), CRM-1/L5 (c), CRM-1/L5ox (d), CRM-1/LD3 (e), CRM-1/LD3ox (f) and CRM-1/LK3ox (g). Concentrations and ratios are indicated. Measurements were performed in aqueous 1×b, pH 7.4, containing 1% HFIP. Ellipticity (θ) plotted over the wavelength between 195 and 250 nm.

4.5.5 Determination of binding affinities to CXCL12 via fluorescence spectroscopy

CXCR4 is known to be a specific receptor and does not share a broad range of substrates. CXCL12 was believed to be its only canonical ligand until the uncover of MIF as an alternative substrate in 2007 [77]. To test whether the CRMs can bind to CXCL12 except for MIF, Fluorescence spectroscopic titrations of labeled peptide with unlabeled protein were carried out under the same experimental setup that was applied in the titrations against MIF. Fluorescence emission of labeled-CRM-1/L4 (26.7 nM) did

not differentiate significantly until 2000 nM of CXCL12, suggesting an app. K_d above this point (Figure 116a, b). Contrariwise, strong binding was noted down for both reduced and oxidized labeled analogs of CRM-1/L5, too. Particularly, Fluos-CRM-1/L5 (26.7 nM) and /L5ox (12.5 nM) bound to CXCL12 with dissociation constants of 13.1 ± 4.4 nM and 27.8 ± 3.6 nM, respectively (Table 52, Figure 116c-f).
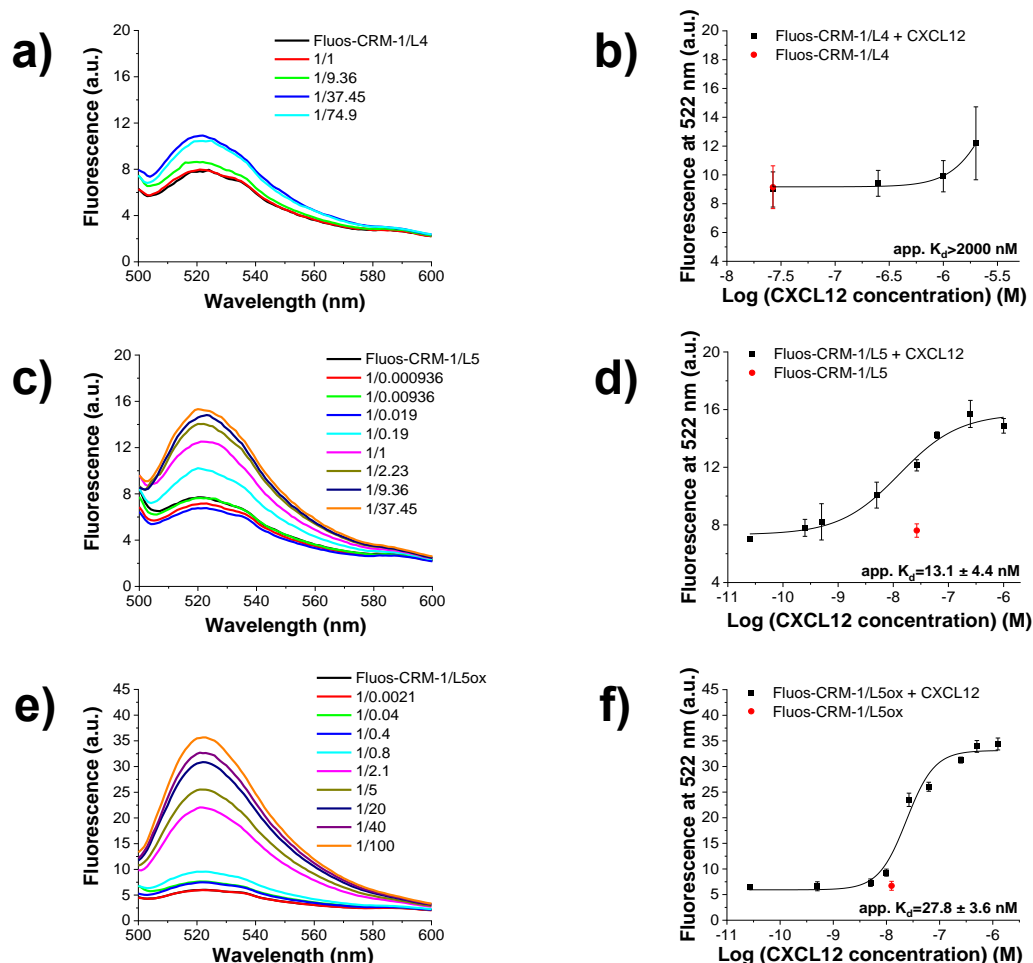
Figure 116. Fluorescence spectroscopic titrations of Fluos-CRM-1/L4, /L5, /L5ox with CXCL12 for the determination of apparent affinities (app. K_{ds}). a, c, e Fluorescence spectra between 500 and 600 nm of 26.7 nM Fluos-CRM-1/L4 (a), 26.7 nM Fluos-CRM-1/L5 (c), and 12.5 nM Fluos-CRM-1/L5ox (e) alone and its mixtures with various amounts of CXCL12; the molar ratios of Fluos-CRMs/CXCL12 are indicated. **b, d, f** Binding curves derived from the fluorescence emission at 522 nm of 26.7 nM Fluos-CRM-1/L4 (b), 26.7 nM Fluos-CRM-1/L5 (d), and 12.5 nM Fluos-CRM-1/L5ox (f) at different concentrations of CXCL12. Data shown are means (±SD) from three independent titration experiments which were performed in aqueous 1×b, pH 7.4, containing 1% HFIP.

The disulfide bridge appeared to be a crucial factor for the interaction between CRM-1/LD3 and CXCL12 (Figure 117a, b). The labeled non-oxidized mimic (26.7 nM) had a very weak affinity for the chemokine and their app. K_d was above 2000 nM. On the contrary, Fluos-CRM-1/LD3ox (12.5 nM) exhibited very strong binding to CXCL12 and the calculated app. K_d was 5.5 ± 0.5 nM (Figure 117c, d). However, the app. K_d of another disulfide bridged mimic, the labeled CRM-1/LK3ox, and CXCL12 was estimated higher than 2000 nM (Table 52, Figure 117e, f). Summarized results and comparison of the binding affinities of the peptides are described in 'Discussion' (see 5.5).
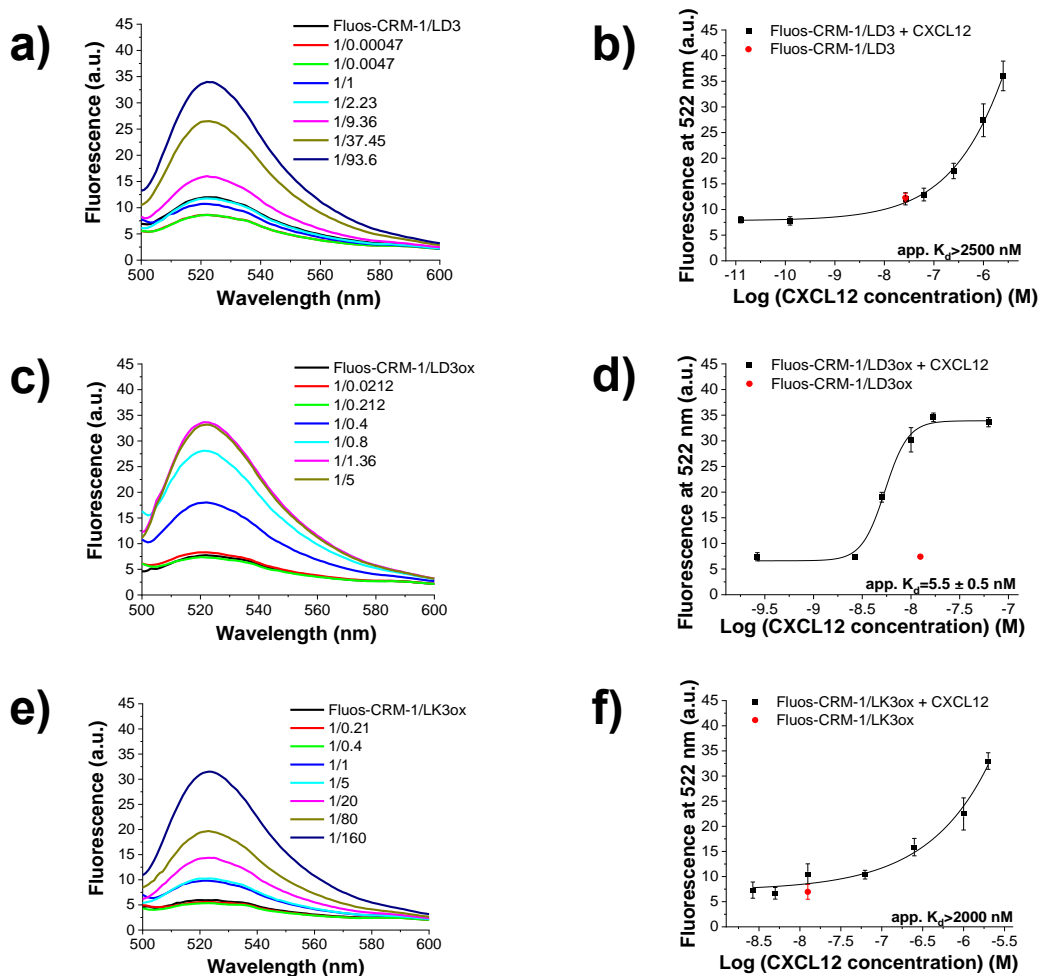
Figure 117. Fluorescence spectroscopic titrations of Fluos-CRM-1/LD3, /LD3ox, /LK3ox with CXCL12 for the determination of apparent affinities (app. K_{ds}). a, c, e Fluorescence spectra between 500 and 600 nm of 26.7 nM Fluos-CRM-1/LD3 (a), 12.5 nM Fluos-CRM-1/LD3ox (c), and Fluos-CRM-1/LK3ox (e) alone and its mixtures with various amounts of CXCL12; the molar ratios of Fluos-CRMs/CXCL12 are indicated. **b, d, f** Binding curves derived from the fluorescence emission at 522 nm of 26.7 nM Fluos-CRM-1/LD3 (b), 12.5 nM Fluos-CRM-1/LD3ox (d), and Fluos-CRM-1/LK3ox (f) at different concentrations of CXCL12. Data shown are means (±SD) from three independent titration experiments which were performed in aqueous 1×b, pH 7.4, containing 1% HFIP.

Table 52. Apparent affinities (app. K_{ds}) of interaction between Fluos-CRMs and CXCL12, as determined by fluorescence spectroscopic titrations.

CRMs	Fluos-CRM/CXCL12 app. K_d (±SD) (nM)[a]
CRM-1/L4	>2000
CRM-1/L4ox	n.d.[b]
CRM-1/L5	13.1 (±4.4)
CRM-1/L5ox	27.8 (±3.6)
CRM-1/LD3	>2500
CRM-1/LD3ox	5.5 (±0.5)
CRM-1/LK3	n.d.[b]
CRM-1/LK3ox	>2000

[a]: App. K_{ds} are means (±SD) from three independent titration experiments which were performed in aqueous 1×b, pH 7.4, containing 1% HFIP. [b]: n.d., non-determined.

4.5.6 Determination of binding affinities to IL-8 via fluorescence spectroscopy

CRMs are designed to mimic the ectodomain segments of CXCR2 and CXCR4 that bind to MIF. Both receptors have ligands, with MIF being their common substrate. CXCR4 is a receptor characterized by specificity, as its CXCL12 has been revealed as its only canonical ligand so far. On the other hand, substrates of CXCR2 consist of CXCL1,-2, 3,-5,-6,-7, and -8, with the last chemokine being considered as the most potent. The sequence of CRMs contains R2ECL2(184-196) linked to the CXCR4 fragments ECL1(102-110), which shares 77.8% identity with the respective CXCR2 analog R2ECL1(112-120), and ECL2(187-195). After investigating whether the mimics can bind to MIF and CXCL12, the next was to examine their binding affinity against the most potent CXCR2 ligand, CXCL8, or in other words IL-8. The experimental setup did not differentiate from the previously described for CXCL12. More specifically, the N-terminus labeled CRMs being titrated against the unlabeled proteins and monitoring the reaction by fluorescence spectroscopy in 1xb, pH 7.4, 1% HFIP.

Neither Fluos-CRM-1/L5 (26.7 nM) nor Fluos-CRM-1/L5ox (12.5 nM) managed to bind with IL-8 with the app. K_{ds} being estimated above 1000 nM and 1250 nM, respectively (Figure 118a-d). On the contrary, the disulfide bridge has a remarkable input in CRM-1/LD3 and the binding to the chemokine. The non-oxidized mimic Fluos-CRM-1/LD3 showed a very weak affinity for IL-8, with dissociation constant above 1250 nM. However, its oxidized analog, Fluos-CRM-1/LD3ox, bound very strongly to the chemokine and the app. K_d was calculated to be 6.1 ± 1.2 nM (Figure 118e-g). No significant change of the fluorescence emission was noticed for the Fluos-CRM-1/LK3ox over the increased concentration of IL-8 and the app. K_d was estimated to be above 1000 nM (Table 53, Figure 118i, j). Summarized results and comparison of the binding affinities of the peptides are described in 'Discussion' (see 5.5).
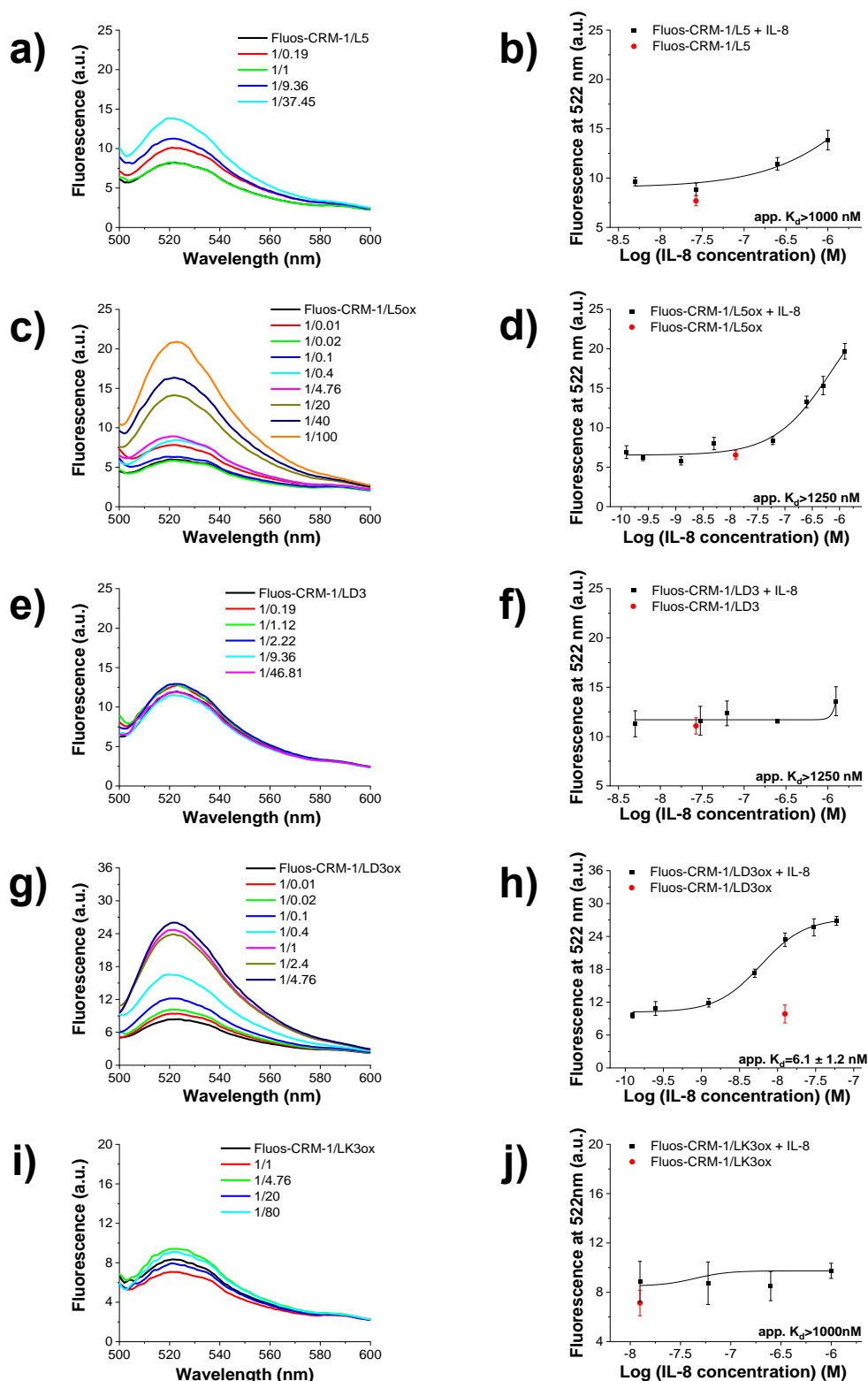
Figure 118. Fluorescence spectroscopic titrations of Fluos-CRM-1/L5, /L5ox, /LD3, /LD3ox, /LK3ox with IL-8 for the determination of apparent affinities (app. K$_{ds}$). a, c, e, g, i Fluorescence spectra between 500 and 600 nm of 26.7 nM Fluos-CRM-1/L5 (a), 12.5 nM Fluos-CRM-1/L5ox (c), 26.7 nM Fluos-CRM-1/LD3 (e), 12.5 nM Fluos-CRM-1/LD3ox (g) and Fluos-CRM-1/LD3ox (i) alone and its mixtures with various amounts of IL-8; the molar ratios of Fluos-CRMs/ IL-8 are indicated. **b, d, f, h, j** Binding curves derived from the fluorescence emission at 522 nm of 26.7 nM Fluos-CRM-1/L5 (b), 12.5 nM Fluos-CRM-1/L5ox (d), 26.7 nM Fluos-CRM-1/LD3 (f), 12.5 nM Fluos-CRM-1/LD3ox (h) and Fluos-CRM-1/LK3ox (j) at different concentrations of IL-8. Data shown are means (±SD) from three independent titration experiments which were performed in aqueous 1×b, pH 7.4, containing 1% HFIP.

Table 53. Apparent affinities (app. K_{ds}) of interaction between Fluos-CRMs and IL-8 as determined by fluorescence spectroscopic titrations.

CRMs	Fluos-CRM/IL-8 app. K_d (±SD) (nM)[a]
CRM-1/L4	n.d.[b]
CRM-1/L4ox	n.d.[b]
CRM-1/L5	>1000
CRM-1/L5ox	>1250
CRM-1/LD3	>1250
CRM-1/LD3ox	6.1 (±1.2)
CRM-1/LK3	n.d.[b]
CRM-1/LK3ox	>1000

[a]: App. K_{ds} are means (±SD) from three independent titration experiments which were performed in aqueous 1×b, pH 7.4, containing 1% HFIP. [b]: n.d., non-determined.

4.5.7 Conclusions on CXCR2 and CXCR4 chimeric receptor mimics (CRMs)

CRMs were synthesized and purified as the other mimics previously with a yield comparable to msR4Ms. Their MALDI-TOF-MS analyses were carried out in a newer solution for sufficient crystalization to confirm the purity of the mimics before testing them. Secondary structure studies revealed an ordered structure for three out of four CRMs and a mixture between β-sheet and random coil for their oxidized analogs. CRM-1/LK3 was the only mimic that lacked any ordered structure in both reduced and oxidized form and remained soluble until 50 μM, contrary to the rest that precipitated in this concentration. All mimics exhibited on their surface hydrophobic residues, with the CRM-1/L4 and /L5 and their oxidized analogs having the highest exposure (Table 54).

Table 54. Defined biophysical properties of CRMs after CD and fluorescence spectroscopy studies with ANS.

Peptide	Secondary structure	Precip. (μM)	Hydrophobic residues on the surface
CRM-1/L4	β-sheet	50	Very high exposure
CRM-1/L4ox	β-sheet + r.c. [a]	50	Very high exposure
CRM-1/L5	β-sheet + r.c. [a]	50	Very high exposure
CRM-1/L5ox	r.c. [a]	50	Very high exposure
CRM-1/LD3	β-sheet	50	Quite high exposure
CRM-1/LD3ox	β-sheet + r.c. [a]	50	Quite high exposure
CRM-1/LK3	r.c. [a]	>50	n.d. [b]
CRM-1/LK3ox	r.c. [a]	>50	High exposure

Peptides were biophysically characterized in aqueous 1×b, pH 7.4, containing 1% HFIP.
[a]: r.c., random coil, [b]: n.d., non-determined.

Even though less ordered, the oxidized CRMs had a significantly stronger tendency to self-assemble than the reduced ones. The non-oxidized mimics had controversial results in their binding studies with MIF. When Fluos-CRMs were applied as the analytes, there was binding in the micromolar range, while the reverse titrations that analyzed the emission of Alexa-488-MIF showed interactions in the low nanomolar range. Contrariwise, MIF and three out of four oxidized CRMs reached saturated in both titration systems, however with reduced affinities when the peptides were labeled. Fluorescence spectroscopy was additionally applied to determine whether the labeled-CRMs interact with CXCL12 or IL-8. As for msR4Ms, oxidation had a pivotal role in the interaction with CXCL12 for CRMs. Both oxidized and reduced CRM-1/L5 together with

CRM-1/LD3ox bound strongly to the chemokine. Noteworthy, only one mimic, the CRM-1/LD3ox recognized IL-8 and notably with a very low dissociation constant (Table 55). Conclusively, CRMs could bind to MIF with strong affinity, and the introduction of a disulfide bridge induced their binding to CXCL12 and maybe to IL-8, depending on the linker. Further studies need to confirm the binding potency of the mimics with the MIF and the chemokines, their selectivity, and their blockade in signaling pathways. However, they seem to be possibly even stronger blockers of atherosclerosis than the previous CXCR4 mimics.

Table 55. Determined app. K_{ds} of self-assembly of CRMs and of their binding interactions with MIF, CXCL12 and IL-8, as derived by fluorescence spectroscopic titrations.

Peptide	app. K_d (±SD) (nM) [a] (self-assembly)	app. K_d (±SD) (nM) [a] (Fluos-CRM/MIF)	app. K_d (±SD) (nM) [a] (Alexa-488-MIF/CRM)	app. K_d (±SD) (nM) [a] (Fluos-CRM/CXCL12)	app. K_d (±SD) (nM) [a] (Fluos-CRM/IL-8)
CRM-1/L4	n.d.[b]	>2000	18.5 (±3.0)	>2000	n.d.[b]
CRM-1/L4ox	20.5 (±6.8)	265.0 (±57.2)	21.2 (±6.1)	n.d.[b]	n.d.[b]
CRM-1/L5	n.d.[b]	>2000	19.8 (±5.9)	13.1 (±4.4)	>1000
CRM-1/L5ox	38.9 (±2.4)	281.1 (±26.3)	22.8 (±3.2)	27.8 (±3.6)	>1250
CRM-1/LD3	>1250	>2000	25.9 (±14.5)	>2500	>1250
CRM-1/LD3ox	67.8 (±13.7)	97.3 (±1.4)	26.4 (±7.7)	5.5 (±0.5)	6.1 (±1.2)
CRM-1/LK3	n.d.[b]	> 500	>250	n.d.[b]	n.d.[b]
CRM-1/LK3ox	>5000	>2000	35.2 (±4.1)	>2000	>1000

[a]: App. K_{ds} are means (±SD) from three independent titration experiments which were performed in aqueous 1×b, pH 7.4, containing 1% HFIP. [b]: n.d., non-determined.

4.6 Studies on [R87A-L87A-R89A]-MIF interaction with CXCR4

MIF was demonstrated as a cytokine with chemokine-like functions that bind to CXCR2 and CXCR4 [77]. Even though it was shown that the binding interface of the MIF with CXCR4 includes the N-like loop of the atypical chemokine, still essential information is missing. Together with the groups of Prof. Bernhagen and Prof. Lolis, we uncovered a pivotal role for the residues R87, L88, R89 of MIF and its interaction with CXCR4. A triple substitution of these residues with alanines was generated and the mutated cytokine, abbreviated as [R87A-L88A-R89A]-MIF, was provided by collaborators from the group of Prof. Bernhagen for biophysical and biochemical assays. Initially, the effects of the simultaneous replacement of the residues in its secondary structure and the exposure of hydrophobic residues on the surface were studied. Moreover, it was determined the effect of the mutation on the interaction to the CXCR4 ectodomain and its mimics, as well as the binding specificity of the RLR residues (Scheme 21).
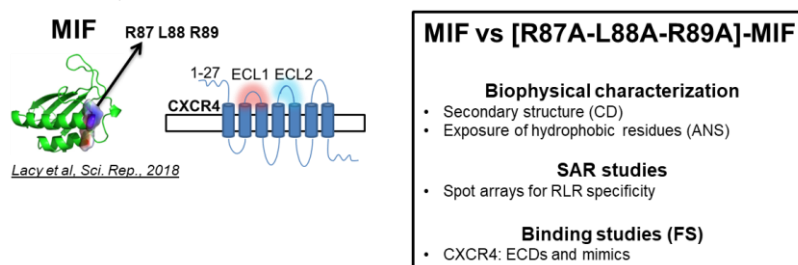
Scheme 21. Overview of the [R87A-L88A-R89A]-MIF studies. The [R87A-L88A-R89A]-MIF was generated from collaborators from the group of Prof. Bernhagen and biophysically characterized. SAR and binding studies were carried out and aimed to shed light on the importance and the specificity of the RLR residues on the interaction with CXCR4 ectodomain segments and mimics.

4.6.1 Biophysical characterization

4.6.1.1 Conformational and concentration dependence studies via CD spectroscopy

As a chemokine-like function protein but without the typical chemokine motif, MIF was structurally studied by many research groups. The protein was already crystallized in a trimeric form, and in each monomer, they were formed two antiparallel α-helices, four-stranded β-sheets, and two β-strands [83]. Except for X-ray and NMR, a more accessible, faster, and more affordable method to extract conclusions for the structure of the proteins is CD spectroscopy, with the MIF spectra being already released twenty years ago. Under very similar measuring conditions to this work, but with a more advanced spectrophotometer, MIF was prepared at 1, 2.5, and 5 µM and its spectra were monitored in aqueous 1×b, pH 7.4. The currently recorded findings are in agreement with the previously released data [76]. MIF did not expose a concentration-dependent- signal in the 1-5 µM range and showed broad minima between 210 and 225 nm. The atypical chemokine reached its minima MRE values at approximately -12000 deg·cm^2·dmol^{-1} that were significantly increased below 210 nm. In particular, MIF reached 0 and ~28000 deg·cm^2·dmol^{-1} at 204.5 and 195 nm, respectively (Figure 119a).

Next, we aimed to compare whether the substitution of the residues R87, L88, and R89 with alanines affected the secondary structure of the protein. The mutated protein was measured with CD spectroscopy under identical conditions and at the same concentration range as MIF. [R87A-L88A-R89A]-MIF exhibited a similar but not identical signal to the wild-type protein at its measured points at 1, 2.5 and 5 µM. Its

spectra showed broad minima at the 207-226 nm range, with the MRE values being approximately -11000 deg·cm^2·dmol^{-1}. After its minima, the signal of the mutated protein began to rise and it reached 0 deg·cm^2·dmol^{-1} at 201.5 nm before its maxima at 195 nm with MRE values at ~20000 deg·cm^2·dmol^{-1} (Figure 119b).
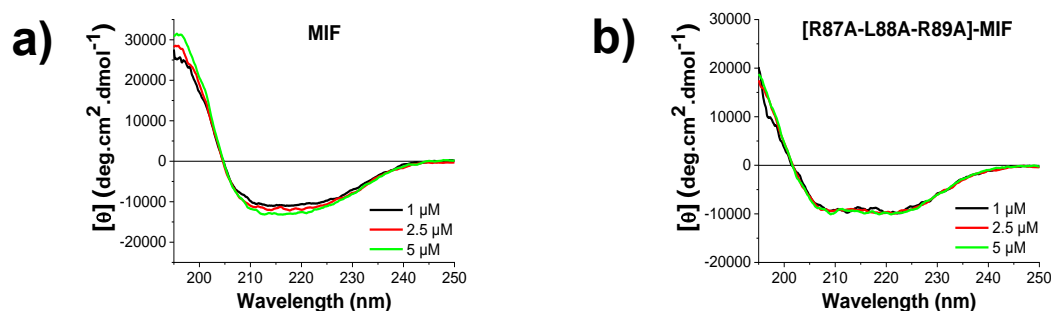
Figure 119. Spectra of MIF and [R87A-L88A-R89A]-MIF in various concentrations for the determination of the conformation, as determined by far-UV CD spectroscopy. a, b CD spectra of MIF (a) and [R87A-L88A-R89A]-MIF (b) at increasing concentrations at final measuring conditions of aqueous 1×b, pH 7.4. Mean residue ellipticity (MRE) plotted over the wavelength between 195 and 250 nm (adapted from Lacy et al., ref.[295]).

4.6.1.2 Estimation of the secondary structure via Dichroweb

CD spectroscopy-derived spectra may provide many valuable insights into the secondary structure of the proteins. However, it is hard to quantify the presence of different species in the structure. Dichroweb is an online server that analyses circular dichroism data via open-source algorithms and quantifies various states. MIF and [R87A-L88A-R89A]-MIF spectra at 5 μM were introduced in the software and analyzed by CONTIN and the reference set 7 (190-240 nm). Data from MIF showed a well-ordered secondary structure and agreed with the previously released works, with 44.7% of the atypical chemokine forming α-helix, 27.8% β-strand, 20.8% in β-turn, while 6.8% remained unordered. [R87A-L88A-R89A]-MIF is suggested to maintain a mainly ordered secondary structure, with 32.3% of the protein being in the α-helix state, 21.0% β-strand, 18.8% in β-turn, and a 28.7% in random coil (Table 56).

Table 56. Quantification of the secondary structure contents of MIF and [R87A-L88A-R89A]-MIF, as determined by the Dichroweb.

Proteins	α-helix (%)	β-strand (%)	β-strand/β-turn (%)	Unordered (%)	NRMSD[a]
MIF	44.7	27.8	48.6	6.8	0.090
[R87A-88A-R89A]-MIF	32.3	21.0	39.8	28.7	0.044

Contents (%) were calculated by deconvolutions of CD spectra and performed after application of ContinLL and the reference spectra set 7 at DichroWeb (http://dichroweb.cryst.bbk.ac.uk/html/home.shtml) [279] [280] [281] (adapted from Lacy et al., ref. [295]). [a] NRMSD (normalized root mean square deviation) of fits.

4.6.1.3 ANS binding studies

The effect of the triple mutations R87A, L88A, and R89A on MIF appeared to have a small but detectable effect on the disruption of the MIF secondary structure, as previously shown. Then, it was questioned whether the substitution of that three residues with alanines might affect the exposed hydrophobic residues on the surface of the protein. To figure this out, MIF and its R87A-L88A-R89A mutant were monitored with fluorescence spectroscopy together with a 2-fold excess ANS as already described. Measurements were carried out in aqueous 1×b, pH 7.4, and the variation of ANS fluorescence emission was recorded at 469 nm. MIF was measured at 1, 2, 5, and

10 μM, without any significant fluorescence emission (Figure 120a, b). In the same concentration range, [R87A-L88A-R89A]-MIF appeared to have a higher tendency for exhibiting hydrophobic residues. The recorded values of ANS fluorescence emission remained in the baseline range for 1 and 2 μM, got slightly increased to 4 a.u. at 5 μM and above 12 a.u. for 10 μM, suggesting exposure of hydrophobic residues over increased mutated cytokine concentration (Figure 120c, d).
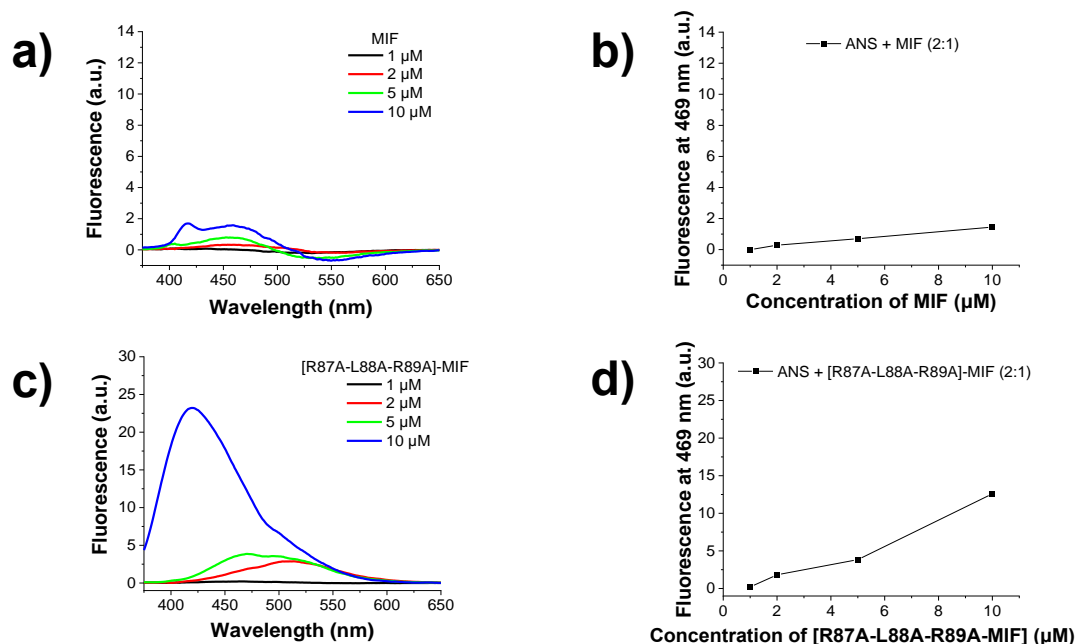

Figure 120. Effect of the binding of ANS to MIF, [R87A-L88A-R89A]-MIF, as recorded by fluorescence spectroscopy. a, c Spectra between 375 and 650 nm of mixtures between ANS and proteins in constant 2:1 proportionality; the concenctrations of MIF (a) and [R87A-L88A-R89A]-MIF (c) are indicated. **b, d** Fluorescence emission at 469 nm over increased concentrations of MIF (b) and [R87A-L88A-R89A]-MIF (d) that was mixed with ANS in a constant 1:2 proportionality. Spectra of ANS alone were subtracted from the spectra of protein/ANS mixtures and measurements were performed in aqueous 1×b, pH 7.4.

4.6.2 Determination of binding affinities of CXCR4 ectodomain peptides and mimics to [R87A-L88A-R89A]-MIF via fluorescence spectroscopy

[R87A-L88A-R89A]-MIF is a recently cloned mutant of MIF. Collaborators from the lab of Prof. Bernhagen discovered that CXCR4-mediated signaling was abrogated when the mutant was applied instead of the wild-type. Consequently, MIF residues 87-89 are considered crucial for the interaction with the chemokine receptor. The follow-up question was whether the ectodomain peptides of CXCR4 that are known to interact with MIF, i.e., CXCR4 (1-27), ECL1 and ECL2, can bind the mutant, and if yes, how strong is their affinity. To address this, Fluorescence spectroscopic titrations of Alexa-488-[R87A-L88A-R89A]-MIF with peptides were applied, under the same conditions that were used for MIF. The lack of change in the Alexa-488 fluorescence emission against the highest measured point of the titrant suggested an app. K_d above 5000 nM for CXCR4 (1-27) and higher than 10000 nM for ECL1 and ECL2 (Figure 121a-f). As previously described in chapter 4.1.1., ECL1 and ECL2 were the two parts that, after chemical linkage, generated the MIF-specific mimics of CXCR4, msR4Ms. Fluorescence emission of the labeled analyte remained unchanged until 1000 nM for

both msR4M-L1 and msR4M-L2, suggesting dissociation constants above this concentration (Figure 121g-j).
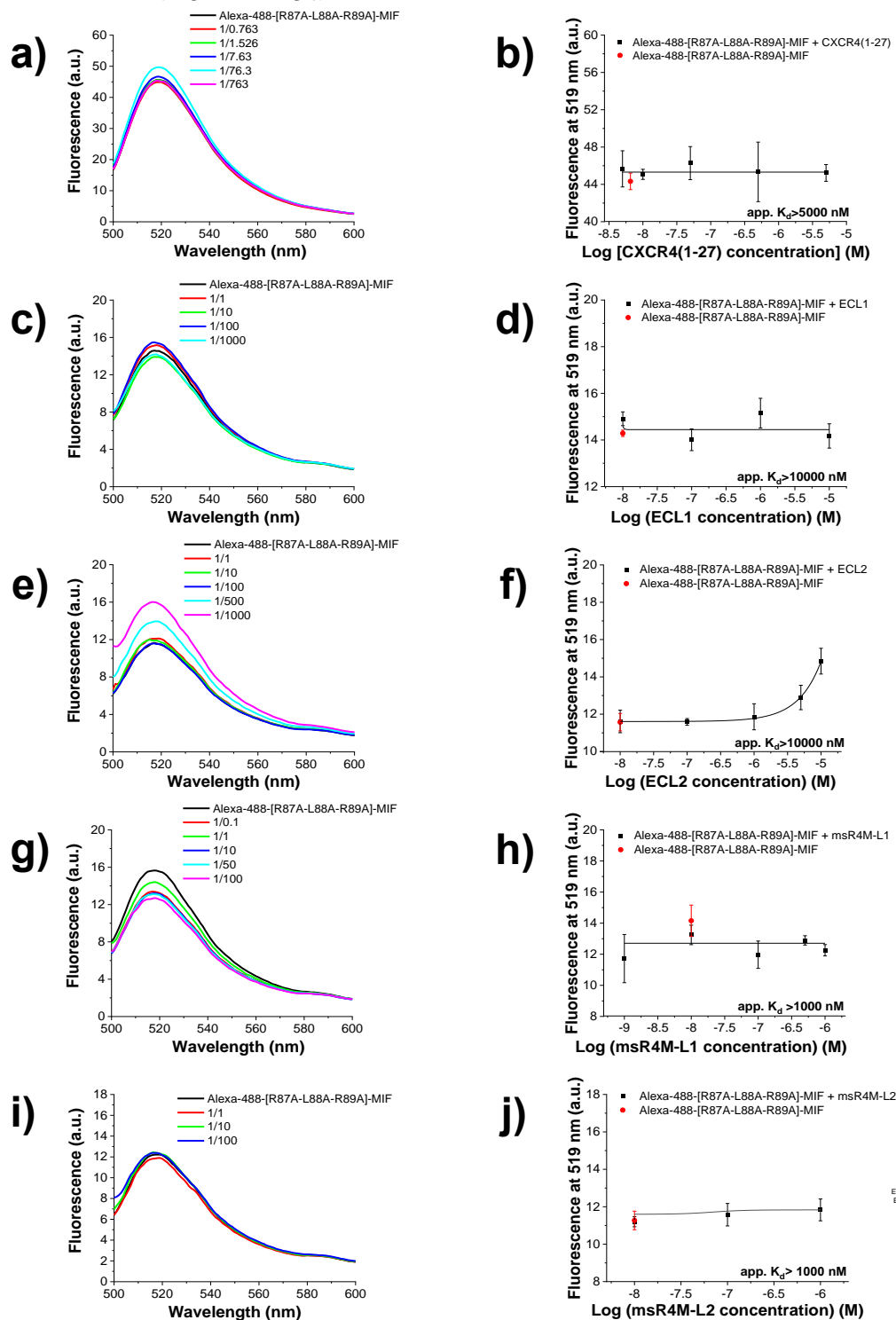
Figure 121. Fluorescence spectroscopic titrations of Alexa-488-[R87A-L88A-R89A]-MIF with CXCR4 (1-27), ECL1, ECL2, msR4M-L1 and msR4M-L2 for the determination of apparent affinities (app. K$_{ds}$). a, c, e, g, i Fluorescence spectra between 500 and 600 nm of Alexa-488-[R87A-L88A-R89A]-MIF (6.55 nM for a, 10 nM for c, e, g, i) alone and its mixtures with various amounts of CXCR4 (1-27) (a), ECL1 (c), ECL2 (e), msR4M-L1 (g) and msR4M-L2 (i); the molar ratios of Alexa-488-[R87A-L88A-R89A]-MIF/peptides are indicated. **b, d, f, h, j** Binding curves derived from the fluorescence emission at 519 nm of Alexa-488-[R87A-L88A-R89A]-MIF (6.55 nM for b, 10 nM for d, f, h, j) at different concentrations of CXCR4 (1-27) (b), ECL1 (d), ECL2(f), msR4M-L1 (h) and msR4M-L2 (j). Data shown are means (±SD) from three independent titration experiments which were performed in aqueous 1×b, pH 7.4, containing 1% HFIP (adapted from Lacy et al., ref. [295]).

To further examine the interactions between the CXCR4 generatied mimics and the mutated MIF binding affinities, the titration roles were reversed. More specifically, the peptides were N-terminus labeled and applied as the analytes, while the protein remained unlabeled as the titrant. As shown in chapter 4.1.4.1., both Fluos-msR4M-L1 and -L2 bound strongly to MIF with respective dissociations constants of 40.7 ± 4.0 and 18.6 ± 2.9. Against [R87A-L88A-R89A]-MIF, Fluos-msR4M-L1 showed a 5-fold decreased-affinity compared to to the wild-type with an app. K_d equal to 211.1 ± 46.3 nM. Likewise, the variation of the fluorescence emission of labeled-msR4M-L2 over rising concentration of the mutated MIF indicated an app. K_d of 212.0 ± 26.4 nM (Table 57, Figure 122).
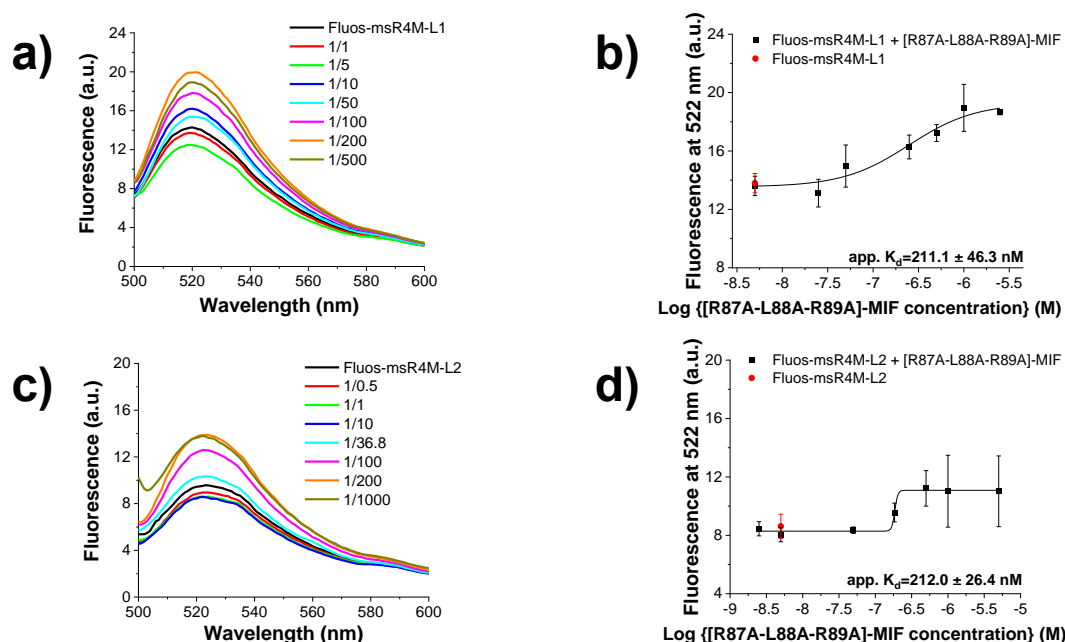
Figure 122. Fluorescence spectroscopic titrations of Fluos-msR4Ms with [R87A-L88A-R89A]-MIF for the determination of apparent affinities (app. K_{ds}). a, c Fluorescence spectra between 500 and 600 nm of 5 nM of Fluos-msR4M-L1 (a) and Fluos-msR4M-L2 (c) alone and their mixtures with various amounts of [R87A-L88A-R89A]-MIF; the molar ratios of Fluos-msR4Ms/[R87A-L88A-R89A]-MIF are indicated. **b, d** Binding curves derived from the fluorescence emission at 522 nm of 5 nM of Fluos-msR4M-L1 (b) and Fluos-msR4M-L2 (d) at different concentrations of [R87A-L88A-R89A]-MIF. Data shown are means (±SD) from three independent titration experiments which were performed in aqueous 1×b, pH 7.4, containing 1% HFIP.

Table 57. Apparent affinities (app. K_{ds}) of interaction between Fluos-peptide and [R87A-L88A-R89A]-MIF or Alexa-488-[R87A-L88A-R89A]-MIF and peptide as determined by fluorescence spectroscopic titrations.

Peptides	Fluos-peptide/[R87A-L88A-R89A]-MIF app. K_d (±SD) (nM)[a]	Alexa-488-[R87A-L88A-R89A]-MIF/peptide app. K_d (±SD) (nM)[a]
CXCR4 (1-27)	n.d.[b]	>5000
ECL1	n.d.[b]	>10000
ECL2	n.d.[b]	>10000
msR4M-L1	211.1 (±46.3)	>1000
msR4M-L2	212.0 (±26.4)	>1000

[a]: App. K_{ds} are means (±SD) from three independent titration experiments which were performed in aqueous 1×b, pH 7.4, containing 1% HFIP. [b]: n.d., non-determined.

4.6.3 SPOT array analysis of specificity between MIF and N-terminus of CXCR4

SPOT peptide array data by the groups of Prof. Bernhagen and Prof. Lolis indicated the importance of MIF residues 87, 88 and 89 for the interaction with the N-terminus of CXCR4. To determine the specificity of the effect, peptide arrays were developed using CelluSpots method and contained MIF (75-90) that included in its sequence the three essential amino acids and five peptides with scrambled sequences of the 16-mer (Figure 123a). To examine their potency, a biotin label together with the spacer 6 Ahx were introduced on the N-terminus of CXCR4 (1-27) and incubated with the slides, after the necessary procedure. The obtained value of chemiluminescence intensity for MIF(75-90) was 0.20 a.u., significantly higher than the 0.03 a.u. and 0.13 a.u., of MIF(75-90)_scr1 and MIF(75-90)_scr2, respectively. Similarly, the rest three scrambled peptides showed low intensity, with MIF(75-90)_scr3 having 0.08 a.u., MIF(75-90)_scr4 0.10 a.u and MIF(75-90)_scr5 0.09 a.u (Figure 123b).
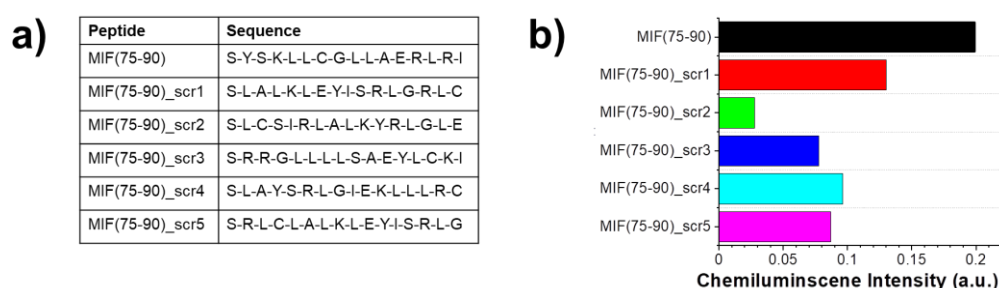
Figure 123. Determination of the interaction specificity between MIF(75-90) and CXCR4 (1-27) through peptide arrays. Abbreviation and sequence of MIF(75-90) and its scrambled peptides. b Chemiluminscence intensity as determined after the incubation of the MIF(75-90) and its scrambled peptides with Biotin-(6 Ahx)-CXCR4 (1-27) (adapted from Lacy et al., ref. [295]).

4.6.4 Conclusions on studies on [R87A-L87A-R89A]-MIF interaction with CXCR4

Conformational studies showed a detectable but not significant effect of the triple alanine mutation of the hot spot residues. Particularly, [R87A-L88A-R89A]-MIF shared a by 80% similar secondary structure with the native protein, while the exposure of hydrophobic residues on the surface was the same until 5 µM for both proteins. The substitution of the RLR residues by alanines reduced the binding affinity to the CXCR4 ectodomains and mimics (Table 58). In the same line, collaborators from the group of Prof. Bernhagen determined the lack of any MIF/CXCR4 mediated signaling when [R87A-L88A-R89A]-MIF was applied. The interaction specificity was confirmed when MIF(75-90) bound to Biotin-CXCR4(1-27), but not its scrambled analogs.

Table 58. Determined app. K_{ds} of the binding interactions between [R87A-L88A-R89A]-MIF or MIF with ECDs or msR4Ms, as derived by fluorescence spectroscopic titrations (adapted from Lacy et al., ref. [295]).

Peptides	Fluos-peptide/ [R87A-L88A-R89A]-MIF app. K_d (±SD) (nM)[a]	Alexa-488-[R87A-L88A-R89A]-MIF/peptide app. K_d (±SD) (nM)[a]	Fluos-peptide/MIF app. K_d (±SD) (nM)[a]	Alexa-488-MIF/peptide app. K_d (±SD) (nM)[a]
CXCR4 (1-27)	n.d.[b]	>5000	n.d.[b]	>9700[c]
ECL1	n.d.[b]	>10000	n.d.[b]	345.2 (±79.4)
ECL2	n.d.[b]	>10000		2458 (±1054)
msR4M-L1	211.1 (±46.3)	>1000	40.7 (±4.0)	31.1 (±16.6)
msR4M-L2	212.0 (±26.4)	>1000	28.9 (±2.5)	30.0 (±6.3)

[a]: App. K_{ds} are means (±SD) from three independent titration experiments which were performed in aqueous 1×b, pH 7.4, containing 1% HFIP. [b]: n.d., non-determined.

4.7 Studies on cyclic MIF analogs

MIF mediates proatherogenic functions through the chemokine receptors CXCR2 and CXCR4 [77]. The MIF/CXCR2 binding interface has been already mapped, and the pseudo-ELR motif together with the region 47-56 of MIF were uncovered as crucial factors from the ligand side [95] [97]. Based on this, the group of Prof. Bernhagen initially tested the decamer MIF(47-56) for its inhibitory potency. After identifying its blockade in the chemotactic activity of the atypical chemokine, cyclized inhibitors were designed as proof-of-concept blockers of atherosclerosis *in vivo*. Herein, it is aimed to determine the secondary structure of MIF(47-56) and its cyclic analogs, as well as whether the linear analog interferes unspecifically with MIF. Based on the conformational properties and the inhibitory potency, the analog MIF(cyclo10) was prioritized and, together with MIF(47-56), were studied if remain stable in human plasma *in vitro* (Scheme 22).
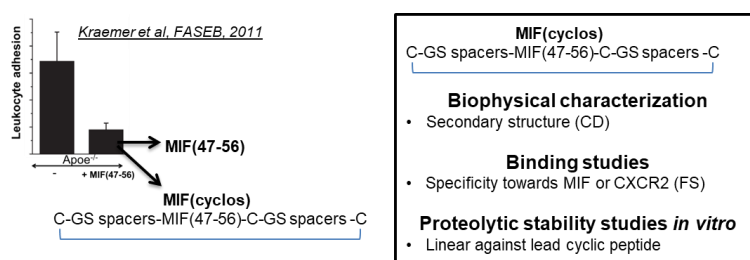
Scheme 22. Overview of the cyclic MIF analogs studies. The secondary structures of MIF(47-56) and its cyclic analogs were estimated. Binding studies were carried out to shed light on the specificity of the MIF(47-56) blockade. The proteolytic stabilities of the prioritized MIF(cyclo10) and the linear analog MIF(47-56) were determined *in vitro* (adapted from Krammer et al., ref. [296]).

4.7.1 Conformational and concentration dependence studies via CD spectroscopy

MIF(47-56) and all its cyclic analogs were purchased by Peptide Specialities GmbH (PSL, Heidelberg, GER). The cyclization occurred on the MIF(47-56) sequence after the conjugation on each terminus of a C and the disulfide bridge formation. However, between each C and the terminuses of MIF(47-56) may be introduced additional G or S residues as additional residues, and their amount varied depending on the peptide. More specifically, in MIF(cyclo0) sequence, there was no additional residue, in MIF(cyclo2) a G on each terminus before the C, in MIF(cyclo4) two G, in MIF(cyclo6) two G and one S, in MIF(cyclo8) a GGSG sequence, in MIF(cyclo10) a GGSGG, while for MIF(cycloAbuAL) an Abu, an A and an L but only in the C-terminus, before the C (Table 59).

Table 59. Sequences of MIF(47-56) and its cyclic analogs.
Adapted from Krammer et al., ref. [296]).

Peptides	Sequences
MIF(47-56)	LMAFGGSSEP
MIF(cyclo0)	CLMAFGGSSEPC
MIF(cyclo2)	CGLMAFGGSSEPGC
MIF(cyclo4)	CGGLMAFGGSSEPGGC
MIF(cyclo6)	CGGSLMAFGGSSEPSGGC
MIF(cyclo8)	CGGSGLMAFGGSSEPGGSGC
MIF(cyclo10)	CGGSGGLMAFGGSSEPGGSGGC
MIF(cycloAbuAL)	CLMAFGGSSEPX$_1$ALC

X_1: Abu, amino-butyric acid; cyclization by disulfide bridge is indicated.

MIF structure is known that contains two α-helices and six β-sheet/β-turn. The MIF region 47-56 is located between β2 (MIF 39-43) and β4 (MIF 58-64) and is partially involved in the β3 formation (MIF 47-50) [83]. However, it is unknown whether MIF(47-56) is ordered as a peptide and not a part of the whole protein sequence. CD spectroscopy was applied to determine the secondary structure and obtain more insights into the linear decamer and its cyclic analogs. MIF-derived peptides were dissolved and measured in aqueous 1×b, pH 7.4, without HFIP in the experimental setup that has been already described previously. Overall, all peptides exposed similar spectra over their tested concentration range with the random coil-characteristic minima at 195 nm. However, the signal variation between 215 and 225 nm indicated differentiation in their structures. MIF(47-56) reached negative MRE values at the 215-225 nm range, and its minima were between -8000 and -10000 deg·cm^2·dmol^{-1} (Figure 124a).

For MIF(cyclo0), a positive band between 215 and 225 nm was detected, suggesting a conformational restriction and a turn-like conformation. The MRE values at the minima were 30% reduced in an absolute value (Figure 124b). Likewise, MIF(cyclo2) and MIF(cyclo4) exhibited MRE values at ~-6000 deg·cm^2·dmol^{-1} at 195 nm and their positive band at 215-225 nm remained but became very weak in the MIF(cyclo4) case (Figure 124c, d). The rest four studied MIF cyclized peptides reached only negative MRE values between 215 and 225 nm in all tested concentrations. Simultaneously, their minima became more intense in three out of four cases, proposing the dissociation of any ordered states formed in the shorter cyclized peptides. Particularly, MIF(cyclo6) exposed its minima at 195 nm and its MRE values varied between -8000 and -20000 deg·cm^2·dmol^{-1}, while MIF(cyclo8) reached -5000 deg·cm^2·dmol^{-1}, MIF(cyclo10) -8000 deg·cm^2·dmol^{-1} and MIF(cycloAbuAL) was in the -11000 to -15000 deg·cm^2·dmol^{-1} range (Figure 124e-h). Summarized results and comparison of the spectra of the peptides are described in 'Discussion' (see 5.7).
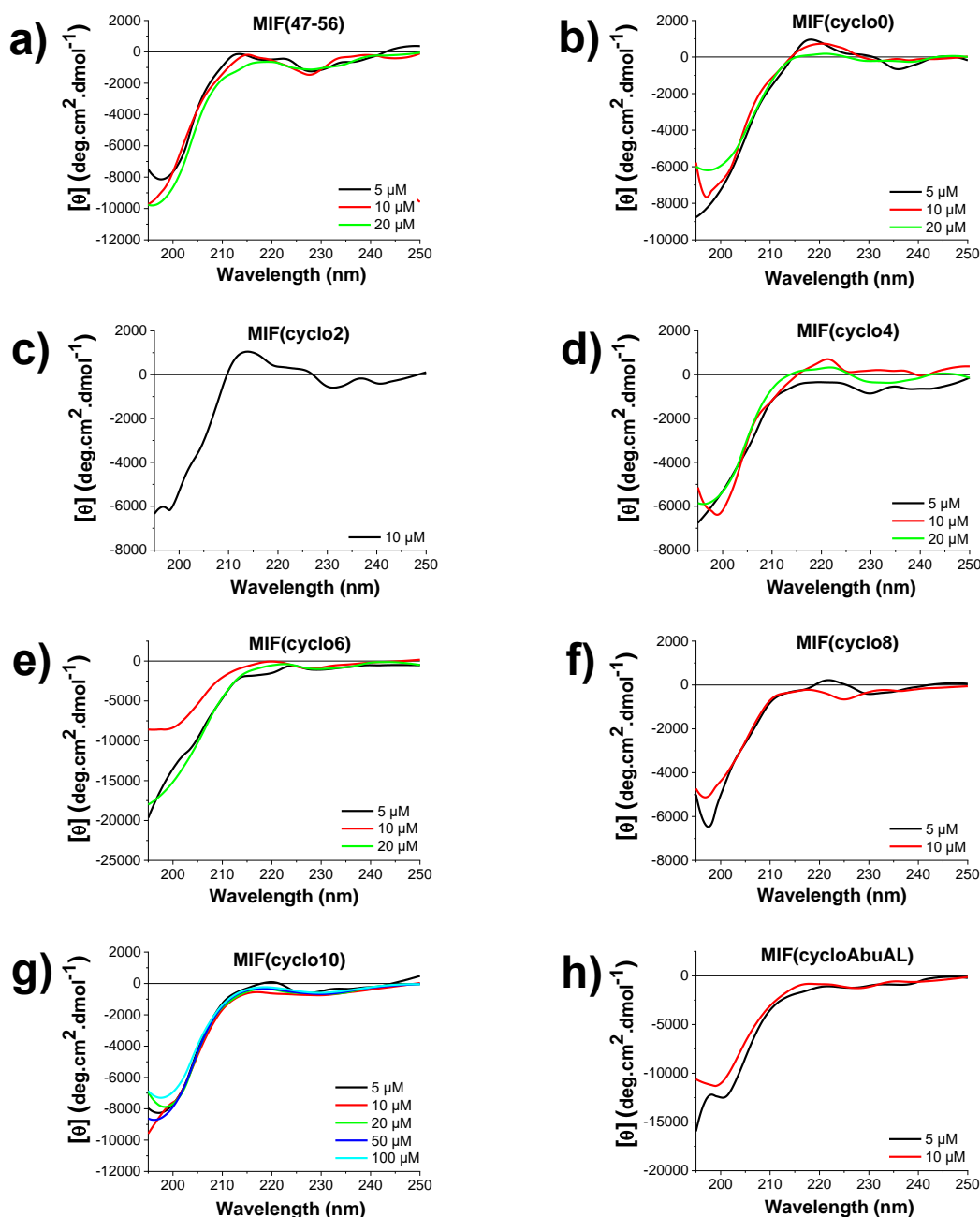
Figure 124. Spectra of MIF(47-56) and its cyclic analogs in various concentrations for the determination of the conformation, as determined by far-UV CD spectroscopy. a, b, c, d, e, f, g, h CD spectra of MIF(47-56) (a), MIF(cyclo0) (b), MIF(cyclo2) (c), MIF(cyclo4) (d), MIF(cyclo6) (e), MIF(cyclo8) (f), MIF(cyclo10) (g) and MIF(cycloAbuAL) (h) at increasing concentrations at final measuring conditions of aqueous 1×b, pH 7.4. Mean residue ellipticity (MRE) plotted over the wavelength between 195 and 250 nm (adapted from Krammer et al., ref. [296]).

4.7.2 Determination of binding affinity of MIF(47-56) to MIF via fluorescence spectroscopy

Collaborators from the group of Prof. Bernhagen examined and determined an inhibitory activity of the decamer MIF(47-56) in the MIF/CXCR2 axis. Next, it was reasoned to control the specificity of MIF(47-56) and whether it has any affinity with MIF or not. To testing this, fluorescence spectroscopic titrations were applied with Alexa-488-MIF as the analyte and non-labeled MIF(47-56) as the titrant under the already described conditions. The fluorescence emission of Alexa-488-MIF did not change

significantly over the increased concentration of MIF(47-56) and the app. K_d was estimated to be above 10000 nM (Figure 125).
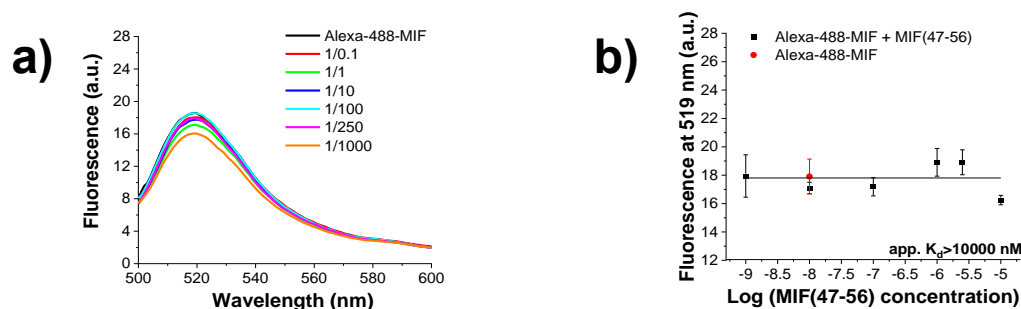
Figure 125 Fluorescence spectroscopic titrations of Alexa-488-MIF with MIF(47-56) for the determination of apparent affinities (app. K_{ds}). a Fluorescence spectra between 500 and 600 nm of Alexa-488-MIF (10 nM) alone and its mixtures with various amounts of MIF(47-56); the molar ratios of Alexa-488-MIF/ MIF(47-56) are indicated. **b** Binding curves derived from the fluorescence emission at 519 nm of Alexa-488-MIF (10 nM) at different concentrations of MIF(47-56). Data shown are means (±SD) from three independent titration experiments which were performed in aqueous 1×b, pH 7.4, containing 1% HFIP (adapted from Krammer et al., ref. [296]).

4.7.3 Proteolytic stability studies of MIF(47-56) and MIF(cyclo10) in human plasma *in vitro*

Overall, peptides are known to be prone to proteolytic degradation, which is considered one of their main disadvantages in drug development. Several peptide research projects focused on chemical modification of the peptide sequence for increasing its resistance against the proteases. Among the implied strategies for improved stability is cyclization. The scope of the current assay was to determine whether MIF(47-56) and the lead cyclized peptide, MIF(cyclo10), are proteolytically stable over time in human plasma. Peptides of interest were incubated in human plasma *in vitro* at 37°C and extracted from the sample after protein precipitation with aqueous 10% TCA and centrifugated. Next, the supernatants were diluted and analysed by RP-HPLC using a Nucleosil 100 C18 column (Grace) (length 33 mm length, ID 8 mm, 7 µm particle size) stationary phase and the program 5 for gradient elution [238].

MIF(cyclo10) exposed remarkable resistance over the degradation due to proteins of plasma. As the integrated area of the eluted peaks indicated, the cyclic peptide remained non-degraded over 8 h in plasma *in vitro* (Figure 126, 127). Its half time is calculated to be between 16 and 24 h. Even with less than half the amount eluted, the peptide was still traced until 48 h in plasma (Figure 128). All peaks were dissolved in MALDI solution A, analyzed by MALDI-TOF-MS, and confirmed the presence of MIF(cyclo10). The linear analog, MIF(47-56), was tested under similar conditions and showed a significantly reduced stability over proteolytic digestion. The half amount of the peptide was already degraded after 30 min and the decamer was barely detected after 2 h (Figure 129, 130). MALDI-TOF-MS was applied as for MIF(cyclo10), and the expected molecular weight of the peptide was determined in every case.
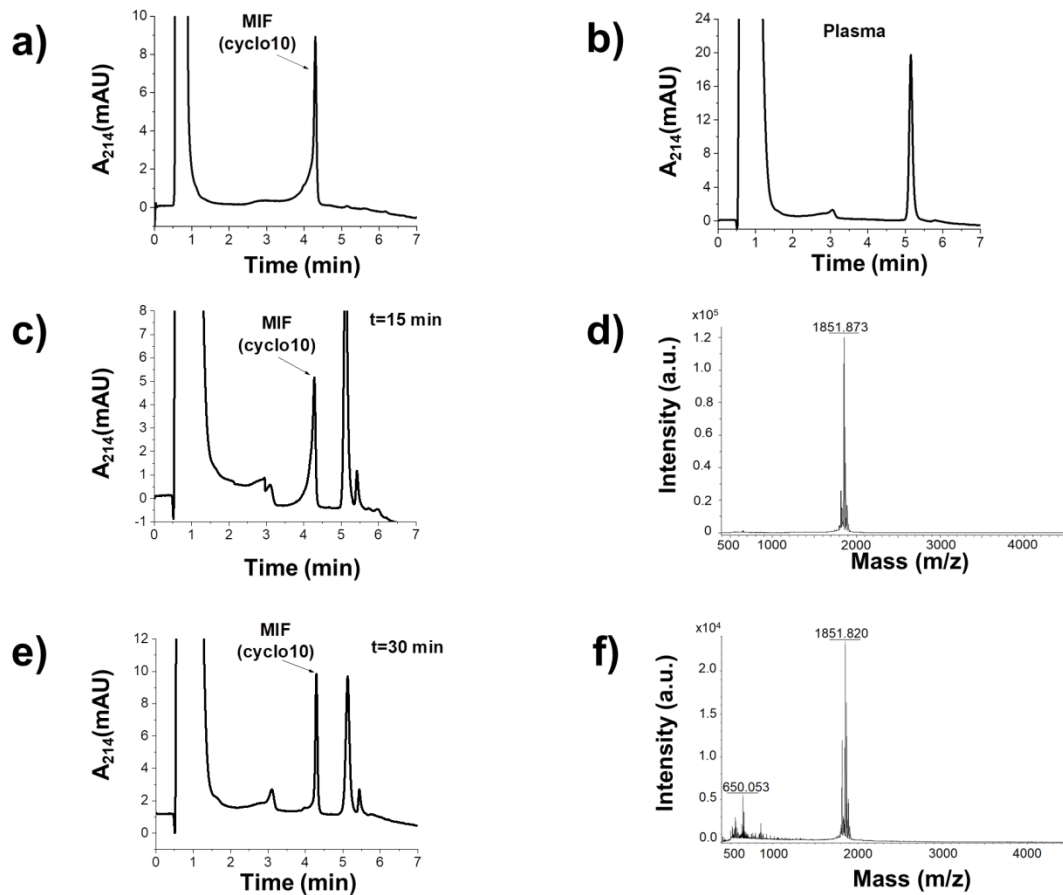
Figure 126. HPLC chromatograms and spectra of MIF(cyclo10) without incubation in plasma, plasma alone and MIF(cyclo10) after incubation in human plasma *in vitro* (37°C) for 15 min and 30 min for the determination of the proteolytic stability.a, b, c, e HPLC Chromatograms of MIF(cyclo10) dissolved in TFA and 80% B (2:8) without any plasma incubation before injection (a), of supernatant of plasma alone after protein precipitation with aqueous 10% TCA (b) and the respective supernatants of MIF(cyclo10) after incubation at 37°C in human plasma (*in vitro*) for 15 min (c) and 30 min (e), as detected by RP-HPLC and their absorbance at 214 nm. **d, f** Spectra of collected peak with $t_R \approx 4.3$ min with the found $[M+Na]^+$ being equal to 1851.873 Da after incubation at 37°C in human plasma (*in vitro*) for 15 min of (d) and 1851.820 Da after 30 min (f), as derived by MALDI-TOF-MS. The calculated $[M+Na]^+$ for MIF(cyclo10) is 1851.68 Da and the incubation shown data are representative from at least three chromatograms and two spectra.
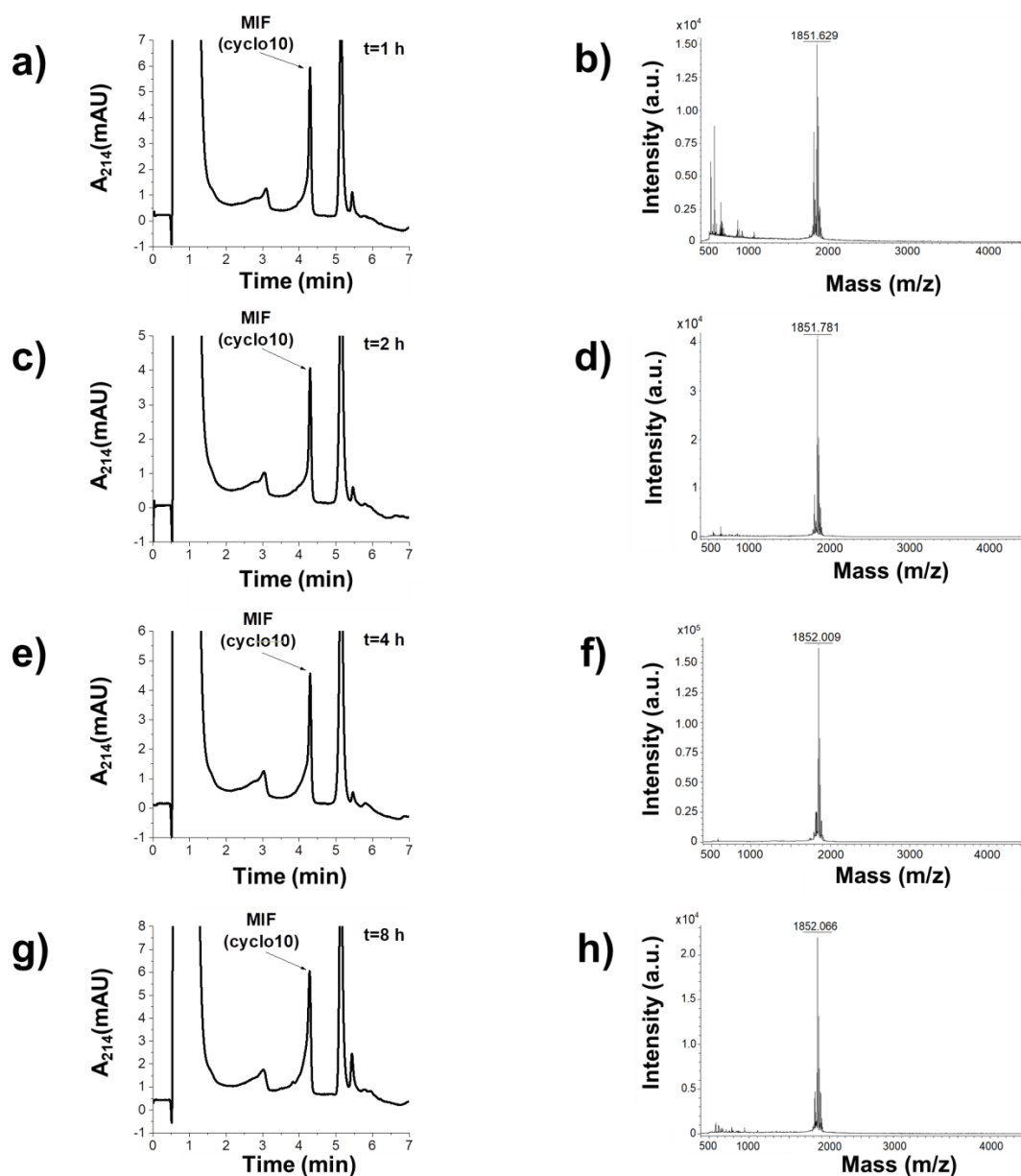
Figure 127. HPLC Chromatograms and spectra of MIF(cyclo10) after incubation in human plasma *in vitro* (37°C) for 1 h, 2 h, 4 h and 8 h for the determination of the proteolytic stability. **a, c, e, g** HPLC chromatograms of supernatant of MIF(cyclo10) incubation at 37°C in human plasma (*in vitro*) for 1 h (a), 2 h (c), 4 h (e) and 8 h (g) and protein precipitation with aqueous 10% TCA, as detected by RP-HPLC and their absorbance at 214 nm. **b, d, f, h** Spectra of collected peak with $t_R \approx 4.3$ min with the found [M+Na]$^+$ being equal to 1851.629 Da after incubation at 37°C in human plasma (*in vitro*) for 1 h (b), 1851.781 Da for 2 h (d), 1852.009 Da for 4 h (f) and 1852.066 Da for 8 h (h), as derived by MALDI-TOF-MS. The calculated [M+Na]$^+$ for MIF(cyclo10) is 1851.68 Da and the incubation shown data are representative from at least three chromatograms and two spectra.
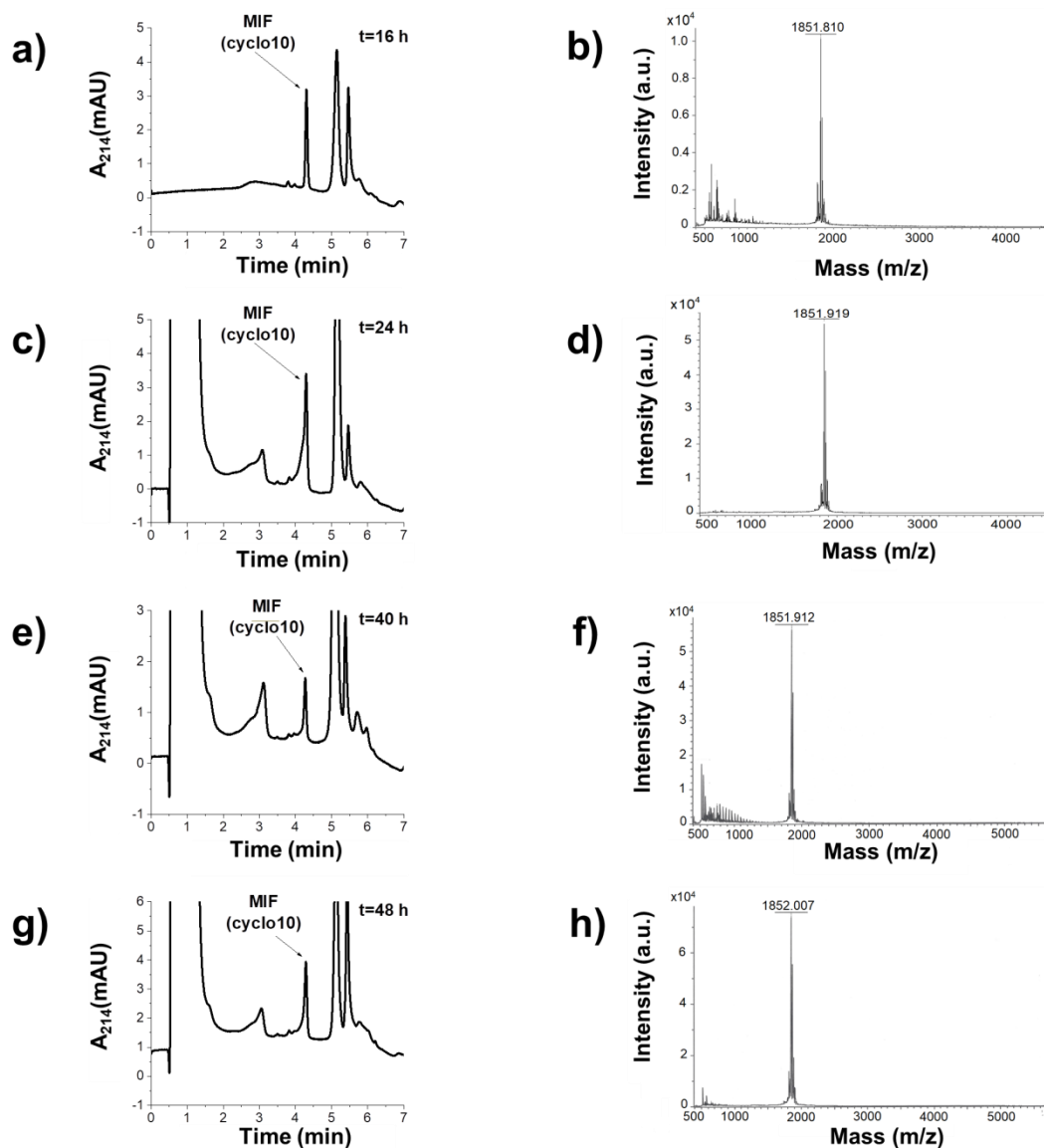
Figure 128. HPLC chromatograms and spectra of MIF(cyclo10) after incubation in human plasma *in vitro* (37°C) for 16 h, 24 h, 40 h and 48 h for the determination of the proteolytic stability. a, c, e, g HPLC chromatograms of supernatant of MIF(cyclo10) after incubation at 37°C in human plasma (*in vitro*) for 16 h (a), 24 h (c), 40 h (e) and 48 h (g) and protein precipitation with aqueous 10% TCA, as detected by RP-HPLC and their absorbance at 214 nm. **b, d, f, h** Spectra of collected peak with $t_R \approx 4.3$ min with the found $[M+Na]^+$ being equal to 1851.810 Da after incubation at 37°C in human plasma (*in vitro*) for 16 h (b), 1851.919 Da for 24 h (d), 1851.912 Da for 40 h (f) and 1852.007 Da for 48 h (h), as derived by MALDI-TOF-MS. The calculated $[M+Na]^+$ for MIF(cyclo10) is 1851.68 Da and the incubation shown data are representative from at least three chromatograms and two spectra (adapted from Krammer et al., ref. [296]).
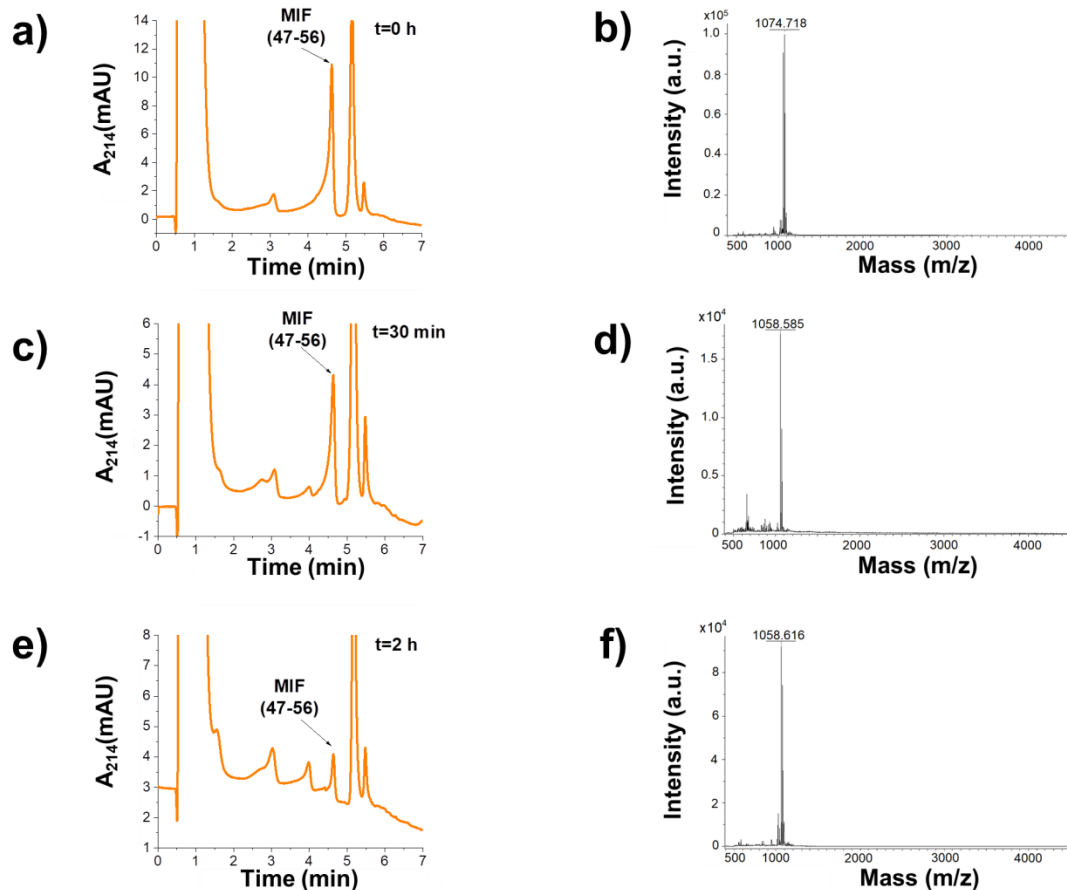
Figure 129. HPLC chromatograms and spectra of MIF(47-56) after incubation in human plasma *in vitro* (37°C) for 0 h, 30 min, and 2 h for the determination of the proteolytic stability.a, c, e HPLC chromatograms of supernatant of MIF(47-56) after incubation at 37°C in human plasma (*in vitro*) for 0 h (a), 30 min (c) and 2 h (e) and protein precipitation with aqueous 10% TCA, as detected by RP-HPLC and their absorbance at 214 nm. **b, d, f** Spectra of collected peak with $t_R \approx 4.6$ min with the found [M+ Na]$^+$ or [M+K]$^+$ being equal to 1074.718 Da after incubation at 37°C in human plasma (*in vitro*) for 0 h (b), 1058.585 Da after incubation at 37°C in human plasma (*in vitro*) for 30 min (d) and 1058.616 Da for 2 h (f), as derived by MALDI-TOF-MS. The calculated [M+Na]$^+$ and [M+K]$^+$ for MIF(47-56) are 1058.42 and 1074.40 Da respectively and the incubation shown data are representative from at least three chromatograms and two spectra.
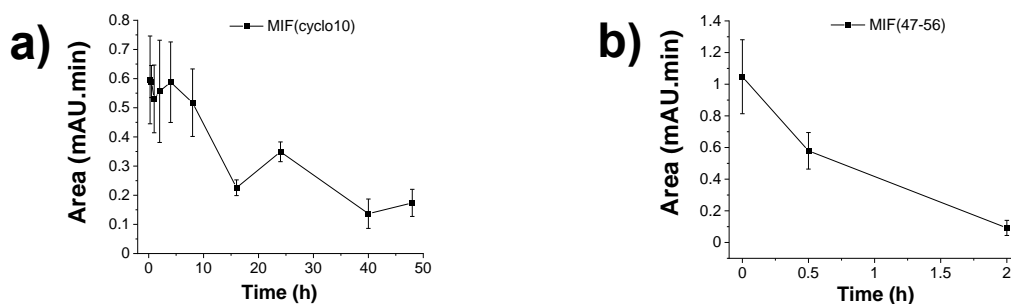
Figure 130. Determination of the proteolytic stability for MIF(cyclo10) and the linear peptide MIF(47-56). a, b The peaks of the eluted recovered intact peptide were integrated and the obtained areas were plotted over the various incubation time points for MIF(cyclo10) (a) and MIF(47-56) (b). Data are from three independent incubations and error bars indicate mean ± SD (adapted from Krammer et al., ref. [296]).

4.7.4 Conclusions on cyclic MIF analogs

Previous studies exhibited a vital role of the MIF region between the 47th and 56th residue for its interaction with CXCR2. Here it is shown that the 10-mer MIF(47-56)

218

is a CXCR2-specific inhibitor that does interfere with MIF. Cyclization of the peptides is known to improve the drug-like properties of the linear ones, and this led us to test various cyclized analogs of the active MIF domain. CD studies of MIF(47-56) and its cyclic analogs recorded in all cases random-coil indicative signal. The linear analog and MIF(cyclo6) and MIF(cyclo10) shared very similar spectra, which exposed flexibility higher than those of the other cyclic peptides. MIF(cyclo10) had the most efficient inhibition of the MIF-mediated B-cell chemotaxis between the two MIF cyclic analogs (data received by the group of Prof. Bernhagen) and was prioritized further. The half lifetime of the cyclic analog in human plasma *in vitro* was more than 8 h, remarkably higher than the 30 min that were determined for the linear. To sum up, MIF(cyclo10) has similar structure and inhibitory potency with the linear (MIF47-56), but its resistance in degradation by the proteases of the human plasma makes it a promising specific blocker of MIF/CXCR2 and therapeutic against atherosclerosis.

5 Discussion

5.1 MIF-specific CXCR4 mimics (msR4Ms)

CVDs remain up to nowadays the main morbidity reason globally. Atherosclerosis is the earlier stage of CVDs, in which the arterial walls are damaged, foam cells are created in the intima, and the plaque is formed before its destabilization and rupture. The atherosclerotic process is identified as a chronic inflammatory vascular disorder with chemokines playing a pivotal role in leukocyte recruitment and adhesion [21a] [297]. Blockade of chemokine-receptor mediated pathways appeals as a promising therapeutic strategy, despite the difficulties due to the complex signal network [198]. MIF is a pleiotropic cytokine with atypical chemokine-like functions. If dysregulated, MIF triggers proinflammatory signaling and gets involved in several diseases, such as cancer, RA, and kidney diseases. Regarding CVDs, MIF acts as a proatherogenic factor that induces its signaling through the chemokine receptors CXCR2 and CXCR4 [77]. However, MIF adapts a cardioprotective role in the ischemic heart via its interaction with the transmembrane protein CD74 [289]. CXCL12/CXCR4 axis is also mainly atheroprotective [198].

Due to its multifunctional properties in many diseases, CXCR4 was at the center of the interest of many therapeutic projects. The second chemokine receptor targeting drug released on the market was AMD3100, an antagonist of CXCR4 for curing patients with non-Hodgkin's lymphoma and multiple myeloma [144]. However, the administration of AMD3100 resulted in mice with increased atherosclerotic plaque progression due to its blockade at CXCL12/CXCR4 axis. Similar results were found for AMD3465, a bicyclam analog of AMD3100 with 10-fold improved efficiency as a CXCR4 antagonist that still inhibits the atheroprotective interaction [207] [196]. Conclusively, another category of compounds with higher specificity is required.

Peptide therapeutics and antibodies (Abs) have increased their market merit in the last years. Both of them are characterized by higher affinity, specificity, and fewer side effects and toxicity than small molecule drugs (SMDs). On the contrary, the Abs still require a high production cost and suffers from a low availability rate in the targeted region due to poor localization [298] [299]. A possible explanation is that Abs could not penetrate the barriers due to their very high affinity with the membrane, and they remain bound. Another issue for Abs is that they are unspecific blockers of the antigen activities [300]. For example, the application of anti-CXCR4 stopped both MIF-and CXCL12-mediated signals by the receptor alone [301].

Peptides may face some of those limitations too, such as poor bioavailability and low permeability. Nevertheless, chemical modification on their sequences, such as introducing N-methylated or D-amino acids amino acids or cyclization, could make peptides capable of overcoming membrane barriers, including BBB, and become more resistant to proteolytic degradation [238]. Overall, peptides are easily synthesized and more affordable than Abs, while they can distinguish between substrates and inhibit more selectively compared to SMDs [238]. Furthermore, following rational design, peptides could be generated as mimics of the protein binding sites and have a therapeutical activity [240].

Herein, it was reasoned to design and synthesize a chemokine receptor mimic with specific blockade of the disease exacerbating interactions and sparing of the protective pathways. Particularly, the mimic had to be a MIF-specific receptor mimic of CXCR4, abbreviated as msR4Ms, that will block the interaction between the

atypical chemokine and the receptor but will not affect the CXCL12/CXCR4 and MIF/CD74 axes. Studies on the binding interface between MIF and CXCR4 uncovered as significant contributors from the receptor side the regions 1-27, located on the N-terminus and termed CXCR4 (1-27), 97-110 on extracellular loop 1 (ECL1), and 182-196 on extracellular loop 2 (ECL2) [98]. ECL1 and ECL2 were chosen to be covalently linked and generate the msR4Ms. CXCR4 (1-27) was excluded due to the presence of many crucial residues for the interaction with CXCL12 and the possible caused problems in the msR4Ms specificity [302].

The applied linkage aimed to mimic the natural distance between the C-terminus of ECL1 and the N-terminus of ECL2. Based on the two available crystal structures of the receptor, the distance between the K110-carboxyl group and the D182-N-terminus varied between 2.18 and 2.25 nm [185] [148]. Several different linkers and combinations were designed and measured in the Moview software and concluded to three different ways for linking. More specifically, the introduction of hydrophobic tandem (6 Ahx)-(12 Ado) between ECDs led to msR4M-L1, while the more hydrophilic O2Oc replaced 6 Ahx to generate msR4M-L2. Of note, ECDs were linked using a similar rational approach by the group of Prof. Eichler for investigating their anti-HIV activity [249]. For the third linked peptide, seven glycines were chosen as linkers (msR4M-LG7), assuming that the polar natural amino acids may result in mimic with high solubility. All available X-Ray structures suggest the presence of a disulfide bridge between their residues C109 and C186, which are present in ECL1 and ECL2, respectively. This native bridge was additionally formed to the msR4Ms linked with non-natural amino acids (msR4M-L1ox, -L2ox) for examing its effect compared to the reduced peptides. The last analog was termed msR4M-LS and was developed to shed light on the role of the linkage. Notably, it was not bonded through linkers between the terminus of ECDs, but only through the disulfide bridge of their cysteines. Overall, the existence of a crystal structure might provide significant important information for the design of a receptor mimic, but it has to be taken into consideration that GPCRs are flexible proteins and could adopt different conformations depending on the environment and the presence of a bound ligand or interacting proteins [303]

Mimics and ECDs were synthesized following Fmoc-SPPS protocols on a Rink resin. In the low yield couplings, HATU replaced HBTU as an activator, and an additional coupling circle might be applied. Cysteines are prone to racemize, therefore it was conjugated with milder base conditions and slightly reduced coupling time [255]. Peptides were cleaved from resin and side-chain deprotected with Reagent K for 3 h, due to the presence of protecting groups that require scavengers [267] [304]. RP-HPLC was applied for the purification of the peptides and MALDI-TOF-MS or ESI-MS for their purity determination. Though, the mass spectra of the first msR4M-L1 synthesis showed next to the expected MW a lower but significant peak with -18 Da.

From the early steps of peptides synthesis, it was found out that similar peaks occurred due to the Asi formation on the side chain of an aspartic acid [263]. Later on, it was discovered that the Asi formation is dependent on the amino acid that was coupled before the acidic residue [261]. Notably, Asi accumulates more as the synthesis proceeds further due to the high exposure to the piperidine. The most recent Asi formation hindering approach targeted the side chain of the aspartic acid and suggested the replacement of the typical tBu protecting group with more bulky

ones [258]. The first prevention method was developed in the late 1970s and focused on milder N-terminus cleavage conditions, with 0.1 M HOBt in 20% piperidine in DMF replacing the 25% piperidine in DMF solution [263] [261]. Several other solutions were tested later, too, with the HOBt/containing one remaining one of the most efficient. Considering its long-term tested efficiency and its lower cost compared to special side-chain protected groups, 0.1 M HOBt in 20% piperidine in DMF substituted the conventional 25% piperidine in DMF as Fmoc-deprotecting solution. Moreover, the two deprotecting circles were reduced from 5 and 20 min that of the conventional method to 3 and 9 min ('Short HOBt protocol').

In the msR4M-L1 sequence there are four aspartic acids of which the carbon of the carboxylic group might be nucleophilic attacked, i.e., D97 in the ECL1 part and D182, D187, D193 in the ECL2 part. Mass spectra of ECL2 recorded already the same reduced peak compared to the expected MW, excluding the possibility of an Asi formation in D97. It is also very unlikely that D182 is the amino acid that the side reaction since it is the last coupled amino acid and was exposed only for 5 and 20 min in the Fmoc deprotecting solution. To be sure to minimize the side reaction, 'Short HOBt protocol' was applied as the Fmoc cleavage method after the coupling of the first aspartic acid, i.e., D193, in ECL2 and all msR4Ms syntheses. For ECL1, the conventional method was followed.

All peptides were purified with typical RP-HPLC methodology, a gradient elution program, and a tandem of a pre-column and a column, and the collected peaks were verified by MALDI-TOF-MS. ECDs were conventional analyzed by mass spectrometry in Matrix solution A and A (matrix), whereas msR4Ms were not detected with this methodology. A possible reason might be the failure of the mimics to crystallize under this solution due to their big size and high hydrophobicity. Therefore, Matrix solutions B and B (matrix) were applied to msR4Ms and brought an improvement to their crystallization. In a few cases, such as for msR4M-L2 and- LS, the obtained spectra were noisy, and among the expected peaks, several others were detected. An amount of purified mimic was provided for an HPLC-ESI-MS analysis to clarify whether those molecular weights correspond to real side products or artifacts that might appear due to the insufficient crystalization of the peptides. After obtaining a pure and sufficient amount of the products, the peptides were biophysically characterized. All peptides were lyophilized to powder and were dissolved just before the beginning of the experiment. Maintanencae of peptides in solid form is a wide applied method to support and enhance their chemical and physical stability and avoid aggregation [305].

Both ECDs were random coil, with ECL1 having few more ordered species on its structure. The mixture of both ECDs in 1 to 1 proportionality remained unorder, too. Nevertheless, things changed when the non-natural amino acids were introduced in the between of the ECDs. Both msR4M-L1 and msR4M-L2 exhibited β-sheet indicative spectra, while their oxidized analogs did not remarkable differentiate to the reduced ones. However, when ECL1 was conjugated to ECL2 via the seven subsequent G, the generated msR4M-LG7 analog lacked structure (Figure 131a). No spectra of msR4M-LS were received due to its unfavorable soluble properties even at 5 µM. All the rest msR4Ms precipitated at 50 µM, except for msR4M-L2ox which remained soluble until this point and the ECDs that precipitated at 20 µM.

An overview of the data shows that msR4M-L1, -L2, and their oxidized analogs are the only ordered peptides. This finding might be correlated with the non-

natural amino acids applied linkage strategy. In both sequences, 12 Ado was the standard linker, followed by 6 Ahx in msR4M-L1 and O2Oc in msR4M-L2. Hydrocarbon chains may be involved in London dispersion forces but are insignificant. However, linkers offer higher flexibility than the very limited rotation and twist of the peptide bond due to its partial double-bond character [306]. The msR4Ms adopted a β-strand, an ordered state which contained several intermolecular hydrogen bonds. Based on their interaction pattern, they could result either in parallel or antiparallel β-sheets [307]. Overall, hydrogen bonds aligned better in antiparallel β-sheets having a more energetically favorable structure [308] [309]. The nature of the sheets might be the reason that the disulphide bridge did not affect the secondary structure of msR4M-L1. A hypothesis is that msR4M-L1 contains antiparallel β-sheets that form a β-hairpin which is stable and not affected by the disulfide bridge [310]. The hairpin formation could be induced by aromatic residues of the mimic and their interactions, such as W/W, W/Y, and Y/Y, which may play a structural stabilization with decreased strength order [311]. Notably, the commonly found in β-sheets aromatic residues are the 25% of residues in msR4M-L1, -L2 sequences [312]. The high percentage of aromatic residues might be the reason for the limited solubility of the mimics, too. The delocalized π-electrons of aromatic residues might be involved in interactions that lead to poor soluble analogs [313]. Additionally, non-natural amino acid linkage might reducing hydrogen bonds and affect the solubility of the mimics [314].

Next, it was aimed to determine the self-association of msR4Ms and ECDs. Both ECDs remained mainly monomers until 10000 nM, but their linkage induces their oligomerization, except for the stabilization of their secondary structure. All CXCR4 mimics tended to self-assemble with dissociation constants in the nanomolar range. Even though the differences were not very significant, msR4M-L1 appears to be the second less prone to self-associate mimic before msR4M-L2ox, followed up from its oxidized analog. The other two mimics, msR4M-L2 and msR4M-LG7, showed a slightly stronger self-assembly propensity (Figure 131b). Other ectodomain mimics that formed β-sheet were shown to self-assemble, too, however, in the micromolar range [248]. The carbonyl-carbonyl interactions that are more abundant in the ordered secondary structures were essential in peptide self-assembly in other cases and might induced the self-association of CXCR4 mimics [315] [316].

Fluorescence spectroscopy was further applied for studies on the hydrophobic surface of selected mimics. Mixtures of ANS and msR4M-L1 exposed an increased emission at 5 μM that became more intense at 10 and 15 μM, before its precipitation at 20 μM. Under the same conditions, msR4M-L2 remained soluble until this concentration with significantly reduced emission (Figure 131c). Overall, peptides containing carboxyhydrates chains in their sequences had an increased tendency for oligomerization [317]. Contrariwise, the polar oxygen atoms of PEG and the hydrogen atoms of water molecules in an aqueous solution are prone to form hydrogen bonds. Those interactions may lead to the burying of hydrophobic residues and could explain the ANS emission differences between msR4M-L1 and -L2 [318].
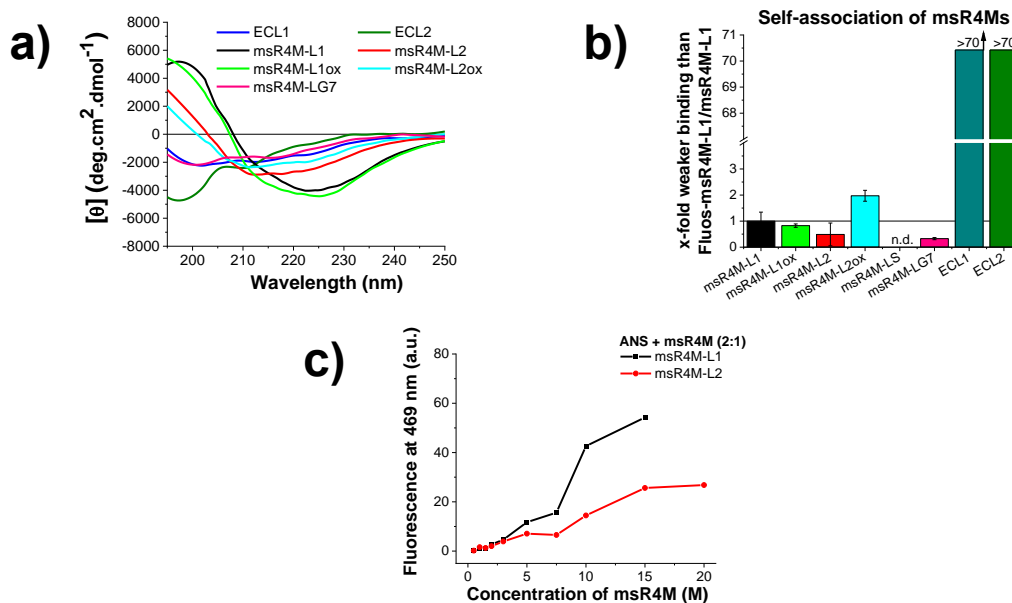
Figure 131. Comparative biophysical characterization of msR4Ms and ECDs. a CD spectra of peptides at 5 µM (except for ECL1 at 10 µM) with their mean residue ellipticity (MRE) being plotted over the wavelength between 195 and 250 nm (HT<1000). **b** Normalized dissociation constants (app. K_{ds}) of the self-association of the peptides with reference to the app. K_d of msR4M-L1 self-assembly. **c** Fluorescence emission at 469 nm over increased concentration of ANS/peptides mixture in a constant 2:1 proportionality. The final measuring conditions were aqueous 1×b, pH 7.4, containing 1% HFIP in all assays (adapted from Kontos et al., ref. [291]).

After the biophysical studies, the binding ones were the next to follow. Previous SPOT-array derived data indicated ECL1 and ECL2 as the binding regions of the receptor for MIF but did not quantify the precise strength of the affinity [98]. Herein, instead of solid-state, the interactions were examined in solution with fluorescence spectroscopic titrations and exhibited a medium and weak affinity of Alexa-488-MIF to ECL1 and ECL2, respectively. The affinity was significantly improved when the two ectodomain segments were linked with non-natural amino acids in the presence or absence of a disulfide bridge. Particularly the app. K_d between the msR4Ms and MIF were in the two-digit nanomolar range, with similar results being obtained with the reverse experimental setup and the peptide as the labeled analyte. Another analog named msR4M-LS, in which the ECDs were linked only with the disulfide bond, showed a remarkable strong affinity for MIF. MsR4M-LG7, the last tested mimic, with the seven glycines between its ectodomains and the only one with random coil structure, failed to bind to MIF (Figure 132).
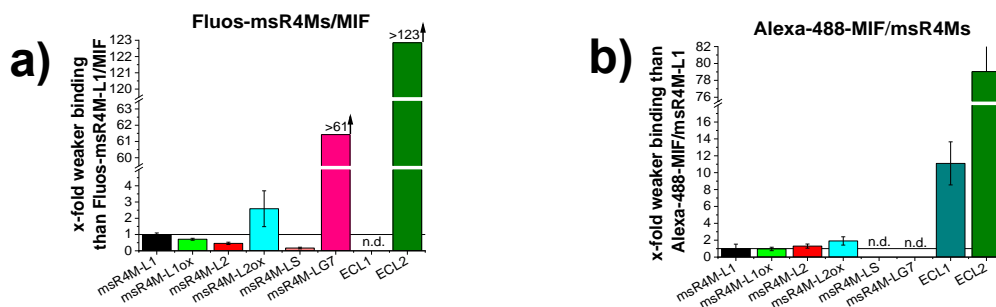
Figure 132. Comparison of binding affinities of msR4Ms or ECDs to MIF. a, b Normalized dissociation constants (app. K_{ds}) of the Fluos-msR4Ms/MIF (a) and Alexa-488-MIF/msR4Ms (b) titrations with reference to the app. K_d of Fluos-msR4M-L1/MIF and Alexa-488-MIF/msR4M-L1, respectively (n.d. not determined, x-fold for ECL2 in Fig 132b is 79±39). The final measuring conditions were aqueous 1×b, pH 7.4, containing 1% HFIP in all assays.

Overall, short linear peptides exhibit conformational freedom in solution, and the limitation of their very flexible conformations during binding may lead to entropic penalty and weak affinities with their substrates [319]. Therefore, peptides that adapt well-ordered structures are more prone to have high affinity [320]. Indeed, all the constrained mimics with non-natural amino acids had an ordered structure and high affinity to MIF, contrary to the random coil ECDs and msR4M-LG7. The presence of a disulfide bridge in msR4M-L1ox and -L2ox had a minor effect on their secondary structures and affinity with MIF compared to their reduced analogs. Surprisingly, msR4M-LS showed a single-digit nanomolar affinity for the atypical chemokine, even without the presence of any linkers between ECL1 and ECL2. However, due to its limited solubility, no CD data were recorded, and its strong affinity with MIF could not be correlated with its secondary structure. A hypothesis might support that due to the lack of restriction between the terminuses of ECDs, aromatic amino acids of msR4Ms were more exposed, and this enhanced the binding with MIF.

Additional binding studies were carried out between the prioritized mimic msR4M-L1 and MIF and monitored with FP and MST. FP was already applied previously for studying protein-ligand interactions, including the ones between MIF and its inhibitors [321] [322] . As in the previous studies, both Fluos-mimic and Alexa-488-MIF were employed as the labeled analytes and titrated against unlabelled protein and peptide, showing app. K_{ds} of 24.4 ± 5.3 nM and 10.6 ± 1.2 nM, respectively. MST is a recently discovered technique and may determine dissociation constants in the low picomolar range with minimum required amounts [286]. As in previous studies, both Fluos-mimic and Alexa-488-MIF were employed as the labelled analytes and against unlabelled protein and peptide with very similar affinities. Microscale thermophoretic titrations between TAMRA-msR4M-L1 and MIF exhibited an app. K_d of 77.2 ± 37.1 nM, confirming their strong affinity.

Next, it was examined whether the binding between msR4M-L1 or other mimics with MIF induces changes in their secondary structures. Spectra of mimic/protein mixtures were recorded and compared to the sum of their individual signals, but the signal remained unchanged in the 10:1 msR4M-L1:MIF mixtures (Figure 133a). Likewise, the oxidized analogs msR4M-L1ox and -L2ox did not cause any structural differentiation to MIF when placed in 10-fold excess (Figure 133a, b). MIF was shown to have a well-ordered structure with remarkable stability, and it might be hard for a peptide to cause alternations in this rigid conformation [83]. Interestingly, the lack of any effect in the MIF secondary structure, including β-strands, is indicative of non-competition with the CD74 for binding to MIF [323].
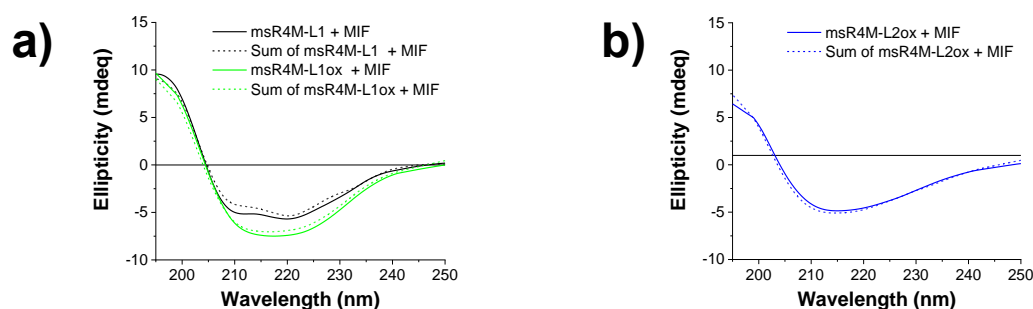
Figure 133. Comparison between the secondary structures of msR4Ms/MIF mixtures. a, b CD spectra of msR4Ms (5 µM)/MIF (0.5 µM) mixtures (line) and the sum of their individual spectra (dashed line). The ellipticity of the spectra is plotted over the wavelength between 195 and 250 nm (HT<1000) and the final measuring conditions were aqueous 1×b, pH 7.4, containing 1% HFIP.

More binding studies were carried out between the msR4Ms that are MIF-binders and the other CXCR4 substrate, CXCL12. Fluorescence spectroscopic titrations of Fluos-msR4Ms with the chemokine showed that binding is dependent on the presence or not of a disulfide bridge. Particularly, the non-oxidized analogs Fluos-msR4M-L1 and L2 failed to bind to CXCL12 until 6340 nM, showing at least 155-fold selectivity over MIF compared to the app. K_{ds} derived by the Fluos-msR4M/MIF titrations. Contrariwise, their oxidized analogs Fluos-msR4M-L1ox and L2ox and the linked via disulfide bridge analog Fluos-msR4M-LS bound strongly to the chemokine, with their determined app. K_{ds} being comparable to their respective ones with MIF (Figure 134). According to the crystal structure models, this disulfide bond exists in the native form of CXCR4 and shapes the entrance of the receptor to the ligand-binding pocket [185] [148]. More structural studies underlined its necessity in the transmission of the signaling throught the receptor [324]. In agreement with these findings, receptor mutation studies showed that single substitutions of the cysteines either of ECL1 or ECL2 decreased to one-third the strength of the CXCL12/CXCR4 interaction [325]. Other peptide or Ab-based CXCR4 mimics that contained the ectodomains of the receptor bonded with the disulfide bridge also had strong binding with CXCL12 [250] [247]. Conclusively, the MIF-specificity of the CXCR4 ectodomain mimics passes through the lack of the disulfide bridge.
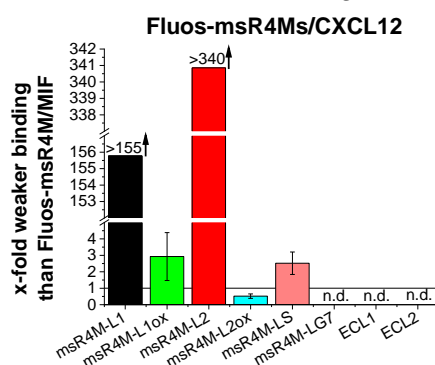
Figure 134. Comparison of the selectivity of msR4Ms towards binding CXCL12 over MIF. The selectivity is determined as the quotient of the app. K_{ds} of Fluos-msR4M/CXCL12 divided by the app. K_d of Fluos-msR4M/MIF. The final measuring conditions were aqueous 1×b, pH 7.4, containing 1% HFIP in all assays.

The msR4M-L1/CXCL12 interaction was investigated further with FP and MST. The experimental conditions were kept identical to when MIF was applied as the titrant and showed dissociation constants above 2500 nM with FP and 3125 nM with MST. Taken together and compare all msR4M-L1 titrations, the mimic exhibited an above 155 times increased affinity for MIF over CXCL12 as determined by fluorescence spectroscopy, higher than 100 times based on FP, and above 40 times, according to MST. None of msR4M-L1 and -L2 inhibited the CXCL12-mediated B-cell chemotaxis as found by the group of Prof. Bernhagen [291]. However, in the same concentration msR4M-L2 exhibited a more intense, even if not significant, trend to block this interaction than msR4M-L1. Alexa-488-CXCL12 measurements were not carried out due to the notion that Alexa-488 might be conjugated on the crucial residue K1 of CXCL12 or another binding-relevant lysine [148]. To summarize, msR4M-L1 has a weaker CXCL12-blocking tendency and aggregation propensity than msR4M-L2, thus it was prioritized for further studies (Table 60).

The next aim was to determine the hot spot regions in msR4M-L1/MIF interaction. Initially, labeled mimic was titrated against various MIF fragments and the MIF region 38-80 was revealed as the binding region of the Fluos-msR4M-L1 with a similar binding affinity to the one of the whole protein. Noteworthy, an MIF targeting antibody that bound to MIF(46-68), which is enclosed in the 38-80 region, was shown to inhibit the cell proliferation [326]. A weak app. K_d for the region 81-95, mainly due to residues C81 and V95, was noted, too. To uncover the precise binding epitope of the atypical chemokine, systematic shortened MIF(38-80) analogs were analyzed even further. MIF(54-80) was found out as the shortest MIF fragment that maintains a comparable to the whole protein affinity with msR4M-L1 (Figure 135). Similar results were obtained for msR4M-L2, -L1ox, while the binding epitope of msR4M-LS was narrowed to MIF(62-80). Even though the regions of 38-80 and 54-80 are located in well-ordered regions of MIF, CD spectra revealed that the 43-mer MIF(38-80) and the 27-mer MIF(54-80) lacked any order. More titrations were performed between Fluos-msR4M-L1 and mutated MIF in the 47-57 region, confirming the N-like loop's importance for the binding. Particularly, the lead mimic failed to get saturated by C57S-MIF and MIF(10xAla), suggesting app. K_{ds} in the micromolar range. [C57S]-MIF had an identical secondary structure with WT-MIF, but with slightly less stability, probably due to the different properties of –SH (Cys) compared to –OH (Ser) [76] [327].
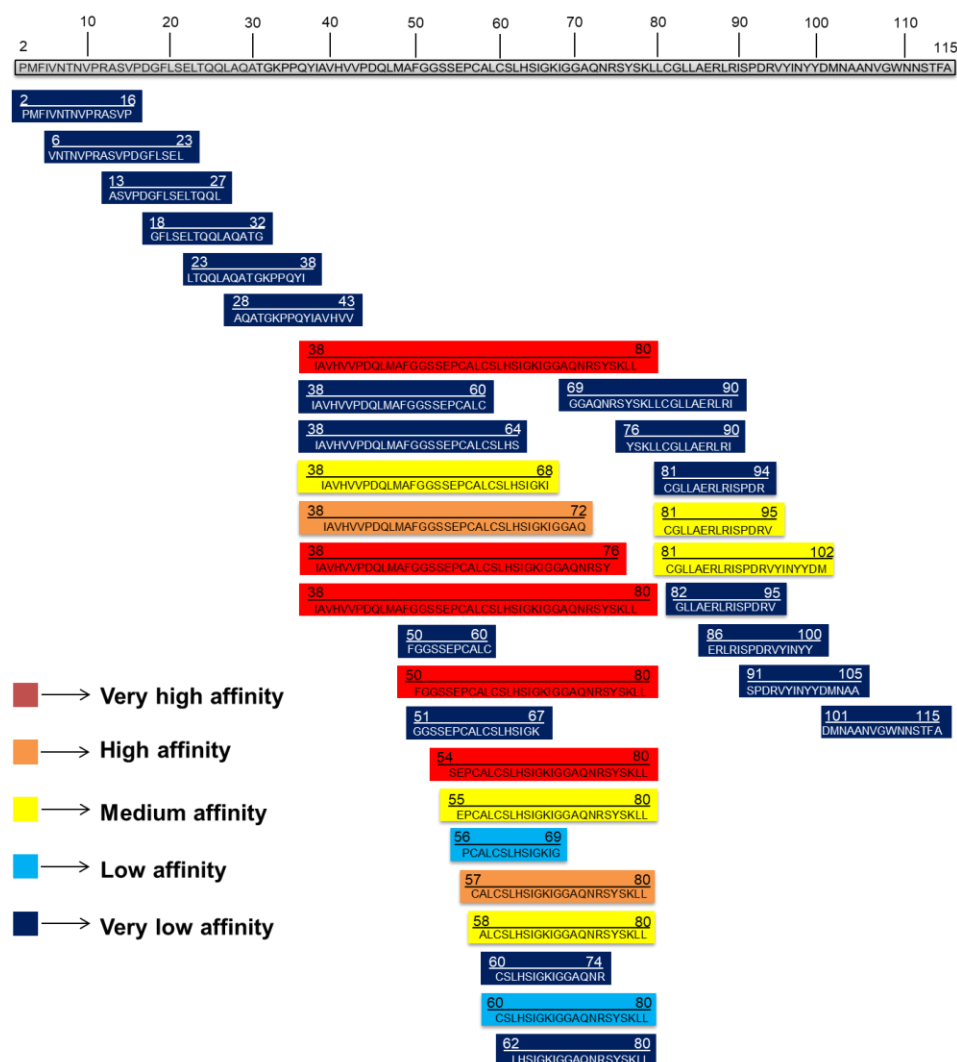
Figure 135. Determination of the MIF binding core in the interaction with msR4M-L1. Based on the derived app. K_{ds} of Fluos-msR4M-L1/MIF fragment fluorescence spectroscopic titrations and how many times is it higher than the one derived by Fluos-msR4M-L1/MIF, the MIF fragments are classified as those with very high affinity (< 3.3-fold higher app. K_d), high affinity (3.3-10-fold higher app. K_d), medium affinity (10-33-fold higher app. K_d), low affinity (33-100-fold higher app. K_d) and very low affinity (>100-fold higher app. K_d) with msR4M-L1 (adapted from Kontos et al., ref. [291]).

SPOT array, a flexible and affordable method for identifying potential essential residues in protein-protein interactions, was applied to uncover the core regions of msR4M-L1 for the interaction with MIF [328] [329]. Even though protein-protein interactions involve large sections, some specific residues, termed as hot spots', play a pivotal role in their complex formation [330] [331]. Mutants of ECL1 and ECL2, the two parts of each msR4M, were synthesized on cellulose membrane via SPOT array methodology and evaluated after incubation with biotinylated MIF. Epitopes 102-108 and 188-196 were determined as the core regions with the aromatic acids W102, Y103, F104, F107 from ECL1 and F189, Y190, W195 from ECL2 being crucial in the binding with MIF. Besides, msR4M-L1 mutants were generated with alanine substitutions on F104, F107 (2xAla), on W102, Y103, F189, Y190, W195 (5xAla), or in all seven residues simultaneously (7xAla).

CD spectroscopy studies revealed that all mutants were mainly unordered, with the amount of random coil being proportionally increased with the number of the substitutions. The double mutant had very similar aggregation and solubility

properties with the native peptide, while msR4M-L1(5xAla) and msR4M-L1(7xAla) remained soluble until 50 μM. Another analog of msR4M-L1 was synthesized with a K3-tag on the N-terminus (K3L1), aiming to be more soluble and maintain the ordered structure. The msR4M-K3L1 kept mainly the ordered structure, though, it precipitated at 50 μM, as the msR4M-L1 (Figure 136). Apparently, the bonds and the forces that induce precipitation were not affected by the K3-conjugate on the N-terminus.

.
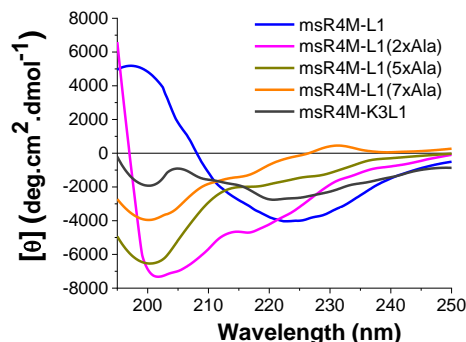
Figure 136. Comparison of the secondary structure of alanine mutants and K3 analog of msR4M-L1 with the native mimic. CD spectra of peptides at 5 μM with their mean residue ellipticity (MRE) being plotted over the wavelength between 195 and 250 nm (HT<1000). The final measuring conditions were aqueous 1×b, pH 7.4, containing 1% HFIP in all assays (adapted from Kontos et al., ref. [291]).

The substitution of an aromatic acid with the smaller alanine might cause interference in the ordered state of the peptide [332]. Interactions that involve aromatic residues, such as cation-π, Cys-Phe, and Cys-Trp are crucial for the stabilization of the β-sheet [333] [334] [335] [336]. Even though weaker, the aromatic interactions might also induce structural stabilization, as most likely occurred in msR4M-L1. In the CXCR4 X-ray structure, the aromatic ring of F104 is located between the aromatic rings of W102 & Y103, in a shorter distance than 0.5 nm for each. A hypothesis is that this short distance is due to π-π interactions between those residues in CXCR4 ectodomain and possibly in msR4M-L1. For that reason, those interactions might be disrupted by the substitution of F104 with a non-aromatic residue, resulting in the destabilization of the secondary structure in msR4M-L1(2xAla) and (7xAla). Notably, F107 does not seem to be located closely to these residues and is less likely to participate in these interactions (Figure 137).
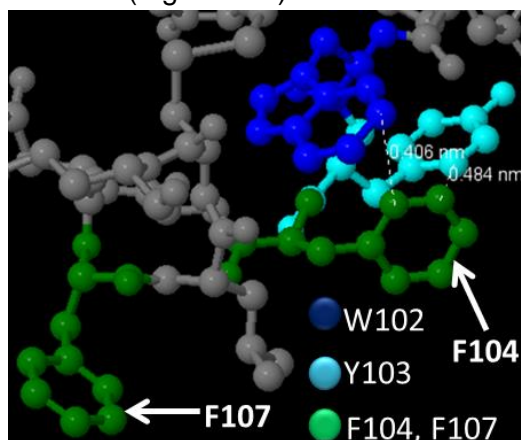
Figure 137. Location of W102, Y103, F104 and F107 on CXCR4 structure. Zoomed view of ECL1 on CXCR4 as spheres, with W102 colored in green, Y103 in cyan and both F104 and F107 in green. The crystal structure was visualized by Jmol (http://www.jmol.org) and obtained from protein data bank (PDB code: 3ODU) as published by Wu and colleagues [185].

Fluorescence spectroscopic titrations of the alanine mutated analogs with MIF shed light to the importance of the aromatic residues for binding MIF. The double alanine mutated analog in F104, F107 had at least 40-fold worse affinity than the wild-type peptide. MsR4M-L1(5xAla) maintained a part of its affinity and had a four-times worse binding, despite the multiple substitutions. However, the additional substitution of F104 and F107 with alanines abrogated the binding for the msR4M-L1(7xAla) analog (Figure 138). Replacement of hydrophobic bulky side chains with the shorter methyl group of alanine may disrupt essential hydrophobic interactions for the peptide binding mechanism [332]. The K3-conjugate did not affect the binding of the mimic to MIF. Conclusively, F104 and F107 are crucial residues not only for the maintenance of the ordered structure of msR4M-L1, but also for its binding to MIF.

Many SAR studies involved CXCR4 with other ligands, but none of them referred to F104 or F107 showing a possible receptor-specific role of the aromatic residues on MIF binding. Particularly for the extracellular loop 1 and 2 of the receptor, a crucial role for the residues D97, D187, F189, N192, and W195 has been suggested for the interaction with CXCL12 [148] [188] [187]. More SAR studies were carried out to investigate the binding interface for another substrate of the CXCR4, the HIV glycoprotein gp120. Several acidic residues of CXCR4, including the ectodomain residues D97, D187, and D193, have been reported to be critical for HIV infectivity [193]. Further studies confirmed the necessity of those residues together with D182, Y190, L194, W195 for the binding to gp120 [337]. The crystallization of CXCR4 with vMIP-II, a CC chemokine encoded by Kaposi's sarcoma-associated herpesvirus, revealed a vital role of D97, W102, D182, I185, C186, D187 for this interaction [150].
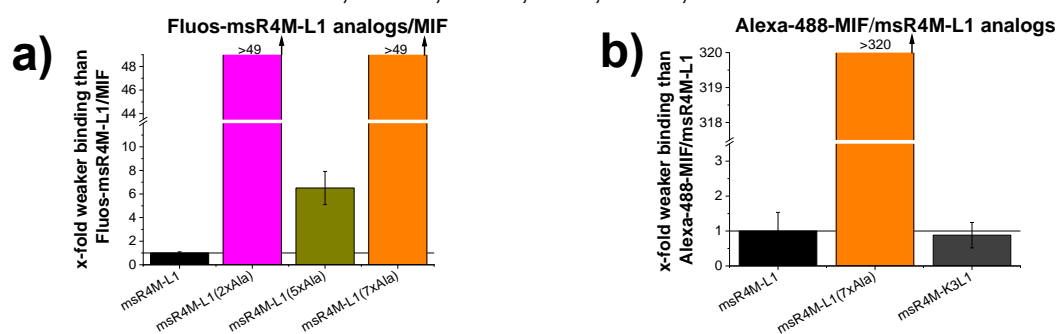
Figure 138. Comparison of binding affinities of alanine mutants or K3 analog of msR4M-L1 to MIF. a, b Normalized dissociation constants (app. K_{ds}) of the Fluos-msR4Ms/MIF (a) and Alexa-488-MIF/msR4Ms (b) titrations with reference to the app. K_d of Fluos-msR4M-L1/MIF and Alexa-488-MIF/msR4M-L1, respectively. The final measuring conditions were aqueous 1×b, pH 7.4, containing 1% HFIP in all assays.

CD74 is a cell-surface receptor of MIF and their signaling pathway may trigger many disease-exacerbating diseases but not in atherosclerosis. Contrariwise, together they exert a cardioprotective effect which is desired to be preserved by a MIF-specific binder and inhibitor [289]. To address whether our lead mimic affects or not the MIF/CD74 complex formation, labeled-MIF was titrated against increasing concentration of sCD74, a soluble CD74 analog, in the presence or absence of msR4M-L1. The titrations were recorded by FP or MST and showed that the presence of CXCR4 mimic did not affect the binding affinity between the cytokine and the transmembrane protein (Figure 139, Table 60). The MIF/sCD74 app. K_d is overall in line with the previously determined by SPR (9 nM) setup [92].
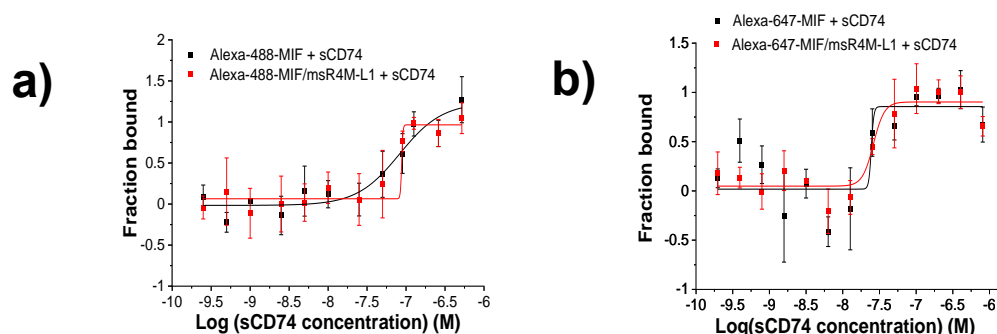
Figure 139. Competitive binding of CD74 and msR4M-L1 for binding to labeled-MIF. **a, b** Normalized titrations between Alexa-488- (a) or Alexa-647-MIF (b) and soluble CD74(73-232) (sCD74) in the presence or absence of msR4M-L1 as recorded by fluorescence polarization (FP) and microscale thermophoresis (MST), respectively. Labeled-MIF was either left untreated (black curve) or was pre-incubated with a 10-fold (for MST) or 20-fold (for FP) molar excess of msR4M-L1 (red curve). Normalization was carried out with reference to the ΔF_{norm} (‰) for MST or FP (mP) at 519 nm of the bound state of the titrations. Data are means ± SD of three independent titration experiments (adapted from Kontos et al., ref. [291]).

Table 60. Apparent affinities (app. K_{ds}) between MIF and msR4M-L1, or MIF and sCD74 in the presence or absence of msR4M-L1, as determined by fluorescence spectroscopic titrations, FP or MST (adapted from Kontos et al., ref. [291]).

	app. K_d (±SD) (nM) [a] Labeled msR4M-L1/ MIF	app. K_d (±SD) (nM) [a] Alexa-488-MIF/ msR4M-L1	app. K_d (±SD) (nM) [a] Labeled msR4M-L1/ CXCL12	app. K_d (±SD) (nM) [a] Labeled MIF/CD74	app. K_d (±SD) (nM) [a] Labeled MIF/CD74 + msR4M-L1
Fluorescence spectroscopy	40.7 ± 4.0 [b]	31.1 ± 16.6	> 6340 [b]	n.d.	n.d.
FP	24.4 ± 5.3 [b]	10.6 ± 1.2	> 2500 [b]	114.4 ± 47.0	89.4 ± 55.3 [d]
MST	77.2 ± 37.1 [c]	n.d.	> 3125 [c]	33.9 ± 5.0	34.5 ± 13.1 [e]

[a] App. K_{ds}, are means (±SD) from three independent titration experiments; [b] Fluos-msR4M-L1; [c] TAMRA-msR4M-L1; [d] Alexa-488-MIF; [e] Alexa-647-MIF, n.d. not determined

The titrations between the msR4M-L1 and MIF fragments uncovered MIF(38-80) and particularly MIF(54-80) as the core MIF binding region. A relatively weak affinity was also determined for the MIF(81-95), which was abolished if C81 or V95 were eliminated. On the other hand, MIF(80-87) appeared to be the binding region of CD74, as SPR data initially suggested [94]. Neutrophil recruitment studies of MIF mutants revealed Y37, K67, and N110 and indirectly P2 as critical residues for the CD74 activation [93]. The vital roles of Y100, located in the terminus of the MIF solvent channel, and of β-strands were highlighted for the activation of CD74, too [323]. Of note, MIF solvent channel is formed in the trimer structure, which has been suggested as the form of MIF that binds to CD74 [338]. Except for K67, the other residues are not included in the MIF(54-80). Conclusively, msR4M-L1 may not affect the MIF/CD74 interaction due to distinguished non-overlapping mechanisms with CD74 for binding to MIF.

5.2   SAR studies on ECL1 and ECL2

Previous SAR studies derived by SPOT array analysis scanned 14-or 15-mers of CXCR4 ectodomain and uncovered ECL1 and ECL2 peptides as the binding interface of the receptor for binding with MIF [98]. As described previously, those peptides were synthesized and characterized before their linkage and the generation of msR4Ms. Notably, the dissociation constants of ECL1 and ECL2 revealed medium and weak affinity for MIF, respectively. Then, it was aimed the identification of even shorter active binders of MIF derived by ECL1 and ECL2, if possible with improved binding properties, and the estimation of their secondary structures. Shorter ECD analogs were synthesized with Fmoc-SPPS as the native peptides, purified by HPLC, and their purity was confirmed with MALDI before testing.

Initially, it was desired to define their secondary structures with CD spectroscopy. As previously shown, both ECDs exposed random coil with ECL1 presenting more ordered species than ECL2. The C-terminus shortened analogs ECL1(97-107), ECL1(97-108) had similar spectra with ECL1, while ECL1(97-109) is more ordered (Figure 140a). Possibly, C109 is prone to form anion-π interactions with any of the aromatic residues of ECL1 (W102, Y103, F104, F107), but the presence of K110 in the native ECL1 sequence hinders this interaction [334] [335] [336]. The N-terminus shorter analogs ECL1(100-110), ECL1(101-110), and ECL1(102-110) presented an overall similar signal shape with the native peptide having a mainly unordered structure with partially ordered traces which were vanished after elimination of W102 and Y103 (Figure 140b). From all analogs, ECL1(97-107) precipitated at 20 µM, as the native peptide, ECL1(101-110), and ECL1(102-110) at 50 µM, while all the others remained soluble until this concentration.

The shortening of the other ectodomain peptide of interest, ECL2, induced the disordering in many cases except for ECL2(187-194) and ECL2(188-195), which have similar CD spectra with the native peptide. The extended analog ECL2(176-200), which contains all the residues of extracellular loop 2, is more ordered than ECL2 but still adapts mainly the random coil structure (see Appendix Figure A3). Notably, the shortening appeared to induce the π-π interaction but only if two of F189, Y190, and W195 are present in the sequence (Figure 140c-e). All peptides remained soluble until 50 µM, except for ECL2(189-194) that precipitated in this concentration and ECL2(176-200) and ECL2(188-195) at 20 µM.

From the C-terminus shortened analogs, only ECL1(97-109) had strong binding with Alexa-488-MIF, particularly 4 times stronger than the native peptide. The further elimination of C-terminus residues resulted in abrogation of binding. Contrariwise, the N-terminus shortening led to ECL1(100-110) with similar binding affinity to the atypical chemokine and to ECL1(101-110) and ECL1(102-110) that are four to five times more potent binders of MIF. However, the additional subtraction of residues disrupted the binding for the analogs ECL1(103-110) and even more for ECL1(104-110) (Figure 141a). The size optimization studies of ECL2 generated the 8-fold stronger binders ECL2(185-195) and ECL2(187-195). The analog ECL2(188-195) had a comparable affinity to the native peptide, while all the rest shorter ECL2 analogs had significantly worse binding with MIF (Figure 141b).
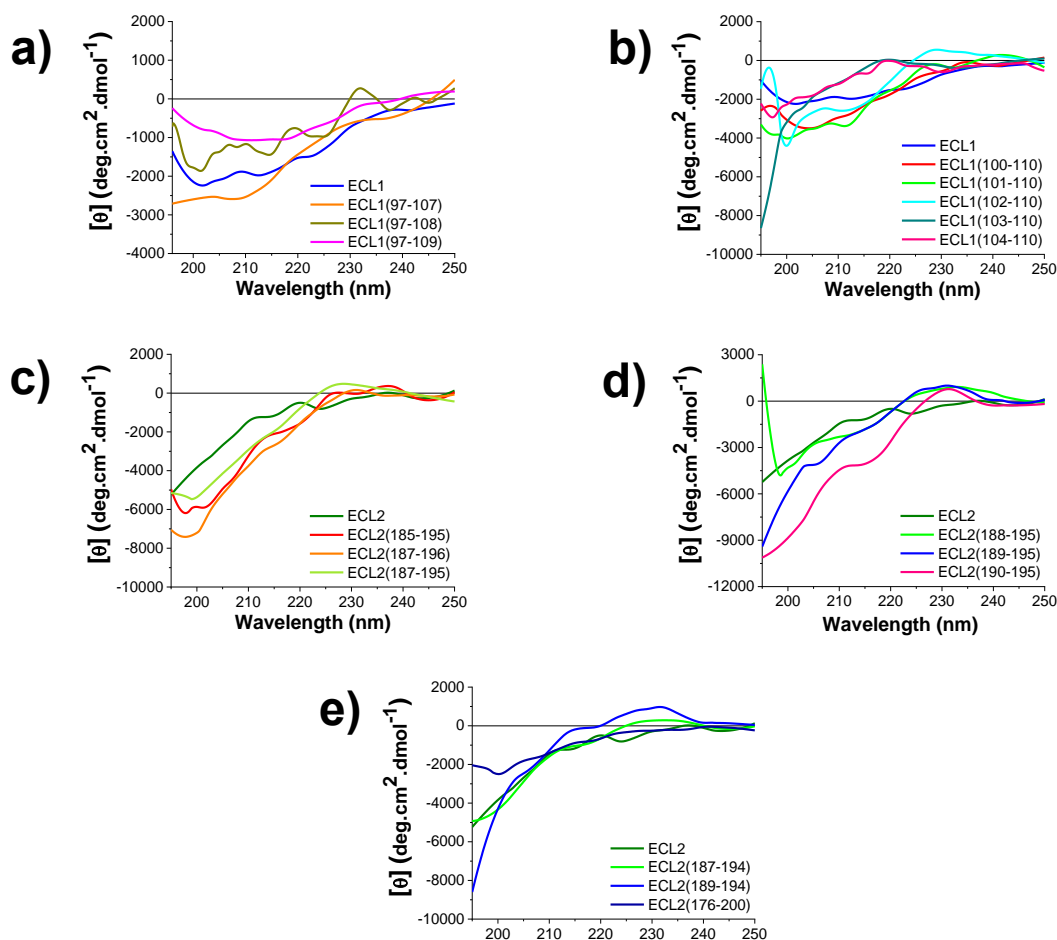
Figure 140. Comparison of the secondary structures of ECL1 and ECL2 shorter analogs. a, b, c, d, e CD spectra of shorter analogs of ECL1 (a, b) and ECL2 (c-e) at 10 µM with their mean residue ellipticity (MRE) being plotted over the wavelength between 195 and 250 nm (HT<1000). **b** The final measuring conditions were aqueous 1×b, pH 7.4, containing 1% HFIP in all assays.
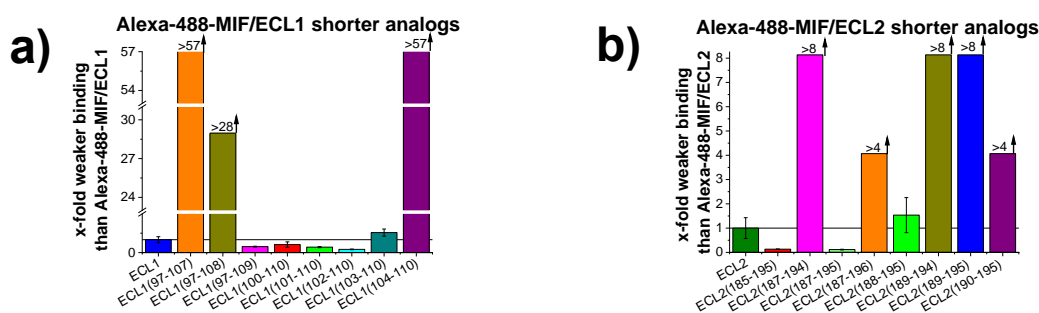
Figure 141. Comparison of binding affinities of ECL1 or ECL2 shorter analogs to MIF. a, b Normalized dissociation constants (app. K_{ds}) of Alexa-488-MIF and shorter analogs of ECL1 (a) or of ECL2 (b) with reference to the app. K_d of Alexa-488-MIF/ECL1 and Alexa-488-MIF/ECL2, respectively. The final measuring conditions were aqueous 1×b, pH 7.4, containing 1% HFIP in all assays.

To summarize, the first part of the SAR studies concluded the existence of shorter peptide fragments than ECL1 and ECL2 that shared even higher affinity with MIF than the native peptides. Notably, the extracellular loop 1 fragments ECL1(101-110), ECL1(102-110), ECL1(97-109), and the extracellular loop 2 fragments ECL2(185-195), ECL2(187-195) bound 4 to 8 times stronger than ECL1 or ECL2 to the atypical chemokine. Among them, the shortest fragments ECL1(102-110) and

ECL2(187-195) were prioritized for additional SAR studies to shed light on the importance of all their residues (Scheme 23). The aim was to determine the effect of specific substitutions on the peptides' secondary structure and the MIF binding and to obtain peptides with even stronger binding to MIF and higher solubility, if possible. Analogs and mutants of the ECL1 and ECL2 9-mers were synthesized and purified as previously and tested.
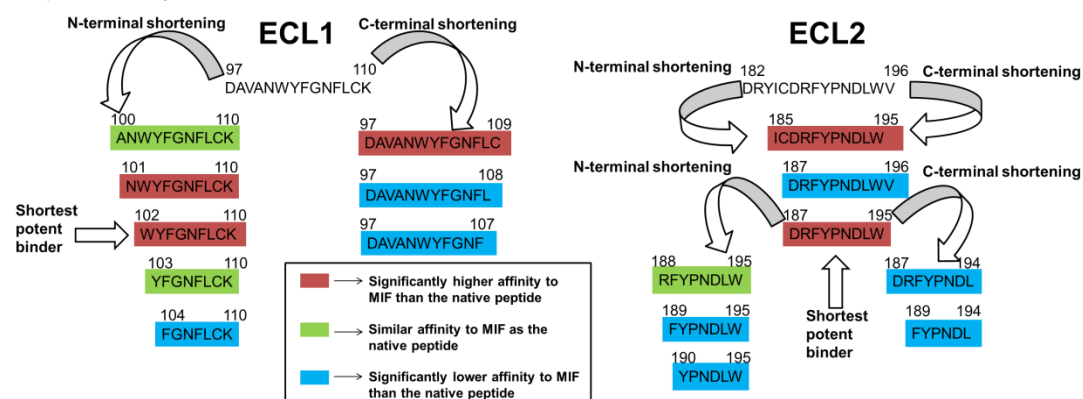
Scheme 23. Summary of SAR studies on ECL1and ECL2 analogs and their affinity with MIF. The affinity between the peptides and the atypical chemokine derived by the Alexa-488-MIF/peptide titrations. The peptides are marked with red and classified with significantly higher affinity (app. K_d with Alexa-488-MIF at least 4-times lower than of the native peptide), green and classified with similar affinity (app. K_d with Alexa-488-MIF between 4-times lower and 4-times higher than of the native peptide), or blue green and classified with significantly lower affinity (app. K_d with Alexa-488-MIF at least 4-times higher than of the native peptide).

ECL1(102-110) exposed a random coil indicative spectra, and this pattern was followed by all its alanine mutants, except for [N106A]-ECL1(102-110) that adapted a β-sheet structure. The substitutions of F104 and F107 led to even more unordered peptides, while the replacement of Y103 or C109 did not significantly affect the secondary structure. All the rest alanine mutants of ECL1(102-110) remained random coil, but with weaker minima and possibly more ordered traces. Π-π interactions were noticed for the native peptide and its single alanine mutants, except for [W102A]-ECL1(102-110) and [Y103A]-ECL1(102-110). All single alanine mutants of ECL1(102-110) were soluble at 50 μM, except for [N106A]-ECL1(102-110) and [K110A]-ECL1(102-110) that precipitated at 50 and 10 μM, respectively (Figure 142a, b). Regarding the rest analogs, the peptides K-ECL1(102-110) and [C109S]-ECL1(102-110) had the same secondary structure as the native peptide. The KK-ECL1(102-110) and [2xPal]-ECL1(102-110) analogs were less ordered, with the first one being the only one that precipitated at 50 μM, while the rest were still in solution. The analogs with the N-terminus lysine conjugation did not maintain the π-π interactions, which were observed for the other two analogs. Notably, the [W102Cha]-ECL1 analog adapted a β-sheet, differentiating significantly from the unordered ECL1 (Figure 142c).
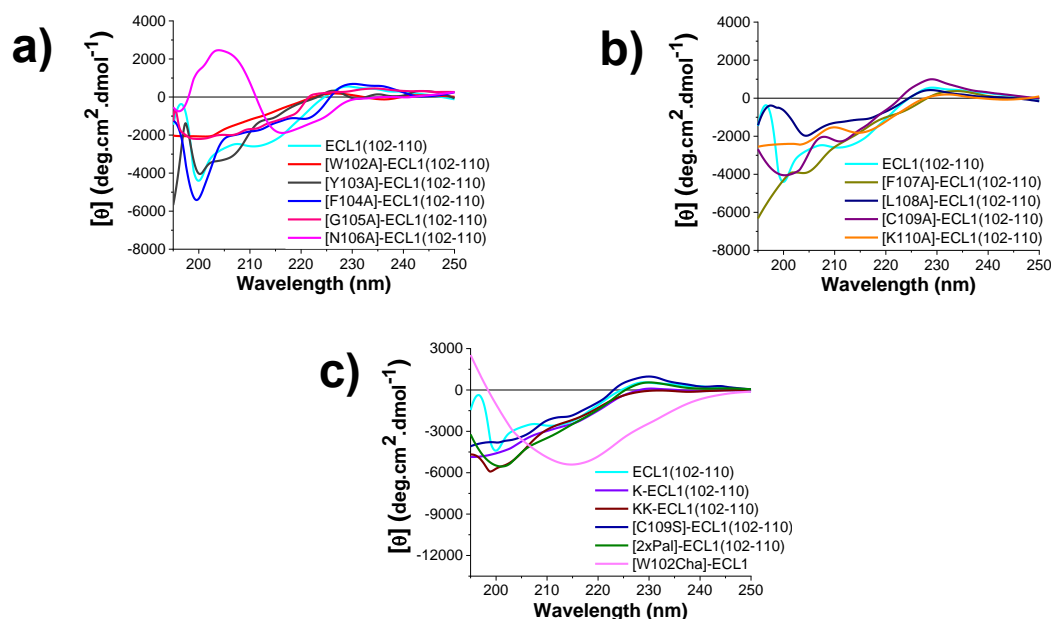
Figure 142. Comparison of the secondary structure of mutants and analogs of ECL1(102-110) and ECL1. a, b, c CD spectra of ECL1(102-110) alanine mutants (a, b), non-alanine mutants, analogs and ECL1 mutant (c) at 10 μM (HT<1000), with their mean residue ellipticity (MRE) being plotted over the wavelength between 195 and 250 nm (HT<1000). The final measuring conditions were aqueous 1×b, pH 7.4, containing 1% HFIP in all assays.

The other ectodomain 9-mer of interest, ECL2(187-195), exposed a random coil indicative spectra with π-π interactions being detected, too. Its alanine mutations at residues Y190, P191, N192, and D193 led to spectra with similar minima and random coil degrees to the native 9-mer. On the other hand, all the rest amino acid substitutions resulted in peptides with weaker minima and even more unordered structure. From those, only the derived spectra by [Y190A]-ECL2(187-195) and [W195A]-ECL2(187-195) did not indicate the presence of π-π interactions, uncovering the two aromatic residues and their role on them (Figure 143a, b). All single alanine mutants of ECL2(187-195) were soluble until 50 μM, as the native peptide. Regarding the other two ECL2 analogs, [R188Cit]-ECL2(184-196) remained unordered and soluble, on the contrary to [Arom]-ECL2. In this case, the simultaneous substitutions of Y184, Y190 with BiP and W195 with 2-Nal increased the hydrophobic character of the peptide and induced a β-sheet/β-turn conformation and its precipitation at 20 μM (Figure 143c).
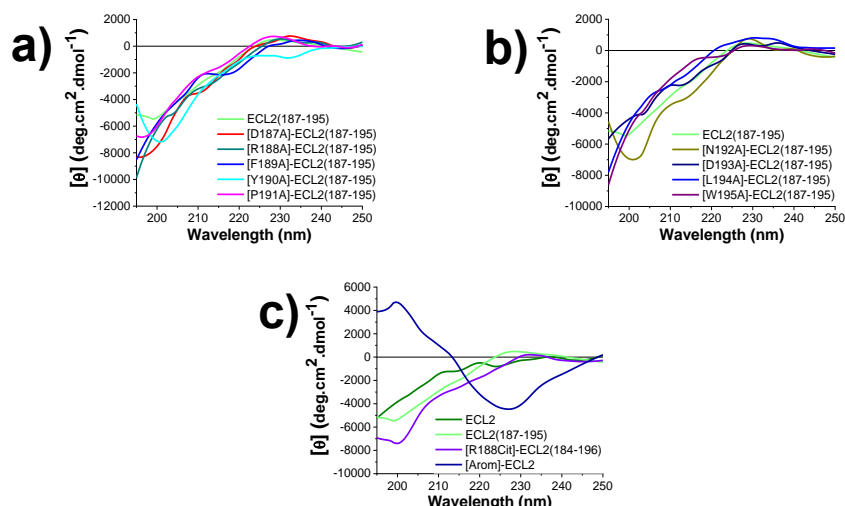
Figure 143. Comparison of the secondary structures of mutants and analogs of ECL2(187-195) and ECL2. a, b, c CD spectra of ECL2(187-195) alanine mutants (a, b) and non-alanine mutants of ECL2 analogs (c) at 10 μM, with their mean residue ellipticity (MRE) being plotted over the wavelength between 195 and 250 nm.

The substitution of F104, F107, or L108 by alanines led to a slightly increased app. K_{ds} between the peptides and labeled-MIF. The mutants [W102A]-ECL1(102-110), [Y103A]-ECL1(102-110), [C109A]-ECL1(102-110) had a 5 to 15-fold decreased affinity with Alexa-488-MIF, while the replacement of G105, N106 or K110 reduced it remarkably more (Figure 144a). The introduction of lysine on the N-terminus did not affect the binding, though; the conjugation of a second one abrogated it. [C109S]-ECL1(102-110) and [2xPal]-ECL1(102-110) had significantly weaker binding with MIF than the ECL1(102-110), while [W102Cha]-ECL1 had similar binding with the 9-mer and improved if compared to ECL1 (Figure 144b). Regarding ECL2 analogs, [R188Cit]-ECL2(184-196), [Arom]-ECL2 and the alanine mutants of ECL2(187-195) had remarkably decreased affinity to MIF, except for the [Y190A] mutant (Figure 144c, d). Substitutions of aromatic amino acids with non-natural ones containing larger aromatic groups, i.e. 2-Nal or BiP may contribute to the π-stacking with the binding region of the protein-ligand, but not in this case [339] [340].
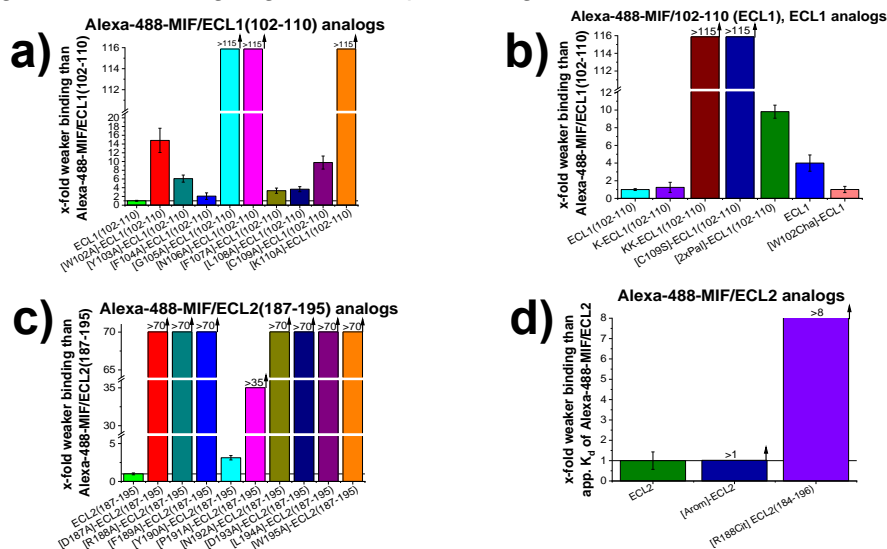
Figure 144. Comparison of binding affinities of ECL1(102-110), ECL1 or ECL2 shorter analogs to MIF. a, b Normalized app. K_{ds} of Alexa-488-MIF and analogs of ECL1(102-110), ECL1 (a) or of ECL2 (b) with reference to the app. K_d of Alexa-488-MIF/ECL1(102-110) or Alexa-488-MIF/ECL2, respectively.

5.3   Next generation of MIF-specific receptor mimics (ngms)

The previously described SAR studies of msR4Ms, ECL1, and ECL2 initiated the development of ngms. The newly developed mimics consist of the shorter ECDs and more potent MIF binders ECL1(102-110) and ECL2(187-195) instead of the 14-mer ECL1 and the 15-mer ECL2. Even though ECL1(102-110) has a strong nanomolar affinity with MIF, it is necessary to include the hot spot region of the ECL2, which often controls the chemokine selectivity of the receptor [341]. As for msR4Ms, the released crystal structure of CXCR4 was imported to Jmol for the calculation of the distance between the ECD terminuses. Linkers were introduced between the two 9-mers to mimic the distance between K110 and D187. Of note, the distance between the terminuses for the ECDs of ngms was less than the half compared to the respective one of msR4Ms.

Initially, the same tandem linker that was applied for msR4M-L1, i.e. 6 Ahx-12 Ado, was used for the generation of ngm-L3 to control the importance of the length in the linkers. 8 Aoc, another linker with carboxyhydrate chains but with size fitting to the K110-D187 distance, connected the shorter ECDs in the ngm-L4 analog. With a similar estimated length, O1Pen-O1Pen was used for ngm-L5. Importantly, PEG molecules such as O1pen are introduced in several drugs due to their contributions to a better pharmacokinetic profile [342]. The measured length of a three natural amino acid chain was found to be very similar to the K110-D187 distance. Based on this, ngms were developed after the introduction of three aspartic acids (ngm-LD3), glycines (ngm-LG3), lysines (ngm-LK3), or arginines (ngm-LR3). A similar three amino acid linkage approach was applied in IAPP mimics and resulted in improved binding and inhibitory potency [237]. However, in this case, the three linking amino acids substituted three non-essential amino acids, and they did not aim to cover the distance of a discontinuous GPCR network as for ngms.

Overall, acidic amino acids were shown to enhance the solubility, while lysine might play the role of an anchor for some domains [241]. Arginines were also tested because, even though they are basic residues as lysines, they have a bigger interaction repertoire and are a ommonly applied for linking amino acid in proteins [343]. Glycines were inserted as non-charged residues to evaluate the effect of the linkage with natural amino acids in the absence of charge. The shortened by one-third compared to msR4Ms ngms aim to be equally potent and specific binders of MIF with the first generation of mimics with higher solubility, yield, and less aggregation propensity. Ngms were synthesized and purified as msR4Ms, while their crystallization and detection were easier with MALDI-TOF-MS than the previously developed mimics.

All ngms were analyzed by CD spectroscopy having remarkably less ordered structure compared to msR4M-L1, while their solubility varied and was dependent on the linkers. The newly developed mimics that their ectodomain segments were linked with non-natural amino acids were less soluble than those with natural amino acids. Particularly, ngm-L3 precipitated already at 2.5 µM, so no spectra were recorded, while ngm-L4 and ngm-L5 precipitated at 20 µM and 50 µM, respectively. Notably, non-natural amino acid linkers may increase lipophilicity and decrease the solubility of the peptides [314] [344]. The triple glycine-linked peptide precipitated at 50 µM as well, but all the rest ngms remained soluble until 50 µM, at least. The introduction of charged natural amino acids appears to be crucial for improving the solubility for ngms, which might correlate with their charge at the

measuring conditions. CD analyses were performed in pH=7.4, in which all peptides that precipitated below 50 μM, i.e., ngm-L3, -L4, -L5, -LG3 have a 0.9 charge. Contrariwise, the acidic linked ngm-LD3 and the basic linked analogs ngm-LK3, -LR3 had -2.1 and 3.9 charges, respectively.

The charged linkers appear to work in favor of less ordered structures, too. All ngms exposed random coil characteristic signal, with the 195 nm minima being more intense for ngm-LK3, followed by ngm-LD3, ngm-LR3, and then the rest of ngms. Overall, the addition of a positive charge might induce repulsion forces that decrease stability [345]. On the other hand, the applied carboxyhydrate chains or PEG groups as linkers for ngm-L4 and -L5 could reduce the hydrogen bond donors/acceptors, contributing to structural stability [314] [346]. Ngm-L4 and ngm-LG3 exposed two significantly weaker minima at 220 and 217 nm, respectively, suggesting the presence of some ordered traces, too. Of note, a broad positive band at 230 nm region was observed for ngm-L5, -LD3, LR3 analogs, which is indicative for π-π interactions (Figure 145a). In general, such short linear peptide sequences tend to be highly flexible in solution and only adopt a defined three-dimensional structure upon binding. The restriction in conformational freedom associated with binding leads to an entropic penalty, resulting in an overall reduced affinity of the short peptide compared to its natural precursor [319]. Therefore, preorganization of peptides into bioactive conformations could increase binding affinity and be a goal for future optimization studies of ngms [320].

IAPP cross-amyloid interaction surface mimics (ISM) were developed in a similar manner. More specifically, shortening studies on IAPP sequence indicated the segments 8-18 and 22-28 as hot spot regions for its interactions. Next, the three PEG unnatural amino acids were introduced between these domains for the development of the 2-AoC3-GI ISM, three arginines for R3-GI, three glycines for the G3-GI, and three lysines for the K3-GI. Of note, the GI indicates the N-methylations on G24 and I26. The secondary structure of 2-Aoc3-GI was well ordered in β-sheet/β-turn and R3-GI was half in ordered state and half in random coil, while the respectively linked CXCR4 mimics ngm-L5 and ngm-LR3 were unordered. G3-,K3-GI, and ngm-LG3 adopted an unordered structure, containing some traces of β-sheet/β-turn, while ngm-K3 exposed a strong random coil indicative minima and signal [237]. Conclusively, the linker might be a pivotal factor in the secondary structure formation of the mimic, but its effect varies on the connected segments.

Although the charged amino acids mediated an increased solubility, they did not hinder the self-association of ngms. Surprisingly, all acidic or basic linked ngms were more prone to self-assemble than msR4M-L1, despite their size reduction by 40%. Charged residues were shown to hinder aggregation, however, this was not the case for ngms [347]. Among all mimics, ngm-LR3 showed the strongest self-assembly and correlates with previous findings of arginines and their importance in aggregation propensity [348]. The substitution of arginines with lysines was expected to disturb the self-association of the mimics significantly, nevertheless, the effect was not as strong as expected [349] [348]. A similar oligomerization propensity was observed for the non-charged linked ngm-L4, -LG3, but not for ngm-L5. The PEG-linked analog did not self-assemble until 500 nM, confirming the disaggregating role of the PEG molecules (Figure 145b) [350] [351]. Contrariwise, peptides containing carboxyhydrates chains in their sequences showed increased tendency for oligomerization [317].

ANS binding has been applied since 1965, and the enhanced fluorescence emission of the label upon binding on peptides and proteins is correlated with increased exposure of hydrophobic residues [283]. Later on, ion-pairing was detected between the negatively charged sulfonate groups of ANS and the basic amino acids. However, complementary interactions, like van der Waals, are needed to stabilize those interactions [352] [353]. The importance of the hydrophobic interactions over the ionic interactions was further confirmed recently [354]. For ngms, the presence of a double PEG molecule (ngm-L5) or of a triple aspartic acid (ngm-LD3) in the linkage hindered the exposure of hydrophobic residues on the surface of the peptide. All other mimics showed a quite high surface hydrophobicity, except for ngm-LR3, which had significantly higher. Of note, the arginine-linked ngm was the only mimic that precipitated at 10 µM, while all the rest remained soluble until 20 µM, at least (Figure 145c).

One possible explanation for the limited solubility of ngm-LR3/ANS mixtures, contrary to the respective CD ones, maybe has to do with an interaction between the label and the mimic. The guanidinium moiety of the arginine side chain has a broad interaction repertoire and it is very likely that the three guanidinium side chains, due to the short distances, would pair to each other and increase the solubility of the peptide in normal conditions [313]. However, if these residues are involved in ionic interactions with ANS, the solubility of the mimic might be decreased.

Another possible interaction of those three arginines is the cation-π one. The three arginines may form a strong positively charged cluster that attracts one or more of the seven aromatic residues (W102, Y103, F104, F107, F189, Y190, W195) of the 21-mer. If ANS and three arginines are coming close due to electrostatic interactions, the label is very close to the aromatic amino acid(s), and for this reason, we obtain these high values until 5 µM. Of note, despite its positive charge, lysines rather interacts with hydrophobic residues via its aliphatic chain than with aromatic amino acids [355]. In a similar rational design approach, an R3 linker linked an 11-mer and a 7-mer of IAPP analogs (ISM R3-GI), containing only one phenylalanine from aromatic residues. Under the same experimental setup, the ANS emission of the label/peptide mixtures obtained similar values to ANS alone emission, excluding the possibility that an R3 linker alone may trigger the ANS emission [237].

Similar very low ANS emission values were observed for ngm-L5 and ngm-LD3, too. Polar amino acids that covered long interlayer distances could be promoters of hydrophilic surface formation. Such a case might be the introduction of the PEG tandem O1Pen-O1Pen as linkers in ngm-L5. Regarding ngm-LD3, aspartic residues were shown that might be in or above the polar headgroup region and exposed to bulk water, depending on their positions on peptide sequence [356]. Another possible factor is that anion-phenylalanine interactions are unfavorable, contrary to the cation-phenylalanine ones [313]. A possible repulsive effect of F104, F107, and/or F189 from the surface due to the location of aspartic acids there might play a role in the low hydrophobicity of the ngm-LD3.
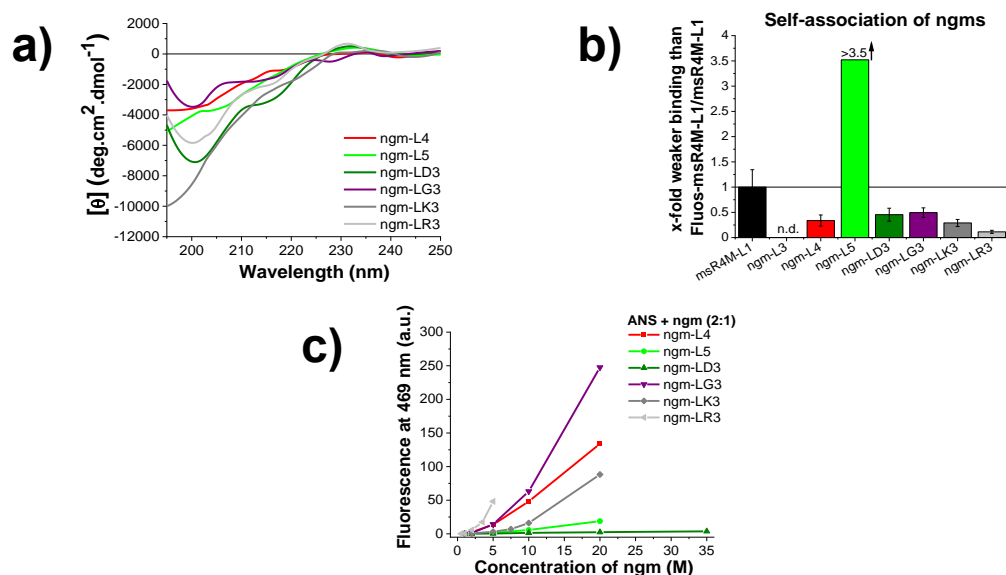
Figure 145. Comparative biophysical characterization of ngms. **a** CD spectra of peptides at 5 µM with their mean residue ellipticity (MRE) being plotted over the wavelength between 195 and 250 nm (HT<1000). **b** Normalized dissociation constants (app. K_{ds}) of the self-association of the peptides with reference to the app. K_d of msR4M-L1 self-assembly. **c** Fluorescence emission at 469 nm over increased concentration of ANS/peptides mixture in a constant 2:1 proportionality. The final measuring conditions were aqueous 1×b, pH 7.4, containing 1% HFIP in all assays.

Initial titrations with the labeled peptide as the analyte determined strong binding between the ngms and the MIF. Of note, Fluos-ngm-L4, -L5, -LR3 had even slightly lower dissociation constants than msR4M-L1 to MIF. Even though in some cases PEG may reduce the binding affinity due to steric hindrance, this did not happen in the ngm-L5/MIF interaction [351]. The rest ngms bound to MIF with very similar app. K_{ds} to the one of msR4M-L1 (Figure 146a). Likewise, Alexa-488-MIF bound to ngm-L3, -L4, -L5, -LK3, -LR3 strongly, as to msR4M-L1. However, the labeled protein shared medium and very weak affinity to ngm-LD3 and ngm-LG3, respectively. Possibly the high tendency of mimics to self-associate might have hindered their binding to the cytokine. Another hypothesis is that the last two mimics might bind in a different way to MIF than the rest ngms, which does not affect the environment of Alexa-488 label, resulting in non-differentiated fluorescence emission, even after binding. Alternatively, the amino group in which the label was coupled might have been crucial for the Alexa-488-MIF/ngm-LD3, -LG3 interactions its interference with the label could hinder their binding (Figure 146b).
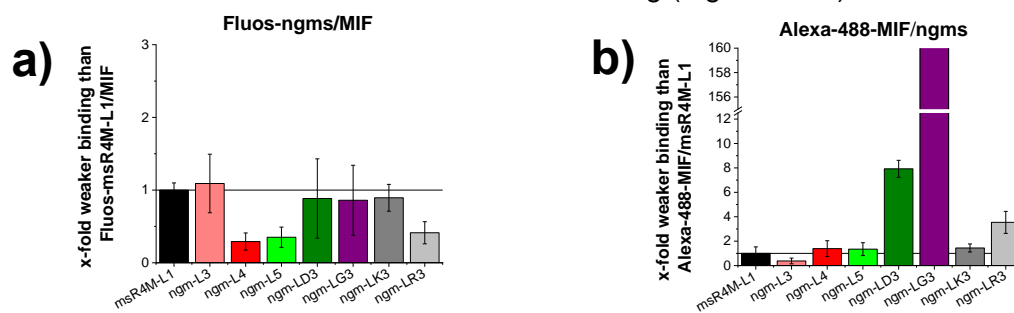
Figure 146. Comparison of binding affinities of ngms to MIF. a, b Normalized dissociation constants (app. K_{ds}) of the Fluos-ngms/MIF (a) and Alexa-488-MIF/ ngms (b) titrations with reference to the app. K_d of Fluos-msR4M-L1/MIF and Alexa-488-MIF/msR4M-L1, respectively. The final measuring conditions were aqueous 1×b, pH 7.4, containing 1% HFIP in all assays.

Next, mixtures of ngms (5 µM) and MIF (1 µM) were analyzed with CD spectroscopy and compared to the expected signal based on the sum of their individual spectra. The non-ordered mimics did not affect the well-structured cytokine, except for the arginine-linked analog. In this case, slightly reduced minima and increased maxima were observed for the ngm-LR3/MIF mixture compared to the sum (Figure 147). Generally, the slight shift of the maximum to the right of the wavelength axis indicates disruption in α-helix in favor of β-sheet formation. However, this is hard to be concluded here due to the decrease of the minima. The arginines (ngm-LR3) contain a longer side chain than aspartic acids (ngm-LD3) or lysines (ngm-LK3) and could locate their guanidinium moiety near to polar protein atoms and disrupt the MIF structure. Moreover, arginines, the most likely charged residues under physiological pH conditions, are likely to participate in electrostatic contributions of charge-charge interactions and might induce a small structural change [357]. Of note, the lack of any structure effect on MIF, including its β-strands, might be indicative for non-competition with CD74 [323].
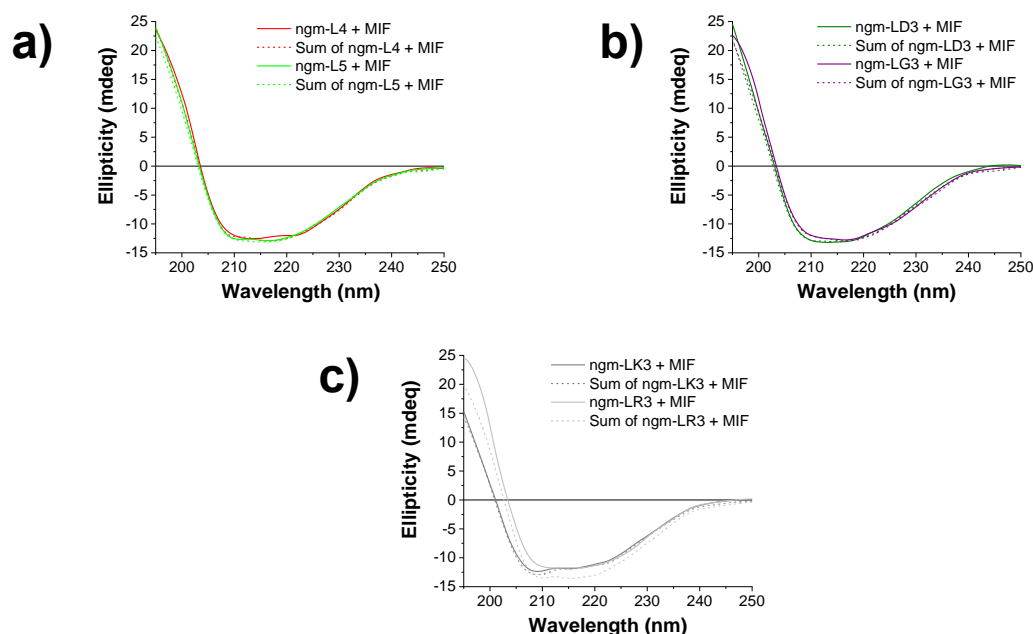
Figure 147. Comparison between the secondary structures of ngms/MIF mixtures. a, b, c CD spectra of ngms (5 µM)/MIF (1 µM) mixtures (line) and the sum of their individual spectra (dashed line). The ellipticity of the spectra is plotted over the wavelength between 195 and 250 nm (HT<1000) and the. final measuring conditions were aqueous 1×b, pH 7.4, containing 1% HFIP.

Additionally, labeled ngms were titrated with MIF(54-80), the binding epitope of Fluos-msR4M-L1. The tested mimics that were linked with non-basic residues (ngm-L5, ngm-LD3) recognized the same binding core regions as msR4M-L1. However, the basic linked analogs ngm-LK3 and ngm-LR3 exhibited a medium and weak affinity to MIF(54-80), respectively (Figure 148). One possible explanation might have to do with repulsive forces between the positively charged ngms (+3.9 at pH=7) and MIF(54-80) (+2 at pH=7). Generally, amino acid residues located on the surface of a protein serve as active sites and/or interact with other molecules and ligands [358]. Maybe the introduction of three arginines mediated the different orientation of some amino acids and led to a limited affinity between ngm-LR3 and MIF(54-80).
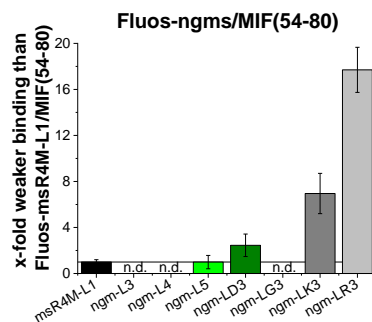
Figure 148. Comparison of binding affinities of ngms to MIF(54-80). Normalized dissociation constants (app. K_{ds}) of the Fluos-ngms/MIF(54-80) titrations with reference to the app. K_d of Fluos-ngm/MIF(54-80) (respectively for msR4M-L1).

       The binding affinities of ngms were determined for CXCL12, as well. Ngms are not disulfide bridged, and the crucial residues D97 of ECL1 and C186 of ECL2 for binding to the chemokine are eliminated [150]. Recent studies revealed an essential role of the receptor residues D187, F189, N192, and W195 for the CXCL12/CXCR4 interaction, which are part of ngms [188]. The linked via-non natural amino acids ngms and the triple aspartic acid linked ngm-LD3 exposed a micromolar affinity with CXCL12. Contrariwise, the rest of the linked with natural amino acids ngms had app. K_{ds} in the two-digit nanomolar range with the chemokine (Figure 149). A hypothesis might correlate this interaction of ngm-LG3, -LK3, -LR3 to their more rigid linkers due to the non-rotating peptide bond, compared to the flexible repeated -CH2- bonds of ngm-L3, -L4, or C-C-O-C of ngm-L5. Nevertheless, usually, the high flexibility of the linker amino acids on a protein does not hinder its interactions with other proteins [359]. It remains unclear why CXCL12 did not bind to the labeled-ngm-LD3, which has a strong positive charge, i.e. a crucial factor of the CXCL12/CXCR4 interaction [360].

       Particularly, the positively charged N-terminus of the chemokine was found to be involved through ionic interactions with acidic residues of the CXCR4 ectodomain [187] [361] [150] [362]. Additional studies with small molecules uncovered more essential residues of the CXCL12 binding interface, mainly basic and hydrophobic ones. [363] [364]. This observation might correlate with the ngms that showed binding with CXCL12 are those with the higher exposure of hydrophobic residues on the surface. Generally, amino acid residues located on the surface of a protein serve as active sites and/or interact with other molecules and ligands [365]. Conclusively, the lack of flexibility and negative charge in the linkers, together with high exposure of hydrophobic residues, may induce the binding of ngms to CXCL12.
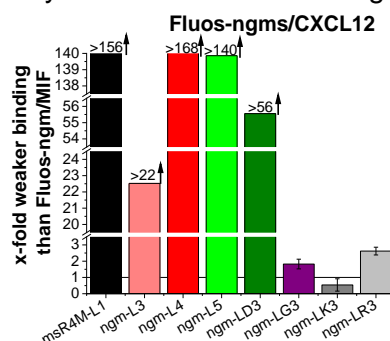
Figure 149. Comparison of the selectivity of ngms towards binding CXCL12 over MIF. The selectivity is determined as the quotient of the app. K_d of Fluos-ngm/CXCL12 divided by the app. K_d of Fluos-ngm/MIF (respectively for msR4M-L1).

5.4   SAR studies on ECL1 and ECL2

Previous dot blot studies revealed 108-120 and 184-198 as binding epitopes of CXCR2 in the interaction with MIF [97]. Herein, it was desired to study those peptides and their shorter analogs, especially their secondary structures and precise dissociation constants with MIF. The aim was to find out the shorter potent binders of MIF. All CXCR2 analogs were synthesized and purified as previously described. Structural studies on the shorter ECDs of CXCR2 provided essential insights into the role of amino acids. Usually, the minimization of the sequence induces the unordering of the secondary structure. However, this was not the case of N-terminus shorter analogs of the partially ordered R2ECL1(108-120), which obtained a β-sheet conformation until the elimination of W112. Similar collected spectra were obtained for the C-terminus shortened R2ECL1(108-119). It appears that the presence of both positively charged terminus residues K108 and K120 destabilized the secondary structure of R2ECL1(108-120), most likely due to repulsive forces. The elimination of one of them induces the packing of the peptides in an ordered state without affecting their solubility. Compared to the respective ECL1 analogs, the R2ECL1(108-120) shorter analogs were remarkably more ordered, most likely due to the more β-sheet stabilization role of I113 and T116 of CXCR2 than the respective residues Y103 and N106 of the CXCR4 analogs (see Appendix Figure A4). All shorter R2ECL2(184-198) analogs retained and obtained an even stronger random coil structure (Figure 150).
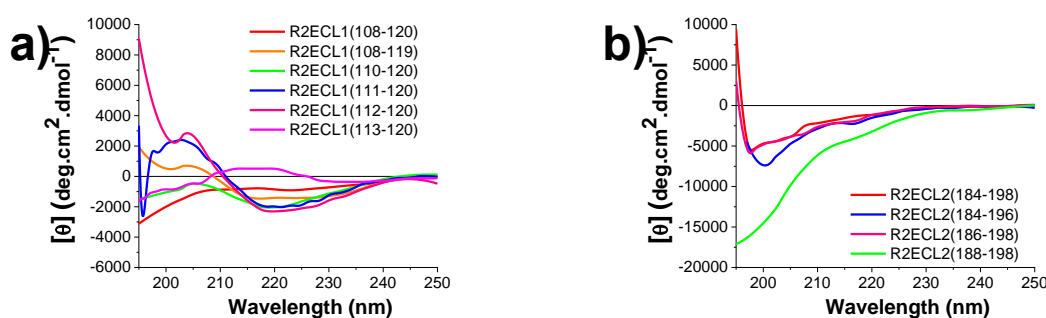
Figure 150. Comparison of the secondary structures of R2ECL1(108-120) and R2ECL2(184-198) analogs. a, b CD spectra of shorter analogs of R2ECL1(108-120) (a) and R2ECL2(184-198) (b) at 10 µM with their mean residue ellipticity (MRE) being plotted over the wavelength between 195 and 250 nm. The final measuring conditions were aqueous 1×b, pH 7.4, containing 1% HFIP in all assays.

SAR studies on the sequence of ECDs with Alexa-488-MIF revealed the hot spot region of the CXCR2 ectodomain in the interaction with the chemokine. Similar to ECL1 findings, the residues of the N-terminus could be eliminated and led to the R2ECL1(112-120) as the core region. Interestingly, the elimination of K120 disrupted the binding with the chemokine (Figure 151a). The respective subtraction enhanced the binding of ECL1 with MIF before its abrogation after C109 elimination. Apparently, the C-terminus C109 and K110 residues have a different binding contribution than their homologous residues of the CXCR2 ectodomain. Of note, R2ECL1(112-120) and ECL1(102-110) share a 77.7% sequence identity. Shortening on the R2ECL2(184-198) sequence led to R2ECL2(184-196), a remarkably more potent binder of MIF than the native peptide. Thus, residues Y197, E198 likely hindered the binding between the peptide and the cytokine. Residue Y197 was shown recently to be crucial in the interaction between IL-8 and CXCR2 [152]. Contrariwise, the N-terminus residues R184, R185 appear to be crucial for the interaction with MIF, since their elimination abolished the binding (Figure 151b).

Docking and MD simulations predicted interactions between the region 187-192 of extracellular loop 2 of CXCR2 and the C-terminus region 101-110 of MIF, among other interactions [96]. Taken together, the peptides R2ECL1(112-120) and R2ECL2(184-198) are the hot spot regions of the CXCR2 ectodomain in the interaction with MIF. Taken together, the peptides R2ECL1(112-120) and R2ECL2(184-198) are the hot spot regions of the CXCR2 ectodomain in the interaction with MIF (Scheme 24).
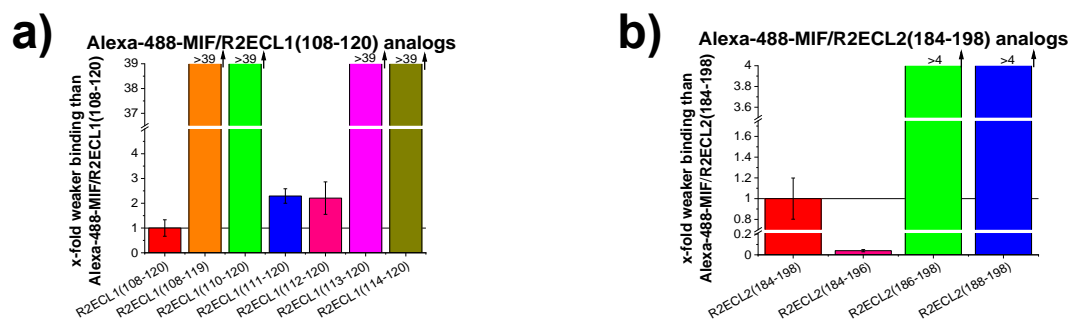
Figure 151. Comparison of the binding affinities of R2ECL1(108-120) or R2ECL2(184-198) shorter analogs to MIF. a, b Normalized dissociation constants (app. K_{ds}) of Alexa-488-MIF and shorter analogs of R2ECL1(108-120) (a) or of R2ECL2(184-198) (b) with reference to the app. K_d of Alexa-488-MIF/R2ECL1(108-120) and Alexa-488-MIF/R2ECL2(184-198), respectively. The final measuring conditions were aqueous 1×b, pH 7.4, containing 1% HFIP in all assays.
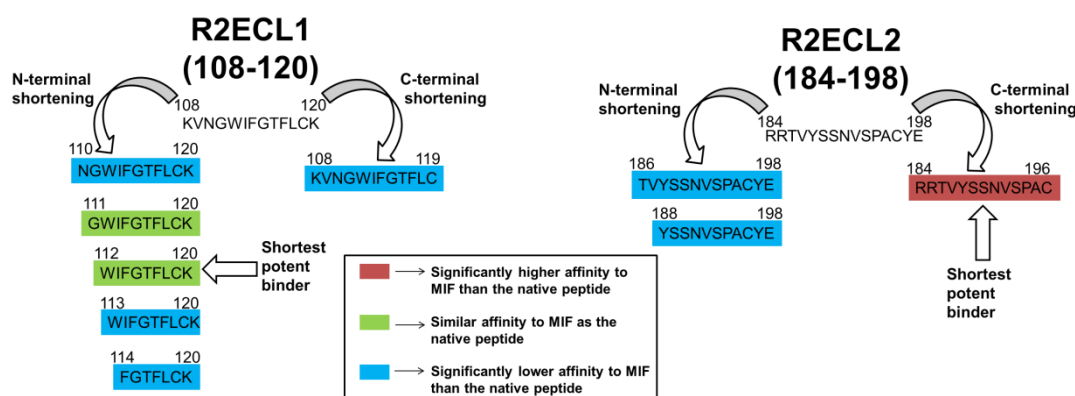
Scheme 24. Summary of SAR studies on R2ECL1(108-120) and R2ECL2(184-198) analogs and their affinities with MIF. The affinity between the peptides and the atypical chemokine derived by the Alexa-488-MIF/peptide titrations. The peptides are marked with red and classified with significantly higher affinity (app. K_d with Alexa-488-MIF at least 4-times lower than of the native peptide), green and classified with similar affinity (app. K_d with Alexa-488-MIF between 4-times lower and 4-times higher than of the native peptide), or blue green and classified with significantly lower affinity (app. K_d with Alexa-488-MIF at least 4-times higher than of the native peptide).

5.5   CXCR2 and CXCR4 chimeric receptor mimics (CRMs)

After the generation of CXCR4 mimics and SAR studies on the extracellular loops 1 and 2 of CXCR2, the next set aim was to imitate the ectodomains of both receptors. Particularly, the goal was to develop chimeric receptor mimics (CRMs) of both MIF receptors with the minimum amount of residues and a strong binding to the atypical chemokine. CRMs were rationally designed as ngms and msR4Ms previously. Thereafter, the previously generated ngms were used as the mimics of CXCR4 instead of the by 60% bigger msR4Ms. The chosen ngms were two that were linked with non-natural amino acids and two with natural ones. More specifically, ngm-L4 and ngm-L5 were prioritized due to the unfavorable soluble properties of ngm-L3. For the same reason ngm-LG3 was excluded as well, while ngm-LD3 and ngm-LK3 were chosen instead of ngm-LR3 due to the high aggregation propensity and self-association of the last mimic.

SAR studies of the CXCR2 extracellular loops 1 and 2 concluded to R2ECL1(112-120) and R2ECL2(184-196) as the hot spot regions of the receptor for the cytokine. Homology studies revealed that R2ECL1(112-120) is 78% identical to the ECL1(102-110) fragment of ngms. Hypothesizing that the ECL1(102-110), which is already present in ngms sequence, may induce similar interactions as its homolog of CXCR2 in binding due to their high rate of sequence identity, it was decided the elimination of R2ECL1(112-120) from the CRM sequence. The applied 12 Ado-G linkage between R2ECL2(184-196) and the ECL1(102-110) of ngms is supposed to mimic the respective distance with the R2ECL1(112-120) on the CXCR2. When CRMs were developed there was no CXCR2 structure available, so the calculations were done with the NMR model of its homologically similar receptor, CXCR1. The later released CXCR2 crystal structure revealed that this distance is slightly shorter than the calculated one by the CXCR1 model. However, the introduced linker 12 Ado is a flexible carbohydrate non-natural amino acid and the slightly larger length of the (12 Ado)-G linkage should not affect the mimicry approach [152].

Notably, all available structures of both chemokine receptors suggest a disulfide bridge connecting the extracellular loops 1 and 2 via their cysteine residues. The same bond was formed in CRMs, but between the C196 of R2ECL2(184-196) and the C109 of ECL1(102-110). Conclusively, ECL1(102-110) is the central part of CRMs with the size optimized extracellular loops 2 of CXCR2 and CXCR4 and the required spacers on the left and right sequence, respectively, with or without an additional disulfide linkage. CRMs were synthesized following the Fmoc-SPPS protocols and purified by HPLC as all peptides previously, but their purity grades were evaluated in a slightly changed way than the previous mimics. Particularly, CRMs were not sufficiently crystallized and detected with MALDI-TOF-MS and the previously applied method with MALDI solution B and B (matrix) as msR4Ms and ngms. Most likely, the reason behind that is the higher molecular weight of the CRMs and their stronger oligomerization propensity compared to the CXCR4 mimics. To solve this, the MALDI solution C (matrix) was applied instead, which was proved to work better for higher molecular weights and proteins, with acceptable crystallization and detection of the newly developed mimics.

CRMs exposed differentiated spectra over increased concentration due to self-association at 10-20 μM before their precipitation at 50 μM. Two exceptions are the CRM-1/LK3, -LK3ox analogs, which remained soluble but aggregated at 50 μM. Most likely, the CRMs precipitation is a result of delocalized π-electrons interactions

like cation-π or anion-π interactions [313]. The secondary structure of the CRMs varied significantly at 5 µM, even though the R2ECL2(184-196) was conjugated with the same linker (12 Ado-G) to the unordered ngms. Spectra of CRM-1/L4, /LD3 at 5 µM indicated the formation of β-sheets, CRM-1/L4ox, /L5, /LD3ox exhibited a mixture of β-sheet and unordered structure, while CRM-1/L5ox, /LK3, /LK3ox were random coil. Noteworthy, all four oxidized CRMs were less ordered in comparison to their reduced analogs (Figure 152a).

It is widely expected that the restriction with the disulfide bond will mediate more ordered structures of the peptides. Indeed, the disulfide bonding on the opposite site of the hydrogen bonds may contribute to the structural stability. However, introducing the disulfide bridge in the hydrogen bonds site might bring about steric repulsion between the sulfur atoms of the cysteines and the carbonyl groups of the cross-strand hydrogen bonds. In this case, the structure is destabilized, and the disulfide bonds more prone to be cleaved [366] [367] [368]. Most likely, in CRMs the disulfide bridge is formed in the site of hydrogen bonds leading to less ordered secondary structures. Newer structural peptide studies discovered that stabilization of parallel β-sheet via an interstrand disulfide might also occur. Nevertheless, the parallel sheet is unable to be elongated further than the disulfide position [369].

The disulfide bridge did not affect only the secondary structure but the self-association of the CRMs, too. The emission of the non-oxidized Fluos-CRM-1/LD3 did not reach any upper plateau until 1250 nM, revealing that it is significantly less prone to self-associate than msR4M-L1. Contrariwise, the oxidized analogs Fluos-CRM-1/L5ox and Fluos-CRM-1/LD3ox were already saturated in this range with dissociation constants of 38.9 ± 2.4 and 67.8 ± 13.7 nM, respectively, and they had a stronger oligomerization propensity than msR4M-L1. Likewise, CRM-1/L4ox had a strong tendency to self-assemble (20.5 ± 6.8 nM). Possibly, the disulfide bridge formation induces the self-association because of its effect on the unfolding of the secondary structure that may result in different orientations and shorter distances between specific residues. However, the triple lysine linkage on the ngm sequence seems to hinder the self-assembly of CRM-1/LK3ox, as it is the only oxidized mimic that did not get saturated at 5000 nM (Figure 152b). A hypothesis is that CRM-1/LK3ox does not self-associate as the other CRMs due to its stronger positive charge (5.9) in comparison to CRM-1/L4ox, /L5ox (2.9), and CRM-1/LD3ox (-0.1) at pH 7 and the possible repulsive forces that might arise and hinder the oligomerization of the peptide.

At canonical pH conditions, like the ANS emission recording ones, hydrophobic proteins tend to have the most intense exposure of hydrophobic residue on their surface [370]. Studies on the CRMs surface presented a quite high to very high exposure of hydrophobic residues, depending on the nature of the applied linker in the ngm sequence. More specifically, the introduction of non-natural amino acids between the ECDs of CXCR4 enhanced the presence of solvent-exposed hydrophobic amino acids in CRMs and their precipitation at 20 µM in the ANS binding measurement conditions. This hydrophobic exposure effect was less obvious when natural amino acids were applied instead, and the respective CRMs remained soluble until 20 µM (Figure 152c). It is hypothesized that the stronger hydrophobic exposure of the last CRMs might be due to the flexibility of the -CH2- chains in 8 Aoc and the C-C-O in O1Pen in comparison to the non-rotating peptide bonds. The presence of a disulfide bond and its effect on the exposed hydrophobic residues, the

solvent-accessible surface, and the enthalpy may cause stabilization or destabilization of the structure. However, it did not affect the presence of the hydrophobic residues on the surface of CRMs or their solubility [371] [372].
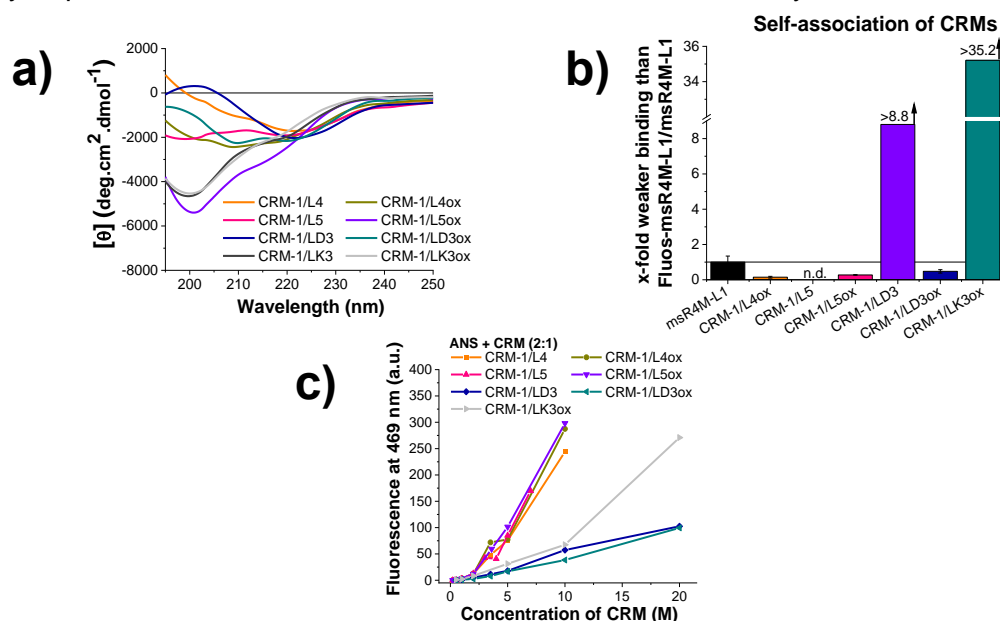
Figure 152. Comparative biophysical characterization of CRMs. a CD spectra of peptides at 5 µM with their mean residue ellipticity (MRE) being plotted over the wavelength between 195 and 250 nm (HT<1000). **b** Normalized dissociation constants (app. K_{ds}) of the self-association of the peptides with reference to the app. K_d of msR4M-L1 self-assembly. **c** Fluorescence emission at 469 nm over increased concentration of ANS/peptides mixture in a constant 2:1 proportionality. The final measuring conditions were aqueous 1×b, pH 7.4, containing 1% HFIP in all assays.

Binding affinity studies appeared to be dependent on analyte and titrant roles for the reduced CRMs. All determined dissociation constants between labeled-non oxidized CRMs and MIF were in the micromolar range (Figure 153a). However, the reverse fluorescence spectroscopic titrations with Alexa-488-MIF as the analyte and the mimics as the titrant exhibited remarkably lower app. K_{ds} between 18.5 and 25.9 nM, comparable to the ones derived by msR4M-L1, except for CRM-1/LK3 (>250 nM) (Figure 153b). The disagreement of these findings might be associated with the two arginines, R184, R185 on the N-terminus, next to the label. For example, the guanidino groups might be involved in a cation-π interaction with the neighboring aromatic group of the Fluos-label. This interaction is likely to lead to non-differentiated fluorescence emission, even if binding occurs, due to the stabilization of the label. This notion could be checked in future studies by introducing a spacer on the N-terminus of CRMs between the Fluos and the mimic sequence, like a PEG molecule, and the repetition of the titrations [373]. Another reason might have to do with the other label, Alexa-488, and its effect on MIF, inducing a stronger binding between the protein and the mimics, maybe because of dissociation of the well-ordered protein structure and the uncovering of hidden binding epitopes. However, the secondary structure of Alexa-488-MIF remained essentially the same as the non-labeled protein (Appendix Figure 5).

The labeled atypical chemokine bound strongly not only to the reduced but to the oxidized peptides, too. Alexa-488-MIF and CRM-1/L4ox, /L5ox, /LD3ox were bound with msR4M-L1 comparable app. K_{ds}, approximately at 20 nM range, as exactly their non-oxidized analogs. In the same range, it was determined the

dissociation constant with CRM-1/LK3ox (35.2 nM), but with the difference that it was significantly improved compared to the affinity of the reduced mimic (250 nM). However, the reverse experimental setup between Fluos-CRM-1/LK3ox and MIF showed a much weaker affinity (>2000 nM). The other labeled oxidized mimics had strong binding with the atypical chemokine (97.3-281.1 nM), but still, 5- to 10-fold reduced compared to the findings from Alexa-488-MIF/CRMs. Compared to the app. K_{ds} of Fluos-msR4M-L1/MIF, Fluos-CRM-1/L4ox, /L5ox, /LD3ox bind approximately 3-to-7 fold weaker to the cytokine . Conclusively, all mimics except for CRM-1/LK3 bound strongly with Alexa-488-MIF, with the three oxidized CRM-1/L4ox, /L5ox and /LD3ox having a quite strong affinity with the cytokine also in the reverse experimental setup (Figure 153). Additional studies might be required to clarify whether the observed differences in the app. K_{ds} with the different experimental setups are due to the label properties or the measuring technique. Fluorescence spectroscopic titrations with a spacer between the label and the CRM sequence, the introduction of Fluos label in a different position, or even its replacement with another label, such as TAMRA, might give additional insights. Other binding techniques, such as FP and MST, could be applied as alternative approaches to determine the binding between CRMs and MIF, as was previously performed with msR4M-L1.
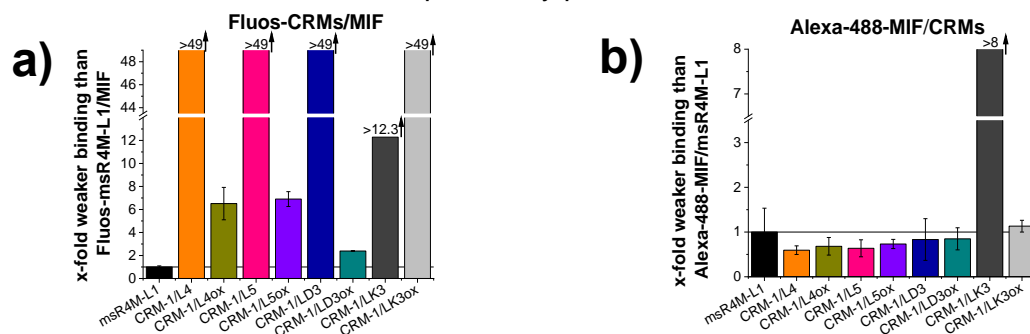
Figure 153. Comparison of binding affinities of CRMs to MIF. a, b Normalized dissociation constants (app. K_{ds}) of the Fluos-CRMs/MIF (a) and Alexa-488-MIF/ CRMs (b) titrations with reference to the app. K_d of Fluos-msR4M-L1/MIF and Alexa-488-MIF/msR4M-L1, respectively. The final measuring conditions were aqueous 1×b, pH 7.4, containing 1% HFIP in all assays.

After the binding affinity studies, mixtures of CRMs (5 µM) and MIF (1 µM) were analyzed by CD spectroscopy and compared with the expected signal. In six out of eight cases, the experimentally and theoretically determined spectra were in agreement, indicating the lack of effect of CRMs in the MIF secondary structure (Figure 154a, c, d). The non-disruption of the MIF conformation and its β-strands might hint at the lack of competition between the CRMs and CD74 for binding to the cytokine [323]. However, CRM-1/L5 and its oxidized analog had a significant interference in the conformation of the atypical chemokine (Figure 154b). The broad minima between 205 and 225 nm had remarkably reduced intensity, especially for the reduced mimic, compared to the sum, suggesting the partial destabilization of the well-ordered MIF secondary structure. The common characteristic between the two mimics that differentiates them from the rest CRMs is the presence of two PEG molecules in the ngm sequence. PEG was shown to bind to hydrophobic sites of the protein and destabilized its structure in other studies [374]. MIF contains some hydrophobic exposed residues, such as Y100 or its C-terminus residues, with an essential role in the order of the MIF structure. A possible interaction of those residues with PEG substrate might have a destabilization effect [84] [86].
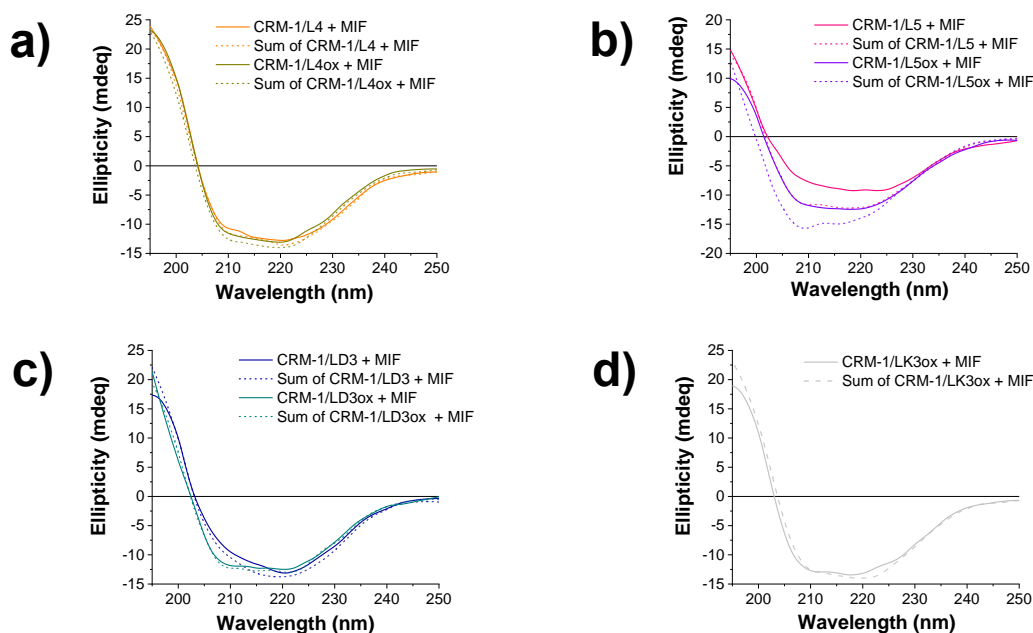
Figure 154. Comparison between the secondary structures of CRMs/MIF mixtures. a, b, c, d CD spectra of CRMs (5 µM)/MIF (1 µM) mixtures (line) and the sum of their individual spectra (dashed line). The ellipticity of the spectra is plotted over the wavelength between 195 and 250 nm (HT<1000) and the. final measuring conditions were aqueous 1×b, pH 7.4, containing 1% HFIP.

Binding affinity studies between CRMs and CXCL12 recorded either strong or very weak interactions. All but CRM-1/LK3ox disulfide bridged mimics bound with high affinity to the CXCR4 ligand. In the respective studies of msR4Ms, it was highlighted already the importance of oxidation in the binding with the chemokine. Contrariwise the non-oxidized analogs CRM-1/L4, /LD3 have app. K_{ds} in the micromolar range, but CRM-1/L5 bound strongly to CXCL12. As explained before, the PEG-applied linkage in the CRM-1/L5 might induce its interaction to the exposed hydrophobic residues on a protein and mediate binding. In the former ngm/CXCL12 studies, it was hypothesized the importance of hydrophobic residues exposure on the surface of the mimics for the interaction with CXCL12. However, this property alone is insufficient since CRM-1/L4, which exposed the same ANS fluorescence emission with CRM-1/L5, failed to bind to the chemokine. Of note, the conjugation of R2ECL2(184-196) on the ngm-L5 alternated completely their binding properties with CXCL12, as the non-CXCL12-binder ngm-L5 was developed to the two-digit nanomolar binder CRM-1/L5. Thus, Fluos-CRM-1/L5, /L5ox, and /LD3ox bind significantly stronger to CXCL12 than MIF, while for the rest tested mimics, no safe conclusions could be extracted, since no upper plateau was reached in their titrations with the proteins (Figure 155a).

The binding potency of CRMs was tested additionally against the IL-8, the most studied ligand of CXCR2. All tested labeled-mimics exhibited a weak affinity with the chemokine except for CRM-1/LD3ox that had a very strong affinity. The oxidized mimic and IL-8 shared a dissociation constant comparable to the one between the receptor and the chemokine and 17-times stronger than the one of CRM-1/LD3ox against MIF (Figure 155b). The recently released crystal structure of the IL-8/CXCR2 complex uncovered an essential role of the N-terminus loop (KTYSKPFHP) and the third β-strand (REL) of the chemokine in the interaction with the receptor, involving both ionic and hydrophobic interactions [152]. Even though the

acidic residues of CXCR2 N-terminus are absent in the CRM sequence, the triple aspartic acids on the ngm part of CRM-1/LD3ox might substitute them and attract the basic residues of the IL-8 N-terminus loop. In the same model, it was shown that the disulfide bond between the N-terminus and ECL3 of the receptor enhanced the alignment of the receptor N-terminus to the binding core of IL-8 [152]. Respectively for the CRM-1/LD3ox case, the disulfide bridge between R2ECL2(184-196) and ECL1(102-110) might align specific residues in a way to interact with the chemokine. The disulfide bridge formation induced the transition from β-sheet to a more unordered state, and this flexibility might be required for the binding. Another factor that might be involved is the lack of positive charge in the sequence, which was present in CRM-1/L4, L5 (+2.9), and CRM-1/LK3 (+5.9), and might cause repulsive forces with the positive charged binding interface of IL-8.

Figure 155. Comparison of the binding affinities of CRMs to CXCL12 and IL-8. a, b Normalized dissociation constants (app. K_{ds}) of the Fluos-CRMs/MIF (a) and Alexa-488-MIF/ CRMs (b) titrations with reference to the app. K_d of Fluos-msR4M-L1/MIF and Alexa-488-MIF/msR4M-L1, respectively (n.d.: non-determined because the titration was not done, n.d.*: non-determined because no upper plateau was reached in the titration and no app. K_d could be calculated). The final measuring conditions were aqueous 1×b, pH 7.4, containing 1% HFIP in all assays.

5.6 Studies on [R87A-L87A-R89A]-MIF interaction with CXCR4

Previous SPOT array studies explained that the initiation of binding between MIF and CXCR4 involves the N-like loop of the atypical chemokine and the N-terminus of the receptor [98]. Collaborators from the groups of Prof. Bernhagen and Prof. Lolis investigated the MIF sequence and revealed a vital role of residues R87, L88, and R89 of MIF in the binding to CXCR4(1-27). Additional studies to test further the potency of those residues required the expression of a triple alanine mutation on MIF sequence in *E.coli* BL21/DE3 and the generation of [R87A-L88A-R89A]-MIF. The mutant was developed from collaborators from the group of Prof. Bernhagen and provided to us for biophysical and binding studies, among others.

Initially, it was studied the structural effect of simultaneous triple alanine substitution on MIF secondary structure. The MRE signal of wild-type and mutated protein did not differentiate over increased concentration (1 to 5 μM). The comparison of their spectra at 5 μM showed a pretty similar signal shape with less intense minima for the mutated protein between 210 and 225 nm and a delay in the increase of the values. All these data indicate that the mutant remains mainly ordered but with more random coil species than the native protein (Figure 156a). This notion was further confirmed with Dichroweb deconvolutions, suggesting that the triple alanine mutation disrupted the one-fourth and the one-fifth of α-helix and β-strand/β-turn content, respectively. R87, L88, and R89 are found at the end of α2 helix, which is located between β4 and β5, and it is hypothesized that their substitutions may affect their stability. Even though the alanines are considered α-helix inducers, it has been shown that the arginine to alanine mutations destabilized α-helixes [375] [376]. However, still 80% of MIF structure did not get affected by the mutations.

Several mutants of MIF have been already structurally studied with CD spectroscopy, revealing that usually, one or two substitutions did not affect the well-ordered structure of the chemokine. Such mutations on MIF sequence were the single P2A, R11A, E22Q, E22A, D44A, L46A, L46G, C60S, Y100G, and the double R11A-D44A and C57A-C60A [88] [95] [377] [378] [86]. Contrariwise, the single mutations L46F, C81S, and Y100F, as well as the elimination of the last 5 or 10 C-terminus residues, had a destabilization impact on the order of MIF structure as derived from CD spectra [377] [379] [86] [84]. Conclusively, an amino acid substitution on the MIF sequence might affect the secondary structure, depending on the residue that is replaced, the substituting residue, and the position.

The structural effect of R87A, L88A, and R89A substitutions was tested further by recording the fluorescence emission of ANS and MIF, native or mutated, mixtures. The label emission of its mixtures with MIF did not change in the 1-10 μM range, contrary to [R87A-L88A-R89A]-MIF mixtures, which got increased values in the last measured points (Figure 156). This different emission behavior of ANS indicates a more significant presence of hydrophobic residues on the protein surface of the mutant compared to the wild-type protein. A hypothesis is that the triple alanine substitution mediated a partial unfolding on protein structure, leading to exposure of hydrophobic residues on the surface. ANS findings agree with the observations of collaborators from the group of Prof. Bernhagen and the higher aggregation propensity of the mutant compared to the wild-type cytokine.
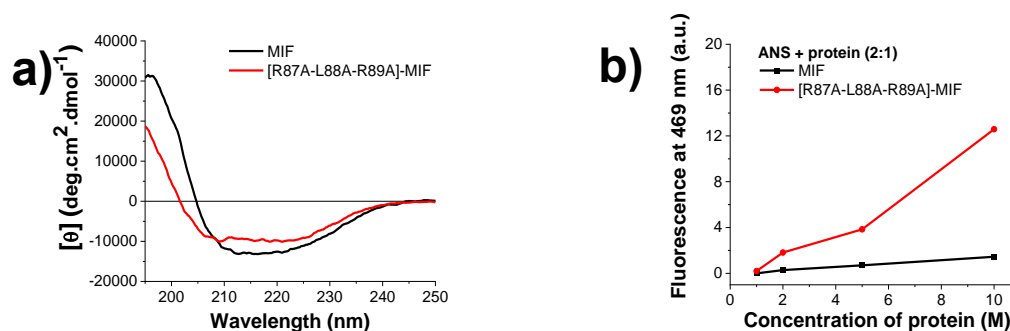
Figure 156. Comparative biophysical characterization of MIF and [R87A-L88A-R89A]-MIF. a CD spectra of proteins at 5 μM with their mean residue ellipticity (MRE) being plotted over the wavelength between 195 and 250 nm (HT<1000). **b** Fluorescence emission at 469 nm over increased concentration of ANS/protein mixture in a constant 2:1 proportionality. The final measuring conditions were aqueous 1×b, pH 7.4, containing 1% HFIP in all assays (adapted from Lacy et al., ref.[295]).

Fluorescence spectroscopic titrations of the labeled mutated protein provided evidence about the importance of the residues on the interaction with CXCR4. Notably, the fluorescence emission of Alexa-[R87A-L88A-R89A]-MIF did not rise against the increased concentration of CXCR4(1-27), ECDs, or msR4Ms. Contrariwise, labeled-MIF bound to all the extracellular domains and had a two-digit nanomolar dissociation constant for the msR4M-L1, -L2. The reverse titration with Fluos-msR4M-L1, -L2, and [R87A-L88A-R89A]-MIF showed a 5 to-10 fold decreased affinity compared to MIF. To sum up, the triple alanine mutation brought about a remarkable decrease in the affinity between the protein and CXCR4 ectodomain parts or mimics. The findings correlate with the data from the lab of Prof. Bernhagen and an abrogation of CXCR4 mediating signaling when the mutated protein substituted the wild-type one. Additional data from SPOT array analysis of MIF(76-90) and its scrambled analogs highlighted the specificity of the interaction with the CXCR4 ectodomain.

5.7   Studies on cyclic MIF analogs

Previous research on MIF/CXCR2 binding interface uncovered the region between the 47th and 56th residue of the atypical chemokine as crucial for binding to the receptor [97]. Later studies from the lab of Prof. Bernhagen determined a MIF-antagonist activity of the 10-mer MIF(47-56) in CXCR2-elicited signaling [380]. To switch in candidates with more drugable properties, MIF(47-56) cyclic analogs were designed and purchased after adding a cysteine on each terminus and forming a disulfide bridge. Cyclic peptides are differentiated based on the number of glycines, serines, or Abu that were introduced between the cysteines and MIF(47-56).

All peptides were studied via CD spectroscopy and exhibited random-coil indicative spectra. However, the application of variable linkers and cyclization affected their secondary structures. The linear MIF(47-56) had very similar spectra with MIF(cyclo6) and MIF(cyclo10) with their minima at -8000 at 195 nm and negative values between 215 and 225 nm. MIF(cycloAbuAL) and MIF(cyclo8) had negative values in the same range too, and -11000 and -6000 at 195 nm, respectively (Figure 157a). However, MIF(cyclo0), MIF(cyclo2), and MIF(cyclo4) had weaker minima and positive values between 215 and 225 nm that suggest a partial conformational restriction and turn-like traces (Figure 157b) [381] [234] [382]. Overall, the linear peptide is unordered, the cyclization partially limits its flexibility which is regained as its linkage between the cysteines and MIF(47-56) gets elongated. Notably, data from the lab of Prof. Bernhagen presented a higher inhibitory potency for the less constrained peptides.

It has been already shown that GS linkers induce conformational flexibility, and this has been correlated more to the glycines, which are the main applied linkage residue on the cyclic MIF analogs [383]. The lack of order in the linear MIF(47-56) is expected due to its small size and its sequence. Other structural studies were carried out with another MIF fragment, the MIF(50-65) that was cyclized via disulfide bridges, as MIF(cyclo0) and generated cyclo-MIF(50–65). Their far-UV CD spectra exposed a random coil structure, with the spectra of the cyclic peptide being partially ordered in β-turn, too. Similar findings were released for its mutant [Asp57,Dap60]MIF(50–65) and its cyclized analog cyclo57,60-[Asp57,Dap60]MIF(50–65) [134]. All MIF(50–65) derived peptides had an MIF agonist activity on the ERK-stimulatory activities, contrary to the MIF-antagonist mediated activity by MIF(47-56) [134]. The specificity of this antagonistic activity was confirmed with lack of any binding between Alexa-488-MIF and MIF(47-56).
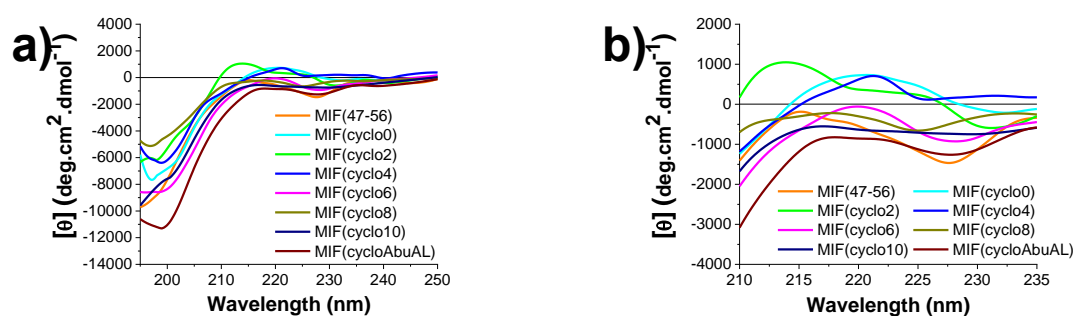
Figure 157. Comparison of the secondary structures of MIF cyclic analogs. a CD spectra of peptides at 5 μM with their mean residue ellipticity (MRE) being plotted over the wavelength between 195 and 250 nm. **b** Same as a but zoomed between 215 and 235 nm. The final measuring conditions were aqueous 1×b, pH 7.4, containing 1% HFIP in all assays (adapted from Krammer et al., ref. [296]).

One of the most significant disadvantages of peptides is their *in vivo* instability, mainly due to their degradation by proteolytic proteases [384]. Overall, poor proteolytic stability might lead to side effects, decreased *in vivo* efficiency, and the failure of peptides in clinical phases [385] [386]. Cyclization is one of the applied chemical modification strategies that may improve resistance against the proteases in plasma [387]. Based on *in vitro* and *ex vivo* data from the lab of Prof. Bernhagen, MIF(cyclo10) was prioritized for stability studies in human plasma *in vitro*. More than half of the lead cyclic analog remained stable above 8 h, and still, one-third was detected in plasma after 48 h. Contrariwise, the $t_{1/2}$ of the linear analog MIF(47-56) was approximately 30 min, and the peptide was barely detected after 2 h of incubation (Figure 158). Conclusively, studies on both peptides confirmed the advantageous effect of cyclization on the proteolytical stability of the peptide.
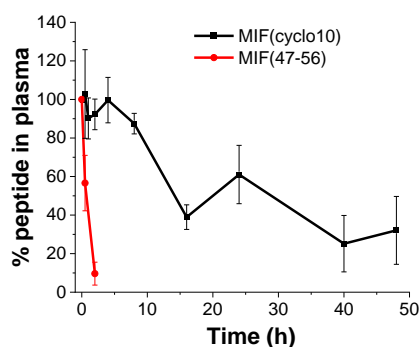
Figure 158. Comparison of the proteolytic stability in human blood plasma between MIF(cyclo10) and MIF(47-56) *in vitro* . Recovered intact peptide (% of total) is calculated based on the area of peptide peak of each time point, normalized based on its area at the earliest time point. and plotted over the various incubation time points (adapted from Krammer et al., ref. [296]).

5.8 CXCR4 and CXCR2/4 mimics as potential therapeutics against atherosclerosis and other inflammatory diseases

Atherosclerosis is classified as a chronic inflammatory disease and is the leading cause of CVDs [21a]. Despite the progress in prevention and therapeutics and the reduction in incidence cases, the prevalence of CVDs increased and remained the main cause of death [388]. Soon the worldwide CVD prevalence is expected to increase further due to the rise of obesity, diabetes, hypertension, and dyslipidemia. The current medical treatment is helpful but still not entirely sufficient [389].

Statins is the most applied treatment for CVD prevention. Several clinical trials showed significant reduction in LDL levels, but side effects were observed in some cases [390]. According to clinical trials, the most common one is muscle toxicity, which should not be a significant reason for discontinuing the drug treatment [391]. Nevertheless, 4 out of 10 statin-receiving patients dropped out of the first year of cure therapy, while the first results of reduced hospitalization require a 2-year treatment [392] [393]. Another health-threatening side effect was the 9% increased risk for the development of diabetes mellitus due to statin treatment [394] [395].

Contrariwise, the other available medicines seem to have fewer side effects. Though, the fibrates' efficiency and to whom of the patients might be beneficial is still debatable [396] [397]. Ezetimibe, a cholesterol absorption inhibitor, did not cause any myalgias, increase in creatine kinase levels, or rhabdomyolysis, nonetheless, it mediated severe cholestatic hepatitis and acute autoimmune hepatitis [398] [399]. PCSK9 inhibitors were shown to lack any side effects, such as myalgia [51] [400]. However, there is still no broad use of them due to their high costs of treatment, their limited benefit against mortality, and in patients with non-high LDL-C concentrations [38] [400] [401]. Even though those molecules appear to be more patient-friendly, statins remain up to nowadays the most applied treatment against atherosclerosis due to their higher efficiency in reducing CVD risk [39]. Still, the risk remains significant, and together with the previously described limitations in patients, it is clear that there is a lot of area for substantial improvement in atherosclerotic therapy [402]. The lack of release of innovative heart-protecting medicines in the market in the last years underlines the importance of finding new ways to attenuate atherosclerosis and reduce CVD events and deaths (Table 61) [54].

Table 62. Currently available medicines on the market against CVDs and their limitations.

Category of medicines	Limitations	References
Statins	• Myalgia and discontinuation of the treatment in 40% of patients • Increased risk for the development of diabetes mellitus	[391] [392] [393] [394] [395]
Fibrates	• Debatable efficiency	[396] [397]
Cholesterol absorption inhibitor	• Severe cholestatic hepatitis (Ezetimibe) • Acute autoimmune hepatitis (Ezetimibe)	[399]
PCSK9 inhibitors	• High cost • Limited benefits against mortality	[38] [400] [401]

Anti-inflammatory pathways appeal as a promising target for the blockade of atherosclerosis. Diabetes patients that were treated with antidiabetic (Rosiglitazone) or antihypertensive (angiotensin-converting enzyme or ACE, inhibitors) or followed a glucose-lowering diet failed to show a reduction in CVD events [403] [404] [405]. Nevertheless, the inhibition of sPLA2 with varespladib not only failed to minimize the CVD risk but induced the risk of MI in patients with ACS [406]. Administration of losmapimod, an inhibitor of p38 MAPK that induces inflammatory mediators production, in patients with acute MI did not decrease the possibility of another severe cardiovascular event [407]. Similarly, treatment of patients with chronic or severe heart failure with TNF-α inhibitor did not bring any improvement [408] [409]. Nevertheless, more promising results were derived by blocking two other cytokines, the IL-1β and IL-6.

Four different FDA-approved drugs that block the two cytokines were administrated for the blockade of CVD events. Methotrexate (MTX) a SMD failed to reduce CVD risk in clinical phase III trial [58]. Colchicine, an alkaloid resulted in the decrease of CVD event in clinical phase III trials in patients after MI or with stable coronary artery disease [410] [64]. Regarding side effects, the colchicine-treated patients in the LoDoCO2 trial were noticed to have a slightly increased possibility of non-cardiovascular related death or myalgia [411]. Canakinumab, a human monoclonal IL-1β antibody decreased heart attack, stroke and death incidences in high risk patients after MI in clinical phase III [67]. However, the high cost of the treatment and the safety concerns led to the final rejection of Canakinumab as an antiatherosclerotic treatment by both FDA and EMA [23] [412] [413]. A possible alternative treatment is Anakinra (Kineret), a recombinant form of IL-1Ra that inhibits the IL-1/IL-1Ra and reduced CRP levels, while it protected against CVDs in clinical trials [69]. An important issue of all successful clinical treatments was the frequent administration of Anakinra, which, together with its high cost, makes routine patient treatment unaffordable [70] [414]. Conclusively, the blockade of proinflammatory cytokines is a promising, innovative therapeutic strategy, but there is still area for improvement on the current approaches, such as reducing side effects, infection risk, and cost. Other proinflammatory cytokines than IL-1β and IL-6 could be possible alternative targets against atherosclerosis, too.

MIF is a pro-inflammatory cytokine that mediates atheroprogressive chemokine-like functions through the chemokine receptors CXCR2 and CXCR4 [77]. The role of MIF in atherogenesis was also confirmed in mouse models, where MIF-deficiency resulted in a reduction of lipid deposition and increased atherosclerotic lesion size compared to wild-type mice [107]. MIF appeals as an attractive target for anti-atherosclerotic drug development, and particularly its signaling through the two chemokine receptors [415].

All the current MIF-orientated therapeutic approaches aim to develop cytokine antagonists in other diseases than atherosclerosis. For example, Ibudilast, an organic molecule that acts as an allosteric MIF inhibitor, decreased the MS progression in clinical phase II, but, adverse effects such as gastrointestinal side effects, headache, and depression appeared [117]. The same side effects, together with nausea and fatigue, were noticed in a clinical phase I trial against ALS, which together with the non-significant therapeutic input led to the discontinuation of the study [416]. Preclinically, neutralizing antibodies inhibited the MIF-mediated lesional inflammation and atherogenesis [417]. A clinical phase I study of Imalumab (BAX69), a

MIF-blocking Ab, revealed mild side effects but almost in 9 out of 10 treated patients [127]. Fatigue, together with vomiting, appeared as side effects in another clinical phase I study but in fewer patients [127]. Imalumab is a blocker of the MIF/CD74 pathway [126]. Anti-CD74 targeting approaches with milatuzumab showed beneficial effects in patients that suffer from specific cancer types in clinical phase I/II [130] [131]. However, targeting this pathway is not desired against atherosclerosis due to the cardioprotective functions of MIF/CD74, even though is targeted by all the current MIF peptide antagonists [418] [133] [419]. The IC_{50} of MIF(47-56), the only CXCR2 inhibitor, and the CD74 inhibitors MIF(80-87), and C36L1 are micromolar, while DRα1-MOG-35–55 inhibits MIF activities at nanomolar range [94] [97] [420] [133] [419]. From all the SMD and peptide antagonists, only ISO-1 was tested and shown to block the CXCR4 [421] [98].

Plexirafor (AMD3100), which was released in the market for the treatment of patients with Non-Hodgkin's lymphoma (NHL) or multiple myeloma (MM), was administrated in atherosclerotic prone mice as well, though it led to increased atherosclerotic lesion areas due to increased neutrophil mobilization [196]. A bicyclam analog of AMD3100, AMD3465, exposed a ten-times increased CXCR4 antagonist potency but with a poor PK [207] [196]. The same issue was faced by 508MCl, a non-cyclam analog of AMD3100, with fast blood clearance lack of oral bioavailability [422]. More organic molecules are currently being tested but still remaining in the preclinical stage [208].

Currently, two different class polyphemusin II-derived peptides, BL-8040 (Motixafortide) and balixafortide, act as CXCR4 antagonists and are in clinical phase III. BL-8040 (Motixafortide) is administrated in combination with cytarabine and showed a potential to treat relapsed/refractory acute myelogenous leukemia [219]. Patients with metastatic breast cancer are treated with the PK optimized balixafortide together with eribulin, and beneficial results were recorded [423] [223]. Another peptide antagonist of CXCR4, LY2510924, combined with Durvalumab (programmed death 1, PD-1, inhibitor) passed in clinical phase II for the treatment of advanced refractory solid tumors [224]. In other clinical studies, the peptide was discontinued either due to toxicological issues in advanced cancer (Clinical Phase I) or lack of efficiency in extensive small cell lung cancer (Clinical Phase II) [424] [425].

From Abs, only the CXCR4-targeting Ab Ulocuplumab reached a clinical phase so far. Particularly, it was administrated together with Lenalidomide or Bortezomib and Dexamethasone in a phase Ib/II trial to treat relapsed MM. The CXCL12/CXCR4 axis blockade had a positive therapeutic effect in patients, however, neutropenia or thrombocytopenia appeared in 4 out of 10 patients [226]. A complete CXCR4 silencing by an Ab might cause trouble to the normal functions of the organism, like short-term myelosuppression or an abnormally increased amount of leukocyte that was mediated by anti-CXCR4 antibodies [426] [427] [428]. Of note, CXCR4 antagonistic activity might differ between peptide and protein. For example, both the peptide LY2510924 and the antibody LY2624587 are subnanomolar inhibitors of SDF-1/CXCR4 but with different mediating effects [225] [230]. Notably, all of the current clinical CXCR4 targeting approaches focus on the inhibition of its interaction with CXCL12 but not with MIF, except for AMD3100 that inhibited both but with an atheroprogressive final outcome [98] [196]. To sum up, the current MIF or CXCR4 therapeutical targeting strategies may be promising in treating some diseases but not suitable against atherosclerosis (Table 62).

Table 63. Currently clinical stage of MIF and CXCR4-targeting approaches and their possible application against atherosclerosis.

Name	Category of molecule	Clinical stage	Disease	Comments on the: ○ **clinical trial** • **possible application against atherosclerosis**	Refer-ences
MIF antagonists					
Imalumab (BAX69)	MIF-blocking Ab	Clinical trial I (finished)	Advanced solid tumours	○ Stabilization in 26% of patients • Non-desirable blockade of the MIF/CD74 cardio-protective pathway	[127]
Milatuzumab	CD74-blocking Ab	Clinical trial I (finished)	Cancer	○ Protective against cancer • Non-desirable blockade of the MIF/CD74 cardio-protective pathway	[130] [131] [429] [430] [431]
CXCR4 antagonists					
AMD3100 (Plexirafor)	SMD	FDA approved	NHL & MM	• Increased atherosclerotic lesion areas	[196]
BL-8040 (Motixafortide)	Peptide	Clinical trial III (ongoing)	Leukemia	○ Ffsf • Blockade of the CXCL12/CXCR4 cardio-protective pathway	[219]
Balixafortide	Peptide	Clinical trial III (ongoing)	Metastatic breast cancer	○ Protective effect • Blockade of the CXCL12/CXCR4 cardio-protective pathway	[423] [223]
LY2510924	Peptide	Clinical trial II (ongoing)	Advanced refractory solid Tumors	○ Protective effect • Blockade of the CXCL12/CXCR4 cardio-protective pathway • Two other clinical studies were withdrawn due to side effects	[424] [425]
Ulocuplumab	Ab	Clinical trial Ib/II (finished)	Relapsed MM	○ Therapeutic input • Blockade of the CXCL12/CXCR4 cardio-protective pathway	[226]

The blockade of MIF/CXCR4 axis is an appealing target for the treatment of atherosclerosis, but not the MIF/CD74 or CXCL12/CXCR4, which mediate cardioprotective signaling. Pharmaceutical targeting of chemokines is challenging due to their multifunctional role and the side effects that might arise due to their inhibition [432]. Herein MIF-specific CXCR4 receptor mimics (msR4Ms) were developed with msR4M-L1 and -L2 interfering only in the atherogenic pathway. The specificity of the mimics is a great advantage compared to the current CXCR4 targeting approaches, which aimed to establish antagonists of the receptors. CXCR4 antagonists blocked totally, and unspecifically the receptor mediating signaling, even the beneficial and resulted in side effects. The lead mimic msR4M-L1 is a specific disease-progressive inhibitor with a MIF-affinity at least 100-fold higher than the one with CXCL12. Notably, the determined dissociation constant of the mimic was

determined with three different techniques (25-78 nM) and proved to be in the same range as the one that the CXCR4 has with the MIF (14 nM) [77]. For most chemokines, the intact receptor is bound with affinities in the range 0.07–60 nM, whereas the peptide binders may have even a 1000-fold reduced affinity [341]. Furthermore, msR4M-L1 adopted an ordered structure, contrary to the other MIF or CXCR4 targeting peptides with no structural data available. Collaborators from the group of Prof. Bernhagen examined further the atheroprotective activity of msR4M-L1. Remarkably, the lead CXCR4 mimic blocked the MIF-mediated inflammatory pathways *in vitro*, the leukocyte adhesion *ex vivo* and the atheroprogression *in vivo* in an Apoe$^{-/-}$ mice model. Conclusively, msR4M-L1 is an ectodomain mimic and a promising therapeutic against atherosclerosis that spares the cardioprotective signaling.

Of note, more than 40% of peptides that entered in clinical trials since 2010 have targeted GPCRs [433]. Currently, three out of four released in the pharmaceutical market peptides contain less than twenty amino acids [434]. Next, SAR studies on the msR4M sequence led to the development of the next generation mimics (ngms) that are within the limits of this size range. All developed mimics adapted a random coil structure with ngm-L5 and ngm-LD3 being prioritized for further studies. Both peptides had a high affinity for MIF and specificity over CXCL12 with the same or improved solubility properties compared to msR4M-L1. Notably, collaborators from the group of Prof. Bernhagen determined an increased inhibitory potency of ngms *in vitro*, if compared to msR4M-L1. Taken together, ngms act as MIF-specific inhibitors like msR4Ms, with the same or improved potency, selectivity and drug-like properties.

One of the current trends in drug development is targeting more than one receptor for the generation of even more effective therapeutics, with dual chemokine receptor antagonists already being in clinical trials [435] [436]. For example, cenicriviroc, a small molecule that acts as an antagonist of CCR2 and CCR5, is in clinical phase III for the treatment of liver fibrosis and a therapeutic candidate against other inflammatory diseases, such as HIV infection and MS [437]. The inhibition of both CXCR4 and CCR5 is suggested to improve the current anti-HIV therapy and hinder the virus resistance that is developed via switching from one receptor to the other [438]. Reparixin, a non-competitive allosteric inhibitor of both CXCR1 and CXCR2, had a protective input in clinical trials against breast cancer and myocardial ischemic reperfusion injury [439] [175] [176] [177]. Even though Reparixin is a blocker of both receptors, it should be classified more as a CXCR1 inhibitor due to its 400-fold higher efficiency in inhibiting it than CXCR2, due to different hydrophobic interactions [440] [177]. An issue for a possible application of the molecule in a routine long-term antiatherosclerotic treatment might be the mild but very common side effects, such as fatigue (3 out of 4 patients) and gastrointestinal disorders (4 out of 10 patients) [175]. MK-7123 (SCH527123), another CXCR2 antagonist, was applied against Chronic Obstructive Pulmonary Disease (COPD) but was withdrawn due to increased blood neutrophil count [179]. Of note, MK-7123 was 100-fold more selective to CXCR2 over CXCR1 inhibitor [441].

The two MIF receptors, CXCR2 and CXCR4, were both targeted in dual receptor antagonism approaches but not simultaneously. A dual receptor antagonist approach against atherosclerosis would involve the inhibition of both of them to minimize the MIF-mediated inflammation and an increased affinity. Following SAR studies on the CXCR2 extracellular loops and the same rational

design principles that were applied for msR4Ms and ngms, chimeric receptor mimics (CRMs) of the ectodomain of both receptors were generated. The labeled MIF bound to 7 out of 8 mimics with a very strong affinity (18-35 nM). Previously dual targeting of CXCR4/CCR5 with organic molecules or of CCR2/CCR3 and CXCR1/CXCR2 with peptide-based ectodomain mimics led to micromolar affinities [442] [251] [252]. Only pyrrolone derivatives managed to inhibit both CCR1 and CCR2 with nanomolar affinities [443]. Additionally, the peptides CRM-1/L5, L5ox bound to CXCL12, the other CXCR4 ligand, with a strong binding affinity. Previously, chimeric inhibitors against HIV have been reported that target either two sites of one protein or two proteins but none of them with three proteins [444] [445] [446]. CRM-1/LD3ox is a mimic of particular interest, which binds to three proteins in total (MIF, CXCL12, IL-8). Notably, its affinity with MIF, CXCL12, and IL-8 is comparable to the ones between the receptors that it imitates and their substrates, i.e., MIF/CXCR4, MIF/CXCR2, CXCL12/CXCR4, and IL-8/CXCR2. The last axis has already been targeted by many clinical approaches, too [447].

For example, patients with COPD were treated with AZD5069, a small molecule with CXCR2 antagonistic activity, in clinical phase II studies but without improvement [448] [449]. Likewise, patients with the same disease and chronic mucus hypersecretion received GSK1325756/danirixin (DNX), another CXCR2 antagonist, but the trial was discontinued after the clinical phase II trial due to the lack of beneficial activity and increased pneumonia cases [448]. One possible reason behind of the lack of efficiency of the clinical trials might be that the blockade of the CXCR2 results in a compensatory induction of its ligands and their signaling through other pathways [450] [451]. Peptide and Ab-based therapeutical strategies exhibited a good anti-inflammatory activity *in vitro* but still remain in preclinical stage [452] [77] [453] [454].

In a more advanced clinical stage is the antibody development for IL-8, the ligand of the CXCR2. Mainly, anti-IL-8 monoclonal antibodies such as HuMax-IL8 (BMS-986253) were applied in patients with metastatic or unresectable solid tumors in clinical phase I. In most patients, only mild side effects occurred, but the treatment was discontinued in some others due to more severe side effects [180]. One possible reason behind these might be the long half-life time of the antibody (11 days) [455]. Abcream is another Ab that has been approved against psoriasis in China by local authorities, but there are still no international literature data [181]. ABX-IL8 is a fully human monoclonal antibody that targets IL-8 and presented some promising results in phase IIa against psoriasis but were not reproduced in the phase IIb trial [181]. However, the necessity for administration by injection, their high production costs, and the risk for allergic reactions or an adverse immune response are crucial problems for developing a long-time routine antibody-based atherosclerotic treatment [297]. Conclusively, the current IL-8/CXCR2 therapeutical approaches are either clinical inefficient (SMDs that act as CXCR2 antagonists) or unaffordable (anti-IL-8 Abs) and not patient-friendly with side effects, thus there is a need for novel strategies (Table 63).

Table 63. Current clinical stage of CXCR2 and IL-8-targeting approaches and their possible application against atherosclerosis.

Name	Category of molecule	Clinical stage	Disease	Comments on the: ◦ **clinical trial** • **possible application against atherosclerosis**	Refer-ences
CXCR1/2 antagonists					
Reparixin	SMD	Clinical trials I (finished)	Breast cancer and MI	◦ Effective against cancer and MI but in small number of patients • High frequency of fatique and gastrointestinal disorders	[439] [175] [176] [177]
MK-7123 (SCH527123)	SMD	Clinical trial II (discontinued)	COPD	◦ Withdrawn due to increased blood neutrophil count • For the same reason is not appropriate against atherosclerosis	[179]
CXCR2 antagonists					
AZD5069	SMD	Clinical trial II (discontinued)	COPD	◦ No improvement in the treated patients • Most likely not sufficient blockade of IL-8/CXCR2	[448] [449]
GSK1325756/ danirixin (DNX)	SMD	Clinical trial II (discontinued)	COPD	◦ No improvement and increased pneumonia cases in the treated patients • Most likely not sufficient blockade of IL-8/CXCR2	[448] [450] [451]
IL-8 antagonists					
HuMax-IL8 (BMS-86253)	Ab	Clinical trial I (finished)	Metastatic or unresectable solid tumors	◦ Efficient ◦ Severe side effects in some patients • Administrated by injection • High cost and risk for allergic reactions	[180] [297]
ABX-IL8	Ab	Clinical trial IIb (discontinued)	Psoriasis	◦ Non reprododucible benefit • Administrated by injection • High cost and risk for allergic reactions	[181] [297]

Overall, peptides have a higher affinity than SMDs but lower than Abs. However, they could inhibit selective pathways and be more affordable and patient-friendly than Abs, with fewer side effects. Furthermore, they could be mimics of protein, or the receptor-binding domain, modulate protein-protein interactions and interfere selectively in many disease-exacerbating pathways [456]. For example, the msR4Ms, ngms, and CRMs that are MIF-specific inhibitors could be applied against inflammatory diseases other than atherosclerosis, such as lung diseases, arthritis or glomerulonephritis [110]. The blockade of MIF/CXCR4 pathway might be beneficial

against various inflammatory diseases, including neurodegenarative diseases, cancer and metastasis (Figure 159) [109] [110].

So far, the CXCL12-binders mimics were not prioritized for further studies due to their interference in the atheroprotective CXCL12/CXCR4 axis. However, this interaction might be a mediator for other diseases. Particularly, CXCL12 induces through CXCR4 progress in tumor progression, angiogenesis, metastasis, and survival in several types of cancer [203] The inhibition of this axis was beneficial against RA and MS too, while it has both disease-inducer and protective role in stroke, psoriasis, kidney diseases [204] [205]. The CXCL12/CXCR4 interaction blockers, such as the oxidized msR4Ms, CRMs or ngm-LK3,-LR3 might be therapeutic candidates in any of these diseases (Figure 159).

CRM-1/LD3ox, as a multiple binder of MIF, CXCL12, and IL-8, could be applied in the described diseases plus the additionally mediated by the IL-8/CXCR2 axis ones, such as COPD and asthma [161] [162]. Besides, blockade of the IL-8/CXCR2 axis led to a reduction in progress of inflammatory bowel disease, MS, and AD [163] [164] [165]. An additional application of the IL-8/CXCR2 inhibition might be beneficial against cancer, too (Figure 159) [166]. Nevertheless, IL-8 is an essential mediator of several aspects of the immune response. Therefore, the complete blockade of IL-8 signaling pathways is not desirable in long-term treatment, such as the one required for atherosclerosis. Thus, it needs to be ensured that the inhibition of the IL-8 signal is carried out in specific tissues. Currently, there is an increasing need for target-selective therapeutic approaches [140]. For that reason, sequence optimization might be required for CRM-1/LD3ox as a possible anti-atherosclerotic treatment. The mimic should localize and inhibit specifically the MIF/CXCR4 and IL-8/CXCR2 disease-exacerbating pathways and not interfere in the CXCL12/CXCR4 and MIF/CD74 cardioprotective ones.
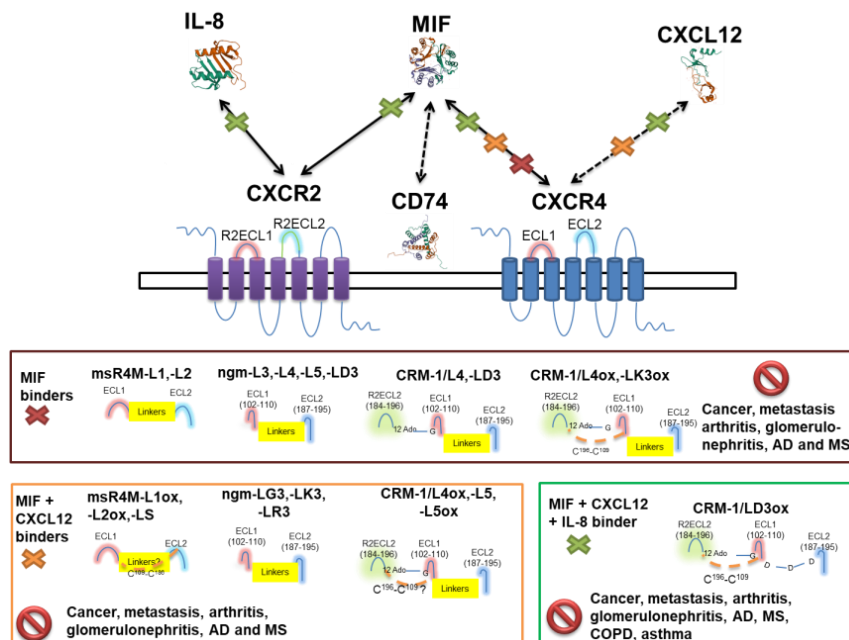
Figure 159. Classification of all generated msR4Ms, ngms and CRMs based on their chemokine binding substrates and their possible therapeutic applications. Depection of the interactions between the chemokines MIF (atypical), CXCL12, IL-8 and the chemokine receptors CXCR2, CXCR4 or the transmembrane protein CD74 and their inhibition by the developed mimics. The mimics are seperated based on their binding properties and the protective role that may have in diseases due to the blockade of the pathways. The chemokines and the transmembrane protein are demonstrated based on their published structures (MIF:1MIF, CXCL12:3HP3, IL-8:1IL8, CD74:1IIE) [83] [101] [158] [102].

Another pharmaceutical approach might aim in even more enhanced blockade of the IL-8. Except for CXCR2, the chemokine mediates signaling through CXCR1, an IL-8 specific receptor, with both receptors sharing a 75% sequence identity all over their sequence [457]. Simultaneous inhibition of both receptors was more efficient than blocking only CXCR2 [441] [458]. Conjugating the CXCR1 ectodomain hot spot regions that interact with the chemokine, such as the N-terminus or the ECL3, to CRM-1/LD3ox might lead to an even stronger blockade of IL-8 [252]. In that case, it would be developed a multiple receptor mimic that, ideally, would imitate the ectodomain of CXCR1, CXCR2, and CXCR4. A similar approach with linking three segments was applied to mimic the binding site of an antibody-heavy chain to an antigen [459]. A dual receptor mimic of CXCR1/2 has already been developed via connection of the N-terminus of CXCR1 with the ECL3 of CXCR2, however, the binding affinity with IL-8 was not very strong. Noteworthy, the two ectodomain segments were not connected with amino acids but stabilized on the B1 domain of Streptococcal protein G that acted as a soluble scaffold [252].

Further studies in the field of chimeric receptor mimics might aim to attach a part of the ACKR3 to generate an even stronger binder of MIF. However, still, no data have been published on the MIF/ACKR3 binding interface. Another strategy might involve introducing additional ectodomain regions so that the mimics would be able to bind with MIF-2, the other member of the MIF family. So far, it remains unknown whether MIF-2 binds to CXCR2 or CXCR4. The fluorescence spectroscopic titration between the CXCR4 mimic msR4M-L1 and MIF-2 suggested that the cytokine behaves as an atypical chemokine and interacts with the receptor. SAR studies on the CXCR4 sequence might provide optimization to the sequence and enhance the binding affinity. Regarding CXCR2, it has been hypothesized that MIF-2 does not activate the receptor since the cytokine does not form a pseudo-(E)LR motif as MIF, which was indispensable for the MIF/CXCR2 interaction.

It might be of particular interest for future experiments to focus on the generation of more structurally stable mimics. Conformational stabilization could hinder their proteolytic degradation of the peptides and enhance their binding and specificity in the protein-protein interactions [240]. [460] [461]. One of the challenges in the peptide pharmaceutical area is developing larger peptides than the currently available ones with an ordered protein-like secondary structure [434]. A chemical modification that might induce both proteolytic and structural stability of the peptide is cyclization, with the bicyclic ones having increased applications in research and medicine [462] [463]. Peptides with β-hairpin might have high selectivity to the protein target, and their structure might get stabilized through hydrogen bonds [464] [465]. In some cases, the structural stability could be improved even by altering the linker length and amino acid composition [466].

Substitutions may also mediate or hinder the self-assembly since it is dependent on the amino acid sequence, its length, and the hydrophobicity degree of the peptide [467]. The self-associated peptides could be stabilized in a low-energy state by hydrophobic or electrostatic interactions, hydrogen bonds, or even van der Waals forces [468]. Interestingly, in some cases, self-association might be desired since self-assembled peptides were proved to be proteolytical stable and have therapeutic applications [469] [470].

6 Appendix

a)

b)
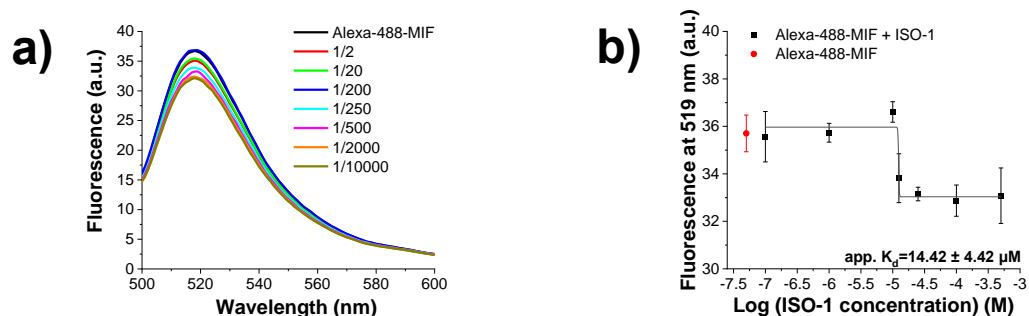
Appendix Figure A1. **Fluorescence spectroscopic titrations of Alexa-488-MIF with ISO-1 for the determination of apparent affinity (app. K_d). a** Fluorescence spectra between 500 and 600 nm of Alexa-488-MIF (10 nM) alone and its mixtures with various amounts of ISO-1; the molar ratios of Alexa-488-MIF/ ISO-1 are indicated. **b** Binding curves derived from the fluorescence emission at 519 nm of Alexa-488-MIF (10 nM) at different concentrations of ISO-1. Data shown are means (±SD) from three independent titration experiments which were performed in aqueous 1×b, pH 7.4, containing 1% HFIP.

a)

b)
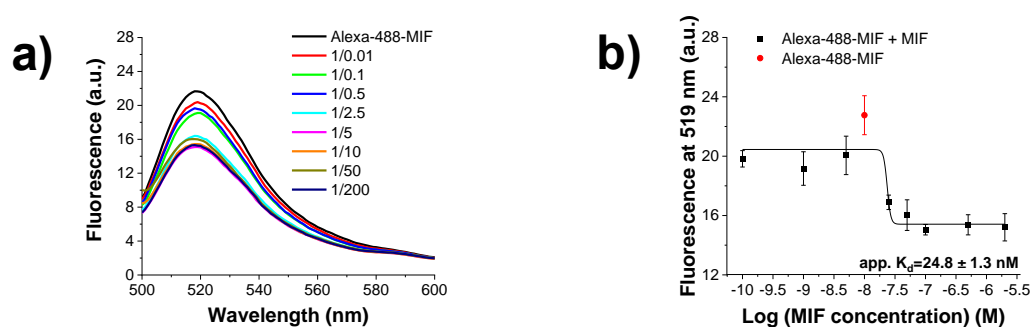
Appendix Figure A2. Fluorescence spectroscopic titrations for the determination of apparent affiniy (app. K_d) for the self-association of MIF. a Fluorescence spectra between 500 and 600 nm of each Alexa-488-MIF (10 nM) alone and its mixtures with various amounts of its respective unlabeled partner MIF; the molar ratios of Alexa-488-MIF/MIF are indicated. **b** Binding curves derived from the fluorescence emission at 519 nm of Alexa-488-MIF (10 nM) at different concentrations of its respective unlabeled partner MIF. Data shown are means (±SD) from three independent titration experiments which were performed in aqueous 1×b, pH 7.4, containing 1% HFIP.
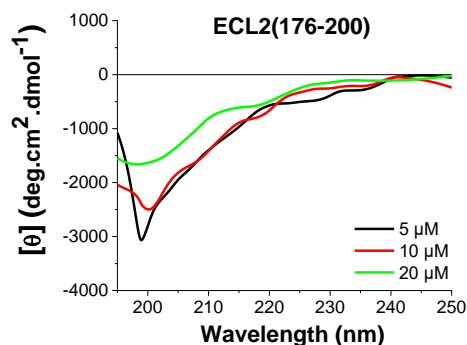
Appendix Figure A3. Spectra of ECL2(176-200) in various concentrations for the determination of the conformation, as determined by far-UV CD spectroscopy. CD spectra of ECL2(176-200) at increasing concentrations at final measuring conditions of aqueous 1×b, pH 7.4, containing 1% HFIP. Mean residue ellipticity (MRE) plotted was plotted over the wavelength between 195 and 250 nm.
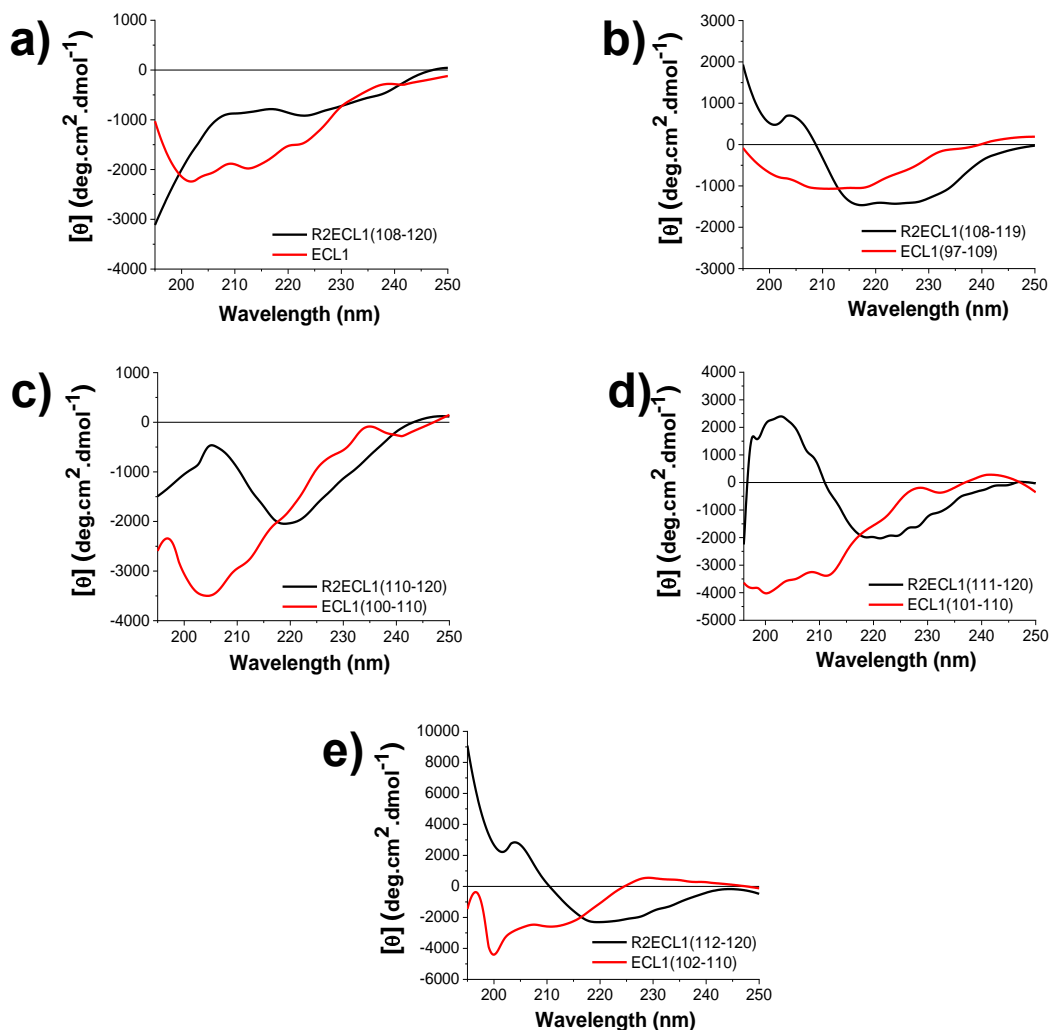
Appendix Figure A4. Comparative spectra of ECL1 with R2ECL1(108-120) analogs for the determination of the conformation, as determined by far-UV CD spectroscopy. a, b, c, d, e CD spectra of ECL1 and R2ECL1(108-120) (a), ECL1(97-109) and R2ECL1(108-119) (b), ECL1(100-110) and R2ECL1(110-120) (c), ECL1(101-110) and R2ECL1(111-120) (d), ECL1(102-110) and R2ECL1(112-120) (e), at 10 µM of the peptide at final measuring conditions of aqueous 1×b, pH 7.4, containing 1% HFIP. Mean residue ellipticity (MRE) plotted over the wavelength between 195 and 250 nm.
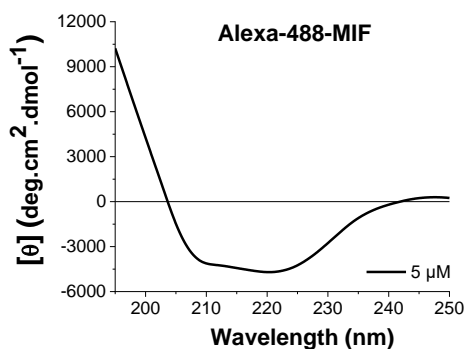
Appendix Figure A5. Spectrum of Alexa-488-MIF, as determined by far-UV CD spectroscopy. Spectrum of Alexa-488-MIF at 5 µM at final measuring conditions of aqueous 1×b, pH 7.4. Mean residue ellipticity (MRE) plotted over the wavelength between 195 and 250 nm.

6.1   List of Tables

6.2 List of Figures

6.3   List of Schemes

6.4   List of Equations

6.5   List of Appendix Figures

6.6   List of Publications and Scientific Presentations

Publications[#][*]

1[#].   **Kontos C**[*], El Bounkari O[*], Krammer C[*], Sinitski D, Hille K, Zan C, Yan G, Wang S, Gao Y, Brandhofer M, Megens R. T. A, Hoffmann A, Pauli J, Asare Y, Gerra S, Bourilhon P, Leng L, Eckstein H.H, Kempf W.E, Pelisek J, Gokce O, Maegdefessel L, Bucala R, Dichgans M, Weber C, Kapurniotu A, Bernhagen J, Nat. Commun., 2020, doi: 10.1038/s41467-020-19764-z

2[#].   Krammer C, **Kontos C,** Dewor M, Hille K, Dalla Volta B, El Bounkari O, Taş K, Sinitski D, Brandhofer M, Megens R. T. A , Weber C, Schultz J. R, Bernhagen J, Kapurniotu A, et al., Chembiochem, 2020, doi: 10.1002/cbic.202000574

3. Sinitski D, Gruner K, Brandhofer M, **Kontos C,** Winkler P, Reinstädler A, Bourilhon P, Xiao Z, Cool R, Kapurniotu A, Dekker F. J, Panstruga R, Bernhagen J, J Biol Chem., 2020, doi: 10.1074/jbc.RA119.009716

4. Sinitski D*, **Kontos C***, Krammer C*, Asare Y, Kapurniotu A, Bernhagen J, J Thromb Haemost., 2019, doi: 10.1055/s-0039-1677803

5[#.] Lacy M*, **Kontos C***, Brandhofer M*, Hille K, Groening S, Sinitski D, Bourilhon P, Rosenberg E, Krammer C, Thavayogarajah T, Pantouris G, Bakou M, Weber C, Lolis E, Bernhagen J, Kapurniotu A, Sci Rep., 2018, doi: 10.1038/s41598-018-23554-5.

6. **Kontos C**, Androutsou M.E, Vlamis-Gardikas A, Tselios T, Anal Biochem., 2017, doi: 10.1016/j.ab.2017.09.016

[#] Papers that included data which are parts of this thesis
* Refers to equal first authorship

Scientific Presentations[#]

Oral Presentation

1[#]. Rationally designed conformationally constrained CXCR4 mimics act as soluble chemokine receptors for MIF but not CXCL12 and block atherogenic inflammation. Kontos C, El Bounkari O, Krammer C, Hille K, Gao Y, Brandhofer M, Megens R, Mägdefessel L, Weber C, Bernhagen J, Kapurniotu A, 15th German Peptide Symposium, Marburg (Germany), 2021

Poster Presentations

1[#]. Identification of an Arg-Leu-Arg motif that contributes to the interface between the cytokine MIF and the chemokine receptor CXCR4. **Kontos C**, Brandhofer M, Lacy M, Hille K, Sinitski D, Krammer C, Bernhagen J, Kapurniotu A. 35th European Peptide Symposium (EPS), Dublin (Ireland), 2018, Published in J. Pept. Sci. 2018;24(S2), S143-S143. doi:10.1002/psc.3127

2. A high throughput recovery method for the quantification of a peptide in plasma using HPLC. **Kontos C**, Androutsou M.E, Vlamis-Gardikas A, Tselios T. 34th European Peptide Symposium (EPS), Leipzig (Germany), 2016, Published in J. Pept. Sci. 2016; 22(S2), S100-S100. doi.org/10.1002/psc.2950

3. Development of a SDS-PAGE methodology for the determination of a peptide in solution. **Kontos C**, Androutsou M.E, Tapeinou A, Tselios T, NMR Applications in Life Sciences-Exploring Peptides & Proteins", Patras (Greece), 2015

4. Development of a UPLC-MS/MS analytical method for the quantification of peptide analogue of myelin oligodendrocyte glycoprotein (MOG) in rat plasma. Androutsou M.E, **Kontos C**, Matsoukas J, Tselios T. 1st Peptides in Paris Symposium (PIPS2014)", Paris (France), 2014

[#] Presentations that included data which are parts of this thesis

7. References

[1]   G. A. Fishbein, M. C. Fishbein, *Archives of Pathology & Laboratory Medicine* **2009**, *133*, 1309-1316.
[2]   V. Kumar, A. Abbas, J. Aster, *Robbins & Cotran Pathologic Basis of Disease*, 9th ed., Saunders, Philadelphia, **2014**.
[3]   M. C. Fishbein, G. A. Fishbein, *Cardiovascular pathology : the official journal of the Society for Cardiovascular Pathology* **2015**, *24*, 335-342.
[4]   K. A. Mowafy, M. Soliman, A. M. Hammoda, R. M. Soliman, *Vascular and Endovascular Review* **2019**, *2*, 48-52.
[5]   F. Marchand., in *Verhandlungen der Kongresse fuer Innere Medizin, Vol. 21 Kongresse*, Leipzig, **1904**.
[6]   aJ. F. Bentzon, F. Otsuka, R. Virmani, E. Falk, *Circulation Research* **2014**, *114*, 1852-1866; bC. Silvestre-Roig, M. P. d. Winther, C. Weber, M. J. Daemen, E. Lutgens, O. Soehnlein, *Circulation Research* **2014**, *114*, 214-226.
[7]   World Health Organization, **2017, May 17**.
[8]   W. Herrington, B. Lacey, P. Sherliker, J. Armitage, S. Lewington, *Circulation Research* **2016**, *118*, 535-546.
[9]   E. Wilkins, L. Wilson, K. Wickramasinghe, P. Bhatnagar, J. Leal, R. Luengo-Fernandez, R. Burns, M. Rayner, N. Townsend, European Heart Network, Brussels, **2017**.
[10]   C. B. Fordyce, M. T. Roe, T. Ahmad, P. Libby, J. S. Borer, W. R. Hiatt, M. R. Bristow, M. Packer, S. M. Wasserman, N. Braunstein, B. Pitt, D. L. DeMets, K. Cooper-Arnold, P. W. Armstrong, S. D. Berkowitz, R. Scott, J. Prats, Z. S. Galis, N. Stockbridge, E. D. Peterson, R. M. Califf, *Journal of the American College of Cardiology* **2015**, *65*, 1567-1582.
[11]   V. Fuster, J. Frazer, M. Snair, R. Vedanthan, V. Dzau, *Journal of the American College of Cardiology* **2017**, *70*, 3140-3156.
[12]   World Health Organization, Geneva, **2013**.
[13]   M. J. Thun, B. D. Carter, D. Feskanich, N. D. Freedman, R. Prentice, A. D. Lopez, P. Hartge, S. M. Gapstur, *New England Journal of Medicine* **2013**, *368*, 351-364.
[14]   S. S. Virani, A. Alonso, E. J. Benjamin, M. S. Bittencourt, C. W. Callaway, A. P. Carson, A. M. Chamberlain, A. R. Chang, S. Cheng, F. N. Delling, L. Djousse, M. S. V. Elkind, J. F. Ferguson, M. Fornage, S. S. Khan, B. M. Kissela, K. L. Knutson, T. W. Kwan, D. T. Lackland, T. T. Lewis, J. H. Lichtman, C. T. Longenecker, M. S. Loop, P. L. Lutsey, S. S. Martin, K. Matsushita, A. E. Moran, M. E. Mussolino, A. M. Perak, W. D. Rosamond, G. A. Roth, U. K. A. Sampson, G. M. Satou, E. B. Schroeder, S. H. Shah, C. M. Shay, N. L. Spartano, A. Stokes, D. L. Tirschwell, L. B. VanWagner, C. W. Tsao, *Circulation* **2020**, *141*, e139-e596.
[15]   US Burden of Disease Collaborators, *The Journal of the American Medical Association* **2013**, *310*, 591-606.
[16]   M. Nagayoshi, S. A. Everson-Rose, H. Iso, T. H. Mosley, K. M. Rose, P. L. Lutsey, *Stroke* **2014**, *45*, 2868-2873.
[17]   C. A. Pope, 3rd, R. T. Burnett, G. D. Thurston, M. J. Thun, E. E. Calle, D. Krewski, J. J. Godleski, *Circulation* **2004**, *109*, 71-77.
[18]   M. Rafieian-Kopaei, M. Setorki, M. Doudi, A. Baradaran, H. Nasri, *International Journal of Preventive Medicine,* **2014**, *5*, 927-946.
[19]   J. H. O'Keefe, L. Cordain, *Mayo Clinic Proceedings* **2004**, *79*, 101-108.
[20]   R. C. Thompson, A. H. Allam, G. P. Lombardi, L. S. Wann, M. L. Sutherland, J. D. Sutherland, M. A.-T. Soliman, B. Frohlich, D. T. Mininberg, J. M. Monge, C. M. Vallodolid, S. L. Cox, G. Abd el-Maksoud, I. Badr, M. I. Miyamoto, A. el-Halim Nur el-din, J. Narula, C. E. Finch, G. S. Thomas, *The Lancet* **2013**, *381*, 1211-1222.
[21]   aR. Ross, *New England Journal of Medicine* **1999**, *340*, 115-126; bA. C. Newby, *Toxicology letters* **2000**, *112-113*, 519-529.
[22]   P. Libby, P. M. Ridker, A. Maseri, *Circulation* **2002**, *105*, 1135-1143.
[23]   M. Vaccarezza, C. Balla, P. Rizzo, *International Journal of Cardiology* **2018**, *19*, 1-2.
[24]   aA. Gisterå, G. K. Hansson, *Nature reviews. Nephrology* **2017**, *13*, 368-380; bI. Tabas, A. H. Lichtman, *Immunity* **2017**, *47*, 621-634.
[25]   G. K. Hansson, L. Jonasson, *Arteriosclerosis, Thrombosis, and Vascular Biology* **2009**, *29*, 1714-1717.
[26]   G. K. Hansson, *New England Journal of Medicine* **2005**, *352*, 1685-1695.
[27]   B.O. Hans, W. Petrine, A. J. Anders, *Current Drug Targets* **2007**, *8*, 169-184.
[28]   H. A. R. Hadi, C. S. Carr, J. Al Suwaidi, *Vascular Health and Risk Management* **2005**, *1*, 183-198.
[29]   G. K. Hansson, P. Libby, I. Tabas, *Journal of Internal Medicine* **2015**, *278*, 483-493.
[30]   A. Schumski, C. Winter, Y. Döring, O. Soehnlein, *Journal of Innate Immunity* **2018**, *10*, 479-486.
[31]   S. J. Hwang, C. M. Ballantyne, A. R. Sharrett, L. C. Smith, C. E. Davis, A. M. Gotto, Jr., E. Boerwinkle, *Circulation* **1997**, *96*, 4219-4225.

[32]   M. T. Nguyen, S. Fernando, N. Schwarz, J. T. Tan, C. A. Bursill, P. J. Psaltis, *Journal of Clinical Medicine* **2019**, *8*, 1109.
[33]   Kathryn J. Moore, I. Tabas, *Cell* **2011**, *145*, 341-355.
[34]   I. Tabas, *Nature reviews. Immunology* **2010**, *10*, 36-46.
[35]   Y. Döring, M. Drechsler, O. Soehnlein, C. Weber, *Arteriosclerosis, Thrombosis, and Vascular Biology* **2015**, *35*, 288-295.
[36]   R. Virmani, F. D. Kolodgie, A. P. Burke, A. Farb, S. M. Schwartz, *Arteriosclerosis, Thrombosis, and Vascular Biology* **2000**, *20*, 1262-1275.
[37]   J. C. Wang, M. Bennett, *Circulation Research* **2012**, *111*, 245-259.
[38]   S. C. Bergheanu, M. C. Bodde, J. W. Jukema, *Netherlands Heart Journal* **2017**, *25*, 231-242.
[39]   K. K. Gupta, S. Ali, R. S. Sanghera, *Cardiology and Therapy |* **2019**, *8*, 5-20.
[40]   C. Stancu, A. Sima, *Journal of Cellular and Molecular Medicine* **2001**, *5*, 378-387.
[41]   The Long-Term Intervention with Pravastatin in Ischaemic Disease (LIPID) Study Group*, *The New England journal of medicine* **1998**, *339*, 1349-1357.
[42]   P. J. Barter, G. Brandrup-Wognsen, M. K. Palmer, S. J. Nicholls, *Journal of Lipid Research* **2010**, *51*, 1546-1553.
[43]   A. Pandor, R. M. Ara, I. Tumur, A. J. Wilkinson, S. Paisley, A. Duenas, P. N. Durrington, J. Chilcott, *Journal of Internal Medicine* **2009**, *265*, 568-580.
[44]   G. Olsson, N. Rehnqvist, A. Sjögren, L. Erhardt, T. Lundman, *Journal of the American College of Cardiology* **1985**, *5*, 1428-1437.
[45]   S. Yusuf, P. Sleight, J. Pogue, J. Bosch, R. Davies, G. Dagenais, *The New England journal of medicine* **2000**, *342*, 145-153.
[46]   K. M. Fox, *Lancet (London, England)* **2003**, *362*, 782-788.
[47]   B. Neal, S. MacMahon, N. Chapman, *Lancet (London, England)* **2000**, *356*, 1955-1964.
[48]   N. H. Kim, S. G. Kim, *Diabetes & Metabolism* **2020**, *44*, 213-221.
[49]   D. Morrone, W. S. Weintraub, P. P. Toth, M. E. Hanson, R. S. Lowe, J. Lin, A. K. Shah, A. M. Tershakovec, *Atherosclerosis* **2012**, *223*, 251-261.
[50]   M. S. Sabatine, R. P. Giugliano, S. D. Wiviott, F. J. Raal, D. J. Blom, J. Robinson, C. M. Ballantyne, R. Somaratne, J. Legg, S. M. Wasserman, R. Scott, M. J. Koren, E. A. Stein, *New England Journal of Medicine* **2015**, *372*, 1500-1509.
[51]   J. G. Robinson, M. Farnier, M. Krempf, J. Bergeron, G. Luc, M. Averna, E. S. Stroes, G. Langslet, F. J. Raal, M. El Shahawy, M. J. Koren, N. E. Lepor, C. Lorenzato, R. Pordy, U. Chaudhari, J. J. P. Kastelein, *New England Journal of Medicine* **2015**, *372*, 1489-1499.
[52]   L. Wallentin, R. C. Becker, A. Budaj, C. P. Cannon, H. Emanuelsson, C. Held, J. Horrow, S. Husted, S. James, H. Katus, K. W. Mahaffey, B. M. Scirica, A. Skene, P. G. Steg, R. F. Storey, R. A. Harrington, A. Freij, M. Thorsén, *The New England journal of medicine* **2009**, *361*, 1045-1057.
[53]   J. M. Lee, M. D. Robson, L. M. Yu, C. C. Shirodaria, C. Cunnington, I. Kylintireas, J. E. Digby, T. Bannister, A. Handa, F. Wiesmann, P. N. Durrington, K. M. Channon, S. Neubauer, R. P. Choudhury, *Journal of the American College of Cardiology* **2009**, *54*, 1787-1794.
[54]   S. M. Paul, D. S. Mytelka, C. T. Dunwiddie, C. C. Persinger, B. H. Munos, S. R. Lindborg, A. L. Schacht, *Nature Reviews Drug Discovery* **2010**, *9*, 203-214.
[55]   H. Ait-Oufella, P. Libby, A. Tedgui, *Arteriosclerosis, Thrombosis, and Vascular Biology* **2019**, *39*, 1510-1519.
[56]   M. E. Weinblatt, *Arthritis Research & Therapy* **2018**, *20*, 103-103.
[57]   A. Aggarwal, R. Misra, *Rheumatology international* **2003**, *23*, 134-137.
[58]   P. M. Ridker, B. M. Everett, A. Pradhan, J. G. MacFadyen, D. H. Solomon, E. Zaharris, V. Mam, A. Hasan, Y. Rosenberg, E. Iturriaga, M. Gupta, M. Tsigoulis, S. Verma, M. Clearfield, P. Libby, S. Z. Goldhaber, R. Seagle, C. Ofori, M. Saklayen, S. Butman, N. Singh, M. Le May, O. Bertrand, J. Johnston, N. P. Paynter, R. J. Glynn, C. Investigators, *The New England journal of medicine* **2019**, *380*, 752-762.
[59]   N. Nerlekar, A. Beale, R. W. Harper, *Medical Journal of Australia* **2014**, *201*, 687-688.
[60]   U. S. Food and Drug Administration, **2015**.
[61]   P. Richette, T. Bardin, *Expert opinion on pharmacotherapy* **2010**, *11*, 2933-2938.
[62]   A. Y. Gasparyan, L. Ayvazyan, M. Yessirkepov, G. D. Kitas, *Expert Opinion on Drug Metabolism & Toxicology* **2015**, *11*, 1781-1794.
[63]   G. J. Martínez, S. Robertson, J. Barraclough, Q. Xia, Z. Mallat, C. Bursill, D. S. Celermajer, S. Patel, *Journal of the American Heart Association* **2015**, *4*, e002128-e002128.
[64]   S. M. Nidorf, J. W. Eikelboom, C. A. Budgeon, P. L. Thompson, *Journal of the American College of Cardiology* **2013**, *61*, 404-410.
[65]   U. S. Food and Drug Administration, **2009**, https://www.accessdata.fda.gov/drugsatfda_docs/nda/2009/125319s000TOC.cfm
[66]   U. S. Food and Drug Administration, **2016** https://www.fda.gov/drugs/postmarket-drug-safety-information-patients-and-providers/colchicine-marketed-colcrys-information
[67]   P. M. Ridker, B. M. Everett, T. Thuren, J. G. MacFadyen, W. H. Chang, C. Ballantyne, F. Fonseca, J. Nicolau, W. Koenig, S. D. Anker, J. J. P. Kastelein, J. H. Cornel, P. Pais, D.

Pella, J. Genest, R. Cifkova, A. Lorenzatti, T. Forster, Z. Kobalava, L. Vida-Simiti, M. Flather, H. Shimokawa, H. Ogawa, M. Dellborg, P. R. F. Rossi, R. P. T. Troquay, P. Libby, R. J. Glynn, *The New England journal of medicine* **2017**, *377*, 1119-1131.

[68]   U. S. Food and Drug Administration, **2020** https://www.accessdata.fda.gov/drugsatfda_docs/label/2020/103950s5189lbl.pdf

[69]   D. L. Mann, in *Inflammation in Heart Failure* (Eds.: W. M. Blankesteijn, R. Altara), Academic Press, Boston, **2015**, pp. 191-203.

[70]   L. F. Buckley, A. Abbate, *European Heart Journal* **2018**, *39*, 2063-2069.

[71]   J. R. David, *Proceedings of the National Academy of Sciences of the United States of America* **1966**, *56*, 72-77.

[72]   W. Y. Weiser, P. A. Temple, J. S. Witek-Giannotti, H. G. Remold, S. C. Clark, J. R. David, *Proceedings of the National Academy of Sciences of the United States of America* **1989**, *86*, 7522-7526.

[73]   J. Bernhagen, T. Calandra, R. A. Mitchell, S. B. Martin, K. J. Tracey, W. Voelter, K. R. Manogue, A. Cerami, R. Bucala, *Nature* **1993**, *365*, 756-759.

[74]   S. Rex, S. Kraemer, G. Grieb, C. Emontzpohl, J. Soppert, A. Goetzenich, R. Rossaint, J. Bernhagen, C. Stoppe, *Mini reviews in medicinal chemistry* **2014**, *14*, 1116-1124.

[75]   E. Rosengren, R. Bucala, P. Åman, L. Jacobsson, G. Odh, C. N. Metz, H. Rorsman, *Molecular Medicine* **1996**, *2*, 143-149.

[76]   R. Kleemann, A. Kapurniotu, R. W. Frank, A. Gessner, R. Mischke, O. Flieger, S. Jüttner, H. Brunner, J. Bernhagen, *Journal of molecular biology* **1998**, *280*, 85-102.

[77]   J. Bernhagen, R. Krohn, H. Lue, J. L. Gregory, A. Zernecke, R. R. Koenen, M. Dewor, I. Georgiev, A. Schober, L. Leng, T. Kooistra, G. Fingerle-Rowson, P. Ghezzi, R. Kleemann, S. R. McColl, R. Bucala, M. J. Hickey, C. Weber, *Nature Medicine* **2007**, *13*, 587-596.

[78]   J. Bernhagen, R. A. Mitchell, T. Calandra, W. Voelter, A. Cerami, R. Bucala, *Biochemistry* **1994**, *33*, 14144-14155.

[79]   T. Roger, L. J. Schlapbach, A. Schneider, M. Weier, S. Wellmann, P. Marquis, D. Vermijlen, F. C. G. J. Sweep, L. Leng, R. Bucala, T. Calandra, E. Giannoni, *Frontiers in immunology* **2017**, *8*, 26-26.

[80]   M. Merk, R. A. Mitchell, S. Endres, R. Bucala, *Cytokine* **2012**, *59*, 10-17.

[81]   G. Odh, A. Hindemith, A. M. Rosengren, E. Rosengren, H. Rorsman, *Biochemical and biophysical research communications* **1993**, *197*, 619-624.

[82]   H. Sugimoto, M. Taniguchi, A. Nakagawa, I. Tanaka, M. Suzuki, J. Nishihira, *Biochemistry* **1999**, *38*, 3268-3279.

[83]   H. W. Sun, J. Bernhagen, R. Bucala, E. Lolis, *Proceedings of the National Academy of Sciences of the United States of America* **1996**, *93*, 5191-5196.

[84]   R. Mischke, A. Gessner, A. Kapurniotu, S. Jüttner, R. Kleemann, H. Brunner, J. Bernhagen, *FEBS Lett* **1997**, *414*, 226-232.

[85]   H. Sugimoto, M. Suzuki, A. Nakagawa, I. Tanaka, J. Nishihira, *FEBS Lett* **1996**, *389*, 145-148.

[86]   G. Pantouris, L. Khurana, A. Ma, E. Skeens, K. Reiss, V. S. Batista, G. P. Lisi, E. J. Lolis, *Cell Chemical Biology* **2020**, *27*, 740-750.e745.

[87]   S. Tillmann, J. Bernhagen, H. Noels, *Frontiers in Immunology* **2013**, *4*.

[88]   R. Kleemann, H. Rorsman, E. Rosengren, R. Mischke, N. T. Mai, J. Bernhagen, *European Journal of Biochemistry* **2000**, *267*, 7183-7193.

[89]   Y. Wang, R. An, G. K. Umanah, H. Park, K. Nambiar, S. M. Eacker, B. Kim, L. Bao, M. M. Harraz, C. Chang, R. Chen, J. E. Wang, T.-I. Kam, J. S. Jeong, Z. Xie, S. Neifert, J. Qian, S. A. Andrabi, S. Blackshaw, H. Zhu, H. Song, G.-l. Ming, V. L. Dawson, T. M. Dawson, *Science* **2016**, *354*, aad6872.

[90]   O. A. Cherepkova, E. M. Lyutova, T. B. Eronina, B. Y. Gurvits, *The International Journal of Biochemistry & Cell Biology* **2006**, *38*, 43-55.

[91]   B. Schröder, *Biochimica et Biophysica Acta (BBA) - Molecular Cell Research* **2016**, *1863*, 1269-1281.

[92]   L. Leng, C. N. Metz, Y. Fang, J. Xu, S. Donnelly, J. Baugh, T. Delohery, Y. Chen, R. A. Mitchell, R. Bucala, *Journal of Experimental Medicine* **2003**, *197*, 1467-1476.

[93]   G. Pantouris, Mansoor A. Syed, C. Fan, D. Rajasekaran, Thomas Y. Cho, Eric M. Rosenberg, R. Bucala, V. Bhandari, Elias J. Lolis, *Chemistry & Biology* **2015**, *22*, 1197-1205.

[94]   D. N. Assis, L. Leng, X. Du, C. K. Zhang, G. Grieb, M. Merk, A. B. Garcia, C. McCrann, J. Chapiro, A. Meinhardt, Y. Mizue, D. J. Nikolic-Paterson, J. Bernhagen, M. M. Kaplan, H. Zhao, J. L. Boyer, R. Bucala, *Hepatology* **2014**, *59*, 580-591.

[95]   C. Weber, S. Kraemer, M. Drechsler, H. Lue, R. R. Koenen, A. Kapurniotu, A. Zernecke, J. Bernhagen, *Proceedings of the National Academy of Sciences* **2008**, *105*, 16278-16283.

[96]   L. Xu, Y. Li, D. Li, P. Xu, S. Tian, H. Sun, H. Liu, T. Hou, *Physical chemistry chemical physics : PCCP* **2015**, *17*, 3370-3382.

[97]   S. Kraemer, H. Lue, A. Zernecke, A. Kapurniotu, E. Andreetto, R. Frank, B. Lennartz, C. Weber, J. Bernhagen, *FASEB journal : official publication of the Federation of American Societies for Experimental Biology,* **2011**, *25*, 894-906.

[98]   D. Rajasekaran, S. Gröning, C. Schmitz, S. Zierow, N. Drucker, M. Bakou, K. Kohl, A. Mertens, H. Lue, C. Weber, A. Xiao, G. Luker, A. Kapurniotu, E. Lolis, J. Bernhagen, *The Journal of biological chemistry* **2016**, *291*, 15881-15895.

[99]   S. Alampour-Rajabi, O. El Bounkari, A. Rot, G. Müller-Newen, F. Bachelerie, M. Gawaz, C. Weber, A. Schober, J. Bernhagen, *FASEB journal : official publication of the Federation of American Societies for Experimental Biology* **2015**, *29*, 4497-4511.

[100]   S. S. Jankauskas, D. W. L. Wong, R. Bucala, S. Djudjaj, P. Boor, *Cellular Signalling* **2019**, *57*, 76-88.

[101]   J. W. Murphy, H. Yuan, Y. Kong, Y. Xiong, E. J. Lolis, *Proteins* **2010**, *78*, 1331-1337.

[102]   A. Jasanoff, G. Wagner, D. C. Wiley, *The EMBO journal* **1998**, *17*, 6812-6818.

[103]   P. Teriete, S. Banerji, M. Noble, C. D. Blundell, A. J. Wright, A. R. Pickford, E. Lowe, D. J. Mahoney, M. I. Tammi, J. D. Kahmann, I. D. Campbell, A. J. Day, D. G. Jackson, *Molecular cell* **2004**, *13*, 483-496.

[104]   D. Aeberli, M. Leech, E. F. Morand, *Rheumatology* **2006**, *45*, 937-943.

[105]   C. Klasen, K. Ohl, M. Sternkopf, I. Shachar, C. Schmitz, N. Heussen, E. Hobeika, E. Levit-Zerdoun, K. Tenbrock, M. Reth, J. Bernhagen, O. El Bounkari, *The Journal of Immunology* **2014**, *192*, 5273-5284.

[106]   Q. Cheng, S. J. McKeown, L. Santos, F. S. Santiago, L. M. Khachigian, E. F. Morand, M. J. Hickey, *The Journal of Immunology* **2010**, *185*, 1238-1247.

[107]   J. H. Pan, G. K. Sukhova, J. T. Yang, B. Wang, T. Xie, H. Fu, Y. Zhang, A. R. Satoskar, J. R. David, C. N. Metz, R. Bucala, K. Fang, D. I. Simon, H. A. Chapman, P. Libby, G. P. Shi, *Circulation* **2004**, *109*, 3149-3153.

[108]   H. Noels, J. Bernhagen, C. Weber, *Trends in Cardiovascular Medicine* **2009**, *19*, 76-86.

[109]   M. R. Guda, M. A. Rashid, S. Asuthkar, A. Jalasutram, J. L. Caniglia, A. J. Tsung, K. K. Velpula, *American Journal of Cancer Research* **2019**, *9*, 2760-2773.

[110]   C. O'Reilly, M. Doroudian, L. Mawhinney, S. C. Donnelly, *Medicinal Research Reviews* **2016**, *36*, 440-460.

[111]   P. Boor, *Der Pathologe* **2019**, *40*, 25-30.

[112]   M. F. Leyton-Jaimes, J. Kahn, A. Israelson, *Proceedings of the National Academy of Sciences of the United States of America* **2019**, *116*, 14755-14760.

[113]   L. C. D. Gibson, S. F. Hastings, I. McPhee, R. A. Clayton, C. E. Darroch, A. Mackenzie, F. L. MacKenzie, M. Nagasawa, P. A. Stevens, S. J. MacKenzie, *European Journal of Pharmacology* **2006**, *538*, 39-42.

[114]   Y. Cho, G. V. Crichlow, J. J. Vermeire, L. Leng, X. Du, M. E. Hodsdon, R. Bucala, M. Cappello, M. Gross, F. Gaeta, K. Johnson, E. J. Lolis, *Proceedings of the National Academy of Sciences of the United States of America* **2010**, *107*, 11313-11318.

[115]   D. Yang, Y. Yang, Y. Zhao, *Medical Science Monitor* **2020**, *26*, e922281-e922281.

[116]   W. Ha, H. Sevim-Nalkiran, A. M. Zaman, K. Matsuda, M. Khasraw, A. K. Nowak, L. Chung, R. C. Baxter, K. L. McDonald, *Scientific Reports* **2019**, *9*, 2905.

[117]   R. J. Fox, C. S. Coffey, R. Conwit, M. E. Cudkowicz, T. Gleason, A. Goodman, E. C. Klawiter, K. Matsuda, M. McGovern, R. T. Naismith, A. Ashokkumar, J. Barnes, D. Ecklund, E. Klingner, M. Koepp, J. D. Long, S. Natarajan, B. Thornell, J. Yankey, R. A. Bermel, J. P. Debbins, X. Huang, P. Jagodnik, M. J. Lowe, K. Nakamura, S. Narayanan, K. E. Sakaie, B. Thoomukuntla, X. Zhou, S. Krieger, E. Alvarez, M. Apperson, K. Bashir, B. A. Cohen, P. K. Coyle, S. Delgado, L. D. Dewitt, A. Flores, B. S. Giesser, M. D. Goldman, B. Jubelt, N. Lava, S. G. Lynch, H. Moses, D. Ontaneda, J. S. Perumal, M. Racke, P. Repovic, C. S. Riley, C. Severson, S. Shinnar, V. Suski, B. Weinstock-Guttman, V. Yadav, A. Zabeti, N. S.-M. T. Investigators, *The New England journal of medicine* **2018**, *379*, 846-855.

[118]   J. B. Lubetsky, A. Dios, J. Han, B. Aljabari, B. Ruzsicska, R. Mitchell, E. Lolis, Y. Al-Abed, *The Journal of biological chemistry* **2002**, *277*, 24976-24982.

[119]   Y. Al-Abed, S. VanPatten, *Future medicinal chemistry* **2011**, *3*, 45-63.

[120]   K. Ioannou, K. F. Cheng, G. V. Crichlow, A. I. Birmpilis, E. J. Lolis, O. E. Tsitsilonis, Y. Al-Abed, *International Journal of Oncology* **2014**, *45*, 1457-1468.

[121]   P. Nagarajan, K. L. Tober, J. A. Riggenbach, D. F. Kusewitt, A. M. Lehman, T. Sielecki, J. Pruitt, A. R. Satoskar, T. M. Oberyszyn, *Molecular Cancer Research* **2014**, *12*, 1292-1302.

[122]   J. Bloom, C. Metz, S. Nalawade, J. Casabar, K. F. Cheng, M. He, B. Sherry, T. Coleman, T. Forsthuber, Y. Al-Abed, *The Journal of biological chemistry* **2016**, *291*, 26502-26514.

[123]   H. Huang, D. Chen, J. Pu, A. Yuan, Q. Fu, J. Li, L. Leng, R. Bucala, S. Ye, L. Lu, *International Immunopharmacology* **2019**, *76*, 105874.

[124]   M. Vujicic, I. Nikolic, T. Krajnovic, K.-F. Cheng, S. VanPatten, M. He, S. Stosic-Grujicic, I. Stojanovic, Y. Al-Abed, T. Saksida, *European Journal of Pharmacology* **2014**, *740*, 683-689.

[125]   L. Mawhinney, M. E. Armstrong, C. O' Reilly, R. Bucala, L. Leng, G. Fingerle-Rowson, D. Fayne, M. P. Keane, A. Tynan, L. Maher, G. Cooke, D. Lloyd, H. Conroy, S. C. Donnelly, *Molecular Medicine* **2015**, *20*, 729-735.

[126]   R. J. Kerschbaumer, M. Rieger, D. Völkel, D. Le Roy, T. Roger, J. Garbaraviciene, W.-H. Boehncke, J. Müllberg, R. M. Hoet, C. R. Wood, G. Antoine, M. Thiele, H. Savidis-Dacho, M.

Dockal, H. Ehrlich, T. Calandra, F. Scheiflinger, *The Journal of biological chemistry* **2012**, *287*, 7446-7455.

[127]   D. Mahalingam, M. R. Patel, J. C. Sachdev, L. L. Hart, N. Halama, R. K. Ramanathan, J. Sarantopoulos, D. Völkel, A. Youssef, F. A. de Jong, A. M. Tsimberidou, *British Journal of Clinical Pharmacology* **2020**, *86*, 1836-1848.

[128]   M. Thiele, R. J. Kerschbaumer, F. W. K. Tam, D. Völkel, P. Douillard, A. Schinagl, H. Kühnel, J. Smith, J. P. McDaid, G. Bhangal, M.-C. Yu, C. D. Pusey, H. T. Cook, J. Kovarik, E. Magelky, A. Bhan, M. Rieger, G. C. Mudde, H. Ehrlich, B. Jilma, H. Tilg, A. Moschen, C. Terhorst, F. Scheiflinger, *The Journal of Immunology* **2015**, *195*, 2343-2352.

[129]   A. Sparkes, P. De Baetselier, L. Brys, I. Cabrito, Y. G. Sterckx, S. Schoonooghe, S. Muyldermans, G. Raes, R. Bucala, P. Vanlandschoot, J. A. Van Ginderachter, B. Stijlemans, *FASEB journal : official publication of the Federation of American Societies for Experimental Biology* **2018**, *32*, 3411-3422.

[130]   M. Haran, V. Mirkin, A. Braester, N. Harpaz, O. Shevetz, M. Shtreiter, S. Greenberg, O. Mordich, O. Amram, I. Binsky-Ehrenreich, A. Marom, I. Shachar, Y. Herishanu, R. Ruchlemer, A. Berrebi, L. Valinsky, M. Shtalrid, L. Shvidel, *British Journal of Haematology* **2018**, *182*, 125-128.

[131]   B. A. Christian, M. Poi, J. A. Jones, P. Porcu, K. Maddocks, J. M. Flynn, D. M. Benson Jr, M. A. Phelps, L. Wei, J. C. Byrd, W. A. Wegener, D. M. Goldenberg, R. A. Baiocchi, K. A. Blum, *British Journal of Haematology* **2015**, *169*, 701-710.

[132]   R. Meza-Romero, G. Benedek, X. Yu, J. L. Mooney, R. Dahan, N. Duvshani, R. Bucala, H. Offner, Y. Reiter, G. G. Burrows, A. A. Vandenbark, *The Journal of Immunology* **2014**, *192*, 4164-4173.

[133]   G. Benedek, R. Meza-Romero, S. Andrew, L. Leng, G. G. Burrows, D. Bourdette, H. Offner, R. Bucala, A. A. Vandenbark, *European Journal of Immunology* **2013**, *43*, 1309-1321.

[134]   M. T. Nguyen, J. Beck, H. Lue, H. Fünfzig, R. Kleemann, P. Koolwijk, A. Kapurniotu, J. Bernhagen, *The Journal of biological chemistry* **2003**, *278*, 33654-33671.

[135]   G.-M. Hu, T.-L. Mai, C.-M. Chen, *Scientific Reports* **2017**, *7*, 15495.

[136]   W. I. Weis, B. K. Kobilka, *Annual Review of Biochemistry* **2018**, *87*, 897-919.

[137]   V. Katritch, V. Cherezov, R. C. Stevens, *Trends Pharmacol Sci* **2012**, *33*, 17-27.

[138]   B. Stephens, T. M. Handel, *Progress in Molecular Biology and Translational Science* **2013**, *115*, 375-420.

[139]   P. B. Wedegaertner, in *Pharmacology and Therapeutics* (Eds.: S. A. Waldman, A. Terzic, L. J. Egan, J.-L. Elghozi, A. Jahangir, G. C. Kane, W. K. Kraft, L. D. Lewis, J. D. Morrow, L. V. Zingman, D. R. Abernethy, A. J. Atkinson, N. L. Benowitz, D. C. Brater, J. Gray, P. K. Honig, G. L. Kearns, B. A. Levey, S. P. Spielberg, R. Weinshilboum, R. L. Woosley), W.B. Saunders, Philadelphia, **2009**, 67-81.

[140]   A. S. Hauser, M. M. Attwood, M. Rask-Andersen, H. B. Schiöth, D. E. Gloriam, *Nature Reviews Drug Discovery* **2017**, *16*, 829-842.

[141]   A. B. Kleist, A. E. Getschman, J. J. Ziarek, A. M. Nevins, P.-A. Gauthier, A. Chevigné, M. Szpakowska, B. F. Volkman, *Biochemical pharmacology* **2016**, *114*, 53-68.

[142]   D. J. Scholten, M. Canals, D. Maussang, L. Roumen, M. J. Smit, M. Wijtmans, C. de Graaf, H. F. Vischer, R. Leurs, *British Journal of Pharmacology* **2012**, *165*, 1617-1643.

[143]   S. Sayana, H. Khanlou, *Expert review of anti-infective therapy* **2009**, *7*, 9-19.

[144]   M. Brave, A. Farrell, S. Ching Lin, T. Ocheltree, S. Pope Miksinski, S. L. Lee, H. Saber, J. Fourie, C. Tornoe, B. Booth, W. Yuan, K. He, R. Justice, R. Pazdur, *Oncology* **2010**, *78*, 282-288.

[145]   Y. L. Kasamon, H. Chen, R. A. de Claro, L. Nie, J. Ye, G. M. Blumenthal, A. T. Farrell, R. Pazdur, *Clinical Cancer Research* **2019**, *25*, 7275-7280.

[146]   M. J. Stone, J. A. Hayward, C. Huang, Z. E. Huma, J. Sanchez, *International journal of molecular sciences* **2017**, *18*, 342.

[147]   R. P. Bhusal, S. R. Foster, M. J. Stone, *Protein Science* **2020**, *29*, 420-432.

[148]   L. Qin, I. Kufareva, L. G. Holden, C. Wang, Y. Zheng, C. Zhao, G. Fenalti, H. Wu, G. W. Han, V. Cherezov, R. Abagyan, R. C. Stevens, T. M. Handel, *Science* **2015**, *347*, 1117-1122.

[149]   P. M. Murphy, H. L. Tiffany, *Science* **1991**, *253*, 1280-1283.

[150]   M. Arimont, S.-L. Sun, R. Leurs, M. Smit, I. J. P. de Esch, C. de Graaf, *Journal of Medicinal Chemistry* **2017**, *60*, 4735-4779.

[151]   M. Veenstra, R. M. Ransohoff, *Journal of Neuroimmunology* **2012**, *246*, 1-9.

[152]   K. Liu, L. Wu, S. Yuan, M. Wu, Y. Xu, Q. Sun, S. Li, S. Zhao, T. Hua, Z.-J. Liu, *Nature* **2020**, *585*, 135-140.

[153]   A. Zarbock, A. Stadtmann, *Frontiers in Immunology* **2012**, *3*.

[154]   C. E. Hughes, R. J. B. Nibbs, *FEBS J* **2018**, *285*, 2944-2971.

[155]   K. J. Eash, A. M. Greenbaum, P. K. Gopalan, D. C. Link, *The Journal of clinical investigation* **2010**, *120*, 2423-2431.

[156]   M. E. Bradley, B. Dombrecht, J. Manini, J. Willis, D. Vlerick, S. De Taeye, K. Van den Heede, A. Roobrouck, E. Grot, T. C. Kent, T. Laeremans, S. Steffensen, G. Van Heeke, Z. Brown, S. J. Charlton, K. D. Cromie, *Molecular pharmacology* **2015**, *87*, 251-262.

[157]   R. Mischke, R. Kleemann, H. Brunner, J. Bernhagen, *FEBS Lett* **1998**, *427*, 85-90.
[158]   G. M. Clore, E. Appella, M. Yamada, K. Matsushima, A. M. Gronenborn, *Biochemistry* **1990**, *29*, 1689-1696.
[159]   H. Ha, B. Debnath, N. Neamati, *Theranostics* **2017**, *7*, 1543-1588.
[160]   Y. Saiman, S. Friedman, *Frontiers in Physiology* **2012**, *3*.
[161]   T. H. Thatcher, N. A. McHugh, R. W. Egan, R. W. Chapman, J. A. Hey, C. K. Turner, M. R. Redonnet, K. E. Seweryniak, P. J. Sime, R. P. Phipps, *American journal of physiology. Lung cellular and molecular physiology* **2005**, *289*, L322-328.
[162]   J. M. Schuh, K. Blease, C. M. Hogaboam, *The Journal of Immunology* **2002**, *168*, 1447-1456.
[163]   Y. Liu, A. T. Holdbrooks, G. P. Meares, J. A. Buckley, E. N. Benveniste, H. Qin, *The Journal of Immunology,* **2015**, *195*, 841-852.
[164]   K. Kishida, M. Kohyama, Y. Kurashima, Y. Kogure, J. Wang, K. Hirayasu, T. Suenaga, H. Kiyono, J. Kunisawa, H. Arase, *International immunology* **2015**, *27*, 307-314.
[165]   J. K. Ryu, T. Cho, H. B. Choi, N. Jantaratnotai, J. G. McLarnon, *Journal of Neuroinflammation* **2015**, *12*, 144.
[166]   Q. Liu, A. Li, Y. Tian, J. D. Wu, Y. Liu, T. Li, Y. Chen, X. Han, K. Wu, *Cytokine & Growth Factor Reviews* **2016**, *31*, 61-71.
[167]   H. Oral, I. Kanzler, N. Tuchscheerer, A. Curaj, S. Simsekyilmaz, T. T. Sönmez, E. Radu, O. Postea, C. Weber, A. Schuh, E. A. Liehn, *Journal of molecular and cellular cardiology* **2013**, *60*, 1-7.
[168]   L. Wang, X.-C. Zhao, W. Cui, Y.-Q. Ma, H.-L. Ren, X. Zhou, J. Fassett, Y.-Z. Yang, Y. Chen, Y.-L. Xia, J. Du, H.-H. Li, *Circulation* **2016**, *134*, 1353-1368.
[169]   B. J. Connell, J. R. Gordon, T. M. Saleh, *Neuroscience letters* **2015**, *606*, 117-122.
[170]   X. Zhao, J. R. Town, A. Yang, X. Zhang, N. Paur, G. Sawicki, J. R. Gordon, *The Journal of surgical research* **2010**, *162*, 264-273.
[171]   X. Z. Wang, L. W. Liu, X. M. Du, R. X. Gu, Z. J. Sun, *Coronary artery disease* **2015**, *26*, 612-619.
[172]   O. Herlea-Pana, L. Yao, J. Heuser-Baker, Q. Wang, Q. Wang, C. Georgescu, M.-H. Zou, J. Barlic-Dicen, *Cardiovascular research* **2015**, *106*, 324-337.
[173]   A. Rousselle, F. Qadri, L. Leukel, R. Yilmaz, J.-F. Fontaine, G. Sihn, M. Bader, A. Ahluwalia, J. Duchene, *The Journal of clinical investigation* **2013**, *123*, 1343-1347.
[174]   E. A. Liehn, I. Kanzler, S. Konschalla, A. Kroh, S. Simsekyilmaz, T. T. Sönmez, R. Bucala, J. Bernhagen, C. Weber, *Arteriosclerosis, Thrombosis, and Vascular Biology* **2013**, *33*, 2180-2186.
[175]   A. F. Schott, L. J. Goldstein, M. Cristofanilli, P. A. Ruffini, S. McCanna, J. M. Reuben, R. P. Perez, G. Kato, M. Wicha, *Clinical cancer research : an official journal of the American Association for Cancer Research* **2017**, *23*, 5358-5365.
[176]   L. J. Goldstein, R. P. Perez, D. Yardley, L. K. Han, J. M. Reuben, H. Gao, S. McCanna, B. Butler, P. A. Ruffini, Y. Liu, R. R. Rosato, J. C. Chang, *Breast cancer research : BCR* **2020**, *22*, 4.
[177]   R. Bertini, M. Allegretti, C. Bizzarri, A. Moriconi, M. Locati, G. Zampella, M. N. Cervellera, V. Di Cioccio, M. C. Cesta, E. Galliera, F. O. Martinez, R. Di Bitondo, G. Troiani, V. Sabbatini, G. D'Anniballe, R. Anacardio, J. C. Cutrin, B. Cavalieri, F. Mainiero, R. Strippoli, P. Villa, M. Di Girolamo, F. Martin, M. Gentile, A. Santoni, D. Corda, G. Poli, A. Mantovani, P. Ghezzi, F. Colotta, *Proceedings of the National Academy of Sciences of the United States of America* **2004**, *101*, 11791-11796.
[178]   P. Nair, M. Gaga, E. Zervas, K. Alagha, F. E. Hargreave, P. M. O'Byrne, P. Stryszak, L. Gann, J. Sadeh, P. Chanez, *Clinical and experimental allergy : journal of the British Society for Allergy and Clinical Immunology* **2012**, *42*, 1097-1103.
[179]   S. I. Rennard, D. C. Dale, J. F. Donohue, F. Kanniess, H. Magnussen, E. R. Sutherland, H. Watz, S. Lu, P. Stryszak, E. Rosenberg, H. Staudinger, *American journal of respiratory and critical care medicine* **2015**, *191*, 1001-1011.
[180]   M. Bilusic, C. R. Heery, J. M. Collins, R. N. Donahue, C. Palena, R. A. Madan, F. Karzai, J. L. Marté, J. Strauss, M. E. Gatti-Mays, J. Schlom, J. L. Gulley, *Journal for ImmunoTherapy of Cancer* **2019**, *7*, 240.
[181]   Y.-C. Tsai, T.-F. Tsai, *Therapeutic Advances in Musculoskeletal Disease* **2017**, *9*, 277-294.
[182]   Y. Feng, C. C. Broder, P. E. Kennedy, E. A. Berger, *Science* **1996**, *272*, 872-877.
[183]   F. Bachelerie, A. Ben-Baruch, A. M. Burkhardt, C. Combadiere, J. M. Farber, G. J. Graham, R. Horuk, A. H. Sparre-Ulrich, M. Locati, A. D. Luster, A. Mantovani, K. Matsushima, P. M. Murphy, R. Nibbs, H. Nomiyama, C. A. Power, A. E. I. Proudfoot, M. M. Rosenkilde, A. Rot, S. Sozzani, M. Thelen, O. Yoshie, A. Zlotnik, *Pharmacological Reviews* **2013**, *66*, 1-79.
[184]   Y.-R. Zou, A. H. Kottmann, M. Kuroda, I. Taniuchi, D. R. Littman, *Nature* **1998**, *393*, 595-599.
[185]   B. Wu, E. Y. Chien, C. D. Mol, G. Fenalti, W. Liu, V. Katritch, R. Abagyan, A. Brooun, P. Wells, F. C. Bi, D. J. Hamel, P. Kuhn, T. M. Handel, V. Cherezov, R. C. Stevens, *Science* **2010**, *330*, 1066-1071.
[186]   M. M. Rosenkilde, L.-O. Gerlach, S. Hatse, R. T. Skerlj, D. Schols, G. J. Bridger, T. W. Schwartz, *Journal of Biological Chemistry* **2007**, *282*, 27354-27365.

[187]   B. S. Stephens, T. Ngo, I. Kufareva, T. M. Handel, *Science signaling* **2020**, *13*, eaay5024.

[188]   M. P. Wescott, I. Kufareva, C. Paes, J. R. Goodman, Y. Thaker, B. A. Puffer, E. Berdougo, J. B. Rucker, T. M. Handel, B. J. Doranz, *Proceedings of the National Academy of Sciences* **2016**, *113*, 9928-9933.

[189]   M. Schiraldi, A. Raucci, L. M. Muñoz, E. Livoti, B. Celona, E. Venereau, T. Apuzzo, F. De Marchis, M. Pedotti, A. Bachi, M. Thelen, L. Varani, M. Mellado, A. Proudfoot, M. E. Bianchi, M. Uguccioni, *Journal of Experimental Medicine* **2012**, *209*, 551-563.

[190]   V. Saini, D. M. Staren, J. J. Ziarek, Z. N. Nashaat, E. M. Campbell, B. F. Volkman, A. Marchese, M. Majetschak, *The Journal of biological chemistry* **2011**, *286*, 33466-33477.

[191]   V. Saini, A. Marchese, W.-J. Tang, M. Majetschak, *The Journal of biological chemistry* **2011**, *286*, 44145-44152.

[192]   M. E. Quiñones-Mateu, M. M. Lederman, Z. Feng, B. Chakraborty, J. Weber, H. R. Rangel, M. L. Marotta, M. Mirza, B. Jiang, P. Kiser, K. Medvik, S. F. Sieg, A. Weinberg, *AIDS* **2003**, *17*, F39-F48.

[193]   A. Brelot, N. Heveker, M. Montes, M. Alizon, *The Journal of biological chemistry* **2000**, *275*, 23736-23744.

[194]   G. Lin, F. Baribaud, J. Romano, R. W. Doms, J. A. Hoxie, *Journal of virology* **2003**, *77*, 931-942.

[195]   Y. Döring, Y. Jansen, I. Cimen, M. Aslani, S. Gencer, L. J. F. Peters, J. Duchene, C. Weber, E. P. C. v. d. Vorst, *Circulation Research* **2020**, *126*, 787-788.

[196]   A. Zernecke, I. Bot, Y. Djalali-Talab, E. Shagdarsuren, K. Bidzhekov, S. Meiler, R. Krohn, A. Schober, M. Sperandio, O. Soehnlein, J. Bornemann, F. Tacke, E. A. Biessen, C. Weber, *Circulation Research* **2008**, *102*, 209-217.

[197]   Y. Döring, H. Noels, E. P. C. van der Vorst, C. Neideck, V. Egea, M. Drechsler, M. Mandl, L. Pawig, Y. Jansen, K. Schröder, K. Bidzhekov, R. T. A. Megens, W. Theelen, B. M. Klinkhammer, P. Boor, L. Schurgers, R. van Gorp, C. Ries, P. J. H. Kusters, A. van der Wal, T. M. Hackeng, G. Gäbel, R. P. Brandes, O. Soehnlein, E. Lutgens, D. Vestweber, D. Teupser, L. M. Holdt, D. J. Rader, D. Saleheen, C. Weber, *Circulation* **2017**, *136*, 388-403.

[198]   H. Noels, C. Weber, R. R. Koenen, *Arteriosclerosis, Thrombosis, and Vascular Biology* **2019**, *39*, 583-592.

[199]   S. M. Davidson, P. Selvaraj, D. He, C. Boi-Doku, R. L. Yellon, J. M. Vicencio, D. M. Yellon, *Basic Research in Cardiology* **2013**, *108*, 377.

[200]   A. Saxena, J. E. Fish, M. D. White, S. Yu, J. W. Smyth, R. M. Shaw, J. M. DiMaio, D. Srivastava, *Circulation* **2008**, *117*, 2224-2231.

[201]   J. Chen, E. Chemaly, L. Liang, C. Kho, A. Lee, J. Park, P. Altman, A. D. Schecter, R. J. Hajjar, S. T. Tarzami, *The American Journal of Pathology* **2010**, *176*, 1705-1715.

[202]   A. Schober, S. Knarren, M. Lietz, E. A. Lin, C. Weber, *Circulation* **2003**, *108*, 2491-2497.

[203]   F. Guo, Y. Wang, J. Liu, S. C. Mok, F. Xue, W. Zhang, *Oncogene* **2016**, *35*, 816-826.

[204]   E. M. García-Cuesta, C. A. Santiago, J. Vallejo-Díaz, Y. Juarranz, J. M. Rodríguez-Frade, M. Mellado, *Frontiers in Endocrinology* **2019**, *10*.

[205]   A. Song, A. Jiang, W. Xiong, C. Zhang, *Kidney Diseases* **2021**, *7*, 176-185.

[206]   E. De Clercq, *Antiviral Chemistry and Chemotherapy* **2019**, *27*, 2040206619829382-2040206619829382.

[207]   S. Hatse, K. Princen, E. De Clercq, M. M. Rosenkilde, T. W. Schwartz, P. E. Hernandez-Abad, R. T. Skerlj, G. J. Bridger, D. Schols, *Biochemical pharmacology* **2005**, *70*, 752-761.

[208]   D. Peng, B. Cao, Y. J. Zhou, Y. Q. Long, *European journal of medicinal chemistry* **2018**, *149*, 148-169.

[209]   D. C. Dale, F. Firkin, A. A. Bolyard, M. Kelley, V. Makaryan, K. J. Gorelick, T. Ebrahim, V. Garg, W. Tang, H. Jiang, R. Skerlj, S. Beaussant Cohen, *Blood* **2020**, *136*, 2994-3003.

[210]   U. N. Vaishampayan, D. F. McDermott, M. R. Matrana, S. Y. Rha, A. J. Zurita, T. H. Ho, B. Keam, J.-L. Lee, R. W. Joseph, S. Ali, W. M. Stadler, N. B. Haas, S. Sundararajan, S. H. Park, R. B. Mowat, J. Picus, A. Z. Dudek, Y. Zakharia, L. Gan, M. B. Atkins, *Journal of Clinical Oncology* **2018**, *36*, 4510-4510.

[211]   G. Thoma, M. B. Streiff, J. Kovarik, F. Glickman, T. Wagner, C. Beerli, H.-G. Zerwes, *Journal of Medicinal Chemistry* **2008**, *51*, 7915-7920.

[212]   J.-S. Song, C.-C. Chang, C.-H. Wu, T. K. Dinh, J.-J. Jan, K.-W. Huang, M.-C. Chou, T.-Y. Shiue, K.-C. Yeh, Y.-Y. Ke, T.-K. Yeh, Y.-N. N. Ta, C.-J. Lee, J.-K. Huang, Y.-C. Sung, K.-S. Shia, Y. Chen, *Proceedings of the National Academy of Sciences* **2021**, *118*, e2015433118.

[213]   H. Tamamura, A. Ojida, T. Ogawa, H. Tsutsumi, H. Masuno, H. Nakashima, N. Yamamoto, I. Hamachi, N. Fujii, *Journal of Medicinal Chemistry* **2006**, *49*, 3412-3415.

[214]   R. A. Wilkinson, S. H. Pincus, J. B. Shepard, S. K. Walton, E. P. Bergin, M. Labib, M. Teintze, *Antimicrobial agents and chemotherapy* **2011**, *55*, 255-263.

[215]   T. Miyata, F. Tokunaga, T. Yoneya, K. Yoshikawa, S. Iwanaga, M. Niwa, T. Takao, Y. Shimonishi, *Journal of biochemistry* **1989**, *106*, 663-668.

[216]   M. Masuda, H. Nakashima, T. Ueda, H. Naba, R. Ikoma, A. Otaka, Y. Terakawa, H. Tamamura, T. Ibuka, T. Murakami, et al., *Biochemical and biophysical research communications* **1992**, *189*, 845-850.

[217] T. Murakami, T. Nakajima, Y. Koyanagi, K. Tachibana, N. Fujii, H. Tamamura, N. Yoshida, M. Waki, A. Matsumoto, O. Yoshie, T. Kishimoto, N. Yamamoto, T. Nagasawa, *Journal of Experimental Medicine* **1997**, *186*, 1389-1393.

[218] H. Tamamura, Y. Xu, T. Hattori, X. Zhang, R. Arakaki, K. Kanbara, A. Omagari, A. Otaka, T. Ibuka, N. Yamamoto, H. Nakashima, N. Fujii, *Biochemical and biophysical research communications* **1998**, *253*, 877-882.

[219] G. Borthakur, Y. Ofran, M. S. Tallman, J. Foran, G. L. Uy, J. F. DiPersio, M. M. Showel, A. Shimoni, A. Nagler, J. M. Rowe, J. K. Altman, M. Abraham, A. Peled, S. Shaw, O. Bohana-Kashtan, E. Sorani, Y. Pereg, A. Foley-Comer, G. Oberkovitz, T. M. Lustig, I. Glicko-Kabir, A. Aharon, A. Vainstein-Haras, S. E. Kadosh, E. Samara, A. N. Al-Rawi, N. Pemmaraju, C. Bueso-Ramos, J. E. Cortes, M. Andreeff, *Cancer* **2021**, *127*, 1246-1259.

[220] B. Bockorny, V. Semenisty, T. Macarulla, E. Borazanci, B. M. Wolpin, S. M. Stemmer, T. Golan, R. Geva, M. J. Borad, K. S. Pedersen, J. O. Park, R. A. Ramirez, D. G. Abad, J. Feliu, A. Muñoz, M. Ponz-Sarvise, A. Peled, T. M. Lustig, O. Bohana-Kashtan, S. M. Shaw, E. Sorani, M. Chaney, S. Kadosh, A. Vainstein Haras, D. D. Von Hoff, M. Hidalgo, *Nature Medicine* **2020**, *26*, 878-885.

[221] S. J. DeMarco, H. Henze, A. Lederer, K. Moehle, R. Mukherjee, B. Romagnoli, J. A. Robinson, F. Brianza, F. O. Gombert, S. Lociuro, C. Ludin, J. W. Vrijbloed, J. Zumbrunn, J.-P. Obrecht, D. Obrecht, V. Brondani, F. Hamy, T. Klimkait, *Bioorganic & medicinal chemistry* **2006**, *14*, 8396-8404.

[222] S. Pernas, M. Martin, P. A. Kaufman, M. Gil-Martin, P. Gomez Pardo, S. Lopez-Tarruella, L. Manso, E. Ciruelos, J. A. Perez-Fidalgo, C. Hernando, F. O. Ademuyiwa, K. Weilbaecher, I. Mayer, T. J. Pluard, M. Martinez Garcia, L. Vahdat, J. Perez-Garcia, A. Wach, D. Barker, S. Fung, B. Romagnoli, J. Cortes, *The Lancet. Oncology* **2018**, *19*, 812-824.

[223] P. Kaufmann, J. Cortes, M. Martin, I. Mayer, L. Vahdat, S. Pernas, P. Schmid, H. McArthur, R. Dent, H. Rugo, C. Barrios, D. Barker, B. Romagnoli, A. Bobirca, *Cancer Research* **2020**, *80*, OT1-08-06-OT01-08-06.

[224] M. H. O'Hara, W. Messersmith, H. Kindler, W. Zhang, C. Pitou, A. M. Szpurka, D. Wang, S.-B. Peng, B. Vangerow, A. A. Khan, M. Koneru, A. Wang-Gillam, *Journal of Pancreatic Cancer* **2020**, *6*, 21-31.

[225] S.-B. Peng, X. Zhang, D. Paul, L. M. Kays, W. Gough, J. Stewart, M. T. Uhlik, Q. Chen, Y.-H. Hui, M. J. Zamek-Gliszczynski, J. A. Wijsman, K. M. Credille, L. Z. Yan, *Molecular Cancer Therapeutics* **2015**, *14*, 480-490.

[226] I. M. Ghobrial, C.-J. Liu, R. A. Redd, R. P. Perez, R. Baz, O. Zavidij, R. Sklavenitis-Pistofidis, P. G. Richardson, K. C. Anderson, J. Laubach, P. Henrick, A. Savell, K. Reyes, K. Hornburg, S. Chuma, P. Sabbatini, M. D. Robbins, P. S. Becker, *Clinical Cancer Research* **2020**, *26*, 344-353.

[227] Y. Zhang, E. Saavedra, R. Tang, Y. Gu, P. Lappin, D. Trajkovic, S.-H. Liu, T. Smeal, V. Fantin, S. De Botton, O. Legrand, F. Delhommeau, F. Pernasetti, F. Louache, *Scientific Reports* **2017**, *7*, 7305.

[228] M. K. Kashyap, C. I. Amaya-Chanaga, D. Kumar, B. Simmons, N. Huser, Y. Gu, M. Hallin, K. Lindquist, R. Yafawi, M. Y. Choi, A.-A. Amine, L. Z. Rassenti, C. Zhang, S.-H. Liu, T. Smeal, V. R. Fantin, T. J. Kipps, F. Pernasetti, J. E. Castro, *Journal of Hematology & Oncology* **2017**, *10*, 112.

[229] S. H. Liu, Y. Gu, B. Pascual, Z. Yan, M. Hallin, C. Zhang, C. Fan, W. Wang, J. Lam, M. E. Spilker, R. Yafawi, E. Blasi, B. Simmons, N. Huser, W. H. Ho, K. Lindquist, T. T. Tran, J. Kudaravalli, J. T. Ma, G. Jimenez, I. Barman, C. Brown, S. M. Chin, M. J. Costa, D. Shelton, T. Smeal, V. R. Fantin, F. Pernasetti, *Blood advances* **2017**, *1*, 1088-1100.

[230] S. B. Peng, X. Zhang, D. Paul, L. M. Kays, M. Ye, P. Vaillancourt, M. Dowless, L. F. Stancato, J. Stewart, M. T. Uhlik, H. Long, S. Chu, V. H. Obungu, *PLoS One* **2016**, *11*, e0150585.

[231] E. Fischer, E. Otto, *Berichte der deutschen chemischen Gesellschaft* **1903**, *36*, 2106-2116.

[232] R. B. Merrifield, *Journal of the American Chemical Society* **1963**, *85*, 2149-2154.

[233] M. Muttenthaler, G. F. King, D. J. Adams, P. F. Alewood, *Nature Reviews Drug Discovery* **2021**, *20*, 309-325.

[234] K. Fosgerau, T. Hoffmann, *Drug discovery today* **2015**, *20*, 122-128.

[235] E. Lenci, A. Trabocchi, *Chemical Society Reviews* **2020**, *49*, 3262-3277.

[236] M. Pelay-Gimeno, A. Glas, O. Koch, T. N. Grossmann, *Angewandte Chemie (International ed. in English)* **2015**, *54*, 8896-8927.

[237] E. Andreetto, E. Malideli, L.-M. Yan, M. Kracklauer, K. Farbiarz, M. Tatarek-Nossol, G. Rammes, E. Prade, T. Neumüller, A. Caporale, A. Spanopoulou, M. Bakou, B. Reif, A. Kapurniotu, *Angewandte Chemie International Edition* **2015**, *54*, 13095-13100.

[238] A. Spanopoulou, L. Heidrich, H. R. Chen, C. Frost, D. Hrle, E. Malideli, K. Hille, A. Grammatikopoulos, J. Bernhagen, M. Zacharias, G. Rammes, A. Kapurniotu, *Angewandte Chemie (International ed. in English)* **2018**, *57*, 14503-14508.

[239] C. A. Rhodes, D. Pei, *Chemistry – A European Journal* **2017**, *23*, 12690-12703.

[240]   A. Groß, C. Hashimoto, H. Sticht, J. Eichler, *Frontiers in Bioengineering and Biotechnology* **2016**, *3*.

[241]   S. Pritz, O. Kraetke, A. Klose, J. Klose, S. Rothemund, K. Fechner, M. Bienert, M. Beyermann, *Angewandte Chemie International Edition* **2008**, *47*, 3642-3645.

[242]   A. C. Conibear, A. Bochen, K. J. Rosengren, P. Stupar, C. Wang, H. Kessler, D. J. Craik, *Chembiochem* **2014**, *15*, 451-459.

[243]   H. Joo, A. G. Chavan, J. Phan, R. Day, J. Tsai, *Journal of molecular biology* **2012**, *419*, 234-254.

[244]   S. Sachdeva, H. Joo, J. Tsai, B. Jasti, X. Li, *Scientific Reports* **2019**, *9*, 997.

[245]   O. Longin, M. Hezwani, H. van de Langemheen, R. M. J. Liskamp, *Organic & biomolecular chemistry* **2018**, *16*, 5254-5274.

[246]   R. Franke, C. Doll, V. Wray, J. Eichler, *Organic & biomolecular chemistry* **2004**, *2*, 2847-2851.

[247]   A. C. Koksal, M. E. Pennini, M. Marelli, X. Xiao, W. F. Dall'Acqua, *MAbs* **2019**, *11*, 725-734.

[248]   A. Datta, M. J. Stone, *Protein Science* **2003**, *12*, 2482-2491.

[249]   K. Möbius, R. Dürr, C. Haußner, U. Dietrich, J. Eichler, *Chemistry – A European Journal* **2012**, *18*, 8292-8295.

[250]   A. Groß, R. Brox, D. Damm, N. Tschammer, B. Schmidt, J. Eichler, *Bioorganic & medicinal chemistry* **2015**, *23*, 4050-4055.

[251]   A. Datta-Mannan, M. J. Stone, *Biochemistry* **2004**, *43*, 14602-14611.

[252]   E. F. Barter, M. J. Stone, *Biochemistry* **2012**, *51*, 1322-1331.

[253]   A. Kazantzis, M. Waldner, J. W. Taylor, A. Kapurniotu, *European Journal of Biochemistry* **2002**, *269*, 780-791.

[254]   Y. Han, F. Albericio, G. Barany, *The Journal of Organic Chemistry* **1997**, *62*, 4307-4312.

[255]   M. Bakou, K. Hille, M. Kracklauer, A. Spanopoulou, C. V. Frost, E. Malideli, L.-M. Yan, A. Caporale, M. Zacharias, A. Kapurniotu, *The Journal of biological chemistry* **2017**, *292*, 14587-14602.

[256]   L. Carpino, G. Han, *The Journal of Organic Chemistry* **1979**, *44*, 3739-3739.

[257]   E. Szczepańska, B. Grobelna, J. Ryl, A. Kulpa, T. Ossowski, P. Niedziałkowski, *Molecules (Basel, Switzerland)* **2020**, *25*.

[258]   K. Neumann, J. Farnung, S. Baldauf, J. W. Bode, *Nature Communications* **2020**, *11*, 982.

[259]   M. Mergler, F. Dick, B. Sax, C. Stähelin, T. Vorherr, *Journal of Peptide Science* **2003**, *9*, 518-526.

[260]   R. Behrendt, S. Huber, R. Martí, P. White, *Journal of Peptide Science* **2015**, *21*, 680-687.

[261]   J. L. Lauer, C. G. Fields, G. B. Fields, *Letters in Peptide Science* **1995**, *1*, 197-205.

[262]   T. Michels, R. Dölling, U. Haberkorn, W. Mier, *Organic letters* **2012**, *14*, 5218-5221.

[263]   J. Martinez, M. Bodanszky, *International journal of peptide and protein research* **1978**, *12*, 277-283.

[264]   E. Kaiser, R. L. Colescott, C. D. Bossinger, P. I. Cook, *Analytical Biochemistry* **1970**, *34*, 595-598.

[265]   V. K. Sarin, S. B. H. Kent, J. P. Tam, R. B. Merrifield, *Analytical Biochemistry* **1981**, *117*, 147-157.

[266]   F. Nissen, T. E. Kraft, T. Ruppert, M. Eisenhut, U. Haberkorn, W. Mier, *Tetrahedron Letters* **2010**, *51*, 6216-6219.

[267]   D. S. King, C. G. Fields, G. B. Fields, *International journal of peptide and protein research* **1990**, *36*, 255-266.

[268]   A. Zernecke, K. Bidzhekov, H. Noels, E. Shagdarsuren, L. Gan, B. Denecke, M. Hristov, T. Köppel, M. N. Jahantigh, E. Lutgens, S. Wang, E. N. Olson, A. Schober, C. Weber, *Science signaling* **2009**, *2*, ra81.

[269]   D. F. H. Winkler, K. Hilpert, O. Brandt, R. E. W. Hancock, in *Peptide Microarrays: Methods and Protocols* (Eds.: M. Cretich, M. Chiari), Humana Press, Totowa, NJ, **2009**, pp. 157-174.

[270]   A. Málnási-Csizmadia, G. Hegyi, F. Tölgyesi, A. G. Szent-Györgyi, L. Nyitray, *European Journal of Biochemistry* **1999**, *261*, 452-458.

[271]   E. Andreetto, L.-M. Yan, A. Caporale, A. Kapurniotu, *Chembiochem* **2011**, *12*, 1313-1322.

[272]   F. He, *Bio-protocol* **2011**, *1*, e44.

[273]   V. V. Andrushchenko, H. J. Vogel, E. J. Prenner, *Journal of peptide science : an official publication of the European Peptide Society* **2007**, *13*, 37-43.

[274]   B. Jirgensons, in *Optical Activity of Proteins and Other Macromolecules*, Springer Berlin Heidelberg, Berlin, Heidelberg, **1973**, 47-56.

[275]   N. J. Greenfield, *Nature Protocols* **2006**, *1*, 2876-2890.

[276]   Y. Wei, A. A. Thyparambil, R. A. Latour, *Biochimica et Biophysica Acta (BBA) - Proteins and Proteomics* **2014**, *1844*, 2331-2337.

[277]   A. Micsonai, F. Wien, L. Kernya, Y.-H. Lee, Y. Goto, M. Réfrégiers, J. Kardos, *Proceedings of the National Academy of Sciences* **2015**, *112*, E3095-E3103.

[278]   E. Andreetto, E. Malideli, L. M. Yan, M. Kracklauer, K. Farbiarz, M. Tatarek-Nossol, G. Rammes, E. Prade, T. Neumuller, A. Caporale, A. Spanopoulou, M. Bakou, B. Reif, A. Kapurniotu, *Angewandte Chemie (International ed. in English)* **2015**, *54*, 13095-13100.

[279]   L. Whitmore, B. A. Wallace, *Nucleic acids research* **2004**, *32*, W668-673.
[280]   N. Sreerama, R. W. Woody, *Analytical Biochemistry* **2000**, *287*, 252-260.
[281]   L. Whitmore, B. A. Wallace, *Biopolymers* **2008**, *89*, 392-400.
[282]   L.-M. Yan, M. Tatarek-Nossol, A. Velkova, A. Kazantzis, A. Kapurniotu, *Proceedings of the National Academy of Sciences* **2006**, *103*, 2046.
[283]   L. Stryer, *Journal of molecular biology* **1965**, *13*, 482-495.
[284]   N. J. Moerke, *Current Protocols in Chemical Biology* **2009**, *1*, 1-15.
[285]   S. A. I. Seidel, P. M. Dijkman, W. A. Lea, G. van den Bogaart, M. Jerabek-Willemsen, A. Lazic, J. S. Joseph, P. Srinivasan, P. Baaske, A. Simeonov, I. Katritch, F. A. Melo, J. E. Ladbury, G. Schreiber, A. Watts, D. Braun, S. Duhr, *Methods* **2013**, *59*, 301-315.
[286]   M. Jerabek-Willemsen, T. André, R. Wanner, H. M. Roth, S. Duhr, P. Baaske, D. Breitsprecher, *Journal of Molecular Structure* **2014**, *1077*, 101-113.
[287]   L. M. Yan, A. Velkova, M. Tatarek-Nossol, G. Rammes, A. Sibaev, E. Andreetto, M. Kracklauer, M. Bakou, E. Malideli, B. Göke, J. Schirra, M. Storr, A. Kapurniotu, *Angewandte Chemie (International ed. in English)* **2013**, *52*, 10378-10383.
[288]   X. M. Gao, Y. Liu, D. White, Y. Su, B. G. Drew, C. R. Bruce, H. Kiriazis, Q. Xu, N. Jennings, A. Bobik, M. A. Febbraio, B. A. Kingwell, R. Bucala, G. Fingerle-Rowson, A. M. Dart, E. F. Morand, X. J. Du, *Journal of molecular and cellular cardiology* **2011**, *50*, 991-999.
[289]   E. J. Miller, J. Li, L. Leng, C. McDonald, T. Atsumi, R. Bucala, L. H. Young, *Nature* **2008**, *451*, 578-582.
[290]   D. Sinitski, C. Kontos, C. Krammer, Y. Asare, A. Kapurniotu, J. Bernhagen, *Thrombosis and haemostasis* **2019**, *119*, 553-566.
[291]   C. Kontos, O. El Bounkari, C. Krammer, D. Sinitski, K. Hille, C. Zan, G. Yan, S. Wang, Y. Gao, M. Brandhofer, R. T. A. Megens, A. Hoffmann, J. Pauli, Y. Asare, S. Gerra, P. Bourilhon, L. Leng, H.-H. Eckstein, W. E. Kempf, J. Pelisek, O. Gokce, L. Maegdefessel, R. Bucala, M. Dichgans, C. Weber, A. Kapurniotu, J. Bernhagen, *Nature Communications* **2020**, *11*, 5981.
[292]   H. Sugimoto, M. Taniguchi, A. Nakagawa, I. Tanaka, M. Suzuki, J. Nishihira, *Biochemistry* **1999**, *38*, 3268-3279.
[293]   V. A. Simossis, J. Heringa, *Nucleic acids research* **2005**, *33*, W289-294.
[294]   S. H. Park, B. B. Das, F. Casagrande, Y. Tian, H. J. Nothnagel, M. Chu, H. Kiefer, K. Maier, A. A. De Angelis, F. M. Marassi, S. J. Opella, *Nature* **2012**, *491*, 779-783.
[295]   M. Lacy, C. Kontos, M. Brandhofer, K. Hille, S. Gröning, D. Sinitski, P. Bourilhon, E. Rosenberg, C. Krammer, T. Thavayogarajah, G. Pantouris, M. Bakou, C. Weber, E. Lolis, J. Bernhagen, A. Kapurniotu, *Scientific Reports* **2018**, *8*, 5171.
[296]   C. Krammer, C. Kontos, M. Dewor, K. Hille, B. Dalla Volta, O. El Bounkari, K. Taş, D. Sinitski, M. Brandhofer, R. T. A. Megens, C. Weber, J. R. Schultz, J. Bernhagen, A. Kapurniotu, *Chembiochem* **2021**, *22*, 1012-1019.
[297]   R. R. Koenen, C. Weber, *EMBO Molecular Medicine* **2011**, *3*, 713-725.
[298]   D. A. Quinteros, J. M. Bermúdez, S. Ravetti, A. Cid, D. A. Allemandi, S. D. Palma, *Nanostructures for Drug Delivery* **2017**, 807-833.
[299]   R. A. Beckman, L. M. Weiner, H. M. Davis, *Cancer* **2007**, *109*, 170-179.
[300]   P. Chames, M. Van Regenmortel, E. Weiss, D. Baty, *British Journal of Pharmacology* **2009**, *157*, 220-233.
[301]   V. Schwartz, H. Lue, S. Kraemer, J. Korbiel, R. Krohn, K. Ohl, R. Bucala, C. Weber, J. Bernhagen, *FEBS Lett* **2009**, *583*, 2749-2757.
[302]   E. K. Gozansky, J. M. Louis, M. Caffrey, G. Marius Clore, *Journal of molecular biology* **2005**, *345*, 651-658.
[303]   A. Jazayeri, J. M. Dias, F. H. Marshall, *The Journal of biological chemistry* **2015**, *290*, 19489-19495.
[304]   F. Albericio, N. Kneib-Cordonier, S. Biancalana, L. Gera, R. I. Masada, D. Hudson, G. Barany, *The Journal of Organic Chemistry* **1990**, *55*, 3730-3743.
[305]   M. T. Cicerone, M. J. Pikal, K. K. Qian, *Advanced drug delivery reviews* **2015**, *93*, 14-24.
[306]   N. V. Bhagavan, C.-E. Ha, in *Essentials of Medical Biochemistry (Second Edition)* (Eds.: N. V. Bhagavan, C.-E. Ha), Academic Press, San Diego, **2015**, 31-51.
[307]   A. Caporale, S. Adorinni, D. Lamba, M. Saviano, *Molecules (Basel, Switzerland)* **2021**, *26*.
[308]   A. Perczel, Z. Gáspári, I. G. Csizmadia, *Journal of Computational Chemistry* **2005**, *26*, 1155-1168.
[309]   N. R. Lee, C. J. Bowerman, B. L. Nilsson, *Biomacromolecules* **2013**, *14*, 3267-3277.
[310]   J. Banerjee, E. Radvar, H. S. Azevedo, in *Peptides and Proteins as Biomaterials for Tissue Regeneration and Repair* (Eds.: M. A. Barbosa, M. C. L. Martins), Woodhead Publishing, **2018**, 245-281.
[311]   L. Wu, D. McElheny, T. Takekiyo, T. A. Keiderling, *Biochemistry* **2010**, *49*, 4705-4714.
[312]   P. Y. Chou, G. D. Fasman, *Biochemistry* **1974**, *13*, 211-222.
[313]   Q. Hou, R. Bourgeas, F. Pucci, M. Rooman, *Scientific Reports* **2018**, *8*, 14661.

[314] B. R. Green, P. Catlin, M.-M. Zhang, B. Fiedler, W. Bayudan, A. Morrison, Raymond S. Norton, B. J. Smith, D. Yoshikami, B. M. Olivera, G. Bulaj, *Chemistry & Biology* **2007**, *14*, 399-407.

[315] G. J. Bartlett, A. Choudhary, R. T. Raines, D. N. Woolfson, *Nature Chemical Biology* **2010**, *6*, 615-620.

[316] R. Sarma, K.-Y. Wong, G. C. Lynch, B. M. Pettitt, *The Journal of Physical Chemistry B* **2018**, *122*, 3528-3539.

[317] A. Malina, Y. Shai, *Biochemical Journal* **2005**, *390*, 695-702.

[318] Q. Xu, J. Mi, C. Zhong, *The Journal of Chemical Physics* **2010**, *133*, 174104.

[319] K. N. Houk, A. G. Leach, S. P. Kim, X. Zhang, *Angewandte Chemie (International ed. in English)* **2003**, *42*, 4872-4897.

[320] A. J. Wilson, *Chemical Society Reviews* **2009**, *38*, 3289-3300.

[321] A. M. Rossi, C. W. Taylor, *Nature Protocols* **2011**, *6*, 365-387.

[322] J. A. Cisneros, M. J. Robertson, M. Valhondo, W. L. Jorgensen, *Journal of the American Chemical Society* **2016**, *138*, 8630-8638.

[323] G. Pantouris, J. Ho, D. Shah, M. A. Syed, L. Leng, V. Bhandari, R. Bucala, V. S. Batista, J. P. Loria, E. J. Lolis, *Angewandte Chemie (International ed. in English)* **2018**, *57*, 7116-7119.

[324] J. J. Ziarek, A. B. Kleist, N. London, B. Raveh, N. Montpas, J. Bonneterre, G. St-Onge, C. J. DiCosmo-Ponticello, C. A. Koplinski, I. Roy, B. Stephens, S. Thelen, C. T. Veldkamp, F. D. Coffman, M. C. Cohen, M. B. Dwinell, M. Thelen, F. C. Peterson, N. Heveker, B. F. Volkman, *Science signaling* **2017**, *10*, eaah5756.

[325] H. Zhou, H.-H. Tai, *Archives of Biochemistry and Biophysics* **2000**, *373*, 211-217.

[326] R. J. Kerschbaumer, M. Rieger, D. Völkel, D. Le Roy, T. Roger, J. Garbaraviciene, W.-H. Boehncke, J. Müllberg, R. M. Hoet, C. R. Wood, G. Antoine, M. Thiele, H. Savidis-Dacho, M. Dockal, H. Ehrlich, T. Calandra, F. Scheiflinger, *Journal of Biological Chemistry* **2012**, *287*, 7446-7455.

[327] G. Rose, A. Geselowitz, G. Lesser, R. Lee, M. Zehfus, *Science* **1985**, *229*, 834-838.

[328] G. B. Bolger, G. S. Baillie, X. Li, M. J. Lynch, P. Herzyk, A. Mohamed, L. H. Mitchell, A. McCahill, C. Hundsrucker, E. Klussmann, D. R. Adams, M. D. Houslay, *Biochemical Journal* **2006**, *398*, 23-36.

[329] R. Volkmer, V. Tapia, C. Landgraf, *FEBS Lett* **2012**, *586*, 2780-2786.

[330] T. Clackson, J. Wells, *Science* **1995**, *267*, 383-386.

[331] A. M. Watkins, M. G. Wuo, P. S. Arora, *Journal of the American Chemical Society* **2015**, *137*, 11622-11630.

[332] D. Migoń, M. Jaśkiewicz, D. Neubauer, M. Bauer, E. Sikorska, E. Kamysz, W. Kamysz, *Probiotics and Antimicrobial Proteins* **2019**, *11*, 1042-1054.

[333] M. S. Smith, E. E. K. Lawrence, W. M. Billings, K. S. Larsen, N. A. Bécar, J. L. Price, *ACS Chemical Biology* **2017**, *12*, 2535-2537.

[334] J. C. Gómez-Tamayo, A. Cordomí, M. Olivella, E. Mayol, D. Fourmy, L. Pardo, *Protein Science* **2016**, *25*, 1517-1524.

[335] H. Drobecq, E. Boll, M. Sénéchal, R. Desmet, J. M. Saliou, J. J. Lacapère, A. Mougel, J. Vicogne, O. Melnyk, *Bioconjugate chemistry* **2016**, *27*, 1540-1546.

[336] C. R. Forbes, S. K. Sinha, H. K. Ganguly, S. Bai, G. P. A. Yap, S. Patel, N. J. Zondlo, *Journal of the American Chemical Society* **2017**, *139*, 1842-1855.

[337] A. Groß, K. Möbius, C. Haußner, N. Donhauser, B. Schmidt, J. Eichler, *Frontiers in immunology* **2013**, *4*, 257-257.

[338] C. Fan, D. Rajasekaran, M. A. Syed, L. Leng, J. P. Loria, V. Bhandari, R. Bucala, E. J. Lolis, *Proceedings of the National Academy of Sciences* **2013**, *110*, 10994-10999.

[339] M. Muraki, H. Morii, K. Harata, *Protein Engineering, Design and Selection* **2000**, *13*, 385-389.

[340] A. Bachmann, D. Wildemann, F. Praetorius, G. Fischer, T. Kiefhaber, *Proceedings of the National Academy of Sciences* **2011**, *108*, 3952-3957.

[341] J. Sanchez, Z. E Huma, J. R. Lane, X. Liu, J. L. Bridgford, R. J. Payne, M. Canals, M. J. Stone, *The Journal of biological chemistry* **2019**, *294*, 3464-3475.

[342] J. M. Harris, R. B. Chess, *Nature Reviews Drug Discovery* **2003**, *2*, 214-221.

[343] R. A. George, J. Heringa, *Protein Engineering, Design and Selection* **2002**, *15*, 871-879.

[344] F. Ditzinger, D. J. Price, A.-R. Ilie, N. J. Köhl, S. Jankovic, G. Tsakiridou, S. Aleandri, L. Kalantzi, R. Holm, A. Nair, C. Saal, B. Griffin, M. Kuentz, *Journal of Pharmacy and Pharmacology* **2019**, *71*, 464-482.

[345] G. R. Grimsley, K. L. Shaw, L. R. Fee, R. W. Alston, B. M. Huyghues-Despointes, R. L. Thurlkill, J. M. Scholtz, C. N. Pace, *Protein Science* **1999**, *8*, 1843-1849.

[346] C. N. Pace, H. Fu, K. Lee Fryar, J. Landua, S. R. Trevino, D. Schell, R. L. Thurlkill, S. Imura, J. M. Scholtz, K. Gajiwala, J. Sevcik, L. Urbanikova, J. K. Myers, K. Takano, E. J. Hebert, B. A. Shirley, G. R. Grimsley, *Protein Science* **2014**, *23*, 652-661.

[347] G. De Baets, J. Van Durme, F. Rousseau, J. Schymkowitz, *Journal of molecular biology* **2014**, *426*, 2405-2412.

[348] J. Warwicker, S. Charonis, R. A. Curtis, *Molecular Pharmaceutics* **2014**, *11*, 294-303.

[349] P. Chan, R. A. Curtis, J. Warwicker, *Scientific Reports* **2013**, *3*, 3333.

[350]   S. Jevševar, M. Kunstelj, V. G. Porekar, *Biotechnology Journal* **2010**, *5*, 113-128.
[351]   P. B. Lawrence, J. L. Price, *Current Opinion in Chemical Biology* **2016**, *34*, 88-94.
[352]   D. Matulis, R. Lovrien, *Biophysical Journal* **1998**, *74*, 422-429.
[353]   O. K. Gasymov, B. J. Glasgow, *Biochimica et biophysica acta* **2007**, *1774*, 403-411.
[354]   C. Ota, S.I. Tanaka, K. Takano, *Molecules (Basel, Switzerland)* **2021**, *26*, 420.
[355]   C. T. Armstrong, P. E. Mason, J. L. R. Anderson, C. E. Dempsey, *Scientific Reports* **2016**, *6*, 21759.
[356]   M. A. Cherry, S. K. Higgins, H. Melroy, H.-S. Lee, A. Pokorny, *The Journal of Physical Chemistry B* **2014**, *118*, 12462-12470.
[357]   O. Keskin, B. Ma, R. Nussinov, *Journal of molecular biology* **2005**, *345*, 1281-1294.
[358]   M. M. Gromiha, S. Ahmad, *Current Computer - Aided Drug Design* **2005**, *1*, 223-235.
[359]   V. P. Reddy Chichili, V. Kumar, J. Sivaraman, *Protein Science* **2013**, *22*, 153-167.
[360]   C. Dealwis, E. J. Fernandez, D. A. Thompson, R. J. Simon, M. A. Siani, E. Lolis, *Proceedings of the National Academy of Sciences of the United States of America* **1998**, *95*, 6941-6946.
[361]   C.-C. Chang, J.-W. Liou, K. T. P. Dass, Y.-T. Li, S.-J. Jiang, S.-F. Pan, Y.-C. Yeh, H.-J. Hsu, *Communications Chemistry* **2020**, *3*, 133.
[362]   M. P. Crump, J. H. Gong, P. Loetscher, K. Rajarathnam, A. Amara, F. Arenzana-Seisdedos, J. L. Virelizier, M. Baggiolini, B. D. Sykes, I. Clark-Lewis, *The EMBO journal* **1997**, *16*, 6996-7007.
[363]   E. W. Smith, Y. Liu, A. E. Getschman, F. C. Peterson, J. J. Ziarek, R. Li, B. F. Volkman, Y. Chen, *Journal of Medicinal Chemistry* **2014**, *57*, 9693-9699.
[364]   E. W. Smith, A. M. Nevins, Z. Qiao, Y. Liu, A. E. Getschman, S. L. Vankayala, M. T. Kemp, F. C. Peterson, R. Li, B. F. Volkman, Y. Chen, *Journal of Medicinal Chemistry* **2016**, *59*, 4342-4351.
[365]   D. Bashford, C. Chothia, A. M. Lesk, *Journal of molecular biology* **1987**, *196*, 199-216.
[366]   C. M. Santiveri, E. León, M. Rico, M. A. Jiménez, *Chemistry – A European Journal* **2008**, *14*, 488-499.
[367]   S. Indu, V. Kochat, S. Thakurela, C. Ramakrishnan, R. Varadarajan, *Proteins* **2011**, *79*, 244-260.
[368]   N. L. Haworth, M. J. Wouters, M. O. Hunter, L. Ma, M. A. Wouters, *Protein Science* **2019**, *28*, 239-256.
[369]   A. M. Almeida, R. Li, S. H. Gellman, *Journal of the American Chemical Society* **2012**, *134*, 75-78.
[370]   H. Lan, H. Liu, Y. Ye, Z. Yin, *AAPS PharmSciTech* **2020**, *21*, 122.
[371]   M. J. Feige, I. Braakman, L. M. Hendershot, in *Oxidative Folding of Proteins: Basic Principles, Cellular Regulation and Engineering*, The Royal Society of Chemistry, **2018**, 1-33.
[372]   A. J. Doig, D. H. Williams, *Journal of molecular biology* **1991**, *217*, 389-398.
[373]   A. Glas, D. Bier, G. Hahne, C. Rademacher, C. Ottmann, T. N. Grossmann, *Angewandte Chemie International Edition* **2014**, *53*, 2489-2493.
[374]   S. Fatima, R. H. Khan, *Journal of biochemistry* **2007**, *142*, 65-72.
[375]   C. A. Rohl, W. Fiori, R. L. Baldwin, *Proceedings of the National Academy of Sciences* **1999**, *96*, 3682-3687.
[376]   J. Wang, J. Chen, J. Li, L. An, Y. Wang, Q. Huang, L. Yao, *Proteins: Structure, Function, and Bioinformatics* **2018**, *86*, 684-692.
[377]   F. El-Turk, B. Fauvet, A. Ashrafi, H. Ouertatani-Sakouhi, M.-K. Cho, M. Neri, M. Cascella, U. Rothlisberger, F. Pojer, M. Zweckstetter, H. Lashuel, *PLOS ONE* **2012**, *7*, e45024.
[378]   R. Kleemann, A. Kapurniotu, R. Mischke, J. Held, J. Bernhagen, *European Journal of Biochemistry* **1999**, *261*, 753-766.
[379]   L.Leng, R. Bucala, *Cell Research, **2006**, 16,* 162–168
[380]   S. Rubin, N. Qvit, *Critical reviews in eukaryotic gene expression* **2016**, *26*, 199-221.
[381]   A. Zorzi, K. Deyle, C. Heinis, *Current Opinion in Chemical Biology* **2017**, *38*, 24-29.
[382]   J. Henninot, J. C. Collins, J. M. Nuss, *Journal of Medicinal Chemistry* **2018**, *61*, 1382-1414.
[383]   X. Chen, J. L. Zaro, W.-C. Shen, *Advanced drug delivery reviews* **2013**, *65*, 1357-1369.
[384]   M. Werle, A. Bernkop-Schnürch, *Amino Acids* **2006**, *30*, 351-367.
[385]   M. Shiota, N. Tokuda, T. Kanou, H. Yamasaki, *Yonsei medical journal* **2007**, *48*, 421-424.
[386]   T. Katsila, E. Balafas, G. Liapakis, P. Limonta, M. Montagnani Marelli, K. Gkountelias, T. Tselios, N. Kostomitsopoulos, J. Matsoukas, C. Tamvakopoulos, *The Journal of pharmacology and experimental therapeutics* **2011**, *336*, 613-623.
[387]   B. J. Evans, A. T. King, A. Katsifis, L. Matesic, J. F. Jamie, *Molecules (Basel, Switzerland)* **2020**, *25*, 2314.
[388]   V. Fuster, B. M. Mearns, *Nature Reviews Cardiology* **2009**, *6*, 669-669.
[389]   G. Riccioni, V. Sblendorio, *Journal of Geriatric Cardiology* **2012**, *9*, 305-317.
[390]   P. H. Jones, R. Nair, K. M. Thakker, *Journal of the American Heart Association* **2012**, *1*, e001800.
[391]   A. Selva-O'Callaghan, M. Alvarado-Cardenas, I. Pinal-Fernández, E. Trallero-Araguás, J. C. Milisenda, M. Á. Martínez, A. Marín, M. Labrador-Horrillo, C. Juárez, J. M. Grau-Junyent, *Expert Review of Clinical Immunology* **2018**, *14*, 215-224.

[392] D. F. Blackburn, R. T. Dobson, J. L. Blackburn, T. W. Wilson, M. R. Stang, W. M. Semchuk, *The Canadian journal of cardiology* **2005**, *21*, 485-488.

[393] R. E. Aubert, J. Yao, F. Xia, S. B. Garavaglia, *The American journal of managed care* **2010**, *16*, 459-466.

[394] D. Preiss, S. R. K. Seshasai, P. Welsh, S. A. Murphy, J. E. Ho, D. D. Waters, D. A. DeMicco, P. Barter, C. P. Cannon, M. S. Sabatine, E. Braunwald, J. J. P. Kastelein, J. A. de Lemos, M. A. Blazing, T. R. Pedersen, M. J. Tikkanen, N. Sattar, K. K. Ray, *Journal of the American Medical Association* **2011**, *305*, 2556-2564.

[395] J. W. Jukema, C. P. Cannon, A. J. de Craen, R. G. Westendorp, S. Trompet, *Journal of the American College of Cardiology* **2012**, *60*, 875-881.

[396] S. Rabar, M. Harker, N. O'Flynn, A. S. Wierzbicki, *The British Medical Journal* **2014**, *349*, g4356.

[397] Expert Dyslipidemia Panel of the International Atherosclerosis Society Panel members, *Journal of clinical lipidology* **2014**, *8*, 29-60.

[398] A. Kashani, T. Sallam, S. Bheemreddy, D. L. Mann, Y. Wang, J. M. Foody, *American Journal of Cardiology* **2008**, *101*, 1606-1613.

[399] M. F. J. Stolk, M. C. J. M. Becx, K. C. Kuypers, C. A. Seldenrijk, *Clinical Gastroenterology and Hepatology* **2006**, *4*, 908-911.

[400] A. Karatasakis, B. A. Danek, J. Karacsonyi, B. V. Rangan, M. K. Roesle, T. Knickelbine, M. D. Miedema, H. Khalili, Z. Ahmad, S. Abdullah, S. Banerjee, E. S. Brilakis, *Journal of the American Heart Association* **2017**, *6*, e006910.

[401] A. F. Schmidt, L. S. Pearce, J. T. Wilkins, J. P. Overington, A. D. Hingorani, J. P. Casas, *Cochrane database of systematic reviews* **2017**, *4*, CD011748-CD011748.

[402] M. Banach, T. Stulc, R. Dent, P. P. Toth, *International journal of cardiology* **2016**, *225*, 184-196.

[403] P. D. Home, S. J. Pocock, H. Beck-Nielsen, P. S. Curtis, R. Gomis, M. Hanefeld, N. P. Jones, M. Komajda, J. J. McMurray, *Lancet (London, England)* **2009**, *373*, 2125-2135.

[404] S. Zoungas, J. Chalmers, B. Neal, L. Billot, Q. Li, Y. Hirakawa, H. Arima, H. Monaghan, R. Joshi, S. Colagiuri, M. E. Cooper, P. Glasziou, D. Grobbee, P. Hamet, S. Harrap, S. Heller, L. Lisheng, G. Mancia, M. Marre, D. R. Matthews, C. E. Mogensen, V. Perkovic, N. Poulter, A. Rodgers, B. Williams, S. MacMahon, A. Patel, M. Woodward, *New England Journal of Medicine* **2014**, *371*, 1392-1406.

[405] The Action to Control Cardiovascular Risk in Diabetes Study Group*, *New England Journal of Medicine* **2008**, *358*, 2545-2559.

[406] S. J. Nicholls, J. J. Kastelein, G. G. Schwartz, D. Bash, R. S. Rosenson, M. A. Cavender, D. M. Brennan, W. Koenig, J. W. Jukema, V. Nambi, R. S. Wright, V. Menon, A. M. Lincoff, S. E. Nissen, *Journal of the American Medical Association* **2014**, *311*, 252-262.

[407] M. L. O'Donoghue, R. Glaser, M. A. Cavender, P. E. Aylward, M. P. Bonaca, A. Budaj, R. Y. Davies, M. Dellborg, K. A. Fox, J. A. Gutierrez, C. Hamm, R. G. Kiss, F. Kovar, J. F. Kuder, K. A. Im, J. J. Lepore, J. L. Lopez-Sendon, T. O. Ophuis, A. Parkhomenko, J. B. Shannon, J. Spinar, J. F. Tanguay, M. Ruda, P. G. Steg, P. Theroux, S. D. Wiviott, I. Laws, M. S. Sabatine, D. A. Morrow, *Journal of the American Medical Association* **2016**, *315*, 1591-1599.

[408] D. L. Mann, J. J. McMurray, M. Packer, K. Swedberg, J. S. Borer, W. S. Colucci, J. Djian, H. Drexler, A. Feldman, L. Kober, H. Krum, P. Liu, M. Nieminen, L. Tavazzi, D. J. van Veldhuisen, A. Waldenstrom, M. Warren, A. Westheim, F. Zannad, T. Fleming, *Circulation* **2004**, *109*, 1594-1602.

[409] E. S. Chung, M. Packer, K. H. Lo, A. A. Fasanmade, J. T. Willerson, *Circulation* **2003**, *107*, 3133-3140.

[410] J.-C. Tardif, S. Kouz, D. D. Waters, O. F. Bertrand, R. Diaz, A. P. Maggioni, F. J. Pinto, R. Ibrahim, H. Gamra, G. S. Kiwan, C. Berry, J. López-Sendón, P. Ostadal, W. Koenig, D. Angoulvant, J. C. Grégoire, M.-A. Lavoie, M.-P. Dubé, D. Rhainds, M. Provencher, L. Blondeau, A. Orfanos, P. L. L'Allier, M.-C. Guertin, F. Roubille, *New England Journal of Medicine* **2019**, *381*, 2497-2505.

[411] S. M. Nidorf, A. T. L. Fiolet, A. Mosterd, J. W. Eikelboom, A. Schut, T. S. J. Opstal, S. H. K. The, X.-F. Xu, M. A. Ireland, T. Lenderink, D. Latchem, P. Hoogslag, A. Jerzewski, P. Nierop, A. Whelan, R. Hendriks, H. Swart, J. Schaap, A. F. M. Kuijper, M. W. J. van Hessen, P. Saklani, I. Tan, A. G. Thompson, A. Morton, C. Judkins, W. A. Bax, M. Dirksen, M. Alings, G. J. Hankey, C. A. Budgeon, J. G. P. Tijssen, J. H. Cornel, P. L. Thompson, *New England Journal of Medicine* **2020**, *383*, 1838-1847.

[412] A. Mullard, *Nature Reviews Drug Discovery* **2018**, *17*, 853-853.

[413] European Medicines Agency, **2018**. https://www.ema.europa.eu/en/documents/withdrawal-report/withdrawal-assessment-report-canakinumab-novartis_en.pdf

[414] W. Clark, P. Jobanputra, P. Barton, A. Burls, *Health technology assessment (Winchester, England)* **2004**, *8*, iii-iv, ix-x, 1-105.

[415] P. V. Tilstam, D. Qi, L. Leng, L. Young, R. Bucala, *Expert Opinion on Therapeutic Targets* **2017**, *21*, 671-683.

[416] S. Babu, B. G. Hightower, J. Chan, N. R. Zürcher, P. Kivisäkk, C.-E. J. Tseng, D. L. Sanders, A. Robichaud, H. Banno, A. Evora, A. Ashokkumar, L. Pothier, S. Paganoni, S. Chew, J. Dojillo, K. Matsuda, M. Gudesblatt, J. D. Berry, M. E. Cudkowicz, J. M. Hooker, N. Atassi, *NeuroImage: Clinical* **2021**, *30*, 102672.

[417] A. Burger-Kentischer, H. Göbel, R. Kleemann, A. Zernecke, R. Bucala, L. Leng, D. Finkelmeier, G. Geiger, H. E. Schaefer, A. Schober, C. Weber, H. Brunner, H. Rütten, C. Ihling, J. Bernhagen, *Atherosclerosis* **2006**, *184*, 28-38.

[418] C. R. Figueiredo, A. L. Matsuo, R. A. Azevedo, M. H. Massaoka, N. Girola, L. Polonelli, L. R. Travassos, *Scientific reports* **2015**, *5*, 14310-14310.

[419] G. Benedek, R. Meza-Romero, K. Jordan, L. Keenlyside, H. Offner, A. A. Vandenbark, *Journal of Neuroinflammation* **2015**, *12*, 123.

[420] C. R. Figueiredo, R. A. Azevedo, S. Mousdell, P. T. Resende-Lara, L. Ireland, A. Santos, N. Girola, R. Cunha, M. C. Schmid, L. Polonelli, L. R. Travassos, A. Mielgo, *Frontiers in Immunology* **2018**, *9*, 1132.

[421] A.-F. Dessein, L. Stechly, N. Jonckheere, P. Dumont, D. Monté, E. Leteurtre, S. Truant, F.-R. Pruvot, M. Figeac, M. Hebbar, C.-H. Lecellier, T. Lesuffleur, R. Dessein, G. Grard, M.-J. Dejonghe, Y. de Launoit, Y. Furuichi, G. Prévost, N. Porchet, C. Gespach, G. Huet, *Cancer Research* **2010**, *70*, 4644-4654.

[422] A. Zhu, W. Zhan, Z. Liang, Y. Yoon, H. Yang, H. E. Grossniklaus, J. Xu, M. Rojas, M. Lockwood, J. P. Snyder, D. C. Liotta, H. Shim, *Journal of Medicinal Chemistry* **2010**, *53*, 8556-8568.

[423] K. Hamesch, P. Subramanian, X. Li, K. Dembowsky, E. Chevalier, C. Weber, A. Schober, *Thrombosis and haemostasis* **2012**, *107*, 356-368.

[424] M. D. Galsky, N. J. Vogelzang, P. Conkling, E. Raddad, J. Polzer, S. Roberson, J. R. Stille, M. Saleh, D. Thornton, *Clinical cancer research : an official journal of the American Association for Cancer Research* **2014**, *20*, 3581-3588.

[425] R. Salgia, J. R. Stille, R. W. Weaver, M. McCleod, O. Hamid, J. Polzer, S. Roberson, A. Flynt, D. R. Spigel, *Lung cancer (Amsterdam, Netherlands)* **2017**, *105*, 7-13.

[426] G. D. Luker, J. Yang, A. Richmond, S. Scala, C. Festuccia, M. Schottelius, H.-J. Wester, J. Zimmermann, *Journal of Leukocyte Biology* **2021**, *109*, 969-989.

[427] P. S. Becker, J. M. Foran, J. K. Altman, A. Yacoub, J. E. Castro, P. Sabbatini, C. Dilea, M. Wade, G. Xing, A. Gutierrez, L. Cohen, B. D. Smith, *Blood* **2014**, *124*, 386-386.

[428] C. Cuesta-Mateos, A. Alcaraz-Serna, B. Somovilla-Crespo, C. Muñoz-Calleja, *Frontiers in Immunology* **2018**, *8*.

[429] L. Alinari, B. Yu, B. A. Christian, F. Yan, J. Shin, R. Lapalombella, E. Hertlein, M. E. Lustberg, C. Quinion, X. Zhang, G. Lozanski, N. Muthusamy, M. Prætorius-Ibba, O. A. O'Connor, D. M. Goldenberg, J. C. Byrd, K. A. Blum, R. A. Baiocchi, *Blood* **2011**, *117*, 4530-4541.

[430] J. L. Kaufman, R. Niesvizky, E. A. Stadtmauer, A. Chanan-Khan, D. Siegel, H. Horne, W. A. Wegener, D. M. Goldenberg, *British Journal of Haematology* **2013**, *163*, 478-486.

[431] P. Martin, R. R. Furman, S. Rutherford, J. Ruan, S. Ely, J. Greenberg, M. Coleman, S. J. Goldsmith, J. P. Leonard, *Leukemia & Lymphoma* **2015**, *56*, 3065-3070.

[432] T. J. Schall, A. E. Proudfoot, *Nature reviews. Immunology* **2011**, *11*, 355-363.

[433] J. L. Lau, M. K. Dunn, *Bioorganic & medicinal chemistry* **2018**, *26*, 2700-2707.

[434] D. J. Craik, D. P. Fairlie, S. Liras, D. Price, *Chemical biology & drug design* **2013**, *81*, 136-147.

[435] R. Horuk, *Nature Reviews Drug Discovery* **2009**, *8*, 23-33.

[436] M. Miao, E. De Clercq, G. Li, *Expert Opinion on Drug Metabolism & Toxicology* **2020**, *16*, 11-30.

[437] L. Fantuzzi, M. Tagliamonte, M. C. Gauzzi, L. Lopalco, *Cellular and Molecular Life Sciences* **2019**, *76*, 4869-4886.

[438] F. Grande, M. A. Occhiuzzi, B. Rizzuti, G. Ioele, M. De Luca, P. Tucci, V. Svicher, S. Aquaro, A. Garofalo, *Molecules (Basel, Switzerland)* **2019**, *24*, 550.

[439] Q. M. Anstee, B. A. Neuschwander-Tetri, V. W. Wong, M. F. Abdelmalek, Z. M. Younossi, J. Yuan, M. L. Pecoraro, S. Seyedkazemi, L. Fischer, P. Bedossa, Z. Goodman, N. Alkhouri, F. Tacke, A. Sanyal, *Contemporary clinical trials* **2020**, *89*, 105922.

[440] A. Moriconi, M. C. Cesta, M. N. Cervellera, A. Aramini, S. Coniglio, S. Colagioia, A. R. Beccari, C. Bizzarri, M. R. Cavicchia, M. Locati, E. Galliera, P. Di Benedetto, P. Vigilante, R. Bertini, M. Allegretti, *Journal of Medicinal Chemistry* **2007**, *50*, 3984-4002.

[441] W. Gonsiorek, X. Fan, D. Hesk, J. Fossetta, H. Qiu, J. Jakway, M. Billah, M. Dwyer, J. Chao, G. Deno, A. Taveras, D. J. Lundell, R. W. Hipkin, *Journal of Pharmacology and Experimental Therapeutics* **2007**, *322*, 477-485.

[442] B. D. Cox, A. R. Prosser, Y. Sun, Z. Li, S. Lee, M. B. Huang, V. C. Bond, J. P. Snyder, M. Krystal, L. J. Wilson, D. C. Liotta, *ACS medicinal chemistry letters* **2015**, *6*, 753-757.

[443] N. V. Ortiz Zacarías, J. P. D. van Veldhoven, L. Portner, E. van Spronsen, S. Ullo, M. Veenhuizen, W. J. C. van der Velden, A. J. M. Zweemer, R. M. Kreekel, K. Oenema, E. B. Lenselink, L. H. Heitman, A. P. Ijzerman, *Journal of Medicinal Chemistry* **2018**, *61*, 9146-9161.

[444] B. D. Quinlan, V. R. Joshi, M. R. Gardner, K. H. Ebrahimi, M. Farzan, *Journal of virology* **2014**, *88*, 3353-3358.

[445] C. Ji, E. Kopetzki, A. Jekle, K. G. Stubenrauch, X. Liu, J. Zhang, E. Rao, T. Schlothauer, S. Fischer, N. Cammack, G. Heilek, S. Ries, S. Sankuratri, *The Journal of biological chemistry* **2009**, *284*, 5175-5185.

[446] B. Zhao, M. K. Mankowski, B. A. Snyder, R. G. Ptak, P. J. Liwang, *The Journal of biological chemistry* **2011**, *286*, 28370-28381.

[447] C. T. Veldkamp, C. Seibert, F. C. Peterson, N. B. De la Cruz, J. C. Haugner, 3rd, H. Basnet, T. P. Sakmar, B. F. Volkman, *Science signaling* **2008**, *1*, ra4-ra4.

[448] A. L. Lazaar, B. E. Miller, A. C. Donald, T. Keeley, C. Ambery, J. Russell, H. Watz, R. Tal-Singer, *Respiratory Research* **2020**, *21*, 149.

[449] A. De Soyza, I. Pavord, J. S. Elborn, D. Smith, H. Wray, M. Puu, B. Larsson, R. Stockley, *The European respiratory journal* **2015**, *46*, 1021-1032.

[450] M. Uddin, C. Betts, I. Robinson, A. Malmgren, C. Humfrey, *Haematologica* **2017**, *102*, e65-e68.

[451] R. B. Moss, S. J. Mistry, M. W. Konstan, J. M. Pilewski, E. Kerem, R. Tal-Singer, A. L. Lazaar, *Journal of cystic fibrosis : official journal of the European Cystic Fibrosis Society* **2013**, *12*, 241-248.

[452] Y. Wu, S. Wang, S. M. Farooq, M. P. Castelvetere, Y. Hou, J.-L. Gao, J. V. Navarro, D. Oupicky, F. Sun, C. Li, *The Journal of biological chemistry* **2012**, *287*, 5744-5755.

[453] M. E. Bradley, B. Dombrecht, J. Manini, J. Willis, D. Vlerick, S. De Taeye, K. Van den Heede, A. Roobrouck, E. Grot, T. C. Kent, T. Laeremans, S. Steffensen, G. Van Heeke, Z. Brown, S. J. Charlton, K. D. Cromie, *Molecular pharmacology* **2015**, *87*, 251-262.

[454] M. J. Alam, L. Xie, C. Ang, F. Fahimi, S. B. Willingham, A. J. Kueh, M. J. Herold, C. R. Mackay, R. Robert, *MAbs* **2020**, *12*, 1856460.

[455] L. Skov, F. J. Beurskens, C. O. C. Zachariae, S. Reitamo, J. Teeling, D. Satijn, K. M. Knudsen, E. P. J. Boot, D. Hudson, O. Baadsgaard, P. W. H. I. Parren, J. G. J. van de Winkel, *The Journal of Immunology* **2008**, *181*, 669-679.

[456] N. Sawyer, A. M. Watkins, P. S. Arora, *Accounts of Chemical Research* **2017**, *50*, 1313-1322.

[457] L. Rajagopalan, K. Rajarathnam, *Journal of Biological Chemistry* **2004**, *279*, 30000-30008.

[458] A. Planagumà, T. Domènech, M. Pont, E. Calama, V. García-González, R. López, M. Aulí, M. López, S. Fonquerna, I. Ramos, J. de Alba, A. Nueda, N. Prats, V. Segarra, M. Miralpeix, M. D. Lehner, *Pulmonary Pharmacology & Therapeutics* **2015**, *34*, 37-45.

[459] C. Haußner, D. Damm, S. Nirschl, A. Rohrhofer, B. Schmidt, J. Eichler, *Chembiochem* **2017**, *18*, 647-653.

[460] J. Meier, K. Kassler, H. Sticht, J. Eichler, *Beilstein The Journal of Organic Chemistry* **2012**, *8*, 1858-1866.

[461] Z. A. Wang, X. Z. Ding, C.-L. Tian, J.-S. Zheng, *RSC Advances* **2016**, *6*, 61599-61609.

[462] A. C. Lee, J. L. Harris, K. K. Khanna, J. H. Hong, *International journal of molecular sciences* **2019**, *20*.

[463] K. Deyle, X.-D. Kong, C. Heinis, *Acc Chem Res* **2017**, *50*, 1866-1874.

[464] A. Luther, M. Urfer, M. Zahn, M. Müller, S.-Y. Wang, M. Mondal, A. Vitale, J.-B. Hartmann, T. Sharpe, F. L. Monte, H. Kocherla, E. Cline, G. Pessi, P. Rath, S. M. Modaresi, P. Chiquet, S. Stiegeler, C. Verbree, T. Remus, M. Schmitt, C. Kolopp, M.-A. Westwood, N. Desjonquères, E. Brabet, S. Hell, K. LePoupon, A. Vermeulen, R. Jaisson, V. Rithié, G. Upert, A. Lederer, P. Zbinden, A. Wach, K. Moehle, K. Zerbe, H. H. Locher, F. Bernardini, G. E. Dale, L. Eberl, B. Wollscheid, S. Hiller, J. A. Robinson, D. Obrecht, *Nature* **2019**, *576*, 452-458.

[465] N. Sawyer, P. S. Arora, *ACS Chemical Biology* **2018**, *13*, 2027-2032.

[466] C. R. Robinson, R. T. Sauer, *Proceedings of the National Academy of Sciences of the United States of America* **1998**, *95*, 5929-5934.

[467] S. Zhang, *Interface Focus* **2017**, *7*, 20170028.

[468] C. J. C. Edwards-Gayle, I. W. Hamley, *Organic & biomolecular chemistry* **2017**, *15*, 5867-5876.

[469] Y. Lee, Y. Chen, N. I. Tarasova, V. Gaponenko, *Nanotechnology* **2011**, *22*, 505101-505101.

[470] S. Lee, T. H. T. Trinh, M. Yoo, J. Shin, H. Lee, J. Kim, E. Hwang, Y.-B. Lim, C. Ryou, *International journal of molecular sciences* **2019**, *20*, 5850.

8. Curriculum vitae

PERSONAL INFORMATION
- Name, Surname: Christos Kontos
- Degree: Chemist, B.Sc., M.Sc., Ph.D. candidate
- Email, Telephone number: kontos@wzw.tum.de, +49 1525 4751956
- Address: Liebigstraße 34, 85354, Freising, Bavaria, Germany

EDUCATION
- Ph.D student (2017 - present): Division of Peptide Biochemistry, TUM School of Life Sciences-Technical University of Munich (TUM), supervisor: Prof. Dr. A. Kapurniotu
- M.Sc. (2013 - 2015): Medicinal Chemistry: Drug Discovery and Design -Departments of Chemistry, Pharmacy and Medicine-University of Patras-Grade: "Excellent" 9.67/10, Master Thesis (2014-2015), supervisor: Assoc. Prof. T. Tselios. Grade: 10/10
- B.Sc. (2009 - 2013): Department of Chemistry – University of Patras-Grade: "Very good" 7.50/10, Diploma Thesis (2012 – 2013), supervisor: Assis. Prof. T. Tselios. Grade: 10/10

WORK EXPERIENCE
- 03/2017 – present: Researcher/ PhD student, Division of Peptide Biochemistry, Technical University of Munich (TUM)
- 06/2016 – 02/2017: Associate researcher, Division of Peptide Biochemistry, Technical University of Munich (TUM)
- 08/2014 - 09/2015: Chemical researcher, Program "GREECE-ISRAEL Collaboration Program: A novel combined approach for the immunotherapy of Multiple Sclerosis" University of Patras
- 10-12/2012: Internship in the context of B.Sc.Thesis at the company ELDRUG S.A.

PUBLICATIONS
1. **Kontos C** *, El Bounkari O *, Krammer C *, et al., Nat. Commun., 2020, doi: 10.1038/s41467-020-19764-z
2. Krammer C, **Kontos C** et al., Chembiochem, 2020, doi: 10.1002/cbic.202000574
3. Sinitski D, Gruner K, Brandhofer M, **Kontos C,** et al., J Biol Chem., 2020, doi: 10.1074/jbc.RA119.009716
4. Sinitski D*, **Kontos C***, Krammer C*, et al., J Thromb Haemost., 2019, doi: 10.1055/s-0039-1677803
5. Lacy M*, **Kontos C***, Brandhofer M*, et al., Sci Rep., 2018, doi: 10.1038/s41598-018-23554-5.
6. **Kontos C**, et al., Anal Biochem., 2017, doi: 10.1016/j.ab.2017.09.016
   * refers to equal first authorship

PATENS, GRANTS AND AWARDS
- Co-inventor in an European Patent application, MIF-binding CXCR4 ectodomain mimics for inflammatory and cardiovascular diseases
- Best Flash talk award in the 15th German Peptide Symposium--Universität Marburg, 04.03.2021
- Travel grant for the 36th European Peptide Symposium (EPS) – 12 International Peptide Symposium (IPS), Sitges (Spain), 28.08-02.09.2022
- Best poster presentation award in the Collaborative Research Programm (CRC) 1123 Atherosclerosis Mechanisms and Networks of Novel Therapeutic Targets Annual Retreat, Oberammergau (Germany), 08-10.10.2018

TUM SEMINARS
- Patents and licencing in Life Sciences (Basic Seminar), 06.02.2020
- Patents in Biology, Chemistry and Biotech (Advanced Seminar), 07.02.2020
- Time Management-Plan your Time Efficiently, 22-23.07.2017

9. Acknowledgements

First of all, I would like to thank my supervisor Prof. Aphrodite Kapurniotu for giving me the opportunity to work on a exciting and challenging topic at the interface of peptide (bio)chemistry and cardiovascular research. I am grateful to her for trusting me with a novel project and giving me enough space, freedom and inspiration to develop as a researcher. I would also like to thank her for her support in various ways, especially in difficult moments, and the keen interest on my progress. It meant a lot to me her effort to motivate, challenge and induce the formation of a multiple comprehensive and objective critique view in a young scientist.

I wish to express my gratitude to another person with significant contribution on the research projects that I worked on, my mentor Prof. Jürgen Bernhagen. I would like to thank him for his guidance and his trust on the projects and me. I am thankfull for his thoughtful comments and recommendations, and for sharing his ideas and knowledge in our meetings. I am grateful for having been a member of the SFB1123 (Atherosclerosis-Mechanisms and Networks of Novel Therapeutic Targets/ Speaker Prof. Christian Weber) and for the support and numerous interactions with the scientists of the SFB1123.

At this point I would like to refer to some colleagues from the past. Particularly, I would like to thank Kathleen Hille for instructing me during the first period in the lab and for her various contributions over these years and Hendrik Wunderlich for the co-operation. Additionally, I thank two former colleagues, Dr. Anna Spanopoulou and Dr. Eleni Malideli for the valuable advises. I also would like to express my thanks to the colleagues Valentina Armiento, Beatrice Dalla Volta, Simon Hornung and Denise Naltsas for our collaboration over these years. Ph.D. is a demanding task and often hides failures, problems and challenges. All obstacles are easier to be overcomed with co-operation, a joke and maybe a bit of philosophy. I am glad that we shared many moments, thoughts, and experiences during this time.

Additionally, I would like to thank the members from the group of Prof. Bernhagen for our collaboration. Particularly, I would like to acknowledge Dr. Omar El Bounkari, Dr. Dzmitry Sinitski and Christine Krammer for their various contributions. Special thanks to Markus Brandhofer for his contribution to MST titrations and organizing the handling of MIF to me and to Simona Gerra for the expression and purification of MIF and related mutants. I would like to thank the Biophysics Core Facility at the School of Biology of LMU Munich and Dr. Sophie Brameyer for flexible access to the MST instrument.

Outside the research related acknowledgement, I feel the need to express my gratitude to my mother for supporting me all these years. She always believed in me, encouraged me and she was willing to help, in any way she could. Special thanks to all my friends that were next to me in the good and the bad moments, independently of the distance. Finally, I would like to acknowledge someone very special to me, who is not anymore with us to see and live that moment, my father. Since I remember myself we were sitting in the same office, studying next to each other and he was always willing to help me. He teached me to insist and follow my dreams and he inspired to overcome obstacles. Without the sacrifices that he did together with my mother to raise me, educate me and offer as many possibilities as they could, I would not have not reached this goal.

10.   Declaration

I, Christos Kontos, declare that I have written this thesis independently, exclusively based on the literature and tools mentioned in the thesis. This document has not previously been submitted for a degree at any other institution than the Technical University of Munich.

Freising, den ....September 2021

Unterschrift

Anhang I

Eidesstattliche Erklärung

Ich erkläre an Eides statt, dass ich die bei der promotionsführenden Einrichtung

School of Life Sciences

der TUM zur Promotionsprüfung vorgelegte Arbeit mit dem Titel:

Design, synthesis, and structure-function studies of peptides as inhibitors of the MIF/chemokine receptor axis

in Technische Universität München (TUM), School of Life Sciences, Professur für Peptidbiochemie

Fakultät, Institut, Lehrstuhl, Klinik, Krankenhaus, Abteilung

unter der Anleitung und Betreuung durch: Prof. Dr. rer. nat. Aphrodite Kapurniotu ohne sonstige Hilfe erstellt und bei der Abfassung nur die gemäß § 6 Ab. 6 und 7 Satz 2 angebotenen Hilfsmittel benutzt habe.

X Ich habe keine Organisation eingeschaltet, die gegen Entgelt Betreuerinnen und Betreuer für die Anfertigung von Dissertationen sucht, oder die mir obliegenden Pflichten hinsichtlich der Prüfungsleistungen für mich ganz oder teilweise erledigt.

X Ich habe die Dissertation in dieser oder ähnlicher Form in keinem anderen Prüfungsverfahren als Prüfungsleistung vorgelegt.

☐ Die vollständige Dissertation wurde in _____ veröffentlicht. Die promotionsführende Einrichtung

_____

hat der Veröffentlichung zugestimmt.

X Ich habe den angestrebten Doktorgrad noch nicht erworben und bin nicht in einem früheren Promotionsverfahren für den angestrebten Doktorgrad endgültig gescheitert.

☐ Ich habe bereits am _____ bei der Fakultät für

_____

der _____ Hochschule

_____

unter Vorlage einer Dissertation mit dem Thema

_____

die Zulassung zur Promotion beantragt mit dem Ergebnis:

_____

Die öffentlich zugängliche Promotionsordnung der TUM ist mir bekannt, insbesondere habe ich die Bedeutung von § 28 (Nichtigkeit der Promotion) und § 29 (Entzug des Doktorgrades) zur Kenntnis genommen. Ich bin mir der Konsequenzen einer falschen Eidesstattlichen Erklärung bewusst.

Mit der Aufnahme meiner personenbezogenen Daten in die Alumni-Datei bei der TUM bin ich

X einverstanden,   ☐ nicht einverstanden.

Freising,

Ort, Datum, Unterschrift

Parts of the results of this thesis were previously published in:

1. **Kontos C** *, El Bounkari O *, Krammer C *, Sinitski D, Hille K, Zan C, Yan G, Wang S, Gao Y, Brandhofer M, Megens R. T. A, Hoffmann A, Pauli J, Asare Y, Gerra S, Bourilhon P, Leng L, Eckstein H.H, Kempf W.E, Pelisek J, Gokce O, Maegdefessel L, Bucala R, Dichgans M, Weber C, Kapurniotu A, Bernhagen J, Nat. Commun., 2020, doi: 10.1038/s41467-020-19764-z
2. Krammer C, **Kontos C,** Dewor M, Hille K, Dalla Volta B, El Bounkari O, Taş K, Sinitski D, Brandhofer M, Megens R. T. A , Weber C, Schultz J. R, Bernhagen J, Kapurniotu A, et al., Chembiochem, 2020, doi: 10.1002/cbic.202000574
3. Lacy M*, **Kontos C***, Brandhofer M*, Hille K, Groening S, Sinitski D, Bourilhon P, Rosenberg E, Krammer C, Thavayogarajah T, Pantouris G, Bakou M, Weber C, Lolis E, Bernhagen J, Kapurniotu A, Sci Rep., 2018, doi: 10.1038/s41598-018-23554-5.